Imperial College London

Department of Earth Science and Engineering

Fuel Cell Hybrid Electric Vehicle Powertrain Modelling and Testing

PhD Thesis

Billy Wu

Mechanical Engineering, Masters with Honours (MEng Hons)
Imperial College London (2010)

Supervisors:

Dr. Gregory J. Offer — Mechanical Engineering
Professor Ricardo Martinez-Botas — Mechanical Engineering
Professor Nigel P. Brandon — Energy Futures Lab
Mr. Hitoshi Igarashi — Nissan Motor Company

February 28, 2014

"Science is not a means of obtaining absolute truth. The real test of a scientific theory is not whether it is 'true' but whether it works"

Niels Bohr

I hereby declare that this thesis and the work presented herein is my own work except where appropriately referenced or acknowledged.

Billy Wu

The copyright of this thesis rests with the author and is made available under a Creative Commons Attribution-Non Commercial-No Derivatives license. Researchers are free to copy, distribute or transmit the thesis on the condition that they attribute it, that they do not use it for commercial purposes and that they do not alter, transform or build upon it. For any reuse or distribution, researchers must make clear to others the license terms of this work.

Abstract

In order to meet the 2050 targets of an 80% reduction in greenhouse gas emissions, electrification of transport is required. Of the zero-emission technologies relating to automotive applications hydrogen fuel cells, lithium-ion batteries and supercapacitors have received the greatest attention.

This thesis presents work on the development and implementation of lithium-ion battery, proton exchange membrane fuel cell and supercapacitor models with the aim of developing the tools and techniques required in assessing their feasibility in automotive applications. Experimental validation of each of these devices is provided with insight given into the physical performance limitations of each device. Analysis is then presented on overall powertrain configurations with a focus on the performance of passive hybridisation as a means of reducing the cost of a vehicle powertrain whilst retaining the advantages of hybridisation.

Four main chapters of content relating to work on: lithium-ion batteries, proton exchange membrane fuel cell, supercapacitors and vehicle system level analysis is presented with distinct conclusions and novel work presented in each chapter.

Lithium-ion batteries

The mathematical framework on the development of a psuedo 2D thermally-coupled electrochemical battery model is presented. This was parameterised using a genetic algorithm based technique against pulsed discharge test data for a 4.8 Ah lithium-polymer cell. This physics-based model was used to develop a means of tracking stoichiometric drift of battery electrodes using a simulated slow rate cyclic voltammetry technique as well as the development of a novel differential thermal voltammetry technique for the extraction of the same information as slow rate cyclic voltammetry but at a much faster rate. The differential voltammetry technique was then used to infer stoichiometric drift in a battery.

The lithium-ion battery model was also used to investigate the scale up effects from single cell to large automotive scale packs. It was found that interconnect resistances in highly parallel packs can cause significant load inhomogeneities due to the increased overpotential caused by the interconnects which can be on the same order as the battery impedance. Cells near to the pack load points were found to experience the highest loads, with highly transient load conditions amplifying the effect.

Proton exchange membrane fuel cells

The mathematical framework for the development of a proton exchange membrane fuel cell model which accounted for transient thermal, mass balance and water management effects and the associated balance-of-plant system was presented. This was validated against experimental data from an in-house developed 9.5 kW 75 cell fuel cell system.

Inhomogeneities in the reactant delivery, and thus performance of cells, in large automotive stacks were investigated with a focus on localised flooding leading to failure through pin-hole formation. It was shown that low pressure systems suffer from the increased risk of flooding, with location of the cell relative to the inlet/ outlets of the reactants being a critical parameter. Flooding was then shown to lead to catastrophic failure of the fuel cell stack through pin-hole formation which lead to a cascading potential instability and decay due to the bipolar coupling of the cells and anode side hydrogen cross over, respectively.

Supercapacitors

A transmission line based supercapacitor model is presented which accounts for the charge redistribution effect caused by slow diffusion of ions in the porous electrodes of supercapacitors. This was experimentally validated against test data for a 150 F and 1500 F supercapacitor. Limitations in terms of high frequency operation are discussed and identified the knee frequency of supercapacitors as being the rate limiting step for their application in highly transient load cycles. A novel method for estimating the low frequency capacitance of supercapacitors based on the complex capacitance is also presented.

Powertrain comparison

Using the developed models of lithium-ion batteries, proton exchange membrane fuel cells and supercapacitors which captures the relevant effects of interest in electric vehicle applications, an analysis of different fuel cell hybrid powertrains is presented.

Analysis of vehicle drive cycles, identified four main load cycle types to be analysed: city, urban, highway and aggressive driving. Through a Reynold's decomposition style analysis, vehicle independent parameters were identified in categorising the vehicle load cycles relative to the power requirements of the load cycle.

Analysis of the different electric vehicle powertrain configurations showed that the 10 year total cost of ownership, assuming an annual mileage of 20,000 km, favoured different powertrains for different load cycles. City driving favoured BEVs whilst highway driving favoured pure fuel cell vehicles with a range of greater than 200 km. The fuel cell-battery active hybrid system under a charge sustaining operation mode was found to have the most benefit in city/ urban driving due to the reduction of transient and idling losses on the fuel cell. Under highway driving conditions, both fuel cell-battery and fuel cell-supercapacitor hybrids showed reduced ranges due to the near steady state operation mode of the fuel cell and the relative inactivity of the secondary energy storage device.

Investigation of the performance of fuel cell-supercapacitor passive hybrid system was also conducted with the construction of a scaled down and large scale demonstrator. The fuel cell-supercapacitor passive hybrid system was experimentally shown to be able to passively smooth loads on the fuel cell without the need for a DCDC converter. It was shown that to maximise the load buffering benefit of the supercapacitors on the fuel cell, the minimum number of supercapacitors in series to match the voltage of the fuel cell is required, due to a reduction in the capacitance with increasing cells in series. The development of a 9.5 kW fuel cell-supercapacitor passive hybrid system is also presented as a proof-of-concept for the passive hybrid system and showed fuel efficiency gains in the region of 5% compared to pure fuel cell mode.

Acknowledgements

First and foremost, I would like to extend my deepest gratitude to my main supervisor Dr. Greg Offer, who I've had the pleasure of working with for 5 years now. Since the days of supervising my undergraduate projects to the conclusion of my PhD, Greg has provided me with the support needed to complete my PhD as well as constantly reminding me of my 'Research Question'. I would also like to thank my other supervisors Professor Nigel Brandon, Professor Ricardo Martinez-Botas and Hitoshi Igarashi. Nigel, Ricardo and Igarashi-san have been extremely supportive of my works over the years and given me every opportunity to succeed. Igarashi-san was the one who helped me get the funding required to continue my studies which I am eternally grateful for.

I would also like to extend my thanks for Dr. Vladimir Yufit and Dr. Fred Marquis. Over the years, Vlad has acted in almost an unofficial supervisor role giving me support and advice (both constructive and destructive). Fred has always supported my work and I'm extremely thankful for the opportunities he's provided me with to teach in the department. The group dynamics in the office is another thing that has made the last 3 years of my studies so eventful and I would like to thank all the past and present members of our research family, with special mention to our current PhDs/post-docs: Farid, Monica, Khalil, Michael, Vladislavs, Marina, Harini and Chris.

Over the 3 years, I've also had the pleasure of working very closely with the undergraduate students who are part of the Racing Green project. I'm extremely thankful for the opportunity given to me by Fred and Greg to help supervise the Fuel Cell division, which over the years has evolved into something quite spectacular and the legacy will live long into the future. Whilst, I don't have room here to mention all 33 of you, it was a pleasure to have worked with every student, with special mentions to Jignesh, Monte, Paul, Sven, Felix, Chris and Yannic whose efforts have helped me in this PhD. Jignesh who helped with the fuel cell model, Monte with the supercapacitor model, Paul with the reduced order battery model, Sven, Chris and Felix with the fuel cell rig construction and Yannic with the HAMSTER cage rig.

I'd also like to thank all my friends outside of Imperial who have helped me to keep my sanity. The years of fun and laugher have definitely made this period much more eventful and special thanks have to go to Olivia and Fiona, who have always been there to support me through our various adventures (good and bad).

And last but by all means not least, I would like to thank the support of my parents and family. It's thanks to them that I was able to come to university in the first place and they were very supportive of my choice of staying in academia.

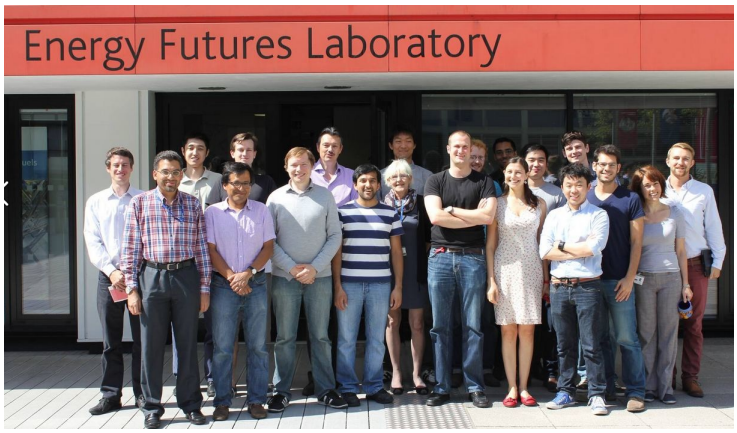


Figure 1: 2013 Fuel Cell and battery research group in front of the Energy Futures Lab

Dissemination

Patents

Billy Wu, Vladimir Yufit, Gregory J. Offer and Nigel P. Brandon. **Segmented fuel cell-battery passive hybrid system**. Submitted 7th June 2013. Imperial Innovations. Reference P56413GB/RGH

Vladimir Yufit, Billy Wu, Farid Tariq and Nigel P. Brandon. **Electrochemical energy storage using a liquid redox couple combined with a solid insertion electrode**. Imperial Innovations. In preparation.

Journal articles

Vladimir Yufit, Farid Tariq, David Eastwood, Billy Wu, Peter D. Lee and Nigel P. Brandon. **In-operandi imaging of dendrite growth during charging in metal-air batteries**. *Advanced Functional Materials*. In preparation.

Billy Wu, Vladimir Yufit, Yu Merla, Monica Marinescu, Ricardo F. Martinez-Botas, Gregory J. Offer and Nigel P. Brandon. **Simulated cyclic voltammetry and novel thermal voltammetry techniques for in-situ monitoring of stoichiometric drift in lithium-ion batteries**. *The Journal of the Electrochemical Society*. In preparation.

Billy Wu, Yu Merla, Vladimir Yufit, Ricardo F. Martinez-Botas, Gregory J. Offer and Nigel P. Brandon. **Segmented fuel cell-battery passive hybrid system**. *Journal of Power Sources*. In preparation.

Billy Wu, Michael A. Parkes, Luca De Benedetti, Vladimir Yufit, Ricardo F. Martinez-Botas, Andrew J. Marquis, Gregory J. Offer and Nigel P. Brandon. **Effect of flooding in PEMFC stacks leading to pin-hole formation**. *International Journal of Hydrogen Energy*. In preparation.

Michael A. Parkes, Thomas Chen, Billy Wu, Vladimir Yufit, Farid Tariq and Gregory J. Offer. **"Can" you make a battery out of that?**. *International Journal of Chemical Education*. In preparation.

Billy Wu, Michael A. Parkes, Luca De Benedetti, Sven Veismann, Christian Wirching, Felix Vesper, Vladimir Yufit, Ricardo F. Martinez-Botas, Andrew J. Marquis, Gregory J. Offer and Nigel P. Brandon. **Design and testing of a 9.5 kWe PEMFC-supercapacitor hybrid system**. *International Journal of Hydrogen Energy*. Submitted.

Yannic Troxler, Billy Wu, Vladimir Yufit, Monica Marinescu, Yatish Patel, Andrew Marquis, Nigel P. Brandon and Gregory J. Offer [202]. **The effect of thermal gradients on the performance of Lithium-ion batteries**. *Journal of Power Sources*. DOI: 10.1016/j.jpowsour.2013.06.084. 2013.

Billy Wu, Vladimir Yufit, Monica Marinescu, Gregory J. Offer, Ricardo F. Martinez-Botas and Nigel P. Brandon [224]. **Coupled thermal-electrochemical modelling of uneven heat generation in lithium-ion battery packs**. *Journal of Power Sources*. DOI: 10.1016/j.jpowsour.2013.05.164. 2013.

Gregory J. Offer, Vladimir Yufit, David A. Howey, Billy Wu and Nigel P. Brandon [150]. **Module design and fault diagnosis in electric vehicle batteries**. *Journal of Power Sources*. DOI: 10.1016/j.jpowsour.2012.01.087. 2012.

Billy Wu, Mardit Matian and Gregory J. Offer [222] **Hydrogen PEMFC system for automotive applications**. *International Journal of Low-Carbon Technologies*. DOI: 10.1093/ijlct/ctr026. 2011.

Conference papers

Billy Wu, Vladimir Yufit, John Campbell, Gregory J. Offer, Ricardo F. Martinez-Botas and Nigel P. Brandon. **Simulated and experimental validation of a fuel cell-supercapacitor passive hybrid system for electric vehicles**. *HEVC 2013, London, UK.* 2013.

Monica Marinescu, Billy Wu, Marie-Therese von Srbik, Gregory J. Offer and Nigel P. Brandon. **Modelling thermal gradients in lithium-ion cells and packs**. *HEVC 2013, London, UK.* 2013.

Billy Wu, Gregory J. Offer, Vladimir Yufit, David A. Howey and Nigel P. Brandon. **Fault analysis in battery module design for electric and hybrid vehicles**. *Power Electronics, Machines and Drives Conference, Bristol, UK.* 2012.

Conference presentations

Fuel cell-supercapacitor hybrid systems for automotive applications. Billy Wu, Vladimir Yufit, John Campbell, Gregory J. Offer, Ricardo F. Martinez-Botas and Nigel P. Brandon *HEVC 2013, London, UK.* 2013.

Modelling and measurement of uneven heat generation in lithium-ion battery packs. Billy Wu, Vladimir Yufit, Monica Marinescu, David A. Howey, Gregory J. Offer, Ricardo F. Martinez-Botas and Nigel P. Brandon *ModVal 10, Bad Boll, Germany.* 2013.

Fault analysis in battery module design for electric and hybrid vehicles. Billy Wu, Gregory J. Offer, Vladimir Yufit, David A. Howey and Nigel P. Brandon. *Power Electronics, Machines and Drives, Bristol University.* 2012.

Posters

Billy Wu, Vladimir Yufit, David A. Howey, Monica Marinescu, Ricardo F. Martinez-Botas, Gregory J. Offer and Nigel P. Brandon **Lithium-ion batteries: Hot or Not? Fault analysis and uneven heat generation in lithium-ion battery packs**. *1st Catapult conference: Energy Storage Technologies, Coventry, UK.* 2013.

Vladimir Yufit, David Howey, Paul Mitcheson, Billy Wu, Gregory J. Offer and Nigel P. Brandon **On-line battery condition monitoring using a low-cost fast electrochemical impedance spectroscopy for automotive applications**. *Electrochemical Impedance Spectroscopy Conference, Okinawa, Japan.* 2013.

Billy Wu, Vladimir Yufit, Monica Marinescu, David A. Howey, Gregory J. Offer, Ricardo F. Martinez-Botas and Nigel P. Brandon **Fault analysis and uneven heat generation in lithium-ion battery packs**. *Vehicle Electrical Systems Integration conference, Warwick University, UK.* 2013.

Billy Wu, Vladimir Yufit, Monica Marinescu, Gregory J. Offer, Ricardo F. Martinez-Botas and Nigel P. Brandon. **Thermal-Electrochemical Modelling and Testing of Lithium-ion Battery Packs for Electric Vehicles**. *International Meeting on Lithium-ion Batteries, Jeju island, South Korea.* 2012.

Billy Wu, Mardit Matian, Gregory J. Offer, Tanya Chong, Nicholas Lee, Ryan Williams, Ashwin Suguna-Balan, Robert Bilinski, Nicholas Higginson, Charles Hudson, Rebecca Nelson,Michael Squire, Alexander Kaldonek, Christoph Mazur, Andrew J. Marquis, Ricardo F. Martinez-Botas and Nigel P. Brandon. **Designing, building and testing a novel low cost proton exchange membrane fuel cell balance of plant system for automotive applications under urban duty cycles**. *Generating the hydrogen and fuel cell society, University of Birmingham, UK.* 2010.

Contents

1 Introduction **1**
- 1.1 Why do we need electric vehicles? . . . 1
- 1.2 Objective of thesis and research questions . . . 2
- 1.3 Hypothesis . . . 4
- 1.4 Thesis structure . . . 4
- 1.5 Deliverables to industrial sponsors . . . 6

2 Literature research **7**
- 2.1 Electrochemical techniques and other analysis tools . . . 7
  - 2.1.1 Electrochemical Impedance Spectroscopy . . . 8
  - 2.1.2 Cyclic voltammetry . . . 12
- 2.2 Lithium-ion batteries . . . 13
  - 2.2.1 Lithium-battery technologies . . . 14
  - 2.2.2 Battery degradation . . . 16
  - 2.2.3 Modelling of lithium-ion batteries . . . 21
  - 2.2.4 Modelling of lithium-ion battery packs . . . 24
  - 2.2.5 Thermal management . . . 26
  - 2.2.6 Summary of lithium-ion battery literature review . . . 26
- 2.3 Proton Exchange Membrane Fuel Cells . . . 27
  - 2.3.1 Fuel cell modelling . . . 30
  - 2.3.2 Water management . . . 33
  - 2.3.3 Studies on larger systems . . . 36
  - 2.3.4 Fuel cell degradation . . . 38
  - 2.3.5 Cost . . . 43
  - 2.3.6 Summary of Proton Exchange Membrane Fuel Cell literature review 44
- 2.4 Supercapacitors . . . 45
  - 2.4.1 Impedance response . . . 47
  - 2.4.2 Charge redistribution effects . . . 47
  - 2.4.3 Voltage dependent behaviour . . . 49
  - 2.4.4 Frequency dependent behaviour . . . 49
  - 2.4.5 Thermal characteristics of supercapacitors . . . 51
  - 2.4.6 Modelling of supercapacitors . . . 52
  - 2.4.7 Supercapacitor degradation . . . 55
  - 2.4.8 Summary of supercapacitor literature review . . . 56
- 2.5 Powertrain comparison . . . 57
  - 2.5.1 Drive cycles . . . 57
  - 2.5.2 Battery electric vehicles . . . 60
  - 2.5.3 Fuel cell vehicles . . . 60
  - 2.5.4 Fuel cell hybrid vehicles . . . 61
  - 2.5.5 Total Cost of Ownership . . . 64
  - 2.5.6 Summary of powertrain comparison literature review . . . 66
- 2.6 Summary of literature review and motivation for work . . . 67
  - 2.6.1 Lithium-ion batteries . . . 67

2.6.2 Proton Exchange Membrane Fuel Cells . . . 67
2.6.3 Supercapacitors . . . 68
2.6.4 Powertrain comparison . . . 68

3 Lithium-ion batteries 69
3.1 Introduction: Lithium-ion batteries . . . 69
3.2 Battery model equations . . . 70
3.2.1 Lithium in the electrolyte phase . . . 72
3.2.2 Lithium in the solid phase . . . 73
3.2.3 Charge in the electrolyte phase . . . 74
3.2.4 Charge in the solid phase . . . 75
3.2.5 Reaction current density . . . 76
3.2.6 Thermodynamic electrode potential . . . 76
3.2.7 Battery thermal model . . . 77
3.2.8 Degradation model . . . 79
3.2.9 Iterative solution routine . . . 80
3.2.10 Convergence analysis . . . 81
3.3 Model reduction - The Single Particle Model . . . 83
3.3.1 Governing equations . . . 83
3.3.2 Thermal model . . . 84
3.4 Experimental set-up . . . 85
3.4.1 Thermal measurements . . . 86
3.5 Experimental results . . . 87
3.5.1 Cell capacity . . . 87
3.5.2 Electrochemical Impedance Spectroscopy . . . 88
3.5.3 Slow Rate Cyclic Voltammetry . . . 93
3.6 Model parameterisation . . . 95
3.6.1 Optimisation methods . . . 95
3.6.2 Electrode thickness . . . 98
3.6.3 Open Circuit Potential . . . 98
3.6.4 Diffusion and charge transfer coefficients . . . 99
3.6.5 Entropy . . . 100
3.7 Comparison between test and modelled data . . . 102
3.7.1 Load cycles . . . 102
3.7.2 Model based investigation of battery performance . . . 104
3.7.3 Model based battery design . . . 106
3.7.4 Degradation . . . 109
3.7.5 Stoichiometric drift . . . 112
3.7.6 Battery pack design . . . 117
3.8 Conclusion . . . 124
3.8.1 Model development and parameterisation . . . 124
3.8.2 Model based performance analysis . . . 124
3.8.3 Novel in-situ diagnosis techniques . . . 125
3.8.4 Pack level analysis . . . 125

4 Proton Exchange Membrane Fuel Cells 126
4.1 Introduction . . . 126
4.2 Fuel cell modelling . . . 127
4.2.1 Operating voltage . . . 127
4.2.2 Saturated partial pressure . . . 133
4.2.3 Mass balances . . . 134
4.2.4 Membrane hydration model . . . 137
4.2.5 Fuel cell thermal modelling . . . 139
4.3 Balance of Plant modelling . . . 141

4.3.1 Compressor modelling . . . 141
4.3.2 Blower modelling . . . 146
4.3.3 Manifold dynamics . . . 147
4.3.4 Cooling system . . . 149
4.4 Experimental set-up: Fuel cell system construction . . . 152
4.4.1 Fuel Cell control . . . 154
4.5 Model implementation and parameterisation . . . 158
4.6 Transient response of the fuel cell . . . 160
4.7 Comparison of models . . . 161
4.8 Fuel cell start-up . . . 162
4.9 Thermal management . . . 164
4.10 Water management . . . 165
4.11 Stack failure through flooding and pin-hole formation . . . 166
4.12 Stack shut-down . . . 169
4.13 Conclusion . . . 170
4.13.1 Fuel cell modelling . . . 170
4.13.2 Development of 9.5 kWe PEMFC system . . . 170
4.13.3 Fuel cell failure through pin-hole formation . . . 171

5 Electrochemical Double Layer Capacitors 172
5.1 Introduction: Electrochemical Double Layer Capacitors . . . 172
5.2 Supercapacitor modelling . . . 172
5.3 Experimental set-up . . . 173
5.3.1 EIS measurements . . . 174
5.3.2 1500 F supercapacitor . . . 176
5.3.3 150F supercapacitor . . . 178
5.3.4 Comparison between small and large cell . . . 179
5.3.5 Constant current tests . . . 181
5.4 Model parameterisation . . . 181
5.5 Conclusion . . . 182

6 Powertrain comparison 184
6.1 Introduction . . . 184
6.2 Vehicle modelling . . . 185
6.2.1 Equations of motion for the vehicle . . . 185
6.3 Electric motors . . . 186
6.4 Drive cycle analysis . . . 188
6.4.1 Drive cycle decomposition . . . 191
6.5 Development of a scaled down powertrain simulator . . . 194
6.6 Total Cost of Ownership . . . 196
6.6.1 Battery costs . . . 196
6.6.2 Fuel cell costs . . . 197
6.6.3 Supercapacitor costs . . . 197
6.7 Powertrain comparison . . . 198
6.7.1 Pure battery electric vehicle . . . 199
6.7.2 Pure fuel cell vehicle . . . 201
6.7.3 Fuel cell-battery active hybrid . . . 203
6.7.4 Fuel cell-supercapacitor active hybrid . . . 206
6.7.5 Passive hybrid system . . . 208
6.7.6 Fuel cell-supercapacitor passive hybrid . . . 209
6.7.7 Large scale fuel cell-supercapacitor passive hybrid system . . . 212
6.7.8 FC-supercapacitor passive system test . . . 215
6.7.9 Estimating buffering effect of the supercapacitors . . . 219
6.7.10 Direct comparison of fuel cell hybrid powertrains . . . 222

6.8 Conclusion 223
6.8.1 Drive cycle analysis 223
6.8.2 Powertrain comparison 224

7 Conclusions **225**
7.1 Future Work 228

List of Figures

1 2013 Fuel Cell and battery research group in front of the Energy Futures Lab . . v

1.1 UK domestic transport GHG emissions in 2007 excluding travel across borders [97] 1
1.2 European passenger car tailpipe CO_2 trajectories (limits are shown for a typical 4-seater C-class vehicle e.g. VW Golf) [97] 2
1.3 Ragone plot showing the energy and power density of PEMFCs, lithium-ion batteries and supercapacitors 3
1.4 Overview of structure of PhD project 5

2.1 Characteristic time scales for different processes occurring in batteries, supercapacitors, fuel cells and electric vehicles. Shaded boxes represent irreversible processes and bolded items represent captured processes in the subsequent works 7
2.2 (a) Relationship between current and overpotential for typical electrochemical systems described by the Butler-Volmer equation and (b) Current oscillation showing resulting voltage magnitude difference and phase shift 8
2.3 Simulated EIS curves (a) a series resistance with a parallel resistance and capacitance with the parallel resistance being varied (b) CPE with constant of 100 over a 0.01-10,000 Hz range, R_3 varied, (d) Short terminus Warburg impedance coefficient T variation 11
2.4 (a) Cyclic potential sweep and (b) resulting cyclic voltammogram. Adapted from Bard and Faulkner [16] 12
2.5 Structure of a lithium-ion battery, showing the cell-scale and particle-scale structures [47] 13
2.6 (A) cyclic voltammetry profiles of a lithium-ion battery components: anode and cathode (green), electrolyte (blue). Counter electrode: Super P carbon; electrolyte EC-DMC, $LiPF_6$. (B) Voltage operation ranges of the $C/LiCoO_2$ electrode combination in comparison with the stability domain of most common liquid electrolytes [184] 18
2.7 (a) Composition of solid electrolyte layer adapted from [157] and (b) A schematic illustration of surface films on graphite electrodes upon prolonged cycling [12] . . 19
2.8 Cause and effects of cathode degradation. Adapted from Vetter *et al.* [207] . . . 20
2.9 Effects of operating a lithium-ion battery outside of the prescribed limits. Adapted from Electropedia [70] 21
2.10 Example of an equivalent circuit model. Adapted from Chen *et al.* [42] 21
2.11 The profiles of potentials on a 3 cell series pack at the end of a 1C and 3C discharge process [91] 25
2.12 Cross-section of PEMFC. Adapted from [112] 27
2.13 (a) CAD drawing of a PEMFC cell and (b) exploded drawing showing typical components 29
2.14 History of modelling studies [241] 30
2.15 Modes of water transport within a fuel cell MEA. Adapted from Larminie and Dicks [115] 33

2.16 Polarisation curves of a PEMFC illustrating the effect of water flooding on cell performance [120] 34
2.17 Cell voltage and cathode side pressure drop measured under various air stoichiometric ratios (symbolized by ξ in the figure) in a 14 cm^2 fuel cell for 0.2 $A.cm^{-2}$, 150 kPa and 80°C wiht the dew point of both H_2 and air at 70°C [213] 35
2.18 (a) Effect of the anode RH on the oscillation behaviour, anode RH of:72% (triangles), 100% (circles) and 137% (diamonds). (b) Effect of the anode flow on the oscillations. Anode flow values: 209 mL/min (triangles), 450 mL/min (diamonds), potentiostatic mode. [177] 36
2.19 Current density distribution measurements at galvanostatic mode with fully humidified MEA at 80°C [125]. Lower current densities in the inlet (top right) suggest higher resistance due to poor humidification resulting in higher current densities at the outet (bottom left) 37
2.20 (a) Simplified diagram of two cell stack with independent media supplies and location of local current density measurements at the stack periphery and (b) 1+2-cell stack showing the changes in cell voltage of the anomalous cell 1 and coupling cells 2 and 3 as a function of the air stoichiometry in the anomalous cell 1 37
2.21 The effect of potential on carbon corrosion rate versus time over commercial conventional-carbon supported MEAs measured at 80°C and 80% relative humidity. The working electrode was fed with N_2 ($50cm^3min^{-1}$), while the counter/reference electrode was purged with H_2 [31] 40
2.22 a PEMFC under start-up/ shut-down conditions showing how the air/hydrogen front causes ORR oxygen reduction reaction, COR carbon oxidation reaction, OER oxygen evolution reaction and HOR hydrogen oxidation reaction 41
2.23 Internal currents and open circuit potentials as a function of time for two different hydrogen inlet flows and for anode initially filled with air or nitrogen. T=22°C. Saturated air and hydrogen at the cathode and anode [131] 42
2.24 Current density distribution measured on a MEA with a pinhole for (a) open circuit conditions and (b) under load (approximately 100 mA/cm^2) [125] 42
2.25 FC cost breakdown [214] 43
2.26 FC system cost sensitivity analysis. Here red represents low values and black high values of the respective parameter. Adapted from Marcinkoski *et al.* [132] . 43
2.27 (a) Diagram showing the structure of a supercapacitor [181] and (b) figure of potential profile across a supercpacitor 45
2.28 Illustration of the basic components and design of an EDLC. Arrows indicate the direction of movement for the cations and anions [102] 46
2.29 Illustration of the electric double layer structure near a planar electrode [57] . . 46
2.30 Bode plot of the absolute impedance of a typical supercapacitor [164] 47
2.31 (a) Schematic of the charge redistribution effect showing ionic diffusion within a supercapacitor pore. Adapted from Kowal *et al.* [109] and (b) cell potential after constant current charging and then variable constant voltage charging of a Spectracarb 2225 in 1 M H_2SO_4 [21] 48
2.32 Voltage and temperature dependency of different parameters for a 2600 F supercapacitor [28] 50
2.33 (a) Schematic of AC signal penetration inside a porous electrode [192] and (b) Nyquist plot of an electrical double layer capacitor [18] 50
2.34 (a) Bode plots of differential capacitance and (b) real impedances at different cell voltages for a 3000 F supercapacitor [164] 51
2.35 (a) Numerically predicted temperature changes as a function of time for cases starting with either a charging step or a discharge step and predicted temperature change change as a function of time for individual heat generation terms where $q_{E,j}$, $q_{E,d}$, $q_{E,s}$ and $q_{S,c}$ represent the ohmic heating, ion diffusion, steric effects and mixing heats [57] 52

2.36 The numerical solutions to the PNP and MPNP systems. The dimensionless charging voltage is ν=10, which corresponds to approximately 0.25 V at room temperature. The very large values of ϵ=0.1 and ν=0.25 are chosen deliberately for illustration. The dimensionless bulk concentration field c is shown in (a), and the dimensionless charge density ρ in (b) [105] 53
2.37 An idealized model of cylindrical pore and distributed capacitance within a pore. [18] 54
2.38 Equivalent circuit model of a supercapacitor [114] 54
2.39 Model parameters changes at 65°C for different voltage [69] 55
2.40 Illustration of the dispersion of pore size and the consequences on ageing [68] . . 56
2.41 Variability of the driving conditions and positioning of the 12 centres of the classes amongst a sample of observations [8] 57
2.42 Variability of the trips and positioning of the centres of the trip classes obtained by cluster analysis [8] 58
2.43 (a) Sankey diagram of a FC system for bus applications [180] and (b) Sankey diagram for FC-battery hybrid system for typical drive cycle Bubna *et al.* [29] . 61
2.44 (a) Diagram of fuel cell-supercapacitor powertrain layout and (b) powertrain causaility flow chart of the model presented by Rodatz *et al.* [173] 62
2.45 Effect of degree of hybridization on fuel economy for city cycle [106] 63
2.46 Power available from the FC and battery in the passive hybrid architecture [20] . 64
2.47 (a) Currents and BUS voltage of triple passive hybrid system and (b) comparison of energy storage systems and PEMFC power distribution during a 300A current peak on different supercapacitor sizes [103] 65
2.48 Predicted cost of a (a) BEV and (b) a FC system for a C/D segment vehicle [135] 65
2.49 Predicted cost of hydrogen delivered at the pump without taxes/excises. Adapted from McKinsey & Company [135] 66

3.1 Schematic of 1D (x-diection) electrochemical cell model with coupled 1D microscopic (r-direction) solid diffusion mode [224] 70
3.2 Solution flow charge for battery code [224] 72
3.3 Convergence of the reaction current density at the start of the simulation for a discharge 81
3.4 Convergence of final cell voltage with absolute error for a simulated 6 Ah cell discharge for 10 s from 60% SOC at a current of 200 A with a 48 node discretization in the x plane and 24 node discretization in the r plane for each node 81
3.5 Convergence analysis of the number of spatial nodes in the x-direction (a) and r-direction (b) for a 10s discharge under 200 A from 60% SOC 82
3.6 Schematic of single particle model 83
3.7 Diagram of experimental set-up used for testing lithium-ion batteries (a) and example EIS measurement taken on a 4.8 Ah Kokam lithium polymer cell with and without isolation of contact resistances at 3.8 V 85
3.8 Diagram of experimental set-up used during SRCV tests and cycling tests 86
3.9 (a) Diagram of thermal test rig, (b) base plate assembly holder and (c) cross section of heating element arrangement [202] 87
3.10 Cell voltage and temperature changes for a 4.8 Ah Kokam lithium-polymer battery under varying discharge rates (a) and cell voltage vs SOC for a 0.25 C discharge (b) 88
3.11 Impedance spectra of a 4.8 Ah lithium-polymer cell from 10 kHz - 0.01 Hz at 4.2 V 89
3.12 Impedance spectra of a Kokam 4.8 Ah lithium-polymer cell at different state-of-charges (a) and isolation of different resistance components (b) for a frequency range between 10,000-0.01 Hz 90
3.13 Fitted series and SEI layer resistance for a 4.8 Ah Kokam lithium-polymer battery at different SOCs 90

3.14 Bode plot of a Kokam 4.8 Ah lithium-polymer cell showing (a) the absolute impedance and (b) the -phase angle between 10 kHz -0.01 Hz at different SOCs . 91
3.15 Exchange current density of the overall 4.8 Ah Kokam lithium-polymer battery at different SOCs 92
3.16 Impedance spectra of a Kokam 4.8 Ah lithium-polymer cell at different isothermal temperatures (a) and fitted charge transfer and series resistance as a function of temperature (b) at 50% SOC [202] 93
3.17 Plot of natural log of the charge transfer resistance against the inverse of the temperature for a 4.8 Ah Kokam lithium-polymer cell at 50% SOC 94
3.18 (a) Slow rate cyclic voltammetry on a 4.8 Ah Kokam lithium-polymer cell and (b) normalised data against the respective peak values 94
3.19 Example of different optimisation solution methods: (a) gradient based solver (b) genetic algorithm solver 96
3.20 Flow chart of genetic algorithm parameterisation technique 97
3.21 (a) Repeated pulse discharge of a 4.8 Ah Kokam lithium-polymer cell under a 3.6 A discharge for 100 s followed by 900 s rest period and the extracted open circuit potential plot and (b) fitted data for one of the 3.6 A pulse discharges . . 99
3.22 Fitted OCV curves for the anode and cathode. Anode values were taken from Smith and Wang [189] 100
3.23 Genetic algorithm fitted charge transfer coefficients (a) and diffusion coefficients (b) for the anode and cathode of a Kokam 4.8 Ah lithium-polymer battery . . . 101
3.24 Experimental whole cell entropy measurements taken from Troxler *et al.* [202] and experimental graphite entropy profile taken from Reynier *et al.* [171] with extracted cathode entropy profile 101
3.25 Comparison between simulated and test data for discharge of a 4.8 Ah Kokam lithium polymer cell under varying discharge conditions 102
3.26 Comparison between experimental and simulated temperature for a 4.8 Ah lithium-polymer battery (a) and comparison of R^2 values between model with and without entropy included 103
3.27 Kokam 4.8 Ah lithium-polymer cell under a 1/238th scale load with 9 ECE EUDC drive cycles with zoomed in current profile for one cycle inset 103
3.28 Comparison between experimental and simulated cell voltage of a 4.8 Ah lithium polymer battery under a single NEDC cycle (a) and 9 in series (b) 104
3.29 (a) Electrolyte phase lithium concentration and (b) solid phase lithium concentration for a 10A discharge of a 4.8 Ah lithium-polymer cell 104
3.30 Reaction current density for a 10A discharge of a 4.8 Ah lithium-polymer cell . . 105
3.31 (a) Percentage of maximum capacity under different isothermal and C-rate discharge conditions and (b) efficiency of cell under varying isothermal and C-rate conditions 106
3.32 Diagram of cell layer arrangement 107
3.33 (a) Thickness and (b) volume fraction of battery layers when varying layer number for a constant cell volume. Each point represents 5 layers of the original 80 layer modelled battery. Normalised current collector value of 1 represents the original parameters 107
3.34 (a) Breakdown of volume fraction of different battery components and (b) cost of raw materials 108
3.35 Ragone plot for varying area of current collection and thickness of electrodes . . 109
3.36 Example of discharge and charge cycle used to characterize degradation rates with different operation regions of the battery SOC. Shaded regions represent energy extracted/ put in during discharge/ charge 110
3.37 (a) Active material available and (b) SEI layer resistance against cycle number for cyclic loading of 10% of the rated capacity at different SOCs at 1C discharge and charge 110

3.38 Simulated (a)eEfficiency at different SOCs and (b) active material available after cycling of 10% of the rated capacity at 1C . . . 111
3.39 Efficiency against active material available during cycling under HEV mode in a 10% SOC window at different SOCs . . . 111
3.40 Potentials of a lithium-ion battery against stoichiometric ratios of lithiations for a carbon MCMB electrode and NMC cathode . . . 112
3.41 Stoichiometric drift of (a) an anode and (b) cathode with increasing loss of active material. Each point represents a 5% increasing loss of active material from the whole cell. Upper and lower limits represents the stoichiometries required for the 4.2-2.7 V cell voltage limits . . . 113
3.42 Slow rate cyclic voltammetry and entropy measurements of a 4.8 Ah lithium-polymer battery [202] . . . 114
3.43 Comparison between simulated and experimental slow rate cyclic voltammetry in the (a) raw and (b) normalised form . . . 114
3.44 Simulated shift in the SRCV for varying loss of active material for a 100 μV.s^{-1} scan rate (a) and normalised current (b) . . . 115
3.45 (a) Comparison between slow rate cyclic voltammetry and differential thermal voltammetry for a 4.8 Ah Kokam lithium-polymer cell and (b) Comparison between simulated and experimental differential thermal voltammetry . . . 115
3.46 Differential thermal voltammetry for increasing loss of active material for a 1C discharge (a) and normalised data (b) . . . 116
3.47 Schematic of a 3P1S battery pack configuration depicting sources of interconnect overpotentials under an applied potential load. The grey arrows depict the direction of the current flow [224] . . . 117
3.48 Ratio between predicted current and equivalent equal split current for cells closest and furthest from the load points for different ratios of interconnect resistance to battery impedance and cells in a single parallel strip. Solid lines and symbols represents the load experienced by cells closest to the load points and dashed lines and hollow symbols represents cells furthest away [224] . . . 118
3.49 (a) Maximum and minimum currents during a 2 C discharge of parallel battery packs with varying numbers of cells in parallel, starting from 60% SOC with a 1 mΩ interconnect resistance. (b) Maximum and minimum temperature of a 8P1S pack under an equivalent 2-4 C loading, starting from 60% SOC [224] . . . 119
3.50 Simulated temperatures and currents during cyclic loading of 6 Ah cells nearest and furthest from the load points in a 8P1S pack, around 60% SOC assuming a 1 mΩ interconnect resistance [224] . . . 120
3.51 Schematic showing current rebalancing in a 3P1S pack under no load conditions, due to differences in SOC induced during previous operation [224] . . . 121
3.52 Simulated cell currents and temperatures of a 8P1S pack under a 3 C discharge for 500 s after which load is removed and OCVs rebalance assuming a 1 m interconnect resistance. Solid symbols represent temperature and hollow symbols represent current [224] . . . 121
3.53 Battery performance map showing pseudo-steady state voltage at different currents and SOCs with superimposed operating points of 2 cells at 40% and 60% SOC to show the rebalancing effect. The no-load contour is shown in black for reference [224] . . . 122
3.54 (a) Current distribution in battery module with equal cell contact resistances for a 150A discharge and (b) with a bad contact [150] . . . 123

3.55 Simulated current of different cells in a 12P7S battery pack with a 100 A load and 10 A superimposed load noise at 1 Hz Simulated temperature of the hottest cell in a 12P7S battery pack under static and dynamic loads with equal (a) and unequal interconnect resistances and simulated current of different cells in a 12P7S battery pack with a 100 A load and 10 A superimposed load noise at 1 Hz (b) [224] 124

4.1 Diagram of inputs, processes and outputs of fuel cell stack model 127
4.2 Open circuit potential and maximum theoretical efficiency of a PEMFC as a function of temperature based on Higher Heating Values 129
4.3 Example polarisation curve for a single PEMFC cell 130
4.4 (a) Simulated polarisation curves of a fuel cell at 80°C, 2.5 bar and 90% relative humidity with decomposed overpotential contributions and (b) separated polarisation resistance components at the same operating conditions 133
4.5 (a) Simulated polarisation curves of a fuel cell at 80°C and 2.5 bar at varying relative humidities and (b) the specific resistance as a function of the cell voltage 133
4.6 Partial pressure of water vapour 134
4.7 (a) Cathode and (b) Anode flow model control volumes of interest. Adapted from Pukrushpan *et al.* [163] 135
4.8 Schematic of inlet and outlets for thermal model of FC stack. Adapted from Yu *et al.* [230] 139
4.9 Diagram of model elements 141
4.10 Compressor block diagram 142
4.11 Compressor efficiency and performance map for different impeller speeds 144
4.12 Transient mass flow rate of a compressor under a constant pressure ratio of 2 under various step load (a) and normalised mass flow rate referenced from the steady state 145
4.13 Transient power a compressor under a constant pressure ratio of 2 under a step load under various step loads (a) and normalised power referenced from the steady state (b) 145
4.14 Experimental set-up for measuring cathode side pressure loss 146
4.15 (a) Cathode side and humidifier pressure drop for the 75-cell Nedstack PEMFC and (b) experimentally measured blower performance map. Adapted from Wu *et al.* [223] 147
4.16 Transient mass flow of a simulated compressor at a pressure of 1.5 bar with and without a 0.2 m^3 manifold volume (a) and the deviation of mass flow from the compressor mass flow caused by the air manifolding effect (b) 148
4.17 Corrugated Louver with splitter plate and triangular channel [39] 149
4.18 (a) Modelled performance of a fan and radiator system for different air and coolant flow rates and (b) multi-objective optimisation for the cooling system showing the Pareto front for minimisation of parasitic energy requirements . . . 151
4.19 Schematic of balance of plant system for a 9.5 kWe PEMFC stack. Adapted from Wu *et al.* [222] 152
4.20 Picture of the 1st generation fuel cell system set-up 153
4.21 (a) Flow of information in compactRIO set-up and (b) diagram of compactRIO modules used 155
4.22 Flow diagram showing the feedback process in the cooling system PID controller 156
4.23 Cooling inlet and outlet temperatures for a 9.5 kWe PEMFC with a pure proportional controller controlled fan cooling systems with K_P=0.5 (a) and K_p=1 for a constant coolant flow rate of 19.4 l/min at an operating power of 2 kWe [223] 157
4.24 Anode pressure, flow rate and stack voltage during operation with a purge frequency of 20s and purge period of 0.5 s 158
4.25 Simulated and experimental polarisation curve under fully humidified conditions at 65°C. Parameters used as indicated in Table 4.8 159

4.26 Comparison between experimental voltage and temperature response of the modelled 75-cell stack under (a) step loads from cold start and (b) a scaled HWFET drive cycle . . . 160
4.27 Stack voltage, current and cathode pressure during operation of the 75-cell system under step loads of 75A . . . 161
4.28 Comparison of the fuel efficiency assuming the Higher Heating Value of the FC model under isothermal steady state conditions and the full unsteady model from cold start conditions . . . 162
4.29 Stack voltage, pressure and flow rate start-up of the 75-cell FC stack . . . 163
4.30 (a) Cell potentials during the start-up of a PEMFC with a hydrogen flow rate of 70 L.min^{-1} after a nitrogen purge. Reactant inlets are at cell 75 and (b) Diagram of U-shaped stack reactant configuration . . . 164
4.31 (a) Thermal properties of the 75-cell system during the heat up stage of the stack and (b) performance of 75 cell stack during flooding . . . 165
4.32 Stack voltage and cathode pressure drop of 75 cell 9.5 kW stack during constant current operation of 30 A . . . 166
4.33 Cell voltages and stack current during a 5 kW test of a 9.5 kWe PEMFC stack . 167
4.34 Cell voltages and stack current during a 6 kW test of a 9.5 kWe PEMFC stack with failure event . . . 167
4.35 Cell voltages of a 9.5 kW PEMFC after pin-hole formation under hydrogen and nitrogen pressure with no external load applied . . . 168
4.36 Cell voltages of a 75-cell 9.5 kW PEMFC after pin-hole formation (a) and close up of one hydrogen pressurisation event (b) . . . 168
4.37 Bar chart plot of cell voltages during cascading potential fall . . . 169
4.38 Cell voltage data during operation and shut-down showing inhomogenities in cell voltage limiting the shut-down procedure . . . 170

5.1 Transmission line equivalent circuit model of a supercapacitor . . . 173
5.2 Experimental set-up used to characterise a supercapacitor . . . 174
5.3 Comparison of different methods of calculating capacitance from EIS data for a 1500 F Maxwell supercapacitor at 2.7 V and room temperature. Dashed lines represents the simple method. Solid lines represent the complex method. . . . 175
5.4 (a) Bode plot of total capacitance for a 1500 F Maxwell supercapacitor at different voltages with inset showing low frequency capacitance as a function of steady state cell voltage at a temperature of 20 °C and (b) Bode plot of imaginary capacitance at different cell voltages. Inset shows the knee frequency dependency with cell voltage at 20 °C . . . 176
5.5 Fitted resistances of a 1500 F Maxwell supercapacitor at room temperature . . . 177
5.6 (a) Nyquist plot of complex capacitance for a 1500 F Maxwell supercapacitor for different potentials at 20 °C (inset shows the equivalent circuit used to fit it) and (b) comparison of different techniques used to extrapolate low frequency capacitance . . . 178
5.7 (a) Bode plot of total capacitance at different cell voltages of a 150 F Maxwell supercapacitor. Inset indicating the cell voltage-knee frequency relationship and (b) Impedance and capacitance for a 150 F Maxwell supercapacitor at different cell voltages . . . 179
5.8 (a)Bode plot of impedance capacitance at different cell voltages of a 150 F Maxwell supercapacitor. Inset indicating the cell voltage-knee frequency relationship and (b) Nyquist plot of capacitance for a 150 F Maxwell supercapacitor at different cell voltages . . . 179
5.9 (a) Normalised capacitance bode plot for a 150 F and 1500 F supercapacitor and (b) comparison of the knee frequencies . . . 180
5.10 (a) Comparison between the impedance at different operating voltages for a 1500 F and 1/10th scale 150 F Maxwell supercapacitor and (b) cell tab configurations 180

5.11 Charge redistribution effect seen in a 150 F Maxwell supercapacitor under a 2 A charge current at different target voltages (a) and change in voltage from target voltage (b) . . . 181
5.12 (a) Comparison between experimental and simulated charging and then relaxation for a 150 F Maxwell supercapacitor after a 2A charge to different target voltages and (b) comparison between experimental and simulated voltages for a 150 F Maxwell supercapacitor during rapid power cycling . . . 182

6.1 Illustration of how forward and backwards facing vehicle models work . . . 185
6.2 (a) Free body diagram of a car and (b) electrical and mechanical schematic of electric motor model . . . 186
6.3 Generated efficiency map of a AFM-140 EVO Electric Axial Flux Machine Motor based on fitting to manufacturers data sheet [73] and coefficients from Shukla [188] 187
6.4 Time-velocity profiles for (a) NYCC (b) JC08, (c) HWFETDS and (d) US06 drive cycles . . . 189
6.5 (a) Average power of vehicle drive cycle assuming a vehicle with a mass of 1500 kg against the average speed × average acceleration of the respective drive cycle and (b) average acceleration against standard deviation of various standard vehicle drive cycles . . . 190
6.6 Energy distribution as a function of power for the (a) NYCC, (b) JC08, (c) HWFETDS and (d) US06 drive cycles . . . 190
6.7 (a) Distance specific losses associated with different drive cycles and (b) pie chart showing relative vehicle losses . . . 191
6.8 (a) Comparison between average simulated drive cycle power assuming a 2000 kg vehicle and only the steady state component, steady state plus fluctuating components and steady state, fluctuating and velocity components and (b) Comparison between the specific aerodynamic and inertia forces for different vehicle drive cycles. The dotted line represents a 1:1 ratio of specific aerodynamic to inertia energy . . . 193
6.9 Diagram of the data logging and control architecture for the hybrid vehicle power train test rig . . . 194
6.10 Picture of (a) 5 cell battery pack and (b) 10 cell supercapacitor pack . . . 195
6.11 Picture of (a) the complete hybrid system rig and (b) the component box . . . 196
6.12 (a) Predicted cost of a battery pack as a function of the battery pack size and time [71] and (b) predicted cost of the battery under different scenarios for 2015 197
6.13 (a) Predicted cost of a fuel cell stack in 2010, 2015 and 2020 with scenarios of optimistic, pessimistic and baseline costs [135] and (b) historical cost of supercapacitors [100] . . . 197
6.14 (a) Example JC08 load cycle on single cell with an 8.88 kWh battery pack (grey lines represent a single drive cycle) and (b) change in SOC for each cycle . . . 199
6.15 (a) Simulated BEV range and (b) range per kWh for different battery sizes . . . 200
6.16 10 year TCO of a BEV under the JC08 and US06 cycles in 2015 under optimistic, baseline and pessimistic scenarios showing (a) capacity and (b) range . . . 200
6.17 (a) Efficiency and (b) range of a pure FCV for different stack sizes and drive cycles with and without BOP power consumption consideration . . . 202
6.18 (a) Fuel efficiency of FC with and without consideration of parasitic power consumption. Here assuming a base value plus 10% of power and (b) 10 year total cost of ownership for the simulated FCVs under different drive cycles assuming a 20,000 km annual usage showing baseline, optimistic and pessimistic scenarios (shaded regions) . . . 203
6.19 (a) Simulated power for a FC-battery hybrid powertrain with a 9.5 kW FC and 8.88 kWh battery pack under the JC08 cycle and (b) variation in SOC . . . 204

6.20 Simulated range (a) and FC efficiency (b) of a FC-battery active hybrid system with charge sustaining operating mode with different battery and FC sizes. Shaded regions represent the equivalent FCV performance 204
6.21 10 year total cost of ownership for a 19 kW FC-battery hybrid under the NYCC and HWFETDS cycles with baseline, optimistic and pessimistic cost assumptions (shaded regions) 205
6.22 Simulated (a) range and (b) FC efficiency of a FC-supercapacitor hybrid system 206
6.23 10 year total cost of ownership for a 38 kW FC-supercapacitor hybrid under the NYCC and HWFETDS cycles with baseline, optimistic and pessimistic cost assumptions (shaded regions) 207
6.24 Figurative representation of voltage, current and overpotentials during dynamic operation for a FC-supercapacitor passive hybrid system 208
6.25 (a) Currents for a FC-SC passive hybrid system under varying step loads and (b) normalised FC currents in the same FC-SC passive hybrid system 209
6.26 Power split between a 100 W PEMFC and 10 x 150 F supercapacitor pack under a scaled down FTP load cycle with a 50 W peak load 210
6.27 Power split between a 100 W PEMFC and 10 x 150 F supercapacitor pack under a scaled down HWFETDS load cycle with a 50 W peak load 211
6.28 Current histograms for the (a) FTP and (b) HWFETDS 211
6.29 Wiring diagram for powertrain components in 9.5 kWe PEMFC-supercapacitor passive hybrid system. Adapted from Wu *et al.* [225] 213
6.30 (a) CAD model of the fuel cell-supercapacitor passive hybrid system and (b) picture of actual system [225] 214
6.31 Dynamic response of a P9.5-75 Nedstack PEMFC and 33×1500 F supercapacitor pack under a 100 A load [225] 215
6.32 Comparison of dynamic fuel cell response to step load in FC-supercapacitor passive hybrid mode [225] 216
6.33 Comparison between pure FC (a) and FC-supercapacitor passive hybrid under 75 A step loads (b) with a frequency of 0.2 Hz [225] 216
6.34 Comparison of fuel cell efficiency between pure FC and FC-SC passive hybrid system with the fuel cell operating with an air stoichiometry of 2 [225] 217
6.35 Dynamic response for the 9.5 kW FC-SC passive hybrid system under a 1/10th scale HWFET drive cycle [225] 218
6.36 (a) Current histogram for the FC-SC passive hybrid system under a HWFETDS and (b) voltage histogram for the FC-SC passive hybrid system under a HWFETDS in pure FC mode and FC-SC mode [225] 219
6.37 Comparison between experimental and simulated data for the FC-supercapacitor passive hybrid system under a 75A 0.2 Hz step load [225] 220
6.38 (a) Comparison of different step loads and supercapacitor pack size with the response time of the FC current assuming the same 1500 F supercapacitors used in this study and (b) Figure showing how increasing the number of supercapacitors in series for the same capacitance increases the pack rate of change of voltage for the same current. The faster the rate of change of voltage for the supercapacitor pack results in faster rate of change of load experienced by the FC [225] 221
6.39 10 year total cost of ownership for different vehicle configurations for (a) the NYCC and (b) HWFETDS cycles. FC size for the FCBEV and FCSC vehicles were 19 and 38 kW respectively for 2015 baseline values 222
6.40 10 year total cost of ownership of different vehicle types against range for two extreme drive cycles: city and highway 223

List of Tables

2.1 Comparison of battery technologies [38] . . . 14
2.2 Comparison of different commonly used cathodes in lithium-ion batteries. Adapted from [111] . . . 15
2.3 Causes of lithium-ion anode aging - causes, effects and influences [207] . . . 17
2.4 Equivalent circuit models and key features. Adapted from [94] . . . 22
2.5 Comparison of different fuel cell technologies. Adapted from Mekhilef *et al.* [136] 28
2.6 Semi-empirical models of fuel cells. Adapted from [241] . . . 32
2.7 Fuel cell operating modes and major types of degradation [187] . . . 39
2.8 Resistance ratio (resistance of slow branch divided by equivalent series resistance) and capacitance of the flow branch as a percentage of the total measured capacitance. Adapted from Graydon *et al.* [87] . . . 49
2.9 Comparison of different vehicle drive cycles . . . 59

3.1 1D electrochemical model equations [189] . . . 71
3.2 Parameterised battery component thicknesses. Separator thickness taken from Smith and Wang [189] . . . 98
3.3 Cost and density of battery materials. All material costs are from Element Energy [71]. Density values are taken from Reddy [168] . . . 108

4.1 Compressor map polynomial regression coefficients . . . 143
4.2 Compressor map parameters . . . 143
4.3 Compressor motor parameters . . . 144
4.4 Parameters of modelled radiator . . . 151
4.5 List of balance of plant components used . . . 154
4.6 National Instruments equipment used for FC test bench . . . 155
4.7 Effect of increasing PID constant . . . 157
4.8 Polarisation coefficients from regression of experimental data . . . 159

6.1 National Instruments equipment and other components used in scaled down hybrid vehicle powertrain simulator rig . . . 195
6.2 Predictions of fuel costs [149] . . . 196
6.3 Comparison of different FC powertrains . . . 198
6.4 Parameters used in simulations . . . 198
6.5 National Instruments equipment for the 9.5 kW FC-supercapacitor passive hybrid system . . . 214

Nomenclature

α	Thermal diffusivity (m^2 s^{-1})
α_a	Anodic transfer coefficient
α_c	Cathodic transfer coefficient
η	Overpotential (V)
κ^{eff}	Effective conductivity of the electrolyte (S cm^{-1})
κ_D^{eff}	Diffusional conductivity of the lithium (A cm^{-1})
ϕ_e	Electrolyte potential (V)
ϕ_s	Solid phase potential (V)
Ψ	Generic physiochemical property
ρ	Density (kg m^{-3})
σ^{eff}	Solid phase effective conductivity (S cm^{-1})
ε_e	Volume fraction of the electrolyte phase
A_s	Convective surface area (m^2)
a_s	Active surface area per electrode unit volume (cm^2 cm^{-3})
c_e	Volume averaged concentration of lithium in the electrolyte phase (mol cm^{-3})
C_p	Specific heat capacity (kJ kg^{-1} K^{-1})
c_s	Volume averaged solid phase lithium concentration (mol cm^{-3})
D_e^{eff}	Effective diffusion coefficient of lithium in the electrolyte (cm^2s^{-1})
D_s	Solid phase lithium diffusion coefficient (cm^2 s^{-1})
E_{act}^{Ψ}	Thermal activation energy (J mol^{-1})
F	Faraday's constant (96,467 C mol^{-1})
$f_{\pm}$	Activity coefficient
h	Convective heat transfer coefficient (W m^{-2} K^{-1})
i_0	Exchange current density (A cm^{-2})
j^{Li}	Reaction current due to the consumption or production of lithium (A cm^{-3})
k	Thermal conductivity (W m^{-1} K^{-1})
q_c	Ohmic heat from contact resistance (W)
q_e	Reversible entropic heat (W)
q_j	Ohmic heat (W)

q_r Reaction heat (W)

R Universal gas constant (8.314 J mol^{-1} K^{-1})

r Radius (cm)

R_c Contact resistance (Ω)

R_{SEI} Solid Electrolyte Interface layer resistance (Ω)

T Absolute temperature (K)

t Time (s)

t_+^0 Transference number of lithium ions with respect to the velocity of the solvent

T_{amb} Ambient temperature (K)

x Negative electrode solid phase stoichiometry or spatial coordinate along the cell width (cm)

y Positive electrode solid phase stoichiometry

AFC Alkaline Fuel Cell

AN Acetonitrile

BEV Battery Electric Vehicle

BMS Battery Management System

BOP Balance-Of-Plant

BTCS Backwards Time Centered Space

CAD Computer Aided Design

CFD Computation Fluid Dynamics

CG Coal Gasification

CL Catalyst Layer

CO_2 Carbon Dioxide

COR Carbon Oxidation Reaction

CPE Constant Phase Element

cRIO compactRIO

CV Cyclic Voltammetry

CVM Cell Voltage Monitoring

DEC Diethyl Carbonate

DMC Dimethyl Carbonate

DME 1,2-Dimethoxyether

DMFC Direct Methanol Fuel Cell

DoD Depth of Discharge

DOE Department of Energy

DOH Degree Of Hybridisation

DRT Distribution of Relaxation Time

DTV Differential Thermal Voltammetry

EC Ethylene Carbonate

ECM Equivalent Circuit Model

EDLC Electrochemical Double Layer Capacitor

EIS Electrochemical Impedance Spectroscopy

EMF ElectroMotive Force

ESR Equivalent Series Resistance

EV Electric Vehicle

FC Fuel Cell

FCEV Fuel Cell Electric Vehicle

FCHEV Fuel Cell Hybrid Electric Vehicle

FCV Fuel Cell Vehicle

FDM Finite Difference Method

FPGA Field Programmable Gate Array

GA Genetic Algorithm

GDL Gas Diffusion Layer

GHG Greenhouse Gas

GUI Graphical User Interface

HEV Hybrid Electric Vehicle

HHV Higher Heating Value

HOR Hydrogen Oxidation Reaction

ICE Internal Combustion Engine

IEA International Energy Agency

IGCC Integrated Gasification Combined Cycle

LPB Lithium Polymer Batteries

MCFC Molten Carbonate Fuel Cell

MCMB MesoCarbon MicroBeads

MEA Membrane Electrode Assembly

MPC Model Predictive Controller

MPL Micro-Porous Layer

MPNP Modified Poisson-Nernst-Planck

NI National Instruments

OCV Open Circuit Voltage

OER Oxygen Evolution Reaction

ORR Oxygen Reduction Reaction

PAFC Phosphoric Acid Fuel Cell

PC Propylene Carbonate

PE Polymer Electrolyte

PEO Polyethylene Oxide

PNP Poisson-Nernst-Planck

PWM Pulse Width Modulation

RDE Rotating Disk Electrode

RHE Reversible Hydrogen Electrode

RT Real Time

SEI Solid Electrolyte Interphase

SOFC Solid Oxide Fuel Cell

SPM Single Particle Model

SRCV Slow Rate Cyclic Voltammetry

STWE Short Terminus Warburg Element

TCO Total Cost of Ownership

TEM Transmission Electron Microscopy

UK Unitied Kingdom

VI Virtual Instrument

Chapter 1

Introduction

1.1 Why do we need electric vehicles?

Levels of Carbon Dioxide (CO_2) emissions have been identified as being a major factor in determining the extent of climate change in the near future with works showing that total Greenhouse Gas (GHG) emissions need to be reduced by 50-60% by 2050 to avoid irreversible damage to the environment [97, 32]. The Grantham Institute for Climate Change has highlighted that, in 2007, the transport sector accounted for 27% of global energy related CO_2 emissions and this figure is likely to increase in the coming years as other sectors decarbonise.

In the United Kingdom (UK), domestic transport GHG emissions account for 92% of total transport emissions with 58% caused by passenger vehicles as depicted in Figure 1.1. On a global scale, 73% of transport related CO_2 emissions were due to road transport [97]. Based on these figures, a target of 50% (globally) and 80% (UK) has been set for the reduction of total GHGs by 2050 [97] and this will only happen if radical changes are made to address the current causes of GHGs.

In 2010, the estimated UK fleet average emissions was 160 gCO_2/km for light duty vehicles as shown in Figure 1.2. With the aims of the 2050 80% reduction in total GHG emissions for the UK, it has been estimated that the automotive sector needs to achieve an average fleet emission of approximately 20 gCO_2/km. Current advances in engine downsizing through the use of turbocharging and vehicle weight reductions will allow for incremental decreases of emissions in the coming years, however the theoretical limit of emission reduction for an typical Internal Combustion Engine (ICE) is approximately 80 gCO_2/km. Hybridisation of the vehicle with a secondary energy storage device coupled with a diesel engine will allow this to be pushed towards the limit of 60 gCO_2/km however this is still not sufficient to reach the long term goal of 20 gCO_2/km. Therefore, in order to meet these targets, automotive powertrains need to become increasingly electrified.

To address the issues of providing a sustainable and low carbon road transport system, the International Energy Agency (IEA) has identified three possible alternative low carbon powertrain technologies [149]. These include Battery Electric Vehicles (BEV), hydrogen Fuel Cell Vehicles (FCV) and vehicles which run off biofuels, the latter of which

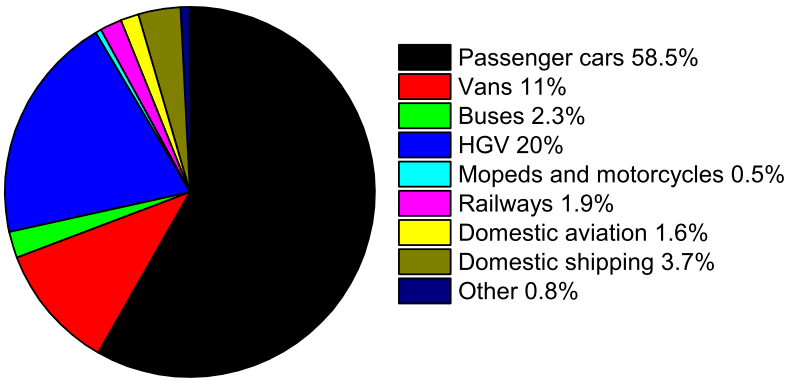


Figure 1.1: UK domestic transport GHG emissions in 2007 excluding travel across borders [97]

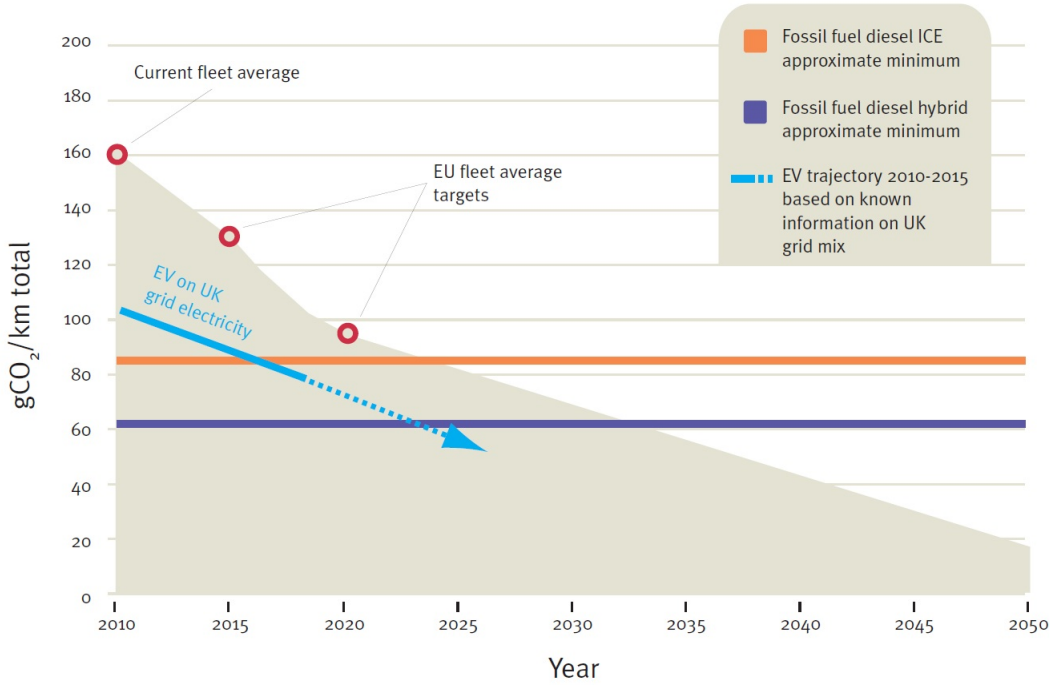


Figure 1.2: European passenger car tailpipe CO_2 trajectories (limits are shown for a typical 4-seater C-class vehicle e.g. VW Golf) [97]

will not be further addressed as it is outside the scope of this study. Development of sustainable low-carbon solutions in transport application is therefore of critical importance in the coming years as sectors decarbonise in order to meet the 2050 targets of a 80% reduction in GHG emissions in order to avoid irreversible climate change.

1.2 Objective of thesis and research questions

The critical technologies identified for the success of Electric Vehicles (EV) are often quoted as being the: hydrogen Fuel Cell (FC), lithium-ion battery and Electrochemical Double Layer Capacitor (EDLC), or supercapacitor. Decades of intense research and development have resulted in these technologies being the current state-of-the-art in terms of energy and power density, and which are close to/ have already been commercialised. The barriers to mainstream adoption of EV technology, however, still remains the high cost of the components, limited durability and lack of hydrogen and charging infrastructure.

Characterising and understanding the electrochemical performance of FCs, lithium-ion batteries and supercapacitors is therefore important in any analysis that looks at their suitability in automotive applications. Figure 1.3 shows the energy and power density of the three electrochemical devices of interest. FCs typically possess the greatest energy density of the three devices owing to the use of a chemical fuel. Power density is typically lower than the other two due to higher operating impedances. Lithium-ion batteries typically have higher power densities due to the lower impedances but have lower energy densities due to the energy carrying capability being directly proportional to the amount of active material used in its construction. Supercapacitors possess the highest power density of the devices due to the absence of charge transfer reactions as the charge storage mechanism is non-Faradic, however their energy density is typically the lowest.

Analysis of these technologies on a individual basis has previously been presented in a number of publications [97, 108, 135]; however, the detailed synergies between these technologies have largely been overlooked [149]. In a study conducted by Offer *et al.* [148]

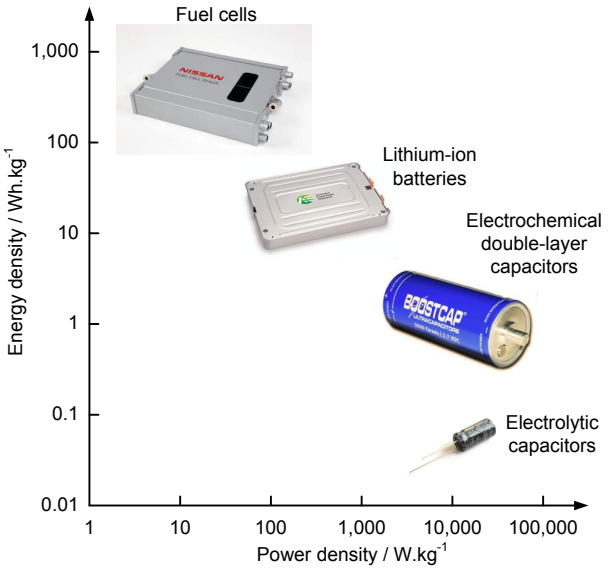


Figure 1.3: Ragone plot showing the energy and power density of PEMFCs, lithium-ion batteries and supercapacitors

the benefits, in terms of lower capital and running cost, of a vehicle using both hydrogen and electricity as fuels, as opposed to pure hydrogen or electricity, were highlighted. Based on the cost sensitivity analysis performed by Offer *et al.* [148] it was concluded that powertrain capital cost, hydrogen cost and electricity cost, in that order, are the most significant factors to consider for a FCV and the greatest benefits are realized when hybridised with batteries to form a Fuel Cell Hybrid Electric Vehicle (FCHEV). In this configuration the FC acts as a range extender for the batteries allowing for the downsizing of the battery pack and FC relative to pure BEV and FCVs.

The performance, lifetime and cost of FCs, batteries and supercapacitors in automotive applications are affected by many variables. The non-linear nature of their operation often means that large scale analysis of the system performance relies on simplifications which may not always be applicable, especially when combining these devices. The area of research of this thesis therefore lies at the interface between the fundamental science of the device operation and the engineering applications with the aims as listed below.

Aims

- To develop a robust mathematical framework and experimentally validated series of models of FCs, batteries and supercapacitors over length and time scales relevant to automotive applications which capture the necessary physics phenomena of interest
- Develop a physics based understanding of the operation of these devices to inform system level design and control rules for electric vehicles
- Use these models to demonstrate their application in assessing the feasibility of different pure electric vehicle powertrain configurations

Through the development of these tools and the methodology it is hoped that a number of different research questions can be answered.

Research questions

- What are the performance limitations of these devices in automotive applications?
- What are optimal operating conditions for these electrochemical devices?
- What is the optimal configuration and combination of these devices in automotive applications?

Where this work hopes to add value to the existing academic literature is to analyse system level problems of automotive powertrain designs with physics driven models that allows for optimisation of variables such as efficiency and durability through knowledge of the fundamental operating principles.

It is important to highlight that the number of different vehicle configurations and control of these devices is near exhaustive and thus within the realms of a thesis not all powertrain configurations can be explored. Rather, this work is aimed at developing the tools and methodology required to answer questions relating to specific vehicle configurations with a few of the main powertrain configurations explored as worked examples.

Similarly, development of detailed full degradation models of each device from a physics point of view is a near exhaustive task and beyond the scope of a single PhD project. Rather, the approach taken here is to be aware of the degradation mechanisms from a physics point of view and design systems and design rules around a more qualitative manner (quantitative where possible) in order to maximise lifetime of these components.

1.3 Hypothesis

Based on the research questions proposed, the following are hypothesises that will be probed in the following thesis.

- Significant gains in efficiency and cost are possible with hybridisation of fuel cells with other electrochemical energy storage devices
- Passive hybridisation can offer the advantages of non-passive hybrids at a reduced cost

1.4 Thesis structure

A literature research on the current research activities and state-of-the-art in the areas of interest is firstly presented with the aim of assessing the gaps in the current literature. This then provides the motivation for the subsequent three chapters which detail the modelling and experimental validation of each electrochemical device with the final chapter presenting work on analysis of drive cycles, total cost of ownership, performance metrics and then combines all elements together for comparison of different drivetrains. The following thus summaries the content of each chapter:

- Chapter 2: **Literature research**
  - This chapter outlines the current state-of-the-art in lithium-ion battery, PEMFC and supercapacitor technology relating to electric vehicles and identifies the current gaps in the academic literature
- Chapter 3: **Lithium-ion batteries**
  - This chapter outlines the mathematic framework for the development of a physics based electrochemical lithium-ion battery model as well as the methodology for its experimental validation. The chapter further expands

into applications of the model to analyse variations in the cell composition and effects on performance, effects of operating range on degradation rates, novel techniques for tracking stoichiometric drift of electrodes and expansion of the single cell model to investigate pack level effects

- Chapter 4: **Proton Exchange Membrane Fuel Cells**
  - This chapter details the FC system model which captures the thermal, mass transfer and water management effects as well as the contributions of the balance-of-plant components. Validation of the model is achieved through the construction and testing of the 9.5 kWe system. System architecture, control issues and failure points are analysed
- Chapter 5: **Electrochemical Double Layer Capacitors**
  - This chapter details the framework for a transmission line based supercapacitor model, its experimental validation and applications to analyse it's dynamic performance. A novel method of extracting the low frequency capacitance through its complex impedance is also presented
- Chapter 6: **Powertrain comparison**
  - This chapter presents the details of the vehicle model, drive cycle analysis, combination of the developed models into a vehicle simulation to answer the research questions and the development of a scaled down powertrain simulator rig and a large scale proof-of-concept rig of a FC-supercapacitor passive hybrid powertrain
- Chapter 7: **Conclusions**
  - This chapter summarises the conclusions from all previous chapters and answers the research questions posed. Future work is also discussed.

The structure of this thesis therefore will be broken down into 4 main sections of technical content as shown in Figure 1.4. The first three chapters outline the modelling frame work, experimental validation and application of the developed models to address component specific problems relating to lithium-ion batteries, PEMFCs and supercapacitors. The final chapter then applies all of the developed models in optimising the vehicle powertrain for different automotive applications.

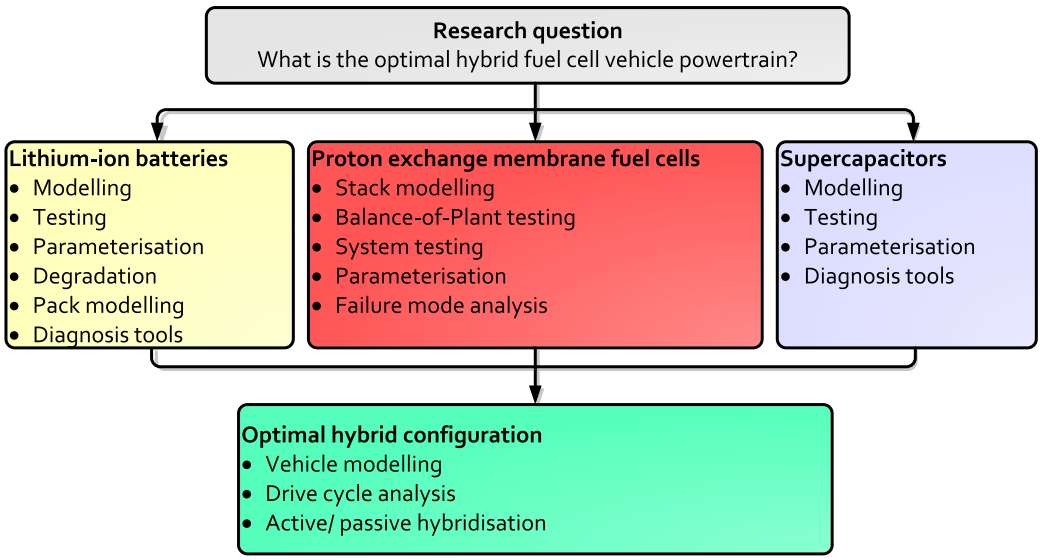


Figure 1.4: Overview of structure of PhD project

1.5 Deliverables to industrial sponsors

This PhD was funded by the kind financial contributions of Nissan Motor Company. Asides from the academic deliverables of the PhD, the industrial deliverables are as follows:

- A literature review of the current state-of-the-art in Proton Exchange Membrane Fuel Cells, Lithium-ion batteries, Electrochemical Double Layer Capacitors and their applications in electric vehicles
- A portfolio of models describing the dynamic behaviour of proton exchange membrane fuel cells, lithium-ion batteries and supercapacitors
  - Models should be able to describe dynamic performance over the relevant time scales and capture relevant thermal and degradation effects
- Experimental validation of the dynamic models of the electrochemical devices
- Comparison of different powertrain configurations for different market segments
- Investigation of feasibility of passive hybrid fuel cell vehicle coupling
- Techno-economic analysis of different powertrain configurations

Chapter 2

Literature research

This chapter outlines the current state-of-the-art in the academic literature relating to aspects of lithium-ion batteries, PEMFCs and supercapacitors in automotive applications and their combinations in electric vehicle powertrains. From this, the current gaps in the academic literature are identified and serves as motivation for subsequent work.

In order to understand the temporal and spatial resolution requirements of the models to be developed, it is useful to compare the different effects occurring of each device and their respective time constants. Figure 2.1 shows, over a range of time constants, the different effects of interest which occur in the three electrochemical devices of interest and also the typical time constants involved in automotive applications.

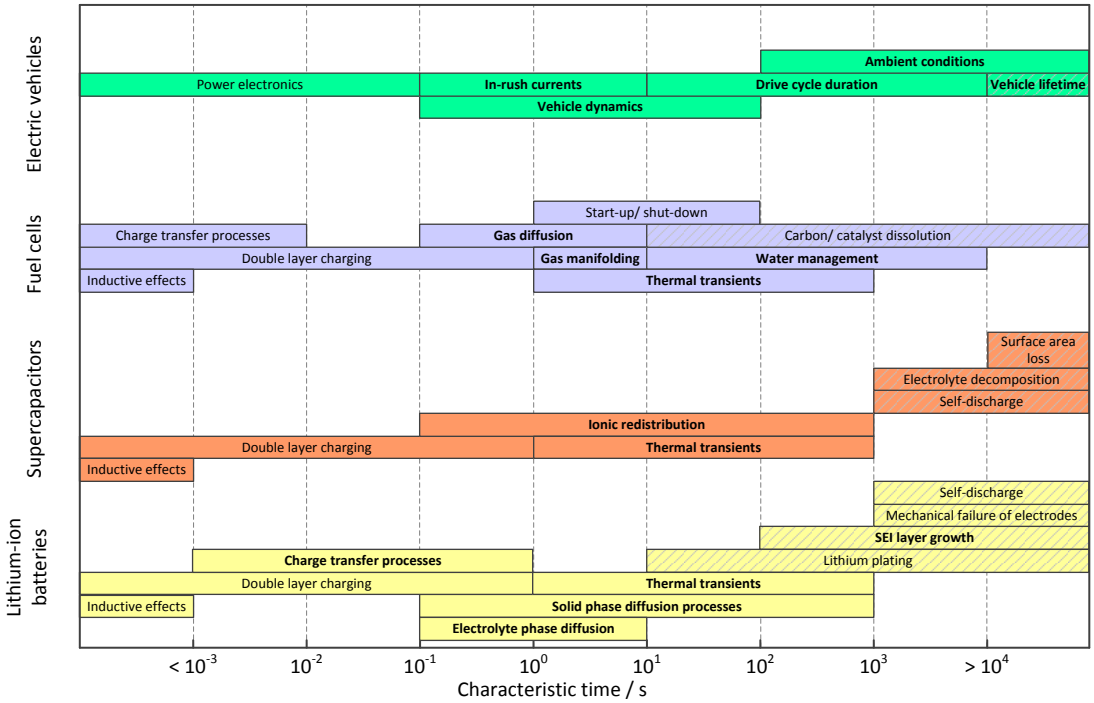


Figure 2.1: Characteristic time scales for different processes occurring in batteries, supercapacitors, fuel cells and electric vehicles. Shaded boxes represent irreversible processes and bolded items represent captured processes in the subsequent works

Multi-scale modelling over all time and length scales is typically impractical due to the computational cost of covering all scales with some effects having a negligible impact on the overall vehicle performance. Therefore, this work will focus on the aspects relating to processes that occur within the time constants relevant to vehicle applications.

2.1 Electrochemical techniques and other analysis tools

Prior to reviewing the literature on the specific electrochemical devices, it is useful to review common electrochemical and non-electrochemical analysis techniques which are often used in the academic literature to probe effects in these devices. Understanding and interpreting the results should be a prerequisite to analysis of the existing works in-order to identify the key conclusions and shortcomings of the work in the academic literature.

2.1.1 Electrochemical Impedance Spectroscopy

Electrochemical Impedance Spectroscopy (EIS) is useful as a diagnostic tool as it is non-invasive and also can isolate parameters from a coupled system. Typically, an alternating voltage or current of a known frequency (ω) and magnitude (V/I) is imposed on system over a pseudo-linear region. Many electrochemical systems can be described by the Butler-Volmer equation which relates the overpotential of a system, which is the deviation from the thermodynamic potential to the current. Equation 2.1 shows the Butler-Volmer equation and Figure 2.2a plots the current-overpotential relationship. Here A represents the area, i_0 the exchange current density, α_a/α_c the anodic and cathodic charge transfer coefficients, n the number of electrons involved in the reaction, F the Faraday's constant, η the overpotential, R the universal gas constant and T the temperature. In a full system considering the processes in both electrodes, anodic and cathodic reactions are occurring at the same time at zero overpotential, with their rates being equal and opposite.]

$$I = Ai_0 \left(\exp\left[\frac{\alpha_a n F \eta}{RT}\right] - \exp\left[-\frac{\alpha_c n F \eta}{RT}\right] \right) \tag{2.1}$$

The magnitude of the EIS excitation signal should be large enough such that the noise-to-signal ratio is sufficiently low to get a good spectra but sufficiently low such that the system remains linear. Whilst some authors have presented works on non-linear EIS [218] the standard technique involves keeping the excitation signal within linear regions. The resulting magnitude and phase of the current or voltage response gives details about the processes occurring in the tested system. Figure 2.2b shows the voltage and current response of a system under a EIS signal excitation as an example.

If a sinusoidal voltage oscillation is applied this is known as EIS under potentiostatic operation and is typically done over a DC voltage (V_{DC}) as shown in Equation 2.2. Depending on the system being investigated and the nature of the experiment, it may be more advantageous to do the EIS measurements under galvanostatic or potentiostatic modes.

$$V(t) = V_{DC} + V_{AC}\sin(\omega t) \tag{2.2}$$

The resulting current output is measured and then compared with the input voltage. Depending on the frequency of the applied voltage there will be a phase difference

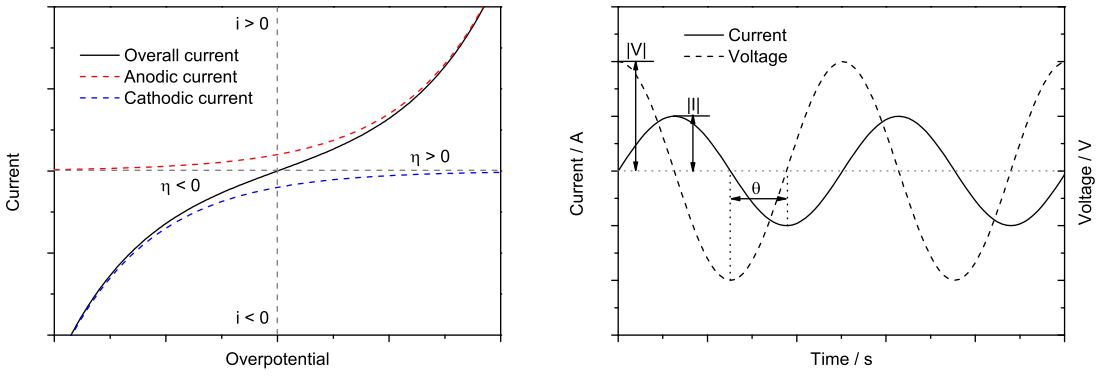


Figure 2.2: (a) Relationship between current and overpotential for typical electrochemical systems described by the Butler-Volmer equation and (b) Current oscillation showing resulting voltage magnitude difference and phase shift

between the signals as shown in Equation 2.3.

$$I(t) = I_{DC} + I_{AC}\sin(\omega t = \theta) \tag{2.3}$$

The impedance of the system ($Z(\omega)$) is therefore defined as the ratio of the applied voltage ($V(\omega)$)and measured current ($I(\omega)$) as shown in Equation 2.4.

$$Z(\omega) = \frac{V(\omega)}{I(\omega)} \tag{2.4}$$

The resulting impedance is a complex number with a real and imaginary component as shown in Equation 2.5.

$$Z = Z' + iZ'' \tag{2.5}$$

Where the magnitude and phase of the impedance can be calculated as shown in Equations 2.6 and 2.7 respectively.

$$\mid Z \mid = \sqrt{(Z')^2 + (Z'')^2} \tag{2.6}$$

$$\varphi = -\tan^{-1}\left(\frac{Z''}{Z'}\right) \tag{2.7}$$

The resulting output from EIS measurements are the real and imaginary components of the impedance as well as the phase angle. These values are commonly plotted on a Nyquist diagram, which shows the real and imaginary components of impedance or as a Bode plot, showing the frequency dependence.

The advantage of EIS is that it is non-destructive and can give information about material properties and electrochemical kinetic rates . The disadvantage of EIS is that decoupling processes with similar time constants can be difficult and measurements should be made when the system is under steady, or pseudo-steady state. Also, measurement of EIS response, in coupled systems, can be difficult and interpretation of the results needs rigorous consideration. Often, EIS can be combined with other complimentary techniques such as half-cell measurements, Slow Rate Cyclic Voltammetry, Distribution of Relaxation Time measurement (DRT), Rotating Disk Electrode (RDE) and various other techniques which provide the user with different information.

Equivalent circuit fitting

Equivalent circuits can be used to match the impedance data measured with EIS and extract useful parameters. The values and arrangements of such components are typically arranged in such a way as to represent physical properties or phenomena of a system. Therefore, changes in the values of these elements when testing can give valuable insight into the underlying processes that are occurring.

Typically, equivalent circuits are made up of a number of different elements [17, 129, 35, 116]. For a pure resistor, the impedance response is equal to the resistance value and is shown as a single point on a Nyquist plot with a zero imaginary impedance value, i.e. no phase shift at all frequencies.

$$Z_R = R \tag{2.8}$$

Typically, there are three main types of resistances users are interested for batteries and fuel cells. These are the series resistance, charge-transfer resistance and diffusion resistance. Series resistance is the bulk resistance to the flow of ions in solution as well as electronic resistance. The charge-transfer resistance is associated with a Faradic reaction mechanisms at the electrode. Diffusion resistance is associated with mass transport limiting factors.

Capacitive circuit elements are useful in EIS analysis to characterise the charge double layer which forms at the interface between a solid electrode and liquid electrolyte in an electrochemical system. For capacitors, the impedance response can be represented by Equation 2.9.

$$Z_C = \frac{1}{i\omega C} \tag{2.9}$$

The impedance response of a pure capacitor is entirely imaginary and negative. Often in equivalent circuits there are two main types of capacitances: double-layer capacitance and geometric bulk capacitances.

For a pure inductor, the impedance response can be represented with reference to Equation 2.10 and is purely imaginary and positive. Inductive effects are dominant at high scan frequencies and are often caused by the finite length and inductive properties of the measurement wires and intrinsic inductive properties of the device.

$$Z_L = i\omega L \tag{2.10}$$

Combinations of purely resistive, capacitive and inductive elements do not necessarily describe the response of all systems and often distributed elements are used to model behaviour. The two main forms of distributed elements are Constant Phase Elements (CPE) and Warburg elements.

The impedance of a CPE can be expressed as shown in Equation 2.11 where T and φ are CPE parameters [17, 116].

$$Z_{CPE} = \frac{1}{T(i\omega^{\varphi})} \tag{2.11}$$

The CPE can be used to describe a pure resistor (φ=0, $T = R^{-1}$), a pure capacitor (φ=1, $T = C$) or a pure inductor (φ=-1, $T = L^{-1}$). A CPE can also be used to represent a Warburg element where φ=0.5. In general the impedance response of CPEs are used to describe the double-layer charging of rough irregular electrode surfaces.

The impedance of Warburg elements arises from one-dimensional diffusion of a species to the electrode. In the general case, describing the effect of the diffusion of species a, is shown in Equation 2.12, where σ_a is a Warburg parameter, dependent on the diffusivity of species a, the reaction rate, the concentration of species a, the current density and the potential [17, 116].

$$Z_{w,a} = \sigma_a(i\omega)^{-1/2} = \frac{\sigma_a}{\omega^{1/2}(1+i)} \tag{2.12}$$

Using a finite length diffusion boundary condition, over a diffusion length of δ, can be used to derive the Short Terminus Warburg Element (STWE). Equation 2.13 describes

the impedance of the STWE where R_w is a Warburg R parameter, and T_w is described in Equation 2.14 where D_a is the diffusivity of species a [17, 116].

$$Z_{w,sh} = \frac{R_w \tanh\left[(iT_w\omega)^{\varphi}\right]}{(iT_w\omega)^{\varphi}} \tag{2.13}$$

$$T_w = \frac{\delta^2}{D_a} \tag{2.14}$$

A STWE behaves like a resistor at low frequencies and has a characteristic 45° behaviour at higher frequencies. For pure diffusive behaviour the φ is typically fixed at 0.5 but for fitting purposes this is typically allowed to be free.

Examples of Nyquist plots of different common equivalent circuits is shown in Figure 2.3. The simplest equivalent circuit typically used to represent the performance of an electrochemical system is shown in Figure 2.3a. This circuit is known as the Randle's circuit and forms a semi-circle in the Nyquist plot. The first resistor represents series resistance of a system which comprises of electronic and ionic resistances of the system. The second resistor typically represents the charge transfer resistance which is directly proportional to the exchange current density of the system. The parallel capacitor typically represents the double layer capacitance of the system. Figure 2.3b represents

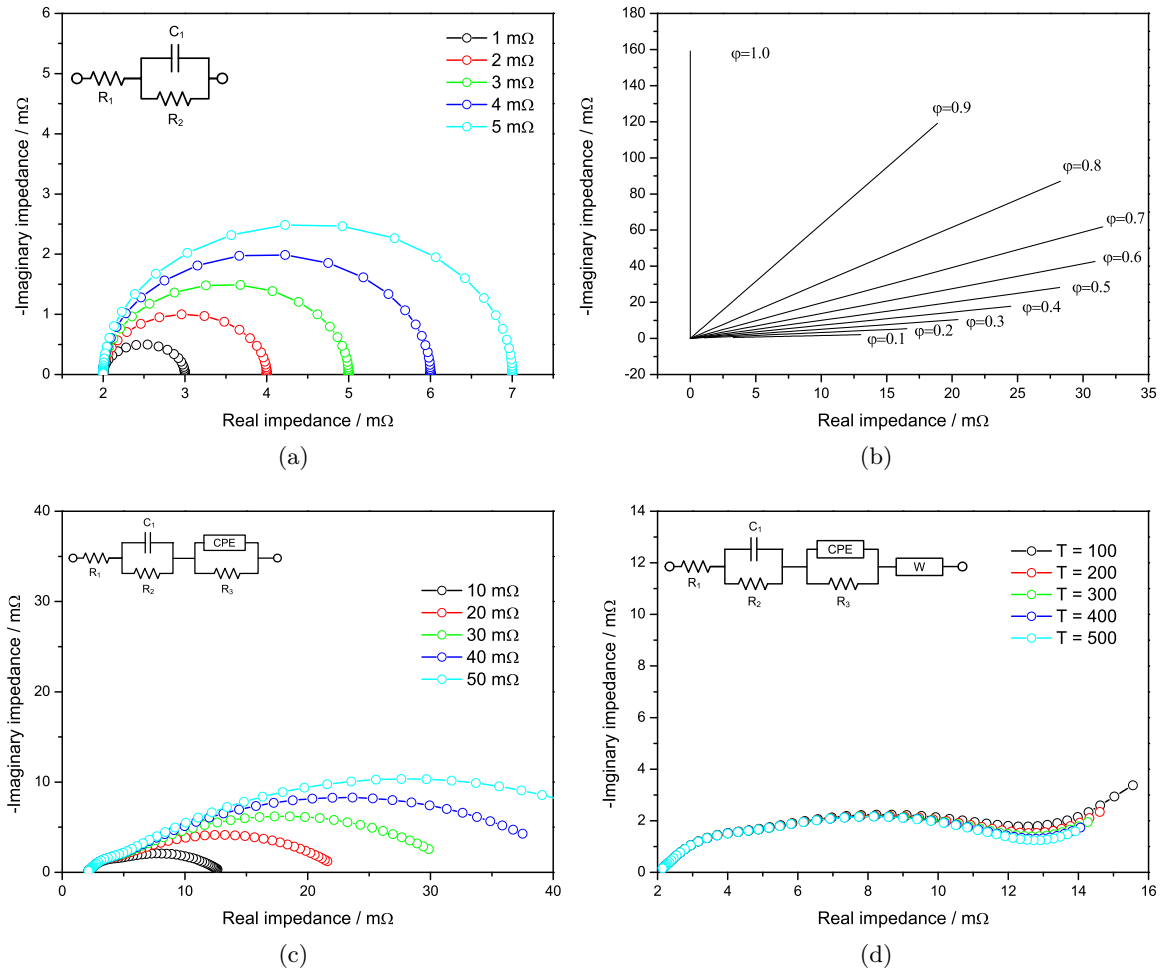


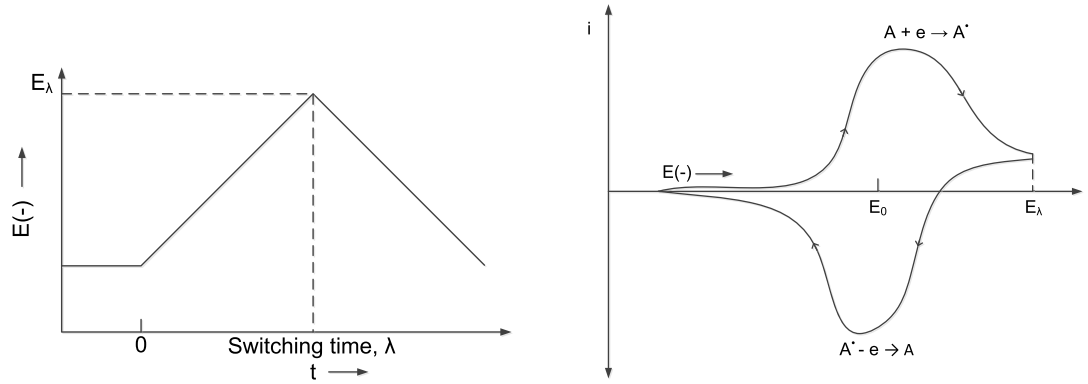
Figure 2.3: Simulated EIS curves (a) a series resistance with a parallel resistance and capacitance with the parallel resistance being varied (b) CPE with constant of 100 over a 0.01-10,000 Hz range, R_3 varied, (d) Short terminus Warburg impedance coefficient T variation

the response of a pure CPE element with different coefficients. This can represent purely capacitive or resistive behaviour as well as a combination of the two. These are typically used in parallel with a resistor to form a semi-depressed circle which better fits the impedance response of highly porous electrodes as shown in Figure 2.3c. Figure 2.3d shows the response of the system with the introduction of a Warburg element which is typically used to represent low frequency diffusion of material.

2.1.2 Cyclic voltammetry

In cyclic voltammetry measurements, the applied potential to a system is varied linearly with respect to time with different ramp rates ranging from 10 mV/s to 1000 V/s for conventional electrodes between set limits [16]. The resulting current is then plotted against the potential to give a voltammogram. An example of the potential and current evolution as a function of time is shown in Figure 2.4.

As a potential is applied at a constant ramp rate the current will increase if it is thermodynamically favourable for a reaction to take place. This is therefore a useful tool to determine the stability limits of electrochemical systems, for example the decomposition potentials of electrolytes used in the battery will largely determine the choice of electrodes and their long term stability. It is also a useful tool for determining potential windows in batteries which contain the most energy as indicated by the peak in the CV plot where the redox reactions occur.



(a) (b)

Figure 2.4: (a) Cyclic potential sweep and (b) resulting cyclic voltammogram. Adapted from Bard and Faulkner [16]

2.2 Lithium-ion batteries

Many thousands of papers have been published in the field of lithium-ion batteries in an expansive array of different areas. The aim of this literature review is to focus on the works relating to battery performance, degradation mechanisms, single cell modelling and pack level modelling with a emphasis on automotive related issues and identify the current gaps in the literature.

The lithium-ion battery is currently the technology of choice in commercially available batteries used in automotive applications due to its superior gravimetric and volumetric energy density compared to other battery technologies. The basic operating principle of a lithium-ion battery is depicted in Figure 2.5 and consists of 5 major components: current collectors, a porous anode, a porous cathode, porous electrically insulating separator and ionically conductive electrolyte. Other materials such as polymeric binder, conductive additives are typically added but are in smaller proportions in the electrodes.

In the fully charged state, lithium is intercalated into the crystalline structure of the anode, which is typically made from carbon. The thermodynamic potential difference between the anode and cathode when lithiated gives rise to the measured cell potential. When the cell is discharged, lithium is split into a lithium-ion and an electron at the interface between the electrode and electrolyte at the anode. The lithium-ion therefore goes into the electrolyte. At the same time, at the cathode, it becomes thermodynamically favourable for lithium-ions to intercalate from the electrolyte into the cathode as electrons are made available from the anode half reaction. Electrons are not allowed to pass through the separator and must therefore flow through an external circuit where useful electrical work can be extracted. The separator is, however, ionically conductive and the generated concentration gradient from the liberation and consumption of lithium-ions at the anode and cathode respectively leads to a movement of ions. Potential field gradients and convective forces can also drive the flux of ions in the electrolyte.

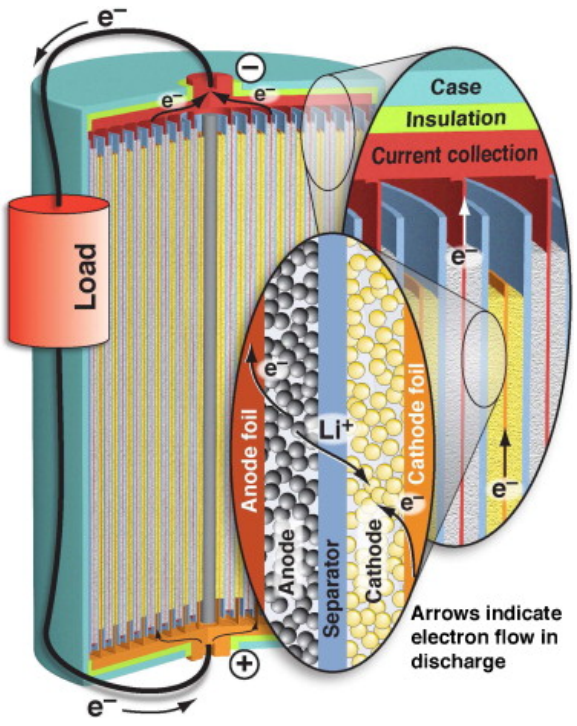


Figure 2.5: Structure of a lithium-ion battery, showing the cell-scale and particle-scale structures [47]

2.2.1 Lithium-battery technologies

Many battery technologies with different electrode and electrolyte chemistries have been developed each with specific performance characteristics. Table 2.1 compares a number of currently available battery technologies.

The key metrics which needs to be considered when selecting a battery technology for vehicle applications are high specific energy, for sufficient range, and high specific power, to meet performance requirements. Decreasing the weight of the system is a key design objective to reduce the eventual motive power required. Based on the information in Table 2.1, lithium-ion and lithium-polymer batteries are the most appropriate battery type for automotive applications. Zn-air and Al-air batteries display higher energy densities compared to lithium-based batteries however their power densities are lower and complications arise when addressing refuelling of a cell which requires replacement of the anode and electrolyte. In a vehicle application, the practical lifetime of a battery pack is of high significance to the end user and therefore lithium-ion batteries are the current battery technology choice for emerging electric vehicles.

Within the realm of lithium-ion batteries, there is still significant choices to be made in terms of the selection of suitable electrodes and electrolyte combinations as well as physical cell design. These will largely determine the resulting energy and power density as well as cost, safety and durability.

Anodes

The most common anode material used in lithium-ion batteries are carbon based due to their relatively safe nature and long cycle lives. Lithium metal anodes have been used in the past and have extremely high theoretical specific energies of ∼1,000 Wh/kg and specific capacity of 3.86 Ah/g; however, the main drawback of pure lithium anodes is the large negative electropotential of lithium and therefore its thermodynamical instability in the majority of electrolytes which is unsuitable in secondary cell applications.

Of the different allotrope of carbon, graphite is most often used due to its excellent intercalation characteristics [12] however other forms of carbon are currently being investigated also such as mesocarbon, coke and carbon fibres [184]. The theoretical

Table 2.1: Comparison of battery technologies [38]

	Specific energy[1] (Wh/kg)	Energy density[1] (Wh/m^3)	Specific power[2] (W/kg)	Cycle life[2] (Cycles)	Projected cost[3] (US$/kWh)
Lead Acid	30-45	60-90	200-300	400-600	150
Ni-Cd	40-60	80-110	150-350	600-1200	300
Ni-MH	60-70	130-170	150-350	600-1200	200-350
Zn-Air	230	269	105	NA[4]	80-120
Al-Air	190-250	190-200	7-16	NA[4]	NA
Na/S	100	150	200	800	250-450
Na/$NiCl_2$	86	149	150	100	230-350
Li-Polymer	155	220	315	600	NA
Li-ion	90-130	140-200	250-450	800-1200	>200

[1] At C/3 rate

[2] At 80% Depth Of Discharge

[3] For reference only

[4] Mechanical recharging

NA: Not Available

capacity of graphite is 372 mAh/g and 186 mAh/g for coke.

Silicon has the potential to be a replacement for carbon based anodes in the future due to its natural abundance and a high theoretical energy density (4,008 mAh/g) compared to the 372 mAh/g for graphite [72]. The main draw back of Silicon anodes is the large volumetric expansion experienced during lithiation which is cited as being approximately 300% compared to 7% for graphite [104]. This leads to extreme mechanical stress in the electrode leading to island formation and also fresh surface being exposed on each cycle leading to rapid consumption of lithium in the passivation layer formation stage.

Cathodes

The most commonly used cathode material is Lithium Cobalt Oxide ($LiCoO_2$) due to its relatively high working potential and structural stability allowing for long cycle lives [147]. However, Lithium Iron Phosphates ($LiFePO_4$) are becoming increasingly popular due to its lower cost, non-toxicity and excellent safety and cycling performance [184]. One of the previous barriers to mainstream adoption was the low electrical conductivity which has been solved by reducing particle size and coating with conductive materials such as carbon, and also doping the result with cations of aluminum, niobium and zirconium [43]. Table 2.2 compares key metrics of the most commonly used battery cathode materials. Many other variants of these materials exist in different proportions, with composite cathodes proving popular. These are commonly known as NMC electrodes.

Many other cathode materials are currently under investigation, however, the materials listed in the table are the ones closest to/ have already been commercialised in automotive applications.

Electrolytes

The role of the electrolyte is to carry lithium-ions, via a lithium containing salt, between the anode and cathode during operation. The selection of a suitable electrolyte will largely define the battery's overall stability and performance, as the ionic conductivity is often one of the limiting factors, especially at low temperatures. The electrolyte used in lithium-ion batteries typically consists of a solution of lithium salts in an aprotic organic solvent. Whilst other technologies such as the rechargeable aqueous lithium-ion battery, which were first proposed in 1994 [196], are currently under development and potentially offer high rates of charge and discharge due to the higher conductivity (approximately two orders of magnitude greater than non-aqueous systems [215]) and also offering superior safety, their energy density is not suited for automotive applications as the operating potential of any aqueous system is limited to lower voltages than organic systems due to the onset of hydrogen and oxygen evolution at elevated potentials.

Table 2.2: Comparison of different commonly used cathodes in lithium-ion batteries. Adapted from [111]

Property	$LiCoO_2$	$LiNiO_2$	$LiMn_2O_4$	$LiFePO_4$
Practical capacity (Ah/kg)	150	170	120	155
Energy density (Wh/kg)	180	170	100	130
Nominal voltage (V)	3.7	3.5	4.0	3.3
Cycling capability (Cycles)	∼500	∼500	∼500	∼2000
Power capability	Best	Good	Average	Good
Safety	Good	Poor	Good	Best
Toxicity	Poor	Poor	Good	Best
Cost	High	Average	Good	Good

One of the initially used electrolytes was Propylene Carbonate (PC) which has good conductivity however poor cyclability due to uncontrollable passivation of the coupled electrodes. Ethylene Carbonate (EC) in recent years has been widely used in commercially available lithium-ion batteries due to its superior cyclability. Typically other species such as Dimethyl Carbonate (DMC), Diethyl Carbonate (DEC) or 1,2-Dimethoxyether (DME) are added in order to control the passivation process and improve conductivity [208].

The choice of the lithium salt has a strong impact on thermal stability, electrochemical stability, toxicity and cost of lithium batteries. $LiClO_4$, $LiPF_6$, $LiAsF_6$ and $LiBF_4$ are some classical salts for liquid electrolytes [208]. The electrolyte can also be solid and is then called a Polymer Electrolyte (PE). This is made with high molecular weight polymer such as Poly(Ethylene Oxide) (PEO) combined with lithium salts (PEO-LiX). Lithium batteries containing a polymer electrolyte are called Lithium Polymer Batteries (LPB). Compared to classical lithium batteries, LPBs have low manufacturing costs and are adaptable to a wide range of shapes. Since lithium is stable in contact with PEO-LiX, high capacities can be achieved by using Li(s) anodes. Unfortunately, LPBs suffer from conductivity problems at room temperature because of the tendency of PEO to crystallize below 70°C. Research efforts are on their way to find a viable solution [9].

2.2.2 Battery degradation

The cause of battery capacity and power fade can be attributed to many different mechanisms, and no one model to date has captured this all and been experimentally validated. These mechanisms include, but are not limited to: dendrite formation, electrode chemical and/or structural distortion, electrolyte decomposition and the formation of a SEI layer. The study of the aging and degradation of individual cells [10, 206] and their response to abuse tests [193] is intrinsically related to that of thermal effects. However, cycling and storage history do impact the cell performance [175, 56], through a variety of factors: the geometry and chemistry of the cell; outside conditions, such as temperature, humidity, and vibrations; load characteristics, such as current and voltage amplitude, frequency and noise.

The following details the commonly identified degradation mechanisms for the anode and cathode.

Anode degradation

Degradation mechanisms commonly associated with that of carbon based anodes are listed in Table 2.3.

Many authors have investigated these effects in great detail in order to probe the fundamental processes which drive their evolution and hopefully in turn allows for the design of better systems in the future. For example, Legrand *et al.* [117] suggests that lithium plating is mainly caused on the anode by the charge transfer process during charging. Diffusion effects are seen as acting over longer time scales and is not the dominating process. This effect is not regularly seen during calendar aging but more when the cell is being regularly cycled. Lithium plating is commonly cited as occurring during charge conditions and especially under heavy charge and low temperatures. This therefore allows for control algorithms to be developed based on knowledge of the fundamental process and would suggest lower charging rates will lead to lower rates of lithium plating due to smaller charge transfer processes.

Authors have also combined this knowledge to develop physics based models that attempt to quantify these losses under different conditions. This helps to inform cell designer

Table 2.3: Causes of lithium-ion anode aging - causes, effects and influences [207]

Cause	Effect	Leads to	Reduced by	Enhanced by
Electrolyte decomposition (→SEI) (Continuous side reaction at low rate)	Loss of lithium, impedance rise	Capacity fade, power fade	Stable SEI (additives), rate decreases with time	High temperatures, high SOC (low potential)
Solvent co-intercalation, gas evolution and subsequent cracking formation in particles	Loss of active material (graphite exfoliation), loss of lithium	Capacity fade	Stable SEI (additives), carbon pre-treatment	Overcharging
Decrease of accessible surface area due to continuous SEI growth	Impedance rise	Power fade	Stable SEI (additives)	High temperatures, high SOC (low potential)
Changes in porosity due to volume changes, SEI formation and growth	Impedance rise, overpotentials	Power fade	External pressure, stable SEI (additives)	High cycle rates, high SOC (low potential)
Contact loss of active material particles due to volume changes during cycling	Loss of active material	Capacity fade	External pressure	High cycling rate, high DOD
Decomposition of binder	Loss of lithium, loss of mechanical stability	Capacity fade	Proposer binder choice	High SOC (low potential), high temperature
Current collector corrosion	Overpotentials, impedance rise, inhomogeneous distribution of current and potential	Power fade, enhances other aging mechanisms	Current collector pre-treatment	Overdischarge, low SOC (high potential)
Metallic lithium plating and subsequent electrolyte decomposition by metallic lithium	Loss of lithium (loss of electrolyte)	Capacity fade (power fade)	Narrow potential window	Low temperatures, high cycling rates, poor cell balance, geometric misfits

through a model driven approach. Christensen [44] developed a mathematical model of diffusion induced stresses in lithium-ion battery electrodes and this was used to compare high power vs high energy cells. It was shown that porous electrode effects, particularly in high energy cells with thicker electrodes amplify the stresses generated under lithiation/delithiation. Variations in the solid-phase diffusion coefficients for different electrode materials was shown to be a key metric in determining the extent of mechanical stresses generated.

Solid Electrolyte Interphase

One of the main degradation mechanism in lithium-ion batteries, with graphite negative electrodes, is understood to be attributed to the growth of a surface film, or Solid Electrolyte Interphase (SEI) layer, at the negative electrode [201]. In this mechanism, lithium reacts with the electrolyte, resulting in the formation of lithium containing compounds on the electrode. This results in an irreversible reduction of cyclable lithium, increased electrolyte resistance due to lower concentrations and increases intercalation resistance leading to power and capacity fade [10]. This process is a function of the overpotential of a cell, thermodynamic potential of the cell and the temperature.

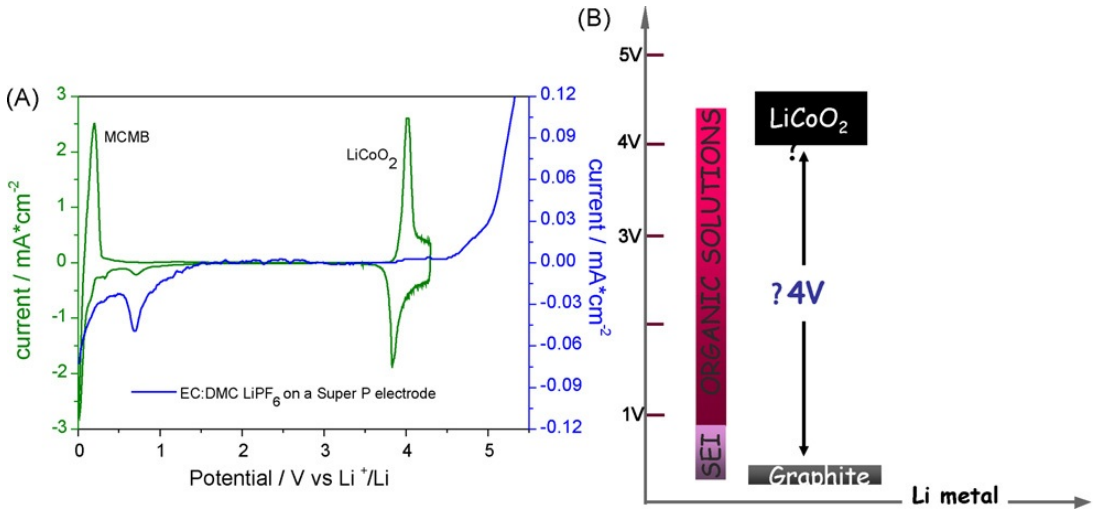


Figure 2.6: (A) cyclic voltammetry profiles of a lithium-ion battery components: anode and cathode (green), electrolyte (blue). Counter electrode: Super P carbon; electrolyte EC-DMC, $LiPF_6$. (B) Voltage operation ranges of the C/$LiCoO_2$ electrode combination in comparison with the stability domain of most common liquid electrolytes [184]

Thermodynamically, lithiated graphite is unstable in the majority of organic electrolytes. Figure 2.6 shows the Cyclic Voltammetry (CV) profiles of the anode, cathode and electrolytes in a battery consisting of a MCMB-$LiCoO_2$ battery in a EC-DMC-$LiPF_6$ electrolyte. The peaks in the CV shows the typical operating potential of that electrode. It can be seen that MCMB anodes typically operate at a potential of 0.3 V vs. Li^+/Li and $LiCoO_2$ operates around 3.9 V. The CV plot of the electrolyte shows the onset of the electrolyte reduction/ oxidation occurs at roughly 4.5 V and 1.5 V vs. Li^+/Li. Based on this it can be seen that the cathode operates near the limit of electrolyte stability whereas the anode operates outside of this.

The only reason why a lithium-ion battery using carbon intercalation electrodes can operate is during the first charging cycle a passivating SEI layer forms which prevents the carbon electrolyte being in direct contact with the electrolyte. Whilst this passivation mechanism allows the lithium-ion battery to operate it is also one of the main causes of degradation as the SEI film growth in continually happening. This leads to the loss of active material, reducing capacity, and also an increase in resistance, leading to power fade. The initial formation of this layer during the first charging cycle is therefore of critical importance to the long term performance of the battery.

The composition of this SEI layer is complex and depends on the type of electrolyte used. Peled *et al.* [157] showed that SEI on Li_xC_6 anodes in non-aqueous solutions consists of materials such as: Li_2O, LiF, LiCl, Li_2CO_3, $LiCO_2$-R, alkoxides and non conducting polymers. Peled [158] suggested that this passivation layer consists of one or two layers. The first being a compact and thin region and a second more porous region that suppresses mass transport of ions. Other authors have since suggested the structure is far more complicated. SEI layer resistance here was quoted as being in the region of 10-1000 $\Omega.cm^2$. Figures 2.7a and 2.7b show proposed compositions of this SEI layer and also how they evolve over time.

Many authors have identified this as being a critical process to model in order to understand degradation. Pinson and Bazant [160] developed a mathematical model based on the capacity fade and power fade of a lithium-ion battery being based on the formation of this SEI layer. They used a single particle model as comparison between low-order and higher order models, and showed the spatial distribution of SEI growth within the through plane direction of the electrode is relative constant. Ramadass *et*

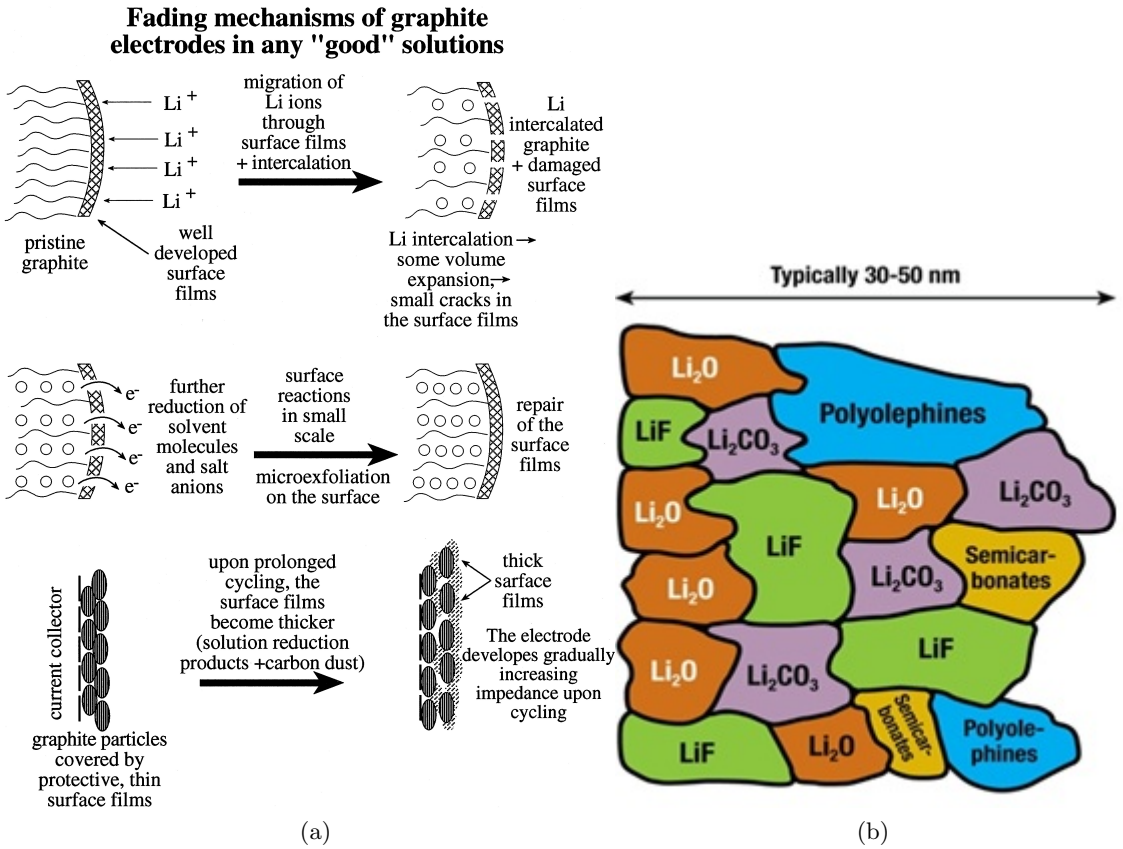


Figure 2.7: (a) Composition of solid electrolyte layer adapted from [157] and (b) A schematic illustration of surface films on graphite electrodes upon prolonged cycling [12]

al. [165] developed a first principles model for capacitance fade in lithium-ion batteries, specifically looking at the degradation caused by solvent reduction and formation of a passive SEI layer. Parameters such as the Depth Of Discharge (DoD), film resistance, exchange current density and over-potential of the parasitic reactions were investigated. Results show highly non-linear rates of SEI layer growth with increasing reaction current density and decreasing cell capacity with increasing number of cycles.

Lin *et al.* [127] also presented a physics based model of the SEI layer formation in lithium-ion batteries; however, also coupled this with other mechanisms of degradation, namely: manganese deposition on the anode, manganese dissolution, electrolyte oxidation and salt decomposition on the cathode. They suggested that with this model three regions of degradation are observed upon cycling, acceleration, stabilization and saturation. In the accelerated stage, capacity fade can be mainly attributed to the anode SEI formation. In the stablisation region, the SEI layer gets thicker and the growth rate decreases, the cathode manganese dissolution rate now occurs faster and the cathode also becomes more intercalated at the end of discharge. In the saturation stage, cathode capacity becomes the limiting factor. This paper therefore highlights the need for coupled models of the anode and cathode to capture the inter-dependancies and effect on the overall cell performance. They also highlight shifting operating stoichiometries which is a hidden problem in that the cell potential is a combination of the anode and cathode potentials, and a decoupling of this is required.

The main caveat with these modelling works is the lack of experimental validation of the works and also in the cases where experimental data is provided how reliable is the data in assigning the observed capacity/power fade is to SEI formation and not any other mechanism.

Cathode degradation

The degradation mechanisms for the battery cathode are different from that of the anode. These are shown in Figure 2.8.

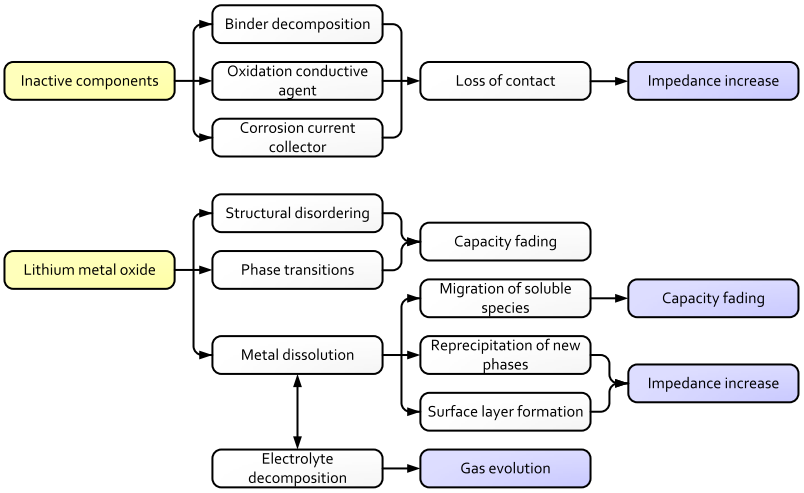


Figure 2.8: Cause and effects of cathode degradation. Adapted from Vetter *et al.* [207]

More dangerous side reactions include the oxidation of the cathode material. Under normal conditions, the battery operates within the oxidative limits of the electrolyte. If there is an overcharge event, and the cathode is operated outside of the potential stability region, no protective film forms on the cathode leading to continued oxidation of the electrolyte, potential gas evolution and catastrophic failure of the cell. Overall, both the anode and cathode decomposition reactions imply a consumption of activate material and electrolyte leading to gas evolution. This results in an irreversible loss of battery capacity [184].

Effects outside of operating limits

Gradual degradation of lithium-ion batteries occurs when kept within the manufacturers prescribed limits; however, if the battery is operated beyond these limits more detrimental effects can occur that can result in catastrophic failure. Depending on which region of operation is exceeded different failure modes can be expected. Figure 2.9 shows typical failure/degradation mechanisms outside of the prescribed limits.

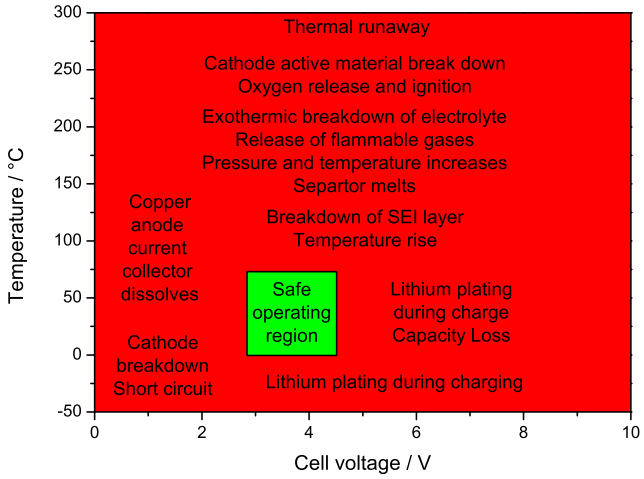


Figure 2.9: Effects of operating a lithium-ion battery outside of the prescribed limits. Adapted from Electropedia [70]

2.2.3 Modelling of lithium-ion batteries

Development of accurate models are essential for the assessment of the performance of EVs. Within the academic literature, there are currently a number of different types of lithium-ion model with the main types including: physics based, equivalent circuit and empirical based models.

Empirical models are the simplest of battery models and in its crudest form represents a look-up table. Here, there is no physics based relationship and the model relies completely on extensive test data for population of the model. These have been implemented commonly in Battery Management Systems (BMS) where the computational cost of any model must be kept low. As no physical information is retained in empirical models, this literature review will focus mainly on the other forms of battery modelling.

Equivalent circuit models

Equivalent Circuit Models (ECM) use a combination of passive electrical components to recreate the electrical response of a lithium-ion cell [42, 94, 86, 119]. This method of modelling a battery has the advantage that the model is computationally cheap; however, suffers from the fact that large data sets are required to parameterise the model and they have no predictive power outside of their parameterised limits due to an absence of fundamental physics. Figure 2.10 shows an example of a typical equivalent circuit model. Typically, more RC branches are added to increase the accuracy of the model however the drawback of this is that it becomes increasingly less based on any physical meaning and requires parameterisation. A look-up table is also commonly required to represent

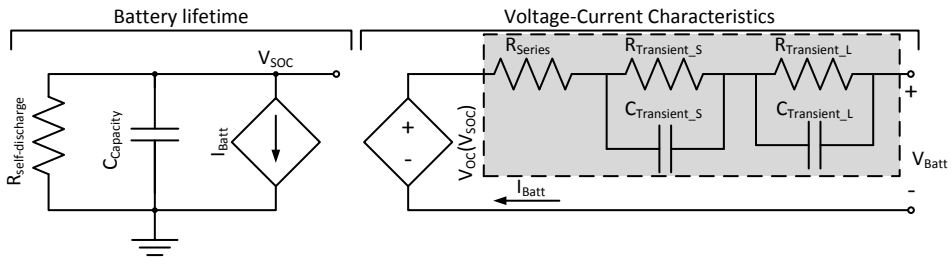


Figure 2.10: Example of an equivalent circuit model. Adapted from Chen *et al.* [42]

Table 2.4: Equivalent circuit models and key features. Adapted from [94]

Model	Features
Shepherd model	The model describes the electrochemical behaviour of the battery directly in terms of voltage and current
Unnewehr Universal model	The model simplifies the Shepherd model and attempts to model the variations in resistance with respect to SOC
Nernst model	The model can be viewed as a modification to the Shepherd model and uses exponential function with respect to SOC
Combined model	The model can be viewed as combination of the previous three models to obtain the most accurate performance
Rint model	The model only has 1 resistance element
Thevenin model	The model connects a parallel RC network in series based on the Rint model, describing the dynamic characteristics of the battery
DP model	The model connects a parallel RC network in series based on the Thevenin model, in order to refine the description of polarisation characteristics ans simulate the concentration polarisation and the electrochemical polarisation separately which may lead to more accurate performance

the thermodynamic potential of the cell which is a function of the state-of-charge. This is represented on the left side of the example model.

Examples of common equivalent circuits include the Shepherd model, Unnewehr Universal model, Nernst model, Rint model, Thevenin model and the DP model [94]. These are listed in Table 2.4 which also lists their features.

Whilst many works have been reported in the academic literature over a range of different fields and applications, care should be taken in interpreting the results. It has been commonly found that many works in the engineering field which use ECMs commonly make assumptions which are not appropriate based on an absence of physical knowledge of the modelled system. For example Gomez *et al.* [86] extensively tested lithium-ion batteries over the whole range of operation to create parameter maps of variables as a function of SOC and temperature to feed into equivalent circuit models. However, a problem with this technique is that all EIS measurements were done under 'no load' conditions and as such the charge transfer resistance correlation with the drawn current was not captured. In reality the charge transfer resistance decreases with increasing load current as the rate of electrochemical reaction typically follows an Arrhenius type relationship, increasing exponentially with current as suggested by the Butler-Volmer equation [16].

Physics based models

Physics based models replicate battery performance by solving equations relating to the fundamental processes occurring within the battery such as diffusion and conservation of charge. In this way, limiting factors relating to performance can be tracked down to the fundamental cause. The drawback of this technique is that a large number of variables are required and need to be parameterised which can be difficult. In addition, physics based models are, in general, regarded as being more computationally intensive than ECMs. As a result, they are rarely employed for simulations at the pack level.

The fundamental equations governing the physical processes occurring in a lithium-ion battery were established in early works by Newman, Doyle and Fuller who set-out the mathematical frame work for a 1D physics based model [82, 61, 62, 151, 11]. Comprehensive models accounting for the relevant physical and chemical processes in a cell in the absence of degradation effects and aging have been developed [63, 75]. Effects such as double layer capacity [238, 64], growth of the SEI layer [165, 52, 167], or electrode volume changes due to intercalation [45] have been subsequently included.

The interplay between these factors and thermal effects plays a crucial role in predicting the life and performance of a cell [205]. Coupled electrochemical-thermal battery models have been focused on the behaviour of single cells [189, 229, 107]. While computationally intensive, these are promising modelling tools for predicting cell lifetime and aging, as they can track the time-evolution of the relevant processes inside a cell from first principles.

The use of these models lies in the fact that limiting performance factors can be traced back to the physical cause. Smith *et al.* [191] used the 1D model to develop a reduced order model which was computationally cheaper. This was shown to be accurate to discharges of up to 50 C to 99%; however, it was shown that when ionic transport is slow, i.e. during low temperature operation or electrolyte depletion, the system exhibits strong spatially varying nonlinearities. Smith and Wang [190] also showed the advantage of using physics based model as they identified using their 1D model that typically the solid phase lithium diffusion is the rate limiting factor in lithium-ion batteries and that during discharge the depletion of the surface lithium concentration is the rate limiting factor.

Since the original works by Newman, Doyle and Fuller, many authors have suggested improvements; however, care must be taken in the methods to validate the models. Martínez-Rosas *et al.* [133] modify the normal Newman equation boundary conditions to solve faster without loss of accuracy; however, validated only on constant current discharge cycles. Therefore, much of the unsteady behaviour has not been tested.

Colclasure and Kee [47] expands on the Newman model to include a description of other competing reaction mechanisms within the lithium-ion battery not captured in the original model without the need for the Butler-Volmer equation. This therefore allows for more fundamental studies of the mechanisms controlling SEI layer growth and lithium plating. The drawback of this approach is that many thermodynamic parameters are required which are often difficult to measure.

Ye *et al.* [229] used the 1D model to investigate thermal effects with their physics thermally coupled model and also integrated the effect of reversible entropy into the analysis. At low temperatures the contribution from lithium concentrations were shown to have a significant impact on the performance of the cell.

In recent years, authors have extended this to 2D [61, 27, 54] and 3D [91, 85, 229, 90] with coupled thermal effects. Gerver and Meyers [85] developed a 3D physics based model which was also thermally coupled to cell performance and showed that in large planar cells and under heavy C-ratings there is significant inhomogeneity in the potential and concentration profiles.

Approaches to reduce the numerical intensity of battery models include the development of the Single Particle Model (SPM) where the electrodes are approximated to a single spherical particle and the electrolyte concentration is assumed to be constant [178]. The advantage of having physical insight into processes in the cell and the lighter computational power is good however the drawback of this is that the model accuracy typically decreases at discharge/charge rates >2C.

Whilst these models capture many of the physical effects occurring within the cell they are limited to what the user programs into them. For example, thermal runaway is not normally integrated into physics based models [27]. Care must also be taken when considering works using the Newman model with newer chemistries where the fundamental physics of the battery operation are not the same as the ones modelled by Newman but with the right parameters the apparent cell voltages appear correct.

Forman *et al.* [76] uses a genetic algorithm based approach to parameterise a lithium-iron

phosphate ($LiFePO_4$) model and achieve a 5% accuracy of model fit when compared to a typical automotive load cycle. This allows for a heuristic approach to parameterization however highlights one of the major caveats of model parameterisation with physics systems in that there are many parameters and there is one school of thought which suggest that with enough parameters any data set can be recreated. In the work by Forman *et al.* [76] they use the Newman model which was originally posed for lithium-ion batteries assuming diffusion based on a constant diffusion coefficient mechanism. Recent works suggest that a staged diffusion process occurs in $LiFePO_4$ batteries and requires further modification in order to retain its physical meaning. Other authors have similarly taken the approach of using the Newman model in its unmodified form for modelling $LiFePO_4$ batteries [228].

In recent years authors have suggested that lithium-ion diffusion in olivine $LiFePO_4$ is strongly related to the phase transition of the electrode which follows a domino-cascade model instead of the more traditional core-shell model [122]. Li *et al.* [122] proposed that this can be modelled using a hybrid domino cascade and core shell model due to the strong anisotropy in the bulk material and the different properties of lithiated and delithiated stages. They attempted to validate this by looking at the linear Warburg diffusion regions of the cell and made distinctions between core shell and domino-cascade mechanisms. Dargaville and Farrell [51] proposed a phase-field model to capture the dynamics of high rate $LiFePO_4$. With their shrinking core battery model however they were not able to produce a good fit with experimental data.

2.2.4 Modelling of lithium-ion battery packs

In order to achieve practical voltages and capacities for use in automotive applications packs are created with many cells in series and parallel. The coupling of cells in series and parallel however does not necessarily mean that homogeneous loads are experienced by all of the cells.

Guo *et al.* [91] developed a mutli-cell model based on the pseudo-2D model to investigate effects of large form factor cells and the effect of interconnect and contact resistances. Large form factor cells were shown to exhibit in cell inhomogeneities in potential, concentration and temperature, which cascades down to other cells. Figure 2.11 shows the potential profile of a 3 cell pack and highlights the fact that linked potentials allow the inhomogeneities in concentration to cascade down to neighbouring cells.

Many authors have commented on the fact that differences between cells due to the manufacturing process, operating conditions and degradation rates can lead to an imbalance in cell performance which limits the overall pack performance [140, 239]. As there are so many cells, the computational cost of this is typically quite high and as such many authors tend to use approximations.

Zheng *et al.* [239] developed a decoupled 3D battery pack thermal model to estimate temperature distributions across the pack. This uses a 3D CFD based thermal model combined with an equivalent circuit battery model within different domains. The focus here was on the thermal generation hence the high fidelity CFD coupling however this was at the expensive of the electrochemical coupling. In addition the paper looks only at cells connected in series with a specific thermal arrangement based on a bespoke pack design.

Dubarry *et al.* [65] presents a 'universal' approach to simulating battery pack performance which takes into account the cell-to-cell variations. They also use a equivalent circuit model to approximate the cell performance and parameterise this against test data and then incorporates this data into a network of equivalent circuit models to achieve better accuracy. The drawback to this is the large amount of experimental data required and

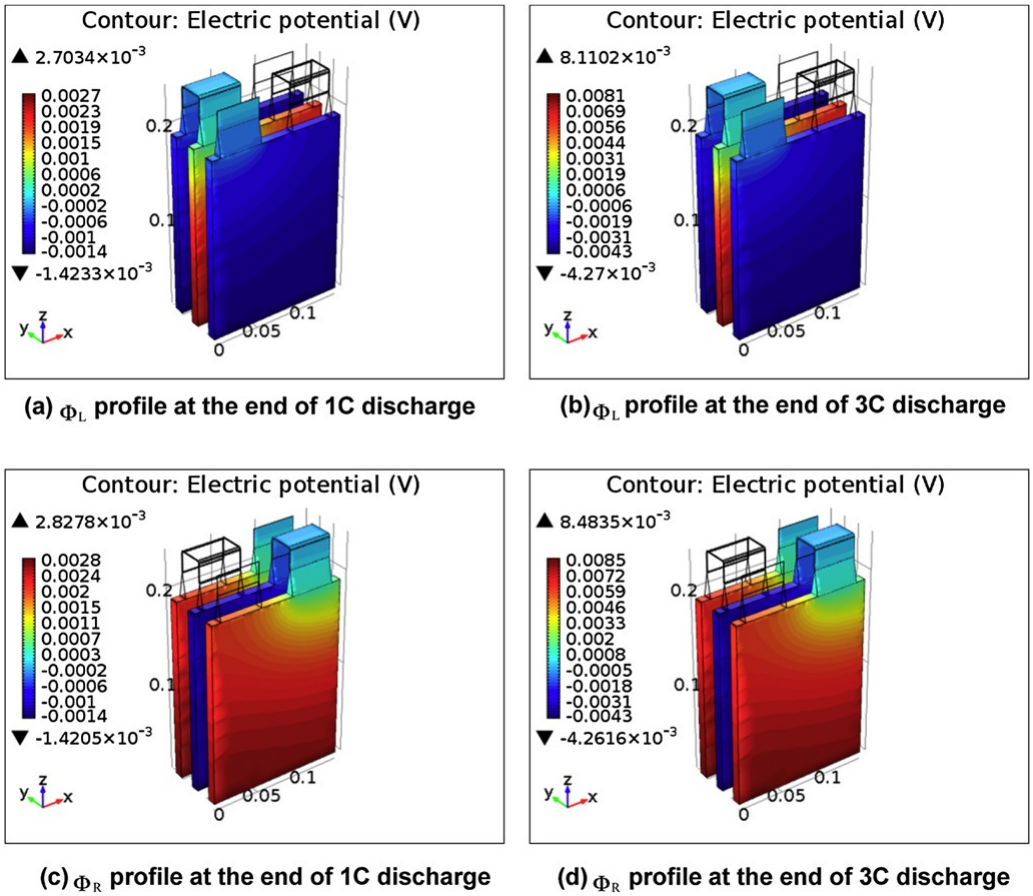


Figure 2.11: The profiles of potentials on a 3 cell series pack at the end of a 1C and 3C discharge process [91]

loss of physics based information.

Li and Mazzola [119] developed a model of a 21.3 kWh automotive lithium-ion pack based on an electrical analogue of the pack performance without consideration of the single cell behaviour. Their model, whilst running fast does not consider thermal effects nor degradation issues and was tested under mild conditions with test currents of only approximately 0.5 C. They do not consider interconnect resistances and lump together all processes in their parameterisation.

Wang and Srinivasan [211] developed a multi-scale battery model using physics based equations from the pore level to cell level and then to stack model. The model is electrochemical and thermally coupled. However, they do not take into account practical interconnection electrical effects which can adversely affect the performance of the pack and make simplifying assumptions in the fundamental equations in order to reduce computational time.

This therefore highlights the gap between the engineering application of the technology in that the physical connections need to be accounted for. One of the things often neglected in pack level modelling is the finite interconnection resistance of connecting cells together, which authors have commented as being significant [162]. Validation of these models have also appears to be under mild, constant current load cycles or load cycles. More aggressive dynamic validation of models is not typically seen and no standard load cycle is current in use that represents automotive load cycles.

2.2.5 Thermal management

As the power and energy requirements increase, a key concern for both cell manufacturers and designers of battery control systems is thermal runaway [202]. If a cell generates more heat than can be dissipated, and the cell heats above 90°C, decomposition of the passivating SEI layer on the surface of the anode takes place [193]. The electrode becomes exposed to the electrolyte, solvent molecules diffuse through the anode and react with the intercalated lithium ions, leading to exothermic reactions, gassing, and partial exfoliation of graphite. When the self-heating rate surpasses 10°C/min, the process is usually irreversible. Depending on its size, design and materials, a cell enters the runaway regime somewhere between 130°C and 220°C [93]. In addition to overcharging/ overdischarging, thermal runaway can also be influenced by the environment in which it operates: external sources of heat and low heat dissipation rates can cause thermal runaway within otherwise normal operating conditions. Separators with shut-down capabilities have been shown to be effective against thermal runaway only for small packs [174].

2.2.6 Summary of lithium-ion battery literature review

Based on the literature review of batteries presented the following can be summarized.

- Lithium-ion batteries are the current technology of choice in automotive applications with carbon based anodes and materials such as $LiCoO_2$ and $LiFeO_4$ being common cathode materials used
- The main battery degradation mechanisms have been identified as being the formation and growth of the SEI layer on the anode which reduces the amount of cyclable lithium and also an increase in cell resistance leading to capacity and power fade over time. Few works have conclusively experimentally validated the SEI growth rate, with a decoupling from other degradation mechanisms and correlated this with performance
- Physics based electrochemical battery models and ECMs are the most commonly adopted battery models with physics based models showing more use when analysing degradation issues. The most commonly used physics model is based on the original Newman models which solve for diffusion and charge conservation assuming continuous mechanics
- Current battery pack modelling is mostly limited to the use of equivalent circuit models and neglects the consideration of contact resistances between cells which can become appreciable with larger capacity cells

The subsequent works will focus on the development of a physics based model which accounts for SEI layer growth and the use of this model to probe pack level effects when scaling to larger systems.

2.3 Proton Exchange Membrane Fuel Cells

Similar to lithium-ion batteries, there have been many thousands of publications in the academic literature relating to PEMFCs. The focus of this literature review is to identify the areas and work relating to PEMFCs in automotive applications with regards to cell level modelling, system level modelling, degradation mechanisms and failure models, with a view of identifying a suitable model fidelity and gaps in the current academic literature to motivate later sections of work.

The wide spread commercialisation of PEMFCs is currently limited by the two main barriers of cost and durability [214]. Lifetime requirements of automotive systems have been quoted as being in the region of 5,000 hours with less than a 10% performance decay [183].

There are currently a number of different FC technologies which are commercially available and which are under development. These include the Alkaline Fuel Cell (AFC), Phosphoric Acid Fuel Cell (PAFC), Solid Oxide Fuel Cell (SOFC), Molten Carbonate Fuel Cell (MCFC), PEMFC and Direct Methanol Fuel Cell (DMFC). Each of these devices have their respective advantages and disadvantages. Details of each device are shown in Table 2.5.

Of the presented FC types PEMFCs show the greatest promise in automotive applications due to their fast start-up and low temperature operation. PEMFCs convert hydrogen into electricity with the only by-product being water at an efficiency typically greater than an ICE. A PEMFC generates electrical power by oxidising hydrogen with oxygen in a controlled reaction. In order to extract useful electrical work, the reaction is facilitated by a ionically conducting but electrically insulating polymer membrane, usually made from a sulfonated tetrafluoroethylene based fluoropolymer-copolymer usually called Nafion. A schematic diagram of a cross section of a FC is shown in Figure 2.12.

The side which is supplied with the hydrogen is known as the anode and the side which is provided with the oxygen is known as the cathode.

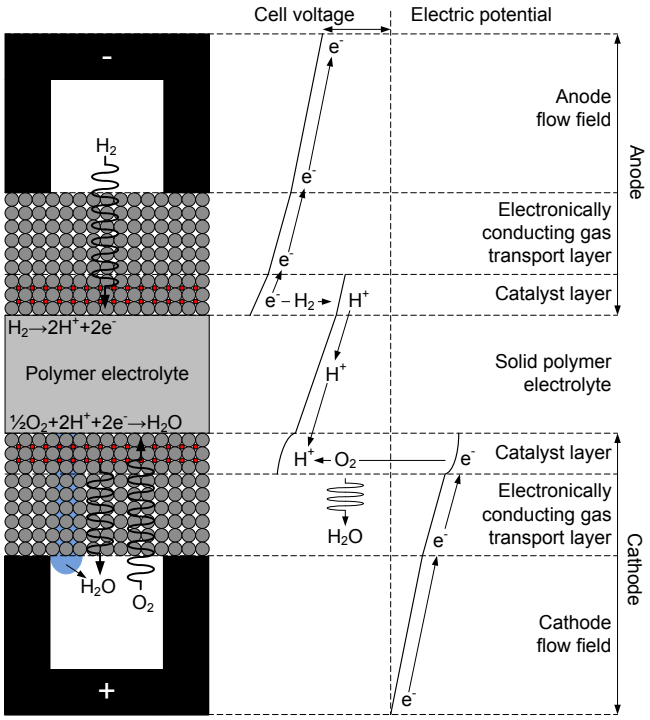


Figure 2.12: Cross-section of PEMFC. Adapted from [112]

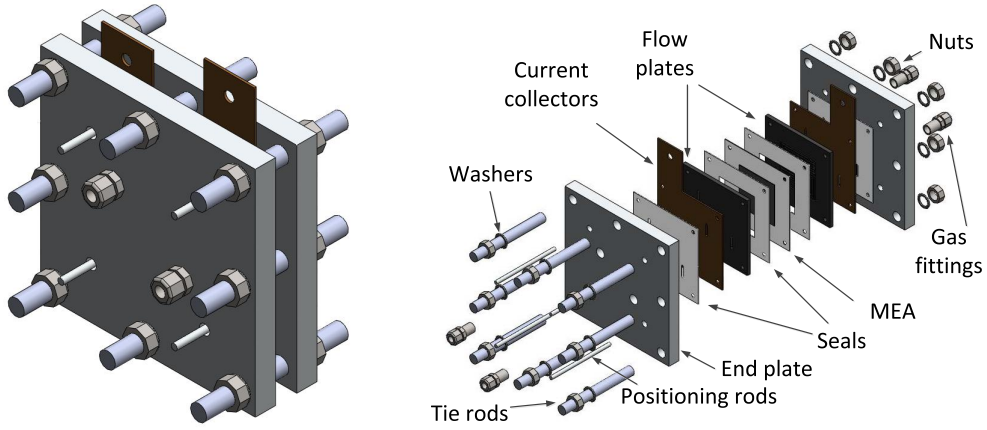
Table 2.5: Comparison of different fuel cell technologies. Adapted from Mekhilef *et al.* [136]

Fuel cell type	Common electrolyte	Fuel	Operating temperature / °C	System output / kW	Electrical efficiency / %	Advantages
Alkaline (AFC)	Aqueous solution of potassium hydroxide soaked in a matrix	Pure H_2	90-100	10-100	60	Cathode reaction faster in alkaline electrolyte, leads to higher performance. Can use a variety of catalysts.
Phosphoric Acid (PAFC)	Liquid phosphoric acid soaked in a matrix	Pure H_2	150-200	50-1000	>40	Higher overall efficiency with CHP. Increased tolerance to impurities in hydrogen.
Solid Oxide (SOFC)	Yttria Stabilized Zirconia	H_2, CO, CH_4, Others	600-1000	<1-3000	35-43	High efficiency. Fuel flexibility. Can use a variety of catalysts. Solid electrolyte reduces electrolyte management problems. Suitable for CHP. Hybrid/ GT cycle.
Molten Carbonate (MCFC)	Liquid solution of lithium, sodium, and/ or potassium carbonates, soaked in a matrix	H_2, CO, CH_4, Others	600-700	<1-1000	45-47	High efficiency. Fuel flexibility. Can use a variety of catalysts. Suitable for CHP.
Polymer Electrolyte Membrane (PEMFC)	Solid organic polymer poly-perfluorosulfonic acid	Pure H_2	50-100	<1-250	53-58	Solid electrolyte reduces corrosion and electrolyte management problems. Low temperature. Quick start-up.
Direct methanol (DMFC)	Solid polymer membrane	CH_3OH	60-200	0.001-100	40	Reduced cost due to absence of fuel reformer.

A typical cell is made up of a number of components. The core of the cell is the polymer electrolyte that allows ionic transport but is electrically insulating. On either side of the membrane is a carbon supported Catalyst Layer (CL) that reduces the activation energy required for the reaction such that it can happen at low temperatures. The catalyst typically used is platinum supported on a carbon support. Typically, the platinum loading on the cathode CL is higher due to the higher bonding energy of oxygen relative to hydrogen. On top of this is a Gas Diffusion Layer (GDL), often made of a porous carbon paper/ carbon felt. Occasionally, a Micro-Porous Layer (MPL) is added between the GDL and CL to aid with reactant distribution and water management [217]. These elements are collectively known as the Membrane Electrode Assembly (MEA). However, the MEA on its own is not usable. Graphite plates, typically, act as reactant distributors to the MEA as well as providing electrical conductivity to extract the useful electrical work. Copper current collectors are typically used to extract the useful electrical work. Stiff end plates are used to apply an even compression to the cell and the flow plate and gaskets provide a gas tight seal for reactants. Coolant flow channels are typically included for high power systems. In smaller open cathode systems, this is sometimes not required as the forced convection from the reactant air is sufficient to remove the excess heat. Figure 2.13 shows a typical construction of a single cell.

A single FC can typically achieve an OCV of approximately 1V with a maximum current density of approximately 1000 $mAcm^{-2}$. In order to achieve practical voltages and currents, these cells are connected in series and can be made with larger active areas. A series of MEAs and bipolar plates is therefore known as a FC stack. In order to increase the voltage of a FC system to practical levels for automotive applications, single cells are stacked together to create a FC stack. The flow plates in this arrangement are bipolar since they share the anode/cathode of two neighbouring cells.

The FC stack itself however cannot produce useful electrical power. Ancillary components know as the Balance-Of-Plant (BOP) are required to deliver the reactants and remove any excess thermal energy. In terms of FC systems, which includes all the associated BOP, their are many factors which determine the overall system efficiency and durability which will be discussed hereafter.



(a) (b)

Figure 2.13: (a) CAD drawing of a PEMFC cell and (b) exploded drawing showing typical components

2.3.1 Fuel cell modelling

In order to predict the dynamic behaviour and thus the efficiency of any FC system, a model is required. Depending on the length and time scales of interest different authors have applied different methods of modelling. The three main forms of FC modelling found in the academic literature are physics, semi-empirical and fully empirical models. This work will focus mainly on physical/ semi-empirical based models as these capture the appropriate length and time scales of interest with an acceptable level of computational cost.

Figure 2.14 show a brief history of models found in the academic literature on modelling of FCs which summarised the level of details and effects captured. It can be seen that over time more and more effects and coupled effects including water and thermal management have been added including a general increase in studies using dynamic models. However, at the same time it can be seen that modelling has not converged into one area with all the coupled effects, with many modern works neglecting certain effects.

Physics based models

One popular type of FC model is the physics based model which takes into consideration the heat and mass balances occurring within the FC stack. This allows for effects in the FC to be investigated with knowledge of the fundamental driving process. The drawback of this is that many parameters are typically needed, some of which are difficult to determine and it typically focuses on the single cell level.

Much of the earlier mathematically framework for later models in the literature was established by Springer *et al.* [194] and Fuller and Newman [81].

Springer *et al.* [194] presented an isothermal, 1D steady-state model of a PEMFC with a Nafion 117 membrane. They focused their modelling efforts on the water transport effects within the membrane and considered the effects of water diffusion coefficients, electro-osmotic drag coefficients, water absorption and membrane conductivities. They used their model to predict that the series resistance of the membrane increases with increasing current density at steady state conditions. The limitations of this model include not being able to handle water saturation situations, being steady state, isothermal and only considering the water transport effect and not of the whole system.

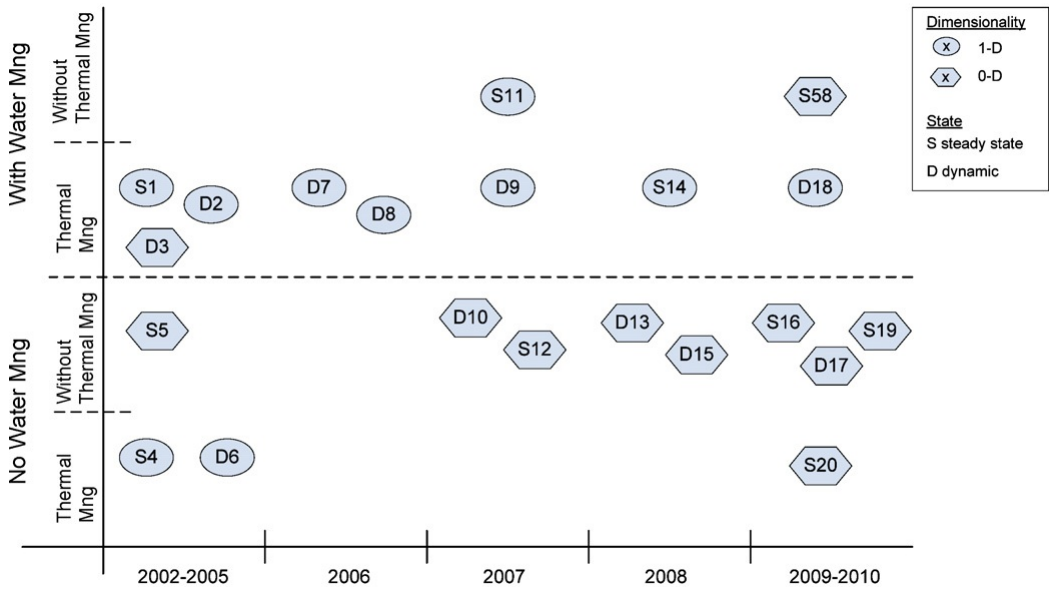


Figure 2.14: History of modelling studies [241]

Fuller and Newman [81] later extended this model to 2D and considered the dependencies between water and thermal management and that of the fuel utilisation on the overall performance of a FC. They identified that temperature is a critical consideration in any water management study and isothermal model results vary from non-isothermal ones.

Weber and Newman [217] later used their physics based model and developed a two phase flow model to investigate the performance implications of the introduction of a MPL into the MEA. Simulations show an increase in performance with using the MPL compared to without due to better oxygen transport and ohmic effects. Ohmic improvements arise due to better structural stability, improved interlayer contact and better CL utilization. The MPL also acts as a 'valve' which pushes water away from the cathode GDL and through the membrane to avoid flooding.

Since then, authors have continually been adding detail to the model. Amphlett *et al.* [4] considers the Stefan-Maxwell, Nernst, Nernst-Planck equations to replicate the FC performance, however with increasing levels of complexity comes increasing numbers of variables, many of which can be difficult to extract, especially when there are so many interdependencies. As such, semi-empirical relationships are often used which arise from parameterisation with modelled data.

Computational Fluid Dynamics (CFD) based models have since been used to combine with the fundamental electrochemistry based equations to allow for detailed analysis of flow field designs however these come at an increasing computational cost. Wang and Wang [212] presented a 143×143 cm FC model which takes into account the geometry of the flow field channels to model the current distribution within a single cell. The generated mesh of 23.5 million nodes took approximately 20 hours to converge to a solution with a 2.8 GHz Intel Pentium 4 CPU. This therefore highlights the need for reduced order models to reduce computational time.

Semi-empirical models

Much of the current literature revolving around control system development of FC systems use semi-empirical models which lump the cell performance owing to the faster computational speed compared to full physics based models. Table 2.6 lists different semi-empirical FC model works in the literature along with a short description of their purpose, mostly of which were developed with the aim of investigating performance implications in different conditions or developing control algorithms. Much of the work is based on the same fundamental physics based processes however the semi-empirical elements of the models needs close consideration when models are used outside of the their parameterised conditions as many semi-empirical models are steady.

Stack models

Beyond modelling the processes within the stack, many authors have also extended to the modelling of the associated ancillary BOP which is important in assessing the dynamic response of systems and also the addition loss required to achieve a certain reactant delivery performance, known as the parasitic power consumption.

Much of the work done on developing system level models has been done with the motivation of development of models for developing more optimized controllers to increase FC dynamic performance with advanced controllers.

Yu *et al.* [230] developed a dynamic PEMFC stack level model based on physical transport phenomena including mass transport effects, electrochemistry, heat transfer and water management. Based on their model results of a Ballard FC stack, it would take the stack approximately 30 minutes to reach a steady state temperature. However, their

Table 2.6: Semi-empirical models of fuel cells. Adapted from [241]

Author	Description and focus
Fowler *et al.* [78]	Study of the voltage degradation and the end of life issue
Ceraolo *et al.* [37]	Identification of numeric values for parameters, assumption of uniform pressure, procedure for evaluation of the parameters
Al-Baghdadi [2]	Investigate the impact of operating conditions to performance, not extensive calculations
Caux *et al.* [36]	Modeling of control auxiliaries, control, boost converters, quasi static, use in vehicular applications
Pathapati *et al.* [156]	Effects of charge double layer and behaviour on sudden load changes, transient phenomena
Wishart *et al.* [220]	Develop a methodology to obtain optimal operating conditions, include BOP. Two performance objectives: maximize net system power and maximize the system exergetic efficiency
Zong *et al.* [242]	Analyze water transport across the membrane and shift change effect, pressure variation along the channel
del Real *et al.* [55]	Development and experimental validation of a dynamic model. Suitable for control studies
Hou *et al.* [96]	Simplified model applied for vehicle applications. Effect of temperature and pressure into performance
Wingelaar *et al.* [219]	Electric circuit representation with small signal and large signal characteristics. Use EIS
Outeiro *et al.* [152]	A parameter optimized model as an electrical equivalent circuit. Optimization method: simulating annealing. Including temperature effect
Li *et al.* [121]	Fast approach to predict the performance. Analysis through a series of experiments
Miansari *et al.* [137]	Thermodynamic approach with study of channel dimension. Effect of temperature, pressure and air stoichiometry on the exergy efficiencies and irreversibilities
Moreira and da Silva [142]	Practical model for performance evaluation with few calculations and sum up into one equation

work considers ideal and fully controlled flow into the stack and does not consider any of the ancillary BOP components.

Pukrushpan *et al.* [163] adopted much of the semi-empirical modelling work of the FC stack from Amphlett *et al.* [4] and incorporated it with transient models of a compressor and gas manifolding effects in order to develop improved control algorithms. This considered all of the heat and mass transfer equations previously set out; however, it did not have an unsteady thermally coupled model for the stack temperature.

Since then, authors such as Özbek *et al.* [153] have adopted the stack modelling work presented by Pukrushpan *et al.* [163] and Amphlett *et al.* [4] in order to investigate controller development for the air subsystem. They show that the typical feedforward controllers reduce system efficiency due to the transient depletion of oxygen under large step-loads and thus propose a novel gain scheduling controller to improved performance. This was for a 1.2 kW system and thus assumed a constant stack temperature; however, larger automotive systems will require cooling systems and consideration of modelling thermal effects also.

Panos *et al.* [155] presented a unsteady heat and mass transfer based model of a FC system, which includes a simplified thermal, cathode and anode subsystem models. The aim of this model was to develop Model Predictive Controllers (MPC). Whilst the work focused on developing the controller to improve the performance of the FC stack to transient load cycles there was no comment on the additional power required to achieve the improved stack performance. Thus one could suggest that the additional power required to achieve improved stack performance may have included the parasitic power consumption leading to a net decrease in system efficiency.

The limitations of many of these developed models for control have been that they are lumped models which considers the performance of the FC as uniform between cells. As larger systems are created, reactant inhomogeneities become increasingly evident and this modelling work of larger systems should be taken with a degree of consideration. For example, Nolan and Kolodziej [145] presented a thermal model of an 120 kWe PEMFC stack but provided a simplified model of the other non-thermally related systems in order to develop their reduced order models to control applications. Whilst their results showed reasonable agreement in the thermal data there was no validation of any electrochemical effects.

Authors have since modified the semi-empirical models of single cells to try and account for reactant and temperature inhomogeneities in large systems. Musio *et al.* [143] presented a MATLAB based model which used semi-empirical steady state equations previously outlines and extended this to a 20 cell open cathode 300 W system. Whilst steady state results showed reasonable agreement, dynamic response was less accurate and open cathode systems have only a niche application in automotive systems due to limited scalability due to thermal management issues.

2.3.2 Water management

Many authors have identified water management in PEMFCs to be of critical importance [120, 183, 30, 66]. Water is the product of the hydrogen PEMFC reaction and a well hydrated membrane allows for good ionic conductivity of the Nafion membrane. Figure 2.15 shows the different mechanisms of water transport that are known to occur within a FC MEA.

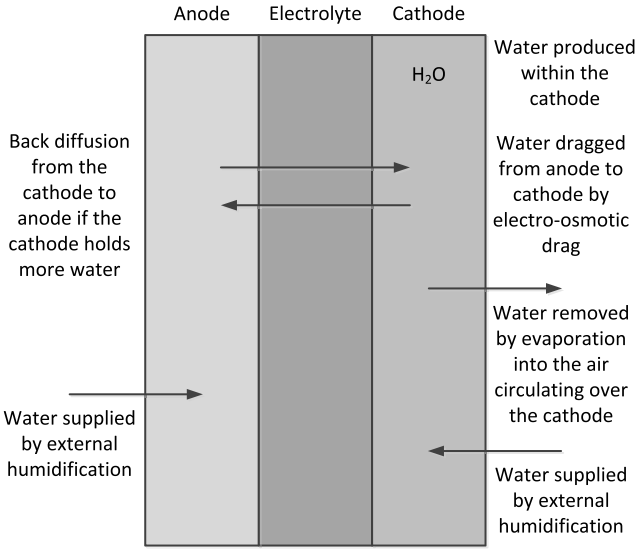


Figure 2.15: Modes of water transport within a fuel cell MEA. Adapted from Larminie and Dicks [115]

Water management is therefore a function of the FC MEA design itself, with the many authors suggesting modifications to the GDL hydrophobic and hydrophilic nature, as well as addition of a MPL to aid with prevention of flooding [217]. External factors also have a significant influence on the water management such as the pressure, temperature humidification of the reactant streams. If this is not suitably managed it can cause either dehydration of the membrane leading to increased ohmic resistance or excessive amounts of water being produced leading to stack flooding whereby water prevents gas diffusion to the MEA.

On a overall cell level, flooding can cause reduced potentials as shown in Figure 2.16. This mainly affects the performance at higher current densities as flooding causes the blockages of gas diffusion channels and gas diffusion rates are higher at higher current densities.

Dutta *et al.* [66] presented a 3D model of a PEMFC flow channel which considered the Navier-Stokes equation and the electrochemical reactions occurring. Their results indicated that flow distribution in both the anode and cathode are significantly affected by the mass consumption patterns of the FC, and thus the current with water transport mainly governed by the electro-osmotic drag and back diffusion effects. These can therefore affect the pressure drop across the cathode. Büchi *et al.* [30] developed a segmented cell system to probe heterogeneous current densities within a single cell. Results show that local current distribution is strongly influenced by the dew point of the air and stoichiometry, with larger inhomogeneities at low stoichiometries and low dew point temperatures.

Observation of anode and cathode pressure drops can therefore be used as an early indicator for stack flooding. Some authors have investigated this effect further by the creation and test of segmented FCs whereby the current density can be measured locally within a single cell. Lin *et al.* [126] tested a 25 cm^2 cell in order to test the effect of local current density under constant voltage operation for different relative humidity conditions. Periodic spikes in the current profile were observed and this suggested local regions of the cell were either being flooded or dehydrated leading to unstable performance. Optimization of the relative humidity to minimise the instabilities was achieved by regulating the relative humidity of both the anode and cathode. Results showed that the relative humidity control of the cathode has more of an influence than the relative humidity of the anode.

These oscillations in performance due to water formation and the removal can also be detected in the pressure drop across the stack. During dynamic operation, pressure drops

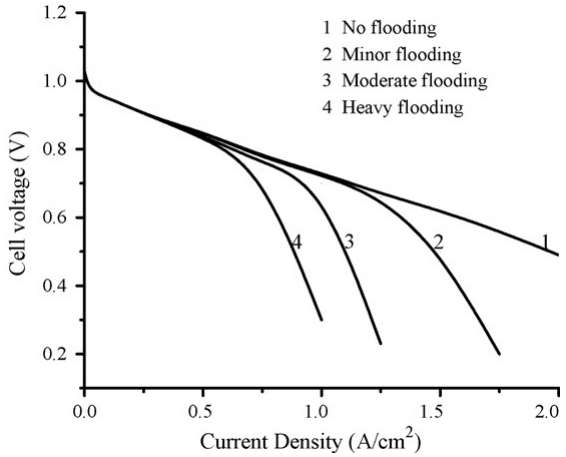


Figure 2.16: Polarisation curves of a PEMFC illustrating the effect of water flooding on cell performance [120]

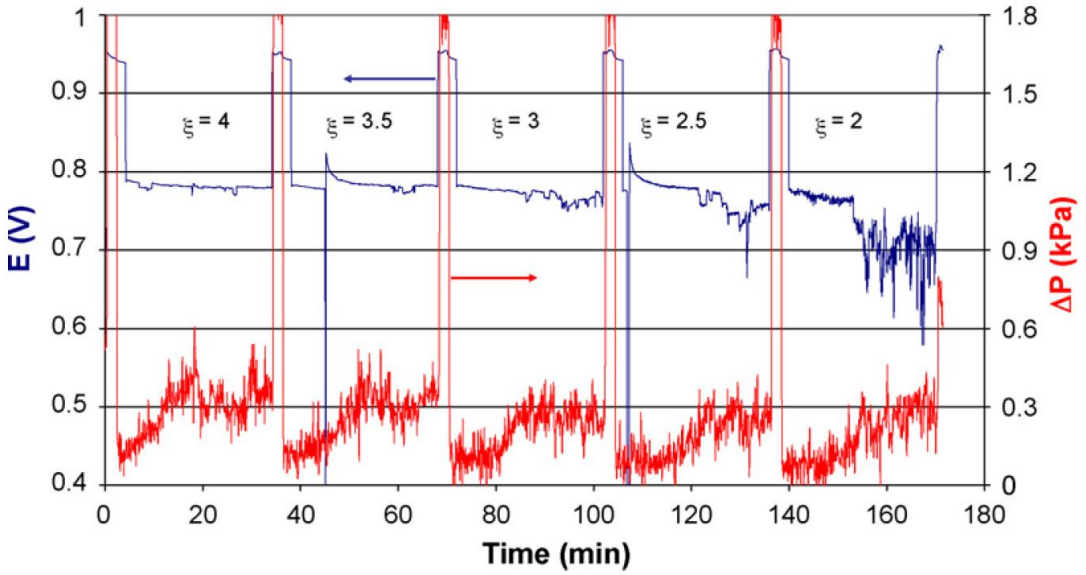
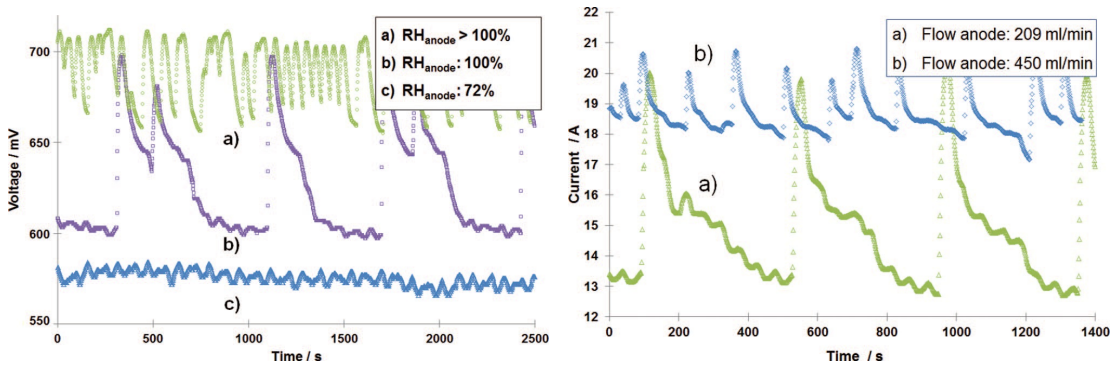


Figure 2.17: Cell voltage and cathode side pressure drop measured under various air stoichiometric ratios (symbolized by ξ in the figure) in a 14 cm^2 fuel cell for 0.2 $A.cm^{-2}$, 150 kPa and 80°C wiht the dew point of both H_2 and air at 70°C [213]

can indicate the presence of excess water. Under dynamic testing of a 10-cell stack, Chen and Zhou [41] showed that long time voltage oscillations could be observed when a change in load was applied. This effect was also noticed in the anode/cathode pressure drops indicating some sort of correlation. In order to relate the variables together, a FFT was performed. It was shown that the dominant frequency of the cathode pressure drop was found to be an early inductor for stack voltage drop. For the dominant frequency for anode pressure drop, this indicated the presence of water in the anode, usually from back diffusion from the cathode.

Wang *et al.* [213] developed a two-phase flow model of a PEMFC to investigate the effect of flooding. Experimental results from their paper, as shown in Figure 2.17, showed that with increasingly low stoichiometries flooding becomes more of an issue as indicated by the drop in cell potential under constant current operation. The onset of flooding can be inferred from the increase in cathode pressure drop due to the formation of liquid water. Periodic pulses of air can be used to mechanically remove this water, as suggested by the data where the pressure drop decreases after each pulse. The ramifications of flooding can include: fuel starvation leading to carbon corrosion of the CCL, oxygen starvation leading to hydrogen evolution on the cathode and further more H_2/O_2 combustion and hot spot formation, flow maldistribution amongst parallel channels leading to operational instabilities and efficiency losses and mass transport losses at high current densities.

Sanchez *et al.* [177] showed the oscillations in the measured cell potential arise when the FC is supplied with dry air and fully humidified hydrogen. They suggested that the periodic oscillations are due to changes in flow type from single to two phase flow in the anodic channels with the orientation of the stack, and design of the flow fields, affecting the oscillatory response observed. Figure 2.18 shows the response of a single cell under different anodic operating conditions. It can be seen that instabilities in the measured cell potential arise when operating the anode near and in excess of the maximum relative humidity, suggesting liquid water formation. Similarly, it was shown that higher anodic flow rates also allows less dynamic oscillations, likely due to the increased water removal capabilities.



(a) (b)

Figure 2.18: (a) Effect of the anode RH on the oscillation behaviour, anode RH of:72% (triangles), 100% (circles) and 137% (diamonds). (b) Effect of the anode flow on the oscillations. Anode flow values: 209 mL/min (triangles), 450 mL/min (diamonds), potentiostatic mode. [177]

2.3.3 Studies on larger systems

The vast majority of the academic literature has focused on the performance of FCs with a relatively small electrode area; however, FC systems for automotive applications will typically have to be on the order of 10-100 kWe in electrical output in order to meet automotive power requirements. Therefore, the scale up of systems needs to be considered and inhomogeneities in performance begin to come about with the increase in the scale of the power output.

With larger systems, reactant inhomogeneities are more likely to occur due to differences in the local pressure drop of the individual cells. This will likely have an impact on the performance of the overall system. Liu and Li [128] showed that these inhomogeneities can significantly affect the performance of the FC stack and suggested the use of a novel manifold design to compensate for the different pressure drops. Whilst their 4-cell stack showed improvements in the stack performance, the eventual integration of this into larger automotive systems seems unlikely due to the additional cost, weight, complexity and pressure drop.

Lin *et al.* [125] also studied current inhomogeneities in large cells and showed that when higher values of current density are measured at the outlet, relative to the inlet, and suggested that there is insufficient humidification in the inlet area which results in higher ohmic resistance resulting in higher currents at the outlet. This is shown in Figure 2.19 and indicates the current density can vary significantly within a single cell. Differences in the local anode and cathode current densities were found to be not significant due to the larger in-plane resistance of the cell, relative to the through plane direction.

The problem arises that when FCs are stacked together for practical applications their behaviour changes compared to when in a single cell format. The cause of this is due to non-uniformities in cell voltages across the stack, temperature differences and variations in reactant concentrations in the flow channels which are not observed at the single cell level [138]. This was demonstrated by Chu and Jiang [46] who compared single cell and a 30 cell stack perform. Here they found that the OCP, Tafel slope and DC resistance of the cumulative number of single cells did add up, however the mass transport effects did not follow the same trend due to variations in heat exchange, humidity and reactant supplied.

Not only are the reactants in a large stack linked but since bipolar plates connect the cells they are also electrically connected. Thus, propagation of performance from one cell to another is possible even with the same reactant delivery. Santis *et al.* [179] developed

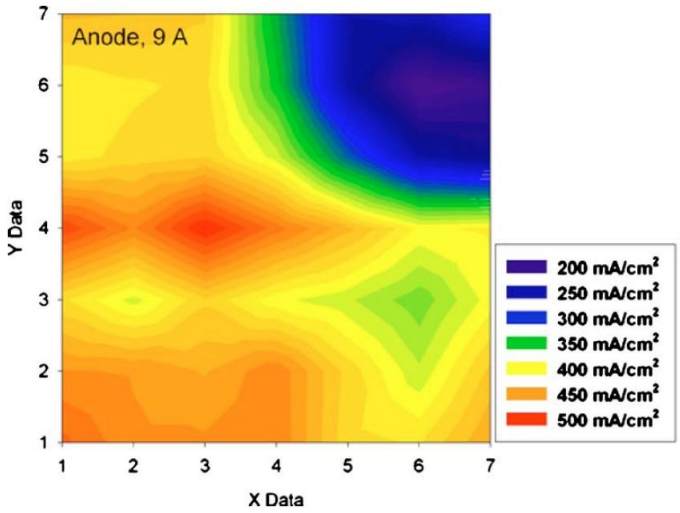
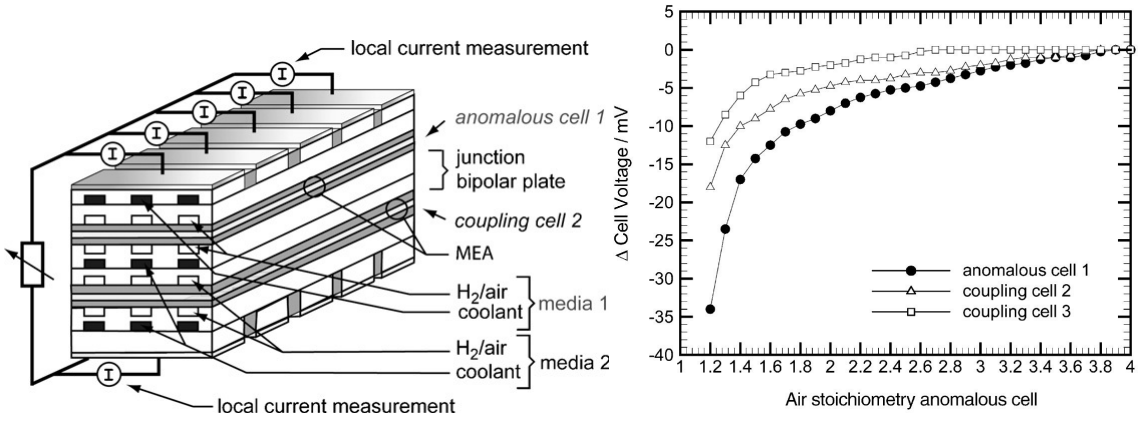


Figure 2.19: Current density distribution measurements at galvanostatic mode with fully humidified MEA at 80°C [125]. Lower current densities in the inlet (top right) suggest higher resistance due to poor humidification resulting in higher current densities at the outet (bottom left)

a segmented cell system to induce reactant and cooling dissimilarities in a single cell of a stack to monitor the performance on the other cells. Results shows that artificially induced air starvation in one cell can propagate to neighbouring cells with the changes in the local reaction current density occurring at the common bipolar plate due to its finite thickness and resistance. Figure 2.20 shows the results of changing the local air stoichiometry in one cell relative to keeping other constant and thus the coupled effect on performance. The effect is more significant at lower operating stoichiometries and could arise when water forms locally within the stack blocking channels within one flow plate.

Rodatz *et al.* [172] confirmed the critical aspects of reactant heterogeneities on cell performance with testing presented on an 6 kW 100-cell system. They highlight the need to monitor individual cell voltages to avoid failures due to reactant under supply, leading to negative potentials and hot spot formation since the cell potential acted as the limiting factor. System level methods suggested to circumvent these issues included



(a) (b)

Figure 2.20: (a) Simplified diagram of two cell stack with independent media supplies and location of local current density measurements at the stack periphery and (b) 1+2-cell stack showing the changes in cell voltage of the anomalous cell 1 and coupling cells 2 and 3 as a function of the air stoichiometry in the anomalous cell 1

current pulsing to impede the build up of platinium oxide layer and the related decrease in performance as well as reactant pulsing to remove liquid water.

2.3.4 Fuel cell degradation

In order for mainstream uptake, a PEMFC for automotive applications is expected to have a lifetime of approximately 5,000 hours for typical consumer vehicles and 20,000 hours for buses [237]. A detailed understanding of the degradation processes is therefore required in order to design systems that maximize the lifetime of the PEMFC. Zhang *et al.* [237] presented a review of PEMFC degradation processes and identified a number of factors, these being: PEM thinning, CL degradation due to platinum sintering or carbon support corrosion and GDL degradation. Among these factors CL degradation has been shown to be the most significant [237].

Carbon-supported platinum is the most commonly used catalyst for the PEMFC Oxygen Reduction Reaction (ORR), with the Cathode Catalyst Layer (CCL) being the most critical factor in the long term durability of the cell performance [58]. Although a variety of catalyst materials are being investigated Pt/C and Pt-modified or alloyed catalysts are the most popular due to their low overpotentials and high catalytic activity for the Hydrogen Oxidation Reaction (HOR) and the ORR as well as their ability to withstand the highly acidic environments inside a PEMFC.

Factors affecting the carbon corrosion rate include the operating current density, where lower current densities and high cell potentials have been shown to accelerate the carbon oxidation reaction [80]. Franck-Lacaze *et al.* [80] investigated carbon corrosion by applying hour long pulse loads between 540 mA.cm^{-2} and 120 or 20 mA.cm^{-2}. Through EIS and Transmission Electron Microscopy (TEM) measurements it was shown that cycles involving the lower 20 mA.cm^{-2} resulted in far more severe degradation with Pt dissolution from the cathode and reformation in the bulk of the perfluorinated sulfonate polymer being shown.

Extensive fundamental experiments have been conducted on single cell PEMFCs over the past decade; however, stack level testing has received less attention [138]. In single cell tests, the focus has primarily been on material properties and transport phenomenon. This includes MEA materials, bipolar plate design, MEA durability and degradation, contamination, water management and thermal management. Stack level research has mainly been focused on macroscopic metrics such as overall performance and durability with semi-empirical models being developed and validated.

The main causes of FC degradation in automotive applications has been attributed to three main factors. These are: FC start-up/ shutdown, load cycling and idling at low currents [187]. The causes and effects of these operating modes are summarized in Table 2.7. Results of studies conducted on FC degradation on real world FCVs showed that the relative contributions of start-up, load cycling and idling caused 44%, 28% and 28% worth of degradation respectively [187].

If not suitably managed, each of these degradation mechanisms can be further agitated causing further increased degradation rates. Rapid load cycling for example can lead to periodic fuel starvation, which can be an acute problem in large area PEMFCs [123]. Under fuel starvation conditions, which are common at high current densities, the current distribution in a cell is highly uneven. Under these conditions the anode potential can rise and the cell potential can reverse. In the inlet of the anode, hydrogen oxidation can occur and the interfacial potential between the anode and the membrane is below the normal PEMFC OCV of 1.23 V. Under fuel starvation conditions, the later parts of the cell do not have sufficient hydrogen so water electrolysis occurs with a local interfacial potential of above 1.23 V. The high interfacial potential at the anode therefore leads to

Table 2.7: Fuel cell operating modes and major types of degradation [187]

Operating mode	Main causes	Degradation
Start-up	Cathode carbon support corrosion by high potential	Cathode catalysts surface area loss Cathodic reactant gas diffusion deterioration
Load cycling	Cathode catalyst dissolution by potential cycling	Cathode catalyst surface area loss
Idling (low current)	Cathode catalyst dissolution by high potential Chemical decomposition by peroxide (radial) attack Cathode catalyst poisoning by membrane fragments	Cathode catalyst surface loss Membrane proton conductivity loss

localised carbon corrosion and catalyst degradation [123]. If not enough water is present to maintain the electrolysis of water then the carbon is typically used to support the current. In their work, Liang *et al.* [123] measured local hydrogen stoichiometries near the anode outlet to be 0.55 with a local potential of 2.6 V creating a CO_2 production rate of 20 ml min^{-1}.

Carbon-support corrosion in PEMFCs

Carbon, in a number of different forms, is commonly used on PEMFCs as a catalyst support, GDL and bipolar plate material. Among these carbon materials, carbon black is often used as a catalyst support for PEMFCs applications due to its high electronic conductivity (1-10 S cm^{-1}) and high surface areas (100-1000 $m^2 g_C^{-1}$) to enable high dispersion of platinum or platinum catalyst and formation of highly porous electrodes [31].

Typically, electrochemical oxidation corrosion of carbon-support proceeds as shown in Equation 6.22 via carbon corrosion and the water shift reaction [58]. This mechanism and reaction kinetics is a strong function of potential (usually on the basis of the Reversible Hydrogen Electrode (RHE)). The carbon oxidation equations are shown in Equations 2.15 and 2.16.

$$C + 2H_2O \rightarrow CO_2 + 4H^+ + 4e^- \qquad E = 0.207V(\text{vs.RHE@}25°C) \tag{2.15}$$

$$C + H_2O \rightarrow CO + 4H^+ + 2e^- \qquad E = 0.518V(\text{vs.RHE@}25°C) \tag{2.16}$$

Carbon corrosion generally occurs when rapid potential cyclic, or oxidizing potentials are applied [185, 13]. Various accelerated stress tests have been developed including fixed potential holding and potential-step cycling. Figure 2.21 shows the carbon corrosion rate of conventionally-supported MEAs as a function of time at 80 °C held at potentials of 1.1 V, 1.2 V and 1.3V versus the RHE. Here the rate at which carbon corrosion occurred increases with potential, with the relationship following a linear log-log trend resulting in non-linear rates of degradation.

Mathias *et al.* [134] performed a number of detailed corrosion studies of conventional carbon-supported MEAs with respect to temperature and potential and showed that for a relative humidity of 100% the carbon corrosion current followed an empirical relationship as shown in Equation 2.17.

$$i_{CO_2} \propto 10^{E/TS} e^{-E_a/RT} t^{-m} \tag{2.17}$$

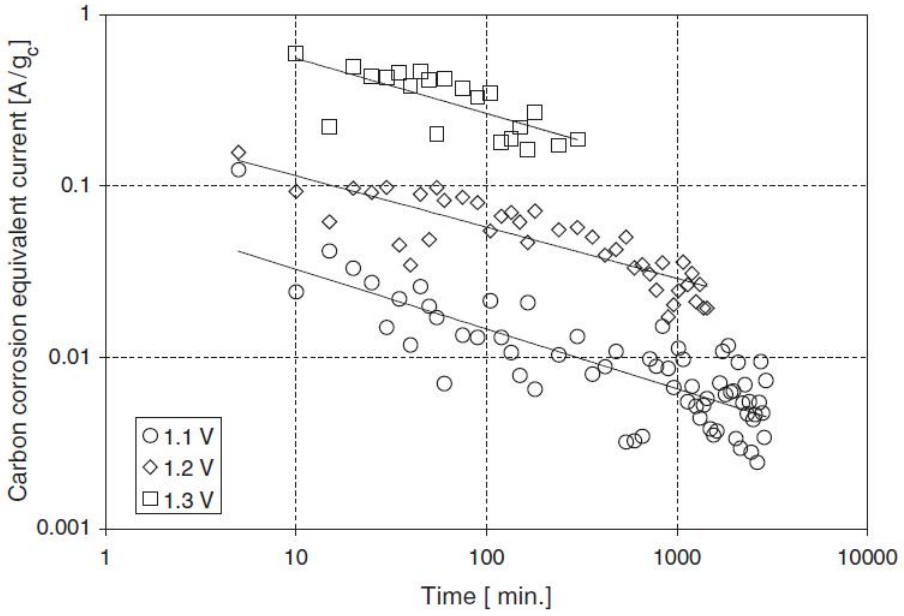


Figure 2.21: The effect of potential on carbon corrosion rate versus time over commercial conventional-carbon supported MEAs measured at 80°C and 80% relative humidity. The working electrode was fed with N_2 ($50 cm^3 min^{-1}$), while the counter/reference electrode was purged with H_2 [31]

Where i_{CO_2} is the carbon corrosion current at time time t, E is the applied potential, and R and T represent the universal gas constant and temperature, respectively. Büchi *et al.* [31] suggests values of E=67 kJ mol^{-1}, Tafel Slope (TS) value of 152 mV per decade and power-law parameter m of 0.32 for time, after fitting with experimental data.

Platinum dissolution

Common to many of the aforementioned degradation mechanisms is the loss of catalytic activity. Shao-Horn *et al.* [186] used TEM to analyse the degradation of MEAs to understand the mechanisms of Pt loss. It was found that the coarsening of Pt particles occurred via two main processes: (1) a nanometer scale Ostwald-ripening process where smaller Pt particles dissolve in the ionomer phase and redeposit on larger Pt particles that are separated by a few nanometers and (2) a micrometer-scale diffusion process, where dissolved Pt species diffuse in the ionomer phase and subsequently precipitate in the ionomer phase of the electrode or the membrane (close to the cathode/membrane interface) via reduction of Pt ions with crossover hydrogen in the anode [134].

Platinum dissolution leads to the decrease of effective catalyst surface area and a loss of electrochemical performance and occurs through a coarsening of the platinum particles in the catalyst layer [221]. Platinum dissolution is still not fully understood and a number of mechanisms have been proposed in the literature including; Oswald ripening [216], diffusion of platinum into the membrane [1] and finally a thermodynamic process in which unstable platinum particles reduce their surface Gibbs free energy through agglomeration [233]. While the mechanism is still debated, platinum dissolution has been linked to fuel cell operating conditions. Mathias et al. [134] showed that platinum dissolution could be reduced by lowering the operating voltage of a fuel cell at low relative humidity, while Borup et al. [26] found that load cycling significantly enhanced platinum dissolution in comparison to steady state operation.

Start-up/shut-down processes

An automotive PEMFC system undergoes an estimated 38,500 start-up/shut-down cycles over a 5,500 hr lifetime [31]. If not correctly managed these start-up/shut-down events can lead to cathode potentials as high as 1.5 V due to the existence of a H_2/air front [169]. Figure 2.22 shows a schematic of this H_2/air front. As in-plane proton transfer can be neglected due to the relative length scales (100 μm perpendicular-to-the-plane vs. several mm in-plane) the H_2/air segment effectively acts as a power source to the air/air segment, which acts as a load. Consideration of the conservation of charge then leads to Equation 2.18.

$$(i_{\mathrm{HOR}} = i_{\mathrm{ORR}})_{\mathrm{H_2/air}} = (i_{\mathrm{ORR}} = i_{\mathrm{COR}} + i_{\mathrm{OER}})_{air/air} \tag{2.18}$$

Where i_{COR} and i_{OER} represent the Carbon Oxidation Reaction (COR) current and the Oxygen Evolution Reaction (OER) current on the cathode side of the air/air segment, which is balanced by the ORR on the opposing side. The current thought the air/air segment is then equal to the current generated by the H_2/air segment [31].

Reiser *et al.* [169] developed a 1D model of the potential profile, which was experimentally validated, and suggests that under start-up/shut-down periods the electrolyte potential drops from 0 to -0.59 V (vs. RHE) when the anode is partially exposed to hydrogen and oxygen. This causes a current flow in the opposite direction to normal operating conditions at the oxygen-exposed region, increasing the cathode interfacial potential difference to 1.44 V which can cause accelerated corrosion of carbon-catalyst supports.

Maranzana *et al.* [131] used a segmented cell to investigate these internal currents and showed that during start-up, the initial flow of hydrogen, pushing out residual gas, can generate currents of up to 1 A.cm^{-2} with most of this due to the charging/discharging of the double layer found at the electrode/electrolyte interface. Contributions from the oxidation of carbon electrodes does occur simultaneously however at a much lower rate (a few mA cm^{-2})[131]. Even with nitrogen purging it has been shown that high hydrogen flow rates during start-up can result in significant internal currents. This charging/discharging of the double layer during start-up also leads to the OCP of the FC momentarily being above that of the steady state value. This is shown in Figure 2.23.

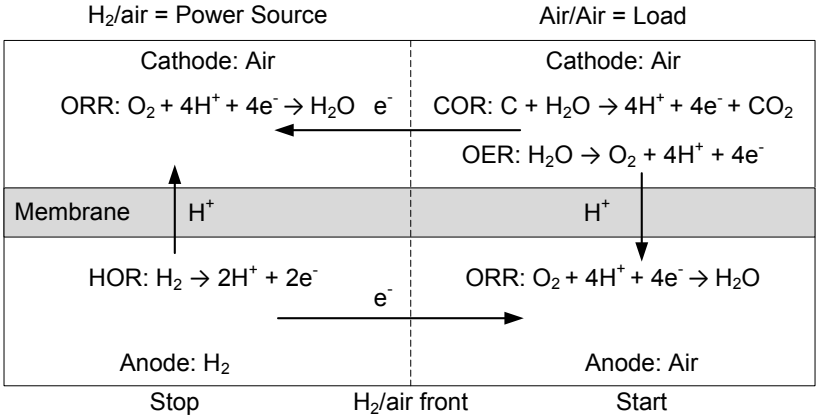
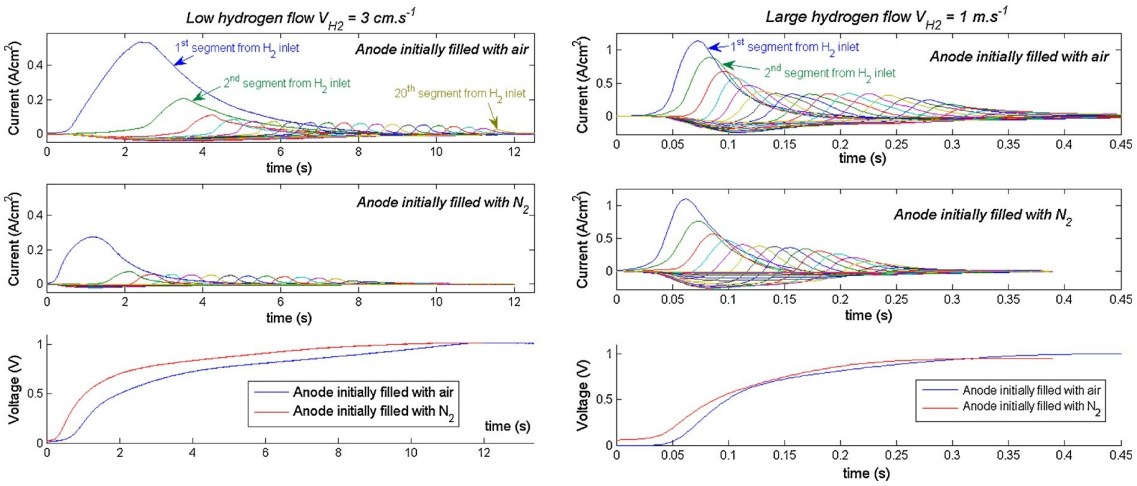


Figure 2.22: a PEMFC under start-up/ shut-down conditions showing how the air/hydrogen front causes ORR oxygen reduction reaction, COR carbon oxidation reaction, OER oxygen evolution reaction and HOR hydrogen oxidation reaction



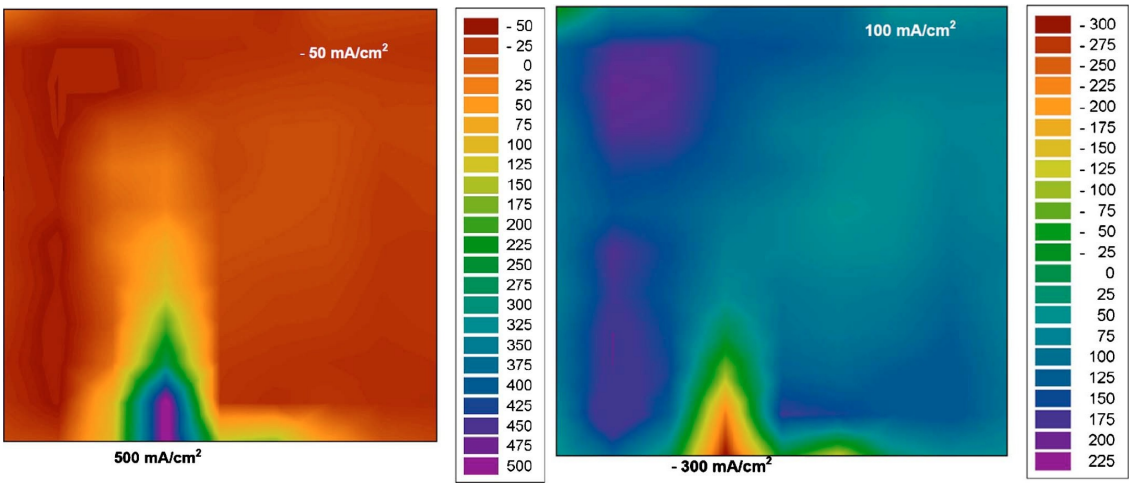
(a) (b)

Figure 2.23: Internal currents and open circuit potentials as a function of time for two different hydrogen inlet flows and for anode initially filled with air or nitrogen. T=22°C. Saturated air and hydrogen at the cathode and anode [131]

FC failure

Asides from gradual degradation of the FC, more rapid failure mechanisms exist, which can be aggravated under unfavourable operating conditions. One mechanism of failure is pin-hole formation, when a hole is formed in the MEA allowing gases to mix between the anode and cathode, resulting in an effective 'mixed potential'. Typically, cathode potentials will be more affected by this reactant mix than the anode potential [125]. This can lead to increased local current densities in the cell and localised heating to cause catastrophic failure of the system.

Lin *et al.* [125] constructed a segmented cell to investigate this effect and showed that significant current inhomogeneities can be observed. Under no load conditions regions near a pin-hole formation would exhibit positive currents at no load conditions and regions away from a pin-hole would experience small negative values. Under external load the regions closest to the pin-hole location leads to large negative currents. The mechanism causing this was identified as being the high crossover rate of hydrogen into



(a) (b)

Figure 2.24: Current density distribution measured on a MEA with a pinhole for (a) open circuit conditions and (b) under load (approximately 100 mA/cm^2) [125]

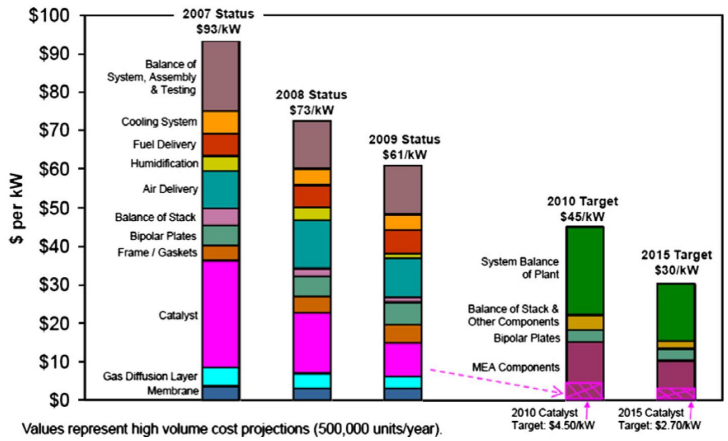


Figure 2.25: FC cost breakdown [214]

the cathode. They also suggest that a sudden pressure drop associated with vaporisation of water and the fast cooling of the cell is assumed to be the trigger for failure of the membrane. This is shown in Figure 2.24.

Residual water in the GDL, CL and gas flow channels can be problematic if ambient temperatures fall below freezing. Failure modes relating to ice formation in the MEA resulting in mechanical failure of the cell, ice blockage of the cathode CL, GDL flow channel leading to high pressure drops have also been reported [101] with ice formation in the cathode CL being the most common failure mode.

2.3.5 Cost

The cost of fuel cells are a major barrier for their commercialization in automotive applications. System cost will have to be competitive with other vehicle technologies in order to gain a market-share required to influence the environment. The U.S. Department of Energy (DOE) has established detailed cost targets for automotive fuel cell systems and components with predictions of costs for mass production [132].

Over past few years, the cost of FCs have dropped from $275/kW in 2002 to $73/kW, which equates to $6,000 for a 80-kW system, which is still twice the cost of an equivalent ICE [214]. In 2009, this was further decreased to $61/ kW ($34/kW for BOP and $27/kW for the stack). A breakdown of the cost evolution of the components in the FC is shown in Figure 2.25.

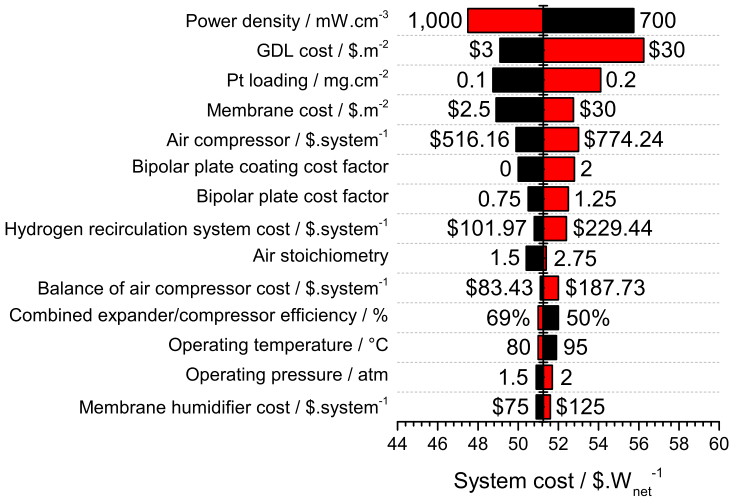


Figure 2.26: FC system cost sensitivity analysis. Here red represents low values and black high values of the respective parameter. Adapted from Marcinkoski *et al.* [132]

Marcinkoski *et al.* [132] presented the cost analysis for a 80 kWe PEMFC suitable for light duty vehicles, including materials and manufacturing. This includes a sensitivity analysis of the costs of per kW as shown in Figure 2.26. The results of the sensitivity analysis they performed, shows which aspects of FCs have the most significant impact on the overall cost per kWe. For different scenarios of best/worst case relative to a base case in 2010, they showed that improvements in the power density of the MEA, GDL costs, platinum loading, membranes and air compressors were the most significant influences on the cost per kWe.

2.3.6 Summary of Proton Exchange Membrane Fuel Cell literature review

Based on the review of the literature for PEMFC systems the following can be concluded.

- Many authors have presented models of FCs and FC systems to different degrees of accuracy, however there is a general trend of increasing length scale and decreasing accuracy such that system level analysis often removes much of the details in place of reduced order models. Even fewer works include this level of accuracy when considering FC system performance in hybrid applications where the load cycles are a function of the degree of hybridisation. The majority of the control development work thus focuses on the improvement of transient performance of only the FC system and rarely considers the parasitic power consumption of the BOP
- Both experimental and simulation based studies of large PEMFCs have shown significant current density and reactant inhomogeneities which can limit performance and accelerate degradation/ failure of the FC
- Operating mode can significantly affect the durability and performance of FCs due to effects on may length scales. Rapid power cycling can lead to catalyst loss, start-up/shut-down cycles as well as no load idling can lead to carbon corrosion. Whilst periodic current pulsing can in come cases improve performance by inhibiting the formation of Pt-oxide layers.
- Water management is of critical importance with flooding being a cause of failure due to localised hot-spots and potential pin-hole formations. Low air temperature and stoichiometry are often the cause with air pulsing techniques current being used to blow the water out
- It has been shown that the most significant cost associated with FC systems is that of the actual FC itself with cost reduction sensitivity greatest in the power density, GDL cost, Pt loading and membrane costs. This suggests that downsizing of the FC, rather than improved control offers to most promising route to affordable FCVs. This also suggests that systems should be designed with the aim of maximising FC durability as it is the most significant cost of a FC system

It was shown that as the length scales of interest in FC systems increase, the detail of the models decrease such that large scale system analysis often used reduced order models. Further to this, most of the large system level modelling work focuses on developing controllers that improve the dynamic response of BOP components to the FC efficiency. Few studies actually consider the impact of the parasitic power consumption required to achieve the performance and no studies retain this information to the hybrid electric vehicle level of modelling where the FC load is a function of the general control of the system and degree of hybridisation. Thus this work will aim to develop a high fidelity model of the FC stack which retains the relevant physics over the time constants of interest, as well as an accurate account of the associated BOP components to allow for analysis of the true system efficiency.

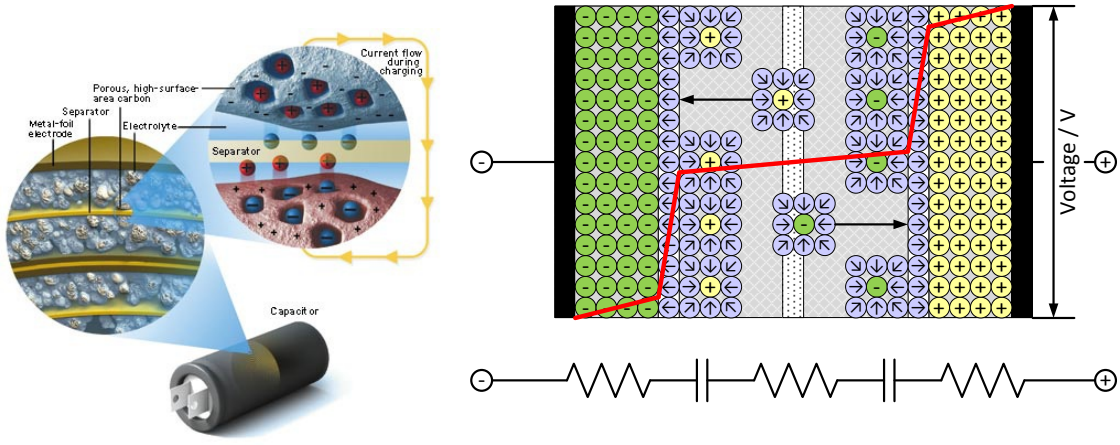
2.4 Supercapacitors

Electrochemical Double Layer (ECDL) capacitors, also known as supercapacitors, store energy via the formation of a charge double layer at the interface between its carbon electrodes and an ionic electrolyte solution. They're typically characterised as having a high power density but low energy density and thus offers another alternative to FCs and lithium-ion batteries. The electrostatic nature of the charge storage mechanism affords them their high power characteristics due to the absence of a charge transfer resistance present in FCs and batteries, with power densities of commercial cells typically quoted in the region of 1-10 kW/kg [164, 161]. This also enables the relatively high lifetimes of these devices due to the absence of the parasitic side reactions typical in other electrochemical energy storage devices. Thus, supercapacitors offer benefits when considering load shaving and regenerative breaking applications where high powers are required. The drawback of these devices, however, are their limited energy densities which are in the region of 1-10 Wh/kg compared to the 200-300 Wh/kg for lithium-ion batteries [164, 161].

The construction of a supercapacitor consists of two porous electrodes on metallic current collectors, separated by an ionically conductive but electrically insulating separator with an organic electrolyte, typically Acetonitrile (AN), as shown in Figure 2.27a. In its uncharged state, the majority of the anions and cations are in the bulk electrolyte. When an external overpotential is applied, anions and cations move to their respective electrodes and adsorb to the surface electrostatically. The accumulation of charge at each electrode gives rise to the measured potential of the cell as shown in Figure 2.27b.

The highly porous nature of the supercapacitor electrodes however means there are different length scales of interest to consider. Figure 2.28 shows one of these length scales of interest in supercapacitors and highlights the highly porous nature of the diffusion of ions. The increase in toruosity in the carbon electrodes results in slower effective diffusion and will have an impact on the extractable energy.

Beyond the diffusion processes, the formation of the double layer also has different regions of interest. Typically, the double layer can be described by two layers (as the name suggest). The inner layer, also known as the Helmholtz or Stern layer, contains solvent molecules which are strongly adsorbed onto the surface of the electrode [209].



(a) (b)

Figure 2.27: (a) Diagram showing the structure of a supercapacitor [181] and (b) figure of potential profile across a supercpacitor

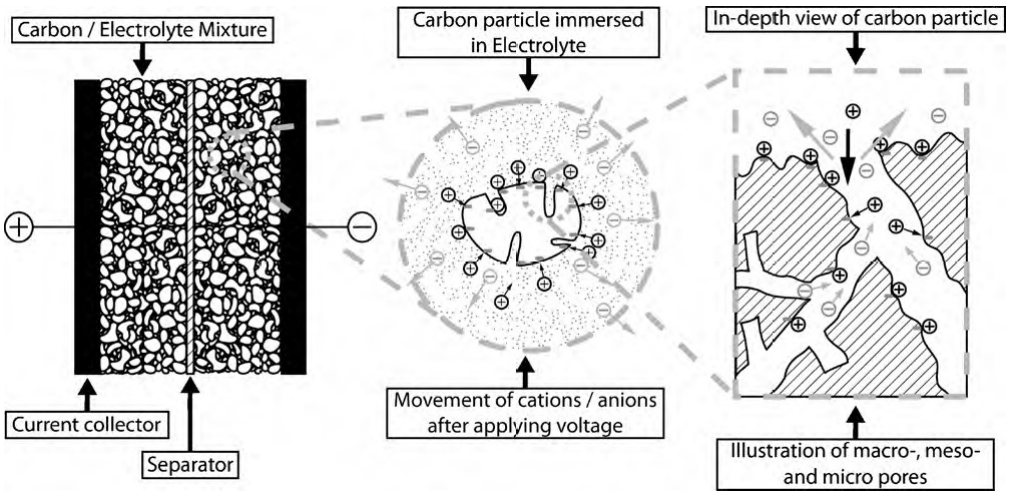


Figure 2.28: Illustration of the basic components and design of an EDLC. Arrows indicate the direction of movement for the cations and anions [102]

This layer can also be subdivided into two regions, the inner and outer Helmholtz layers, with the inner layer containing adsorbed ions and the outer layer containing solvated ions interacting only via long-range electrostatic forces and diffusion. The region of decaying electrostatic attraction into the bulk material is thus known as the diffuse layer [16].

The earliest model of the double layer is based on the Helmholtz model which assumed a single layer of adsorbed ions. Later, the Gouy-Chapman model introduced the concept of the diffuse layer, where the electric potential decreases exponentially towards the bulk fluid from the electrode. In highly charged systems the Gouy-Chapman model breaks down, with the later Gouy-Chapman-Stern model combining both Helmholtz layer and diffuse layer models together. Figure 2.29 shows an illustration of this double layer.

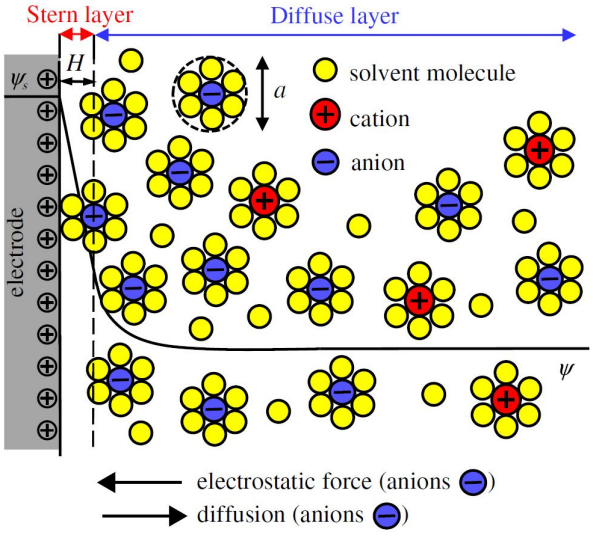


Figure 2.29: Illustration of the electric double layer structure near a planar electrode [57]

2.4.1 Impedance response

EIS is a usful tool for analysing any electrochemical device and supercapacitors are no different. The porous nature of supercapacitors thus results in frequency dependent performance characteristics. The impedance response of a typical supercapacitor is shown in Figure 2.30.

Here it can be seen that supercapacitor impedance behaviour can typically be broken down into four main frequency dependent regions [164]. These are shown in the list below:

(a) Zone I with a frequency range between 1 and 10 mHz is dominated by electronic leak current through the separator, charge redistribution effects and self-discharge

(b) Zone II with a frequency range between 10 mHz-10 Hz is dominated by the effects of the series and ionic impedance of the system giving rise to the characteristic Equivalent Series Resistance (ESR). The frequency impedance arises due to ions being able to travel deeper into the porous carbon electrodes resulting in a longer ionic diffusion path

(c) Zone III with a frequency range between 10 Hz-1 kHz is characterised by the series resistance which arises due to the impedance of the electrodes, current collectors and contacts

(d) Zone IV with a frequency range between 1-10 kHz is dominated by the intrinsic inductance of the supercapacitor and of the connecting cables

2.4.2 Charge redistribution effects

An effect commonly seen is that after constant current charging and load removal, the potential will rapidly fall. This is attributed to ions preferentially absorbing onto the larger pores nearer the bulk electrolyte due to the lower ionic resistance. When load is removed the concentration gradient will allow diffusion of the surface ions into deeper pores. The measured cell potential will be a function of the surface concentration of ions and thus a diffusion of ions into deeper pores results in an observed cell potential decrease after charging. The opposite effect is observed during discharge, whereby the cell voltage gradually increases after load removal. This is due to ions nearer the surface of the pore preferentially liberating their ions relative to ions in deeper pores. This

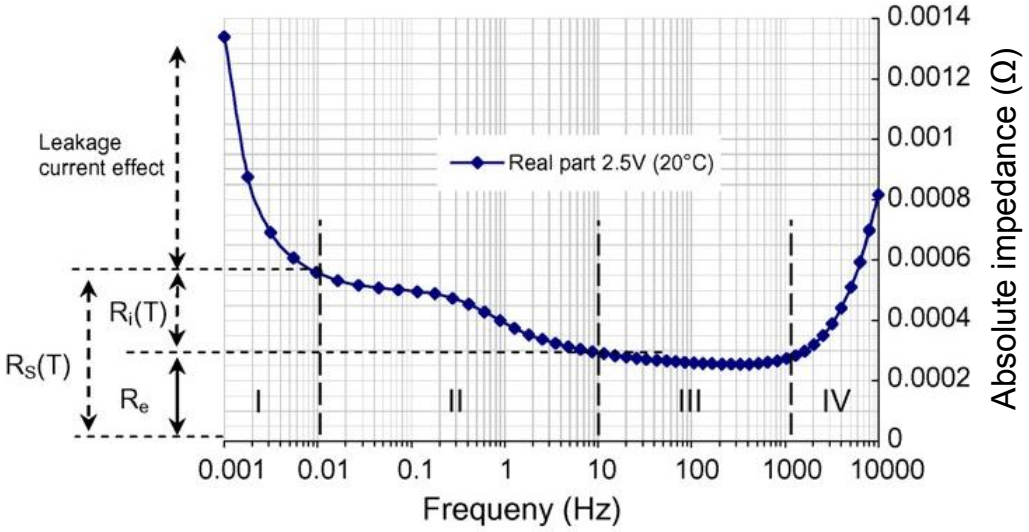
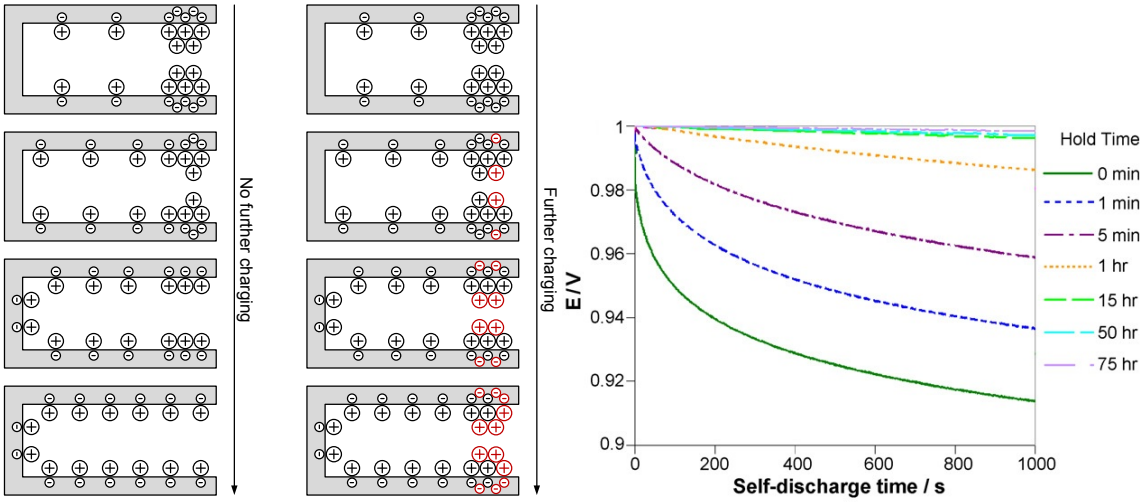


Figure 2.30: Bode plot of the absolute impedance of a typical supercapacitor [164]



(a) (b)

Figure 2.31: (a) Schematic of the charge redistribution effect showing ionic diffusion within a supercapacitor pore. Adapted from Kowal *et al.* [109] and (b) cell potential after constant current charging and then variable constant voltage charging of a Spectracarb 2225 in 1 M H_2SO_4 [21]

generates a concentration gradient which results in the ions in the deeper pores diffusing to the surface, even after load removal. This can be mitigated somewhat by saturation of the pores. This is commonly known as the charge redistribution effect and arises due to the higher ionic resistance to diffusion experienced by ions within smaller pores of the carbon electrodes. This is illustrated in Figure 2.31a and 2.31b.

It has been shown that the redistribution effect in supercapacitors can have a significant impact on performance, with the highly porous nature of the carbon electrodes meaning that the redistribution effect can have a time constant on the order of tens of hours rather than hundreds of seconds [102, 109, 21, 22]. This has previously been misinterpreted as self-discharge where some authors have tried to adopt a variable leakage current model to compensate for this effect [226, 59]. In the charge redistribution effect, the energy is not dissipated but rather the ions associated with the charge move deeper into the porous electrodes. Works have shown that this is a function of the short-term history including variables such as the charge/discharge duration and temperature [109]. The self-discharge profile typically exhibits three main regions. An initial region governed purely by the activation-controlled discharge, a second combining charge redistribution and activation controlled discharge and finally a pure activation-controlled profile [22].

Graydon *et al.* [87] developed a 2 branch (2 capacitor transmission line) equivalent circuit model to account for this charge redistribution effect and found that a substantial fraction of the capacitance is found in the smaller pores where the ionic resistance can be up to 4 orders of magnitude higher than in the bulk electrolyte. Table 2.8 highlights the differences between the rated capacitance and the flow branch capacitance for different capacitors.

It can be seen that in all cases the surface, or flow, capacitance values are substantially lower than the rated capacitance and similarly the ionic resistance within these regions which define the speed at which the charge can be accesses is significantly large. This thus highlights the need for a model to account for this charge redistribution effect especially when considering applications over longer periods.

Table 2.8: Resistance ratio (resistance of slow branch divided by equivalent series resistance) and capacitance of the flow branch as a percentage of the total measured capacitance. Adapted from Graydon *et al.* [87]

Source	Manufacturer	Rated capacitance / F	Resistance ratio / $\times 10^{-3}$	Capacitance / %
Faranda [74]	Epcos	110	1.74	13.4
Faranda [74]	Epcos	200	0.99	14.9
Faranda [74]	Maxwell	350	1.16	15.7
Faranda [74]	Epcos	600	1.09	14.6
Belhachem *et al.* [19]	Maxwell	2700	1.25	6.88
Diab *et al.* [59]	Not mentioned	2600	4.30	9.18
Rafik *et al.* [164]	Maxwell	2600	2.72	13.3
Kaus *et al.* [102]	Nesscap	600	6.07	2.66
Zhang and Yang [235]	Cooper Bussmann	22	5.25	17.7
Yang and Zhang [226]	Panasonic	10	1.10	22.3

2.4.3 Voltage dependent behaviour

A commonly found misconception in the literature revolving around supercapacitors is that their performance can be replicated fully through a simple electrical capacitor model. In reality, both the impedance and the capacitance varies as a function of voltage (or SOC). Rafik *et al.* [164] highlighted that the vast majority of engineering works that considered supercapacitors do not account for this affect and by using a linear approximation for capacitance, as a function of potential, can increase modelling accuracy of the cell voltage by approximately 10%, with respect to the absolute R^2 value between simulated and experimental results.

At higher potentials, the measured capacitance is greater as result of several physical phenomena such as reduction of the solvent layer thickness, increase of the solvent dielectric constant [88], increase in the electronic state density in the carbon pore walls [92] and higher ion penetration in mesopores [176].

Figure 2.32 shows the temperature and voltage dependency of a number of critical supercapacitor parameters for a 2600 F supercapacitor. Here it can be seen that the capacitance clearly increases with cell voltage and similarly there is an increase in series and electrolyte resistance. The term γ in the works by Briat *et al.* [28] represents the fitted CPE exponent to their EIS data which physically represents a metric relating to the porosity and thus diffusion properties of the supercapacitor.

2.4.4 Frequency dependent behaviour

The impedance of an electrode is also frequency dependent with Figure 2.33a illustrating the effect in supercapacitors. Here r_1 and r_2 are the radii of the pores and λ_1 and λ_2 are the penetration lengths of the excitation signal. Song *et al.* [192] demonstrated that with higher frequencies or smaller pores, the penetration depth of the signal becomes reduced. Thus, at high frequencies only large pores and external surfaces take part if the interactions.

Figure 2.33b shows the impedance response of a supercapacitor. The labelled point called the knee frequency represents the transition frequency between full access of the electrode surface and the electrolyte penetration. It also represents the point of 50% charge storage efficiency [18].

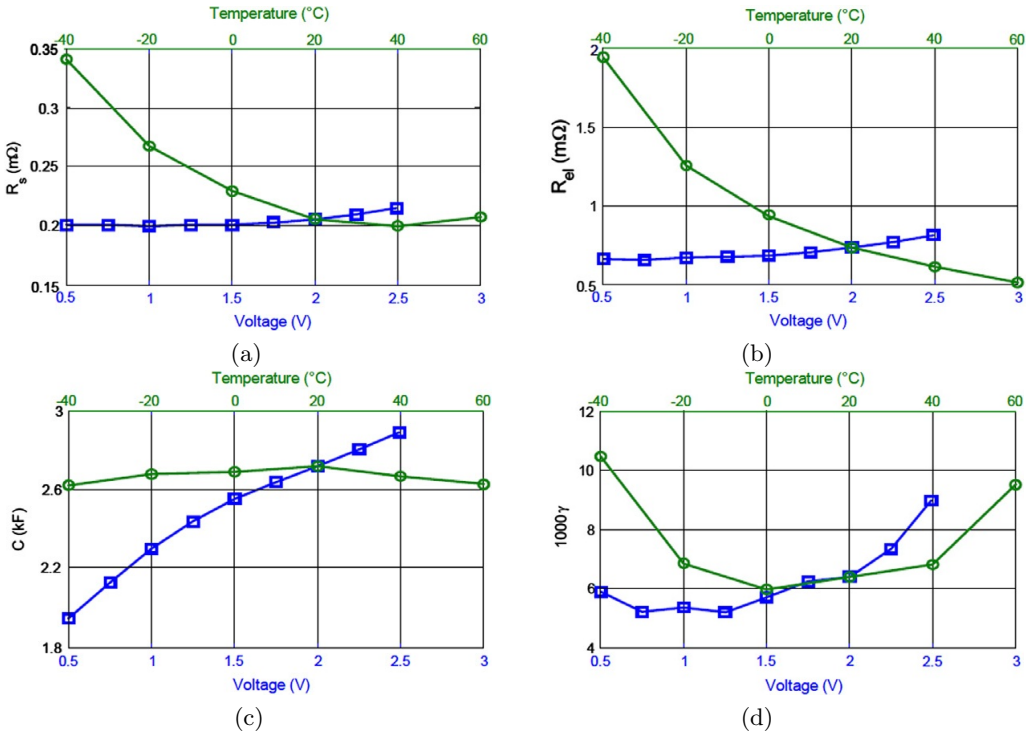


Figure 2.32: Voltage and temperature dependency of different parameters for a 2600 F supercapacitor [28]

This frequency dependent behaviour is illustrated in Figure 2.34. This shows that the capacitance, of a supercapacitor, decreases with higher frequency operation due to the penetration depth and limited ionic diffusion at those time constants. The behaviour of the supercapacitor also becomes potential independent at that stage. The real impedance of the device is also frequency dependent with high frequencies only representing the series and bulk electrolyte resistance and lower frequencies representing the addition of the electrolyte resistance.

Wang and Pilon [209] developed a physics based model of a supercapacitor and showed that the double layer capacitance is constant for a frequency below a critical value. At high frequencies it was shown that ion transport could not follow the fast variations in electric potential. Many authors have used EIS measurements to represent the

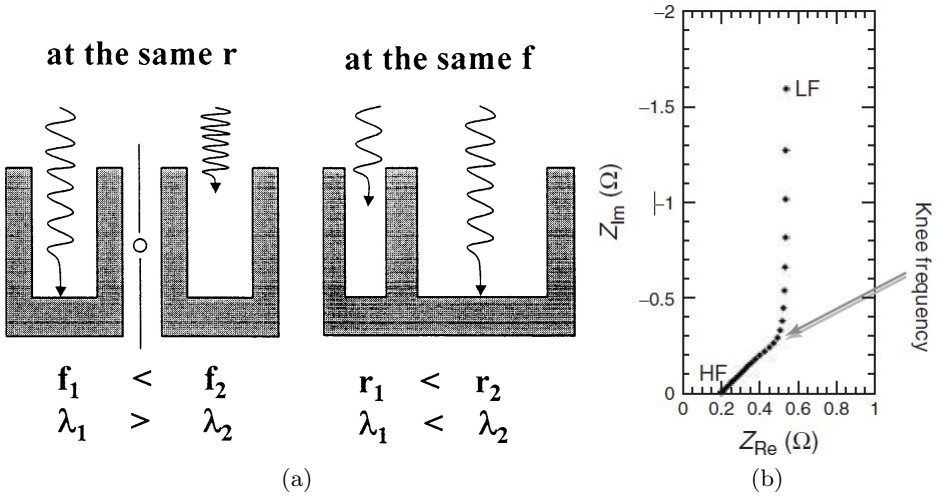
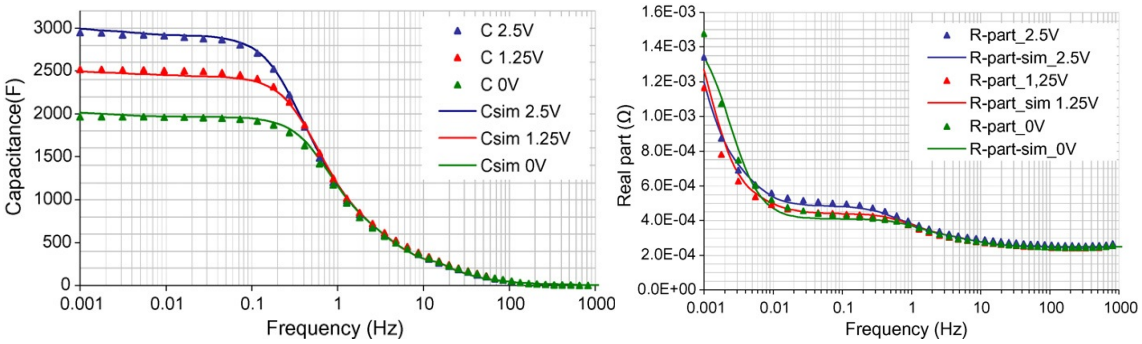


Figure 2.33: (a) Schematic of AC signal penetration inside a porous electrode [192] and (b) Nyquist plot of an electrical double layer capacitor [18]



(a) (b)

Figure 2.34: (a) Bode plots of differential capacitance and (b) real impedances at different cell voltages for a 3000 F supercapacitor [164]

frequency dependency of the capacitance using only the imaginary impedance according the Equation 2.19 [164, 3].

$$C = -\frac{1}{2\pi Im(f)f} \tag{2.19}$$

Whilst this gives the general trend and the low frequency capacitance, the transition frequency between zero capacitance and 100% of the rated charge capacitance is often represented at higher frequencies than in reality.

2.4.5 Thermal characteristics of supercapacitors

The temperature of supercapacitors affects its' performance, as the ionic resistance and electronic resistance are a function of the temperature. Heat generation in supercapacitors can typically be attributed to two main sources: irreversible ohmic heats and reversible entropic heats [182, 50]. The irreversible ohmic heat generation from the movement of ions and electrons and the reversible entropic heat generation caused by the change in order of the ions when charging/discharging a supercapacitor [182].

Various authors have developed models of supercapacitors which account for the thermal effects. Gualous *et al.* [89] developed a thermal model of the supercapacitor and also embedded thermocouples into the cell to validate their results. Whilst their results appear to match with their simulations they do not account for entropic effects.

Schiffer *et al.* [182] showed that the heat generation within supercapacitors was the superposition of the irreversible joule heating and the reversible entropy effects as the heat generation under charge and discharge conditions was found to differ. They proposed a thermal model which accounts for this ordering of the ions during charging based on the thickness of the Helmholtz layer.

D'Entremont and Pilon [57] later developed a more advanced physics based model which accounted for coupled ion transport and heat transfer. Their model accounts for the presence of the Stern layer and the finite size of ions by using the modified Poisson-Nernst-Planck model. The model accounts for the irreversible ohmic heats as well as reversible contributions from diffusion, steric effects and entropy changes, with results showing that the reversible heat terms are exothermic during charging and endothermic during discharge. Figure 2.35 shows the predicted temperature as well as the predicted temperature contribution from the different effects.

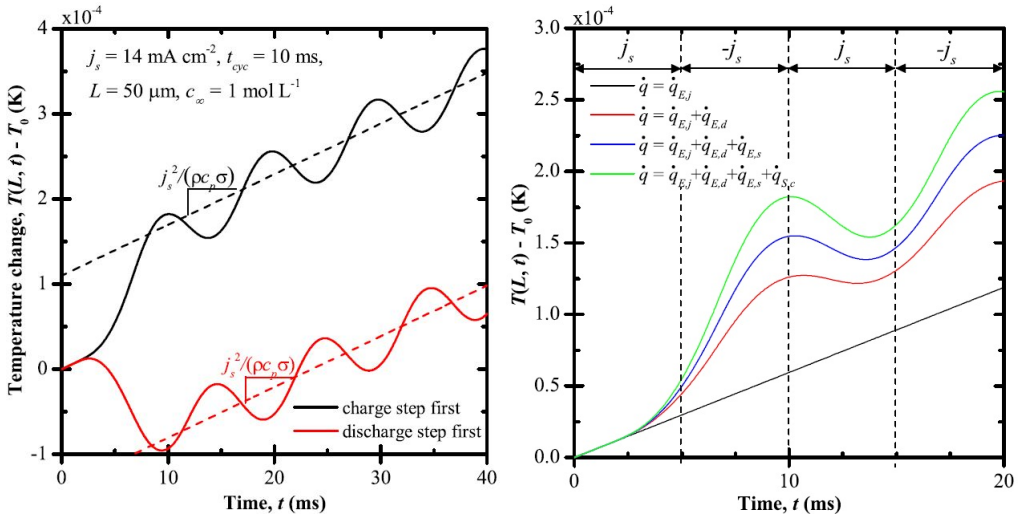


Figure 2.35: (a) Numerically predicted temperature changes as a function of time for cases starting with either a charging step or a discharge step and predicted temperature change change as a function of time for individual heat generation terms where $q_{E,j}$, $q_{E,d}$, $q_{E,s}$ and $q_{S,c}$ represent the ohmic heating, ion diffusion, steric effects and mixing heats [57]

2.4.6 Modelling of supercapacitors

Models of supercapacitors found in the academic literature can typically be subdivided into a two main categories: equivalent circuit and physics based, with the vast majority of works focusing on equivalent circuits due to their ease of implementation and low computational cost.

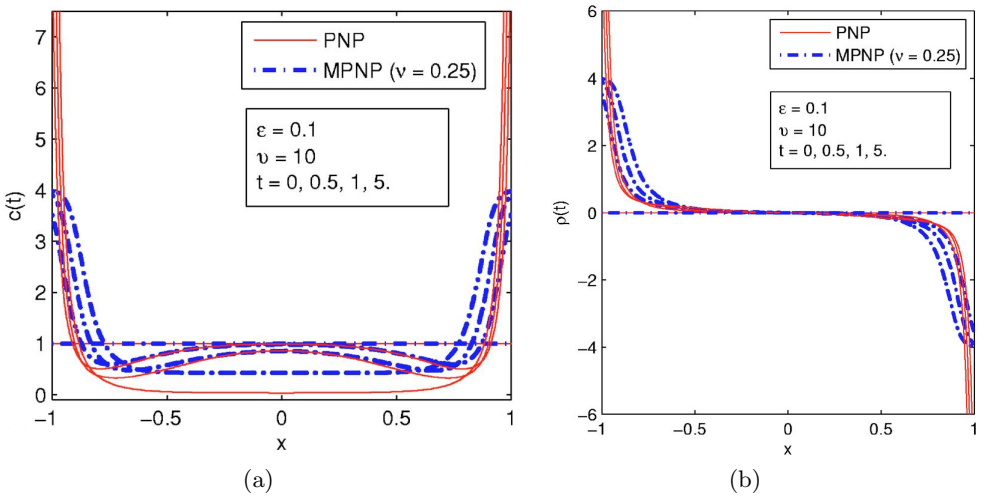
Physics based models

The use of physics based models allows for the investigation of performance metrics from a first principles point of view. Within physics based models there are different approaches to modelling depending on the length scale of interest.

Starting at the larger bulk cell level, authors have used continuum mechanics to model the performance of supercapacitors. Verbrugge and Liu [204] developed a 1D physics based model using porous electrode theory of a supercapacitors intended for analysis of hybrid electric vehicle optimisation. They used their model to probe the effects of charge distribution in electrodes under high discharge conditions and found that under high discharge/charge rates, electrode regions closest to the separator experienced the greatest current density due to the relative increase in resistance the further the electrode was from the separator. The limitation of this work is that it assumes a constant porosity based on the porous electrode theory and does not account for the different pore length scales as previously mentioned.

Continuing down the length scales, authors have used the Poisson-Nernst-Planck (PNP) equations to provide the standard description of the linear response dynamics based on the same assumptions of dilute solutions of pointlike ions interacting though a mean field. Depending on the length scales and regions of operation, this assumption is reasonable; however, as energy densities of supercapacitors increase, steric effects due to the finite ion size and particle-particle interactions become increasingly significant meaning that the pointlike assumption breaks down.

Additions to this model have since been made. Kilic *et al.* [105] presented a physics based model using a Modified PNP (MPNP) equations accounting for ionic transport to account for additional steric effects. The steric effects account for the finite size of



(a) (b)

Figure 2.36: The numerical solutions to the PNP and MPNP systems. The dimensionless charging voltage is ν=10, which corresponds to approximately 0.25 V at room temperature. The very large values of ϵ=0.1 and ν=0.25 are chosen deliberately for illustration. The dimensionless bulk concentration field c is shown in (a), and the dimensionless charge density ρ in (b) [105]

each charge carrying molecule and the size of the pores have an impact on each other at a small enough length scale meaning that eventually bulk continuum mechanics as adopted by the porous electrode theories breakdown. The steric effects have been shown to have a significant influence on the performance, especially at higher potentials, as ionic packing becomes greater and the diffuse layer has a reduced capacitance compared to the classical theory. Figure 2.36 shows a comparison between the PNP and MPNP models in both the concentration and potential domains. Here -1 and 1 represent the electrode of a system in dimensionless form.

It can be seen that in both domains, as a load is applied over time, charged species will accumulate on the electrodes with the respective charge density increasing/ decreasing. The example shown is for large potential steps and it can be seen that the PNP model overestimates the concentration profiles at the electrodes and also underestimates the bulk electrolyte concentration in comparison to the MPNP model. The result on the charge density is also an overestimation. This is caused by the fact that the PNP model does not account for steric effects.

Authors have since probed the impact of the steric effects. D'Entremont and Pilon [57] developed a physics based model of a supercapacitor which coupled the electrodiffusion, heat generation and thermal transport processes occurring within a cell. Transient electrodiffusion in a binary and symmetric electrolyte was done with a MPNP. The thermal model also accounted for irreversible ohmic heating as well as reversible heat generation from entropy related effects.

Wang and Pilon [209] developed a physics based model of a supercapacitor for numerical simulation of the EIS profile and determination of the true double layer capacitance. They used the classical PNP model, with and without the Stern layer, and a MPNP model with Stern layer. They found that there was a characteristic time constant for ionic diffusion which is a function of the ionic concentration, and that at high frequency oscillations, ionic diffusion is not fast enough to follow the imposed potential field. From their models, they suggest that EIS measurements of the double layer capacitance can typically overestimate the true value for dilute electrolytes and underestimate for concentrated electrolytes subjected to large potentials.

Wang and Pilon [210] later extended this work to model 3D structures using their physics based models which accounted for the effects of the Stern and diffuse layers, finite ion size and dependency of the electrolyte permittivity on the local electric field.

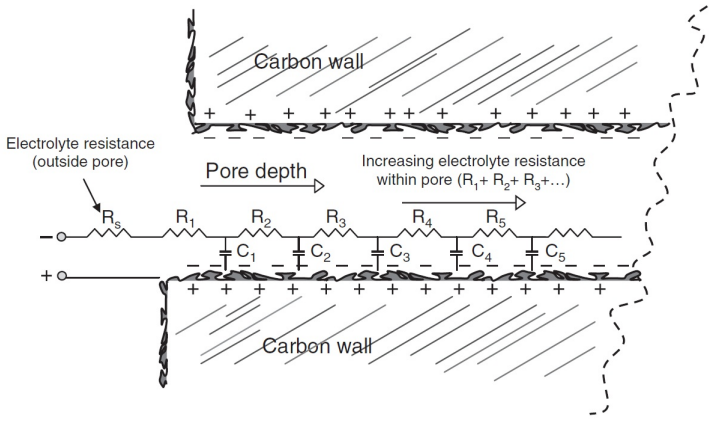


Figure 2.37: An idealized model of cylindrical pore and distributed capacitance within a pore. [18]

Equivalent circuit models

Equivalent circuit models have been the preferred choice of modelling approach adopted by more engineering works due to ease of implementation and speed of computation. The original concept of the equivalent circuit model for supercapacitors was based on the work by de Levie [118] who investigated the capacitance effects of porous electrodes in electrolyte solutions. Mathematical evaluation of potential and current distributions in porous electrodes showed that processes do not occur evenly throughout the thickness of a porous electrode due to the relatively large IR drop in the solution of the pores, resulting in faster dynamics at the mouth of the pore closer to the counter electrode [227]. As such, a de Levie brush model, or transmission line type model was proposed as shown in Figure 2.37.

In the transmission line model, a network of resistors and capacitors represent the increase of ionic resistance deeper into pores and the related capacitance. Many authors have used this approach with variations made over the years to incorporate different effects [102, 164, 114, 21, 22]. For example Rafik *et al.* [164] developed an equivalent circuit model that also accounted for the varying capacitance as a function of the voltage.

A figure of one of the variations of equivalent circuits proposed is shown in Figure 2.38. As one can see different parts of the model are used to represent different processes with different time constants of interest.

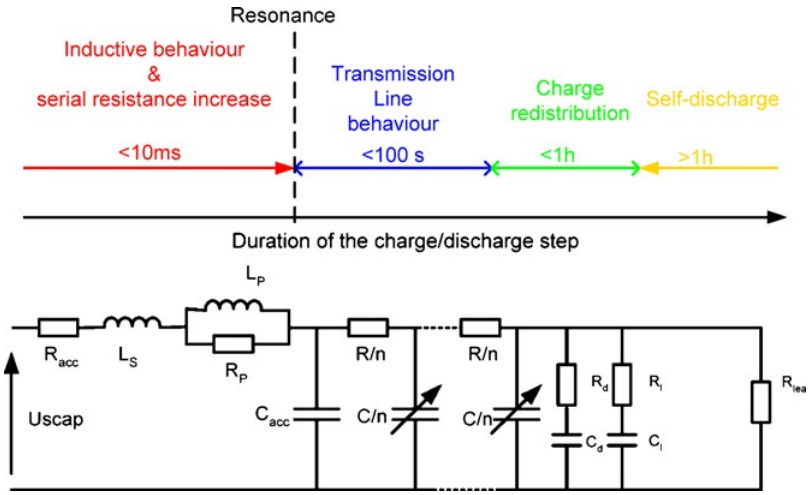


Figure 2.38: Equivalent circuit model of a supercapacitor [114]

Whilst the use of equivalent circuit models becomes more wide spread, the limitations of their validity must also be considered. Miller [139] used a simple series-RC model to model the performance of supercapacitors. It was shown that in lower capacitance cells, this showed good agreement however in higher energy dense cells, the deviation of the simple approximation began to increase. This is likely due to the pore porous nature of the higher energy dense cells and the resulting charge redistribution effects. The earlier physics based works would suggest that this is caused by the fact that higher energy dense supercapacitors have smaller pores and in those cases the increasing influence of steric effects results in a decrease in capacitance.

2.4.7 Supercapacitor degradation

Whilst supercapacitors are typically quoted as having extremely high lifetimes due to the absence of electrochemical charge transfer process, and thus the normally associated parasitic side reactions, these do still exist but at much smaller magnitudes and are caused by by oxygenated functional groups leading to the degradation of performance [24]. The general observed trend is such that as supercapacitors age their resistance increases and capacitance decreases [23] with many authors commenting that higher temperatures and potentials accelerates the rate of degradation [3, 182, 89].

Bohlen and Kowal [23] showed that there is a close coupling between the thermal effects and degradation, with a feedback effect whereby, in large supercapacitor packs, the cell that get hottest degrade faster, which results in higher resistance and consequently higher rates of heat generation. This is obviously dependent on the pack architecture and cooling system, but highlights the importance of thermal considerations. Schiffer *et al.* [182] showed that the temperature dependency of degradation follows an Arrhenius rate law, and thus degradation rates will have an exponential dependency with temperature.

Zhu *et al.* [240] showed that the aging of carbon materials in AN based electrolytes is mainly attributed to structural changes with micro/mesopores being destroyed by the polymerisation of AN. Their measurements suggested that degradation is faster on the anode than cathode and they highlight the criticality of trace water amounts causing the chemical aging.

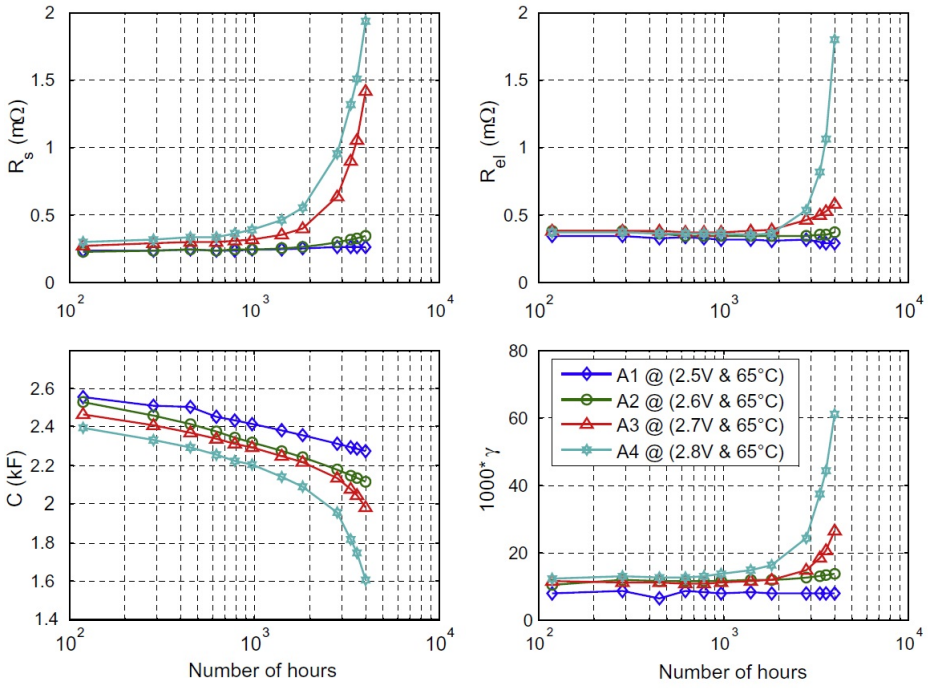
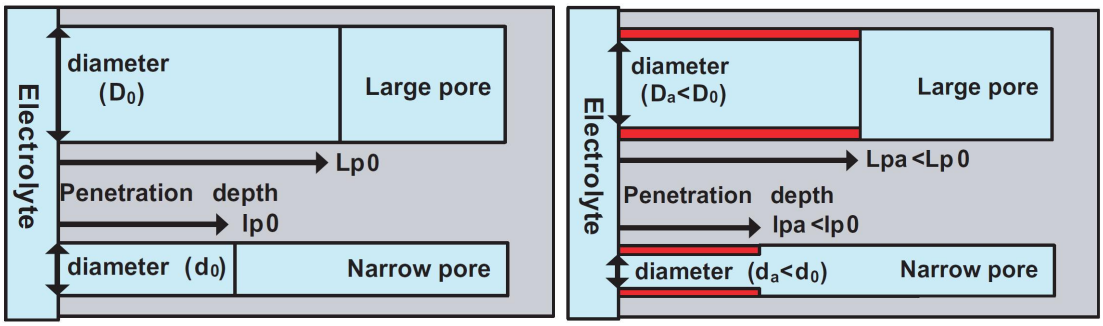


Figure 2.39: Model parameters changes at 65°C for different voltage [69]



(a) (b)

Figure 2.40: Illustration of the dispersion of pore size and the consequences on ageing [68]

The sensitivity of the degradation rate to cell potential also supports the side reaction mechanism as the thermodynamic equilibrium potential often defines the kinetics of a reaction in addition to temperature. Figure 2.39 shows how storage at different potentials affects the rate of degradation of different parameters over time. Here γ represents a fitted parameter from the equivalent circuit which represents the porosity of the electrode as would be suggested by its close trend correlation to the capacitance.

Further work by El Brouji *et al.* [68] on calendar aging and power cycling tests, found that calendar aging leads to a decrease in cell capacitance due to the deposition of impurities in the pores of the electrode materials leading to a loss of active surface area. Power cycling tests by contrast more radially modified the pore size distribution. Figure 2.40 illustrates the impact of calendar aging.

2.4.8 Summary of supercapacitor literature review

The literature review of supercapacitor technology for automotive applications has resulted in the following conclusions.

- Many studies of supercapacitors in the pure engineering field fail to account for variations in the capacitance as a function of the SOC and also the frequency dependency of supercapacitor performance
- Equivalent circuit models are the main form of model used in the academic literature to replicate supercapacitor performance, with many models adopting a de Levie brush type model to account for porous electrode effects
- Lower energy dense cells show better agreement with equivalent circuits, with deviations increasing in larger energy dense cells. From physics based modelling of cells using MPNP based models this has been attributed to the increasing steric effects at higher potentials where charge carrying species can no longer be considered pointlike charges in a mean field
- The main degradation mode in supercapacitors is attributed to structural changes in the electrode causes by the parasitic side reactions of impurities from the manufacturing process which reduce the effective surface area of the supercapacitor

The literature would thus suggest that for system level analysis using supercapacitors, consideration of the charge redistribution effects needs to be accounted for. Whilst physics based models do give additional insight into the performance limitations of supercapacitors, no current model from the length scale of the Helmholtz layer has been developed that is suitable for large system level analysis. Of the physics based model continuum mechanics based models appear most suitable.

2.5 Powertrain comparison

The term powertrain refers to all components within a vehicle which delivers or converts energy for motive power. The selection, arrangement and control of a vehicle powertrain has a significant impact on the performance, efficiency, cost and lifetime of the vehicle and therefore needs careful consideration. The simplest configuration for an electric vehicle is one where there is only one main prime mover which includes either pure BEV or pure Fuel Cell Vehicle (FCEV). Depending on the application, there may be advantages and disadvantages which makes one technology favourable over the other.

As seen from previous sections, the three main electrochemical devices have different advantages and disadvantages. Therefore, to achieve the most benefit, many authors have suggested hybridisation, whereby multiple devices are used to provide the motive power for the vehicle. However, before consideration of different configurations an understanding of the load cycles that are applied to the vehicle is needed.

2.5.1 Drive cycles

One of the critical metrics of interest in the analysis of vehicle powertrains is which drive cycle is used for the analysis. Depending on the load cycle, the results may show that one powertrain is preferred over another whilst the opposite is true for a different load cycle. Thus an understanding of the type of drive cycle being applied is needed. Segmenting the market for automotive applications is therefore a key requirement.

Many studies have looked into the impact of driving cycles when assessing the performance of vehicles [8, 7, 14, 130, 6] and it is generally agreed that a single drive cycle to characterise the entire market does not give a true representation of energy efficiency of different powertrains [7].

Typical metrics used to characterise drive cycles include average speed, peak speed, duration, average acceleration and peak acceleration [8, 146]. André [8] analysed a large dataset of different vehicle drive cycles with the aim of categorising them with the aim of deriving a common set of reference real-world driving cycles, hereafter termed the ARTEMIS cycles. They categorised drive cycles into 12 distinct classes based on their

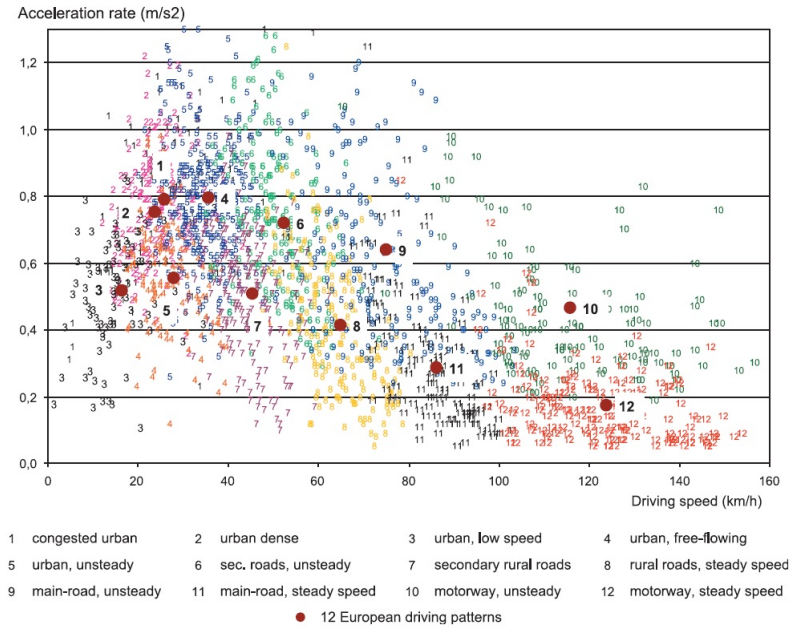


Figure 2.41: Variability of the driving conditions and positioning of the 12 centres of the classes amongst a sample of observations [8]

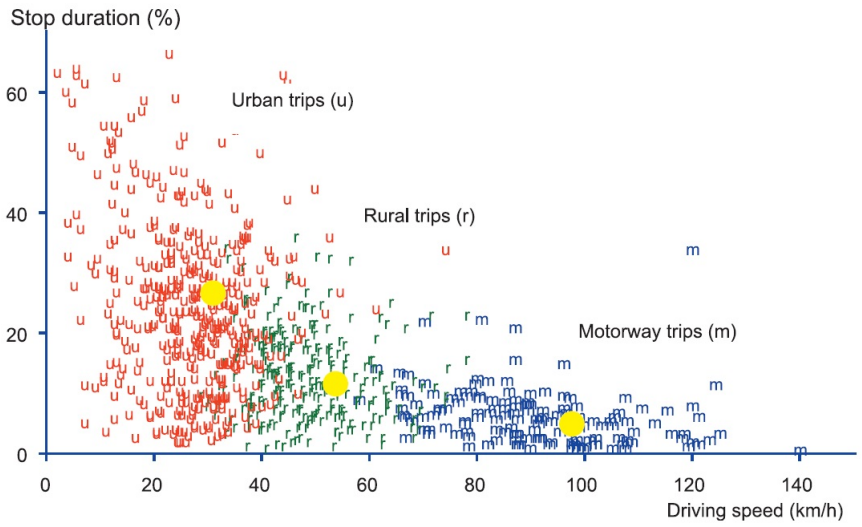


Figure 2.42: Variability of the trips and positioning of the centres of the trip classes obtained by cluster analysis [8]

speed and acceleration profiles and eventually derived three main drive cycles that they claim to be representative of real world driving conditions. The subcategories include: urban, rural road and motorway driving. Figure 2.41 shows the distribution of the average acceleration and speed for the different drive cycles. Trends in the drive cycles can thus be seen.

In addition, André [8] also looked at the intermittency of the drive cycles and the variations between different categories. Figure 2.42 shows the percentage stop duration against average speed for different driving styles. It becomes apparent that low speed urban driving contains many more stop-start events than high speed motorway trips. This would thus become a consideration in powertrain configurations where there is a significant parasitic power consumption under idling conditions.

Many works have studied the performance of vehicles under different duty cycles. Baptista *et al.* [15] analyses the life cycle emissions for a London taxi using the CENEX-PCO drive cycle specifically designed for characterising taxi driving behaviour. Liaw and Dubarry [124] uses fuzzy logic pattern recognition to characterise drive cycles. They describe the concept of a driving pulse which includes information about the average speed and distance travelled during active periods of a drive cycle. A driving cycle profile is then created from a number of driving periods to characterise the whole cycle.

Table 2.9 compares different standard drive cycles against their retrospective metrics. Typically, the differentiation between different vehicle drive cycles is very much qualitative however it is the aim of the author to make drive cycle analysis much more quantitative.

Table 2.9: Comparison of different vehicle drive cycles

Name	Description	Duration / s	Distance / km	Average (peak) speed / KPH	Average (peak) acceleration / $m.s^{-1}$
Mode 10-15	Japanese drive cycle for light duty vehicles	891	6.34	25.6 (70)	0.14 (0.81)
JC08	Japanese drive cycle to considered to be more 'real world' than the Mode 10-15	1204	8.17	24.4 (81.6)	0.15 (1.69)
New European Drive Cycle (NEDC)	For light duty vehicles	1180	11.01	33.6 (120.0)	0.12 (1.04)
The Heavy duty Urban Dynamometer Driving Schedule (HUDDS)	For heavy duty vehicle testing	1060	8.94	30.3 (93.3)	0.13 (1.95)
US06	High acceleration, aggressive drive cycle	600	12.89	77.2 (129.2)	0.30 (3.76)
New York City Cycle (NYCC)	Represents low speed, stop/start events typical of city driving	598	1.89	11.4 (44.6)	0.20 (2.68)
Highway Fuel Economy Test Driving Schedule (HWFETDS)	Represents highway driving below 100 KPH	1544	33.01	76.9 (96.4)	0.09 (1.43)
Urban Dynamometer Driving Schedule (UDDS)	Represents city driving for light duty vehicles	1369	11.99	31.5 (91.3)	0.20 (1.48)
Federal Test Procedure (FTP)	Extension of the UDDS with cold, transitions and hot periods	1873	17.69	34.1 (91.3)	0.20 (1.48)
LA92	Similar to the FTP but more aggressive	1435	15.80	39.6 (108.0)	0.25 (2.82)
IM240	Road side vehicle testing	240	3.15	47.1 (91.3)	0.38 (1.48)
CENEX-PCO	Drive cycle for a London Taxi	2710	13.30	16.5	0.53

2.5.2 Battery electric vehicles

Lithium-ion batteries are currently the main battery technology of choice in BEVs applications, and whilst other battery technologies are being developed it is expected that lithium-ion batteries will play a large part in near and far term EV futures [84]. BEVs only use battery to store energy for the vehicle powertrain. BEVs potentially have the capacity of providing the lowest GHG emissions of all EV technologies. This is highly dependent on the fuel type being used to generate the electricity for charging with values ranging from 0 gCO_2/km using renewable sources and 155 gCO_2/km using coal based electricity generation [203].

The limitations with pure BEVs has always been the range of the vehicle. Campanari *et al.* [34] showed through simulations that battery weight and energy consumption of the vehicle increased dramatically with the driving range. This would also mean that the cost of the vehicle increase. Durability is also a concern with many authors quoting that a BEV should last for at least 10 years or 150,000 miles [161]; however, as the range of comsumer operating conditions is quite wide, it is difficult to guarantee this.

Cost is another limitation for the commercialisation of BEVs. van Vliet *et al.* [203] showed that in 2010 with a cost level of 1,280 $/kWh for lithium-ion batteries, the Total Cost of Ownership (TCO) of a BEV was $3,600/ year more than an ICE based vehicle. Driving costs down to 530 $/kWh would still result in a TCO difference of $1,000/year.

2.5.3 Fuel cell vehicles

Pure FCVs only use FCs as their main form of power generation. These have been generally acknowledged as being the best potential all electric technology for long range vehicles. Thomas [198] showed that when comparing BEVs with FCVs, FCVs exhibited superior benefits in terms of mass, volume, cost, initial GHG reductions, refuelling time, well-to-wheel energy efficiency and life cycle costs than BEVs when the vehicle range is greater than 160 km.

Various works have been presented in the academic literature demonstrating FCVs. Bonnet *et al.* [25] developed an 80 kWe PEMFC system. Here they compared the normalised performance between different stack sizes. They reported that under low humidification all systems performed the same; however, at higher humidifications (60%) variations in performance could be seen. This has been attributed to condensed water causing the differences in normalised performance, with water management more difficult in larger systems.

Saxe *et al.* [180] analysed the performance of 27 FC buses that were operated in 9 different European cities with consideration of the energy systems and different load cycles. They found that the FC system efficiency under real world operation to range between 36-41%. They suggested that via hybridisation the fuel consumption could be improved by 5-10%. Figure 2.43a shows the Sankey diagram for a 38 kW system. From the starting potential energy of the fuel it can be seen that only approximately 52% of this is useful electrical energy. Further inefficiencies down the powertrain result in as low as 23.5% of the total energy being useful motive energy. This highlights the fact that whilst FCs possess a relatively high energy density they are still relatively inefficient when compared to batteries or supercapacitors.

The drawback of a pure FC system is that the FC time constants are dominated by temperature and fuel delivery systems, with highly dynamic loads resulting in large voltage drops due to fuel starvation effects with these effects leading to accelerated degradation and potential failure of the FC [221, 197]. As such many authors suggest

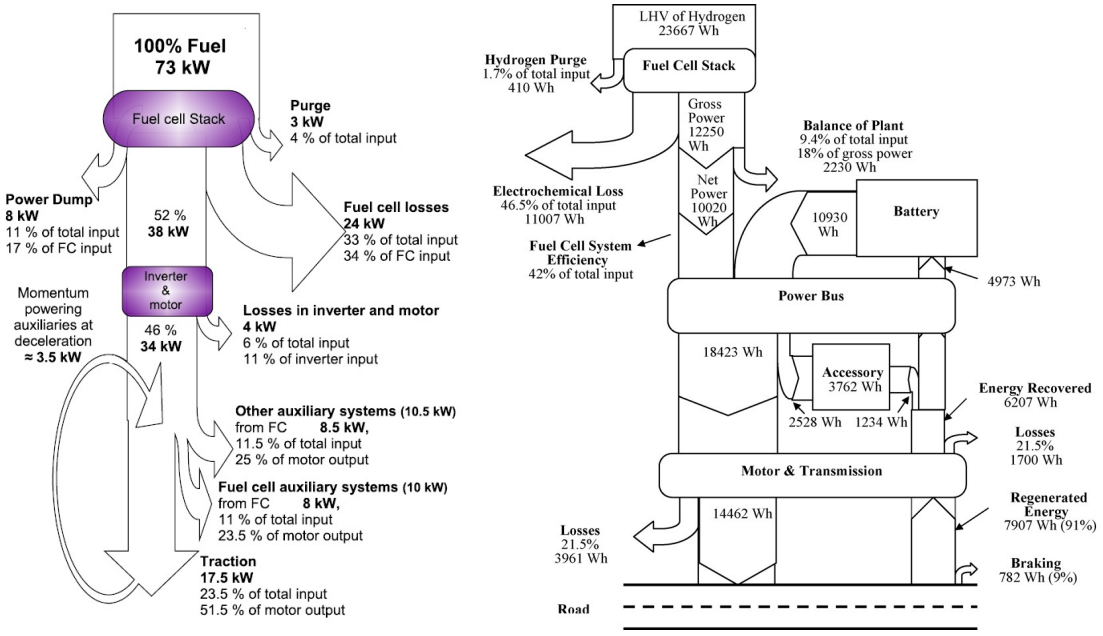


Figure 2.43: (a) Sankey diagram of a FC system for bus applications [180] and (b) Sankey diagram for FC-battery hybrid system for typical drive cycle Bubna *et al.* [29]

limiting the load ramp rate of a FC with values of 4 A/s for a 500 W-12.5 V FC [199], 2.5 kW/s for a 40 kW-70V FC [173], 50 A/s for a 20 kW-48V FC [48]. Of course limiting the ramp rate of current then has a knock on effect that the performance of the vehicle suffers.

2.5.4 Fuel cell hybrid vehicles

A hybrid powertrain is one in which there are multiple power sources to drive the vehicle. Typically, one component is used for chemical conversion and the other energy storage.

Many authors have suggested hybridisation of a FC with batteries and/ or supercapacitors as a means of both downsizing the FC stack and also reducing the rate of potential cycling [173, 15, 5, 154, 33]. Yufit and Brandon [231] developed a FC-battery hybrid system which was actively controlled using a DCDC converter where the lithium-ion battery was used to meet peak power requirements whilst the DCDC converter maintained the FC under a constant current load. Hosseinzadeh *et al.* [95] investigated the theoretical optimisation of an FC-lead acid battery system for a forklift truck power train. An optimal design was found to give theoretical reductions in hydrogen consumption by up to 26% while García *et al.* [83] modelled the performance of a FC-battery-SC powertrain for use on the Urbos 3 tramway in Spain. Using lithium-ion batteries and SCs connected via DCDC converters, the hybrid powertrain was found to theoretically smooth power cycling and enable the fuel cell to operate at conditions close steady state. Efficiencies of the FC were predicted at 60.9% while the hybrid vehicle had a theoretical system efficiency of 55.6%. Hwang and Chang [98] investigated the performance of a FC-lithium ion battery hybrid for use in a light electric vehicle. This powertrain was found to have an efficiency of 46%. Hwang [99] also reported on the performance of a FC-lithium ion battery generator. This system was able to smooth sudden changes in load while allowing FC efficiencies between 52-58%.

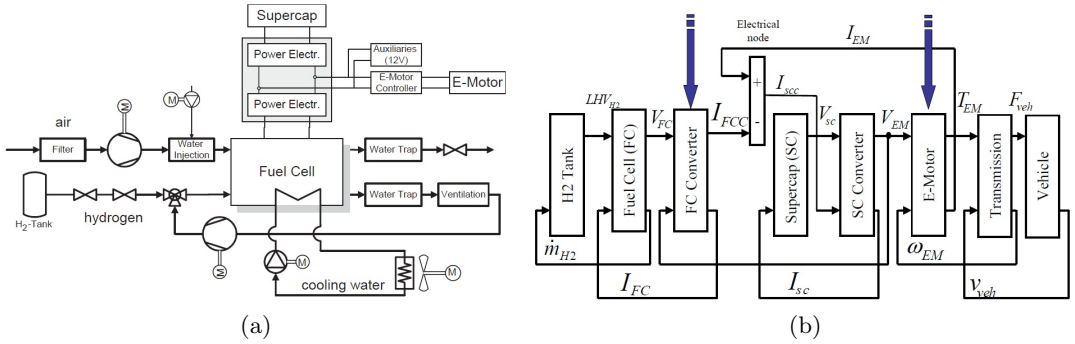


Figure 2.44: (a) Diagram of fuel cell-supercapacitor powertrain layout and (b) powertrain causaility flow chart of the model presented by Rodatz *et al.* [173]

Corbo *et al.* [48] developed a 20 kWe PEMFC system hybridised with a lead acid battery pack for a minibus application. In the hybrid operation mode they quote FC system efficiencies between 45-48% with overall powertrain efficiency of 30%. Here they identified the air management strategies as the critical parameter which affected the stack uniformity performance and suggested that higher air stoichiometries should be used in dynamic conditions compared to steady state. They also compared different hybridisation strategies where the FC dynamics were kept to a minimum (hard) and one where it was allowed to vary more (soft). When the operation mode was switched from soft to hard the DCDC converter efficiency varied from 78 % to 84 % whilst FC efficiency increased from 45 % to 48%. The overall hard operation mode efficiency was approximately 30% compared to the 26% soft mode. This suggests that reduced dynamics on the FC have a significant impact on the overall efficiency of the powertrain.

Varying degrees of FC hybridisation have been reported. Some authors have used the FC as a range extender to battery packs in order to keep the cost of the FC and hydrogen storage low [5]. Andaloro *et al.* [5] reported a FC-battery hybrid system for BUS applications where a 5 kWe PEMFC combined with a ZEBRA battery was used as a range extender. In this configuration, the FC was operated in a constant current mode, with load variations handled by the battery. Here a simple Simulink model of both the battery and FC was used to predict the performance of the system. Whilst a system was reportedly built this was not validated. The FC model was just a static look-up table based on the manufacturers provided data sheet.

Paladini *et al.* [154] developed a vehicle model of a FC-battery-supercapacitor hybrid and optimised for different drive cycles for hydrogen consumption using multi-objective optimisation and genetic algorithms. Here DCDC converter models regulate the power from the FC, nickel metal hydride batter and supercapacitors, in a backwards facing modelling approach. A fixed battery recharging efficiency of 80% was assumed. The FC model used is the semi-empirical model proposed by Amphlett *et al.* [4] for the polarisation curve but does not include any dynamic effects. The battery model is based on a look-up table.

Rodatz *et al.* [173] developed a FC-supercapacitor hybrid system. Here they used a forward facing model with 2 DCDC converters to maintain a constant BUS voltage as shown in Figure 2.44. The FC model used here whilst considering temperature effects does not account for water management and transient effects, nor does the FC model consider the energy requirement from the ancillary components. No detailed description of the supercapacitor model is given and thus it was assumed that at best they used a simple equivalent circuit to model the performance of the supercapacitor.

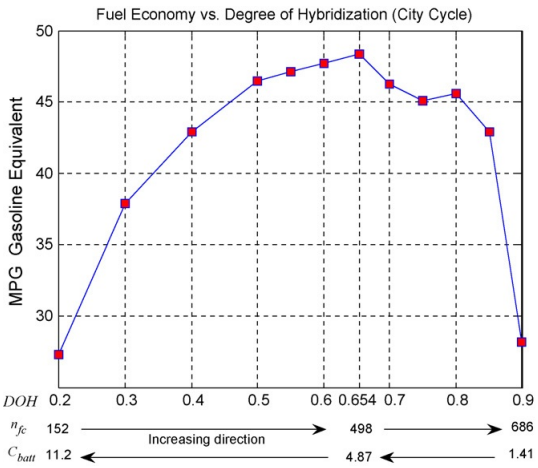


Figure 2.45: Effect of degree of hybridization on fuel economy for city cycle [106]

Baptista *et al.* [15] conducted a life cycle analysis of different vehicle technologies with a London taxi application. They found that FCPHEV had the highest CO_2 emission reduction of 69% when compared against an equivalent ICE taxi. The FCHEV and BEV also showed CO_2 reductions over the lifetime of operation with reduction values of 39% and 64% respectively.

Thounthong *et al.* [200] investigated triple active hybrid systems using a FC, battery and supercapacitor. Small scale validation was achieved. Here they developed a control system to regulate the 3 DCDC converters which regulated power from the different devices. The focus here was on using the controllers to enable the supercapacitors to have the fastest dynamics, batteries to maintain the SOC of the supercapacitors and the FC to have a very low dynamic and meet the average power requirement of the system.

Bubna *et al.* [29] presented work on the development of a FC-battery heavy hybrid bus. Here a 19.4 kW PEMFC stack with a 12.8 kg hydrogen storage capacity. was combined with a 300 V 200Ah NiCd battery system. They have gone for a plug-in configuration where the FC acts as a range extender. Figure 2.43b shows the Sankey diagram for the FC-battery hybrid system. It can be seen that with the incorporation of the battery, relative to pure FCVs it can recover some of the regenerative energy.

Kim and Peng [106] developed a power management optimisation procedure for FC-hybrid vehicle applications. Here they use a pseudo steady state FC model where the polarisation curves are in the form of look up tables but vary depending on the pressure ratio of the compressor. Also, a simple battery model was used based on a single resistance and integration of the SOC to find the OCV. They showed that the most significant efficiency gains come from aggressive downsizing of the FC and increased Degree Of Hybridisation (DOH). Figure 2.45 shows how varying the DOH affects the equivalent MPG of the vehicle. Here DOH represents the ratio of FC power to battery power. They found that excessively smaller FCs and excessively large batteries are not the optimal solution and there is often an intermediate DOH that is best with a ratio of 0.65 for city driving.

Within the hybrid vehicle domain however considerable variations in the results are found due to the near infinite variations in control strategies in power regulation.

Passive hybrid systems

Passive hybridisation involves the direct coupling of electrochemical devices without the need for additional power electronics such as DCDC converters whilst still achieving the

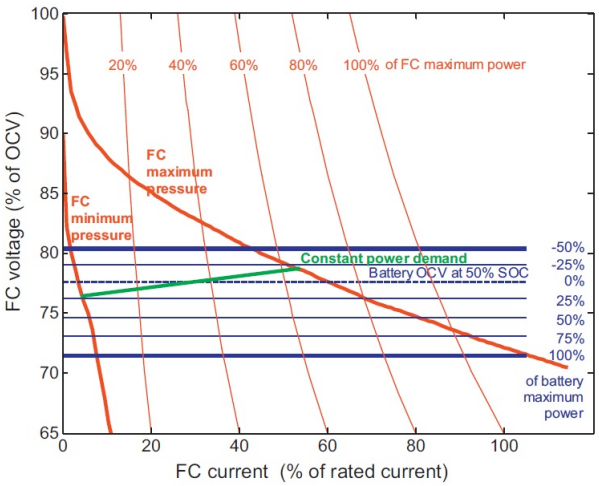


Figure 2.46: Power available from the FC and battery in the passive hybrid architecture [20]

benefits of traditional hybrids in decoupling energy and power requirements. This has the advantage of lower cost due to one less component and no loss from the addition level of power conversion. The disadvantage of this system however is that active power control is often lost.

Several studies have previously looked into the effect of passive hybrid systems. Kuperman *et al.* [113] used a frequency domain approach based analysis to investigate the potential benefits of a battery-supercapacitor passive hybrid. It was shown that supercapacitors act as a low-pass filter for the battery terminals under pulse loading reducing battery stress. The disadvantage of passive hybridisation is therefore the loss of active power regulation control. In the work by Bernard *et al.* [20] they investigated alternative control strategies to counteract the loss of control. This was achieved by active pressure control of the FC stack thereby regulating the operating voltage. As the devices share the same potential, this controls the current flowing out the stack through regulation of the electrochemical overpotential. This is shown in Figure 2.46. Nishizawa *et al.* [144] developed a FC-battery passive hybrid system for aircraft applications and showed that there was an increase in efficiency compared to equivalent systems using DCDC converters and that the lower impedance response of the battery resulted in more mild transient loads for the FC.

Keränen *et al.* [103] developed a FC-supercapacitor-battery triple hybrid. Due to the differences in the impedance of the devices the supercapacitors responded fastest to load changes, whilst the battery gradually ramped up and followed slower dynamics. The FC responded to even slower dynamics and effectively met the average power requirement of the load cycle. This is shown in Figure 2.47a. They showed that benefits of passive hybridisation could be achieved with a relatively small supercapacitor pack as shown in Figure 2.47b. They created a 16 kW system for fork lift applications and developed an model of the powertrain, however this model used an empirically determined FC model, equivalent circuit battery model and a supercapacitor model which did not capture the charge redistribution effects.

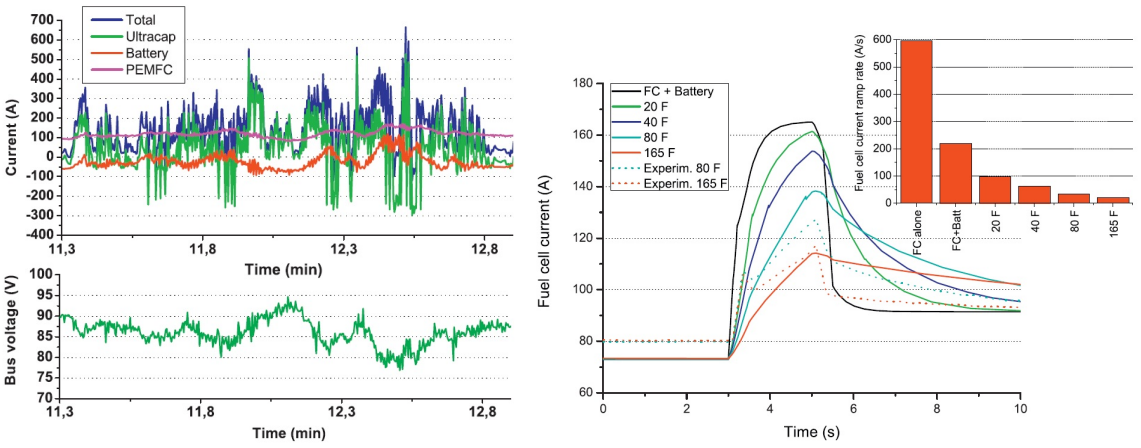
2.5.5 Total Cost of Ownership

One of the important metrics to consider when evaluating a hybrid electric vehicle is the costs involved. When considering the cost of a vehicle there are two main things to consider; the capital cost of acquisition and the running cost of the vehicle. Combined, this is known as the TCO.

It is generally acknowledged that during the early uptake of EVs, the capital cost of acquisition will be higher than an ICE equivalent. Thus, for EVs to be an economically viable option for mainstream adoption, rather than just for niche applications, EVs need to allow for cost savings in other areas. BEVs, FCVs and FCHEVs are generally acknowledged as having higher efficiencies than the ICE counterpart with (in some cases) cheaper fuel resulting in lower running costs. The question thus arises, in which applications would EVs result in a lower TCO than an ICE equivalent and how long would this pay back period be?

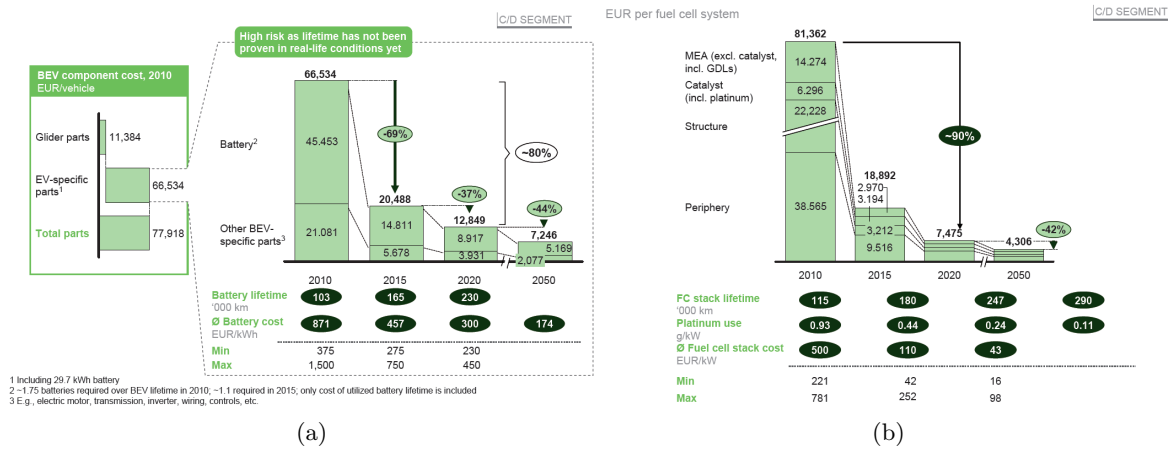
It was shown by McKinsey & Company [135] that the cost of all vehicle powertrains after 2025 converge. It was predicted that the cost of a FC system would decrease by 90% and 80% for a BEV against the 2010 value by 2020 due to economies of scale and incremental improvements in the technology. They also show that PHEVs are more economic than BEVs and FCVs in the short term, however the gap gradually closes and by 2030 PEHVs are cost competitive with BEVs for smaller vehicles with both BEVs and FCEVs for medium cars and less competitive than FCEVs for larger vehicles. Trends in the predicted vehicle costs are shown in Figure 2.48.

The cost of hydrogen will be another critical metric which ultimately determines the success of FC based powertrains. Figure 2.49 shows the predicted cost of hydrogen from



(a) (b)

Figure 2.47: (a) Currents and BUS voltage of triple passive hybrid system and (b) comparison of energy storage systems and PEMFC power distribution during a 300A current peak on different supercapacitor sizes [103]



(a) (b)

Figure 2.48: Predicted cost of a (a) BEV and (b) a FC system for a C/D segment vehicle [135]

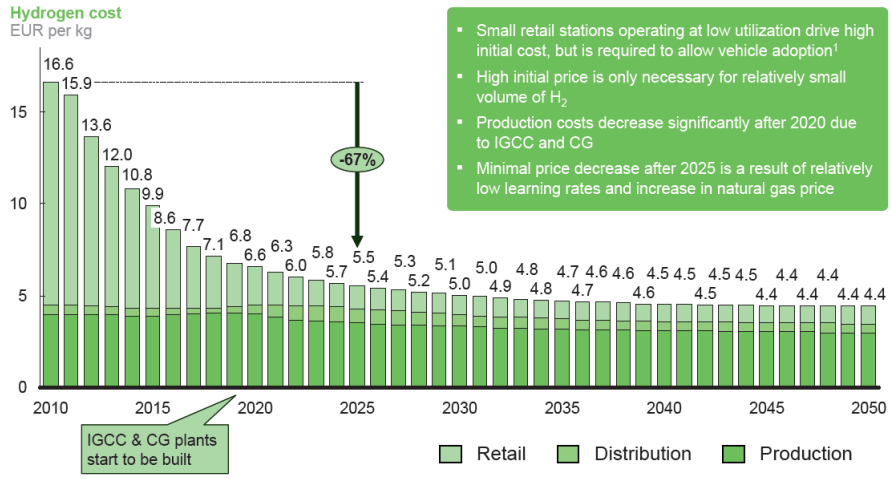


Figure 2.49: Predicted cost of hydrogen delivered at the pump without taxes/excises. Adapted from McKinsey & Company [135]

2010-2050 and suggests that the production costs will significantly decrease by 67% by 2020 due to the introduction of Integrated Gasification Combined Cycle (IGCC) and Coal Gasification (CG) plants.

2.5.6 Summary of powertrain comparison literature review

This section presented the relevant literature relating to academic works on FCV, BEV and FCHEV powertrain studies. The below thus lists the key findings:

- The selection of a vehicle load cycle has been acknowledged as being a critical parameter in assessment of different vehicle technologies
- Much of the techno-economic analysis of electric vehicles uses oversimplified models of the electrochemical devices
- Few studies on the comparison of different FC hybrid configurations subdivide the market (i.e. applied load cycles)
- Many hybrid system analysis works use steady state models which do not account for water management issues
- Works on FC hybrid vehicles have mainly focused on active hybrids with few works detailing FC passive hybrid systems
- No studies exist that comprehensively compare FC hybrid configurations with other all electric alternatives with detailed, experimentally validated models
- Passive hybrid systems have been identified as being one possible powertrain configuration which allows for cost reductions through removal of the DCDC converter, but few works have been published in this area with none focused on FC-supercapacitor passive hybrid systems

The motivation for subsequent work based on the review of the current literature will therefore focus on initially developing a rigorous understanding of vehicle load cycles, integration of the high fidelity models developed into a vehicle modelling platform to probe efficiency and cost metrics and to investigate the feasibility of FC-supercapacitor passive hybrid systems, which has currently not been investigated.

2.6 Summary of literature review and motivation for work

The previous sections have detailed the current state-of-the-art regarding lithium-ion batteries, PEMFCs, supercapacitors and their application in EVs. As mentioned, the focus on this PhD work is on developing the tools and techniques required to assess the feasibility of these technologies in different configurations. The presented literature review thus provides a framework to build upon and has highlighted a number of different areas which are currently missing in the academic literature which this work hope to contribute towards.

As such, the below lists the main gaps in the current academic literature which will act as motivation for the work in the subsequent chapters.

2.6.1 Lithium-ion batteries

Physics based models have been shown to offer significant advantages in providing additional information about the performance of batteries in automotive systems, with the Newman model being the current standard. Temperature effects in batteries have been identified as being a critical parameter, both in terms of efficiency but also in terms of safety. Thus, the motivation for the development of a battery model will focus on a coupled thermal-electrochemical model. Whilst, works have been presented on the application of these models in predicting the performance of an EV, simplifying assumptions have been made about the scale up effects from single to multi-cell level system with the effect of interconnect resistances neglected.

The analysis of the degradation mechanisms in lithium-ion batteries has shown the cause to be many and varied depending on the chemistry used, cell design, operating conditions and many other factors. Capturing all of these effects, thus has been identified as being beyond the scope of this project but the developed models will focus on the most significant which has been identified as being the growth and evolution of the SEI layer.

In addition, diagnosis techniques of batteries are limited somewhat to laboratory based EIS measurements and currently very few detailed in-situ techniques exist which allows for additional electrochemical information to be extracted. Addition to the academic literature in this area will thus be addressed.

2.6.2 Proton Exchange Membrane Fuel Cells

Analysis of the literature regarding PEMFCs in automotive applications have shown that the critical effects that need to be captured are: mass transport from BOP components, thermal and water management issues. The vast majority of the academic literature revolving around the analysis of FC systems for automotive applications use steady state models and/or neglect the effect of the BOP. Thus, the this work will focus on the development of a PEMFC stack model that assumes lumped performance but considers transient thermal, mass transport and water balances. This will also include models of the BOP components, which are critical metrics in assessing the parasitic power consumption.

The critical degradation modes in FCs under automotive load cycles were identified as being start-up/shut-down, rapid power cycling and no load idling. System design cannot affect the number of start-up/shut-down cycles but can affect the rate of power cycling and no-load idling. Analysis of the literature has shown that there is no comprehensive model of these two modes of degradation suitable for system level analysis and it is beyond the scope of this project to develop new models for quantifying these effects however consideration of these factors will be made in a qualitative manner.

2.6.3 Supercapacitors

It has been shown that the vast majority of the academic literature use equivalent circuit models to describe the performance of supercapacitors. The critical effects to consider have been identified as being the charge redistribution effect and the frequency dependent performance. Thus, the modelling efforts of subsequent chapters will focus on the development of a transmission line base model that accounts for charge redistribution and frequency dependent effects. The relatively low impedance of the devices relative to FCs and batteries means that heat generation will be lower and thus a thermal model will not be included as the literature suggest a weak temperature dependency of capacitance with temperature within the normal EV operating range.

No comprehensive degradation model of supercapacitors which is suitable for system level modelling exists and due to the already high durability of supercapacitors this will not be developed within the framework on this PhD.

The capacitance behaviour with voltage and frequency, however is seen as a critical metric to understand and there will be efforts made to develop diagnosis tools for extracting this information from the supercapacitor in novel ways.

2.6.4 Powertrain comparison

Whilst it was acknowledged in many publications that the selection of a load cycle will have a dramatic effect on the merits of one vehicle powertrain over another, the vast majority of the academic works have not taken this into consideration with works presents on a single load cycle only. Further to this, the vast majority of system level analysis works use over simplified models and techno-economical works typically make further high level assumptions about the efficiency and performance of different systems.

Thus, the motivation for the powertrain comparison work is to assess different vehicle load cycles and then use the developed models of lithium-ion batteries, PEMFCs and supercapacitors to answer system level questions. The study of power flows within active hybrid systems is near exhaustive and thus a detailed analysis of different energy management strategies will not be covered. Rather a few case studies will be investigated and compared against each other to demonstrate the developed tools and techniques, which are the main focus of this work.

Passive hybrid systems were in particular identified as being a promising means of cost reduction due to the removal of the DCDC converter and thus this will be investigated in more detail, with the focus being on FC-supercapacitor hybrids, of which there are currently no publications in this area.

Chapter 3

Lithium-ion batteries

3.1 Introduction: Lithium-ion batteries

This chapter presents the modelling and experimental work relating to the development of a physics based lithium-ion battery model and its subsequent application to investigating performance limitations in automotive applications and the development of novel diagnosis techniques. This will provide the foundation for subsequent system level analysis of hybrid systems. The below therefore lists the contents on this chapter.

- **Formulation of a pseudo 2D thermally coupled-physics based lithium-ion battery model**
  - This section sets the mathematical framework and solution methods for the thermally coupled-physics based lithium-ion battery model which includes details of the SEI based degradation model
- **Formulation of reduced order single particle-thermally coupled-physics based battery model**
  - This section sets the mathematical framework and solution methods for the thermally coupled-physics based lithium-ion battery model which is based on the single particle approximation for improved speed of operation
- **Experimental set-up and model parameterisation**
  - This section outlines the experimental set-up and techniques used to acquire data needed to parameterise and validate the developed model. It then details the genetic algorithm based techniques used to parameterise the developed battery model and substantially validates the result with experimental data collected
- **Model based investigation of battery performance**
  - The section uses the validated model to investigate rate limiting effects in lithium-ion batteries when used in automotive applications and explores how the model can be used to select optimal operating points and cell designs
- **In-situ monitoring techniques of stoichiometric drift**
  - This section presents the work done on using the models to develop in-situ diagnosis techniques to monitor battery electrode stoichiometric drift over the lifetime of use and includes a novel thermal-entropy based monitoring technique
- **Model based investigation of battery pack design**
  - This section presents the work on taking a single cell model and expanding this to a pack level model and investigating pack architecture designs and implications on performance driven by fundamental physics based phenomena

For a vehicle with an electric powertrain that uses batteries, it is important to understand the limitations on performance, the dynamics of the transient behaviour and the modes of degradation. Understanding the operating characteristics of batteries as a form of energy storage will enable the effective development of a hybrid powertrain utilising FCs and/or supercapcitors.

3.2 Battery model equations

Analysis of the existing academic literature has shown that physics based models assuming continuum mechanics can be solved at speeds suitable for system level analysis and that they provide significant insight into the performance of batteries and their rate limiting processes. In addition to this, the high temperature dependency of these systems necessitates a thermally coupled model. The following works will therefore focus on the development of a model based on this.

The most generally used electrochemical model of the lithium-ion battery is based the original works by Newman, Doyle and Fuller [82, 61, 62] which is currently accepted as being the standard for cell level, physics based modelling of lithium-ion batteries [189]. This model couples the reaction current density with mass and charge conservation equations to describe the physics occurring within the battery.

The unit cell of a lithium-ion battery typically consists of five main components. A porous negative electrode, positive electrodes and separator, immersed in an ionically conductive electrolyte with metallic current collector connected to each electrode. Other materials such as binder for the anode and conductive additives are also typically present, however in smaller proportions. In order to reduce the internal impedance to increase power capabilities of the cell, the thickness of the electrode layers and separators are typically kept to as small as possible. The unit cells are then stacked in parallel within the cell to increase the available capacity. Figure 3.1 shows the different spatial domains of a lithium-ion battery which were modelled.

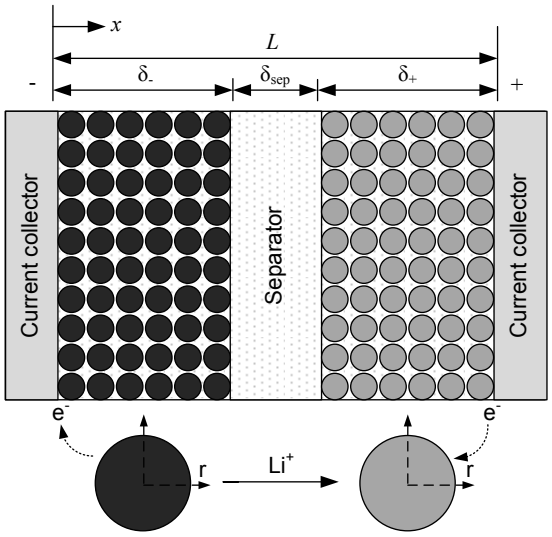


Figure 3.1: Schematic of 1D (x-diection) electrochemical cell model with coupled 1D microscopic (r-direction) solid diffusion mode [224]

The 1D macroscopic model uses concentrated solution theory to describe the transport of lithium-ions and lithium in the solution and solid phases respectively with a Bruggeman modified Fick's diffusion rate law equation to account for bulk porosity. The electrolyte is assumed to be a binary salt in a single solvent. The composite negative and positive electrode as been assumed to be a single phase with volume fractions of binding and conductive additives considered. The porous electrode theory used assumes the various phases can be superimposed to create a continua. The intercalation electrodes were assumed to be spherical particles of constant diameters [61]. The effect of double layer capacitance has not been incorporated due to the relative time constant of this process being outside of the region of interest.

Table 3.1: 1D electrochemical model equations [189]

Lithium, electrolyte phase (c_e)	$\frac{\partial(\varepsilon_e c_e)}{\partial t} = \frac{\partial}{\partial x}\left(D_e^{eff}\frac{\partial}{\partial x}c_e\right) + \frac{1-t_+^0}{F}j^{Li}$ $\frac{\partial c_e}{\partial x}\Big\|_{x=0} = \frac{\partial c_e}{\partial x}\Big\|_{x=L} = 0$
Lithium, solid phase (c_s)	$\frac{\partial c_s}{\partial t} = \frac{D_s}{r^2}\frac{\partial}{\partial r}\left(r^2\frac{\partial c_s}{\partial r}\right)$ $\frac{\partial c_s}{\partial r}\Big\|_{r=0} = 0, -D_s\frac{\partial c_s}{\partial r}\Big\|_{r=R_s} = \frac{j^{Li}}{a_s F}$
Charge, electrolyte phase (ϕ_e)	$\frac{\partial}{\partial x}\left(\kappa^{eff}\frac{\partial}{\partial x}\phi_e\right) + \frac{\partial}{\partial x}\left(\kappa_D^{eff}\frac{\partial}{\partial x}\ln c_e\right) + j^{Li} = 0$ $\frac{\partial \phi_e}{\partial x}\Big\|_{x=0} = \frac{\partial \phi_e}{\partial x}\Big\|_{x=L} = 0$
Charge, solid phase (ϕ_s)	$\frac{\partial}{\partial x}\left(\sigma^{eff}\frac{\partial}{\partial x}\phi_s\right) = j^{Li}$ $-\sigma_-^{eff}\frac{\partial \phi_s}{\partial x}\Big\|_{x=0} = \sigma_+^{eff}\frac{\partial \phi_s}{\partial \phi_x}\Big\|_{x=L} = \frac{I}{A}, \frac{\partial \phi_s}{\partial x}\Big\|_{x=\delta_-} = \frac{\partial \phi_s}{\partial x}\Big\|_{x=L-\delta_+} = 0$
Electrochemical kinetics reaction rate (j^{Li})	$j^{Li} = a_s i_0\left\{exp\left[\frac{\alpha_a F}{RT}\left(\eta - \frac{R_{SEI}}{a_s}j^{Li}\right)\right] - exp\left[-\frac{\alpha_c F}{RT}\left(\eta - \frac{R_{SEI}}{\alpha_s}j^{Li}\right)\right]\right\}$
Overpotential (η)	$\eta = \phi_s - \phi_e - U$
Electrolyte ionic diffusional conductivity (κ_D^{eff})	$\kappa_D^{eff} = \frac{2RT\kappa^{eff}}{F}(t_+^0 - 1)\left(1 + \frac{dlnf_\pm}{dlnc_e}\right)$
Specific interfacial surface area (a_s)	$a_s = \frac{3\varepsilon_s}{r_s}$

The model presented is based on the equations presented by Smith and Wang [189] and consists of 4 partial differential equations describing solid and electrolyte phase species concentrations and potentials. These are linked to a Butler-Volmer reaction rate equation. The equations which define the model are shown in Table 3.1. The solution of these partial differential equations is achieved by use of Finite Difference Method (FDM) numerical methods.

Figure 3.2 shows a flowchart of the solution method employed to solve the set of partial differential equations for the battery mass and charge conservation and diffusion processes. An iterative approach to converging to the a valid solution for the reaction current density is adopted which is also described. The code was written in the Matlab programming environment and later integrated into the Simulink modelling environment by the use of an embedded MATLAB function block.

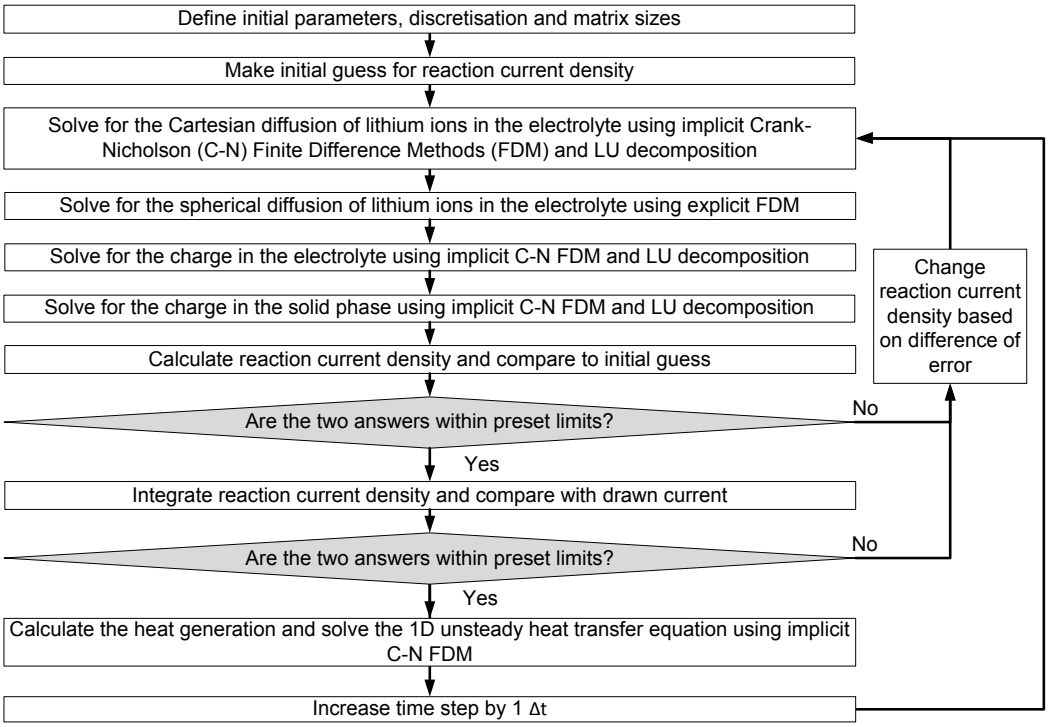


Figure 3.2: Solution flow charge for battery code [224]

3.2.1 Lithium in the electrolyte phase

During operation, lithium-ion concentration gradients are established in the electrolyte phase which results in a relative ionic motion that can be characterised by a Fick's diffusion law equation with a electrochemical source term as shown in Equation 3.1, where ε_e is the volume fraction of the electrolyte phase, c_e is the volume averaged concentration of lithium in the electrolyte phase (mol cm^{-3}), t is time (s), x is the distance along the cell width (cm), D_e^{eff} is the effective diffusion coefficient of lithium in the electrolyte (cm^{2}s^{-1}), t_+^0 is the transference number of lithium ions, F is Faraday's constant and j^{Li} is the reaction current due to the consumption or production of lithium (A cm^{-3}). The inclusion of the transference number in equation 3.1 and in the conductivity equation account for the effect of the counter ions needed to maintain charge neutrality. No ionic flux is allowed at the current collectors dictating that there are two zero gradient Neumann boundary conditions at these points, as represented in Equation 3.2.

$$\frac{\partial(\varepsilon_e c_e)}{\partial t} = \frac{\partial}{\partial x}\left(D_e^{eff}\frac{\partial}{\partial x}c_e\right) + \frac{1-t_+^0}{F}j^{Li} \tag{3.1}$$

$$\left.\frac{\partial c_e}{\partial x}\right|_{x=0} = \left.\frac{\partial c_e}{\partial x}\right|_{x=L} = 0 \tag{3.2}$$

Equation 3.1 is a parabolic partial differential equation. This was solved by using a implicit Crank-Nicolson Finite Difference Method solution scheme. The Crank-Nicolson scheme is a combination of the Backwards Time Centered Space (BTCS) scheme used to solve the first order time derivative and the average of the central difference scheme for the second order spatial derivative.

Assuming no source term for Equation 3.1 the discretised form of the parabolic partial differential equation is shown in Equation 3.3 where i represents the spatial node evaluated

at time step j, δt is the size of the time step and δx is the size of the spatial discretization.

$$\frac{c^e_{i,j+1} - c^e_{i,j}}{\delta t} = \frac{D^{eff}_e}{2}\left\{\frac{c^e_{i+1,j+1} - 2c^e_{i,j+1} + c^e_{i-1,j+1}}{\delta x^2} + \frac{c^e_{i+1,j} - 2c^e_{i,j} + c^e_{i-1,j}}{\delta x^2}\right\} \tag{3.3}$$

Rearranging this so that all the $j+1$ terms are on the LHS and the j terms are on the RHS results in Equation 3.4 where $\beta = D^{eff}_e \frac{\delta t}{\delta x^2}$.

$$-\beta c^e_{i-1,j+1} + (2+2\beta)c^e_{i,j+1} - \beta c^e_{i+1,j+1} = -\beta c^e_{i-1,j} + (2+2\beta)c^e_{i,j} - \beta c^e_{i+1,j} \tag{3.4}$$

To apply the zero gradient boundary conditions in Equation 3.2, central difference theorem is used on the end nodes and rearranged to eliminate the non-existing nodes. The resulting set of equations are written in matrix form as shown below and a solution is found using LU decomposition which writes a matrix as the product of a lower and upper triangular matrix to find the implicit solution for the next time step. The advantage of using an implicit solution is that it is more numerically stable and it gives more accurate solutions than explicit schemes like forward or backwards differencing.

$$\begin{pmatrix} 2+2\beta & -2\beta & & & & \\ -\beta & 2+2\beta & -\beta & & & \\ & \ddots & \ddots & \ddots & & \\ & & -\beta & 2+2\beta & -\beta & \\ & & & -2\beta & 2+2\beta \end{pmatrix} \begin{pmatrix} c^e_{i,j+1} \\ c^e_{i+1,j+1} \\ \vdots \\ c^e_{n-1,j+1} \\ c^e_{n,j+1} \end{pmatrix} = \begin{pmatrix} (2-2\beta)c^e_{i,j} + 2\beta c^e_{i+1,j} \\ \beta c^e_{i-1,j} + (2-2\beta)c^e_{i,j} + \beta c^e_{i+1,j} \\ \vdots \\ \beta c^e_{n-2,j} + (2-2\beta)c^e_{n-1,j} + \beta c^e_{n,j} \\ 2\beta c^e_{n-1,j} + (2-2\beta)c^e_{n,j} \end{pmatrix}$$

The electrochemical source term attributed to the reaction current for each node was then added to the solution of the differential diffusion equation.

3.2.2 Lithium in the solid phase

It has been assumed that within each discretization node in the through plane direction there is a single spherical solid particle representing the porous electrode material. The diffusion of lithium within the particle is represented by a spherical Fick's diffusion law equation shown in Equation 3.5 where c_s is the volume averaged solid phase lithium concentration (mol cm^{-3}), r is the radius (cm) and D_s is the solid phase lithium diffusion coefficient (cm^2 s^{-1}).

$$\frac{\partial c_s}{\partial t} = \frac{D_s}{r^2}\frac{\partial}{\partial r}\left(r^2\frac{\partial c_s}{\partial r}\right) \tag{3.5}$$

When a battery is discharged/charged lithium ions are deintercalated/intercalated from the negative electrode, this is interpreted as a species surface flux with the boundary conditions shown in Equation 3.6, where a_s is the active surface area per electrode unit volume (cm^2 cm^{-3}) and R_s is the radius of the spherical particles (cm).

$$\left.\frac{\partial c_s}{\partial r}\right|_{r=0} = 0, -D_s\left.\frac{\partial c_s}{\partial r}\right|_{r=R_s} = \frac{j^{Li}}{a_s F} \tag{3.6}$$

This equation is a parabolic partial differential equation; however, the problem with using the Crank-Nicolson solution scheme is that the equation is solved in spherical polar

coordinates which means that at the centre of the radial coordinate system $r \rightarrow 0$ which leads to an asymptote solution. Therefore, to solve the solid phase lithium diffusion in the spherical co-ordinate system an explicit solution scheme is used as shown in the below Equation [49].

$$\frac{1}{r^2}\frac{\partial}{\partial r}\left(r^2\frac{\partial c_s}{\partial r}\right) = \begin{cases} \frac{1}{i(\delta r)^2}\{(i+1)c^s_{i+1,j} + 2ic^s_{i,j} + (i-1)c^s_{i-1,j}\} & \text{if i}\neq 0 \\ \frac{6}{(\delta r)^2}(c^s_{1,j} - c^s_{0,j}) & \text{if i}=0 \end{cases}$$

The explicit form of the discretised equation was then combined with the surface flux boundary conditions, written in the below matrix form and solved explicitly for the next time step.

$$\frac{D_s\delta t}{(\delta r)^2}\begin{pmatrix} -6 & 6 & & & \\ \frac{i-1}{i} & -\frac{2i}{i} & \frac{i+1}{i} & & \\ & \ddots & \ddots & \ddots & \\ & & \frac{(i+1)}{i} & -\frac{2i}{i} & \frac{i+1}{i} \\ & & & \frac{n+1}{N} & -\frac{2n}{n} \end{pmatrix}\begin{pmatrix} c^s_{i,j} \\ c^s_{i+1,j} \\ \vdots \\ c^s_{n-1,j} \\ c^s_{n,j} \end{pmatrix} = \begin{pmatrix} c^s_{i,j+1} - c^s_{i,j} \\ c^s_{i+1,j+1} - c^s_{i+1,j} \\ \vdots \\ c^s_{n-1,j+1} - c^s_{n-1,j} \\ c^s_{n,j+1} - c^s_{n,j} + (n+1)\frac{j^{Li}2\delta t}{a_s F n \delta r} \end{pmatrix}$$

3.2.3 Charge in the electrolyte phase

Consideration of electrolyte charge conservation yields Equation 3.7, where κ^{eff} is the effective conductivity of the electrolyte (S cm^{-1}), κ_D^{eff} is the diffusional conductivity of the lithium (A cm^{-1}) and ϕ_e is the electrolyte potential (V). As there is no electrolyte phase potential flux at the current collectors, zero gradient boundary conditions defined as shown in Equation 3.8 where L is the length of the electrode domain (cm).

$$\frac{\partial}{\partial x}\left(\kappa^{eff}\frac{\partial}{\partial x}\phi_e\right) + \frac{\partial}{\partial x}\left(\kappa_D^{eff}\frac{\partial}{\partial x}\ln c_e\right) + j^{Li} = 0 \tag{3.7}$$

$$\left.\frac{\partial \phi_e}{\partial x}\right|_{x=0} = \left.\frac{\partial \phi_e}{\partial x}\right|_{x=L} = 0 \tag{3.8}$$

The diffusional conductivity of lithium ions in the electrolyte can be defined with consideration of Equation 3.9 where $f_\pm$ is the activity coefficient which is assumed constant, R is the universal gas constant and T is absolute temperature (K).

$$\kappa_D^{eff} = \frac{2RT\kappa^{eff}}{F}(t_+^0 - 1)\left(1 + \frac{d\ln f_\pm}{d\ln c_e}\right) \tag{3.9}$$

The problem with Equation 3.7 is that it is a steady state problem with two zero-gradient boundary conditions. This leads to a zero determinant and is therefore singular. To solve this problem a node must be fixed as a reference value and since only potential differences can be measured, the boundary condition for ϕ_e becomes arbitrary. Based on [40] the reference node was chosen to be the positive electrode/current collector interface which was set to zero potential.

The solution method used was an explicit forward differencing FDM scheme. The discrete form of the partial differential equation for charge in the electrolyte is shown in Equation 3.10.

$$\kappa^{eff}\left\{\frac{\phi^e_{i+1,j} - 2\phi^e_{i,j} + \phi^e_{i-1,j}}{\delta x^2}\right\} + \kappa_D^{eff}\left\{\frac{\ln c^e_{i+1,j} - 2\ln c^e_{i,j} + \ln c^e_{i-1,j}}{\delta x^2}\right\} + j^{Li} = 0 \tag{3.10}$$

The zero gradient boundary conditions are then accounted for by use of central difference method being applied at the end node to eliminate nodes which are not within the accounted spatial domain. The equations are then written into matrix form as shown below and solved using LU decomposition.

$$\frac{\kappa^{eff}}{\delta x^2}\begin{pmatrix} -2 & 2 & & & \\ 1 & -2 & 1 & & \\ & \ddots & \ddots & \ddots & \\ & & 1 & -2 & 1 \\ & & & 0 & 1 \end{pmatrix}\begin{pmatrix} \phi^e_{i,j} \\ \phi^e_{i+1,j} \\ \vdots \\ \phi^e_{n-1,j} \\ \phi^e_{n,j} \end{pmatrix} = \frac{\kappa^{eff}_D}{\delta x^2}\begin{pmatrix} 2\ln ci^e_{i,j} + 2\ln c^e_{i+1,j} \\ -\ln c^e_{i-1,j} + 2\ln c^e_{i,j} - \ln c^e_{i+1,j} \\ \vdots \\ -\ln c^e_{n-2,j} + 2\ln c^e_{n-1,j} - \ln c^e_{n,j} \\ 0 \end{pmatrix} - j^{Li}$$

3.2.4 Charge in the solid phase

Consideration of the conservation of charge in the solid phase results in Equation 3.11, where ϕ_s is the solid phase potential (V) and σ^{eff} is the solid phase effective conductivity (S cm^{-1}).

$$\frac{\partial}{\partial x}\left(\sigma^{eff}\frac{\partial}{\partial x}\phi_s\right) = j^{Li} \tag{3.11}$$

The solid phase is not continuous over the whole spatial domain of the cell meaning that Equation 3.11 is only valid within each electrode and the solution should be divided into two sections. At the electrode/separator interface there is no charge flux giving a zero gradient Neumann boundary condition. At the electrode/current collector interface there is a charge flux which is a function of the drawn current. The boundary conditions for the conservation of charge in the solid phase are therefore shown in Equation 3.12.

$$-\sigma^{eff}_{-}\frac{\partial\phi_s}{\partial x}\bigg|_{x=0} = \sigma^{eff}_{+}\frac{\partial\phi_s}{\partial\phi_s}\bigg|_{x=L} = \frac{I}{A}, \frac{\partial\phi_s}{\partial x}\bigg|_{x=\delta_-} = \frac{\partial\phi_s}{\partial x}\bigg|_{x=L-\delta_+} = 0 \tag{3.12}$$

For the solution of charge in the solid phase an explicit forward differencing scheme was used. The steady nature of the governing equation means that a Crank-Nicolson scheme is not needed in conjuncture with this solution. Since this is a steady problem with two gradient boundary conditions within each electrode domain a singularity solution would arise if not further constrained as with the charge conservation in the electrolyte phase. Therefore, the electrode/separator node in both domains was fixed to a reference potential found by using Equation 3.14 which is a form of the Butler-Volmer equation [40]. The discretised form Equation 3.11 can therefore be written as in Equation 3.13.

$$\frac{\sigma^{eff}}{\delta x^2}\left\{\phi^s_{i+1,j} - 2\phi^s_{i,j} + \phi^s_{i-1,j}\right\} = j^{Li} \tag{3.13}$$

Central difference theorem is used to account for flux boundary conditions. The resulting set of equations are written into matrix form as shown below for the negative and positive electrode respectively.

$$\frac{\sigma^{eff}}{\delta x^2}\begin{pmatrix} -2 & 2 & & & \\ 1 & -2 & 1 & & \\ & \ddots & \ddots & \ddots & \\ & & 1 & -2 & 1 \\ & & & 0 & 1 \end{pmatrix}\begin{pmatrix} \phi^s_{i,j+1} \\ \phi^s_{i+1,j+1} \\ \vdots \\ \phi^s_{n-1,j+1} \\ \phi^s_{n,j+1} \end{pmatrix} = \begin{pmatrix} -j^{Li} - \frac{2I}{A\delta x} \\ -j^{Li} \\ \vdots \\ -j^{Li} \\ \phi^s_{ref} \end{pmatrix}$$

$$\frac{\sigma^{eff}}{\delta x^2}\begin{pmatrix} 1 & 0 & & & \\ 1 & -2 & 1 & & \\ & \ddots & \ddots & \ddots & \\ & & 1 & -2 & 1 \\ & & & 2 & -2 \end{pmatrix}\begin{pmatrix} \phi^s_{i,j+1} \\ \phi^s_{i+1,j+1} \\ \vdots \\ \phi^s_{n-1,j+1} \\ \phi^s_{n,j+1} \end{pmatrix} = \begin{pmatrix} \phi^s_{ref} \\ -j^{Li} \\ \vdots \\ -j^{Li} \\ -j^{Li} - \frac{2I}{A\delta x} \end{pmatrix}$$

LU decomposition is then used to solve for the steady solution at that time step.

3.2.5 Reaction current density

A reaction current term links the four governing partial differential equations. This reaction current is defined by the charge/discharge rate imposed and represents the relative rate of lithium intercalation/deintercalation. The reaction rate equation is shown in Equation 3.14 and is a form of the Butler-Volmer equation, where i_0 is the exchange current density (A cm^{-2}), η is the overpoential (V), α_a and α_c anodic and cathodic transfer coefficients respectively and R_{SEI} is the SEI layer resistance (Ω).

$$j^{Li} = a_s i_0 \left\{ \exp\left[\frac{\alpha_a F}{RT}\left(\eta - \frac{R_{SEI}}{a_s} j^{Li}\right)\right] - \exp\left[-\frac{\alpha_c F}{RT}\left(\eta - \frac{R_{SEI}}{\alpha_s} j^{Li}\right)\right]\right\} \tag{3.14}$$

Here a_s is the specific interfacial surface area of the discretised particles and is a function of the electrode porosity and radius as defined by Equation 3.15.

$$a_s = \frac{3\varepsilon_s}{r_s} \tag{3.15}$$

η represents the overpotential which is the deviation in potential from the theoretical thermodynamic potential. This is shown in Equation 3.16 where U represents the Open Circuit Voltage (OCV) or the thermodynamic equilibrium potential.

$$\eta = \phi_s - \phi_e - U \tag{3.16}$$

The exchange current density (i_0) is a function of the electrolyte and solid phase lithium concentrations according to Equation 3.17. Where k is a rate constant and α_a and α_c represent the anodic and cathodic transfer coefficients, respectively [62, 229].

$$i_0 = Fkc_e^{\alpha_a}\left(c_{s,max} - c_{s,surface}\right)^{\alpha_a} c_{s,surface}^{\alpha_c} \tag{3.17}$$

This follows the general form for the exchange current density equations when derived from the equating the forward and backwards rate constants of a reaction as presented by Bard and Faulkner [16]. Modifications appear in the form of the difference in maximum to surface lithium concentration in the solid phase, which act as a rate constant modifier as suggested by Doyle and Newman [62].

3.2.6 Thermodynamic electrode potential

The OCV is a function of surface lithium concentration, electrode material and temperature. For the purposes of this model, the OCV of each electrode is initially based on empirical data from [189] which is a function of surface lithium stoichiometry for the negative electrode (x)(graphite) and positive electrode (y)(lithium cobalt oxide). This will be later reparameterised for the specific battery chemistry under investigation. The electrode

potential equations as a function of lithiation is shown in Equations 3.18 and 3.19 respectively. If modelling different electrode chemistries, this can replaced with the respective equation.

$$\begin{aligned} U_{-} &= 8.00229 + 5.0647x - 12.578x^{0.5} - 8.6322 \times 10^{-4}x^{-1} + 2.1765 \times 10^{-5}x^{1.5} \\ &\quad -0.46016\exp(15[0.06 - x]) - 0.55364\exp(-2.4326x - 0.92) \end{aligned} \tag{3.18}$$

$$\begin{aligned} U_{+} &= 85.681y^{6} - 357.7y^{5} + 613.89y^{4} - 555.65y^{3} + 281.06y^{2} - 76.648y \\ &\quad -0.30987\exp(5.657y^{115}) + 13.1938 \end{aligned} \tag{3.19}$$

The measured voltage of a cell is therefore defined as the potential difference between the two end nodes and the instantaneous potential drop caused by contact resistances (R_c) as shown in Equation 3.20.

$$V = \phi_s|_{x=L} - \phi_s|_{x=0} - \frac{R_c}{A}I \tag{3.20}$$

3.2.7 Battery thermal model

For the thermal model, temperature dependent terms (Ψ) vary according to a general Arrhenius rate law as shown in Equation 3.21 where Ψ_{ref} is the reference parameter at the reference temperate T_{ref} (K) and E_{act}^{Ψ} is a thermal activation energy (J mol^{-1}).

$$\Psi = \Psi_{ref}\exp\left[\frac{E_{act}^{\Psi}}{R}\left(\frac{1}{T_{ref}} - \frac{1}{T}\right)\right] \tag{3.21}$$

Heat generation in a cell can be divided into four main contributions: reaction heat (q_r), Ohmic heat from ionic transfer through the solid and electrolyte phase (q_j), Ohmic heat from contact resistance (q_c) and reversible entropy heats (q_e) associated with phase transitions in the electrode materials during intercalation/ deintercalation.

The volume specific reaction heat is calculated as the product of the overpotential and the reaction current as shown in Equation 3.22. Since there is no reaction current in the separator domain of the battery there will also be no reaction heat within this domain.

$$q_r = A\int_{x}^{x+dx} j^{Li}(\phi_s - \phi_e - U)\mathrm{d}x \tag{3.22}$$

Within the electrode-separator-electrode spatial domain, ohmic heat is generated due to the current carried and also by the resistive properties of that phase. By using the conservation of charge relationship for each phase, the ohmic heat can be calculated from the potential gradients generated. This is shown in Equation 3.23 where the first term represents the ohmic heat of the solid phase and the other terms represent the ohmic heat of the electrolyte phase.

$$q_j = A\int_{x}^{x+dx}\left[\sigma^{eff}\left(\frac{\partial\phi_s}{\partial x}\right)^2 + \kappa^{eff}\left(\frac{\partial\phi_e}{\partial x}\right)^2 + \kappa_D^{eff}\left(\frac{\partial \ln c_e}{\partial x}\right)\left(\frac{\partial\phi_e}{\partial x}\right)\right]\mathrm{d}x \tag{3.23}$$

Ohmic heating also arises due to the contact resistance between the electrode and the current collectors. This heat source only acts on the end nodes and is shown in Equation 3.24.

$$q_c = I^2 \frac{R_c}{A} \tag{3.24}$$

Reversible heating in the cell arises due to phase transitions and related entropic changes in the electrode structures during lithiation/delithiation. This can be represented with the equation shown in Equation 3.25, where $\partial U/\partial T$ is the temperature dependency of the potential of each electrode.

$$q_e = aj^{li} T \frac{\partial U}{\partial T} \tag{3.25}$$

The unsteady heat equation is applied with the heat terms acting as source terms and natural convection boundary conditions at the two end surfaces of the cell. This is shown in Equations 3.26 with boundary conditions shown in Equation 3.27, where ρ is the density (kg m^{-3}), C_p is the specific heat capacity (kJ kg^{-1} K^{-1}), k is the thermal conductivity (W m^{-1} K^{-1}), h is the convective heat transfer coefficient (W m^{-2} K^{-1}) , A_s is the convective area (m^2) and T_{amb} is the ambient temperature (K).

$$\rho C_p \frac{\partial T}{\partial t} = \frac{\partial}{\partial x}\left(k \frac{\partial T}{\partial x}\right) + (q_r + q_j + q_c + q_e) \tag{3.26}$$

$$\left.\frac{\partial T}{\partial x}\right|_{x=0} = \left.\frac{\partial T}{\partial x}\right|_{x=L} = \frac{h}{k} A_s (T - T_{amb}) \tag{3.27}$$

The model was fully discretised to account for localised heat generation and natural convection. For the contact resistance heat this is only applied at the two end nodes as this is where the current collectors are. For the reaction heat this is only applied in the positive and negative domains as there is no reaction current in the separator domain. For the ohmic heat this is applied over the whole domain due to the existence of either solid phase or electrolyte phase in all regions of the battery. There is no solid phase in the separator domain, therefore there is no solid phase ohmic heat in this region.

The parabolic partial differential equation was solved by using an implicit Crank-Nicolson FDM. The discretised form of this is shown in Equation 3.28 where q_{tot} represents the total heat generation for that node.

$$\frac{T_{i,j+1} - T_{i,j}}{\delta t} = \frac{k}{2\rho C_p}\left\{\frac{T_{i+1,j+1} - 2T_{i,j+1} + T_{i-1,j+1}}{\delta x^2} + \frac{T_{i+1,j} - 2T_{i,j} + T_{i-1,j}}{\delta x^2}\right\} + \frac{q_{tot}}{\rho C_p} \tag{3.28}$$

Applying the convective gradient boundary conditions by using central difference theorem at the end nodes allows the reformulation of the discretised equation to be written in matrix form, which is shown below, where α is the thermal diffusivity (m^2 s^{-1})

$$\begin{pmatrix} 2+2\alpha & -2\alpha & & & & \\ -\alpha & 2+2\alpha & -\alpha & & & \\ & \ddots & \ddots & \ddots & & \\ & & -\alpha & 2+2\alpha & -\alpha & \\ & & & -2\alpha & 2+2\alpha & \end{pmatrix} \begin{pmatrix} T_{i,j+1} \\ T_{i+1,j+1} \\ \vdots \\ T_{n-1,j+1} \\ T_{n,j+1} \end{pmatrix} =$$

$$\begin{pmatrix} (2-2\alpha)T_{i,j} + 2\alpha T_{i+1,j} - 4\alpha h A_s(T_{1,j} - T_{amb})/k \\ \alpha T_{i-1,j} + (2-2\alpha)T_{i,j} + \alpha T_{i+1,j} \\ \vdots \\ \alpha T_{n-2,j} + (2-2\alpha)T_{n-1,j} + \alpha T_{n,j} \\ 2\alpha T_{n-1,j} + (2-2\alpha)T_{n,j} - 4\alpha h A_s(T_{1,j} - T_{amb})/k \end{pmatrix} + \frac{1}{\rho C_p} \begin{pmatrix} q_c + q_r + q_j \\ q_r + q_j \\ \vdots \\ q_r + q_j \\ q_c + q_r + q_j) \end{pmatrix}$$

3.2.8 Degradation model

There are many different mechanisms of battery degradation and failure. To date there has not been a comprehensive model that accounts for all mechanisms of failure and coupled this to performance loss. The majority of the academic literature has identified the SEI layer growth as the most significant degradation mechanism in lithium-ion batteries and thus this will be the focus of this model. The degradation model used in this work is based on the approach taken by Ramadass *et al.* [166] that the side reaction involves the decomposition of the solvent (Etyhlene Carbonate) and lithium-ions to form groups such as Li-alkyl carbonates, Li_2CO_3, leading to the formation of a passivating SEI layer on the anode. Formation of this passivating SEI layer consumes cyclable lithium, reducing cell capacity and also increases cell impedance, reducing peak power.

The are many different possible reactions between the carbon electrodes and electrolyte which depend on the materials that have been used. As many commercially available batteries use EC as one of their organic solvents for the electrolyte the reaction mechanism as shown in Equation 3.29 has been assumed. Where S refers to the solvent and P the products formed.

$$S + 2Li^+ + 2e^- \rightarrow P \tag{3.29}$$

It has been assumed that the products which are formed for the side reaction are a mixture of organic and inorganic compounds. This is due to the low conductivity of pure Li-alkyl groups resulting in an overestimate of eventual film resistance.

The reaction current density is therefore the sum of the intercalation (j_{int}) and the side reaction (j_s) as shown in Equation 3.30.

$$j_{total} = j_{int} + j_{SEI} \tag{3.30}$$

The reaction current density of the side reaction can also be described by using a the Butler-Volmer equation. Using the Tafel approximation for irreversible reactions and neglecting concentration dependencies, and thus a constant exchange current for the side reaction, the Butler-Volmer equation can be reduced to Equation 3.31.

$$j_{SEI} = -i_{o,s} a_s^- \exp\left(\frac{F}{2RT}\eta_s\right) \tag{3.31}$$

As there is no side reaction occurring in the cathode, the side reaction current density there is zero. This is a reasonable assumption as it is typically assumed that no SEI forms at the cathode [184]. The side reaction overpotential can therefore be expressed as shown in Equation 3.32.

$$\eta_s = \phi_s - \phi_e - \frac{j_{tot} R_{SEI}}{a_s^-} \tag{3.32}$$

The growth of the SEI layer can then be modelled according to Equation 3.33 and then the growth of new SEI is related the the reaction current density of the side reaction as according to Equation 3.34.

$$R_{SEI} = R_{SEI,t-1} + \frac{\delta_{SEI}}{\kappa_p} \tag{3.33}$$

$$\frac{\partial \delta_{SEI}}{\partial t} = -\frac{j_{SEI} M_P}{a_s^- \rho_p F} \tag{3.34}$$

Due to this parasitic side reaction taking place on the anode to reduce the solvent, some of the reaction current does not contribute to pulling lithium out of the active electrode. Therefore, the boundary equation for the spherical diffusion of lithium in the anode must be modified as shown in Equation 3.35.

$$D_s^- \frac{\partial c_s}{\partial r}\bigg|_{r=R_s^-} = \frac{j_{int}}{a_s^- F} = \frac{j_{tot} - j_{SEI}}{a_s^- F} \tag{3.35}$$

This therefore allows for the evolution of the SEI layer resistance, which is only applicable to the anode. Increases in the SEI layer resistance therefore results in a lower peak power as the battery ages due to increased resistance, however this does not account for the loss of capacity. To do this the side reaction current density is integrated accounting for the electrochemical current which is used to for the SEI and therefore represents the amount of cyclable lithium lost. This is shown in Equation 3.36.

$$Q_s = -\int_0^{\Delta t} \int_0^{L_{neg}} j_s dx dt \tag{3.36}$$

3.2.9 Iterative solution routine

In order to solve for the coupled differential equations an initial guess for the reaction current density must be made and then this is iterative converged to a valid solution to maintain conservation of charge and mass. This is shown in Figure 3.3. The reaction current density is used as either a boundary condition or within the differential equation for the four government equations defining the solution and solid phase charge and mass conservation equations. At the first time step an initial guess of the reaction current density is made based on if the cell is charged or discharged. The 4 differential equations relating to the charge and mass conservation of the solution and solid phase are solved using this initial guess and the Butler-Volmer equation is then used to calculate the reaction current density distribution across the cell in the through-plane direction. The initial guess value and the calculated reaction current density from the Butler-Volmer equation are then compared and the initial guess and modified based on the error between the two results. A relaxation factor is added to the reaction current density modifications for numerical stability.

This iterative process is continued until the reaction current density value used and the calculated value has a residual error lower than a predetermined value. A smaller residual results in a more accurate solution however at the cost of computational time through the need for increased number of iterations. When all reaction current density values have converged, current conservation is considered within each electrode domain using Kirchoff's current law. This is where the reaction current density in each node is summed over the electrode domain and compared to the drawn current. The reaction current is then converged to the drawn current with consideration of the absolute error

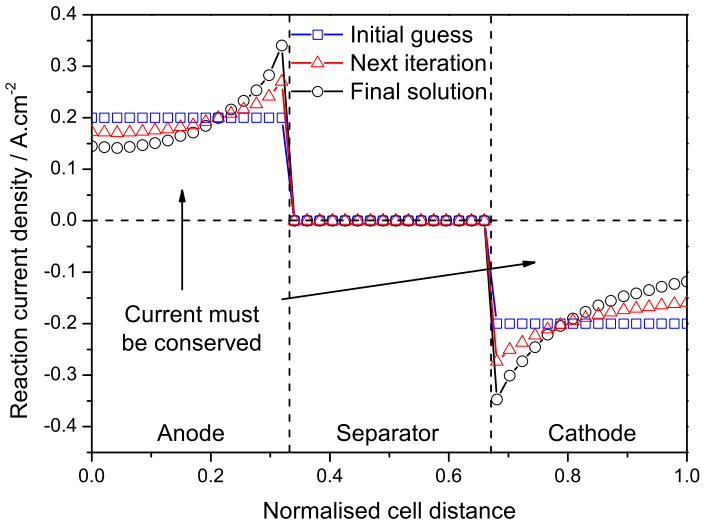


Figure 3.3: Convergence of the reaction current density at the start of the simulation for a discharge

and a relaxation factor. Once both valid values for the reaction current and current conservation are found, the iteration is allowed to go to the next time step where the process is repeated until the end time is achieved.

3.2.10 Convergence analysis

When setting the value for the absolute error tolerance the solution accuracy and computation time must be considered; a lower error tolerance will give a more accurate solution however the number of calculation iterations required to achieve this increases exponentially. The parameters used by Smith and Wang [189] will therefore be used in the developed model for a convergence analysis of required nodes. Figure 3.4 shows how the final voltage of a simulated 6 Ah cell discharged under a 200 A load for 10 s varies with different absolute errors and also the number of iterations required to achieve this.

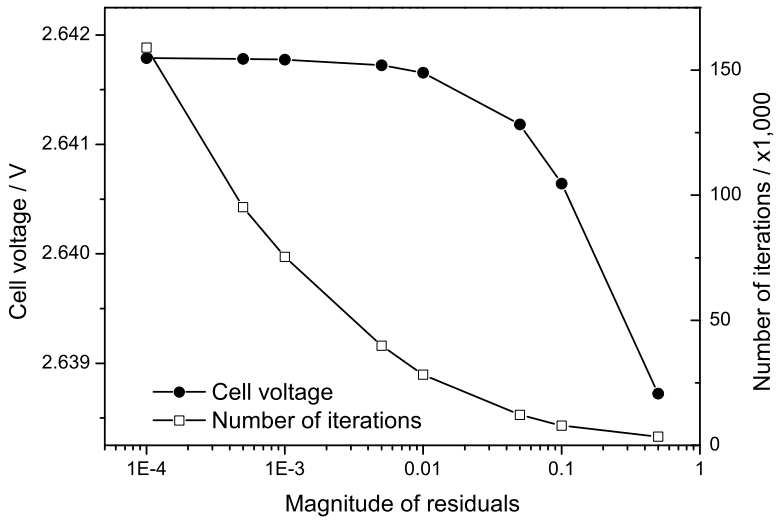


Figure 3.4: Convergence of final cell voltage with absolute error for a simulated 6 Ah cell discharge for 10 s from 60% SOC at a current of 200 A with a 48 node discretization in the x plane and 24 node discretization in the r plane for each node

A 200A discharge over 10 s was chosen as it represents the likely extreme of operation of batteries of this type.

Based on the results, the absolute error tolerance chosen was 0.01 with respect to reaction current density of each node and overall current conservation in each electrode domain. This results in a convergence accuracy of 99.99%.

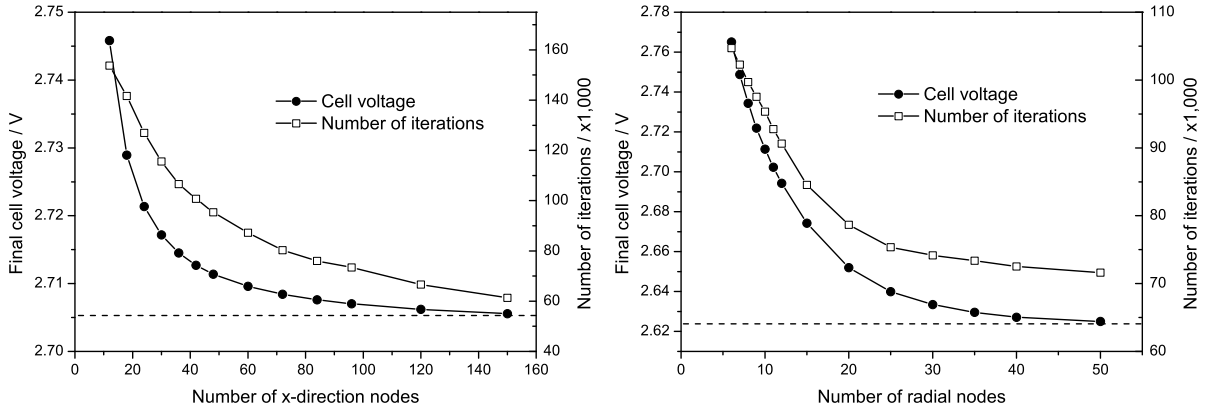
As the spatial and temporal domains have been discretised for the model, their relative resolutions also need to be considered. Figure 3.5a shows how the final value of cell voltage converges with varying degrees of spatial discretization in the x direction for a simulated 6 Ah cell with an absolute error tolerance of 0.01 and radial discretization of 24 nodes. Based on this analysis a discretization of 48 nodes was chosen, whereby the solution is 99.7% accurate. Figure 3.5b similarly shows the solution convergence for the same conditions for the radial discretisation for each node point, where a spherical diffusion problem is being solved at each node. Based on this analysis a 24 radial node discretization was chosen, allowing for a convergence accuracy of 99.4%.

For the temporal convergence, selection of an appropriate time discretization is more dependent on the stability of the numerical method used. For the solution of the diffusion of lithium in the solid and electrolyte phase an explicit and implicit Crank-Nicolson scheme was respectively used. The limitation on time discretisation for both schemes are shown in Equations 3.37 and 3.38 respectively, where k_1 represents the coefficient on the time derivative side and k_2 represents the coefficient on the spatial derivative side of the parabolic equations.

$$\delta t < k_1 \frac{(\delta x)^2}{2k_2} \tag{3.37}$$

$$\delta t < k_1 \frac{(\delta x)^2}{k_2} \tag{3.38}$$

In the case of the diffusion of lithium in the electrolyte phase shown in Equation 3.37, k_1 is represented by the volume fraction of which the values range from 0.3-0.5 in the different regions and k_2 represents the lithium-electrolyte diffusion coefficient which is has been set at $2.6\times10^{-6}\text{cm}^2/\text{s}$. Therefore, with a spatial discretisation of 48 nodes over



(a) (b)

Figure 3.5: Convergence analysis of the number of spatial nodes in the x-direction (a) and r-direction (b) for a 10s discharge under 200 A from 60% SOC

a 15 μm domain in the x-direction the maximum time discretisation is 0.011 s using the stability criteria for an implicit scheme.

In the case of solid phase lithium diffusion shown in Equation 3.38, k_1 is 1 and k_2 represents the solid phase lithium diffusion coefficient which ranges from 2×10^{-12}-3.7×10^{-12}. Therefore, with a radial spatial discretization of 24 nodes over a 1 μm domain the maximum time discretization is 2.35 s using the stability criteria for an explicit scheme. Therefore, an allowable time discretization of 0.011 s is allowed, and hence a simulation time step of 0.01 s was chosen. Due to the fast dynamics in the solution phase diffusion, numerical instabilities are most likely to occur in that phase first.

Combining all convergence solution errors from the relative error tolerance and spatial discretization allows for a convergence accuracy that is 99.09% accurate which has been decided is within acceptable levels.

3.3 Model reduction - The Single Particle Model

In addition to the development of the pseudo-2D battery model a SPM was created. The SPM neglects the contributions from the electrolyte phase and models each electrode as a single spherical particle. As the contributions from the electrolyte phase have been neglected and the solid phase is approximated to a single particle rather than a network of particles, the model is much less computationally expensive. The drawback of this is that the model is only accurate up to discharge/charge rates of 2C [166]. Figure 3.6 shows a diagram of the reduced order model domains.

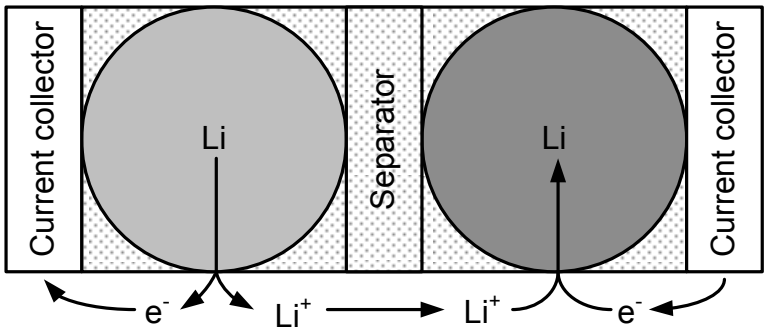


Figure 3.6: Schematic of single particle model

3.3.1 Governing equations

In the SPM the electrolyte concentration is assumed to be constant, which is an assumption which holds under low discharge currents when the rate of lithium-ion release and consumption from the electrode is sufficiently slow relative to the diffusion rate of the ions. Thus $c_e(x,t) = c_e^0$. As the concentration of lithium-ions in the electrolyte phase have been assumed to be constant, it then follows that the electrolyte phase overpotential becomes zero ($\phi_e = 0V$) due to constant electrolyte concentration assumption. The overpotential of the electrodes however is not zero and can be calculated by using a simplified version of the Butler-Volmer equation as shown in Equations 3.39 and 3.40.

$$\eta^- = \frac{2RT}{F}\sinh^{-1}\left(\frac{i_{app}(t)}{2a_s^- L^- k_{eff}\sqrt{c_e^0 c_s^-(t)(c_{max}^- - c_s^-(t))}}\right) \tag{3.39}$$

$$\eta^{+} = \frac{2RT}{F}\sinh^{-1}\left(\frac{i_{app}(t)}{2a_s^{+}L^{+}k_{eff}\sqrt{c_e^0 c_s^{+}(t)(c_{max}^{+} - c_s^{+}(t))}}\right) \tag{3.40}$$

Where $c_s(t)$ is the lithium concentration at the surface of the electrode (mol), c_{max} is the maximum lithium concentration in the electrode (mol) and $i_{app}(t)$ is the applied current density (A/m^2).

The potential of each electrode can then be calculated by subtracting the overpotential losses from the thermodynamic equilibrium potentials of each electrode which are a direct function of its lithiation state as shown in Equation 3.41 and 3.42. The anode has an additional overpotential term due to the presence of the SEI passivation layer which only forms on the anode.

$$V_{anode} = U^{-} + \eta^{-} + \frac{R_{film} i_{app}(t)}{a_s^{-} L^{-}} \tag{3.41}$$

$$V_{cathode} = U^{+} + \eta^{+} \tag{3.42}$$

The solid phase lithium concentration is then derived assuming diffusion in a spherical polar coordinates, using a Fick's diffusion law, with a surface flux of lithium based on the reaction current density as shown in Equation 3.43 with boundary conditions as shown in Equations 3.44 and 3.45.

$$\frac{\partial c}{\partial t} = \frac{1}{r^2}\frac{\partial}{\partial r}\left(Dr^2\frac{\partial c}{\partial r}\right) \tag{3.43}$$

$$\left.\frac{\partial c^{-}}{\partial r}\right|_{r=0} = 0, \left.\frac{\partial c^{-}}{\partial r}\right|_{r=R_s^{-}} = -\frac{i_{app}(t)}{D^{-}Fa_s^{-}L^{-}} \tag{3.44}$$

$$\left.\frac{\partial c^{+}}{\partial r}\right|_{r=0} = 0, \left.\frac{\partial c^{+}}{\partial r}\right|_{r=R_s^{+}} = -\frac{i_{app}(t)}{D^{+}Fa_s^{+}L^{+}} \tag{3.45}$$

The solution of the spherical diffusion equation is again solved using FDMs with consideration of the singularity at the centre of the particle as shown below.

$$\frac{1}{r^2}\frac{\partial}{\partial r}\left(r^2\frac{\partial c_s}{\partial r}\right) = \begin{cases} \frac{1}{i(\delta r)^2}\{(i+1)c_{i+1,j}^s + 2ic_{i,j}^s + (i-1)c_{i-1,j}^s\} & \text{if i}\neq 0 \\ \frac{6}{(\delta r)^2}(c_{1,j}^s - c_{0,j}^s) & \text{if i}=0 \end{cases}$$

The improvement in computational speed, of the SPM, not only arises due to the course discretisation, but also due to the fact that the reaction current density does not need to be iteratively solved.

3.3.2 Thermal model

For the thermal mode a lumped capacitance model has been assumed and therefore temperature is space invariant. The three main sources of heat that have been modelled include the ohmic heat from internal resistance, the ohmic heat from ionic motion and reaction heat which is described by Equations 3.46, 3.47 and 3.48.

$$q_{ohm} = I^2 R \tag{3.46}$$

$$q_{ionic} = A\int_0^{R_s^-} \frac{4\pi r^2}{\sigma^{eff}}\left(FD^-\frac{\partial c_s}{\partial r}\right)^2 dr + A\int_0^{R_s^+} \frac{4\pi r^2}{\sigma^{eff}}\left(FD^+\frac{\partial c_s}{\partial r}\right)^2 dr \tag{3.47}$$

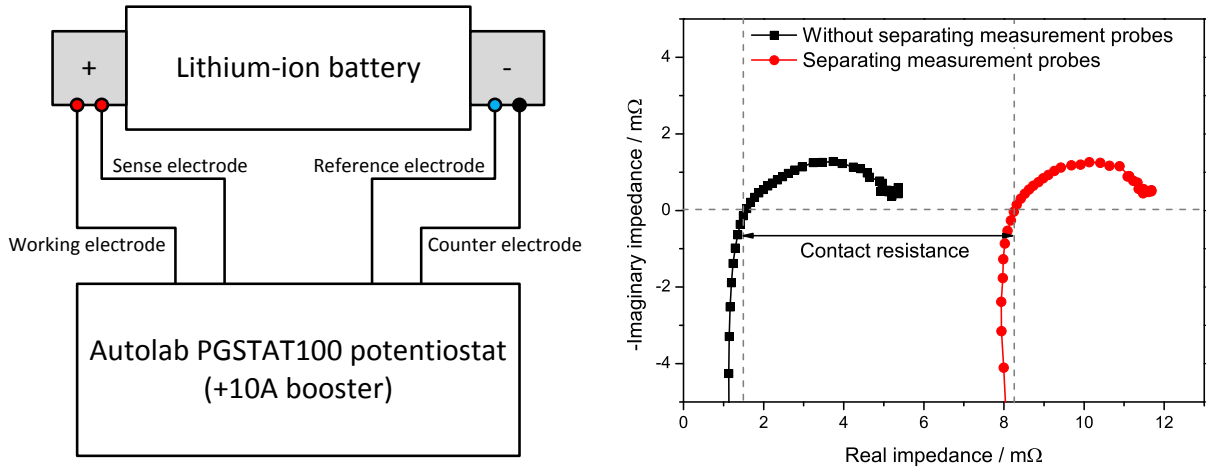
$$q_{reaction} = I(\eta^- + \eta^+) \tag{3.48}$$

3.4 Experimental set-up

The battery used in this study was a 4.8 Ah Kokam lithium-polymer battery. These cells are pouched form factor batteries which use a carbon anode with a Lithium Cobalt Manganese Nickel Oxide (MNC) cathode in an electrolyte of lithium hexafluorophosphate ($LiPF_6$) in a mixture of organic solvents including EC and Ethyl-Methyl Carbonate (EMC) [60]. All experiments and parameterisation hereafter refer to this cell.

An Autolab PGSTAT100 potentiostat with a 10A booster controlled by the Nova software was used to perform electrochemical tests on the lithium-ion battery. Experiments were conducted in 4 electrode mode where the working and counter electrodes were connected to the cathode and anode of the battery respectively. Sense and reference electrodes were also placed on the cathode and anode respectively however were connected at separate points in order to minimise the influence of the contact resistance of the crocodile connectors to the battery cell tabs. Figure 3.7 shows a diagram of the experimental set-up as well as two EIS spectra taken in 2 electrode and 4 electrode mode to highlight the need to isolate the contact resistances for the low impedance devices being tested. The shape of the spectra are the same however the series resistance has been shifted across due to current flowing through the connectors giving an extra overpotential.

Good EIS measurements rely on the system being in equilibrium. Therefore, before every EIS measurement, the cell was left to rest for at least 30 minutes such that any solid phase/solution phase concentration gradients within the electrodes/ electrolyte have sufficient time to equilibrate. All EIS measurements on batteries hereafter were done in galvanostatic mode with a 200 mA RMS current signal amplitude which was determined to be the best trade off between linearity and noise reduction.



(a) (b)

Figure 3.7: Diagram of experimental set-up used for testing lithium-ion batteries (a) and example EIS measurement taken on a 4.8 Ah Kokam lithium polymer cell with and without isolation of contact resistances at 3.8 V

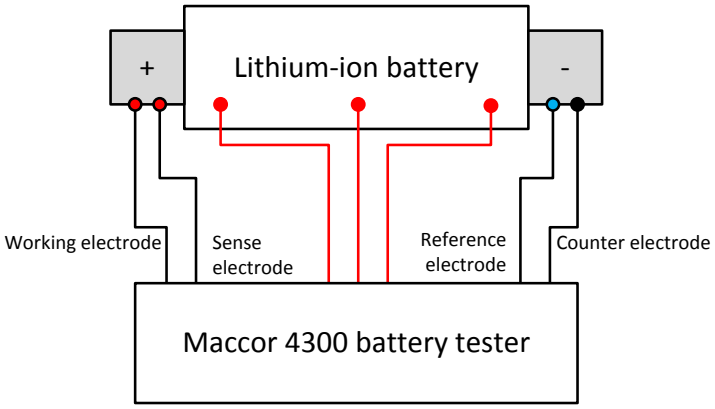


Figure 3.8: Diagram of experimental set-up used during SRCV tests and cycling tests

As the Autolabs were not equipped with synchronized temperature measurements, a different battery tester was used for the discharge and SRCV experiments. This was the Maccor 4300 battery tester which has 8 channels of 5 A which can be combined to create a single channel with 40 A. 8 temperature sensors allow for the measurement of these 8 different cells or multiple temperature measurements on a single cell. During discharge tests three temperature measurements were made. One in the centre and one near each cell tab. This is because at higher currents and in large form factor cells there may be significant temperature inhomogeneities on a single cell. Typically, the temperature near the current collectors is higher due to larger reaction current densities within this area. Again the sense probes were isolated from the load bearing probes.

3.4.1 Thermal measurements

The isothermal measurements of cell performance were taken by use of the rig presented by Troxler *et al.* [202] who used the same Kokam 4.8 Ah cell used in this study. Known as the HAMSTER CAGE (**H**eat **A**nd **M**as**S** **T**ransf**E**r **R**ig for **C**ontrolled **A**nd **G**auged **E**xperiments), this rig uses Peltier elements, which are thermoelectric components, to independently heat/cool either side of the cell through direct conduction. PID controllers through a LabVIEW interface allowed for regulation of the temperature to the set-point value. The inherent advantage of this rig over conventional thermal test chambers is that it allows a much faster transient response due to the heat removal mechanism being conduction rather than convection and also the ability to independently control the temperature on either side of the cell.

Figure 3.9a shows a diagram of the rig which is made up of two main compartments. Compartment A is where the battery sits on the removable base plate. A polycarbonate wall separates the battery compartment with the compartment which houses the electrical components such as pumps and data loggers. Banana connectors and quick connectors allow for easy connection of electrical and water connections between the two compartments. They are separated in case the battery fails in order to preserve the valuable electronic equipment. The outside of the unit houses a water header tank which is used to top up the cooling fluid and a radiator and fan to dissipate excess heat.

Figure 3.9b shows the base plate unit which holds the cell and heating elements. The adjustable holding column allows for accommodation of different sized pouch cells. This base plate is removable for easy of operation if the user wants to install a new cell or make adjustments to the rig. Figure 3.9c shows a cross-section of the heating element/cell arrangement. Peltier elements are installed into a plastic holder. On the cell side, a copper plate acts as the interface between the Peltier element and the cell to allow for

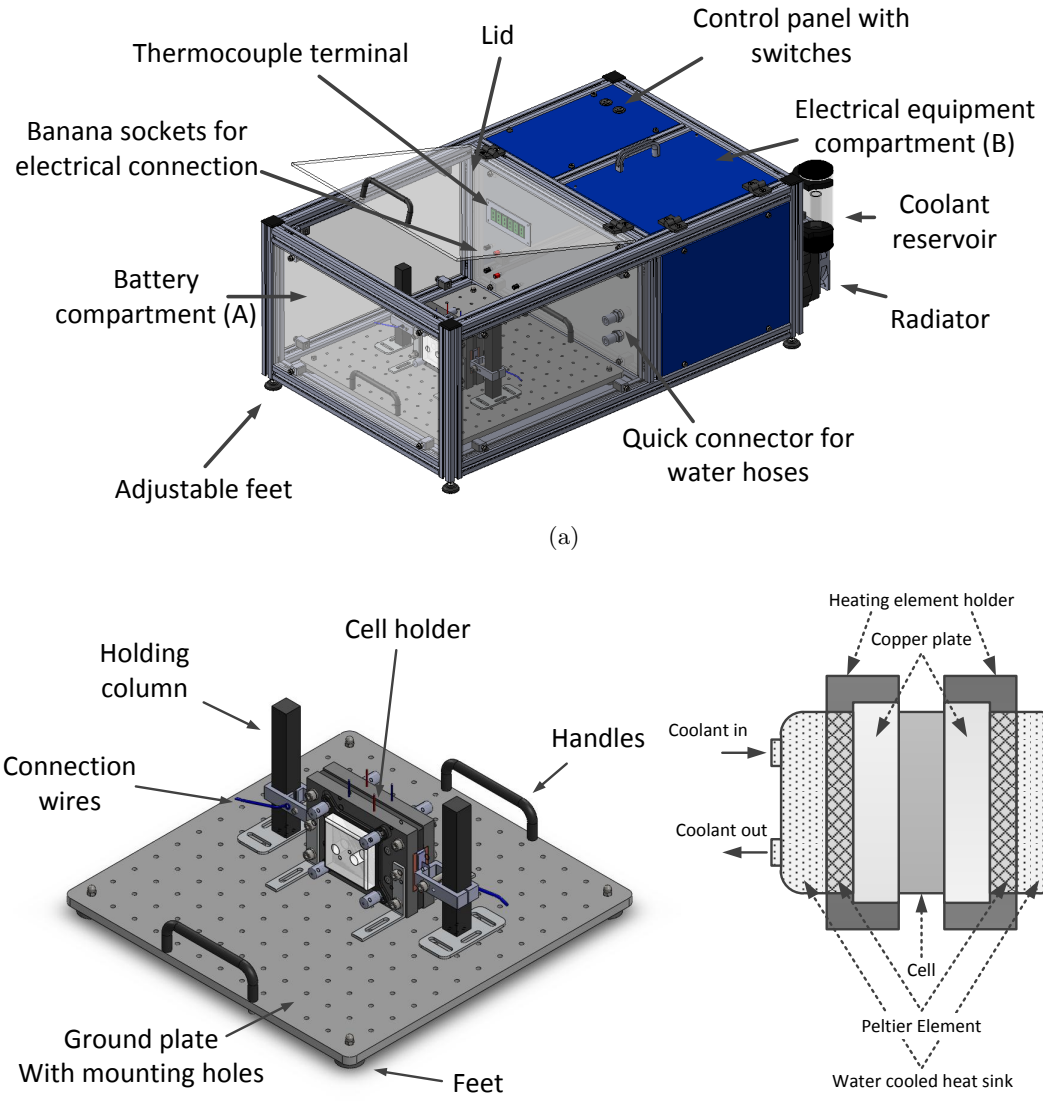


Figure 3.9: (a) Diagram of thermal test rig, (b) base plate assembly holder and (c) cross section of heating element arrangement [202]

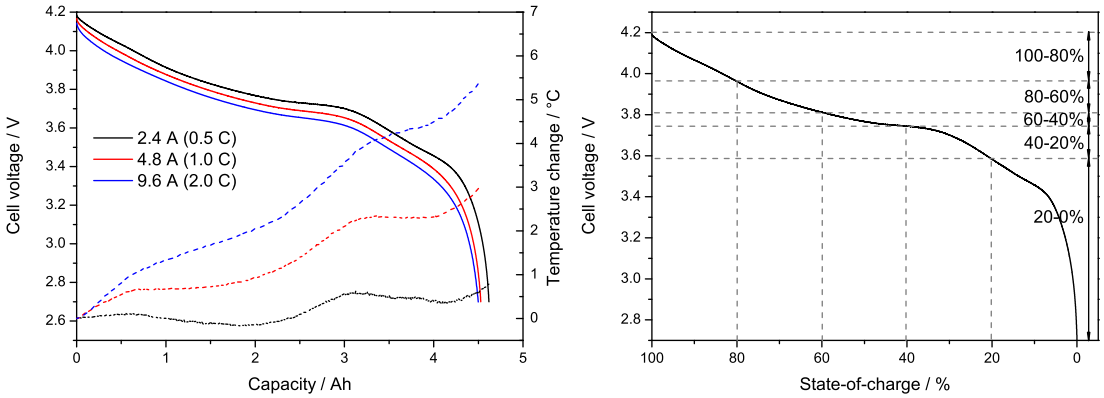
an even temperature distribution. On the other side a water heat exchanger is installed to remove excess heat. Peltier elements are analogue to heat pumps and can drive thermal energy in either direction depending on the direction of current. Therefore, to allow for larger temperatures to be achieved relative to the ambient temperature the excess heat should be removed. This arrangement is mirrored on the other side of the cell and the top and bottom sides are insulated.

3.5 Experimental results

The following outlines the experimental results taken that is subsequently required for parameterisation and validation of the model.

3.5.1 Cell capacity

Constant current discharge tests are useful for the determination of the capacity of a cell and also the energy available within a certain voltage range. This is needed for the parameterisation as it will allow for the estimation of electrode thicknesses or available



(a) (b)

Figure 3.10: Cell voltage and temperature changes for a 4.8 Ah Kokam lithium-polymer battery under varying discharge rates (a) and cell voltage vs SOC for a 0.25 C discharge (b)

active material. Typically, the lower the discharge current, the closer the measured capacity is to the theoretical value due to fewer losses. The constant current discharge curves for a 4.8 Ah Kokam lithium-polymer cell under varying discharge rates is shown in Figure 3.10a.

It can be seen that at higher rates of discharge, the capacity of the cell at the rated voltage cut-off of 2.7 V decreases. This is caused by the increased overpotential losses associated with higher current operation. The lower the current, the closer the cell voltage operation to the thermodynamic equilibrium potential. As the rate of discharge increases the heat generation also increases due to the increased losses which are approximately to the square of the load current. The non-linear temperature increases observed are in part due to the non-linear increase in the polarization resistance of the cell, mainly due to the increase in the anode charge transfer resistance but also in part due to the entropy reversible heat term associated with phase transitions of the battery electrode materials. Reversible entropic heat can be either exothermic or endothermic.

If the cell voltages are plotted against the SOC, where 100% SOC is when the battery has 100% of its energy and 0% SOC is when it has used all of its energy then the voltage profile changes slightly as shown in Figure 3.10b. Compared against the plot of cell voltage against capacity, it can be seen that when factoring the energy in the system the last 20% of the available energy results in a relatively large fraction of the voltage decrease. These values represent the near steady state potentials and therefore it is unlikely that this remaining 20% will be usable due to the additional losses under higher currents.

3.5.2 Electrochemical Impedance Spectroscopy

The use of constant current discharge tests however do not allow for the decoupling of different loss mechanisms. Thus different experimental techniques should be employed. EIS is a technique that allows the user to decouple different phenomena in a battery to be separated. Figure 3.11 shows the impedance response of the 4.8 Ah lithium-polymer cell used.

Conventionally the complex response of a battery is plotted on a Nyquist plot with the negative of the imaginary component against the real component. The inset in Figure 3.11 shows the equivalent circuit found to best fit the battery spectra measured. At high frequencies the imaginary component is positive and this represents mainly

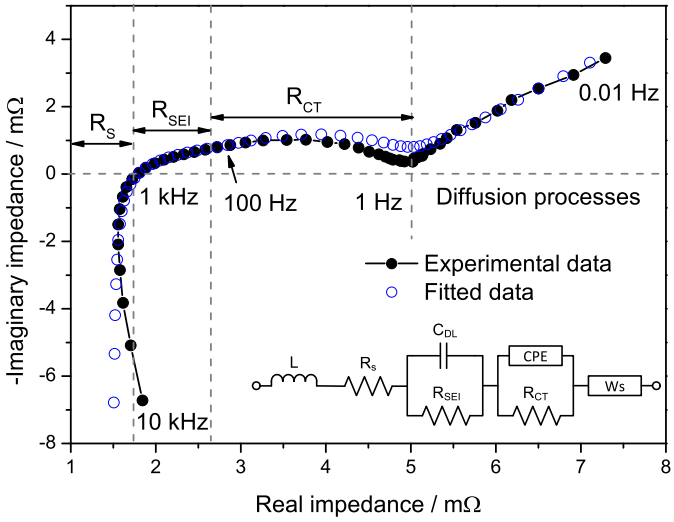
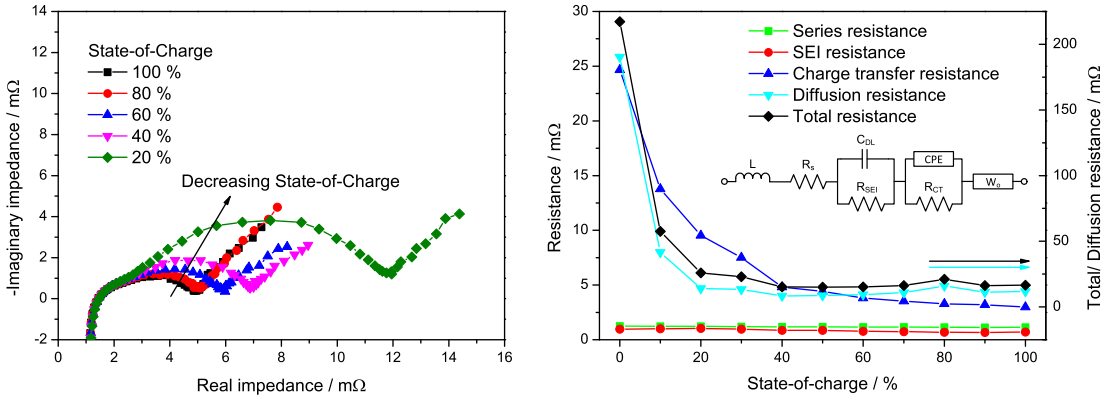


Figure 3.11: Impedance spectra of a 4.8 Ah lithium-polymer cell from 10 kHz - 0.01 Hz at 4.2 V

inductive behaviour. Where the imaginary component changes from positive to negative represents the series resistance of the battery which represents the resistance of the electrode materials, current collectors and contact resistances. Subsequent response can be represented by RC branches. The first one typically represents the response of the SEI layer resistance and the double layer capacitance. The larger response is typically that of the charge transfer processes related to the intercalation processes of lithium in the electrodes. This is in parallel with a CPE to account for the porous electrodes. Low frequency behaviour is characteristic of diffusion processes and this is usually characterised by use of a Warburg element.

The magnitude of the various resistance change with different temperatures and SOCs. Figure 3.12a shows the impedance spectra of the 4.8 Ah lithium-polymer cell at room temperature over a frequency range of 10,000-0.01 Hz in galvanostatic mode with an RMS current amplitude of 0.2 A. Measurements were taken at 10% SOC intervals with 1A discharge current being used to move from one SOC to another and rest periods of 30 minutes given after discharge from one SOC to another to allow for equilibrium of cell potential. Figure 3.12b then shows the fitted parameters of the series, SEI, charge transfer and diffusion resistance from the data at different SOCs. Fitting was done with the ZView software which uses the Simplex solution algorithm and this was done against the equivalent circuit shown inset of Figure 3.12. Care was taken to ensure a suitable fit my allowing the time constant for the SEI/ double layer capacitance branch to be faster than the charge transfer process.

It can be seen that the main contribution to battery resistance is the diffusion resistance which is an order of magnitude larger than the charge transfer resistance. The diffusion resistance however has a long time constant and in reality does not manifest itself fully under most automotive load cycles. The charge transfer, series resistance and SEI layer resistance are much smaller, with the charge transfer resistance providing the next most significant resistance contribution. In the case of both the charge transfer resistance and the diffusion resistances, it can be seen that they both increase with decreasing SOC. The increase in diffusion resistance can be attributed to the variation of diffusion coefficient with stoichiometry of the electrode, with diffusivity dropping significantly in the cathode at low stoichiometric values. This is in-line with findings in the literature [170].



(a) (b)

Figure 3.12: Impedance spectra of a Kokam 4.8 Ah lithium-polymer cell at different state-of-charges (a) and isolation of different resistance components (b) for a frequency range between 10,000-0.01 Hz

The dominating influence of the charge transfer and diffusion resistance relative to the series and SEI layer resistances mean that they appear relatively constant however they are also a function of the SOC. Figure 3.13 shows how the series and SEI layer resistance varies as a function of SOC.

In the case of the series resistance there is a general increase in series resistance with decreasing SOC. This can be attributed to possible volumetric changes in the graphite anode with changing lithiation states, with values of approximately 7% being typically being quoted in the literature [104]. Therefore, as the graphite particles shrink as lithium is deintercalated from its crystal structure, the mechanical contact between particle decreases as a whole, resulting in some loss of interconnectivity and the resulting increase in the observed series resistance. In the case of the SEI layer resistance there is the same general trend of increasing resistance with decreasing SOC. The SEI layer forms as a passivating layer over the graphite particles. Therefore, it can be envisaged that

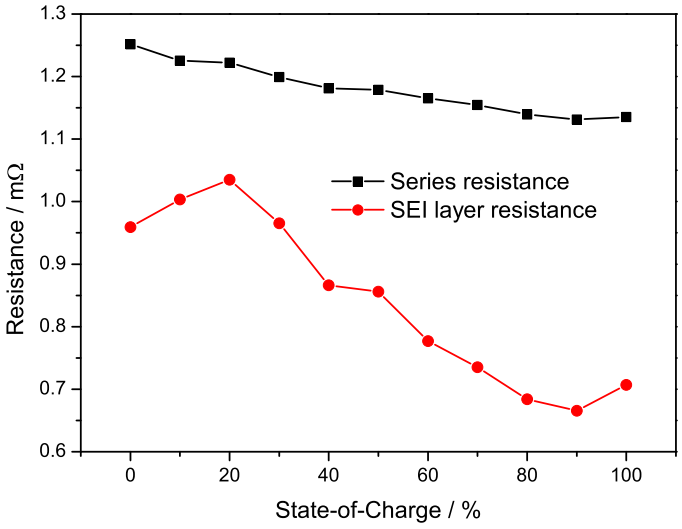
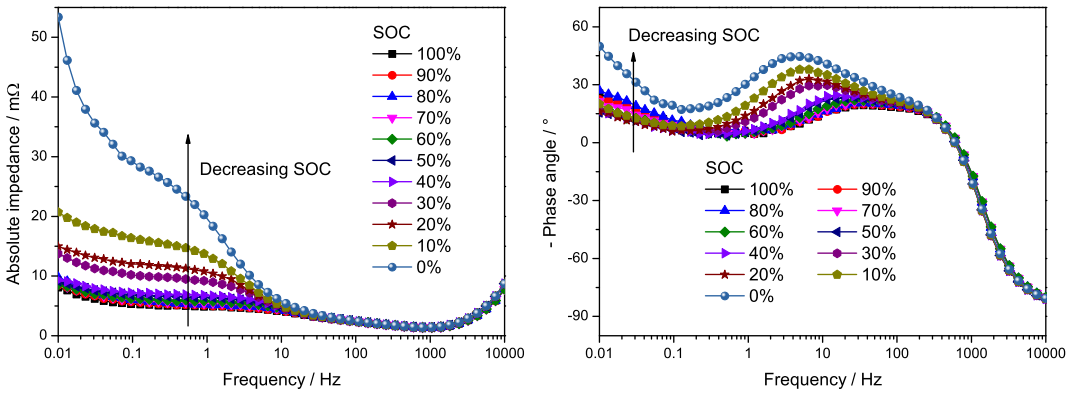


Figure 3.13: Fitted series and SEI layer resistance for a 4.8 Ah Kokam lithium-polymer battery at different SOCs



(a) (b)

Figure 3.14: Bode plot of a Kokam 4.8 Ah lithium-polymer cell showing (a) the absolute impedance and (b) the -phase angle between 10 kHz -0.01 Hz at different SOCs

upon particle shrinkage, during delithiation, the interface resistance between the SEI material and graphite increases, as the two phases are pulled apart. There is a slight decrease in the resistance at low SOCs which may suggest the formation of new SEI which compensated for the SEI-graphite contact resistance increase.

Whilst a Nyquist plot is good at displaying both the complex and real impedance components it doesn't contain information about the frequency that the measurements were taken. Figure 3.14 shows the same impedance data but this time plotted on a Bode plot to show the frequency dependency of the absolute impedance and the phase angle measured between 10 kHz and 0.01 Hz.

It can be seen that at frequencies above 1 kHz all of the impedance spectras converge to the same value for both absolute impedance and the phase angle. When the phase angle is zero this means the impedance measured is purely resistive meaning that this is only the resistive contribution from the electrodes, current collectors and electrolyte. Variations in the series resistance is relatively small as a function of SOC and therefore it appears that all values converge. At higher frequencies the phase angle becomes positive indicating inductive behaviour. At lower frequencies the impedance increases. An effect which becomes more apparent at lower SOCs. This is due to the low frequency operation resulting in a deficit of ion concentration in the electrolyte and electrode resulting in higher mass transport losses and thus the resulting higher impedance.

It then becomes apparent that to maximise efficiency and thus reduce the operating impedance of the cell the frequency of operation should be high. However, practically this may not be possible and it may also be detrimental to the lifetime of the cell from the point of view of mechanical fatigue of the electrode material from volumetric changes as suggested by Vetter *et al.* [207].

Exchange current density

The exchange current density is related to the charge transfer resistance of a battery. Measured cell response is a combination of both the anodic and cathodic contributions. These values change during operation as a function of the lithium concentration in the solid phase, the lithium-ion concentration in the electrolyte phase and temperature. The magnitude of the exchange current density affects the resulting charge transfer resistance and therefore the charge transfer overpotentials when the cell is under load.

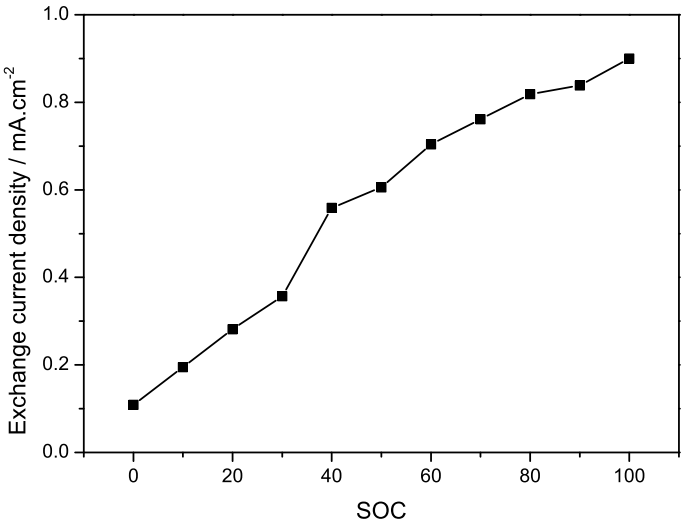


Figure 3.15: Exchange current density of the overall 4.8 Ah Kokam lithium-polymer battery at different SOCs

EIS can be used to find the overall cell charge transfer resistance and from this value the exchange current density can be derived as shown in Equation 3.49.

$$i_0 = \frac{RT}{eR_{CT}F} \tag{3.49}$$

Figure 3.15 shows how the exchange current density varies with SOC for the 4.8 Ah lithium-polymer battery. It can be seen that as the SOC decreases the overall exchange current density decreases, indicating an increase in polarisation resistance for the whole battery which increase at a rate proportional to the inverse of the SOC. The values are also of the same order of magnitude as literature values [189].

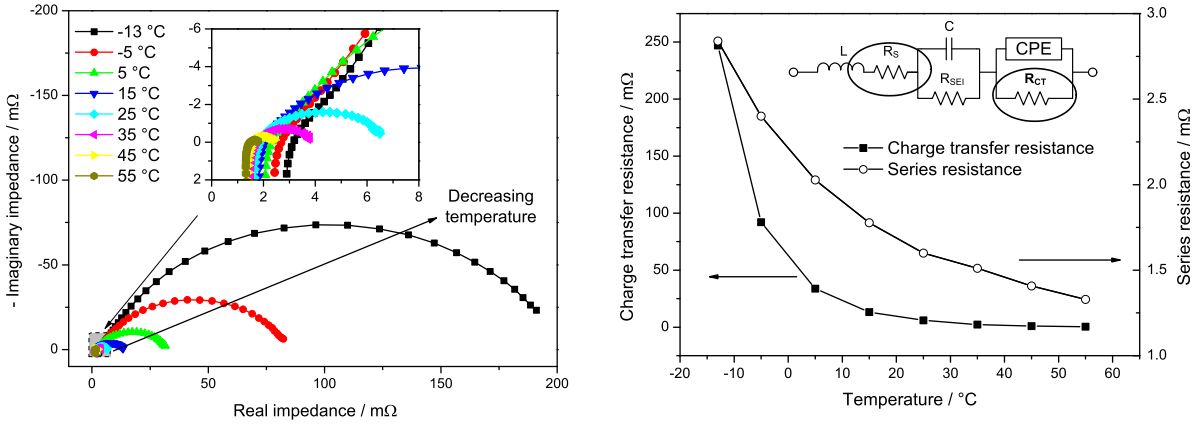
This linear dependence is in general agreement with the modelled approach of estimating the exchange current density as a function of the solid phase and solution phase lithium/ lithium-ion concentrations as shown in Equation 3.50. As it can be seen from the equation, assuming the electrolyte concentration of lithium-ions to be constant and the coefficient α to also be constant, the exchange current density is inversely proportional to the surface lithium concentration in the electrode. As the general trend of the overall cell exchange current density is decreasing this would suggest that the anode contribute more the the charge transfer resistance than the cathode.

$$i_0 = Fkc_e^{\alpha_a} \left(c_{s,max} - c_{s,surface}\right)^{\alpha_a} c_{s,surface}^{\alpha_c} \tag{3.50}$$

Thermal measurements

Measurements of cell EIS responses at different temperatures allows for the extraction of an activation energy coefficient that determines the temperature-exchange current density relationship. This is important to accurately model the polarisation losses at low temperatures when these losses dominate. Figure 3.16 shows the EIS specta of a 4.8 Ah cell held under different isothermal conditions [202].

Between the temperature range of -13-60°C the charge transfer resistance varies from 247 mΩ to 0.4 mΩ, an increase of 583 fold at low temperatures. The dramatic increase



(a) (b)

Figure 3.16: Impedance spectra of a Kokam 4.8 Ah lithium-polymer cell at different isothermal temperatures (a) and fitted charge transfer and series resistance as a function of temperature (b) at 50% SOC [202]

in charge transfer resistance is mainly attributed to lower rates of chemical kinetics making the intercalation and deintercalation processes increasingly difficult. The series resistance also increases with decreasing temperature, but with a much lower sensitivity. Series resistance is a combination of contact resistance between electrode and current collector, electrode resistance and electrolyte resistance. At lower temperatures the conductivity of the electrolyte drops which causes the observed increase in resistance at low temperatures. It can be seen that the variations of charge transfer resistance vary exponentially with temperature and fits well to an Arrhenius rate law form as shown in Equation 3.51.

$$R_{CT} = R_{CT,ref} \exp\left(\frac{E_a}{R}\left(\frac{1}{T} - \frac{1}{T_{ref}}\right)\right) \tag{3.51}$$

The constant E_a which represents the activation energy can be determined by plotting the natural logarithm of the charge transfer resistance against the reciprocal of the temperature minus the reciprocal of the reference temperature. Here the reference temperature is taken to be 25°C. This is shown in Figure 3.17 for 50% SOC. The fit from the data shows a strong correlation with a R^2 value of 0.999 and activation energy of 65.47 kJ/mol at 50% SOC.

3.5.3 Slow Rate Cyclic Voltammetry

Slow Rate Cyclic Voltammetry (SRCV) is a technique which can be used to find information about the location of phase transitions within battery electrodes. Assuming that the electrolyte is fully stable within the range of potentials tested, the resulting current has to come from the intercalation reaction occurring at the electrodes. Each peak within the SRCV typically represents a phase transition which corresponds to plateaus in the voltage-capacity profile; however, SRCV measurements on a whole cell can only give information about combined anode and cathode processes without addition of a reference electrode. Figure 3.44 shows the SRCV response of a 4.8 Ah Kokam lithium-polymer cell under different scan rates in both the charge and discharge direction.

For better results, SRCV should be done at a slow scan rate to minimise the electrode overpotentials. A higher scan rate results in higher currents and higher overpotentials as

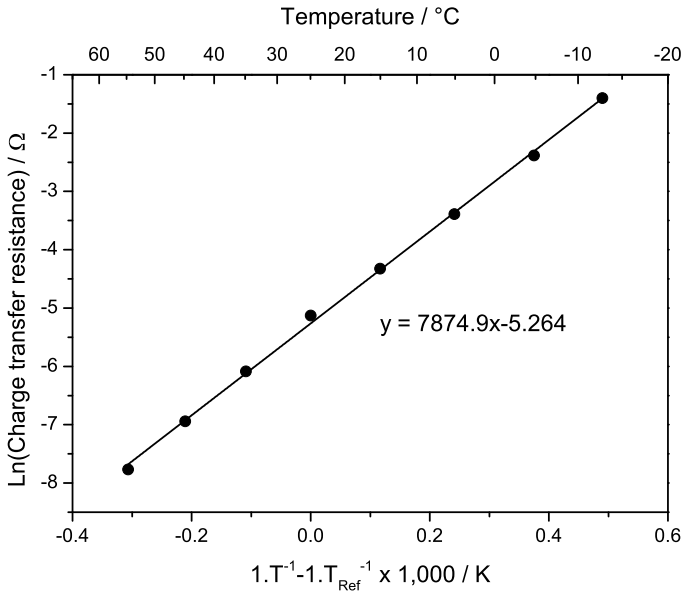


Figure 3.17: Plot of natural log of the charge transfer resistance against the inverse of the temperature for a 4.8 Ah Kokam lithium-polymer cell at 50% SOC

seen in Figure 3.18a. Operation as close as possible to the thermodynamic equilibrium potential is preferred. Slower scan rates therefore allow for more information to be extracted as seen in the normalised data plot shown in Figure 3.18b. With increasing scan rate both the location of the peaks and also the number of peaks is changed. Fewer peaks are observed due to the higher overpotentials masking some of the processes. The higher overpotentials also means that the location of the peak is more shifted. This is why the charge and discharge SRCV plots do not give peaks in the same location as they have not been IR-corrected. The half-cell SRCV data provides information about the stability region of the cell. In the whole cell measurements this provides insight into potential windows where most of the energy is, which is represented by the area under the graph. However, some authors have suggested that cycling around phase transitions results in faster rates of degradation.

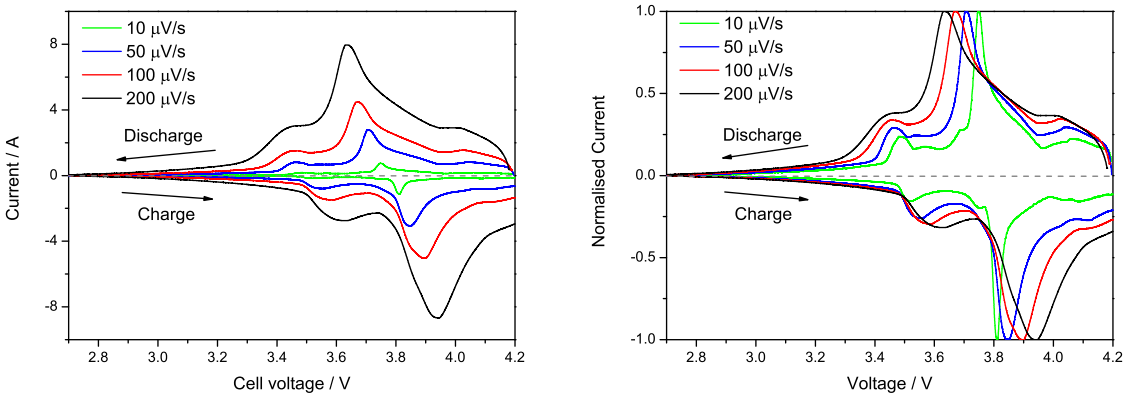


Figure 3.18: (a) Slow rate cyclic voltammetry on a 4.8 Ah Kokam lithium-polymer cell and (b) normalised data against the respective peak values

3.6 Model parameterisation

With so many different variables in the model, many of which are interrelated, fitting appropriate values for each constant in the model can be difficult. Therefore, different tests should be conducted to isolate certain parameters to be fitted in a systematic way.

3.6.1 Optimisation methods

The performance of a system can be a function of many variables, which depending on the nature of the problem can vary linearly or non-linearly. When modelling and parameterising systems, finding the global residuals minimum can be difficult, especially with increasing number of variables.

There are two main types of solvers used in MATLAB. Gradient based solvers and heuristic based solvers of which Genetic Algorithms (GA) are one form.

Gradient based solvers

Gradient based solvers use the gradient of the solution domain to decide on the size of the search area for the next iteration. An example of a gradient based solvers in MATLAB include `fmincon`, which can handle, linear and non-linear constraints. These solvers tend to find a solution relatively quickly; however, the problem is that they do not handle discontinuities very well and often do not find global minima, with this being highly dependent on the initial starting point. An example can be seen in Figure 3.19a where the objective is to find the global minima of the the function $Z(X, Y)$.

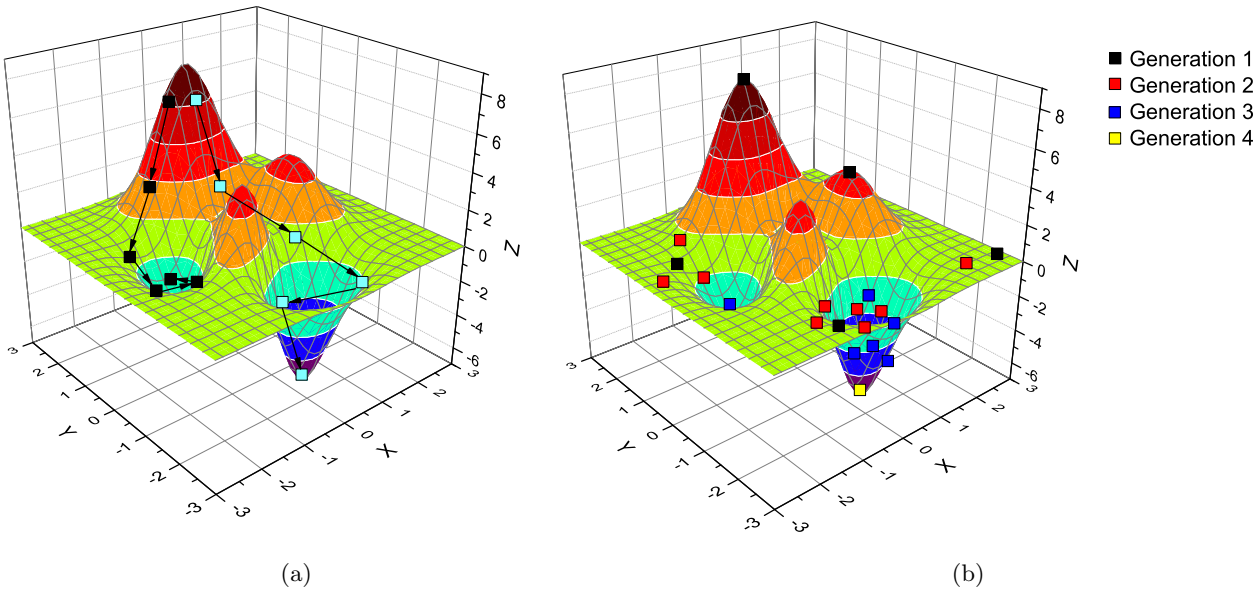
It can be seen in 3.19a that a gradient based solver can converge to a global minimum if the starting point is sufficiently good, however if the starting point is close to the global minimum then the gradient based solver can converge to a local minima instead as depicted by the black squares in Figure 3.19a. It also becomes apparent that if there are discontinuities, the gradient cannot be evaluated and also if the function is noisy it will be again difficult to evaluate the gradient.

A way around this problem is to iterate the solver and use random start points. The resulting spread of results can then find global minima if a sufficiently large number of points are used; however, this still does not get around the problem of handling discontinuities or noisy functions and increases the number of required function calls.

Genetic Algorithm

GAs are one of the heuristic based optimisation tools available in MATLAB. This search method mimics the process of natural evolution and is part of a larger class of evolutionary algorithms. GAs work by generating an initial population of samples which are spread over the solution domain and then the solution is allowed to iteratively evolve. Each set of initial guesses is known as a generation. In each generation, the fitness (how ideal the solution is) of the population is evaluated and then multiple individuals of this population are selected based on their fitness and modified to form a new population according to user set crossover, mutation and migration algorithms in order to effectively explore the solution domain.

The individuals with the appropriate fitness then undergo crossover where variables defining that state is then combined with other individuals that have continued to the next generation. The resulting individuals then undergo the mutation stage whereby there is a probability that one of the variables determining the state of that individual is changed. These points then become the new population used for the next iteration of



(a) (b)

Figure 3.19: Example of different optimisation solution methods: (a) gradient based solver (b) genetic algorithm solver

the algorithm. The GA continues until either the maximum number of generations has been reached, a suitable fitness has been achieved or the variable tolerance decreases to a certain value. In the termination case of maximum generations a suitably fit solution may not have been reached.

This concept is depicted in Figure 3.19b. Here it can be seen that a 1st generation of random points is generated across the function map. A second generation is then generated based on the fitness of these points; the better the solution the more larger to subset population from that parent point. This process is continued until a sufficiently fit solution is achieved.

GAs tend to be slower than gradient based solvers due to the larger number of function calls required in finding a solution but their advantage is that they can handle more non-linear problems, discontinuities and also find a global minimum more consistently the gradient based solvers. In addition, GAs don't require an initial guess as it searches the entire function space given a large enough population.

Another advantage of the GA function in MATLAB, is the ability to run the code on parallel cores. Gradient based solvers often make single function evaluations at a time and based on the returned function value makes a decision of which point to set as the variables next. Therefore, the next function call requires that the previous one is complete before being able to start the next. The optimisation therefore cannot run in parallel. GAs, by contrast evaluate, the function multiple times that are independent of each other within the same population set. The computational evaluation of each set of variables for a function can therefore be done on a separate core to decrease computational time. It's only when the fitness functions of each set of variables and crossover of variables is evaluated when the next function call is dependent on the last ones finishing.

Parameterisation code parallalisation

In order to speed up the parameterisation process the GA parameterisation process was parallelized to run on multiple cores of a computer. A flowchart showing the processes

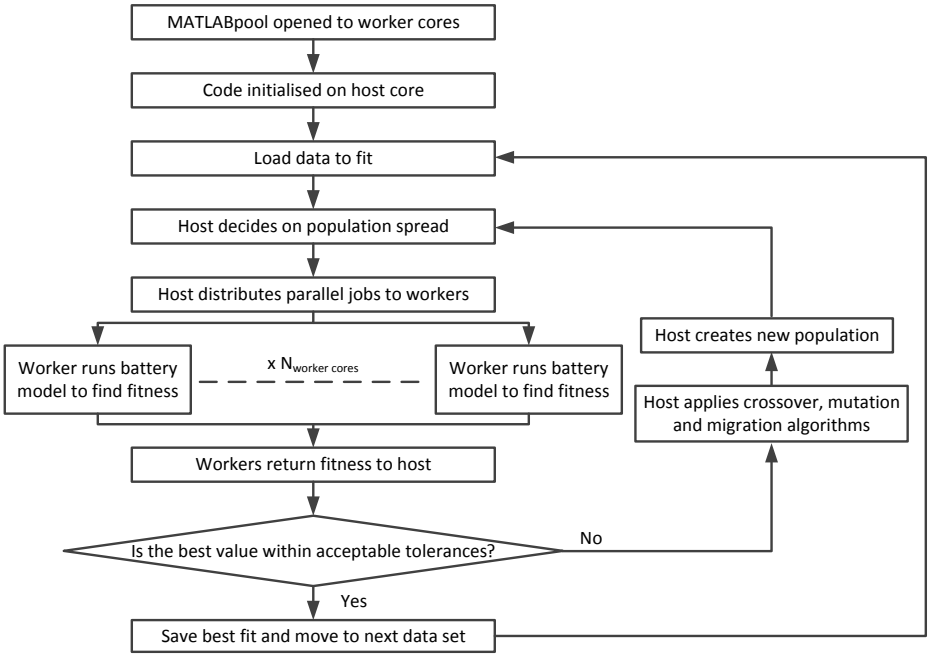


Figure 3.20: Flow chart of genetic algorithm parameterisation technique

in the GA code is shown in Figure 3.20.

Initially, the user must use the '`matlabpool`' command to open a specified number of MATLAB workers that will allow for parallel computing. Not all codes can be run on parallel processes and some which can do not always benefit from being parallelised. In problems where the solution depends on the a process occurring before it, the two calculations cannot be done in parallel. In the case of GAs, a population spread is created and the function is evaluated at those points independent of the values from other functions calls.

In the case of the GA parameterisation for the battery code, once the MATLAB workers are called, the code loads the first data set to be fitted. The host MATLAB will then create a population distribution which is a set of variables to try for the free variables that the user wants to fit. These can be evaluated independently of the others. The host then distributes the function evaluation to the worker cores to calculate the fitness function which it is trying to minimise. In this case it is the RMS of the error between the model results and the loaded test data for the variables being fitted. This process is continued until the best fitness is to within a certain limit, rate of change of the solution be below a certain value or the number of generations reached is at its limits.

All calculations hereafter were completed on a computer with 6 Intel Xeon 3.2 GHz real cores and an additional 6 virtual cores on a 64-bit operating system with the 64-bit verson of MATLAB 2012b and 16 GB RAM.

Electrode area

The electrode area, with respect to the in-plane area, represents the area of the current collectors. This was determined by analysis of the physical dimensions of the cell. The number of layers was determined by analysis of the work by Yufit *et al.* [232] where they used X-ray tomography to investigate the failure of the same 4.8 Ah Kokam lithium-polymer cell that is being parameterised. Delamination of the layers allowed for the counting of the individual layers. 80 individual layers were noted and an electrode area of 9,408 cm^2 was derived based on the measured in-plane dimensions of the cell.

Table 3.2: Parameterised battery component thicknesses. Separator thickness taken from Smith and Wang [189]

Component	Thickness / μm
Current collector[a]	48.1
Anode	40.1
Separator	25.4
Cathode	23.9

[a] Thickness of aluminium and copper current collectors assumed to be the same

3.6.2 Electrode thickness

The thickness of the anode and cathode determine the capacity of the cell as this determines the available active material, whilst the thickness of the separator determines part of the electrolyte resistance. Conservation of charge and species means that the overall reaction current density in the anode must equal and opposite to that of the cathode (assuming no parasitic side reactions are occurring). The stoichiometric limits of each electrode determine the ideal 100% and 0% SOC lithium saturation fraction.

In an ideal situation, the SOC of each electrode should be the same throughout use, where SOC of the electrode is determined from the stoichiometric lithium content of each electrode as shown in Equation 3.52. In this way, the whole range of electrode stoichiometry can be used. If one of the electrodes reaches its SOC limit before the other, some of the active material of the other electrode is wasted. In reality, the cathode is normally operated in excess of lithium and saturation and depletion limits are not reached due to the nature of battery construction whereby large amounts of lithium-ions are consumed for the formation of the SEI layer on the first few cycles.

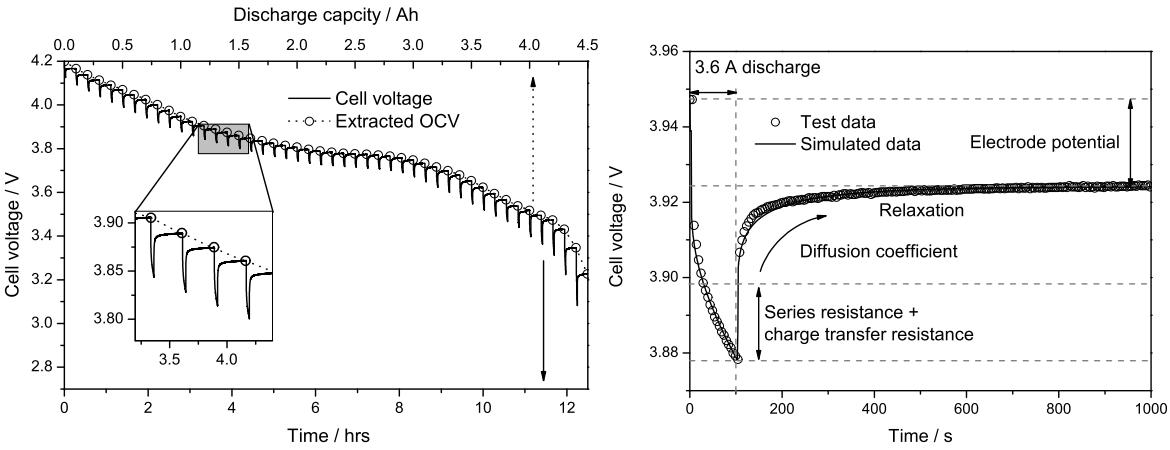
$$Electrode_{SOC} = \frac{stoi(x) - stoi_{100\%}}{stoi_{100\%} - stoi_{0\%}} \tag{3.52}$$

Assuming a certain electrode porosity, in order to have both electrodes maintain the same SOC under quasi-static conditions over the whole range of operation, the ratio of the electrode thicknesses has to be maintained at a certain value. The first stage of model parameterisation is therefore to ensure that both electrode SOCs reach 0% SOC at the rated capacity of the battery. The calculated values are shown in Table 3.2, where the thickness of the separator is assumed to be the same as that quoted by Smith and Wang [189]. Current collector thickness was calculated from the difference in thickness of the measured cells physical dimensions and the calculated thicknesses of the active battery components.

3.6.3 Open Circuit Potential

The thermodynamic potential of each battery electrode is a function of the material composition, lithium concentration and temperature. The difference between the potentials of the anode and cathode result in the OCV of the cell.

To establish the OCV relationship for the Kokam 4.8 Ah lithium-polymer batteries, a pulse discharge of 3.6 A was applied for 100 s followed by a 900 s rest period to allow concentration gradients in the solution and solid phase to equilibrate. The OCV is then taken as the steady state value after the rest period. The OCV curve was established in this manner rather than under a lower C-rate constant current discharge as it allows for the establishment of the true OCV provided the relaxation time is sufficient for the lithium concentration gradients in the electrodes to equilibrate. Using 100 s pulses at 3.6 s with a 900 s relaxation time, 46 pulses could be achieved. Data for each pulse was



(a) (b)

Figure 3.21: (a) Repeated pulse discharge of a 4.8 Ah Kokam lithium-polymer cell under a 3.6 A discharge for 100 s followed by 900 s rest period and the extracted open circuit potential plot and (b) fitted data for one of the 3.6 A pulse discharges

then extracted and, assuming the same anode as in Smith and Wang [189], the cathode OCV could be determined through fitting of the model.

The resulting voltage profile is shown in Figure 3.21a with a single pulse shown in Figure 3.21b.

Each pulse data set was fitted to the model using MATLAB's GA solver enabled in parallel computing model. The objective function to minimise was set-up to be the chi-squared value of the error between the simulated and test voltage. This was iteratively done for each pulse starting from 100% SOC. In this way the cathode stoichiometry-potential relationship can be determined independently of other pulses. The starting point was fixed such that the starting potential of the whole cell is 4.2 V, which represents 100% SOC.

Figure 3.22 shows the OCV curves for the fitted anode and cathode after the GA minimisation. The cathode curve was then fitted to a 9th order polynominal as shown in Equation 3.53 to be used in the model as polynomial functions are evaluated faster than interpolation functions in Matlab. The stoichiometric limits have been assumed to be the same as that of a $LiCoO_2$ cathode as studied by Zhang *et al.* [236].

$$\begin{aligned} U_y &= -1.59 \times 10^5 y^9 + 9.25 \times 10^5 y^8 - 2.36 \times 10^6 y^7 + 3.48 \times 10^6 y^6 - 3.27^6 y^5 \\ &\quad +2.03 \times 10^6 y^4 - 8.29 \times 10^5 y^3 + 2.16 \times 10^5 y^2 - 3.25 \times 10^4 y + 2150 \end{aligned} \quad (3.53)$$

3.6.4 Diffusion and charge transfer coefficients

The solid phase diffusion coefficient defines the rate of lithium diffusion in the electrode phase. The implications on performance are such that at high C-rates of discharge, bulk lithium cannot diffuse to the surface fast enough and the cell voltage cut-offs are reached faster and the whole cell capacity cannot be achieved. Fitting the diffusion coefficient correctly is therefore important in determining high C-rate performance limits which are common in HEV and EV load cycles.

The fitting of the diffusion coefficients for the anode and cathode was again done with the use of GAs and the pulse discharge data. After each pulse, the relaxation curve of the battery cell voltage contains information about the diffusion coefficient at that particular

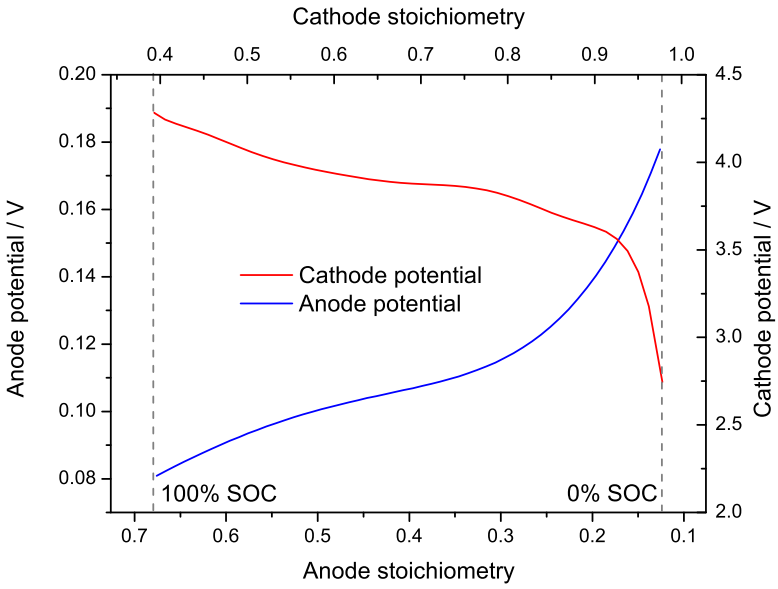


Figure 3.22: Fitted OCV curves for the anode and cathode. Anode values were taken from Smith and Wang [189]

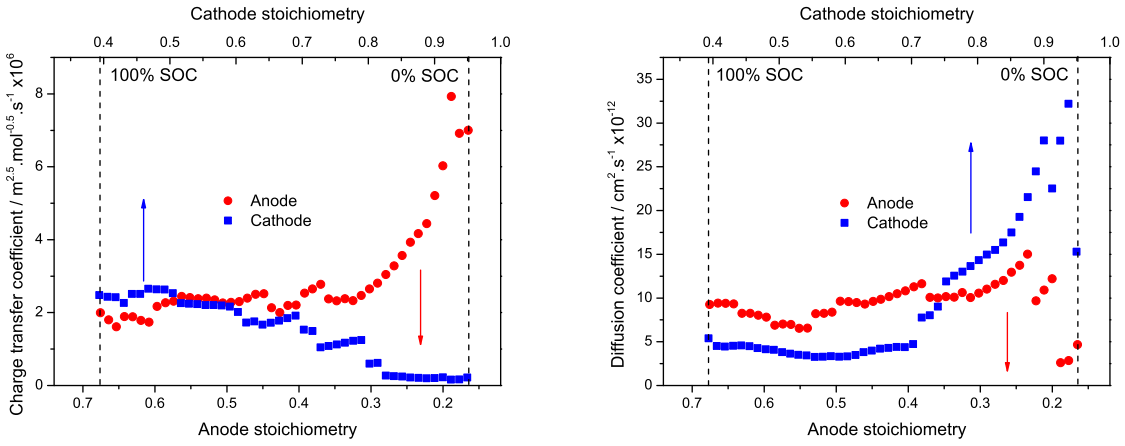
electrode stoichiometry. The diffusion coefficient varies as a function of the electrode stoichiometry due to the associated changes in the electrode crystallographic structure. In terms of impact on the cell voltage, the relative change in the electrode OCV is larger for the cathode. Therefore, the rate of cell voltage recovery after a pulse discharge is more indicative of the dynamic performance of the cathode than anode and as such it is easier to fit for the cathode diffusion coefficient than the anodes. The diffusion coefficient of the cathode is also normally lower than that of the anode and as such the cathode performance is often the rate limtiing step in solid phase mass transport.

The charge transfer coefficient for each electrode describes the charge transfer resistance, with a lower coefficient representing a higher charge transfer resistance. Figure 3.23a shows the result of the GA fitting of the charge transfer coefficient for both the anode and cathode at different electrode stoichiometries. A 3-point rolling average was used to reduce the rolling standard deviation of the results. It can be seen that at high SOCs, the cathode contributes slightly more to the charge transfer resistance than the anode. As the cell discharges the cathode charge transfer resistance decreases and the anode one increases, most likely due to the increase/ decrease in lithiation state. By the fully discharged state the anode contributes to the majority of the charge transfer resistance due to being nearly fully delithiated.

Figure 3.23b shows the fitted diffusion coefficient of the anode and cathode as a function of stoichiometry. It shows that the diffusion coefficient of the anode remains relative constant over the range of stoichiometries but the cathode increases significantly at low SOCs. This is perhaps due to the higher concentration of lithium intercalated into the cathode at low SOCs.

3.6.5 Entropy

During the intercalation/ deintercalation process, the electrodes often undergo phase transitions which lead to changes in the thermodynamic OCV and also leads to an additional reversible entropic heat. In a complete cell the observed temperature dependency of the OCV is a combination of both the anode and cathode entropy profiles with are a direct function of the state of lithiation.



(a) (b)

Figure 3.23: Genetic algorithm fitted charge transfer coefficients (a) and diffusion coefficients (b) for the anode and cathode of a Kokam 4.8 Ah lithium-polymer battery

Figure 3.24 shows the OCV dependency with temperature as a function of electrode stoichiometries. The whole cell entropy profile was taken from [202] which used the same 4.8 Ah cell parameterised and the anode was taken from Reynier *et al.* [171] which is for a graphite anode.

The total voltage dependency with electrode phase is a function of both electrodes according to Equation 3.54. The contribution from the anode and cathode are in opposite directions to give the total cell entropy due to the fact that the cell voltage is the difference of the two electrodes. Thus, an increase in anode potential leads to a decrease in overall cell potential and vice versa.

$$\frac{\partial E_0}{\partial T}_{cell} = \frac{\partial E_0}{\partial T}_{cathode} - \frac{\partial E_0}{\partial T}_{anode} \tag{3.54}$$

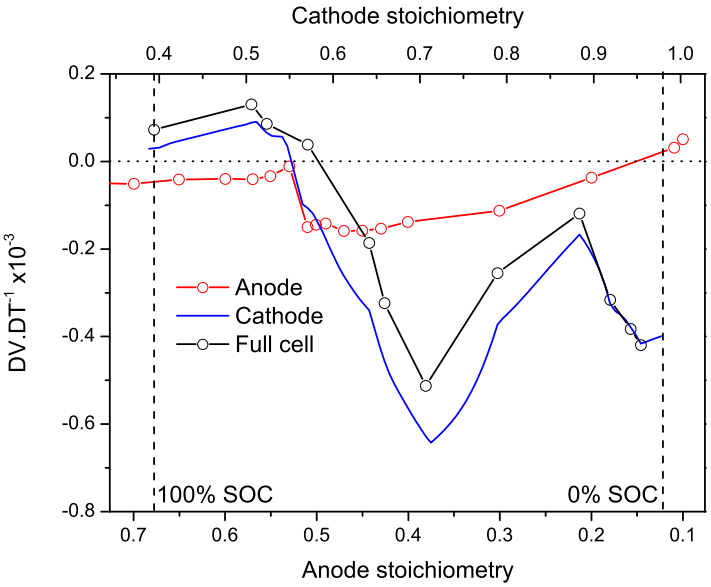


Figure 3.24: Experimental whole cell entropy measurements taken from Troxler *et al.* [202] and experimental graphite entropy profile taken from Reynier *et al.* [171] with extracted cathode entropy profile

3.7 Comparison between test and modelled data

Figure 3.25 compares the test and simulated data under different constant C-rate discharges. It can be seen that in general there is good agreement between the model and experimental data over the whole range of operation.

Figure 3.26a shows the comparison of the experimental and simulated temperature change of the cell under discharge under different discharge currents with no entropic heat generation. It can be seen that the general trend and magnitude of change for the cell between the modelled and experimental data is in good agreement. The oscillations of the experimental temperature around the simulated values are due to reversible entropic heating effects caused by intercalation/deintercalation of the electrodes. When adding the entropic heat generation to the model it can be seen that the accuracy of the model increases as shown in Figure 3.26b which shows the R^2 value of the model and test data. The most significant improvement in accuracy is experienced at low discharge currents, where the relative magnitude of the entropic heat is greater. At higher discharge rates, the entropic heat generation is approximately the same however the ohmic and reaction heat generation terms now account for more as this increases to the square of the applied current. Thus there is a smaller improvement in the accuracy of the solution.

3.7.1 Load cycles

The aim of the development of these battery models is to use them to predict the cell potentials for automotive drive cycles. The performance of a cell can vary significantly depending on the type of load applied to it and the question therefore arises of what is an appropriate load cycle. Automotive manufacturers typically benchmark their vehicles against a standard drive cycle. In Europe this is commonly the ECE EUDC or NEDC. These are time-velocity traces which, if combined with a vehicle model, generates a power-time profile which can be used as an input for battery testing.

The scaling of these load cycles is also a common question. Ideally, the load cycle should recreate real world conditions as closely as possible. Here, the NEDC cycle has been used as a benchmark for the scaling of other load cycles. Typically, a 100 km range for a BEV is expected. An NEDC cycle is 11 km in length. Vehicle models allow for the estimation of the power required for the entire vehicle. Here, the battery load cycles were

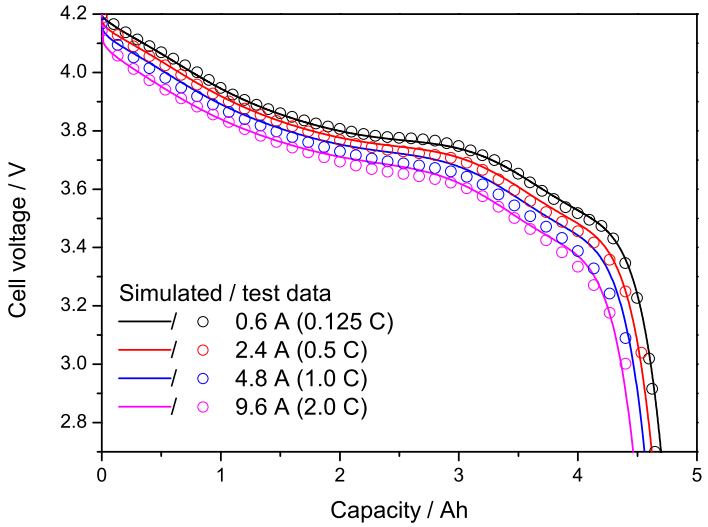
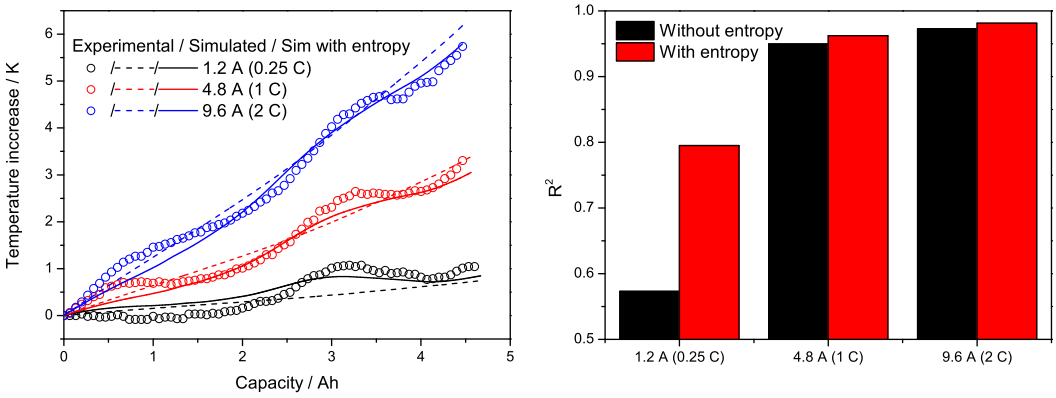


Figure 3.25: Comparison between simulated and test data for discharge of a 4.8 Ah Kokam lithium polymer cell under varying discharge conditions



(a) (b)

Figure 3.26: Comparison between experimental and simulated temperature for a 4.8 Ah lithium-polymer battery (a) and comparison of R^2 values between model with and without entropy included

scaled such that an individual cell is able to provide the equivalent of 9 NEDC cycles which equate to approximately the 100 km range of electric vehicles assuming a mass of 1500 kg and accounting for losses such as inertia, rolling resistance and aerodynamic drag. Figure 3.27 shows the current and voltage of a 4.8 Ah Kokam lithium-polymer cell under 9 NEDC cycles. The load profile is a 1/238th scale that allows for the 9 cycles to be complete on this battery.

As the load cycle applied to the battery is a power-time trace, it can be seen that as the number of cycles increases the current load on the batteries also increases. This is due to the lower cell potential resulting in needing higher currents for the same power, and also the increased polarisation losses associated with operation at lower SOCs. Figure 3.28 show the comparison between experimental and simulated cell voltage under one NEDC load cycles and all of them. It can be seen that in general there is good agreement between the experimental and simulated data over the whole range of battery operation.

In the final NEDC cycle large potential drops are observed due to the lower potential and higher currents required to maintain the required power profile. Thus the remaining 10%

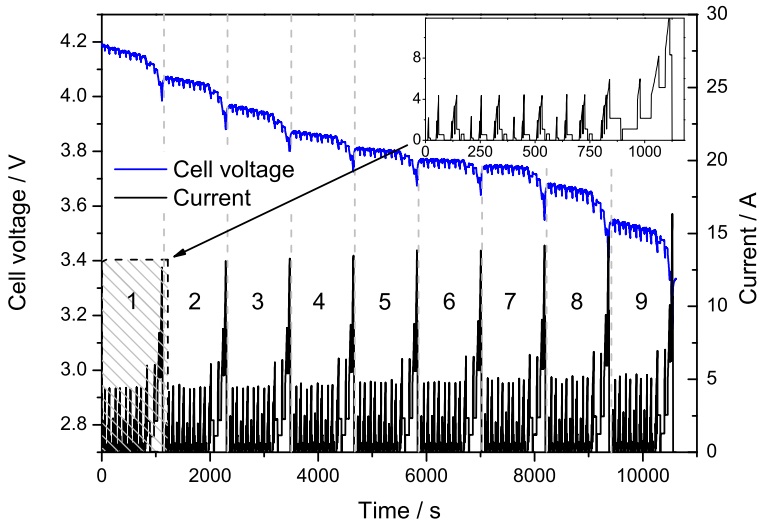
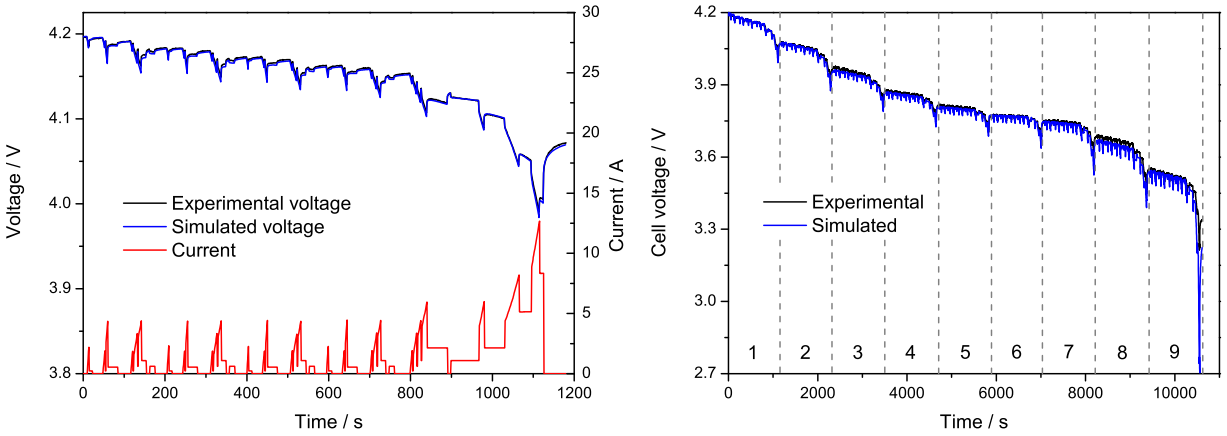


Figure 3.27: Kokam 4.8 Ah lithium-polymer cell under a 1/238th scale load with 9 ECE EUDC drive cycles with zoomed in current profile for one cycle inset



(a) (b)

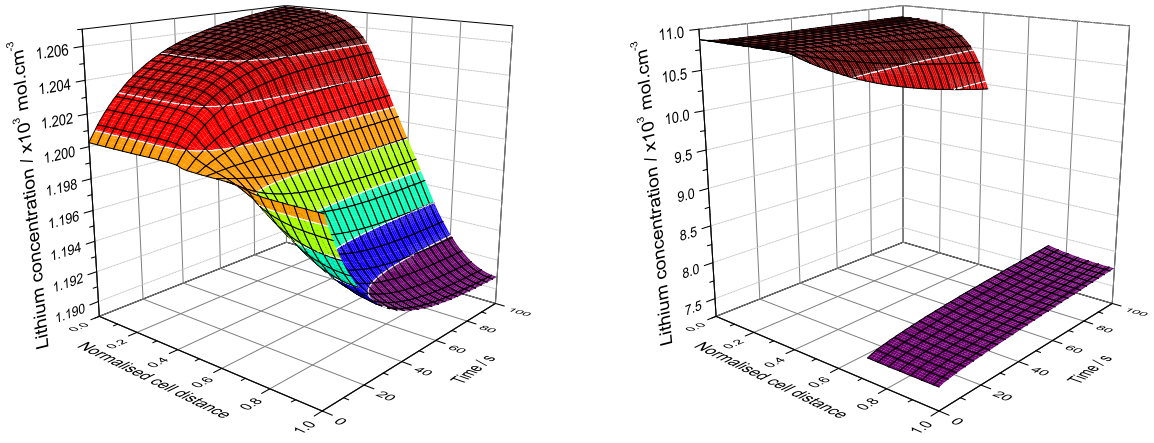
Figure 3.28: Comparison between experimental and simulated cell voltage of a 4.8 Ah lithium polymer battery under a single NEDC cycle (a) and 9 in series (b)

SOC range is typically not used as an additional safety factor in real world applications to avoid damage to the battery through overdischarging and also over heating of the cell since currents and resistances are higher in this region of operation.

3.7.2 Model based investigation of battery performance

Having a fully paramertised physics based model allows the user to probe the physical effects and limitations occurring in a lithium-ion battery as well as eventually relating these effects with overall cell performance. Understanding these effects allows for the design of a better overall system. Figure 3.29 shows the electrolyte and solid phase lithium concentration profiles within a single cell for a 10 A discharge.

As can be seen from Figure 3.29 over time there is an excess of lithium-ions in the electrolyte within the anode domain and a deficit at the cathode. This is because under discharge conditions lithium is deintercalated from the anode and enters the electrolyte phase, at the same time lithium-ions are intercalated at the cathode which removes



(a) (b)

Figure 3.29: (a) Electrolyte phase lithium concentration and (b) solid phase lithium concentration for a 10A discharge of a 4.8 Ah lithium-polymer cell

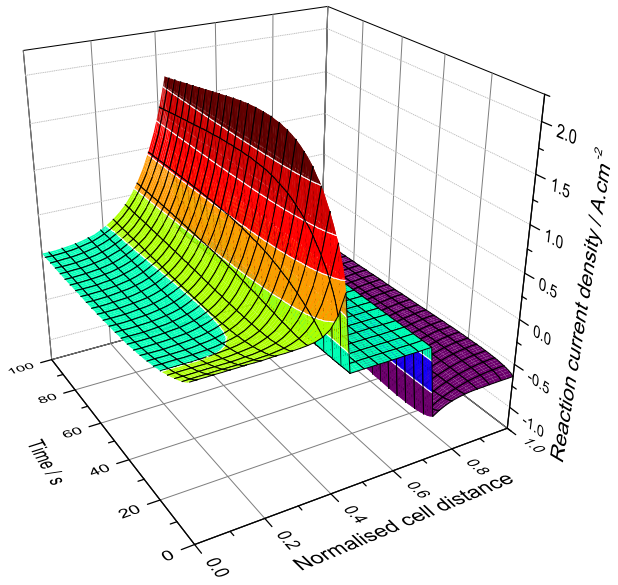


Figure 3.30: Reaction current density for a 10A discharge of a 4.8 Ah lithium-polymer cell

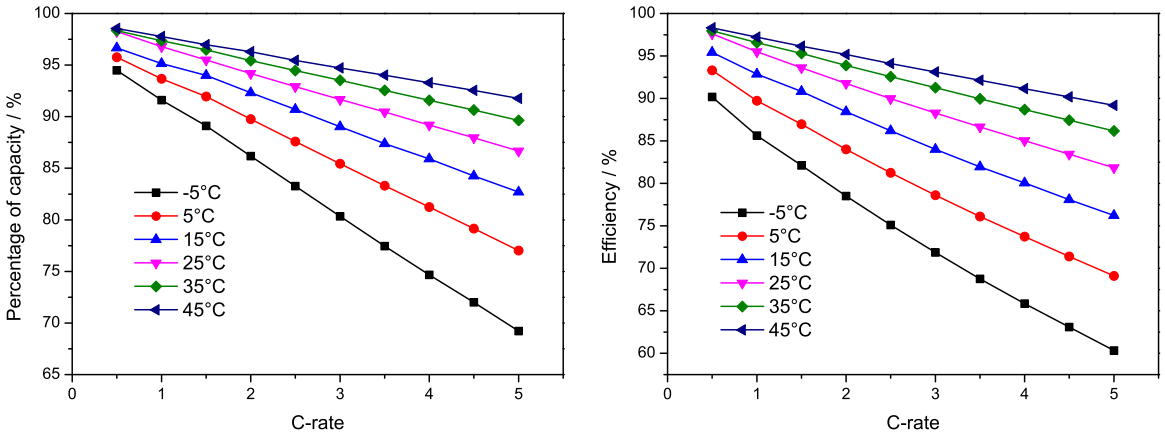
lithium-ions from the electrolyte. The flux of lithium-ions is therefore driven by the developed concentration gradient within the solution.

It can also be seen that in the solid phase, the regions closer to the separator, especially for the anode becomes much more lithium depleted than solid regions closer to the current collector. This is due to the fact that the reaction current density is much higher at the interface due to that having an initially lower resistance pathway. This difference in solid phase lithium concentration isn't as evident in the cathode as the lithium diffusion coefficient is often higher than the anode meaning that concentration gradients are smaller. Figure 3.30 then shows how the reaction current density evolves over time.

As it can be seen, the higher reaction current density is found at the anode at the electrode-separator interface due to the lower resistance. Over time the peak location will move towards the electrode-current collector interface as lithium concentration becomes lower in the separator interface regions leading to higher resistance and less preferred reaction sites. At high C-rates of discharge; however, this inhomogeneity may mean regions of the cell reach the prescribed limits before other regions thus not achieving the cells theoretical maximum capacity. More concerning is that potential of the cell is only measured at the electrode/current collector interface. Results show that the region experiencing the highest reaction current densities are at the electrode-separator interface. Therefore, there it becomes a risk that at low SOCs and high discharge rates regions of the cell will have already reached the prescribed cut-off point however the terminal voltage of the cell does not indicate this.

The effect of temperature and C-rate on the efficiency and capacity of the battery can be investigated by running the model under isothermal conditions. Figure 3.31a shows the percentage of capacity available under varying C-rate discharges and temperatures. Here the 100% of capacity is taken as the slow rate 0.1 C discharge capacity at 45°C. It can be seen that there is a near linear dependency of decreasing available capacity with C-rate at all temperatures. This is due to increased diffusion limitations. At higher temperatures, the C-rate dependency is less due to the increased solid phase diffusivity of lithium in the electrodes.

Figure 3.31b shows how the efficiency of the battery, under discharge, varies as a



(a) (b)

Figure 3.31: (a) Percentage of maximum capacity under different isothermal and C-rate discharge conditions and (b) efficiency of cell under varying isothermal and C-rate conditions

function of temperature and C-rate. Efficiency is taken as being the ratio between the extracted energy and the extracted energy of the cell under 0.1 C discharge at 45°C which represents the near 100% available energy. Inefficiencies indicated by the model therefore arise due to series, charge transfer and mass transfer resistances. Again it can be seen that at higher temperatures and lower C-rates the battery performs within a higher efficiency regime. At low temperature and high C-rate discharge the efficiency of the cell can drop to 60% at 5 C and -5°C.

3.7.3 Model based battery design

Now that a physics based model for a lithium-ion battery has been established and validated it is possible to use the model in order to probe the effects of varying the characteristics of the battery from a fundamental point of view. Batteries of the same chemistry can have very different dynamic characteristics which depend on the thickness of the electrodes used and the area of the current collectors. In high power applications, more current collectors are used in order to reduce the internal resistance which is a function of the area specific resistance. The drawback of this is that the volumetric energy density suffers as more space within the cell is taken up by current collector material. In high energy batteries, the electrode thicknesses are increased at the cost of increased cell resistance due to lower though plane current collection area. Using a physics based model, it is possible to probe the effects of sizing the electrodes and the relative impact on performance without having to construct the cell.

The thickness of the electrodes used in a battery will largely define its power and energy density. A cell with thicker electrodes will have a higher energy density as, per unit volume, there is less current collector material. The draw back of this is that the series resistance becomes higher resulting in a lower power density. A diagram of a typical arrangement of cell layers in a battery is shown in Figure 3.32. It can be seen that each current collector, apart from the end ones, share two sets of electrodes. Removal of current collectors will obviously allow for more room for electrode material.

In this study, the volume of the cell was kept constant, and the same parameters as initially parameterised against were used. Therefore, the space which is freed up when removing layers was added to the electrodes assuming the same ratio of anode to cathode active materials in order to ensure the stoichiometries of both electrodes remain similar

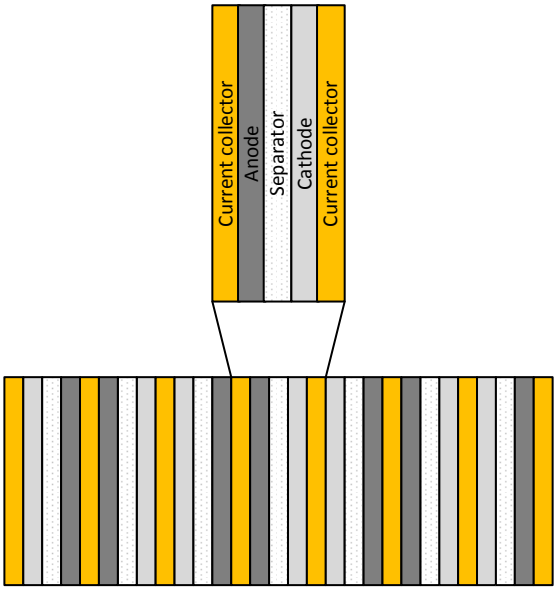
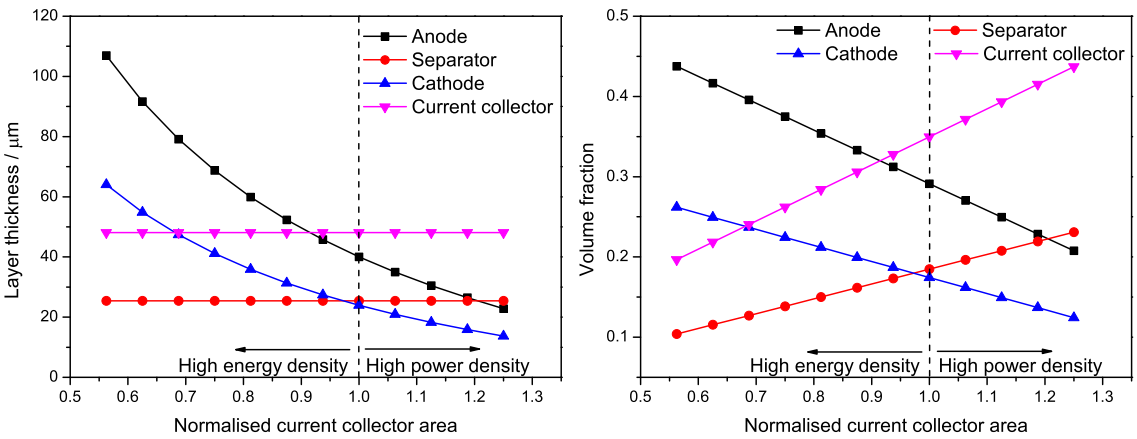


Figure 3.32: Diagram of cell layer arrangement

during the whole range of discharge. Figure 3.33a shows how the thicknesses of each layer varies when changing the relative current collector area relative to the original. In the parameterised Kokam 4.8 Ah battery it was shown that there are 80 individual battery layers. Each point therefore represents a change of 5 layers with the normalised current collection area of 1 representing the original parameters. It has been assumed that the thickness of the separator and current collector remains constant.

Figure 3.33b shows how the relative volume fraction of the different components of the cell varies when changing the available current collector. In the higher energy battery domain the available active material is evidentially larger and the space occupied by the current collector and separator is decreased due to fewer layers.

Of course, varying the amounts of active materials will affect the cost of the cell which will be analysed in later chapters as one of the objective functions to minimise. The cost



(a) (b)

Figure 3.33: (a) Thickness and (b) volume fraction of battery layers when varying layer number for a constant cell volume. Each point represents 5 layers of the original 80 layer modelled battery. Normalised current collector value of 1 represents the original parameters

Table 3.3: Cost and density of battery materials. All material costs are from Element Energy [71]. Density values are taken from Reddy [168]

Component	Cost ($/kg[a])	Density (g/cm^3)
NMC[b]	42	2.69
Carbon conductor	30	1.1
Separator	2 $/m^2	-
Graphite[c]	30	1.1
Binder[d]	10	1.78
Aluminium foil	14.8	2.7
Copper foil	16.8	8.96
Electrolyte[e]	21.6 $/dm^3	-

[a] Unit for cost is $/kg unless otherwise stated

[b] Assumed to be NMC 11 BC-618 from 3M taken from chapter 26.12 of [168]

[c] Assumed to be 818 Natural Graphite taken from chapter 26.25 of [168]

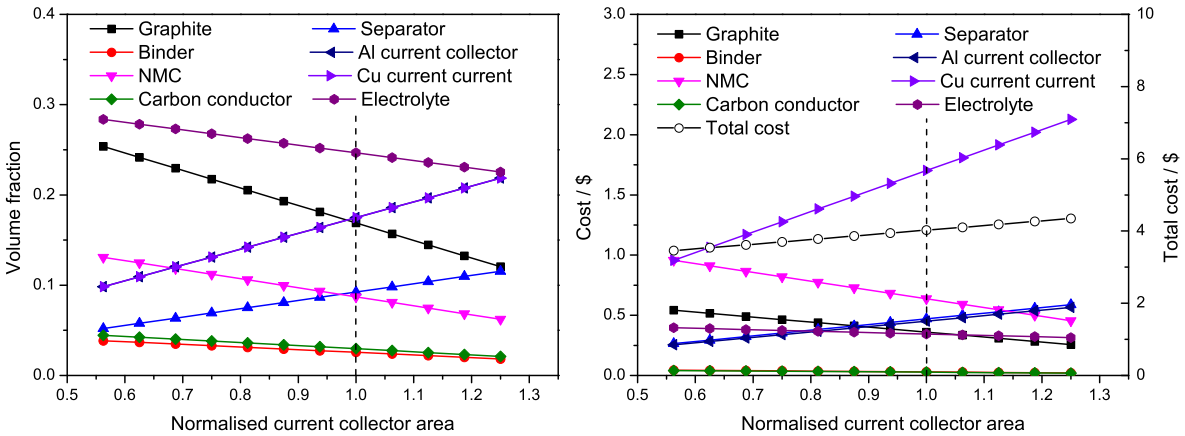
[d] Assumed to be Polyvinylidene Fluoride

[e] Assumed to be Ethylene Carbonate

of the main components of the battery are shown in Table 3.3. This does not include any overhead costs and is purely indicative of the raw material costs.

Figure 3.34a shows a detailed breakdown of the volume fractions of materials used in a battery based on simulation parameters previously established. It can be seen that electrolyte constitutes the largest proportion of the cell volume and that this decreases in higher power cells due to the larger proportion of current collectors. The graphite anode is the next largest proportional material however the volume of the current collectors increases above this in high power cells. The amount of NMC cathode material is much lower and lower still is the proportion of anode binder to give mechanical strength to the graphite and carbon conductor material in the NMC to increase electrical conductivity.

Figure 3.34b shows the relative cost of the individual components and how they change with increasing power density. It can be seen that a higher power cell costs more to produce from a purely materials point of view due to the increased cost of the current collectors. The low proportion of binder and carbon conductor in the anode and cathode



(a) (b)

Figure 3.34: (a) Breakdown of volume fraction of different battery components and (b) cost of raw materials

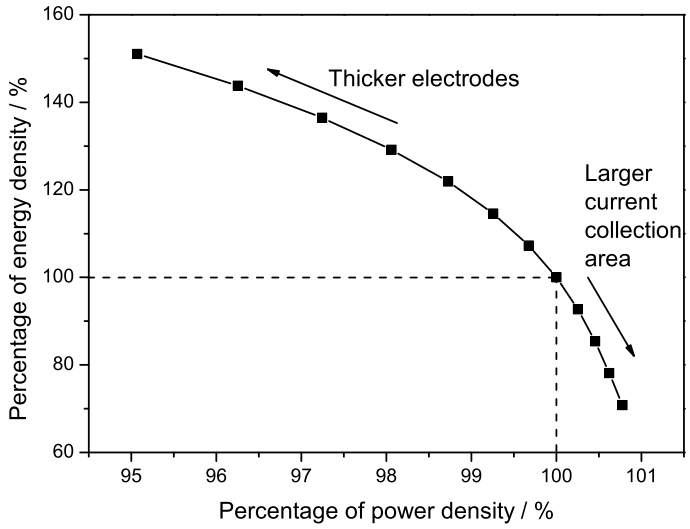


Figure 3.35: Ragone plot for varying area of current collection and thickness of electrodes

have a negligible impact on the overall cost. Of the two electrodes the NMC is nearly twice as costly as the graphite. The reader should bear in mind that this is just the cost of materials and does not include any overhead costs or system integration costs.

The resulting Ragone plot can then be plotted for these alterations to the cell configuration as shown in Figure 3.35. The axis have been plotted against the performance of the originally parameterised cell which represents the performance at 100% of the reference state. The energy density was established by integrating the energy under a 0.5 C (2.4 A) discharge of the model. The power density was established by the initial power after a 10 C (48A) discharge. Each point represents the removal or addition of 5 layers of the original 80 layer cell. It can be seen that if the area of the current collection is reduced by 45% the energy density increases by 50% with a decrease of 5% of the power density. By comparison, increasing the current collection area by 25% results in a 30% reduction in capacity but only a 1% increase in power. This indicates that for the cell modelled the power density has been reasonably optimised for this cell.

3.7.4 Degradation

The developed battery model can be used to analyse not only the most efficient operating points and battery dynamics but also the rates of degradation if operated within a certain operating range. HEV applications where the battery is cycled around a narrow SOC range have many possible options for operating conditions. In order to probe this, the battery model was cycled around different SOC operating points. Figure 3.36 shows a discharge followed by a charge process. Shaded regions represent the energy extracted under discharge and put in during charge. The dotted line represents the OCP. For this analysis the removed capacity was fixed to 10% of the rated capacity. The efficiency calculated, was taken as the ratio of the discharge energy to the charge energy with the charge removed and replenished remaining was the same.

Figure 3.37a shows how the active material available to the cell decreases with increasing number of cycles for different SOC operating regions and Figure 3.37b shows the SEI layer resistance evolution under the same cyclic conditions. Active material loss and SEI growth are linked to each other as the lost active material is used to grow the SEI. Operation at higher SOCs leads to accelerated rates of active material loss and SEI resistance due to the increases in the potentials driving the side reaction which are

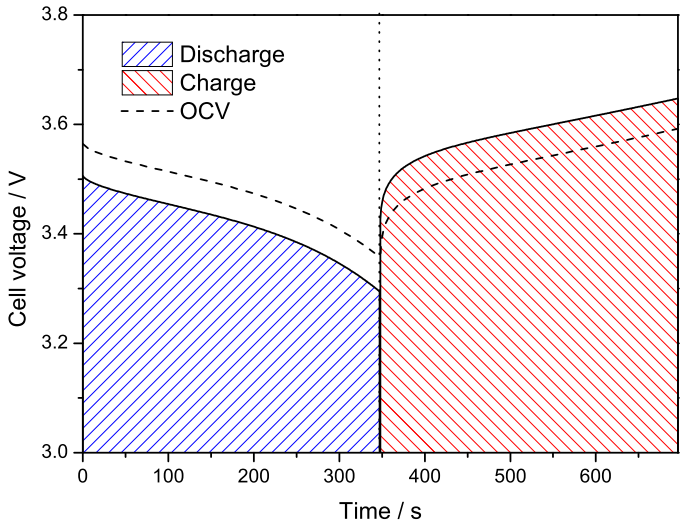
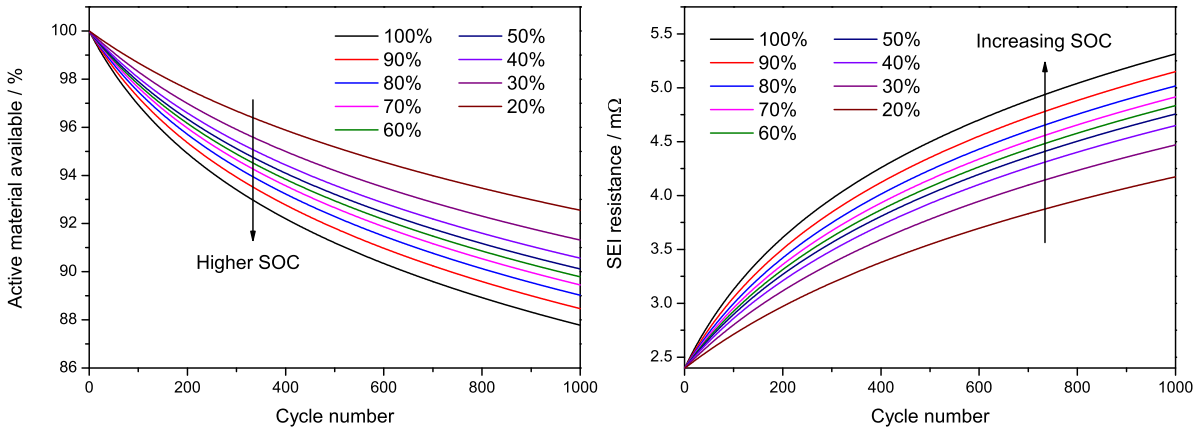


Figure 3.36: Example of discharge and charge cycle used to characterize degradation rates with different operation regions of the battery SOC. Shaded regions represent energy extracted/ put in during discharge/ charge

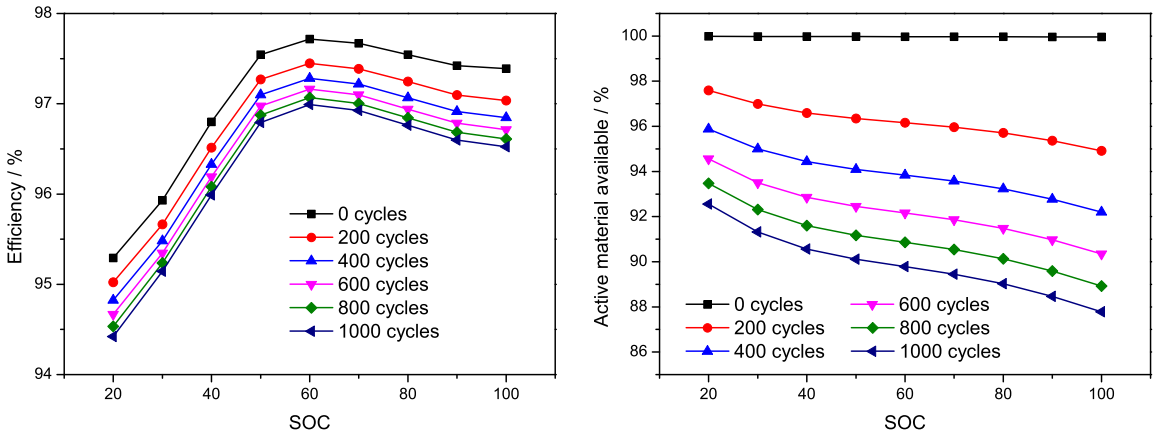
correlated to the potential of the electrode and electrolyte.

The degradation rates are most strongly a function of the operating SOC. At higher SOCs, the degradation rate is greater. Decreasing the operating SOC will therefore help with minimising the rates of degradation however this reduces the available energy, and depending on the region of use mean the user operates the battery in a less efficient regime. It therefore becomes a trade off between efficient operation, available energy and durability of the battery. Figure 3.38a shows how the efficiency of the battery varies at different SOC operating points under a 1C discharge and charge cycle within a 10% capacity of the rated capacity over 1000 cycles. It can be seen that the peak efficiency is achieved at a SOC operating point of 60%. Above 60% and the cathodic overpotentials dominate. Below 60% and the anodic overpotentials dominate.



(a) (b)

Figure 3.37: (a) Active material available and (b) SEI layer resistance against cycle number for cyclic loading of 10% of the rated capacity at different SOCs at 1C discharge and charge



(a) (b)

Figure 3.38: Simulated (a)eEfficiency at different SOCs and (b) active material available after cycling of 10% of the rated capacity at 1C

Figure 3.38b then shows how the degradation, which is taken as the available active material changes when cycled at different SOCs over 1000 cycles. The shape of the SOC degradation rate curve for each number of cycles follows the SOC-anode potential curves since this drives the side reaction process.

Direct comparison between the efficiency of the battery and the available active material can be seen in Figure 3.39. It becomes evident here that the same efficiency can be achieved at SOC operating points above 60% SOC and below it however at points below 60% the degradation rates are smaller. Operating SOCs between 60% and 45% appear to be the best for maximising efficiency and minimising degradation rates before the anodic charge transfer processes increases polarisation resistance significantly to reduce the efficiency too much.

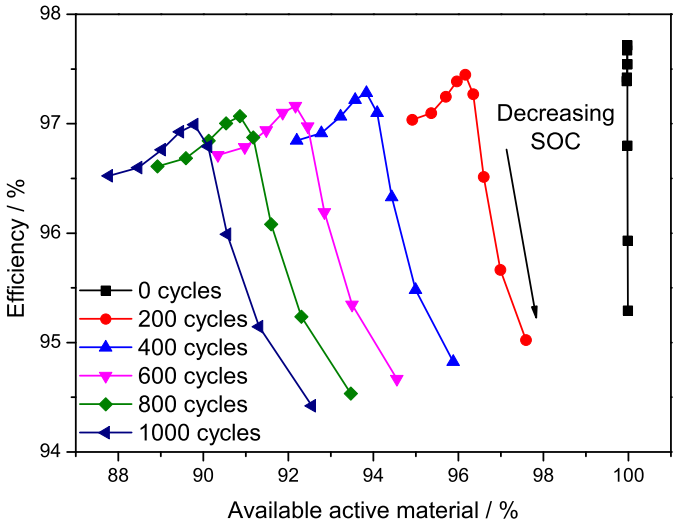


Figure 3.39: Efficiency against active material available during cycling under HEV mode in a 10% SOC window at different SOCs

3.7.5 Stoichiometric drift

In a galvanic cell, the measured cell potential at steady state is the difference between the anode and the cathode. The potentials of each electrode is a direct function of the material composition of the electrode, relative lithium content, electrolyte and the temperature. Normally, the stoichiometric operating window of each electrode is predetermined by the battery manufacturer; however, over the lifetime of the battery, irreversible losses can result in the loss of cyclable lithium due to phenomenon such as SEI layer formation and lithium plating as well as loss of capacity due to mechanical failure of parts of the battery electrode effectively forming isolated islands and therefore loss of electro-active surface area. All these factors combine to lead to an effect known as stoichiometric drift where the measured cell potential may be within a safe range but the individual electrodes themselves are operating in a regime where they are unstable leading to accelerated capacity fade [234].

In the majority of conventional cells, the lithium-ion cell consists of a graphite anode, for example MesoCarbon MicroBeads (MCMB), a lithium metal oxide cathode (e.g. $LiMnO_2$ or $LiCoO_2$) and an electrolyte consisting of a solution of lithium salts (e.g. $LiPF_6$) in a mixed organic solvent (e.g. ethylene carbonate-dimethyl carbonate (EC-DMC) imbedded in a separator [184]. Cyclic voltammetry tests indicate that MCMB redox processes occur at approximately 0.05 V vs. Li and for $LiCoO_2$ this is approximately 4 V vs. Li. The stability region of the electrolyte is typically 0.8 V vs Li to 4.5 V vs Li [184]. It is therefore apparent that MCMB anodes operate outside the stability limit of the electrolyte, whilst the lithium metal oxide cathode is just at the limit. The MCMB/$LiCoO_2$ battery is therefore a thermodynamically unstable system in this electrolyte; however, in reality the formation of the SEI layer allows for the passivation of the side reactions.

Under conditions where overcharging of a battery occurs, therefore leading to the possibility of oxidative processes at the cathode, no passivation film forms leading the severe accelerated degradation [184]. Therefore, if over time the anode stoichiometry drops leading to a large anode potential at 100% SOC, there is a risk that the cathode could be accidentally overcharged due to the apparent cell voltage.

Figure 3.40 shows the electrode potentials for a lithium-ion battery using a MCMB carbon electrode and the parameterised NMC cathode. Here the same anode stoichiometry

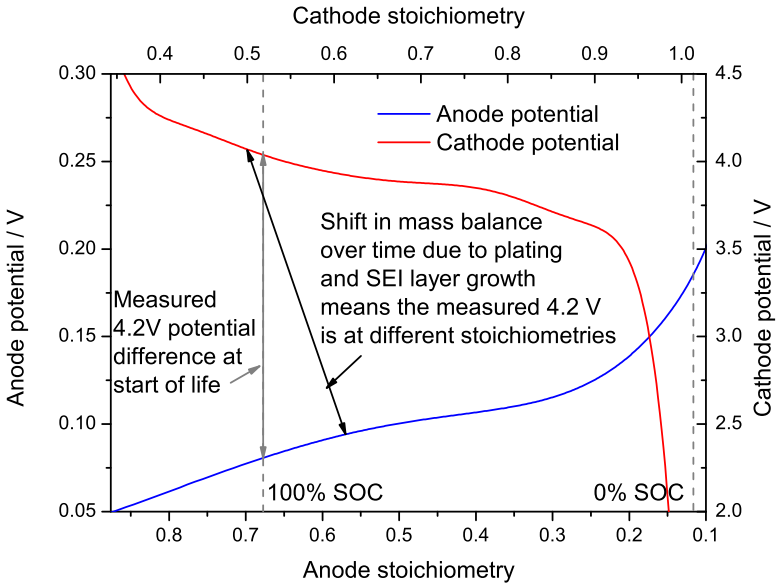
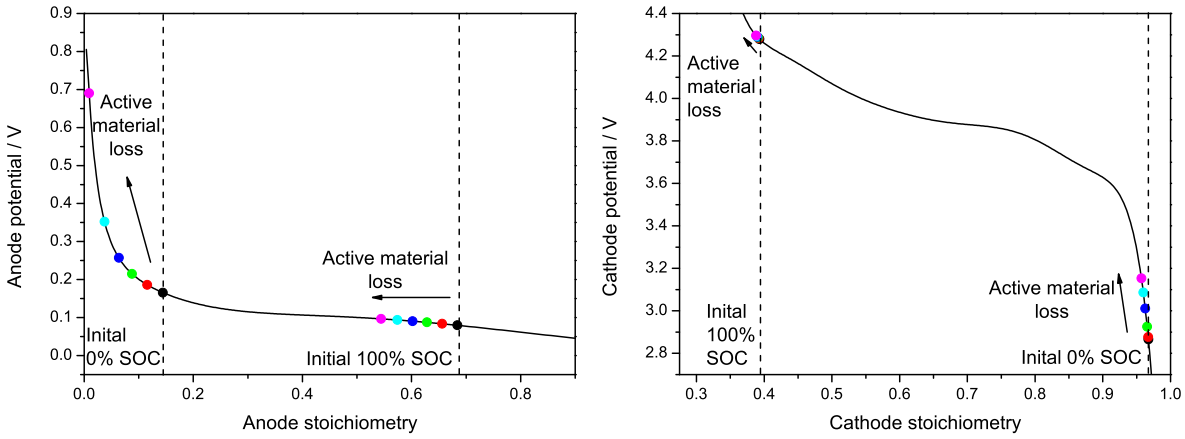


Figure 3.40: Potentials of a lithium-ion battery against stoichiometric ratios of lithiations for a carbon MCMB electrode and NMC cathode



(a) (b)

Figure 3.41: Stoichiometric drift of (a) an anode and (b) cathode with increasing loss of active material. Each point represents a 5% increasing loss of active material from the whole cell. Upper and lower limits represents the stoichiometries required for the 4.2-2.7 V cell voltage limits

curve as the one presented by Smith and Wang [189] was used to determine the cathode stoichiometry-potential relationship, assuming the same stoichiometric limits as in suggested by Smith and Wang [189].

It can be seen that there can be multiple combinations of anode/cathode stoichiometries that result in the same overall cell voltage. Over the duration of use the operating point will inevitably shift due to irreversible side reactions. Having a reference electrode that allows for the separation of anodic and cathodic potentials allows for access to this information, however the majority of commercial cells do not have reference electrodes and thus this information is difficult to derive.

Using SRCV is it proposed that it is possible to monitor stoichiometric drift in lithium-ion batteries without the need for a reference electrode. This is because the location of the peaks in the SRCV correspond to a phase transition in the battery electrodes which occur at a specific lithium stoichiometry.

Figure 3.41 shows the change of the electrode stoichiometries over time with the loss of active material due to the growth of the SEI layer. This assumes the cell voltage limits remain at 4.2-2.7 V. Each incremental point represents a 5% loss of active material. It can be seen that over time as cyclable lithium is lost from the system the starting stoichiometry of the cathode decreases (increasing cathode potential), whilst the starting stoichiometry of the anode also decreases (increases the anode potential). The increase in cathodic potential is therefore balanced by the anodic increases to result in the same 4.2 V cell voltage that the user experiences. The risk of this is that in the discharged state the anode gets increasingly close to fully depleted, whereby the anode potential increases significantly.

Slow Rate Cyclic Voltammetry

SRCV applies a constant voltage which changes at a constant ramp rate. The peaks in the resulting current profile represent the location of redox potentials or phase transitions of the electrode. In chromopotentiometry mode this is akin to a plateau during constant current discharge. Figure 3.42 shows the discharge half of the SRCV taken at 10 μV.s^{-1} superimposed with the dV/dT measurements, which are an indicator of entropic changes,

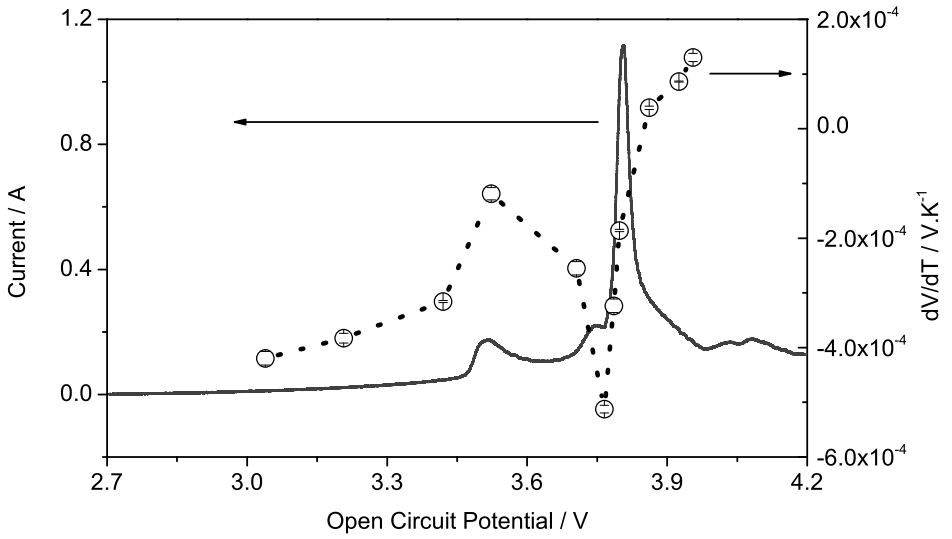


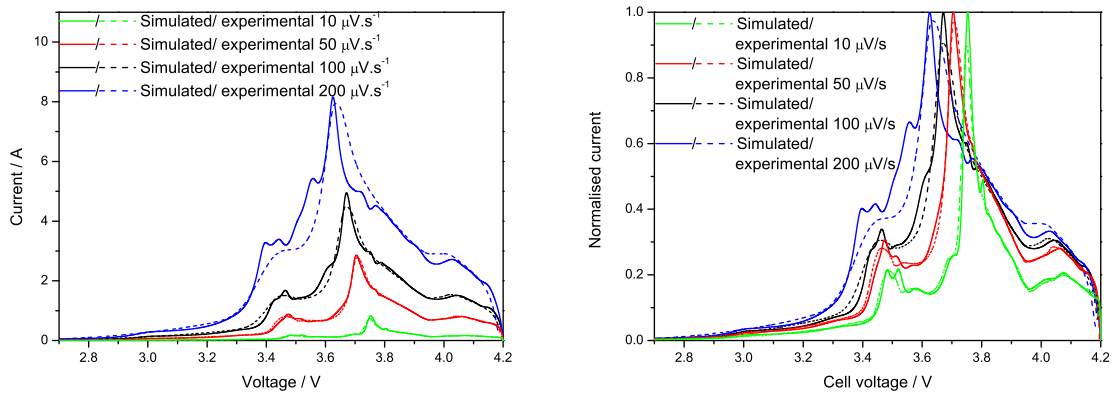
Figure 3.42: Slow rate cyclic voltammetry and entropy measurements of a 4.8 Ah lithium-polymer battery [202]

taken by monitoring the cell voltage as the temperature is varied. Rapid changes in the entropy typically represent phase transitions in the electrode materials.

Using the developed model it is also possible to simulate the response of the SRCV. This is shown in Figure 3.43a and 3.43b.

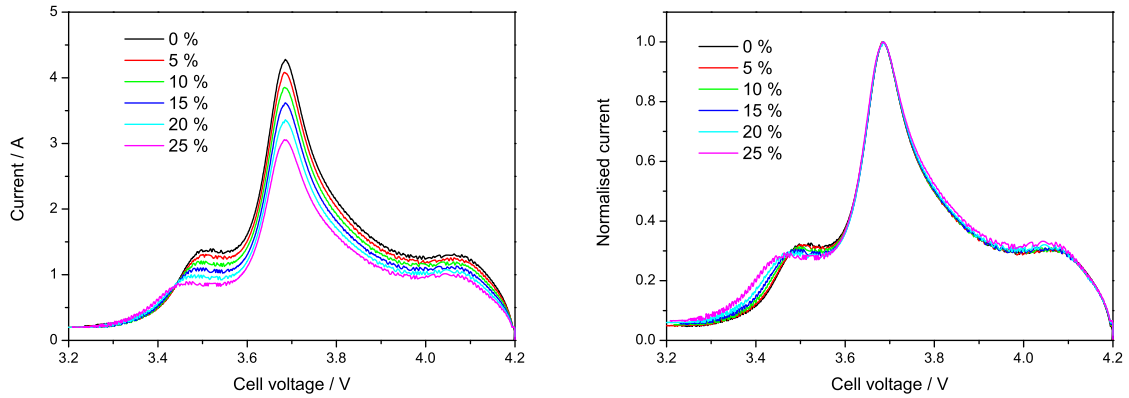
As shown in Figures 3.43a and 3.43b, the simulated and experimental results show good agreement. With the model it is then possible to artificially induce this stoichiometric drift which is shown in Figure 3.44a for different amounts of lost active material assumed to have been used in the formation of the SEI layer.

In the raw simulations, without normalisation, it can be seen that the area under the SRCV decreases indicating the loss in active material. The main peak between 3.6-3.8 V however does not significantly move location which is evident from the normalised plot. The secondary peak between 3.4-3.6 V; however, does move more and could be used as an in-situ indicator for stoichiometric drift.



(a) (b)

Figure 3.43: Comparison between simulated and experimental slow rate cyclic voltammetry in the (a) raw and (b) normalised form



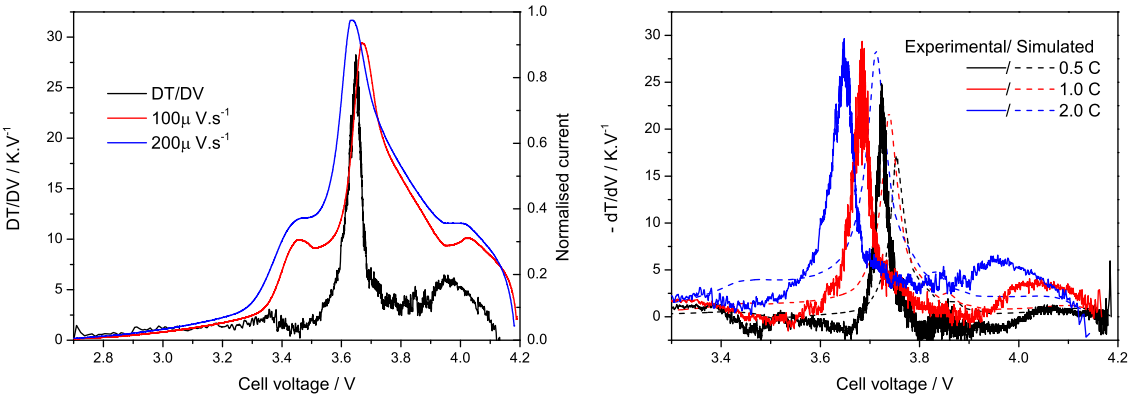
(a) (b)

Figure 3.44: Simulated shift in the SRCV for varying loss of active material for a 100 μV.s^{-1} scan rate (a) and normalised current (b)

Differential Thermal Voltammetry

As previously discussed, the peaks in the SRCV plots allow for information on the phase transitions of electrodes to be inferred. This can ultimately be used as a indicator for the stoichiometry of each electrode. The draw back of this technique is that SRCV can take quite a long time to conduct. However, herein we introduce the concept of Differential Thermal Voltammetry (DTV) as a means of deriving the same information as the SRCV experiments, i.e. the location of the peaks and therefore phase transitions but in a shorter time.

The DTV technique consists of a constant current discharge or charge, where voltage and temperature are monitored. The differential of voltage and temperature, with respect to time, are then taken and the ratio of the two (DT/DV) is presented. Physically, entropy changes in each electrode induce a reversible temperature change which can act as a indicator for a certain electrode SOC. Figure 3.45a compares the experimental DTV with SRCV measurements. Here it can be seen that the general shape of the DTV measurements are similar to that of the SRCV, with the peak occurring at approximately



(a) (b)

Figure 3.45: (a) Comparison between slow rate cyclic voltammetry and differential thermal voltammetry for a 4.8 Ah Kokam lithium-polymer cell and (b) Comparison between simulated and experimental differential thermal voltammetry

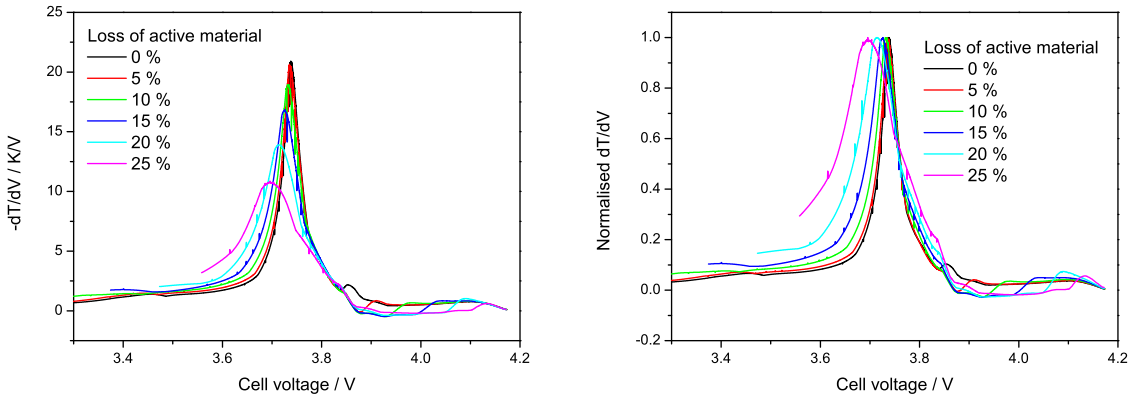
the same voltage.

The presented data was taken with the cell under ambient conditions with free convection. A K-type thermocouple was attached to the centre of the cell and used as the measured temperature. A discharge of 1 C (4.8 A) previously resulted in a temperature change of approximately 3 °C, suggesting that the amount of heat loss via free convection is not significant relative to the electrochemical and electronic heat generated from the cell. Measurements, were taken under ambient conditions as to replicate in-situ conditions for a typical cell in an electric vehicle.

Figure 3.45b then compares the experimental DTV measurements to the modelled ones. The general shape of both the simulations and the experimental results show good agreement with a main peak and two sub-peaks either side, however the simulation results show an approximate 0.1 V shift to the right in all cases. This could be attributed to insufficient accuracy in the resolution of the entropy measurements previously made. However, even with this error, the concept still holds as one can use the temperature changes as a marker for individual electrode stoichiometries.

Figure 3.46a shows the DTV plots when there is a simulated loss of active material leading to a shift in the operating stoichiometry of the electrodes to compensate. It can be seen that the main difference is the main peak is shifted to lower voltages and is smaller in magnitude. The smaller peak near 3.85 V is then shifted to higher potentials. The reason for this is that as the battery loses active material through the formation of the SEI layer, the starting anode and cathode stoichometries get increasingly lower. The shift in the location of the main peak is therefore much more evident than in the simulated SRCV.

For the data sets for >15% active material loss the solution did not converge for all time steps before the cut-off voltage was reached. This is due to the fact that the surface stoichiometry of the anode particles reached 0 and the dominant potential of the cathode had not dropped. The model cannot handle stoichiometric values <0 and therefore did not converge. Physically this would mean that the anode is fully depleted of lithium. In reality the potential of the anode should increase significantly in this case however in the used anode-stoichiometry relationship used, which was taken from Smith and Wang [189] this was outside the range of operation and therefore this physical mechanism was not captured.



(a) (b)

Figure 3.46: Differential thermal voltammetry for increasing loss of active material for a 1C discharge (a) and normalised data (b)

3.7.6 Battery pack design

In order to achieve practical voltages and capacities for lithium-ion battery packs for automotive applications, usually hundreds of cells are connected in series and parallel. Under ideal conditions, one would expect each cell in the pack to experience the same loading; however, in reality depending on the pack architecture, operating conditions and a range of other things one cell can experience a significantly different load.

In a BMS it is impractical to monitor the condition of each cell of the pack and therefore it is normal for a reduced number of measurements to be made in areas where the battery pack developer expects to be the most critical; however, without a detailed understanding of the performance of lithium-ion batteries the location of the most critical cells may not be monitored. Using the developed model it is possible to probe pack level effects.

Many authors in the academic literature neglect the effect in interconnect resistances when modelling battery packs and those that do typically use simplified equivalent circuit models. As cell designers continue to drive the internal impedance of cells ever lower the relative magnitude of the interconnects becomes increasingly important.

Uneven loads in parallel battery strings

In a highly parallel pack, where interconnect resistances have equal values, an applied external load does not necessarily cause the individual cells to supply equal amounts of current. This effect arises due to the existence of different current paths, some of which pass through a different number of interconnect resistances, as shown in Figure 3.47. Non-uniform ohmic overpotentials arise throughout the pack, making the careful consideration of the current paths and the position of the load terminals essential for maintaining performance and safety.

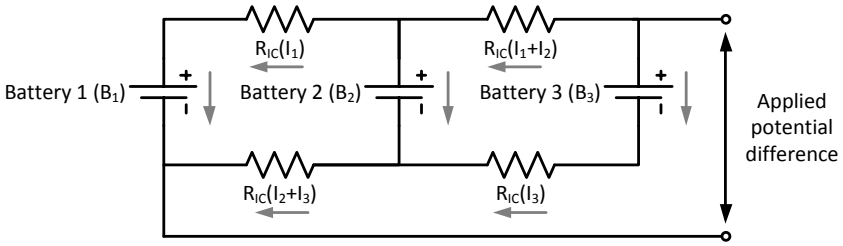


Figure 3.47: Schematic of a 3P1S battery pack configuration depicting sources of interconnect overpotentials under an applied potential load. The grey arrows depict the direction of the current flow [224]

In the 3P1S pack configuration shown in Figure 3.47, the external load is applied as a potential difference at diagonal corners. Kirchhoff's Voltage Law (KVL) dictates that within any close loop formed within the circuit, the overall potential difference must be equal to zero: $\Sigma_{k=1}^{n} V_k = 0$, where n is the number of voltage source/sinks. Assuming that the initial state of each battery is the same and that the resistances of all interconnects are equal, three simultaneous equations govern the current flow through the system as shown in Equations 3.55-3.57, where η represents the overpotential of the subscripted cell.

$$V_{app} = OCV_1 + \eta_1 + R_{IC}\left(2I_1 + I_2\right) \tag{3.55}$$

$$V_{app} = OCV_2 + \eta_2 + R_{IC}\left(I_1 + 2I_2 + I_3\right) \tag{3.56}$$

$$V_{app} = OCV_3 + \eta_3 + R_{IC}\left(I_2 + I_3\right) \tag{3.57}$$

The system can be written in a generalised matrix form for any number of batteries (N_{cell}) as shown below, where the battery overpotentials have been represented as the product of the battery current and polarisation resistance ($I_i R_{cell,i}$). Here i and j are indices for the row and column numbers in the matrix. The dependence of load on polarisation resistance is neglected. As the polarisation resistance varies with temperature, SOC and load, the assumption is valid only when the pack is in steady state.

$$\begin{pmatrix} OCV_i + I_i R_{cell,i} \\ \vdots \\ OCV_n + I_i R_{cell,n} \end{pmatrix} + \begin{pmatrix} N-1-|i-j| & \cdots & N-1-|i-N_{cells}| \\ \vdots & \ddots & \vdots \\ N-1-|N_{cells}-j| & \cdots & N-1-|N_{cells}-j| \end{pmatrix} \begin{pmatrix} I_i \\ \vdots \\ I_N \end{pmatrix} R_{IC} = \begin{pmatrix} V_{app} \\ \vdots \\ V_{app} \end{pmatrix}$$

Assuming that all cells are at the same SOC initially, they also have the same OCVs and polarisation resistances. The set of simultaneous equations can then be solved for the currents I_i by multiplication of the inverse matrix as shown below where $\beta_{i,j} = (N-1-|i-j|)\frac{R_{IC}}{R_{cell}}$ if $i \neq j$ and $\beta_{i,j} = (N-1-|i-j|)\frac{R_{IC}}{R_{cell}} + 1$, with $i = j$ for convenience.

$$\begin{pmatrix} I_i \\ \vdots \\ I_N \end{pmatrix} = \frac{1}{R_{cell}} \begin{pmatrix} V_{app} - OCV_i \\ \vdots \\ V_{app} - OCV_N \end{pmatrix} \begin{pmatrix} \beta i, j & \cdots & \beta_{i,N} \\ \vdots & \ddots & \vdots \\ \beta_{N,i} & \cdots & \beta_{N,N} \end{pmatrix}^{-1}$$

As the same external potential is applied to all of the cells and their OCVs are initially the same, the current flowing through each cell cannot be the same if R_{IC} is finite, as the inverse matrix would be non-zero.

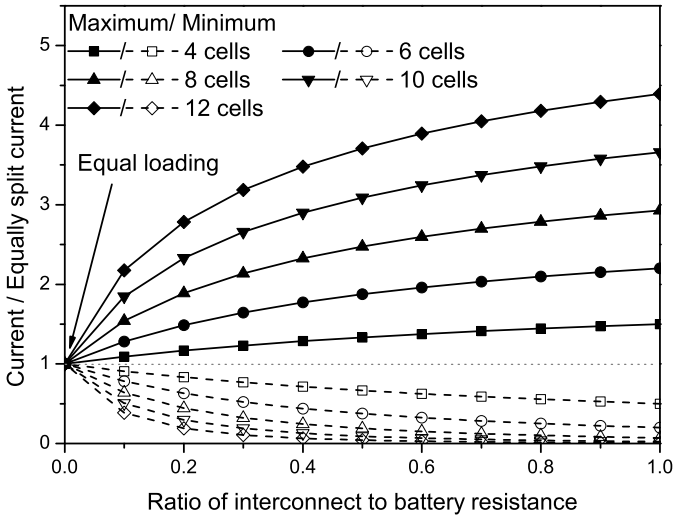


Figure 3.48: Ratio between predicted current and equivalent equal split current for cells closest and furthest from the load points for different ratios of interconnect resistance to battery impedance and cells in a single parallel strip. Solid lines and symbols represents the load experienced by cells closest to the load points and dashed lines and hollow symbols represents cells furthest away [224]

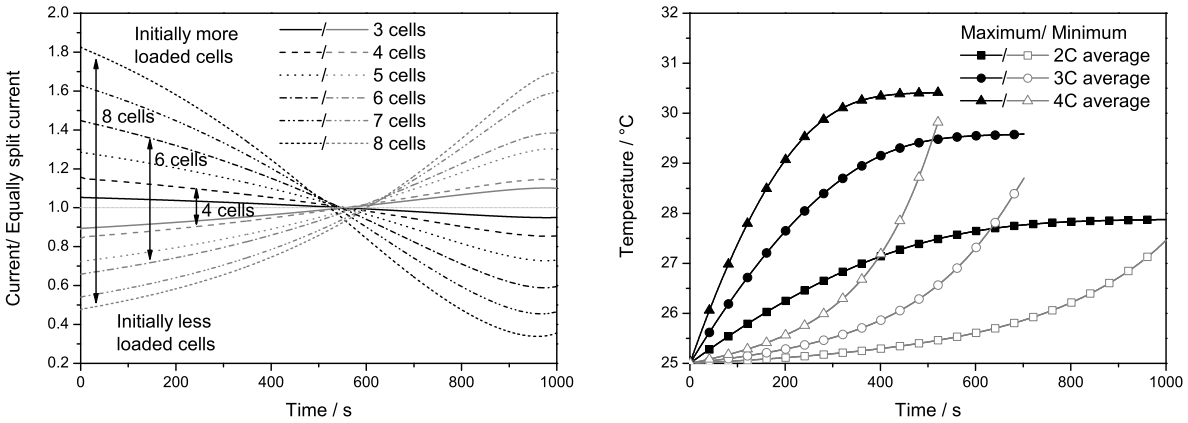
Figure 3.48 shows the effect of increasing the ratio of interconnect to battery impedance for different numbers of cells in parallel. When interconnect resistances are not considered $R_{IC}/R_{cell} = 0$ the same current flows through each parallel cell giving a current/equivalent split current ratio of 1. As the ratio of interconnect to battery impedance increases, the deviation in initial load from the ideal case of no interconnect resistances also increases. The magnitude of the load on a cell is dependent on the position of the cell relative to the point at which the external load is applied. Cells nearer the pack terminals experience a greater load due to lower interconnect overpotentials. Cells further away from the load terminal experiences higher interconnect overpotentials and thus provide less current initially. When additional cells are added in parallel, the number of interconnects is increased, and so the effect is amplified.

The load imbalance increases linearly with increasing number of cells in parallel and logarithmically with increasing R_{IC}/R_{cell}. In an 8P1S pack with a $R_{IC}/R_{cell} = 0.1$, the cell nearest the load point experiences an initial load 2.2 times greater than for $R_{IC} = 0$. This highlights the need to consider the interconnect resistance contribution to pack performance.

Constant current discharge

Under continuous discharge or charge, the impedance of a cell changes as a function of the SOC, temperature and load current, leading to the variation of load imbalance over time. The same type of effect is known at the cell level, where the reaction current density distribution is greatly affected by the position of the cell tabs. The maximum and minimum current through a parallel battery pack with a varying number of parallel cells, assuming a 1 mΩ interconnect resistances, is shown in Figure 3.49a.

As the SOC of the cells decreases, their internal resistance increases due the increased polarisation resistance. After a sufficient time, the changing impedance of the cell nearest the load point matches that of the additional interconnect overpotentials, and the situation is reversed: the cells furthest away from the load points provide the most current. This load redistribution can take on the order of hundreds of seconds and relies on the presence of a constant load. The characteristic time of the load distribution is highly dependent on the load profile, cell chemistry and position of the load point.



(a) (b)

Figure 3.49: (a) Maximum and minimum currents during a 2 C discharge of parallel battery packs with varying numbers of cells in parallel, starting from 60% SOC with a 1 mΩ interconnect resistance. (b) Maximum and minimum temperature of a 8P1S pack under an equivalent 2-4 C loading, starting from 60% SOC [224]

As the load is eventually redistributed to the initially less loaded cells, the difference in heat generation from the different cells is not as large as expected from the initial load distribution. Figure 3.49b illustrates the time evolution of the cell temperature as calculated for the different cells of a 8P1S battery pack under an equivalent 2-4 C discharge.

The shift in the peak load current towards the cells further from the load point caused by changing cell impedances does not result in significant inhomogeneities in temperature distribution under constant discharge/charge conditions. A problem arises, however, if the cells are continuously kept within a narrow SOC range as is common in Hybrid Electric Vehicle (HEV) applications, where the battery pack is used for load shaving of another prime mover. Cells could also be kept within a narrow SOC window relative to each other under the conditions where the load profile allows for sufficient time to rebalance cell SOCs such as pulse loading followed by rest periods. In such pulse loading situations the cell impedance differences do not compensate for the interconnect resistance imbalances leading to cells nearest the load points to continually be loaded more.

Cyclic loading

Under cyclic charge/discharge loading of a pack, cell impedances do not have sufficient time to balance and thus the cells nearest the load points continually experience higher currents, leading to them heating up considerably more than the cells further from the load points, as shown in Figure 3.50.

As there is insufficient time for the impedances to balance the relative change of the SOCs, the cell closest to the load point is constantly loaded more heavily than cells further away. This situation results in considerably more heating in that region of the pack and significantly inhomogeneous temperatures in comparison to constant current loading. The load imbalance caused by interconnects is more critical in applications where the battery pack is kept within a narrow range of SOC, such as commonly found in hybrid electric vehicle applications, because the impedances do not have sufficient time to balance. As shown in Figure 3.49a, the balancing time is on the order of hundreds of seconds. The exact value depends on the cells used: higher capacity cells are expected to require longer balancing times.

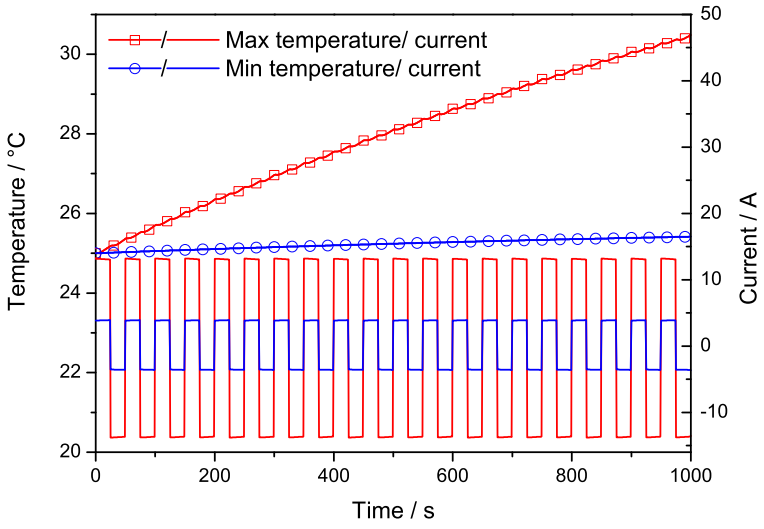


Figure 3.50: Simulated temperatures and currents during cyclic loading of 6 Ah cells nearest and furthest from the load points in a 8P1S pack, around 60% SOC assuming a 1 mΩ interconnect resistance [224]

Internal pack currents after load removal

During operation with imbalanced loads, the SOCs of the cells in a parallel strip become different from one another. When the load is removed, the cells OCVs are different, and current must flows from the cells with higher SOC to those with lower SOC, as shown in Figure 3.51. This rebalancing current leads to further heat generation beyond the removal of the load, a process detrimental to all cells.

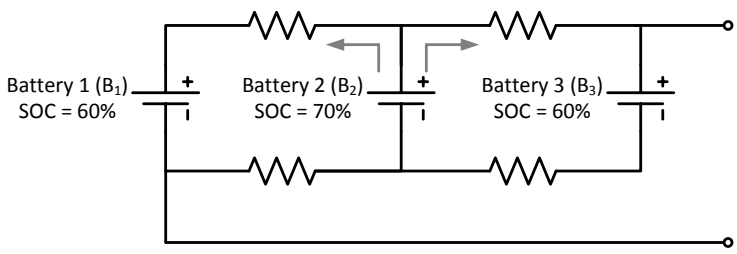


Figure 3.51: Schematic showing current rebalancing in a 3P1S pack under no load conditions, due to differences in SOC induced during previous operation [224]

Figure 3.52 shows the effect of current rebalancing for a 8P1S pack after a 3 C discharge from 60% SOC. Again it can be seen that the cell nearest the load point is initially overloaded. When load is removed after 500 s, the difference in SOCs results in higher OCVs for the furthest cells than for the nearest ones, and a rebalancing current is present in the pack.

The rate of current rebalancing within cells of the same parallel strip is determined by the difference in SOC and also by the type of cells used. Figure 3.53 shows the performance map of the modelled battery to depict the driving forces of this rebalancing. Assuming the cells are identical, each must operate along the surface contour defined in Figure 3.53. If two cells of different SOC are connected in parallel, their potentials must be equal (minus the small interconnect overpotentials); their OCVs, however, are different, and

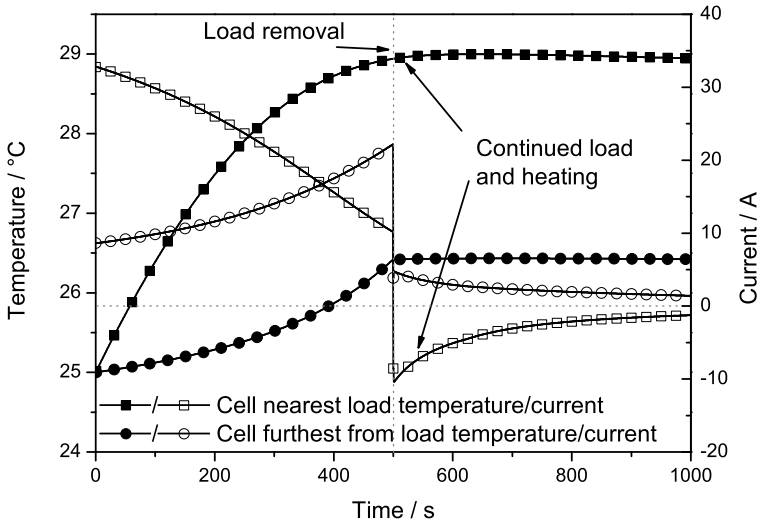


Figure 3.52: Simulated cell currents and temperatures of a 8P1S pack under a 3 C discharge for 500 s after which load is removed and OCVs rebalance assuming a 1 m interconnect resistance. Solid symbols represent temperature and hollow symbols represent current [224]

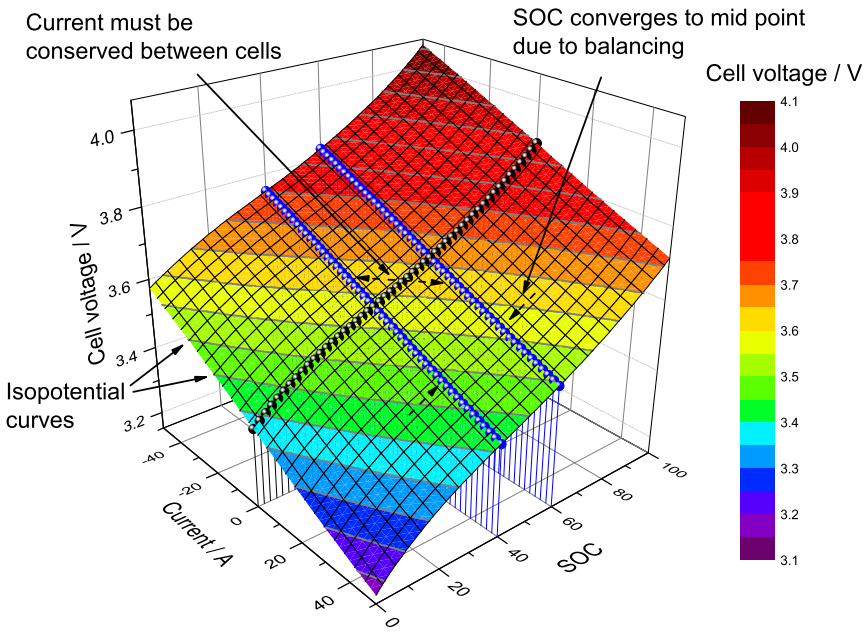


Figure 3.53: Battery performance map showing pseudo-steady state voltage at different currents and SOCs with superimposed operating points of 2 cells at 40% and 60% SOC to show the rebalancing effect. The no-load contour is shown in black for reference [224]

the resulting overpotential to match the potential between the cells drives a rebalancing current. In this closed system charge is conserved, and thus the operating point is at the iso-potential where the net positive current matches the net negative current.

Larger packs

Battery packs for automotive applications typically use hundreds of cells and the effect of uneven current loads can be further amplified if the design is not appropriately considered. As the size of the pack increases the likelihood of inhomogeneous load distribution increases. This can be attributed to a number of factors: in larger systems the statistical distribution of cell characteristics and physical interconnects.

Figure 3.54a shows the current distribution for the module with oppositely connected electrical terminals with even contact resistances for a 150A discharge just after the load has been applied. As it can be seen, the highest observed currents are at the electric connection points at opposite corners of the module, with the highest currents being observed diagonally across the module as this is the path of least resistance. The cells that are at the opposite corner, relative to the electrical connections, experience a much lower discharge current. This effect also occurs when the electrical connection points are on the same side. In the no-fault case, the maximum discharge current is still double that of the minimum. This effect therefore leads to cell unbalancing and internal currents flowing when no load is applied. Figure 3.54b, then shows the current distribution in the module with the high interconnection resistance.

In Figure 3.54b, the uneven current distributions observed in Figure 3.54a are further accentuated, especially near the location of the high resistance. This high resistance restricts current flow from the cells isolated by the high contact resistance, drastically increasing the load on the cells near the current collection and decreasing the load on the cells isolated by the high contact resistance. Under the same discharge conditions, the model predicts the maximum discharge current to be 6 times that of the minimum discharge current. This highlights the importance of minimising contact resistances and ensuring equal balancing.

In automotive applications the battery packs are larger than the ones analysed so far. The effect of uneven current loading can limit performance and safety. Large interconnect resistances between cells, such as due to assembly faults, were shown to magnify the problem of uneven resistance pathways in a 12P7S battery pack of 4.8 Ah cells [150]. The effect of a high interconnect resistance is explored here as a worked example. The case is hypothetical, as the fault was fortunately resolved in the real life tests.

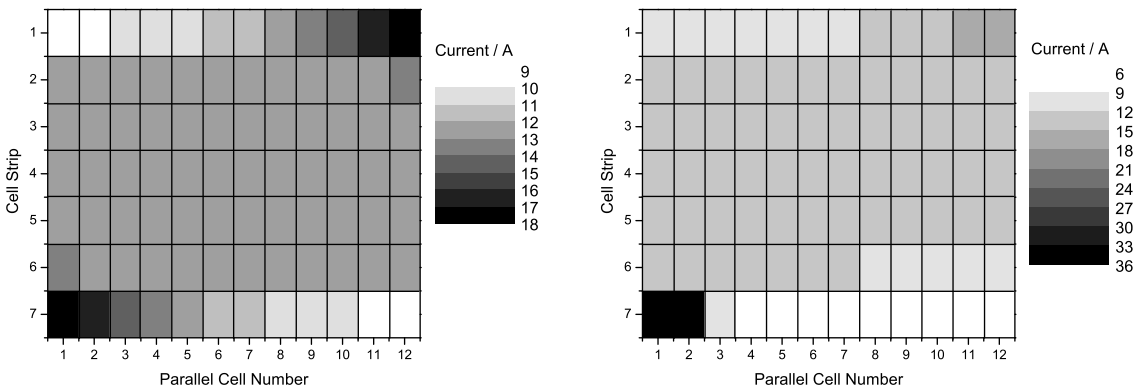
Load cycles typically seen in automotive applications tend to be highly dynamic. The difference in current loads through different cells and resulting heat generation do not scale linearly with size for highly parallel battery packs. Figure 3.55a shows simulated cell currents for a 12P7S battery pack under a 100 A load with a superimposed 1 Hz 10 A sine wave.

As a result of oscillating current load, a larger proportion of the noise amplitude is imposed on cells which are on the path of least resistance. This means that heat generated from both the steady state current and the oscillating current is higher in the worst positioned cells, showing that noise worsens any pre-existing problems.

In order to explore the consequences of the relatively high intercell resistance reported in previous work due to assembly problems [150], simulated temperatures and currents for the hottest cell in a 12P7S battery pack with and without a higher interconnect resistance in as shown Figure 3.55b. The effect of dynamic versus static loads is compared, where the latter is chosen equal to the average current of the real world cycle. The current profile is taken from the test data presented previously [150] and corresponds to a relatively aggressive drive cycle.

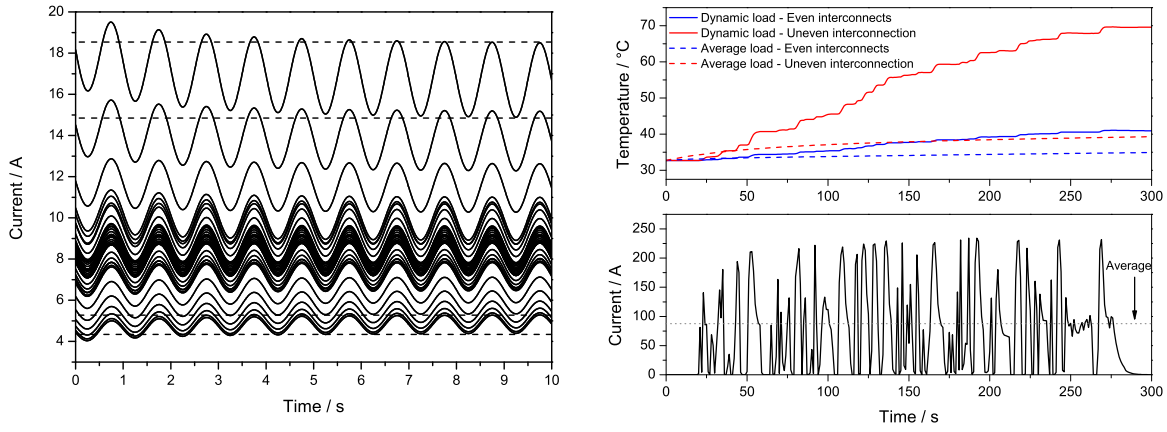
If the average current of the drive cycle were to be used as the model input, the predicted hottest cell temperature would be significantly lower than that for the real dynamic load. This difference is due to the non-linear distribution of current in the parallel cell strips. The cells positioned after the high interconnect resistance, away from the current collector, become isolated from the rest of the parallel strip. As a result, certain cells provide a current significantly larger than intended, and the temperature of the hottest cells increases.

In the case of dynamic load and high interconnection resistance, the hottest cell reached a temperature of 70°C, which is outside the 60°C maximum operating range recommended by the cell manufacturer. If the load cycle were to be allowed to continue, the hottest cell would enter thermal runaway.



(a) (b)

Figure 3.54: (a) Current distribution in battery module with equal cell contact resistances for a 150A discharge and (b) with a bad contact [150]



(a) (b)

Figure 3.55: Simulated current of different cells in a 12P7S battery pack with a 100 A load and 10 A superimposed load noise at 1 Hz Simulated temperature of the hottest cell in a 12P7S battery pack under static and dynamic loads with equal (a) and unequal interconnect resistances and simulated current of different cells in a 12P7S battery pack with a 100 A load and 10 A superimposed load noise at 1 Hz (b) [224]

If the assembly problem had not been identified during assembly and resolved, and if the vehicle had been run with a single faulty interconnect resistance (out of over one thousand) then it is likely a thermal runaway event would have occurred. The importance of understanding the effects reported here when designing battery packs and the BMS sensors and safety cut-offs cannot be underestimated.

3.8 Conclusion

3.8.1 Model development and parameterisation

The development of a pseudo-2D lithium-ion battery model has been presented which has coupled temperature dependent behaviour and an SEI based degradation model. Parameterisation of the developed battery model has been achieved by use of a GA based approach combined with pulsed discharge testing. Incorporation of experimentally derived entropy profiles for the whole cell showed increased accuracy of the thermal model. The development of a reduced order SPM was also presented as a means to reduce computational time for longer simulations. Comparison with the experimental voltage response of a 4.8 Ah Kokam cell to an NEDC load cycle showed good agreement.

3.8.2 Model based performance analysis

The development of a physics based model allowed for the investigation of varying the internal parameters of the battery and the subsequent impact on performance. Using the model it was possible the investigate the impact on performance of varying the power and energy density of the parameterised battery. By removing current collectors from battery, for a fixed volume, allows for more active electrode material to be used resulting in a greater capacity. The drawback of this is that the resulting cell resistance, which is area specific, is larger resulting in lower power. Analysis of the cost of the raw materials, shows that higher power batteries cost more due to the relative cost of the copper and aluminum current collectors.

The selection of the operating SOC range when a battery is cycled over a narrow SOC range as is a commonly found problem in HEV applications and has been shown to have a significant impact on the lifetime of the battery. The lower the SOC the slower the rate of SEI growth which is driven by the thermodynamic potential of the carbon electrodes in the organic electrolyte. However, operation at lower SOCs has the drawn back of

increased polarisation resistances. An optimal was found to be between 60-50% SOC range as the point where charge/discharge efficiency and lifetime are maximised.

3.8.3 Novel in-situ diagnosis techniques

The developed models were used to investigate novel means of tracking stoichiometric drift between battery electrodes which occurs over time as the side reaction current consumes cyclable lithium for the formation of the SEI layer. It was shown that as the stoichiometry of the electrodes drift from their initial state a change in the SRCV can be seen, thus indicating stoichiometric drift. If left unmonitored it could result in cells being operated when the overall cell voltage is within acceptable limits but the individual electrodes with operated in regions which are detrimental to their lifetimes. Further to this, it was shown that a differential thermal voltametry technique can be used to derive the same information as the SRCV at a much greater speed and with only need for voltage and temperature measurements allowing for the possibility of in-situ monitoring of battery state during charge conditions.

3.8.4 Pack level analysis

Scaling the single cell model up to a multi-cell pack model has allowed for the investigation of inhomogeneous current and heat generation within larger automotive sized packs. In highly parallel packs with smaller cells, it was found that the magnitude of the interconnect resistances affected the current drawn from cells within the same parallel strip, with cells nearest the load points experiencing initially the highest currents. This is due to interconnect overpotentials reducing the potential applied across cells further from the load point. It was found that in constant discharge profiles the maximum current point would propagate to the initially less loaded cells due to an increase in polarisation resistance of the more initially loaded cells when discharged to a lower SOC. However, in applications where the pack was cycled within a small SOC window or pulsed loaded periodically with sufficient time for SOC imbalances to arise, it was found that the cells nearest the load points continually experiences a considerably higher load than other cells, increasing the likelihood of premature failure of that cell or even thermal runaway if not monitored.

Chapter 4

Proton Exchange Membrane Fuel Cells

4.1 Introduction

This chapter presents the modelling and experimental work relating to the development of a semi-empirical based model for a PEMFC stack and associated BOP. This will form the foundation of later high level system analysis work. The below therefore summarises the contents in this chapter.

- **Formulation of the semi-empirical based fuel cell stack model and balance of plant components**
  - This section sets the mathematical framework for the fuel cell stack model which considers all heat and mass transfer assuming lumped performance and a membrane hydration model as well as the interactions of the BOP components required to deliver the reactants needed and provide thermal management
- **Experimental set-up of a large scale PEMFC test rig**
  - This section outlines the experimental development of a 9.5 kWe PEMFC system used to validate the developed model as well as the control systems implemented
- **Model implementation, parameterisation and validation**
  - This section outlines the implementation method, parmeterisation and validation work done for the FC model and BOP components. Simulations and data are validated against slower transient data and more rapidly varying automotive type load cycles. Comparison is then made against simpler and steady models
- **Thermal and water management issues**
  - This section investigates thermal and water management issues in large scale stacks and shows air temperature being a critical parameter for water and thermal management due to cathode side water production and smaller heat capacity. Thermal transient times from cold start-up have been shown to be on the order of minutes during which water removal rates are significantly limited. Operation at low cathode pressures also poses a water management issue in that large stoichiometries are needed to avoid water accumulation and thus flooding. An air purging technique is used to mechanically remove water
- **Stack failure through pin-hole formation**
  - This section presents data on pin-hole formation in large stacks caused by flooding and inhomogeneous current distributions causing localised heating and failure of the membrane which has been shown to have a cascading failure mode from one cell to another due to the mixing of hydrogen into the cathode. Observations of internal currents during no-load conditions of the failed cell is suggested from the instability of neighboring cells due to the bipolar coupling of cells in the stack

4.2 Fuel cell modelling

When operating a fuel cell system on the scale required for automotive applications, a number of technical challenges must be addressed. These included how the reactants are delivered, water management and thermal management. The components which address these issues are known as the BOP.

A FC has many length scales of interest which can be modelled in its' own right. The aim of this work is to investigate system level effects and efficiency of the system on a larger scale. Therefore, detailed aspects of modelling the distribution of reactants and charge within the length scale of the MEA will not be covered. The focus of the modelling work will be aimed at heat and mass balances within the system and transient phenomena such as gas manifolding and thermal effects, i.e. metrics which can be adjusted through system design and control rather than material development which is outside the scope of this study.

Parameters such as temperature, pressure, flow rate and relative humidity of the reactants, the temperature of the stack itself, the hydration of the membrane and the load current all affects the performance of a FC stack. Many of these operating conditions are linked to each other and therefore the heat and mass balances must be considered as shown in Figure 4.1. The following sections thus present the equations used to define each subsystem. These are based on the fundamental work presented by Springer *et al.* [194], Amphlett *et al.* [4] and Pukrushpan *et al.* [163] who developed the mass balance and electrochemical coupled relationships with the addition of the heat balance based the work by Yu *et al.* [230].

4.2.1 Operating voltage

Accurately modelling the cell voltage is critical in assessing the efficiency of the system. In order to do this one must have a detailed understanding of the thermodynamic and electrochemical processes occurring within a FC.

The OCV of a FC is the no load, thermodynamic potential which can be calculated by

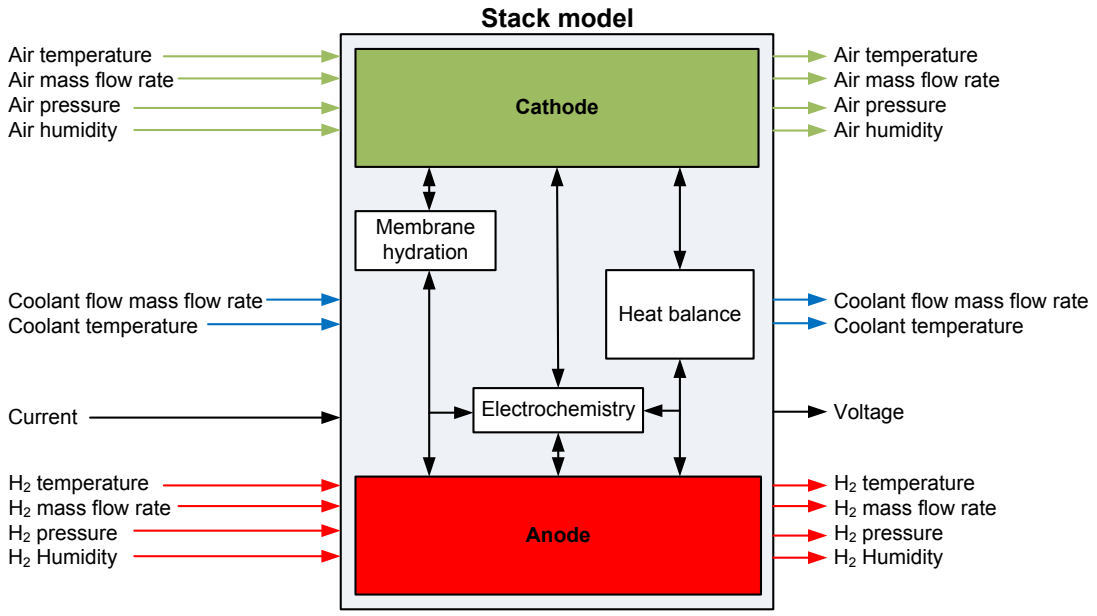


Figure 4.1: Diagram of inputs, processes and outputs of fuel cell stack model

considering the reaction that occurs in a PEMFC as shown in equation 4.1.

$$H_2 + \frac{1}{2}O_2 \rightarrow H_2O \tag{4.1}$$

The theoretical maximum OCV can then be calculated by considering the change in the Gibbs free energy of the products and reactants in this reaction, which are a function of the enthalpy, temperature and entropy of the various states. The equation which arise are therefore:

$$\begin{array}{rcl} \Delta\bar{g}_f & = & \bar{g}_{f|products} - \bar{g}_{f|reactants} \\ \Delta\bar{g}_f & = & \bar{g}_{f|H_2O} - \bar{g}_{f|H_2} - \bar{g}_{f|O_2} \end{array} \tag{4.2}$$

The theoretical maximum OCV for a PEMFC can therefore be found by considering this Gibbs free energy as shown in equation 4.3.

$$E = \frac{-\Delta\bar{g}_f}{2F} \tag{4.3}$$

Where the change in the Gibbs free energy of the system also varies with temperature and pressure relative to its reference state as shown in equation 4.4. Where p_x represents the partial pressure of the reactant x.

$$\Delta\bar{g}_f = \frac{-\Delta\bar{g}_f^0}{2F} - \bar{R}T\ln\left[\frac{p_{H2}p_{O2}^{1/2}}{p_{H2O}}\right] \tag{4.4}$$

The maximum efficiency of this reaction is often defined as the ratio of the Gibbs free energy to the enthalpy of reaction as shown in equation 4.5. Analysis of the temperature dependency of the FC reaction shows that the maximum theoretical efficiency drops as a function of temperature as shown in figure 4.2. This is contrary to the trend observed in ICEs and the Carnot efficiency where at higher temperatures the efficiency is higher. However, in practice the trend in FC efficiency is opposite once the temperature dependency of the chemical kinetics has been considered.

$$\eta_{max} = \frac{\Delta\bar{g}_f}{\Delta\bar{h}_f} \times 100\% \tag{4.5}$$

When a FC is under load there are a number of losses that reduce the operating potential from its OCV value. The three main overpotential losses can be attributed to: activation losses, ohmic losses and mass transport losses. An example polarisation curve is shown in figure 4.3.

This polarisation curve can be divided into 3 main regions. In region 1, at low current densities, the electrochemical losses are dominated by activation losses which is caused by the energy required to drive the chemical reaction and transfer the electrons to and from the electrodes. Typically, the charge transfer resistance of electrochemical processes decreases with increasing current density as indicated by the Butler-Volmer equation. Region 2 is a near linear region that is characteristic of the ohmic losses caused by the resistance of the various interconnectors, electrodes and ionic flow through the electrolyte. In region 3, the losses are dominated by mass transport/ concentration losses where the reactants cannot be supplied to the reaction sites at a fast enough rate that it is being consumed and there as a rapid drop in the cell potential due to local reduction of the reactant partial pressure. Mass transport losses arise at high current densities or during periods of reactant starvation.

The cell terminal voltage that is measured is therefore the OCV minus the three main losses previously mentioned as shown in equation 4.6.

$$V_{cell} = E_{OCV} - \eta_{act} - \eta_{ohm} - \eta_{conc} \tag{4.6}$$

Stack voltage can then be found by multiplying this cell voltage by the number of cells. This assumes uniform reactant distribution and lumped cell behaviour. In reality the cell voltages will vary due to varying reactant concentrations through the stack, pressure drops and a number of other parameters. This has not been considered from a modelling perspective for this study in order to minimise computational cost.

The mathematical framework presented is based on the governing equations presented by Springer *et al.* [194], Amphlett *et al.* [4] and Pukrushpan *et al.* [163] who developed the mass balance and electrochemical coupled relationships with the addition of the heat balance based the work by Yu *et al.* [230].

Open Circuit Potential

The thermodynamic, no load potential of the FC reaction shown in equation 4.1 is defined by the Nernst equation as shown in equation 4.7. Where n is the number of electrons in the reaction.

$$E = E^0 - \frac{RT}{nF} \ln \left(p_{H_2} p_{O_2}^{0.5} \right) \tag{4.7}$$

The standard state for the reference potential E^0 is taken to be 1.229 V at 298.15 K and 1 atm [4]. This reference potential will vary as a function of the temperature according to equation 4.8. Where T_0 is the reference temperature, taken to be 298.15 K, and ΔS is the change of entropy.

$$E^0 = E_0 + (T - T_0) \left(\frac{\Delta S^0}{nF} \right) \tag{4.8}$$

It has been assumed that for this given reaction, the entropy will remain relatively constant as the change of the specific heats of the reactants remains reasonably constant over typical operating temperatures of PEMFCs. Above 100°C, this assumption breaks

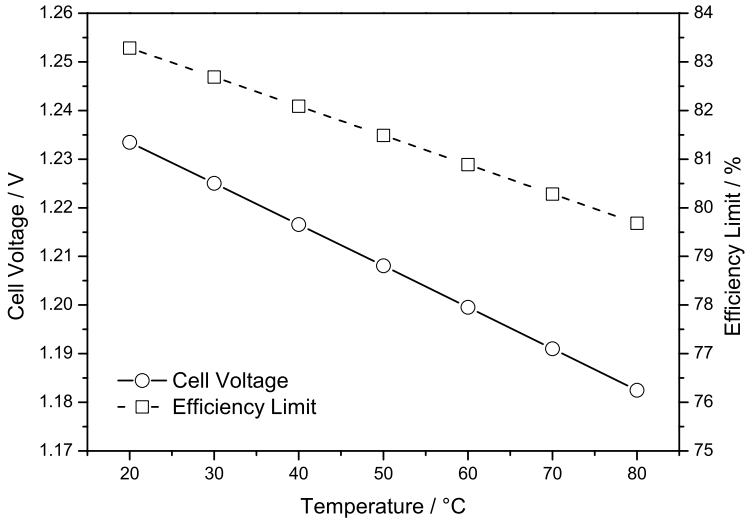


Figure 4.2: Open circuit potential and maximum theoretical efficiency of a PEMFC as a function of temperature based on Higher Heating Values

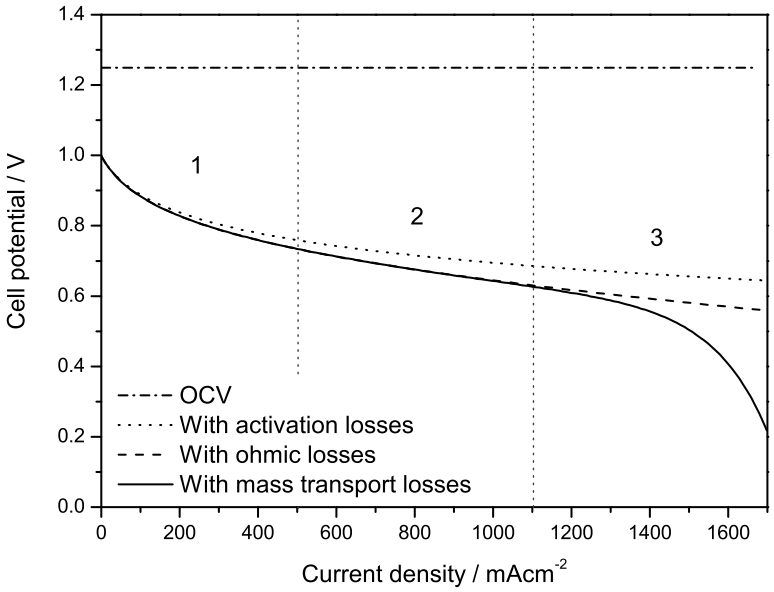


Figure 4.3: Example polarisation curve for a single PEMFC cell

down due to the phase transition of water. Therefore, the reference potential is directly proportional to the temperature. Taking literature based values from the work by Amphlett *et al.* [4], the relationship between the reference potential, temperature and pressure can be written according to the semi-empirical relationship shown in equation 4.9.

$$E_0 = 1.229 - 0.85 \times 10^{-3}(T_{fc} - T_{ref}) + 4.3085 \times T_{fc}[\ln(P_{H2}) + 0.5\ln(P_{O2})] \quad (4.9)$$

Activation overpotential

Activation overpotentials result from the losses associated with charge-transfer processes at the anode and cathode. In general the hydrogen oxidation reaction on platinum is considered to be very rapid with the Tafel slope being approximately 0.03 V/decade and an exchange current density of 46 mA/cm^2. The oxygen reduction reaction over platinum by contrast is seen as being much slower due to the higher bond energy of the oxygen molecule, with a Tafel slope of approximately 0.07 V/decade and exchange current density of 92μA/cm^2 [4]. A typically overall equivalent exchange current density for a low temperature PEMFC is in the region of 0.1 mA/cm^2 [115]. Therefore, oxygen reduction is the predominant contributor to activation overpotentials in PEMFC reactions.

These activation losses can be approximated by considering the Tafel equation, shown in equation 4.10. Where a is a constant, i is the current density and i_0 is the exchange current density.

$$\eta_{act} = a\ln\left(\frac{i}{i_0}\right) \quad (4.10)$$

The problem with the Tafel equation is that it is only valid for $i > i_0$. Therefore, for simulation purposes this can be modified to equation 4.11 [163]. Where v_0 is the voltage

drop at no load, and v_a and c_1 are constants which depend on temperature and oxygen partial pressure.

$$\eta_{act} = v_0 + v_a(1 - e^{-c_1 i}) \tag{4.11}$$

Expansion of the coefficients to account for the effects of temperature and pressure result in equation 4.12 as presented by Pukrushpan *et al.* [163]. Where p_{sat} represents the saturated partial pressure of the cathode with all pressures and temperatures in bar and Kelvin.

$$\eta_{act} = \left\{ a_1 + a_2 \left(T_{fc} - T_{ref}\right) + a_3 T_{fc} \left[\frac{\ln(p_{ca} - p_{sat})}{1.101325} + \frac{1}{2}\ln\frac{0.1173(p_{ca} - p_{sat})}{1.01325} \right] \right\} + \left\{ (b_1 T_{fc} + b_2) \left(\frac{p_{O2}}{0.1173} + p_{sat} \right)^2 + (b_3 T_{fc} + b_4) \left(\frac{p_{O2}}{0.1173} + p_{sat} \right) + b_5 T_{fc} + b_6 \right\} \left(1 - e^{-c_1 i_{fc}}\right) \tag{4.12}$$

The resulting coefficients: a_x, b_x and c_x can be determined by non-linear regression fitting of the system under investigation.

Ohmic overpotential

The ohmic resistance arises from the ionic resistance of the polymer membrane to the motion of protons, the electrical resistance of the electrode materials, contact resistances and current collection resistance. This can be calculated from equation 4.13. Where t_m and σ_m represent the thickness and conductivity of the membrane.

$$\eta_{ohmic} = i\frac{t_m}{\sigma_m} \tag{4.13}$$

Here it has been assumed that the majority of the ohmic resistance arises from ionic resistance of the polymer membrane as indicated by the correlation with the membrane thickness and conductivity. Ideally, a thinner membrane allows for lower resistance; however, there are practical limitations for the manufacture of ultra thin membranes, including: the mechanical stability and gas permeability of the separators.

The conductivity of this polymer membrane is a strong function of its hydration and can be defined as equation 4.14 [163].

$$\sigma_m = d_1 e^{\left(d_2 \left(\frac{1}{303} \right) - \frac{1}{T_{fc}} \right)} \tag{4.14}$$

Where d_1 can be approximated by equation 4.15 and d_2 is a experimentally determined constant.

$$d_1 = (d_{11}\lambda_m - d_{12}) \tag{4.15}$$

Here λ_m is the membrane water content which will be considered in later sections. Again the aforementioned coefficients can be parameterised based on the system under investigation using non-linear regression from test data.

Mass transport overpotential

Mass transport, or concentration, overpotentials result from a drop in reactant partial pressure at high operating current densities due to the rate of chemical consumption being higher than the rate of diffusion through the GDL. This can be a significant problem at lower temperatures and high current densities as these are operating conditions which risk stack flooding where the water carrying capacity of the cathode air is low and therefore liquid water can form in the pores of the GDL blocking active reaction sites. Mass transport overpotentials can also arise under highly dynamic loads where the reactant delivery to the stack flow channels is not sufficiently fast and thus there are brief periods when local supply stoichiometry is below the set value.

The mass transport losses can thus be calculated from equation 4.16 [163].

$$\eta_{conc} = i\left(c_2 \frac{i_{fc}}{i_{max}}\right)^{c_3} \tag{4.16}$$

Again the presented coefficients are typically found from a non-linear regression of test data.

Charge double layer

Due to the nature of the FC construction, the interface between the electrodes and electrolyte forms a charge double layer. This double layer capacitance behaves like an electrical capacitor and affects the dynamics of a FC when there are load changes. The collection of charges generates an electrical voltage which corresponds to the combination of activation and concentration overpotentials. Therefore, when there is a load change there is also a finite transient time associated with this double layer which affects the activation and mass transport overpotentials. The ohmic resistance is not affected by this capacitance.

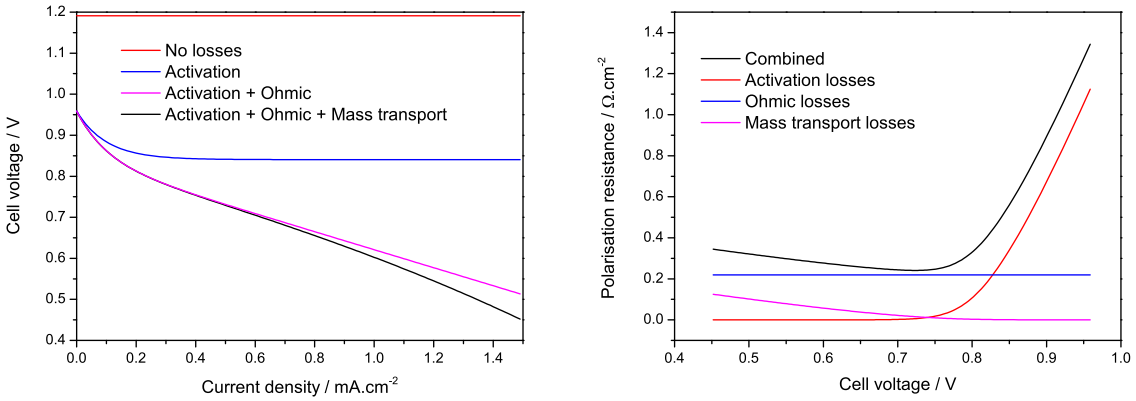
Studies have shown that the time constant of this double layer capacitance and charge transfer resistance is typically < 1 s [77]. Given that the relative speed is so fast it has not been captured in the current FC model. Double layer effects during start up will be more evident due to the larger relative changes in cell potential; however, it is not the aim of this model to capture the dynamics during FC start-up.

Trends in polarisation curves

This semi-empirical model thus allows for observation of general trends in performance caused by changing operating conditions. Figure 4.4 shows a polarisation curve at 80°C, 2.5 bar and 90% relative humidity with separated losses components.

It can be seen that initially when the FC is under a low load the polarisation resistance is reasonably high due to the relatively high contribution of the activation losses. This decreases with increasing current density. At its lowest point this roughly corresponds to the ohmic resistance which is not a function of the load. At higher loads the mass transport concentration overpotentials begin to increase. The ohmic polarisation resistance remains constant, with respect to current. At higher currents mass transport related polarisation resistance is experienced. It therefore becomes apparent that the maximum efficiency (point of lowest resistance) do not normally correspond to the point of maximum power. This is a critical issue to address when optimising the powertrain of FC hybrid vehicles which will be addressed in later chapters.

Figure 4.5 shows the simulated polarisation curves for a PEMFC at 80°C and 2.5 bar for varying relative humidities as well as the respective polarisation resistance with



(a) (b)

Figure 4.4: (a) Simulated polarisation curves of a fuel cell at 80°C, 2.5 bar and 90% relative humidity with decomposed overpotential contributions and (b) separated polarisation resistance components at the same operating conditions

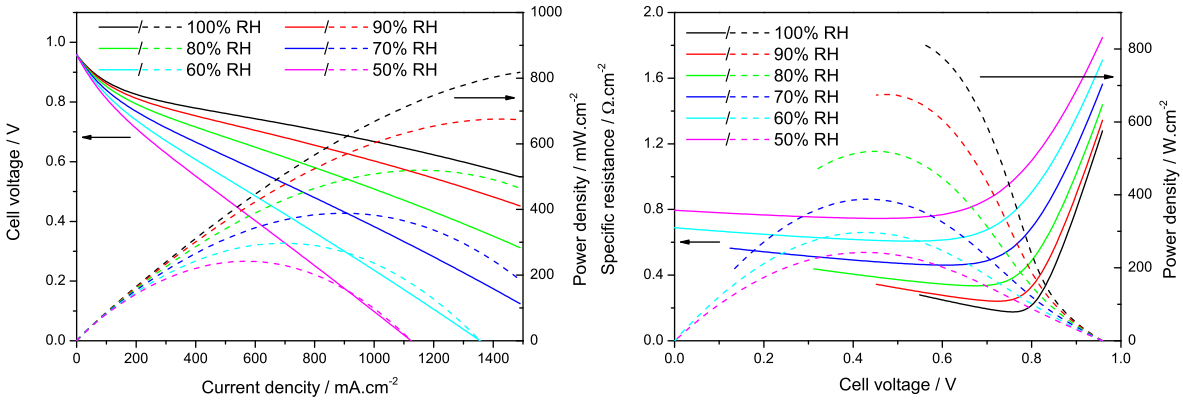
coefficients taken from Pukrushpan *et al.* [163].

It can be seen that the relative humidity of the reactants and thus the hydration of the membrane critically affects the performance of the FC due to the sensitivity of the ionic conductivity to the water content of the membrane. Water management thus becomes a critical consideration in the operation of PEMFC systems.

4.2.2 Saturated partial pressure

As previously mentioned, water balances within the FC are of critical importance, affecting both the hydration of the membrane and the limits of operation before the on-set of flooding. Therefore, consideration of the relative humidity and thus the saturated partial pressure of the reactant gases is required.

The saturated partial pressure represents the limit of water carrying capacity of the gas and the relative humidity is the ratio of the partial pressure of water vapour to this



(a) (b)

Figure 4.5: (a) Simulated polarisation curves of a fuel cell at 80°C and 2.5 bar at varying relative humidities and (b) the specific resistance as a function of the cell voltage

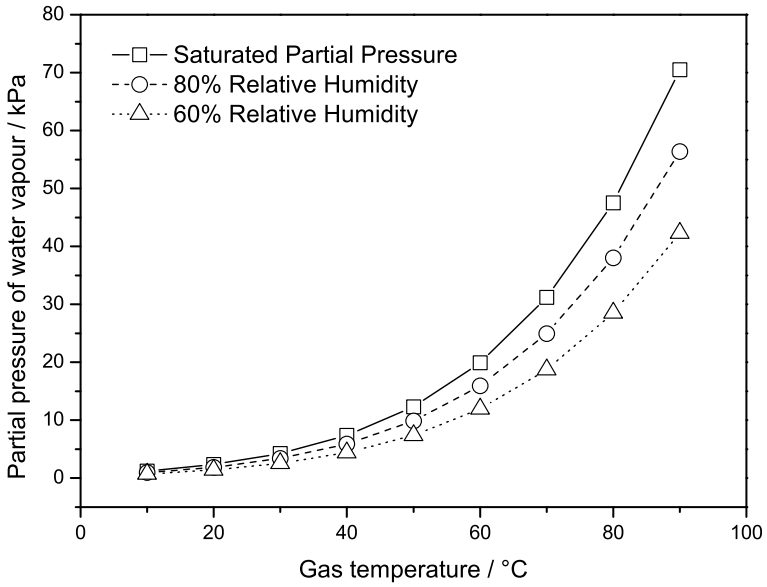


Figure 4.6: Partial pressure of water vapour

saturated value. Using the Magus-Teten approximation, the saturated partial pressure can be calculated as shown in equation 4.17 [115].

$$\log_{10}(p_{sat}) = \frac{7.5T}{T + 237.3} + 0.7858 \tag{4.17}$$

It can be seen that the saturated vapour pressure is only a function of temperature. Consideration of the relative humidity of the gas stream then allows for the calculation of the partial pressure of water vapour. This is shown in figure 4.6.

As it can be seen at lower temperatures the partial pressure of water vapour at saturation is low indicating a low water carrying capability. As the temperature increases so does the saturated partial pressure, which represents the limit of water capacity. If the water generation inside the stack is greater than the amount of water the air can remove then liquid water will form within the stack which not only increases the mass transport limitations but also reduces the heat removal capabilities since some heat is removed through the latent heat of evaporation of water but it also increases the likelihood of catastrophic failure of the system through pin-hole formations which can arise due to localised hot-spots due to higher local reaction current densities which come about through stack flooding [110].

4.2.3 Mass balances

The mass balances inside the stack model are critical in determining the overall performance of the system as it will define the operating partial pressure, temperature and water balance of the stack, as well as give information to the BOP components about their theoretical operating points. This is broken down into two main sections: flow in the cathode and flow in the anode.

Flow in the cathode

The flow in the cathode accounts for air provided externally, the rate of reactant consumption and water generation which occurs on the cathode side of a PEMFC. The subscript v

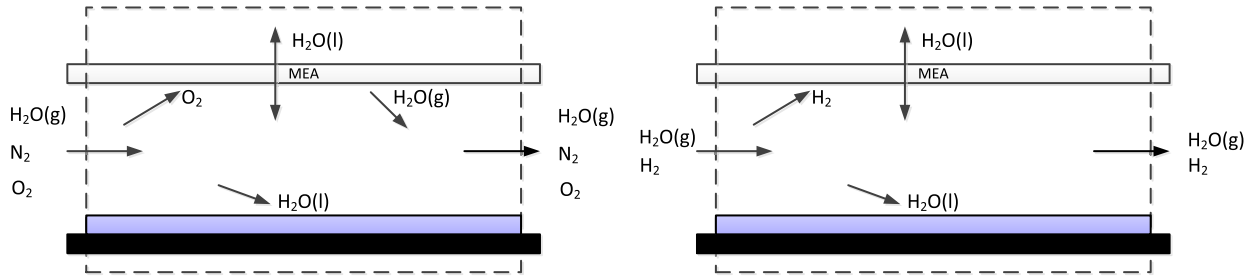


Figure 4.7: (a) Cathode and (b) Anode flow model control volumes of interest. Adapted from Pukrushpan *et al.* [163]

refers to water vapor, *ca* refers to the cathode and the subscript l represents the liquid phase. All other phases are gaseous. Figure 4.7a shows a diagram of the mass balances being considered in the cathode flow model as presented by Pukrushpan *et al.* [163].

Equations 4.18 - 4.20 show the equations governing the mass balances within the cathode for oxygen, nitrogen and water.

$$\frac{dm_{O2,ca}}{dt} = \dot{m}_{O_2,ca_{in}} - \dot{m}_{O_2,reacted} - \dot{m}_{O_2,ca_{out}} \tag{4.18}$$

$$\frac{dm_{N_2,ca}}{dt} = \dot{m}_{N_2,ca_{in}} - \dot{m}_{N_2,ca_{out}} \tag{4.19}$$

$$\frac{dm_{water,ca}}{dt} = \dot{m}_{v,ca_{in}} - \dot{m}_{v,ca_{out}} + \dot{m}_{v,ca_{gen}} + \dot{m}_{v,ca_{mem}} - \dot{m}_{l,ca_{out}} \tag{4.20}$$

Water inside of the FC can be in either vapour or liquid form depending on the operating conditions with the largest mass of water vapour the air can hold being defined by equations 4.21.

$$m_{v,max,ca} = \frac{p_{sat} V_{ca}}{R_v T} \tag{4.21}$$

If the amount of water calculated by the mass balance in equation 4.20 is more than the saturated state of the cathode air then the additional water is assumed to condense within the stack. The water then accumulates within the stack until it can be removed. The current model does not account for the effect of flooding on the performance of the FC.

The partial pressures of the oxygen, nitrogen and water vapour in the cathode can be calculated by considering ideal gas laws as shown in equation 4.22 where the subscript x represents the gas of interest.

$$p_x = \frac{m_x R_x T}{V_{ca}} \tag{4.22}$$

The pressure of the cathode inlet is the sum of the partial pressures of oxygen, nitrogen and the water vapour pressure as shown in equation 4.23.

$$p_{ca} = p_{O_2,ca} + p_{N_2,ca} + p_{v_{ca}} \tag{4.23}$$

The mole fraction of the oxygen is then calculated as the ratio of oxygen partial pressure and the dry air partial pressure as shown in equation 4.24.

$$y_{O_2,ca} = \frac{p_{O_2,ca}}{p_{a,ca}} \tag{4.24}$$

The relative humidity of the cathode gases (ϕ_{ca}) can then be defined as the ratio of the cathode vapour partial pressure to the saturated partial pressure which is a function of temperature as shown in equation 4.25.

$$\phi_{ca} = \frac{p_{v,ca}}{p_{sat}} \tag{4.25}$$

The dry partial pressure of air can then be defined by considering the total pressure of the cathode and the partial pressure of the water vapour as shown in equation 4.26.

$$p_{a,ca,in} = p_{ca,in} - p_{v,ca,in} \tag{4.26}$$

The humidity ratio (ω), which is the ratio of water vapour to dry air, can the be defined as:

$$\omega_{ca,in} = \frac{M_v}{M_{a,ca,in}} \frac{p_{v,ca,in}}{p_{a,ca,in}} \tag{4.27}$$

Where the molecular mass of the the air $M_{a,ca,in}$ is defined as:

$$M_{a,ca,in} = y_{O_2,ca,in} \times M_{O_2} + (1 - y_{O_2,ca,in}) \times M_{N_2} \tag{4.28}$$

The mass flow rate of the dry air and vapour entering the stack can then be calculated from:

$$\dot{m}_{a,ca,in} = \frac{1}{1 + \omega_{ca,in}} \dot{m}_{ca,in} \tag{4.29}$$

$$\dot{m}_{v,ca,in} = \dot{m}_{ca,in} - \dot{m}_{a,ca,in} \tag{4.30}$$

Where the oxygen and nitrogen mass fractions can be defined as:

$$\dot{m}_{O_2,ca,in} = x_{O_2,ca,in} \dot{m}_{a,ca,in} \tag{4.31}$$

$$\dot{m}_{N_2,ca,in} = (1 - x_{O_2,ca,in}) \dot{m}_{a,ca,in} \tag{4.32}$$

Where $x_{O_2,ac,in}$ is the oxygen mass fraction which can be defined as:

$$x_{O_2,ca,in} = \frac{y_{O_2,ca,in} \times M_{O_2}}{y_{O_2,ca,in} \times M_{O_2} + (1 - y_{O_2,ca,in}) \times M_{N_2}} \tag{4.33}$$

Calculation of the cathode out flows are done with the same governing equations as the inlets however also consider the consumption of the reactant oxygen, whereby the oxygen mole fraction is not 0.21 as in in the inlet, but is a function of the operating current and the size of the stack.

The rate of oxygen consumption and water generation can then be calculated from the drawn current from the stack as shown in equations 4.34 and 4.35 where I is the total current per cell.

$$\dot{m}_{O_2,reacted} = M_{O_2} \times \frac{N_{cells} \cdot I}{4F} \tag{4.34}$$

$$\dot{m}_{v,ca_{gen}} = M_v \times \frac{N_{cells} \cdot I}{2F} \tag{4.35}$$

Where N_{cells} is the number of cells in the stack.

Flow in the anode

The anode flow model considers compressed hydrogen and the water balance of the flow. Again it has been assumed that all gases can be treated as ideal gases and the cells behave homogeneously. Equations 4.36 and 4.37 thus shows the hydrogen and water mass balances.

$$\frac{dm_{H_2,an}}{dt} = \dot{m}_{H_2,an_{in}} - \dot{m}_{H_2,reacted} - \dot{m}_{H_2,an_{out}} \tag{4.36}$$

$$\frac{dm_{water,an}}{dt} = \dot{m}_{v,an_{in}} - \dot{m}_{v,an_{out}} + \dot{m}_{v,an_{mem}} - \dot{m}_{l,an_{out}} \tag{4.37}$$

Flow equations for the water transport and and partial pressure was done in a similar way to the cathode flow model.

Consumption of hydrogen is again directly proportional to the current drawn and number of cells in the stack as shown in equation 4.38.

$$\dot{m}_{H_2,reacted} = M_{H_2} \times \frac{N_{cells} \cdot I}{2F} \tag{4.38}$$

4.2.4 Membrane hydration model

The governing equations as presented by Pukrushpan *et al.* [163], also accounts for the changing membrane hydration as a function of the water generation, removal and deposition rates based on the condition of the stack and reactant gases. Water transport across a Nafion membrane is assumed to occur due to two main mechanisms: electro-osmotic drag and back diffusion.

In the electro-osmotic drag mechanism water is dragged from the anode to the cathode by the movement of the protons in the FC reaction. The rate of electro-osmotic drag is thus a function of the operating current density. The amount of water transported is represented by the electro-osmotic drag coefficient n_d, which is the number of water molecules carried by each proton as shown in equation 4.39, where $N_{v,osmotic}$ is the water flow rate from electro-osmotic drag (mol.s^{-1}.cm^{-2}). The number of water molecules dragged by each proton varies as a function of the membrane hydration.

$$N_{v,osmotic} = n_d \frac{I}{F} \tag{4.39}$$

The back diffusion mechanism of water transport arises due to differences in the water concentration. Since water is generated in the cathode, this results in a higher water

concentration and thus a concentration based flux from the cathode to the anode which can be described by a Fick's diffusion law as shown in equation 4.40, where $N_{v,diff}$ is the flow rate of water due to back diffusion (mol.s^{-1}.cm^{-2}), D_w is the diffusion coefficient of the process (cm^2.s^{-1}), c_v the concentration of water (mol.cm^{-3}) and y the through plane direction of the membrane (cm). The diffusion coefficient is a function of the water content.

$$N_{v,diff} = D_w \frac{dc_v}{dy} \tag{4.40}$$

Combining the two water movement mechanisms results in equation 4.41, where the distribution of water has been assumed to be linear over the membrane.

$$N_{v,membrane} = n_d \frac{I}{F} - D_w \frac{(c_{v,ca} - c_{v,an})}{t_m} \tag{4.41}$$

The total water flow rate across the membrane is then approximated from equation 4.42, where M_v is the molecular mass of water.

$$\dot{m}_{v,membrane} = N_{v,membrane} \times M_v \times A_{FC} \times N_{cells} \tag{4.42}$$

The average water content between the anode and cathode can then be taken to represent the water content in the membrane, however typically the water content in the anode is less than in the cathode especially at high current densities when the rate of electro-osmotic drag outweighs that of the back diffusion. The membrane water diffusivity and the number of water molecules per proton can then be calculated by considering the activity of the anode and cathode gases as shown in equation 4.43, where x represents either the anode or cathode, and $y_{v,x}$ the mole fraction of vapour.

$$a_x = \frac{y_{v,x} p_x}{p_{sat,x}} = \frac{p_{v,x}}{p_{sat,x}} \tag{4.43}$$

The detailed derivation of the electro-osmotic drag coefficient and membrane water diffusion coefficient can be found in the work by Dutta *et al.* [66] which provides much the fundamental physics. The experimental data used to parameterise the model is based on the work presented by Springer *et al.* [194] of a Nafion 117 membrane. The water content in the membrane (λ_x) is calculated from the respective anode/ cathode water activities as shown below, where a_m is the water activity of the membrane which is taken as the average between the anode and cathode.

$$\lambda_m = \begin{cases} 0.043 + 17.81 a_m - 39.85 a_m^2 + 36 a_m^3 & 0 < a_m \leq 1 \\ 14 + 1.4(a_m - 1) & 1 < a_m \leq 3 \end{cases}$$

The membrane water content can then be used to calculate the electro-osmotic drag coefficient n_d and the water diffusivity D_w according to equations 4.44 and 4.45.

$$n_d = 0.0029 \lambda_m^2 + 0.05 \lambda_m - 3.4 \times 10^{-19} \tag{4.44}$$

$$D_w = D_\lambda \exp\left(2416 \left(\frac{1}{303} - \frac{1}{T_{FC}}\right)\right) \tag{4.45}$$

$$D_\lambda = \begin{cases} 10^{-6} & \lambda_m < 2 \\ 10^{-6}(1 + 2(\lambda_m - 2)) & 2 \leq \lambda_m \leq 3 \\ 10^{-6}(3 - 1.67(\lambda_m - 3)) & 3 < \lambda_m < 4.5 \\ 1.25 \times 10^{-6} & \lambda_m \geq 4.5 \end{cases}$$

The water content of the membrane will therefore affect the previously mentioned conductivity of the membrane and thus affect performance.

4.2.5 Fuel cell thermal modelling

The thermal characteristics of the FC stack and the reactant gases will have a significant impact on the performance of the system and the relatively slow time constants of operation warrant understanding of the processes occurring to avoid over heating of the system.

Following the approach is based on the equations presented by Yu *et al.* [230], the thermal performance of the fuel cell stack was based on assuming a lumped thermal mass of the whole fuel cell stack. A energy balance considering the maximum theoretical energy of the hydrogen (q_{theo}) electrical work, (q_{elect}), sensible heat (q_s), latent heat (q_{latent}) and heat loss via convection (q_{conv}) from the stack itself, were considered.

Transient thermal performance was then characterised by considering conservation of energy with the unsteady heat transfer equation, assuming lumped thermal behaviour. This is shown in equation 4.46.

$$q_{theo} - q_{elec} - q_s - q_{latent} - q_{conv} = m_{stack} C_{p,stack} \frac{dT_{stack}}{dt} \tag{4.46}$$

Figure 4.8 shows schematically the inputs and output from the thermal model and highlights the link between the heat and mass balances.

The theoretical maximum energy content on one mol of hydrogen can be calculated based on the heat of reaction $\Delta H_{reaction}$ as shown in equation 4.47.

$$q_{theo} = N_{H_2,cons} \Delta H_{reaction} \tag{4.47}$$

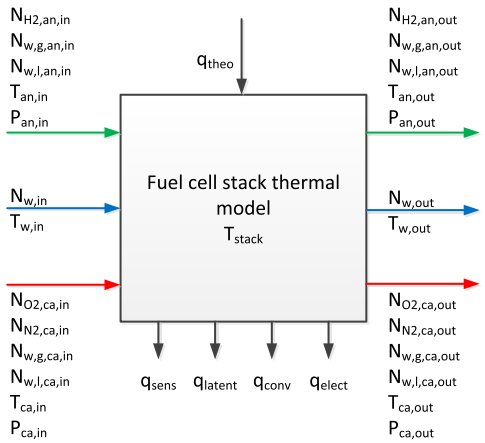


Figure 4.8: Schematic of inlet and outlets for thermal model of FC stack. Adapted from Yu *et al.* [230]

The q_{elect} is useful electrical energy generated by the FC reaction which is calculated from the current and voltage as shown in equation 4.48.

$$q_{elect} = N_{cell} V_{cell} I \tag{4.48}$$

q_s is the sensible heat from the reactant flows and the coolant (assumed to be completely water) as show in equations 4.49-4.52 for the anode and cathode.

$$q_s = q_{s_{an}} + q_{s_{ca}} + q_{s_{H_2O}} \tag{4.49}$$

$$\begin{aligned} q_{s_{an}} = &(\dot{m}_{H_2,an_{out}} Cp_{H_2} + \dot{m}_{vap_{H_2O},an_{out}} Cp_{vap_{H_2O}} + \dot{m}_{l_{H_2O},an_{out}} Cp_{l_{H_2O}})(T_{an_{out}} - T_0) \\ &+ (\dot{m}_{H_2,an_{in}} Cp_{H_2} + \dot{m}_{vap_{H_2O},an_{in}} Cp_{vap_{H_2O}} + \dot{m}_{l_{H_2O},an_{in}} Cp_{l_{H_2O}})(T_{an_{in}} - T_0) \end{aligned} \tag{4.50}$$

$$\begin{aligned} q_{s_{ca}} = &(\dot{m}_{O_2,ca_{out}} Cp_{O_2} + \dot{m}_{N_2,ca_{out}} Cp_{N_2} + \dot{m}_{vap_{H_2O},ca_{out}} Cp_{vap_{H_2O}} + \dot{m}_{l_{H_2O},ca_{out}} Cp_{l_{H_2O}})(T_{ca_{out}} - T_0) \\ &+ (\dot{m}_{O_2,ca_{in}} Cp_{O_2} + \dot{m}_{N_2,ca_{in}} Cp_{N_2} + \dot{m}_{vap_{H_2O},ca_{in}} Cp_{vap_{H_2O}} + \dot{m}_{l_{H_2O},ca_{in}} Cp_{l_{H_2O}})(T_{ca_{in}} - T_0) \end{aligned} \tag{4.51}$$

$$q_{s,H_2O} = N_{H_2O,out} C_{p,H_2O,l} (T_{H_2O,out} - T_0) - N_{H_2O,in} C_{p,H_2O,l} (T_{H_2O,in} - T_0) \tag{4.52}$$

q_{latent} is the latent heat of the water during phase transition from liquid to gas or vice versa during condensation/evaporation which is shown in equations 4.53-4.55. The freezing/melting of water is not considered here.

$$q_{latent} = q_{latent_{an}} + q_{latent_{ca}} \tag{4.53}$$

$$q_{latent,an} = H_{vaporization,an} (\dot{m}_{vap_{H_2O},an_{out}} - \dot{m}_{vap_{water},an_{in}} + \dot{m}_{membrane}) \tag{4.54}$$

$$q_{latent,ca} = H_{vaporization,ca} \dot{m}_{l_{H_2O},ca_{in}} + H_{vaporization,ca} (\dot{m}_{vap_{H_2O},ca_{out}} - \dot{m}_{l_{H_2O},ca_{in}} - \dot{m}_{membrane}) \tag{4.55}$$

Where $H_{vaporization}$ is taken as shown in equation 4.56 [163].

$$H_{vaporization} = 45070 - 41.9T + 3.44 \times 10^{-3} T^2 + 2.54 \times 10^{-6} T^3 + 8.98 \times 10^{-10} T^4 \tag{4.56}$$

q_{conv} is the heat lost through free convection of the stack as shown in equation 4.57. Where A_{conv} represents the area for convection and h_{stack} is the convective heat transfer coefficient.

$$q_{conv} = A_{conv} h_{stack} (T_{FC} - T_{amb}) \tag{4.57}$$

4.3 Balance of Plant modelling

The BOP accounts for all components which deliver reactants to and from the FC stack and which provide control and cooling to maintain the system. An efficient BOP system should provide the required reactants and remove heat for the least amount of energy. The energy requirement to operating the BOP components reduces the overall efficiency of any FC system and are known as parasitic losses.

At system level consideration of the associated ancillary components also needs to be made as this will determine many of the heat and mass balances since some reactant flows are fed back. The implementation of the governing equations previously shown was done in the MATLAB Simulink environment. Each subsystem was built into a group allowing for modularity of the model design. This will later allow for interfacing the FC model with other EV components for whole system level analysis as well as replacement of component models if different configurations are desired. Figure 4.9 shows a block diagram of the different model elements.

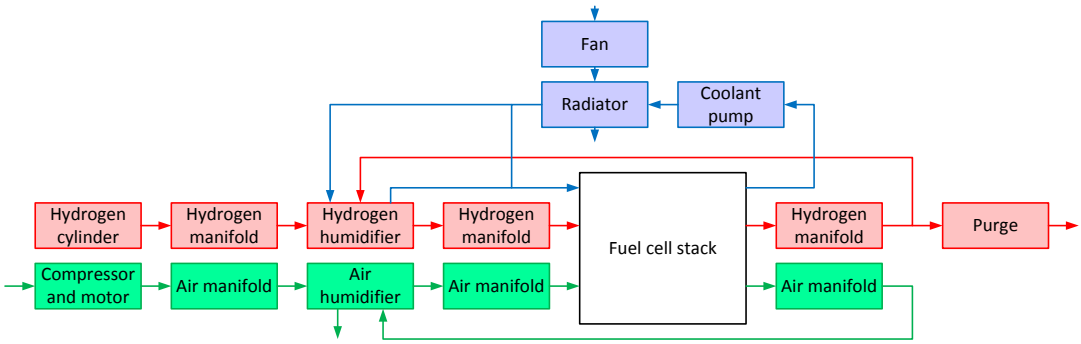


Figure 4.9: Diagram of model elements

The subsections here after detail the component models.

4.3.1 Compressor modelling

Air delivery is typically the largest of the parasitic losses and usually comprises of a motor coupled to a compressor. Compressor inertia and gas manifolding time constants can be on the order of seconds and therefore highly transient loads will incur additional localised mass transport losses on FC performance as well as additional inefficiencies from the coupled motor due to inertia losses under highly transient loads. The compressor model presented is based on the work presented in Pukrushpan *et al.* [163].

The compressor model is broken down into two parts. The first is a static compressor map which determines the air flow rate combined with thermodynamic equations to determine the exit air temperature and required compressor power. The second is a model of the compressor and motor inertia which defines the blade speed of the compressor and which is used in the static compressor map. The speed of the compressor is used to find the air mass flow rate. Figure 4.10 shows a schematic of the compressor model, where p_{sm} is the supply manifold pressure, p_{atm} is atmospheric pressure, $p_{cp,in}$ is the compressor inlet pressure, p_{cp} which is the compressor pressure, $T_{cp,in}$ is the inlet air temperature (K), $T_{cp,out}$ is the outlet temperature (K), v_{cm} is the voltage command to the compressor motor (V), $\dot{m}_{cp}$ is the mass flow rate of air $(kg.s^{-1})$ and ω_{cp} is the compressor speed $(rad.s^{-1})$.

The only dynamic state in this model is the compressor speed. The input air supply is assumed to be atmospheric air at 25°C and 1 atm. The downstream pressure is

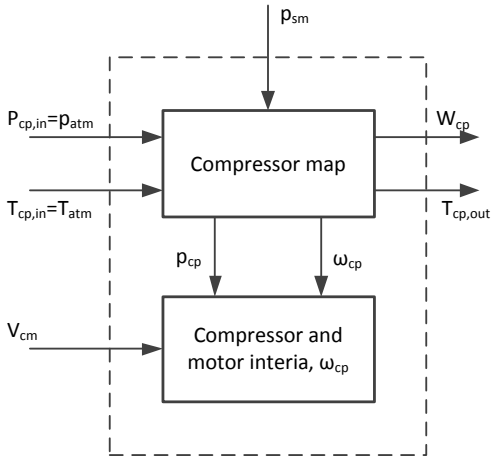


Figure 4.10: Compressor block diagram

determined by the supply manifold and the back pressure of the stack. The compressor air flow rate is determined through the compressor map, pressure ratio and the speed of the compressor. However, use of a look-up table is not well suited for dynamic models as standard interpolation routines are not continuously differentiable and extrapolation is unreliable. Therefore, a non-linear curve fitting method is used instead as adopted by Jensen and Kristensen as described by Moraal and Kolmanovsky [141]. In this approximation, the 'corrected' compressor speed $N_{cr} = N_{cp}/\sqrt{\theta}$ and corrected temperature $\theta = T_{cp,in}/288$ are used to calculate the dimensionless head (Ψ) as shown in equation 4.58.

$$\Psi = C_p T_{cp,in} \left(\left(\frac{p_{cp,out}}{p_{cp,in}}^{\frac{\gamma-1}{\gamma}} - 1 \right) \right) / \left(\frac{U_c^2}{2} \right) \tag{4.58}$$

Where $T_{cp,in}$ is the inlet air temperature (K), γ is the specific heats ratio of air at constant pressure and U_c is the compressor blade tip speed ($m.s^{-1}$), as defined in equation 4.59. Where d_c is the compressor diameter (m).

$$U_c = \frac{\pi}{60} d_c N_{cr} \tag{4.59}$$

The normalised compressor flow rate (ϕ) is defined by equation 4.60. Where ρ_a is the density of air (kg.m^{-3}).

$$\phi \frac{W_{cr}}{\rho_a \frac{\pi}{4} d_c^2 U_c} \tag{4.60}$$

The normalised compressor flow rate (ϕ) is then correlated with the head parameter (Ψ) by equation 4.61. Where ϕ_{max}, β and Ψ_{max} are polynomial functions of the Mach number (M) as shown in equations 4.62.

$$\phi = \phi_{max} \left(1 - \exp \left(\beta \left(\frac{\Psi}{\Psi_{max}} - 1 \right) \right) \right) \tag{4.61}$$

Table 4.1: Compressor map polynomial regression coefficients

Parameter	Value	Parameter	Value	Parameter	Value
a_0	2.21195×10^{-3}	b_0	2.44419	c_0	0.43331
a_1	-4.63685×10^{-5}	b_1	-1.34837	c_1	-0.68344
a_2	-5.36235×10^{-4}	b_2	1.76567	c_2	0.80121
a_3	2.70399×10^{-4}			c_3	-0.42937
a_4	-3.699069×10^{-5}			c_4	0.10581
				c_5	-9.78755×10^{-3}

$$\begin{aligned}\phi_{max} &= a_4M^4 + a_3M^3 + a_2M^2 + a_1M + a_0 \\ \beta &= b_2M^2 + b_1M + b_0 \\ \Psi_{max} &= c_5M^5 + c_4M^4 + c_3M^3 + c_2M^2 + c_1M + c_0\end{aligned} \tag{4.62}$$

The polynomial coefficients a_i, b_i and c_i were taken from Pukrushpan *et al.* [163], where a non-linear regression was performed to find the constant. The regression coefficients are shown in table 4.1.

The inlet Mach number is defined by equation 4.63. Where R_a is the air gas constant ($\text{J.mol}^{-1}\text{.K}^{-1}$).

$$M = \frac{U_c}{\sqrt{\gamma R_a T_{cp,in}}} \tag{4.63}$$

The air mass flow rate is then calculated using equation 4.64.

$$W_{cr} = \phi\rho_a\frac{\pi}{4}d_c^2U_c \tag{4.64}$$

Table 4.2 lists the parameters used for the compressor map.

A look-up table of the compressor efficiency (η_{cp}) is used to find the efficiency from the mass flow rate and the pressure ratio across the compressor. The maximum efficiency of the compressor is 80%. The temperature of the exit air is calculated from equation 4.65.

$$\begin{aligned}T_{cp,out} &= T_{cp,in} + \frac{T_{cp,in}}{\eta_{cp}}\left(\left(\frac{p_{cp,out}}{p_{cp,in}}\right)^{\frac{\gamma-1}{\gamma}} - 1\right) \\ &= T_{atm} + \frac{T_{atm}}{\eta_{cp}}\left(\left(\frac{p_{sm}}{p_{atm}}\right)^{\frac{\gamma-1}{\gamma}} - 1\right)\end{aligned} \tag{4.65}$$

The torque required by the compressor can then be derived by equation 4.66 which considers the energy required to compress the air and the inefficiencies of the compressor.

Table 4.2: Compressor map parameters

Parameter	Value	Units
R_a	2.869×10^2	$J.kg^{-1}K^{-1}$
ρ_a	1.23	$kg.m^{-3}$
d_c	0.2286	m

Table 4.3: Compressor motor parameters

Parameter	Value	Units
k_v	0.153	$V.s.rad^{-1}$
k_t	0.153	$N.m/\ A$
R_{cm}	0.82	Ω
η_{cm}	98	%

Where τ_{cp} is the torque needed to drive the compressor $(N.m)$ and ω_{cp} is the compressor speed $(rad.s^{-1})$.

$$\tau_{cp} = \frac{C_p}{\omega_{cp}} \frac{T_{atm}}{\eta_{cp}} \left(\left(\frac{p_s m}{p_{atm}} \right)^{\frac{\gamma-1}{\gamma}} - 1 \right) W_{cp} \tag{4.66}$$

The transient behaviour of the compressor is then modelled by assuming a lumped rotational mass model as shown in equation 4.67. Where J_{cp} is the combined inertia of the compressor and motor $(kg.m^2)$ and τ_{cp} is the compressor motor torque input $(N.m)$.

$$J_{cp} \frac{d\omega_{cp}}{dt} = (\tau_{cm} - \tau_{cp}) \tag{4.67}$$

The compressor torque is then calculated using assuming the use of a static DC motor model as shown in equation 4.68. Where k_t, R_{cm} and k_v are motor constants and η_{cm} as defined in table 4.3.

$$\tau_{cm} = \eta_{cm} \frac{k_t}{R_{cm}} (v_{cm} - k_v \omega_{cp}) \tag{4.68}$$

Figure 4.11 shows the resulting compressor map for constant compressor speeds between 10 - 100 kRPM and also the compressor efficiency map. In reality, it not possible to operate in some pressure ratio regions due to the surge limitation of the device.

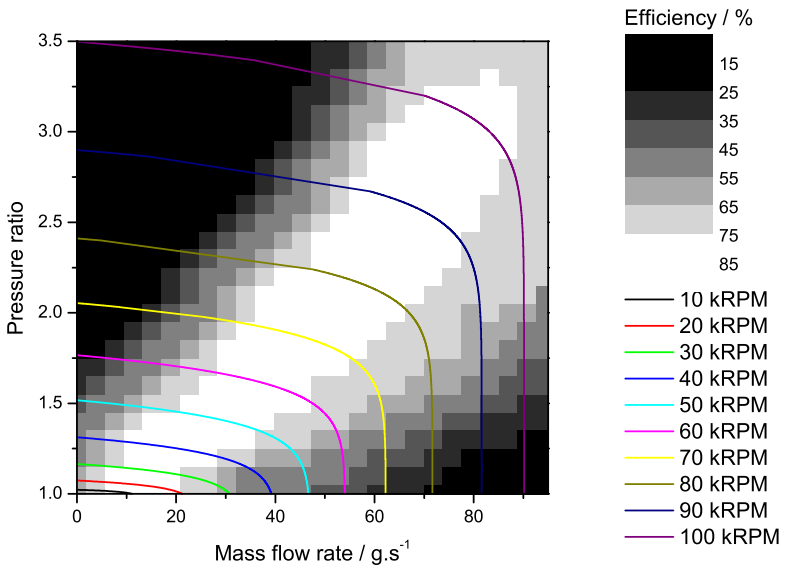
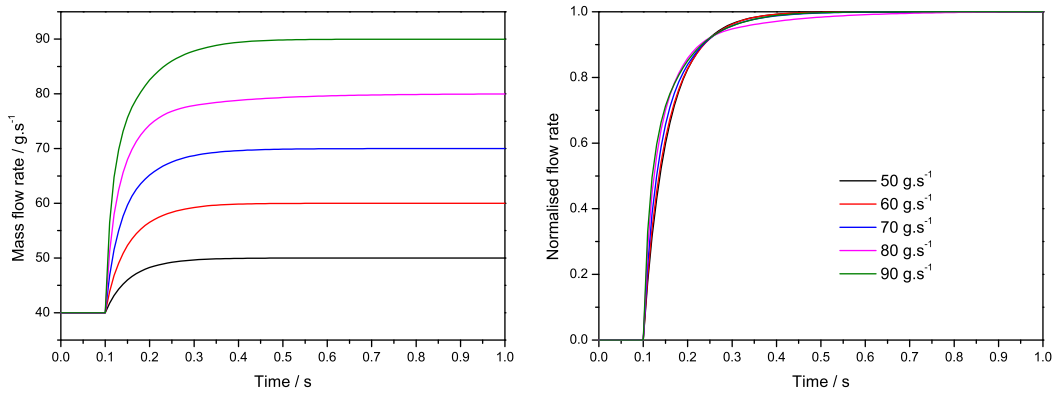


Figure 4.11: Compressor efficiency and performance map for different impeller speeds



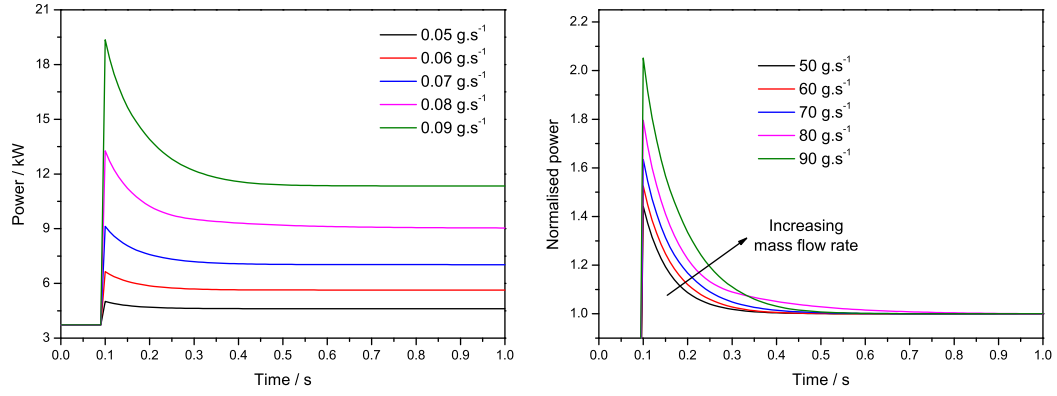
(a) (b)

Figure 4.12: Transient mass flow rate of a compressor under a constant pressure ratio of 2 under various step load (a) and normalised mass flow rate referenced from the steady state

The operating point of the compressor at a certain RPM will be the point at which the iso-speed curve matches with the pressure drop of the stack, manifolds and any back pressure regulation. Efficiency can vary significantly and thus close consideration of the operation point needs to be considered. At low flow rates and low pressures, the efficiency of the compressor is typically low and thus it is not normally recommended to operate within this region. Similarly, at higher flow rates the optimal efficiency point shifts towards higher pressures and operation in this region is not recommended.

Figure 4.12 shows the transient response of the compressor under a step load from a steady state mass flow rate of 40 $g.s^{-1}$ operated under a pressure ratio of 2.

It can be seen that for all step conditions it takes approximately 0.25 s for to reach 90% of the new steady state value. This transient ramp up time is linked to the performance of the electric motor and associated compressor inertia. When normalising the data it can be seen that the transient step time for all steps under the test conditions are approximately the same. The rate of electrochemical reactions in a FC are on a time scale many orders of magnitude faster than that of the compressor, thus when a step load on a FC is applied, the FC will draw current near instantaneously whilst the oxygen required takes on the order of ms to reach the FC. In that time the operating air stoichiometry of the FC is below optimum and this affects the efficiency of the FC. Figure 4.13 then



(a) (b)

Figure 4.13: Transient power a compressor under a constant pressure ratio of 2 under a step load under various step loads (a) and normalised power referenced from the steady state (b)

shows the transient power requirements of the compressor motor.

Here it can be seen that the larger the step the larger the power requirement. Moreover, the additional power required to achieve a certain transient performance can be quantified. The normalised power, with each series being references to the steady state power shows that with larger step sizes the additional power requirements to overcome the inertia of the motor increases. The power requirements to overcome the inertia of the compressor is thus and additional power requirement which combined with the additional electrochemical mass transport losses of the FC makes the FC increasingly inefficient under transient loads.

4.3.2 Blower modelling

Whilst the mathematical framework for a high pressure compressor has been presented, the work on a low pressure blower is also presented due to later experimental validation of the system with a blower rather than a compressor. The modelling framework for the compressor and subsequent analysis remains valid due to this being of use larger in large scale system analysis where high pressure compressors would normally be used rather than low pressure blower and thus presents a more likely situation.

The blower model works in much the same way as the compressor model. The same DC motor equations are used to model the rotational speed of the blower which gives the blower its transient response time. The main difference is the correlation of the rotational speed to flow rate is based upon an experimentally derived look-up table, combined with experimentally measured pressure drops across the stack.

Initial testing was required to quantify the cathode side pressure drop. The two main sources of pressure drop across the cathode side were identified as being from the humidifier and the FC stack. The experimental set-up is shown in figure 4.14, where T and P represent points where pressure and temperature were measured.

To avoid an excessive pressure difference between the anode and cathode sides which could cause damage to the MEAs, the anode side was pressurised with nitrogen to a pressure of 30 kPa. Air was supplied by an Eaton roots M24 supercharger powered via a belt drive connected to a Lemco LEM-200-127 DC electric motor with a maximum power output of 11 kW. A 4.8 kW 48 V Murata D1U-W-1600 power shelf unit provided the power required of the motors. A 4QD 300 motor controller was used for speed control of the motor with a manual potentiometer control.

Data logging of the volume flow rate, temperatures and pressures was done on the cRIO with a sample rate of 2 Hz. A running mean and running standard deviation script of the measured values was programmed into the cRIO. Volume flow rate of air was measured with an ABB FS4000 Swirl Flow Meter, the output of which was calculated by measuring the voltage across a 500 Ω resistor with the 9205 analog input module.

Figure 4.15a shows the cathode side pressure drop across the 75-cell PEMFC stack as

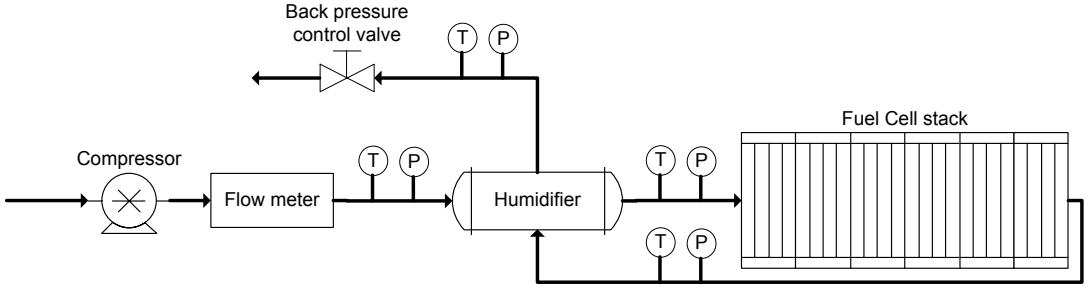


Figure 4.14: Experimental set-up for measuring cathode side pressure loss

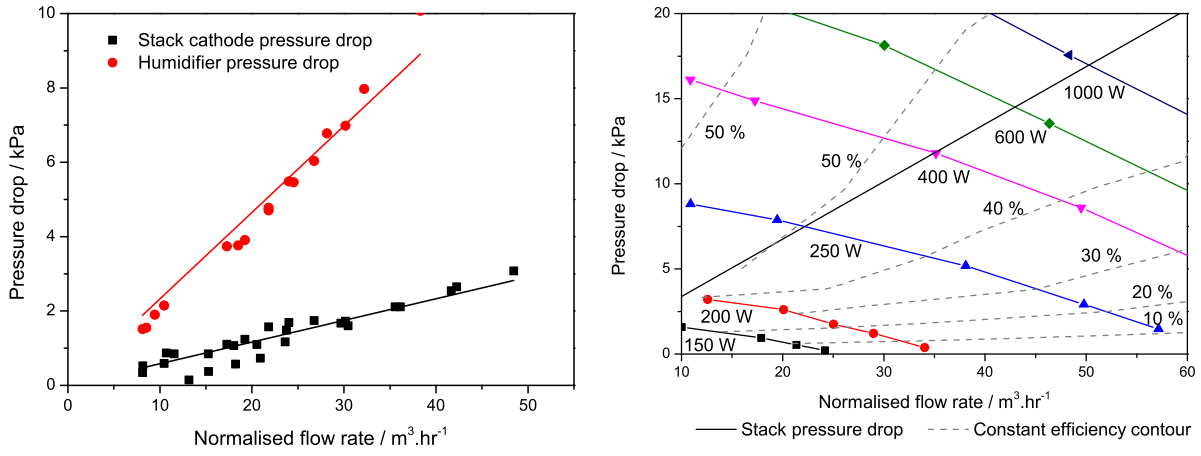


Figure 4.15: (a) Cathode side and humidifier pressure drop for the 75-cell Nedstack PEMFC and (b) experimentally measured blower performance map. Adapted from Wu *et al.* [223]

well as the pressure drop across the humidifier used. As the air circuit passes through the humidifier twice the total pressure drop is the stack pressure drop in addition to two passes of the humidifier pressure drop. This compounded pressure drop can then be used to determine the operating point of the blower. In reality during operation the pressure drop of the stack can vary due to reactant consumption and the onset of flooding leading to the blockage if flow channels. Figure 4.15b shows the performance map of the tested low pressure blower with the superimposed total cathode side pressure drop. As the blower approached its maximum power the pressure ratio it can achieve is only approximately 1.2.

4.3.3 Manifold dynamics

In dynamic FC system models the volume of the pipe and connection between devices has to be considered as the time constant of pressure changes can be significant. This is represented by a lumped manifold model as presented by Pukrushpan *et al.* [163].

If a control volume is drawn around the manifold volume of interest, equation 4.69 shows that the mass accumulated is equal to the difference of the mass flow into and out of the system.

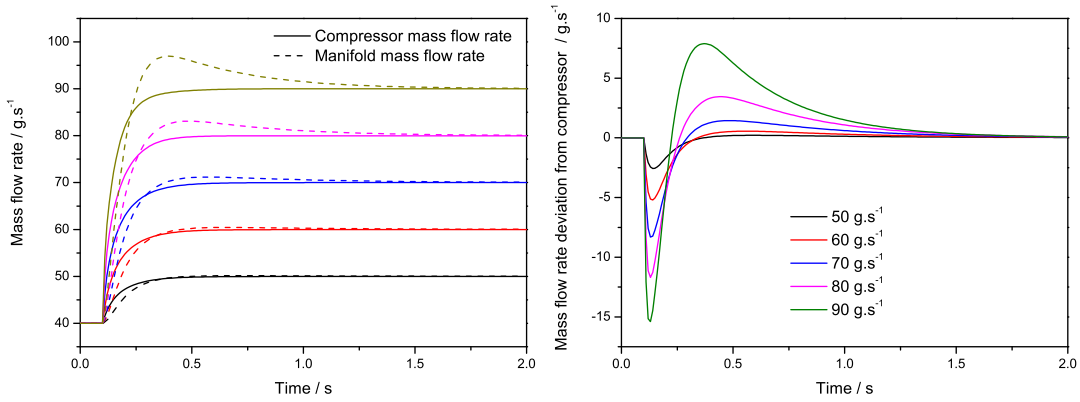
$$\frac{dm}{dt} = \dot{m}_{in} - \dot{m}_{out} \tag{4.69}$$

Where m is the mass of reactant (kg s^{-1}). If it is then assumed that the air temperature is constant in the manifold the relationship then becomes isothermic as represented by equation 4.70.

$$\frac{dp}{dt} = \frac{R_a T}{V} \left(\dot{m}_{in} - \dot{m}_{out}\right) \tag{4.70}$$

Where R_a is the gas constant of air, (J K^{-1} mol^{-1}), V is the manifold volume (m^3). If the air temperature is expected to change in the manifold equation 4.70 then becomes equation 4.71.

$$\frac{dp}{dt} = \frac{\gamma R_a}{V} \left(\dot{m}_{in} T_{in} - \dot{m}_{out} T_{out}\right) \tag{4.71}$$



(a) (b)

Figure 4.16: Transient mass flow of a simulated compressor at a pressure of 1.5 bar with and without a 0.2 m^3 manifold volume (a) and the deviation of mass flow from the compressor mass flow caused by the air manifolding effect (b)

Where γ is the heat capacity ratio.

The nozzle flow equation is then used to calculate the outlet manifold flow which is a function of the inlet pressure and temperature, as well as the outlet temperature. This can be divided into two regions divided by the critical pressure ratio as shown in equation 4.72.

$$\left(\frac{p_2}{p_1}\right)_{crit} = \left(\frac{2}{\gamma+1}\right)^{\frac{\gamma}{\gamma-1}} \tag{4.72}$$

Where $\gamma = 1.4$ and the critical pressure ratio is 0.528. When the flow pressure is below the critical pressure ratio the mass flow rate can be calculated from equation 4.73.

$$W = \frac{C_D A_T p_1}{\sqrt{\bar{R}T_1}} \left(\frac{p_2}{p_1}\right)^{\frac{1}{\gamma}} \left\{\frac{2\gamma}{\gamma-1}\left[1-\left(\frac{p_2}{p_1}\right)^{\frac{\gamma-1}{\gamma}}\right]\right\}^{\frac{1}{2}} \quad \text{if} \quad \frac{p_2}{p_1} > \left(\frac{2}{\gamma+1}\right)^{\frac{\gamma}{\gamma-1}} \tag{4.73}$$

For flows where the pressure drop is equal to or greater than the critical pressure ratio, equation 4.74 is used.

$$W_{choked} = \frac{C_D A_T p_1}{\sqrt{\bar{R}T_1}} \gamma^{\frac{1}{2}} \left(\frac{2}{\gamma+1}\right)^{\frac{\gamma+1}{2(\gamma-1)}} \quad \text{if} \quad \frac{p_2}{p_1} \leq \left(\frac{2}{\gamma+1}\right)^{\frac{\gamma}{\gamma-1}} \tag{4.74}$$

Where C_D is the discharge coefficient of the nozzle, A_T is the opening area of the nozzle (m^2) and $\bar{R}$ is the universal gas constant. If the pressure difference between the inlet and outlets of the manifolds is small and is also sub-critical the mass flow rate equation can be linearised to give equation 4.75.

$$W = k\,(p_1 - p_2) \tag{4.75}$$

Figure 4.16 show the transient performance of a compressor with the manifold dynamics included. Where k is the nozzle coefficient.

4.3.4 Cooling system

The performance of the cooling system is critical to the operation of the FC in order to not allow the system to overheat. Accurate modelling of the radiators performance will allow for more accurate description of the coolant parasitic power consumption.

The design of a radiator is such that it maximises the surface area and also the convective heat transfer coefficients of the working fluids. This is typically achieved through the use of thermally conductive materials, fin plates to increase surface area and air flow channel designs (typically known a louvre fins) with the aim of increasing turbulent flow which typically has much better heat transfer properties than laminar flows.

A semi-empirical model has been implemented to characterise the break-up of the thermal boundary layer caused by the louvre fin geometries of automotive radiators. This break-up causes an increase in turbulence in the air channels of the radiator which improves convective heat transfer. A diagram of the arrangement of typical automotive radiator fins is shown in figure 4.17.

To evaluate the effect that the louvre fins have on convective heat transfer coefficient, a Davenport correlation was applied to find a variable known as the j-factor which was used to relate Reynolds number (Re) to Stanton number (St) and Prandtl number (Pr). This is shown in equation 4.76 and 4.77.

$$j = 0.249 Re_{Lp}^{-0.42} L_h^{0.33} \left(\frac{L_h}{F_l}\right) F_l^{0.26} \qquad 300 < Re_{Dh} < 4000 \tag{4.76}$$

$$j = StPr^{2/3} \tag{4.77}$$

Where L_h is the louvre fin height (m) and F_l is the fin length (m).

The convective heat transfer coefficient of the air side can then be calculated by considering equation 4.78, where all properties refer to the working air and is density (kg/m^3), C$_p$ is the specific heat capacity (kJ/kg.K) and U_{mean} is the mean flow rate (m/s).

$$h_{air} = St\rho CpU_{mean} \tag{4.78}$$

The convective heat transfer from the coolant is then calculated by considering the physical dimensions of the radiator and the conditions of the flow through it as shown in

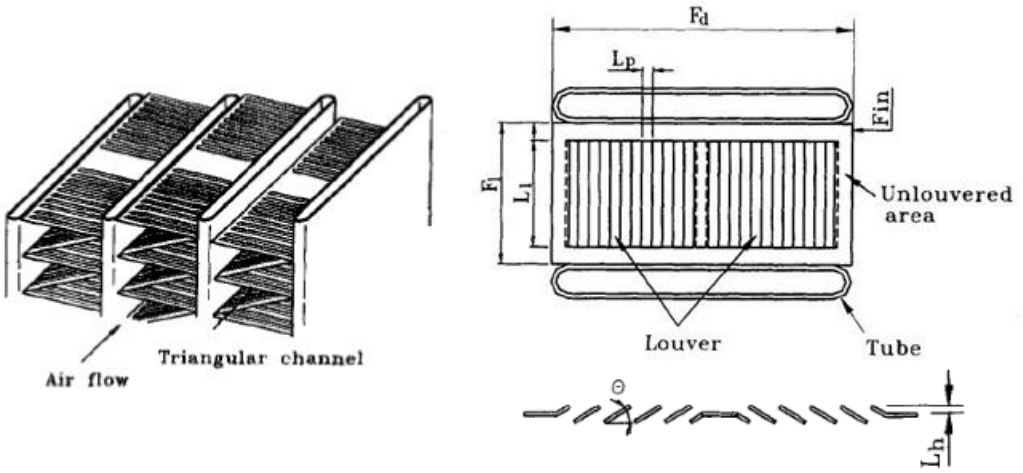


Figure 4.17: Corrugated Louver with splitter plate and triangular channel [39]

equations 4.79-4.85. Equation 4.79 shows calculates the flow velocity within each tube of the radiator assuming incompressible flow.

$$V_{coolant} = \frac{\dot{m}_{coolant}}{D_{duct} W_{duct} \rho_{coolant} N_{ducts}} \tag{4.79}$$

As the cooling tubes are not cylindrical a hydraulic diameter needs to be calculated which is shown in equation 4.80.

$$D_{h,duct} = \frac{2 W_{duct} D_{duct}}{W_{duct} + D_{duct}} \tag{4.80}$$

This can then be used to calculate the Reynolds number (Re) of the coolant flow as shown in equation 4.81, and subsequently the Graetz number (Gz) which characterises laminar flow in a conduit as shown in equations 4.82.

$$Re_{coolant} = \frac{V_{coolant} \rho_{coolant} D_{h,duct}}{\mu_{coolant}} \tag{4.81}$$

$$Gz_{coolant} = \frac{H_{duct}}{D_{h,duct} Re_{coolant} Pr_{coolant}} \tag{4.82}$$

The Nusselt number, which presents the ratio of convection to conduction across a boundary, can then be calculated based on the Graetz number as shown in equations 4.83 and 4.84.

$$Nu_{coolant} = \frac{1.615}{Gz_{coolant}^{1/3}} - 0.2 \qquad Gz_{coolant} < 0.03 \tag{4.83}$$

$$Nu_{coolant} = \frac{0.0499}{Gz_{coolant}} + 3.66 \qquad Gz_{coolant} \geq 0.03 \tag{4.84}$$

The convective heat transfer coefficient of the coolant side can then be calculated as shown in equation 4.85 and combining this with the convective heat transfer coefficient of the air side, the overall heat transfer coefficient can then be found as shown in equation 4.86.

$$h_{coolant} = \frac{Nu_{coolant} k_{coolant}}{D_{h,duct}} \tag{4.85}$$

$$UA_{rad} = \left(\frac{1}{h_{coolant} A_{duct,total}} + \frac{1}{h_{air} A_{fin,total}} \right)^{-1} \tag{4.86}$$

The ratio of the specific heat capacities is then taken as the smaller over the larger value and this is then used to calculate the Number of Transfer Units (NTU) which is used in calculating the effectiveness of the system as shown in equations 4.87, 4.88 and 4.89 respectively.

$$Cr_{rad} = \frac{\min(C_{p,coolant}, C_{p,air})}{\max(C_{p,coolant}, C_{p,air})} \tag{4.87}$$

$$NTU_{rad} = \frac{UA_{rad}}{\min(C_{p,coolant}, C_{p,air})} \tag{4.88}$$

Table 4.4: Parameters of modelled radiator

Parameter	Value		Parameter	Value	
Height	0.352	m	Coolant C_p	4185	J/kgK
Width	0.347	m	Coolant μ	0.462×10^{-3}	kg/ms
Depth	0.032	m	Coolant ρ	983	kg/m^3
Duct spacing	0.0085	m	Coolant k	0.653	W/mK
Number of ducts	34		Coolant Pr	2.96	
Radiator fin pitch	2.85	mm	Air C_p	1006	J/kgK
Louvre fin height	2.81	mm	Air μ	1.81×10^{-5}	kg/ms
Air ρ	1.205 kg/m^3	Air k	0.025	W/mK	

$$eff_{rad} = \frac{1 - e^{-NTU_{rad}(1-Cr_{rad})}}{1 - Cr_{rad}e^{-NTU_{rad}(1-Cr_{rad})}} \tag{4.89}$$

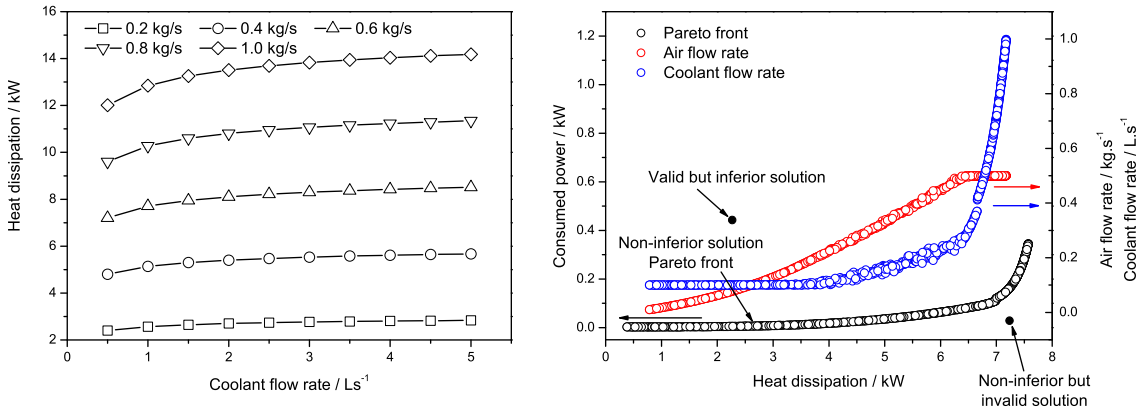
The overall heat dissipation of the system is then calculated by using equation 4.90.

$$q_{cooling} = eff_{rad}\min(C_{p,cooling}, C_{p,air})(T_{cooling} - T_{amb}) \tag{4.90}$$

It has been assumed that over the surface of the radiator the flow is uniform and that the fan speed can change instantaneously based on the control signal. This is valid due to the relative time constant of any thermal changes being several orders of magnitude slower than fan dynamic response times. It has also been assumed that the radiator is at a uniform temperature and than the ambient temperature remains constant.

Table 4.4 shows the parameters that were used which are based on parameters for a Honda Civic V radiator.

Power consumption for the fan and pump were based on manufacturers supplied data sheets. Modelling results of the fan and radiator showed that the air velocity through the radiator had the greatest impact on the cooling performance of the combined system. At low air flow rates, increasing the coolant flow rate had negligible increases in the overall heat transfer of the cooling system. This is shown in figure 4.18a.



(a) (b)

Figure 4.18: (a) Modelled performance of a fan and radiator system for different air and coolant flow rates and (b) multi-objective optimisation for the cooling system showing the Pareto front for minimisation of parasitic energy requirements

Plotting the same system as the percentage of cooling power consumed for a certain FC operating power it can be seen that to dissipate the same amount of heat it is more beneficial to increase the air flow rate than that of the coolant flow rate due to its higher sensitivity. However, at high rates of heat dissipation it may be beneficial for more of the coolant to be flowed as shown in figure 4.18b which shows the multi-objective optimisation for the cooling system with 2 free variables of coolant flow rate and fan speed, with the two objectives of maximise heat rejection whilst minimising power required.

In practice, having too low a coolant flow rate for a give power dissipation can have a detrimental impact on the long term performance of the FC stack due to the larger thermal gradients that arise due to the slower coolant flow rate. Thermal gradients within the FC stack and single FC cell can result in inhomogeneities in the current density and also result in thermal stresses.

4.4 Experimental set-up: Fuel cell system construction

In order to validate the developed FC stack model and BOP components a full FC system was constructed. The stack used 75 200 cm^2 MEAs from Johnson Matthey with the stack assemblers being Nedstack B.V. resulting in a 9.5 kWe system. The BOP systems were all developed in-house. Supervisory control was achieved though the use of a National Instruments (NI) compactRIO (cRIO). Figure 4.19 shows a schematic of the designed system with the location of various sensors.

Figure 4.20 shows an image of the first generation experimental FC system set-up with BOP components. Later generations of the system with improved aesthetics and portability are presented in later chapters.

The air subsystem consisted of a low pressure 24 VDC Domel blower which drew in ambient air. The air flow then went through a Permapure humidifier and then into the cathode inlet of the stack. Oxygen depleted air from the cathode outlet was then channeled back into the humidifier which recovered waste heat and also excess water and then the air was exhausted to ambient conditions through a back pressure regulator. During normal operation this back pressure regulator was set in the wide open position due to the low pressure operation of the system.

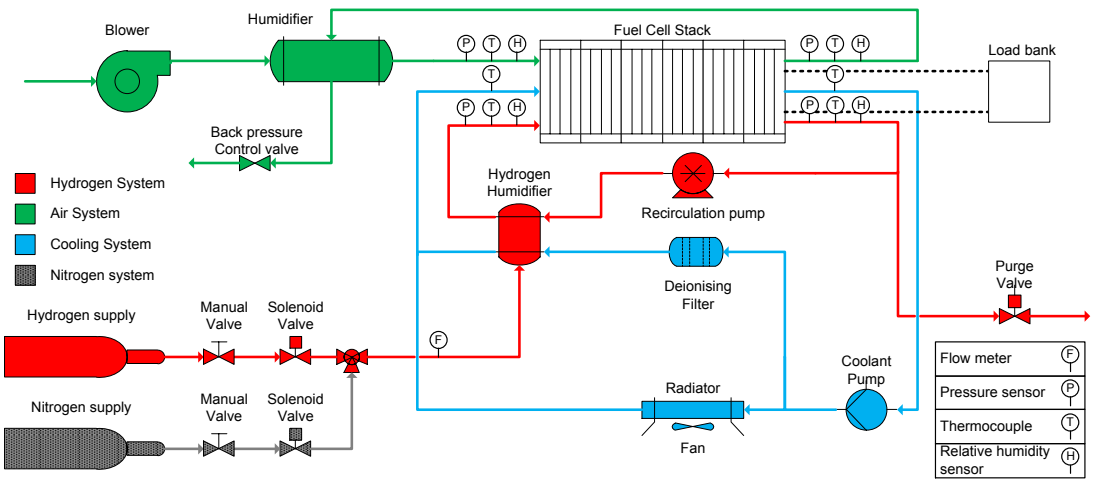


Figure 4.19: Schematic of balance of plant system for a 9.5 kWe PEMFC stack. Adapted from Wu *et al.* [222]

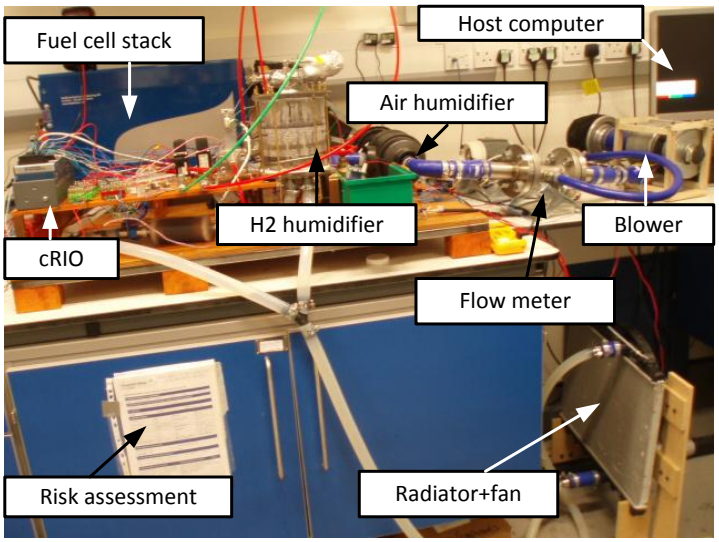


Figure 4.20: Picture of the 1st generation fuel cell system set-up

The anode subsystem was supplied from a high pressure hydrogen supply. Typically a 5×50 litre tank bank at 200 bar, when fully filled, was used from the lab supply line. Pressure regulators reduced this down to approximately 10 bar on the local line pressure and the another regulator then reduce this to 1.5 bar absolute. Solenoid valves are used to turn on and off the supply as needed. This dry hydrogen then enters into a in-house designed hydrogen humidifier which bubbles the dry hydrogen through de-ionised water to increase the relative humidity. The de-ionized water used to bubble the hydrogen also recovers waste heat from the cooling loop through a heat exchanger to increase the temperature of the hydrogen from the cylinder. This hydrogen then enters into the stack. Exhaust hydrogen is then recirculated with a diaphragm pump to increase the working stoichiometry. During high current density operation inhomogenities in the single cell can mean that regions of the cell do no recieve enough hydrogen without higher operating stoichiometries. This is a problem commonly encounter in dead-ended systems. In addition, literature works have previously shown that higher anode side flow rates result in more homogeneous conditions due to water removal [177].

The anode gas loop is also connected to a purge valve which periodically removes all the gas in the anode. This is done to remove nitrogen which crosses over from the cathode during operation and also to remove excess water which may cause localised cell flooding. This is likely to occur if the hydrogen loop is over humidified due to the low pressure and temperature operation.

The anode subsystem is also connected to a nitrogen supply which during normal operation is not active. This is only used during start-up/shut-down events. During start-up, due to the MEAs gas permeability, it is likely that the anode contains air. If hydrogen is supplied during start-up this can cause large internal currents due to the formation of a hydrogen-air boundary which accelerated carbon corrosion of platinum supports. Therefore, a nitrogen supply is used to purge the air prior to supplying hydrogen to minimise the impact of start-up degradation.

During shut-down the nitrogen supply is also used to purge the remaining hydrogen in the gas manifolds. This is done to reduce the potential of the cell as quickly as possible during shut-down. Prolonged operation at elevated potentials again accelerates the rate of carbon oxidation of the catalyst supports in PEMFCs. A cell will stay at potential until internal currents consume all of remaining hydrogen in the anode gas manifolds, thus nitrogen is used to remove remaining hydrogen.

Table 4.5: List of balance of plant components used

Component	Manufacturer/ supplier	Use
Air system		
Air blower	Domel - 497.3.265	Supply air to the FC
Humidifier	Permapure - FC4000-2500	Humidifies the air supply
Air filter	Pipercross	Filters dust from air inlet
Hydrogen system		
Recirculation pump	Thomas - 7015Z DC	Recirculates the anode gases
Solenoid values	Burkert	Turns on/ off gases
Mass flow meter	Bronkhorst	Measures H_2 flow
Cooling system		
Radiator	Honda Civic V	Cools coolant
Water pump	Jabsco - 50870	Circulates coolant
Axial push fan	Comex	Cools the radiator
Control/ sensors		
Data logger/controller	National Instruments[a]	Logs data and controls components
Pressure sensors	Omega	Measures pressure
Humidity sensors	Sensirion - SHT75x	Measures relative humidity
Thermocouple	RS	Measures temperature

[a] Further details about the exact specifications of the National Instruments equipment will be provided later

The cooling loop of the stack is needed to remove excess heat from the stack. Typically, operating efficiencies of PEMFCs can range from 50-40%. The cooling loop of the rig consists of a centrifugal pump which moves de-ionised water through a radiator and fan which are controlled by PID controller to maintain a constant operating temperature of 60°C. A de-ionising filter is placed in parallel with the radiator to maintain low conductivity of the coolant. This de-ionising filter has a relatively larger pressure drop across it, therefore it has been placed in parallel with the lower pressure drop circuit of the radiator.

The electrical terminals of the stack are then connected directly to a Dynaload WCL 488-400-1000-12000 water cooled load bank with an operational range of upto 400 V, 1000 A and 12 kW, with 50 mm^2 wires to ensure low resistance. Sense terminals for the load bank were connected directly to the FC stack terminals to minimise the impact of contact resistance overpotentials at high operating currents.

All BOP components operate from a low voltage 24 VDC supply unless otherwise stated. This low voltage supply is provided via an external power supply. Table 4.5 lists all the BOP components used.

4.4.1 Fuel Cell control

In order to control all the BOP components and monitor the state of the FC a NI cRIO was used. This was interfaced with a host computer running NI LabVIEW. Figure 4.21 shows architecture of the program.

Typically, the host computer runs LabVIEW which allows the user to design a custom user Graphical User Interface (GUI). This consists of a front panel which displays all graphical information with user controls. This is linked to a back panel where the computational logic is defined. Users create programs known as Virtual Instruments (VI) which does a specific process, for example convert uncalibrated temperatures. The two main VIs created are the RT VI which does the graphical presentation, low speed computation and data logging, and also a FPGA VI which handles high speed computation such as CAN messages and also acquires the raw data from the modules.

Table 4.6: National Instruments equipment used for FC test bench

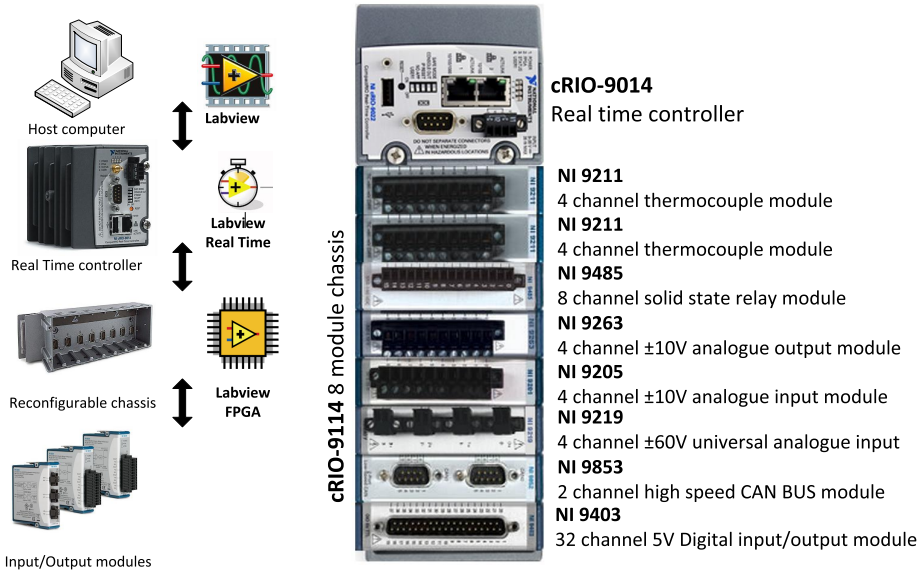
Component		Channels/Range	Use
Real Time controller	cRIO-9014		Real time data processor
FPGA chassis	cRIO-9114	8-slot	FPGA processor
Analog Output module	NI 9263	4-channel / ±10 V	Controls fan, pump and recirculation pump
Thermocouple module	NI 9211	4-channel	Measure temperatures
Analog Input module	NI 9205	4-channel / ± 10 V	Measure analogue based sensors
Universal Analog Input module	NI 9219	4-channel / ± 60 V	Measure stack voltage
Digital Input/ Output module	NI 9403	32-channel / 5 V	Generates PWM signal for blower control
CAN BUS module	NI 9853	2-channel	Reads CAN signals from FC CVM

It is ideal to divide the program into these main sections due to the nature of having to recompile the raw HDL language onto the FPGA, which for large programs can be time intensive. The cRIO is powered by a separate and dedicated 24 VDC supply to the BOP to avoid oscillations in the working voltage since measurements such as thermocouples and pressure transducers would need to share a common ground and this could potentially be a source of electrical error.

A list of the modules used as well as their purpose is shown in table 4.6

The NI cRIO control program is primarily controlled by a host computer running NI LabVIEW. This then communicates with the cRIO's Real Time controller (RT) which does the majority of the data calculation and logging. This is also connected to the Field Programmable Gate Array (FPGA) module which directly interfaces with the C-series modules aforementioned that acquire the data and provides the control signals.

The host computer running LabVIEW also controls the load bank. The load bank is connected to the host computer via an RS232 to COM connector. Read/write commands



(a) (b)

Figure 4.21: (a) Flow of information in compactRIO set-up and (b) diagram of compactRIO modules used

are then sent via the registered COM port on the computer via an in-house written equipment driver. Command refresh rates were limited to 0.25 s due to the speed of the equipment.

Fan, coolant pump and recirculation pump control

The radiator fan, coolant pump and recirculation pump all work off 24 V, rather than 12 V to reduce losses. Control of these devices was achieved by combining each device with a SyRen10 A motor controller which allows for direct regulation of the supply power from a low voltage BUS by changing the input analogue 0-5 V sense terminal. This 0-5 V sense was supplied by the cRIO NI 9263 ±10 V analogue output module. The sense terminal of the motor controller should in all cases, share the same ground as the cRIO NI 9263 module. The motor controller then regulates the output voltage which is connected to the device, which depending on the internal resistance, will draw a set amount of current. The motor controller needs to be connected to the 24 VDC low voltage BUS supply.

Temperature control

The temperature of the 9.5 kWe stack was controlled by using a centrifugal water pump in series with a radiator and fan. During normal operation the flow rate of the coolant was set to a fixed speed and temperature control was achieved by use of a PID controller varying only the fan speed. Use of differential based control constants proved to introduce too many instabilities of the system due to the noise of the thermocouple measurements which acted as the measured variable. Due to the slow transient nature of the system caused by the lengths of pipe in the system only low integral control constants were used to remove steady state errors from the controller.

Figure 4.22 shows the process of a PID controller where the PID control function is defined as shown in equation 4.91 where K_P, K_I and K_D are the proportional, integral and differential control constants, e is the error between the reference value and the actual value of the control variable and τ is the integration time window which is between 0 and t.

$$u(t) = K_P e(t) + K_I \int_0^t e(\tau)d\tau + K_D \frac{d}{dt} e(t) \tag{4.91}$$

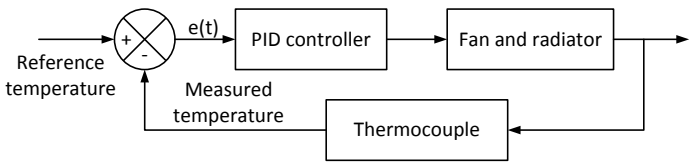


Figure 4.22: Flow diagram showing the feedback process in the cooling system PID controller

Determination of the PID constants can affect the dynamic and steady state response time of the system. Table 4.7 shows the typical effect of increasing different PID constants in a system being controlled by a PID controller.

Oscillations in the temperature control were observed due to the finite transient time to took the coolant to move from the radiator to the stack, and also due to the use of the integral gain which will have some overshoot, but was needed to remove the steady state error and also prevent rapid changes in fan speed due to pure proportional control.

Figure 4.23 shows the temperature response of the cooling system in a 9.5 kWe PEMFC. Here a pure proportional controller was used to regulate the power to the fan. The

Table 4.7: Effect of increasing PID constant

Parameter	Rise time	Overshoot	Settling time	Steady-state error	Stability
K_P	Decrease	Increase	Small change	Decrease	Degrade
K_I	Decrease	Increase	Increase	Eliminate	Degrade
K_P	Small change	Decrease	Decrease	No effect	Improved

control variable was the stack coolant outlet temperature and this was regulated against a set-point of 61°C.

As it can be seen the temperature of the coolant is maintained within ±1.5°C for a proportional gain of 0.5 and ±1°C. The observed oscillations in the temperature are due to the finite time required to transport a package of fluid between the stack, where the temperature was measured, and the radiator where the fan acts to dissipate the excess thermal energy. The phase shift between the inlet and outlet is also due to the finite amount of time required to transport a package of fluid between the two measurement points. The period of these oscillations is approximately 40 s with a phase shift of approximately 10 s. Increasing the coolant flow rate will decrease the period of the oscillations; however, at the cost of increased parasitic power consumption.

Purge control

The hydrogen system periodically needs to be purged in order to remove any nitrogen that crosses through the MEA from the cathode and any condensated water which may hinded gas diffusion through the GDL. This was achieved by using a solenoid valve that periodically opened removing the gases from the system. This also served the purpose of removing any condensed water in the anode by the pressure differential created by the purge.

Figure 4.24 shows the anode pressure, flow rate and stack voltage under constant current operation when a purge with a frequency of 20 s and duration of 0.5 s is applied. During non-purge events there steady difference between the anode inlet and outlet pressures

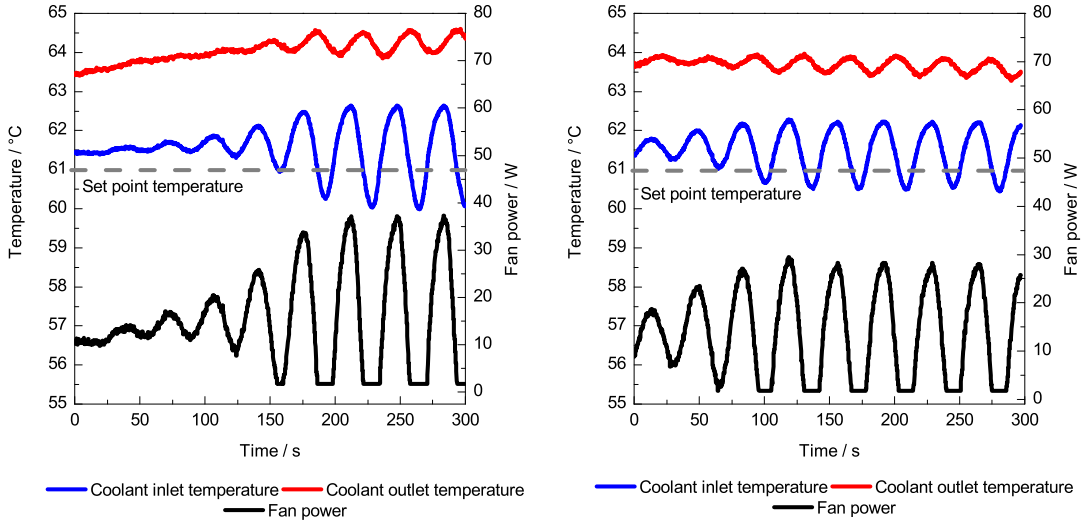


Figure 4.23: Cooling inlet and outlet temperatures for a 9.5 kWe PEMFC with a pure proportional controller controlled fan cooling systems with K_P=0.5 (a) and K_p=1 for a constant coolant flow rate of 19.4 l/min at an operating power of 2 kWe [223]

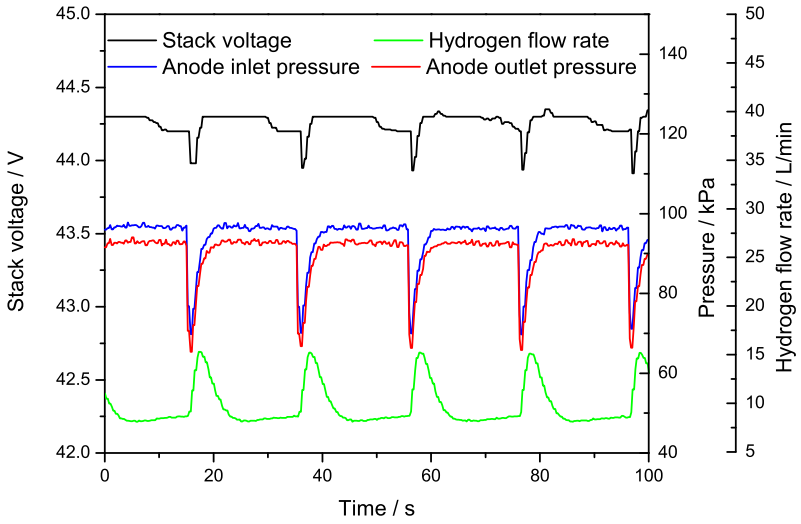


Figure 4.24: Anode pressure, flow rate and stack voltage during operation with a purge frequency of 20s and purge period of 0.5 s

due to the pressure drop across the anode flow channels. During the purge event the pressure drops rapidly to near ambient pressure. Once the solenoid value is closed again, the pressure recovers until the steady state pressure is achieve again. The finite time required to achieve the steady pressure is a function of the supply pressure and the total anode manifold volume. When the pressure drops due to the purge the stack voltage drops due to the decrease in operating pressure.

Blower control

The blower comes with its own controller that can operate in either analogue input or digital mode. The control of the blower was achieved by generating a Pulse Width Modulation (PWM) signal with frequency of 1000 Hz and output voltage of 5 V nominal. The power of the blower is then proportional to the applied duty cycle. A base PWM duty cycle of 20% needs to be applied in order to overcome stationary frictional losses. The specified blower operates from the 24 V low voltage BUS circuit.

Cell voltage monitoring

The 9.5 kWe FC stack used has 75 individual cells. With larger and larger systems the probability of inhomogeneous performance becomes ever higher. This is especially true in the case of low pressure system where uniform reactant distribution can be a major issue. The Nedstack system used has an in-built Cell Voltage Monitoring (CVM) system which operates over a CAN BUS interface outputting the voltages of all cells in the stack. The CAN interface of the Nedstack system requires a 24 V supply and was therefore connected to the 24 V low voltage BUS.

4.5 Model implementation and parameterisation

All of the governing equations were put into the MATLAB Simulink modelling environment. This is to allow for later integration of the FC system model with other component models developed.

For the fitting of the polarisation curve, test data from the 9.5 kW PEMFC was taken at different operating conditions and a pattern search based fitting algorithm was used to find constants that best fit the polarisation curves. This proved to be better than the GA based fitting previously employed by the battery fitting. Figure 4.25 shows the fit of

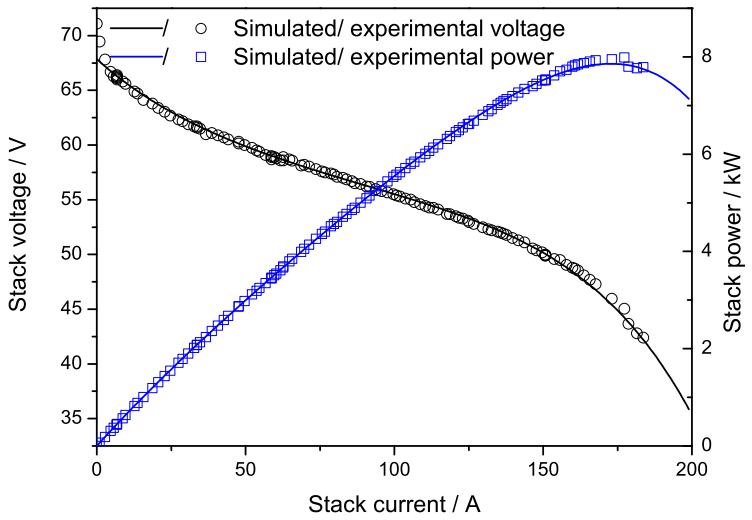


Figure 4.25: Simulated and experimental polarisation curve under fully humidified conditions at 65°C. Parameters used as indicated in Table 4.8

the experimental polarisation curve at 65°C. The results from the regression are shown in table 4.8.

Figure 4.26a shows the comparison between a cold start for the experimental and simulated data. Flow rate for the coolant was set to a constant value with the fan speed off during the heat up phase. It is ideal to have a small flow rate in order to measure accurately the coolant temperature. Without a small flow rate large differences in the local coolant temperature in the stack and at the measurement points would be evident and also buoyancy and convective mass transfer of the coolant in the stagnant flow could affect measurements. Prior to the introduction of the hydrogen into the anode, the blower was set to a constant flow rate and the system was purged with Nitrogen to minimise the effect of the formation of an air-hydrogen boundary in the anode which is know to lead to large internal currents and accelerate degradation [131].

Once the anode manifold volumes were purged with Nitrogen, the Nitrogen solenoid was closed and the anode was again purged of all gases. If hydrogen was introduced with the anode under nitrogen pressure, and if the nitrogen pressure in the anode is higher than the hydrogen pressure, back flow could occur. With the anode pressure at near ambient, the pressurized hydrogen flows faster. This is seen by the sharp increase in potential in figure 4.26a. The sharp increase in potential followed by a steady decay could indicate the rapid charging of the double layer due to internal currents, the implications of this will be discussed in later sections. As load is applied, the temperature of the reactants and coolant increase, representing an increase in the stack temperature. The cathode temperature increases are more significant than the anodes due to a combination of a number of effects. The water generation in the cathode results in large amounts of evaporation in the cathode which improves heat transfer allowing the air to remove more

Table 4.8: Polarisation coefficients from regression of experimental data

Parameter	Value	Parameter	Value	Parameter	Value
a_1	0.3362	b_1	-1.62×10^{-5}	c_1	5.730
a_2	-8.50×10^{-4}	b_2	0.0162	c_3	5.389
a_3	4.31×10^{-5}	b_3	1.8×10^{-4}		
		b_4	-0.166		
		b_5	-5.8×10^{-4}		
		b_6	0.471		

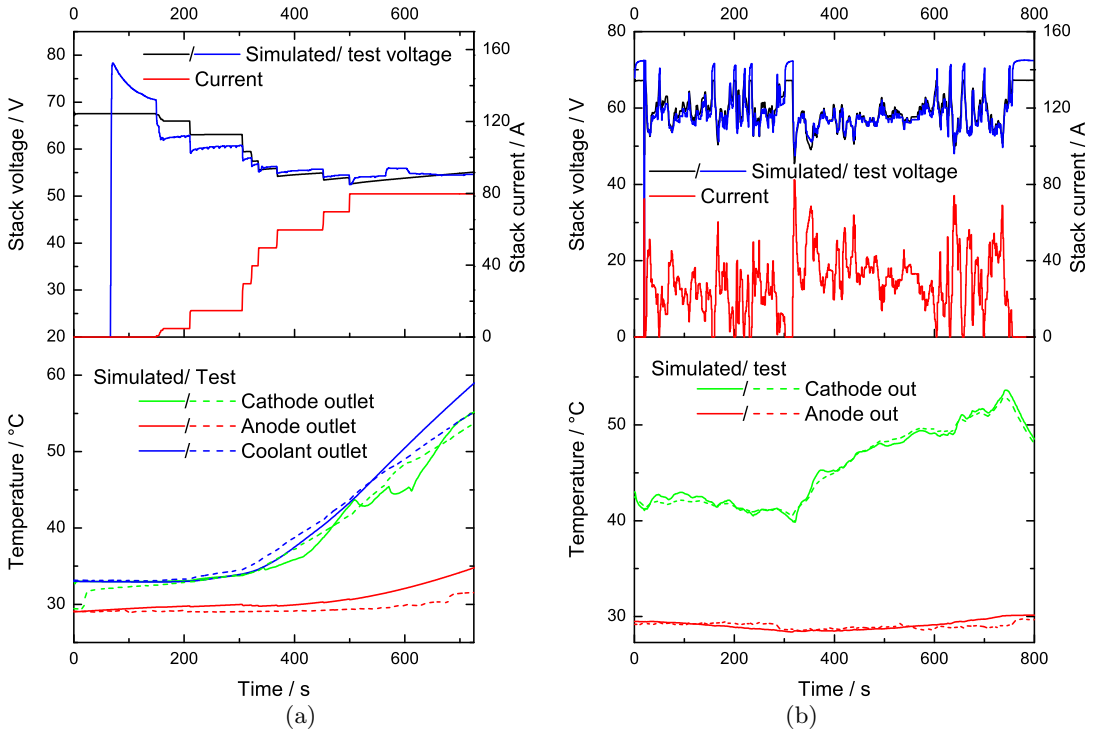


Figure 4.26: Comparison between experimental voltage and temperature response of the modelled 75-cell stack under (a) step loads from cold start and (b) a scaled HWFET drive cycle

heat. The specific heat capacity of hydrogen (14.3 $J.g^{-1}.K^{-1}$) is also approximately 14 times greater than that of air (1 $J.g^{-1}.K^{-1}$) thus meaning a greater temperature change is observed per joule of energy. This is combined with the fact that the hydrogen is being expanded from a high pressure to a lower one, this being a function of how full the hydrogen tank is, and may be one cause of error between the model and test data. In general however, the trend in the simulated and experimental voltage are in good agreement. Larger errors arise at lower current densities due to the poorer fitting; however, with regards to the absolute error in predicted power accuracy at larger current densities is more critical.

Comparison of the model result to experimental under more real-world type load cycles is preferable to increase confidence in the model results. Figure 4.26b shows a comparison between the model results and experimental results under a HWFET drive cycle under pure FC mode operation. Air stoichiometry was set to a value of 2 with a feed forward controller for the blower. Fan and pump speeds were set to a constant value. It can be seen that under the scaled load cycle, the modelled voltages match the experimental values to a good degree of accuracy. Larger deviations in the no load potential are evident which arise due to the poorer fit at low current densities. Predicted temperatures are in good agreement. Unfortunately, coolant temperature measurements were unavailable due to a fault with those thermocouples during the test.

4.6 Transient response of the fuel cell

The transient performance of the FC is of critical importance and much varied from steady state performance due to gas manifolding effects, membrane hydration and thermal effects. These effects have different times scales, with gas manifolding occurring on the order of seconds, thermal effect taking on the order of seconds and minutes to take full effect and membrane hydration taking many minutes to hours to take full effect.

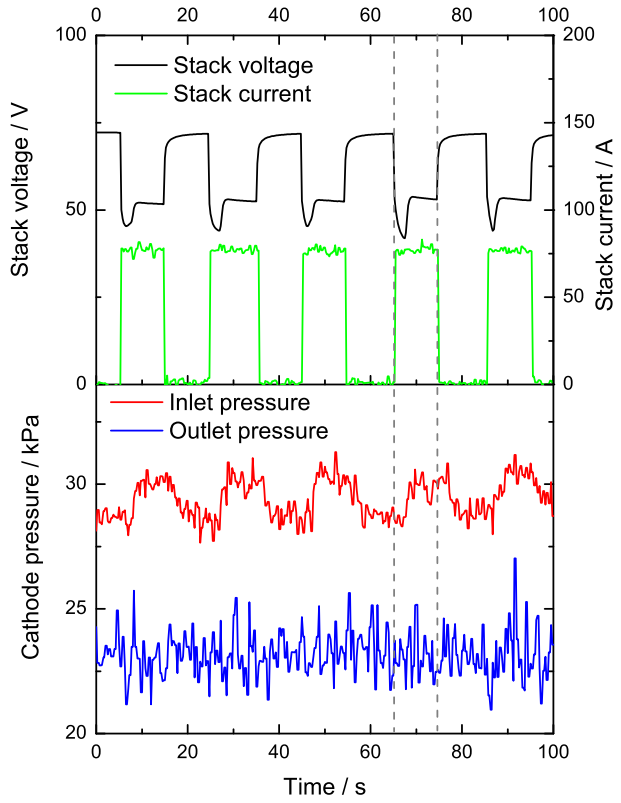


Figure 4.27: Stack voltage, current and cathode pressure during operation of the 75-cell system under step loads of 75A

Figure 4.27 shows the performance of the 75-cell stack under step loads of 75 A from no load conditions where the blower is operated with a feedforward control system. It can be seen that upon application of the load current the FC voltage drops instantaneously due to activation and ohmic losses; however, after the initial drop there is a slower continuous drop which is caused by the delay in the blower response time as inferred from the cathode inlet pressure. Locally, within the stack, the partial pressure of oxygen gets lower due to the near instantaneous electrochemical rate of oxygen consumption. The blower cannot supply the air fast enough and potential falls. Once the blower catches up, the stack potential increases again, with a slight overshoot due to the excess of oxygen supplied as suggested by earlier simulations due to the step load of the blower and the manifolding effect. Upon load removal, there is an instantaneous increase due to the reduced overpotentials but then there is a gradual increase in potential likely due to a combination of gas manifolding due to an excess of air being in the cathode and thus the higher pressure, and the double layer charging effects of the FC [115].

4.7 Comparison of models

With the model implemented and parameterised, different fidelities of the model were simulated to see the impact of different effects of the eventual result. Many authors in the academic literature make simplifying assumptions, such as isothermal conditions, no water hydration model or use a steady state look-up table for the polarisation curve. The critical metric for this work is to have a model that accurately models the efficiency of the FC as this will have an impact on the results of the hybrid system analysis.

Figure 4.28 shows the different fuel efficiencies under different automotive load cycles scaled for the validated 9.5 kWe stack with comparison of the efficiencies gained when using different models. Load cycles were generated from a vehicle model discussed in later chapters. Three cases have been considered: 25°C isothermal steady operation with fully

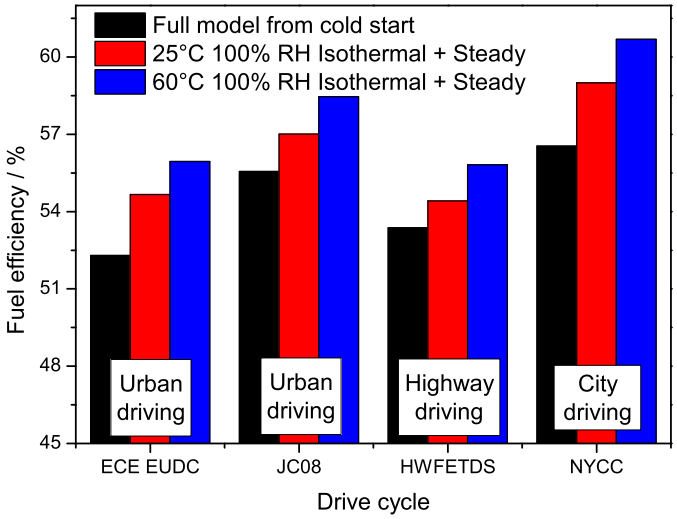


Figure 4.28: Comparison of the fuel efficiency assuming the Higher Heating Value of the FC model under isothermal steady state conditions and the full unsteady model from cold start conditions

humidified gases and membrane, 65°C isothermal steady operation with fully humidified gases and membrane and the unsteady model accounting for cold start conditions, partial membrane humidification and finite reactant delivery delay times due to gas manifolding and blower inertia. The fuel efficiency calculated is based on equation 6.21 which takes the Higher Heating Value (HHV) of hydrogen (285.84 kJ/mol).

$$\eta_{FC} = \frac{\text{Energy per mol of hydrogen}}{-\Delta \bar{h}_f} \tag{4.92}$$

It can be seen that the same trend in efficiencies is observed in all drive cycles with the 65°C fully humidified, steady and isothermal model giving the highest fuel efficiency. Comparison between that and 25°C operation under fully humidified conditions reduces efficiency by between 1.2-1.7%. Comparison then between the 65°C operating condition and the cold start, unsteady, partially humidified model results in differences in efficiency of between 2.9-4.2% with the NYCC and ECE EUDC drive cycles showing the most significant deviation due to lower average power consumption resulting in lower temperature operation and also higher transient loads compared to the other drive cycles resulting in greater mass transport losses due to lower reactant partial pressures from manifolding and inertia effects. This therefore highlights the need for transient models which account for the different phenomena occurring within the FC stack to avoid overestimation of the performance.

Further discussion of the implications of each different load cycle will be presented in later chapters.

4.8 Fuel cell start-up

The start-up of PEMFCs has previously been identified as one of the major causes of degradation in automotive applications. This has been attributed due to the internal currents which arise due to the formation of a hydrogen front as the hydrogen is introduced leading to local potential differences drive a currents. These internal currents can be significant with values of 1 A/cm^2 quoted in the literature [131]. In order to minimise the impact of this effect, nitrogen is used to purge to air from the anode volume prior to introduction of the hydrogen. Figure 4.29 shows the response of the 75-cell stack during start up.

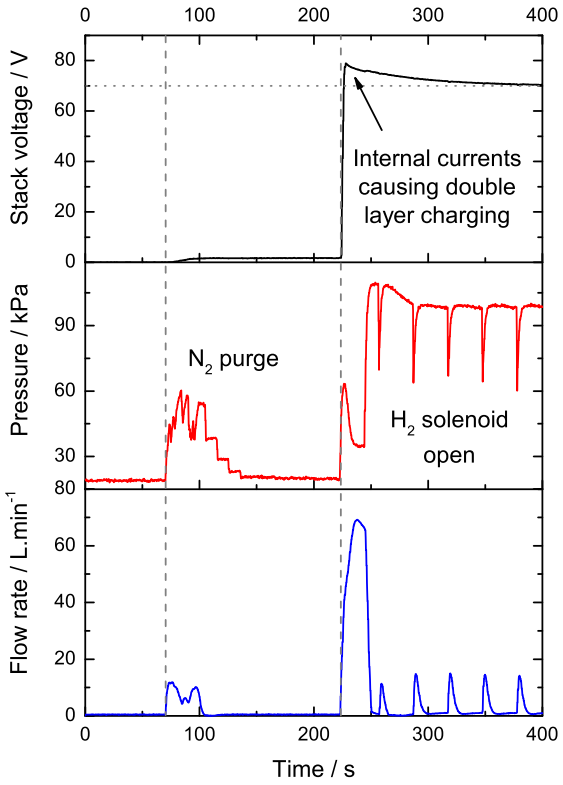


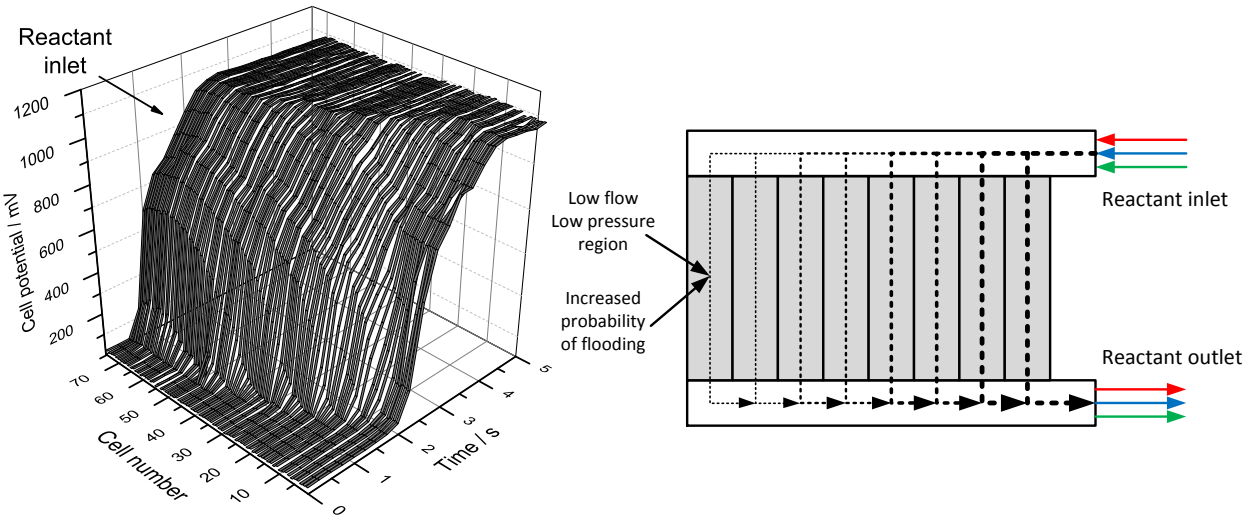
Figure 4.29: Stack voltage, pressure and flow rate start-up of the 75-cell FC stack

An initial nitrogen purge is observed where no significant cell voltages are observed. Upon introduction of the hydrogen the stack voltage increases rapidly and an overshoot in the stack voltage is observed, relative to the steady state voltage. This has been attributed to internal currents charging the double layer of the FC.

The Nedstack 9.5 kW stack has a U-shaped stack configuration where the air, hydrogen and cooling inlets/outlets are on the same side. Figure 4.30b shows a diagram of a U-shaped stack reactant configuration. As it can be seen the length of the reactant flow path varies from cell to cell, with cells furthest from the entrance of the stack having the longest path and therefore the highest pressure drop. This will likely result in cells furthest from the stack inlets having less flow than cells closest to the inlets.

Figure 4.30a shows the cell potentials during start-up. Hydrogen flow rate was 70 $L.min^{-1}$ and this was after a nitrogen purge. The reactant inlets are both near cell number 75. It can be seen that upon application of the hydrogen, the cell potentials increase rapidly however this increase is not uniform, with cells nearest the inlets rising first due to gas manifolding effects. Voltage increases up to a peak after which there is a small decrease due to the double layer effects.

This has implications from the point of view of water management and flooding of the system. As cells furthest from the inlets experience a lower pressure differential across an individual cell than cells closest to the inlet, this means water removal becomes more difficult. When the Nafion membrane is fully saturated with water, additionally produced water forms in the channels in the form of beads. These water beads can then block the flow field channels, preventing reactant diffusion. Locally, within a single cell the reactant depleted region will experience significantly higher overpotentials. As the global cell current must be the same as every other cell due to the series nature of a stacks construction, it can result in other regions of the cell experiencing extremely high current densities, localised heating and ultimately premature failure of the stack.



(a) (b)

Figure 4.30: (a) Cell potentials during the start-up of a PEMFC with a hydrogen flow rate of 70 L.min^{-1} after a nitrogen purge. Reactant inlets are at cell 75 and (b) Diagram of U-shaped stack reactant configuration

4.9 Thermal management

The thermal management system of the stack is of critical importance, both in respect of the efficiency and durability. Low temperature operation leads to increased inefficiencies due to slower chemical kinetics and also the increased risk of flooding at high current densities due to the reduced capacity of the reactant air to remove water. Excessively high temperatures leads to possible dehydration of the membrane leading to mechanical failure.

Figure 4.31a shows the main thermal problems of the stack during thermal transients to get the stack up to steady state temperature. The risk of applying maximum current upon cold start-up of the stack is the increased risk of flooding due to the high rates of water generation and limited capability of the reactant gases to remove the water due to the lower temperatures. Assuming that the temperature of the stack can be inferred from the coolant temperature, it can be seen that for an applied 80 A current on the 75-cell stack the rate of heat generation is approximately 3.1 °C/min. This will change as the temperature of the stack increases as the ohmic losses decrease; however, it becomes apparent that the thermal transient period is considerable.

It can be seen that in all cases the outlet of the stack is hotter than the inlet representing heat removal. The temperature of the coolant and the air follow each other much closer than the hydrogen temperature. This is partly due to the the lower heat transfer rates of the hydrogen humidifier compared to the air humidifier. The air heats up much more due to the recirculate air recovering waste heat from the humidifier. The oscillations in the temperature at the three stages represent when the PID cooling system was activated at different target temperatures. It can be seen from the power consumption that another disadvantage of operation at lower temperatures is that the required BOP power to maintain that temperature is higher for lower temperatures due to the smaller temperature difference to drive heat transfer for the radiator fan and also due to the higher rate of heat generation in the stack at lower temperatures due to increased losses.

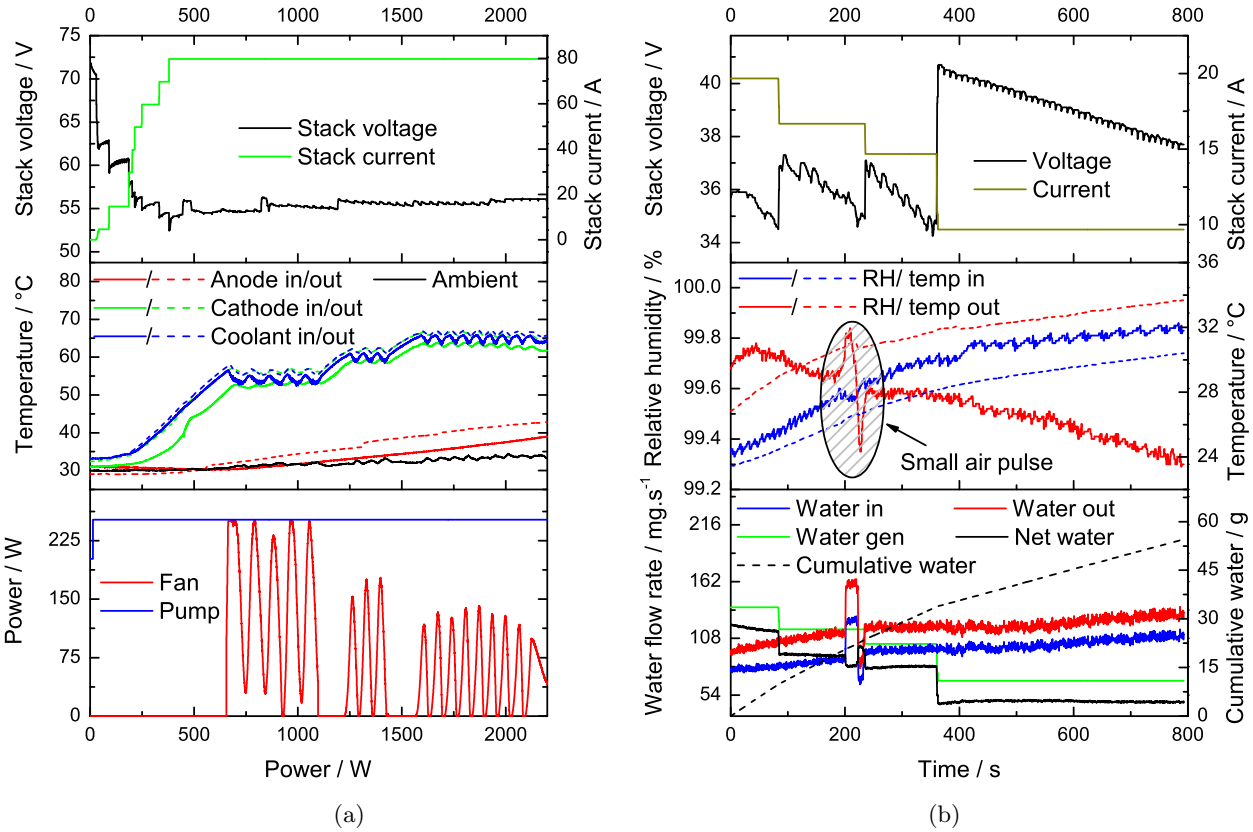


Figure 4.31: (a) Thermal properties of the 75-cell system during the heat up stage of the stack and (b) performance of 75 cell stack during flooding

4.10 Water management

Closely linked to thermal management is the water management of the system. Too low a water content leads to reduced conductivity of the Nafion membrane, too much water leads to the saturation of the membrane and GDL leading to the formation of liquid water in the stack, which if left unattended can prevent gas diffusion to the FC.

Indicative signs of stack flooding can be inferred from the stack voltage during constant current operation. Figure 4.31b show the performance of the stack during operation when flooding was occurring. It can be seen that under constant current operation the voltage decays at a constant rate. The smaller oscillations in the voltage are due to the regular hydrogen purging of the system. Measurements during this test were made with a constant ambient air flow rate of 4.8 g/s which represents an air stoichiometry of 9 at 20 A. As the stack voltage decayed the current was stepped down to avoid the stack voltage becoming too low. Upon reduction of the current the voltage recovered slight due to the lower ohmic overpotential however the decay in potential continued.

During operation it can also be seen that the outlet relative humidity started decreasing whilst the inlet increased suggesting that water is condensing within the stack. Conducting a water balance of the system using the temperature, pressure and relative humidity measurements show that whilst the outlet contains more water that the inlet this was not enough to offset the water generation from the FC reaction resulting in a net deficit of water meaning that this must have been condensed within the stack, assuming minimal water back diffusion to the anode. When the current was reduced to 10 A and water production decreased it can be seen that whilst the stack voltage does still decay the rate is slower which is likely to be attributed to slower rate of accumulation.

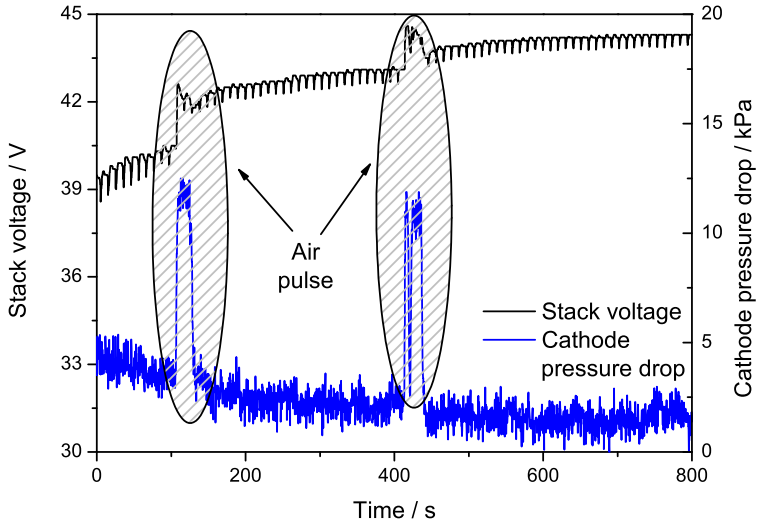


Figure 4.32: Stack voltage and cathode pressure drop of 75 cell 9.5 kW stack during constant current operation of 30 A

The fact that flooding occurs at high stoichiometries of 9 highlights the risk of operation at low temperatures and pressures due to the limited water carrying capabilities of the air.

One technique employed to remove the excess water was air purging of the system, where the blower power was increased momentarily to mechanically remove the water. Figure 4.32 shows the stack voltage and cathode side pressure drop of the 75 cell stack under two air pulses after a flooding event had occurred. It can be seen that upon application of the air pulse the stack voltage significantly increased upon the first pulse and the pressure drop decreased. The second pulse had similar effects but smaller in magnitude, likely due to water having been removed already. The oscillations in the stack voltage are due to the periodic purging of the anode side which also helps with removing water but to a much smaller extent.

4.11 Stack failure through flooding and pin-hole formation

In large PEMFC systems for automotive systems, where stacks of hundreds of cells are often used, significant inhomogenities in both the reactant distribution and temperature can lead to large variations in the cell potential and current density. This can be caused by a number of factors such as stack design, operating conditions etc. Figure 4.33 shows the 75 cell voltages of a 9.5 kW PEMFC stack during a 5 kW test.

In figure 4.33 the reactant inlets are nearest cell 75. It can be seen that since the inlets and outlets for the stack are on the same side the pressure drop across the first cell will therefore be lower than that of the last cell. The effect this will have is that reactants will preferentially flow through the first cell. This is confirmed by the fact that upon partial start-up of the stack when hydrogen is flowed through the system the cells nearest cell 75 increase their cell potentials faster than cells further from the inlet/outlets.

Figure 4.34 shows the cell voltages during a 6 kW test where a stack failure occurred.

It can be seen that at a time step of approximately 1500 s, cells 11-13 experiences an abrupt drop in potential. Prior to failure, this region was exhibiting higher overpotentials, possibly indicating flooding events as formation of liquid water on the GDL would result in increased mass transport losses due to limited gas diffusion. After the fall in cell voltage was observed, the load was removed from the FC, hydrogen supply closed and an unassisted shut-down was performed. In this case an external load was not applied to

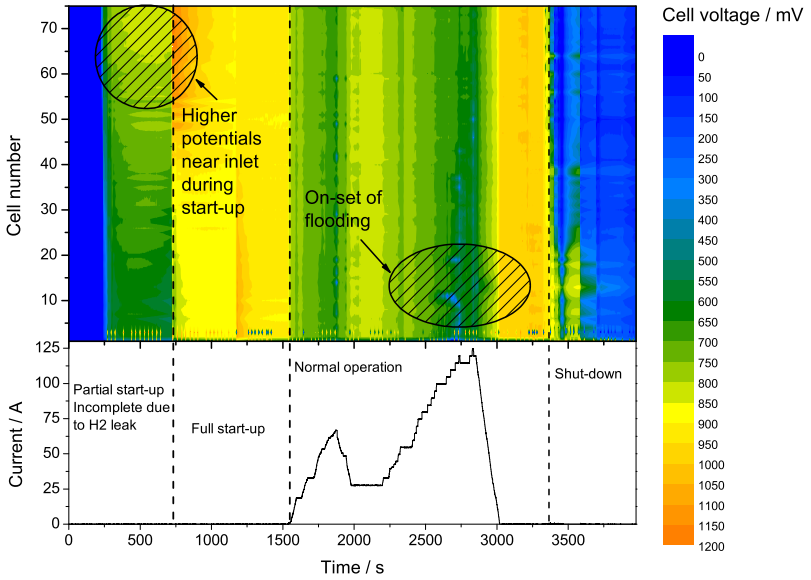


Figure 4.33: Cell voltages and stack current during a 5 kW test of a 9.5 kWe PEMFC stack

consume all remaining hydrogen in the GDL and gas manifolds due to the fault.

Subsequently, the stack was started up again under no load conditions under hydrogen and nitrogen atmospheres on the anode. The cell voltages and pressures during this test are shown in figure 4.35.

From the CVM data it can be seen that upon application of the hydrogen the cells which failed continue to have a zero potential; however, over time it causes the surrounding cells to have an erratic voltage fluctuations. The cause of this has been attributed to the bipolar nature of the FC flow plates. Inhomogenous current distributions in one cell can cascade to other cells as shown by the work by Lin *et al.* [125].

Figure 4.36 shows the cell potentials of the 75-cell stack after the pin-hole formation. It can be seen that upon application of hydrogen at a time step of 440 s all cell potentials initially increase to their OCV value apart from cells 11-13 which have been identified as the source of the pin-hole formation. After this cells beyond the pin-hole formation drop in potential back to 0 V extremely rapidly. Cells closer to the reactant inlets subsequently gradually drop in potential with this effect cascading from the location of the pin-hole. Once the hydrogen pressure had reached a steady state, indicating that

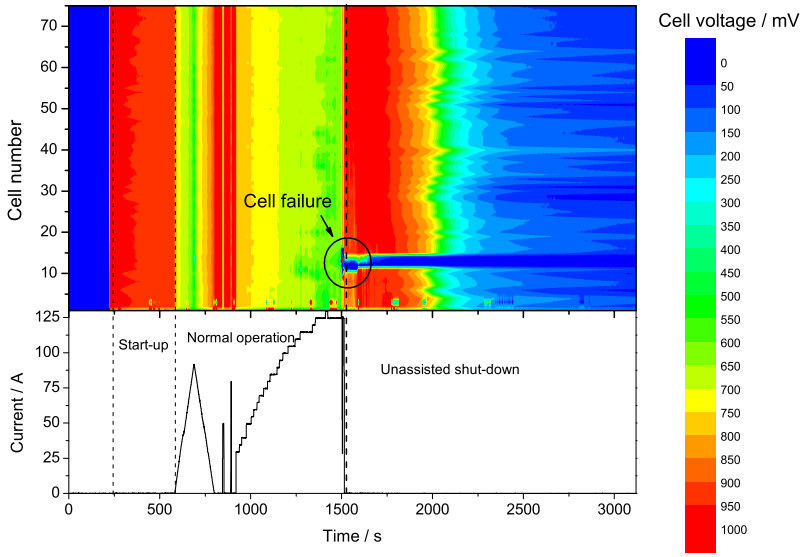


Figure 4.34: Cell voltages and stack current during a 6 kW test of a 9.5 kWe PEMFC stack with failure event

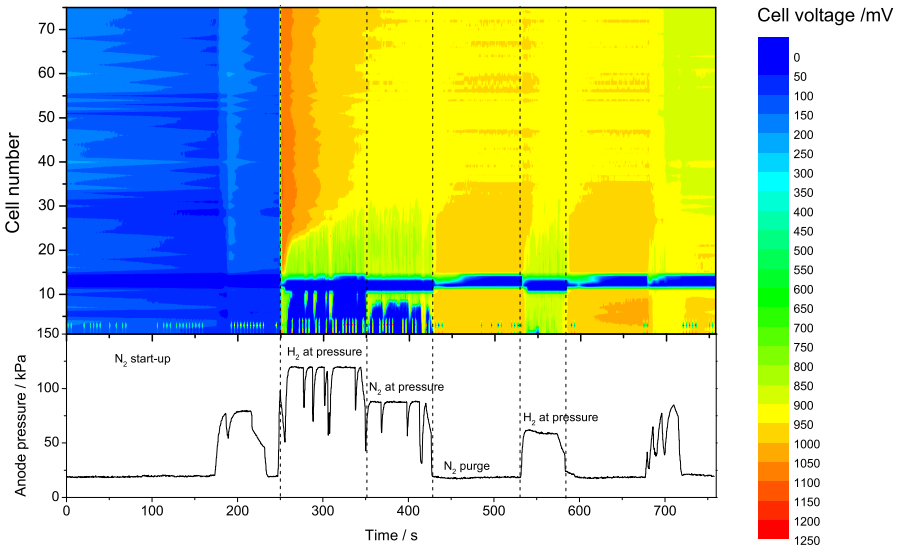
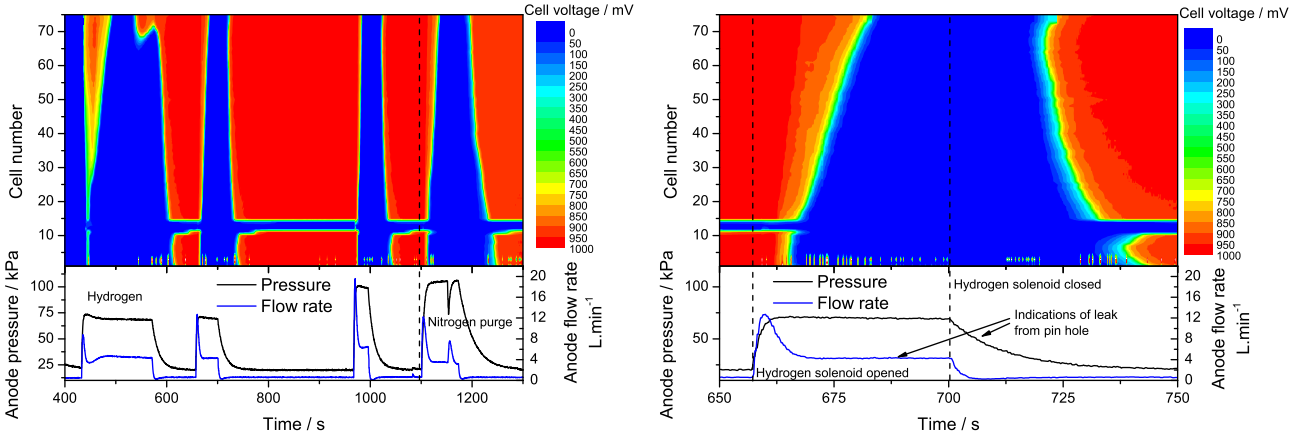


Figure 4.35: Cell voltages of a 9.5 kW PEMFC after pin-hole formation under hydrogen and nitrogen pressure with no external load applied

the manifolds have filled with hydrogen, the flow meter indicates a steady flow. This therefore suggests that hydrogen is crossing over from the anode to the cathode due to the pin hole since the anode is normally operated in a closed mode. Upon closing of the hydrogen solenoid, the pressure of the anode decreases supporting the earlier suggestion. The possible cause of the potential drop is attributed to the cross-over of hydrogen from the anode to the cathode resulting in a hydrogen-hydrogen system and therefore no potential difference being generated. Hydrogen crosses over from the anode to cathode rather than the other way around as the anode pressure is higher than the cathode pressure.

Figure 4.37 shows the cell voltages at a time step of 660 s in 5 s increments to visualize this effect more clearly.

At a time step of 660s the anode compartment is at ambient pressure as it has just been purged. All cell voltages are approximately at an OCV value of 1 V apart from the aforementioned failed cells. Upon application of hydrogen pressure of 70 kPa the cells next to the pin hole towards the end of the stack decay in potential. Cells increasingly



(a) (b)

Figure 4.36: Cell voltages of a 75-cell 9.5 kW PEMFC after pin-hole formation (a) and close up of one hydrogen pressurisation event (b)

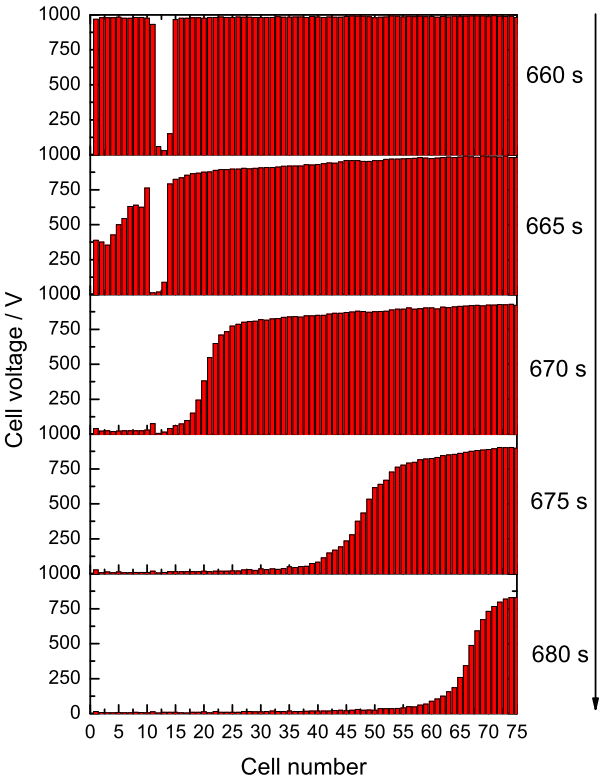


Figure 4.37: Bar chart plot of cell voltages during cascading potential fall

closer to the reactant inlet from the pin-hole decrease in cell potential. This potential drop continues, taking approximately 40 s to propagate to all cells after pressurizing the anode. Hydrogen crossover from the anode to the cathode is the likely cause of this resulting in a potential difference of 0V in the eventual H_2/H_2 cell.

4.12 Stack shut-down

After operation, rapid shut-down of the stack is ideal to lower the potential of the cells to minimise the rate of carbon corrosion. After the hydrogen solenoids are closed, residual hydrogen in the anode manifolds keeps the stack at elevated potentials. Internal currents and gas crossover would remove all hydrogen to return the cell potential back to 0 V, however the time required for this can be quite significant and not ideal from a durability perspective. To assist with shut-down, nitrogen is purged in the anode to remove hydrogen in the gas manifold volume. Adsorbed in the GDL is more difficult to remove and therefore a load is typically applied to consume the remaining adsorbed hydrogen.

Figure 4.38 shows the cell potentials during shut-down. Here a constant voltage load is applied to the stack gradually from 70 V down to 30 V in 5 V increments. As it can be seen the nitrogen flushing is more effective nearer the gas inlets/outlets due to the greater pressure difference. During shut-down, since the same current flows through each cell as they are in series, cells closest to the inlet/outlet reach lower potentials faster. Figure 4.38 shows that when cell 75 has reached a potential of 100 mV cell 1 is still at a potential of 600 mV. At this stage further loading of the FC may result in the inversion of the cell potential which is not idle as it causes catalyst coarsening by reactant starvation decreasing FC durability.

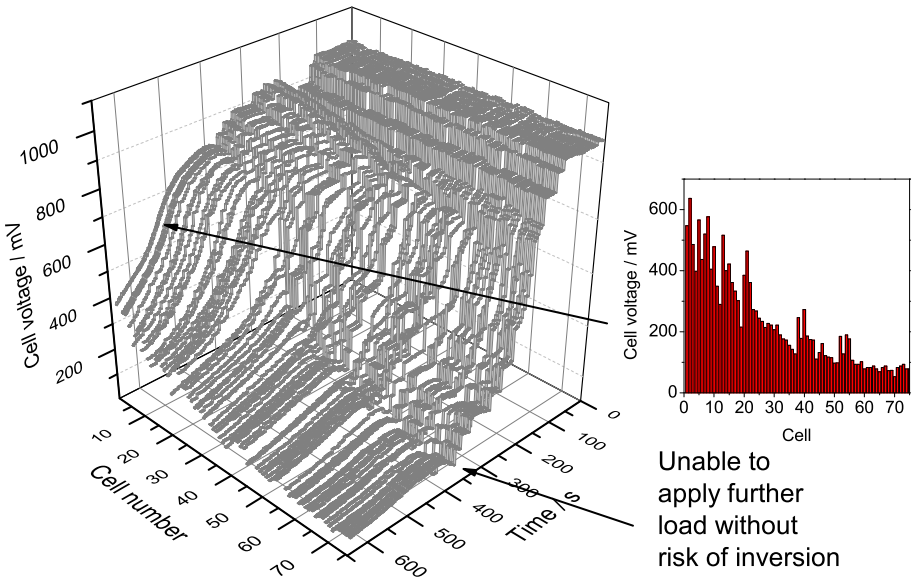


Figure 4.38: Cell voltage data during operation and shut-down showing inhomogenities in cell voltage limiting the shut-down procedure

4.13 Conclusion

4.13.1 Fuel cell modelling

A semi-empirical/physics based model of the FC stack and associated BOP has been presented. This accounts for heat and mass transients which are critical to assess when modelling efficiencies of FC systems, as well as incorporating a membrane hydration model. This provides the framework for later system level analysis work of hybridised systems. Comparison of different model fidelities showed that for typical automotive load cycles, fuel efficiency overestimations of up to 4.2% can be experienced when comparing against isothermal, steady models.

Simulations suggest that the compressor response time compounded with manifolding effects can result in reactant delivery delays on the order of seconds which can lead to additional mass transport losses due to lower reactant partial pressures.

4.13.2 Development of 9.5 kWe PEMFC system

In order to validate the developed model a 75-cell 9.5 kWe PEMFC system was created with in-house developed BOP components and controllers. The control of the system was achieved by use of a NI compactRIO running LabVIEW with a user defined interface system. All control logic and systems were developed in house and mainly used feedforward controllers for the air system and PID based control system for temperature regulation. Optimisation and analysis showed that to minimise BOP power consumption from the cooling system, a constant pump speed with vary fan speed was ideal for lower FC power. At higher rates of heat generation, increases in the coolant flow rate have a more significant impact.

After parameterisation of the polarisation curve, the dynamic response of the voltage showed good agreement with the modelled data and similarly the temperatures of the reactant hydrogen, air and coolant showed good agreement. The model was not able to

capture start-up effects where double layer charging effects were evident but this was outside the scope of work.

Transient response analysis showed that under step loads with feedforward controllers the FC voltage does indeed suffer from additional losses due to the finite time required to deliver the reactants.

Analysis of the start-up characteristics of the FC stack suggested that even with nitrogen purging significant internal currents can arise which were observed in the form of a voltage overshoot during start-up above the thermodynamic potential of the stack. CVM measurements suggest that due to the size of the stack, significant delays in the reactant delivery within the stack itself is evident and the U-shaped configuration of its construction leads to uneven pressure drops and thus reactant flow rates through each cell.

Analysis of the thermal transient data suggests significant time constants, on the order of minutes, are present for the heating of the stack under no external heating. This has implications in terms of water management where it was shown that even at an operating stoichiometry of 9, at low temperatures and low pressures the water carry capability of the air is significantly limited such that the water balance inside the stack results in deposition of liquid phase water and the onset of flooding leading to significant performance decay. Use of air purging was seen as a means of removing excess water and recovering performance.

4.13.3 Fuel cell failure through pin-hole formation

Low pressure operation with U-shaped FC stacks run the risk of stack flooding at high current densities due to the inability to remove liquid water products from deep within the stack where the driving pressure differential is smaller. Low temperatures can further agitate the problem with water balance calculations showing that during initial operation of the stack, operating stoichiometries in excess of 9 were not sufficient to prevent water accumulation within the stack. This water can then block areas of an MEA leading to localised heating and reduction of mechanical strength. Purge events where the pressure differential can incur a mechanical stress can then lead to pin-hole formation within the MEA. The result is that there is a cascade effect where all other cells within the stack drop in potential, with the cascade originating from the failure point. This has been attributed to the cross over of hydrogen to the cathode side thereby reducing the potential difference. Under no-load conditions after the pin-hole formation unstable behaviour of neighbouring cells around the failure point were observed suggesting internal currents were causing the cascading effect due to the bipolar electronic coupling of the plates.

Experimental results also suggest that after the pin-hole formation internal currents are present under no-load conditions which result in unstable potential profiles in neighboring cells due to the bipolar coupling and relatively large in-plane to through plane resistance of the bipolar plates.

Closing remarks

This chapter sets the mathematical framework for the development of a FC stack and BOP model that allows for accurate modelling of the transient performance of the FC stack over a range of time scales. The model has been experimentally validated against data from a 75 cell 9.5 kWe system with insight gained into the real world requirements of operating large PEMFC system and potential failure points. This model with thus be used in later chapters for system level analysis.

Chapter 5

Electrochemical Double Layer Capacitors

5.1 Introduction: Electrochemical Double Layer Capacitors

This chapter outlines the modelling and validation work done on supercapacitors. The work probes supercapacitor limits of operation in automotive applications and provides the foundation for later analysis of whole systems efficiencies for powertrains using supercapacitors. This chapter therefore contains the following sections.

- **Modelling of supercapacitors**
  - This section outlines the modelling framework used to develop a dynamic model of a supercapacitor with an equivalent circuit based model that accounts for variable capacitance and the charge redistribution effect
- **Experimental set-up and parameterisation**
  - This section details the experimental set-up used to acquire the data required for the model parameterization and validation of the model
- **Analysis of supercapacitor performance metrics**
  - This section presents the work done on analysing the performance metrics of supercapacitors, including the variation of capacitance as a function of operating potential and frequency
- **Novel techniques for performance analysis**
  - This section outlines a novel technique proposed to predict the low frequency capacitance of a supercapacitor without having to scan to lower frequencies by the use of a complex capacitance Nyquist plot

5.2 Supercapacitor modelling

Analysis of the academic literature showed that the majority of works use equivalent circuit models of supercapacitors of varying degrees of complexity. The main physical phenomena to capture were identified as being the charge redistribution effect, variable capacitance as a function of voltage and capacitance dependency with frequency. Relative to batteries and FCs, supercapacitors have a much longer lifetime and lower impedance, meaning that degradation and thermal management are less of an issue and thus were secondary to accurate modelling of the voltage response. As such, the modelling and validation of supercapacitors will focus on a equivalent circuit based model. Thermal coupling and degradation will not be captured in this model.

The work by de Levie [118] on the capacitance effects of porous electrodes showed that current and potential profiles within electrodes was not uniform due to the increased ionic resistance within nano-meso sized pores the deeper inside the pore you go. To account for this, authors have proposed a transmission line type model to account for the increase in resistance in order to reach all of the surface area in supercapacitors [21, 159].

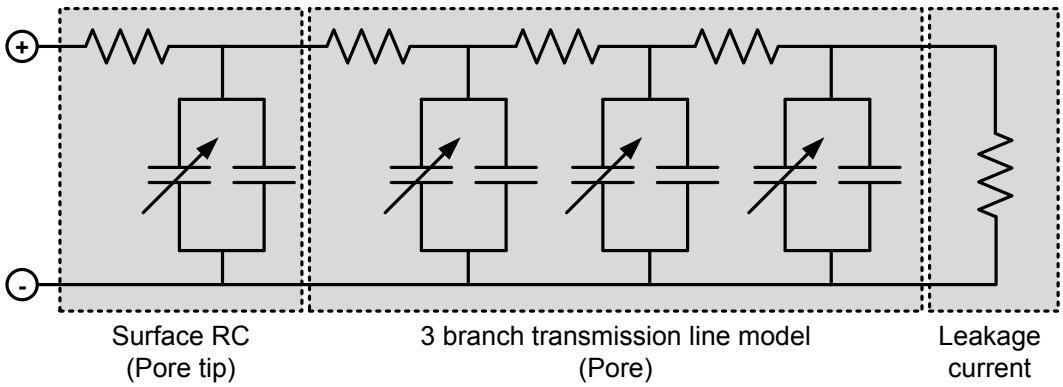


Figure 5.1: Transmission line equivalent circuit model of a supercapacitor

The charge storage ability of supercapacitors is directly proportional to the available surface area of the electrode materials. Supercapacitors have higher energy densities relative to traditional electrolytic capacitors due to the maximisation of the surface area of the electrodes by using porous materials such as activated carbons. The approach taken to modelling the performance of supercapacitors is based on the use of resistors and capacitors to create a transmission line model.

Figure 5.1 shows a diagram of the model and how different parts of the model represents different time constants. Inductive behaviour has been ignored as the typical inductance for a supercapacitor is on the order of nHs and thus the time constant of the process would not cause appreciable differences in the results. Addition of inductive elements would also slow later simulation speeds. The surface RC portion of the model accounts for the pore tip performance and series resistance from the material ohmic resistance and bulk ionic resistance. The transmission line portion of the model then accounts for the slower diffusion of ions within the smaller pores of the supercapacitors. Authors in the literature have previously commented on the fact that the surface capacitance is a small fraction of the total capacitance. The last part of the model is a leakage current resistor which accounts for the slow self-discharge effects in supercapacitors. This has the slowest time constant.

This model was implemented in the MATLAB's Simulink environment with the Simpower systems toolbox. This was mainly due the fact that it will allow for later integration of the supercapacitor model with other models, as described in previous chapters, and also due to the fact that the Simpower systems toolbox has ready made electrical elements and solvers for ease of implementation.

5.3 Experimental set-up

In order to parameterise the model, tests were performed to extract the information needed to parameterise the model. In later sections two distinct scales of systems will be experimentally investigated and thus the choice of supercapacitors experimentally investigated were the Maxwell BCAP0150 and BCAP1500 which have respective capacitances of 150F and 1500F.

Figure 5.2 shows the experimental set-up used to test the supercapacitors. An Autolab potentiostat with 10A booster was used to conduct all potentiometric and EIS measurements. Due to the relatively low impedance characteristics of supercapacitors, it was very important to conduct the tests under 4-electrode mode in order to isolate the effects of contact resistance from the connection between the potentiostat and cell terminals.

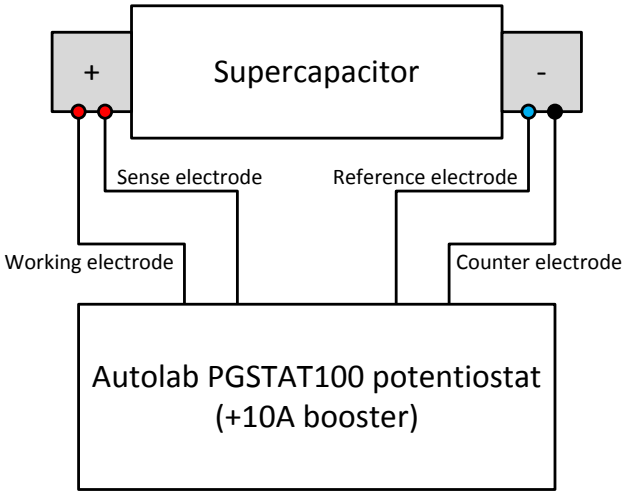


Figure 5.2: Experimental set-up used to characterise a supercapacitor

5.3.1 EIS measurements

The use of EIS allows for the decoupling of different effects occurring within the supercapacitor that would previously not be possible under chromopotentiometry mode, and also gives insight into the frequency dependency of these effects.

The EIS measurements were done at set voltages. The below lists the procedure followed for the 1500 F supercapacitor tested:

1. Charge supercapacitor at 1A under chromopotentiometry to target potential
2. Once target potential is achieved switch to chromoamperometry mode and keep charging until the current drops below 10 mA
3. Remove load from the supercapacitor and let it settle for 30 minutes
4. perform EIS measurements under poteniostatic mode with a 1 A RMS current
5. Repeat as needed

The procedure for the 150 F supercapacitor was the same however the current threshold was set to 1 mA and RMS current excitation signal was set to 200 mA. These values were found to give the best noise to signal ratio whilst keeping the system linear.

From the real and imaginary components, and the shape of the EIS plot, a number of different metrics can be calculated. For example the capacitance as a function of frequency. Whilst many authors in the academic literature have used the simple approximation of only considering the imaginary component as a representative metric of the capacitance according to equation 5.1, it is believed a better approximation is achieved by considering the influence of both real and imaginary components. Often using the simple approximation a "resonance point" is measured where the capacitance value tends to infinity as the imaginary component of the impedance switches from inductive to capacitive behaviour. This, we believe is inaccurate and arises due to the nature of the expression given by the simple approximation.

$$C = -\frac{1}{2}\pi f \mathrm{Im(Z)} \tag{5.1}$$

A better approximation would be to consider the contributions from the real and imaginary capacitances as suggested by Taberna and Simon [195] with the form given in equations 5.2-5.4.

$$C_{Tot} = C_{Re} - jC_{Im} \tag{5.2}$$

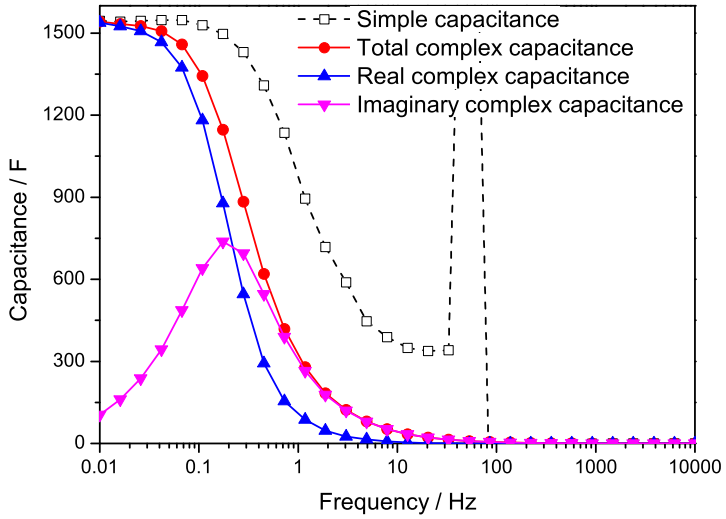


Figure 5.3: Comparison of different methods of calculating capacitance from EIS data for a 1500 F Maxwell supercapacitor at 2.7 V and room temperature. Dashed lines represents the simple method. Solid lines represent the complex method.

$$C_{Re} = -\frac{Z_{Im}}{\omega}|Z|^2 \tag{5.3}$$

$$C_{Im} = \frac{Z_{Re}}{\omega|Z|^2} \tag{5.4}$$

Figure 5.3 shows the capacitance-bode plot for a 1500 F Maxwell supercapacitor at 2.7 V and room temperature using the simple and complex methods for finding the capacitance as a function of frequency from the impedance data.

It can be seen in the case of the simple approximation, at the "resonant frequency" the capacitance tends to infinity which is not a feasible result. Relative to the complex method, which considers the real and imaginary components, the simple method overestimates the capacitance at higher frequencies as the transition point from full capacitance to zero capacitance is suggested to occur at higher frequencies than according to the complex method. However, the low frequency capacitance does tend to the same solution.

The impedance of the cell also varies with the cell voltage. A typical equivalent circuit of a supercapacitor has an inductor in series with a resistance which is in series with a constant phase element to represent the porous effects of the porous electrode de Levie equation as shown in equation 5.5 [53].

$$Z_p = \sqrt{R_i Z_i}\coth\sqrt{R_i/Z_i} \tag{5.5}$$

Where R_i is ionic resistance inside the pores and Z_i is the interfacial resistance which, in absence of any Faradaic process, is simply a capacitance of Double Layer (DL): $Z_i = 1/(jC_{DL})$. It then follows that the equation can be re-arranged to give equation 5.6-5.7.

$$Z_P = R_i\frac{\coth\sqrt{\mathrm{j}\omega\tau}}{\sqrt{j\omega\tau}} \tag{5.6}$$

$$\tau = R_i C_{DL} \tag{5.7}$$

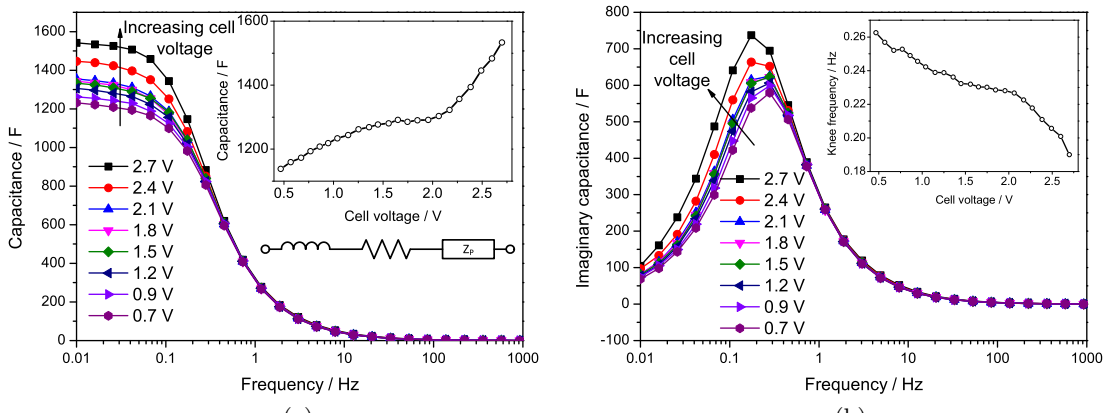
This approach to calculating the double layer capacitance is taken to be a more suitable method than taking the low frequency capacitance from the capacitance Bode plot as the frequency would have the tend to infinity in order to get the correct answer.

5.3.2 1500 F supercapacitor

Characterisation of the 1500 F supercapacitor will be useful in later chapters during the construction of testing of a large scale test rig.

Figure 5.4a shows the Bode plot of the total capacitance of the supercapacitor for different steady state cell voltages. Capacitance is shown to be frequency dependent; at higher frequencies AC signals cannot penetrate into mesopores thus limiting the active surface area for ionic absorption resulting in a lower capacitance. At lower frequency, ions have sufficient time to diffuse into all pores and access the full surface area [102]. At higher potentials the measured capacitance is greater. Explanations for this effect vary in the literature but include: possible reduction of the solvent layer thickness caused by increasing coulombic forces on the ions when the electric field of the double layer is increased, increase of the solvent dielectric constant caused by the compression of the solvent layer [88], increase in the electronic state density in the carbon pore walls with voltage [92] and the potential dependency of ionic penetration in nanopores [176]. The inset of figure 5.4a shows the correlation between low frequency capacitance and cell potential. This was calculated by fitting the EIS data to the inset equivalent circuit in figure 5.4a and deriving the capacitance from the parameters of the pore impedance (Z_P). At 2.7 V a capacitance of 1533 F was measured compared with 1138 F at 0.47 V resulting in a decrease of 25.8 % or 177 F.V^{-1} if a linear correlation is assumed. Therefore, to achieve the highest capacitance the operating potential should be as high as possible.

Figure 5.4b shows the Bode plot for the imaginary component of the capacitance for different steady state cell voltages. The peak value in the imaginary impedance represents half of the low frequency capacitance and occurs at a frequency known as the knee frequency which represents the boundary between full access of the electrode surface area and the electrolyte penetration region. This frequency also represents the 50%



(a) (b)

Figure 5.4: (a) Bode plot of total capacitance for a 1500 F Maxwell supercapacitor at different voltages with inset showing low frequency capacitance as a function of steady state cell voltage at a temperature of 20 °C and (b) Bode plot of imaginary capacitance at different cell voltages. Inset shows the knee frequency dependency with cell voltage at 20 °C

median charge storage efficiency [195]. The inset in figure 5.4b shows the voltage dependency of the knee frequency. Due to the discrete measurement frequency of the EIS measurements, fitting of the curve allowed for a more accurate estimate of the knee frequency. The exact value for the knee frequency was estimated by fitting the natural log of the frequency-imaginary capacitance data to a Gaussian distribution in the form shown in equation 5.8 where μ is the mean and σ is the standard deviation. In this case $F(f)$ represents the imaginary capacitance and f is the natural log of the frequency (Hz). Taking the first derivative with respect to x results in equation 5.9, where $A = 1/\sigma\sqrt{2\pi}$. Setting the first derivative to zero and solving for the frequency finds the inflection point, or maximum in this case, which occurs when $f = \mu$.

$$F(f) = \frac{1}{\sigma\sqrt{2\pi}}\exp\left(-\left(\frac{f-\mu}{2\sigma}\right)^2\right) \tag{5.8}$$

$$\frac{dF(f)}{df} = \frac{A\mu\exp\left(-\left(\frac{\mu-f}{2\sigma}\right)^2\right)}{2\sigma^2} - \frac{Af\exp\left(-\left(\frac{\mu-f}{2\sigma}\right)^2\right)}{2\sigma^2} \tag{5.9}$$

As potential of the cell decreases it can be seen that the knee frequency increases with values of 0.19 Hz at 2.7 V and 0.26 Hz at 0.47 V giving a rate of change of -30.4 mHz.V^{-1}. Therefore, at higher potentials it is more difficult to access the full pore depth. This is perhaps due to the decrease in effective pore radius as the adsorbed ionic double layer becomes thicker with higher cell voltage, thus occupying the free pore space. It also becomes apparent that below the knee frequency, the complex and real capacitance becomes cell voltage independent.

The impedance of the cell also varies with the cell voltage. Figure 5.5 shows the fitted EIS results for the series and diffusion impedances. As SOC decreases, the series impedance increases. Series resistance consists of the electronic resistance of the electrodes, contact resistances and bulk electrolyte resistances. As the series resistance is measured at high frequencies, ions do not have sufficient time to penetrate the full depth of the pore nor cell [102]. The observed decrease in series resistance is likely due to an increase in electronic conductivity of the carbon electrodes due to an increase in the electronic state density [92]. For the diffusion resistance, at higher SOCs the resistance increases, this is due to the lower concentration of ions in the electrolyte as in the more charged state, more ions move to the double layer, therefore reducing the ionic conductivity of

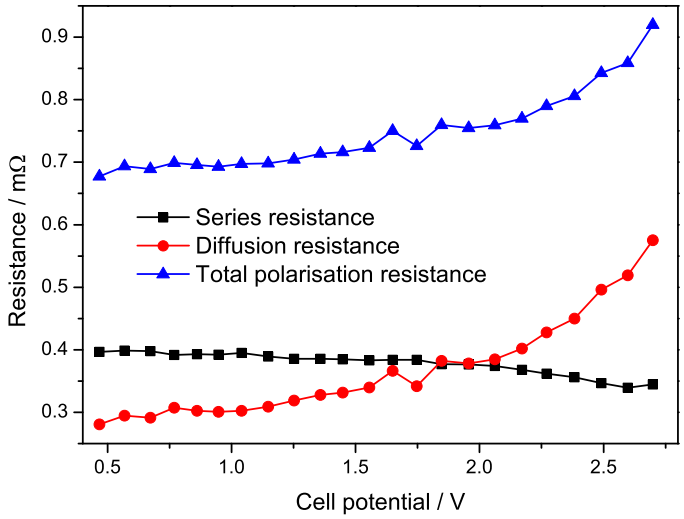


Figure 5.5: Fitted resistances of a 1500 F Maxwell supercapacitor at room temperature

the electrolyte. The total polarisation that the cell experiences though increases with increasing SOC due to the dominating effect of reduced electrolyte conductivity within the bulk electrolyte. The impedance of a single 1500 F supercapacitor is therefore between 0.68-0.92 mΩ.

Novel method of extracting low frequency capacitance

As both the real and imaginary components of the capacitance are available, it is also possible to present the complex capacitance data in the form of a Nyquist plot in a similar fashion to Nyquist plots of impedance. This is shown in figure 5.6a for different cell voltages. The same trends can be concluded; however, relationship between the complex variations of capacitance is now more evident, as is the low frequency capacitance which is the point at which the semi-depressed circle would meet the x-axis if extrapolated forward.

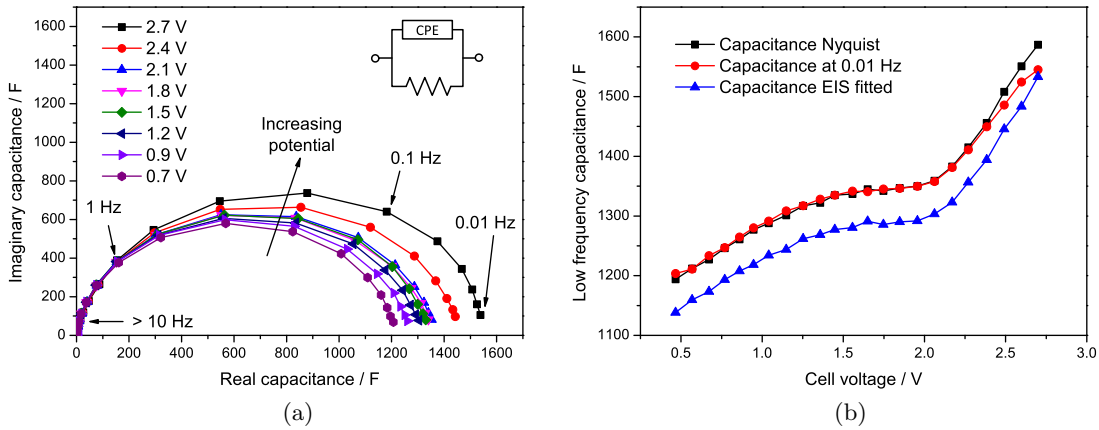
This was fitted against the inset equivalent circuit of figure 5.6a which was found to best fit the complex capacitance plot for frequencies <10 Hz. If frequencies above were considered the inductive effects cause complications in the fitting due to no electrical element having the same response when considering the complex capacitance. In this equivalent circuit, the resistive element represents the low frequency capacitance. Figure 5.6b shows a comparison of the capacitance values from the different techniques: capacitance Nyquist, capacitance at low frequencies (0.01 Hz) and capacitance derived from the EIS fitted parameters.

It can be seen that in all cases the general trend is the same. The capacitance Nyquist matches with with low frequency capacitance trend quite well. However, both of these overestimate the values derived from the EIS fitted parameters.

5.3.3 150F supercapacitor

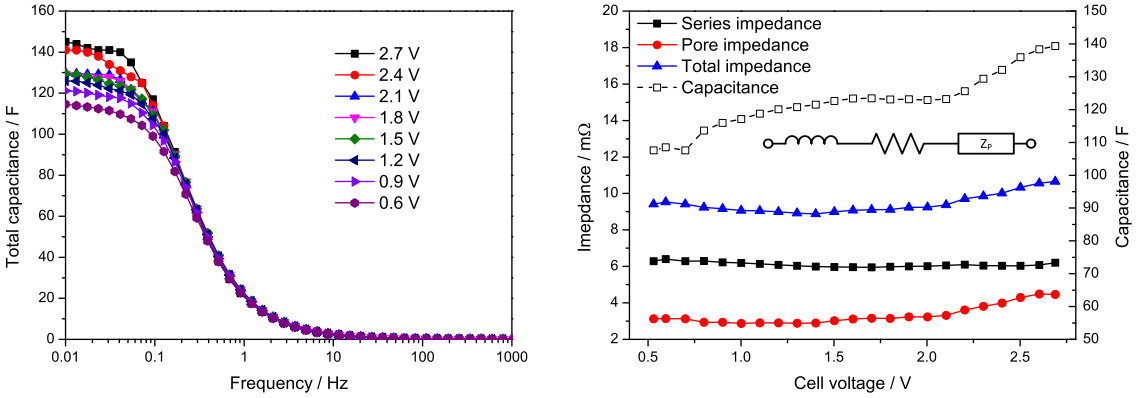
The same analysis as the 1500 F supercapacitors can also be performed on the 150 F supercapacitors. This analysis will be useful in later chapters during the development of a scaled down hybrid electric vehicle test rig.

Figure 5.7a shows the Bode plot of the total complex capacitance and 5.7b shows the impedance and low frequency capacitance dependency with cell voltage for a Maxwell 150 F supercapacitor. Figure 5.8a shows the imaginary capacitance component of a 150



(a) (b)

Figure 5.6: (a) Nyquist plot of complex capacitance for a 1500 F Maxwell supercapacitor for different potentials at 20 °C (inset shows the equivalent circuit used to fit it) and (b) comparison of different techniques used to extrapolate low frequency capacitance



(a) (b)

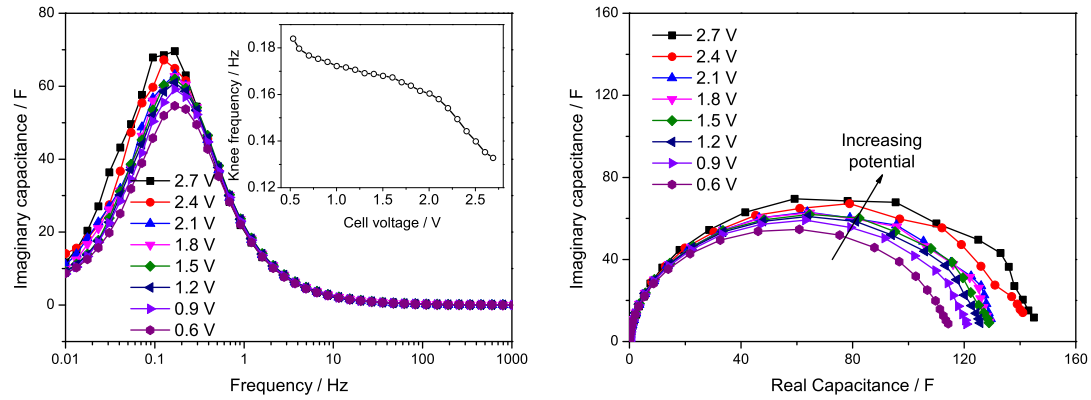
Figure 5.7: (a) Bode plot of total capacitance at different cell voltages of a 150 F Maxwell supercapacitor. Inset indicating the cell voltage-knee frequency relationship and (b) Impedance and capacitance for a 150 F Maxwell supercapacitor at different cell voltages

F Maxwell supercapacitor. The inset shows the cell voltage-knee frequency relationship. Figure 5.8b then shows the capacitance Nyquist plot.

5.3.4 Comparison between small and large cell

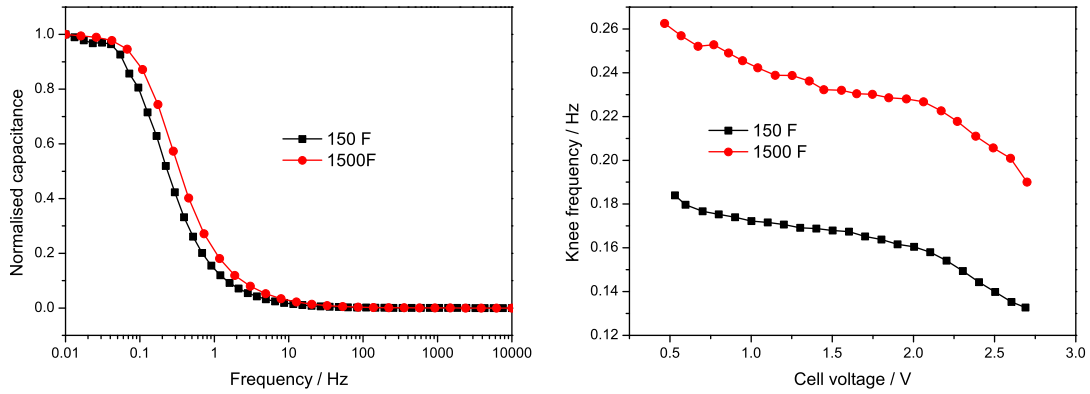
The differences in the resistance of a large and smaller cell are evident and commonly acknowledged due to the difference in the area of electrodes use. However, no studies have looked at the differences in the knee frequency of supercapacitors of different devices which is important in determining the limitations of performance when operated at higher frequencies, where limitations of ionic diffusivity are reduce the capacitive performance as the ionic movement cannot follow the rapid changes in the applied potential field.

Figure 5.9 shows how the knee frequency varies at different potentials for a small and large supercapacitor. It can be seen that in both cases with a increase in operating potential the knee frequency decreases which can perhaps be attributed to the increased ionic packing of the pores of the porous electrodes, limiting further the ionic resistance and thus the ability to access the capacitance of deeper pores. The difference between the two devices however is that the larger 1500 F supercapacitor has a higher knee



(a) (b)

Figure 5.8: (a)Bode plot of impedance capacitance at different cell voltages of a 150 F Maxwell supercapacitor. Inset indicating the cell voltage-knee frequency relationship and (b) Nyquist plot of capacitance for a 150 F Maxwell supercapacitor at different cell voltages

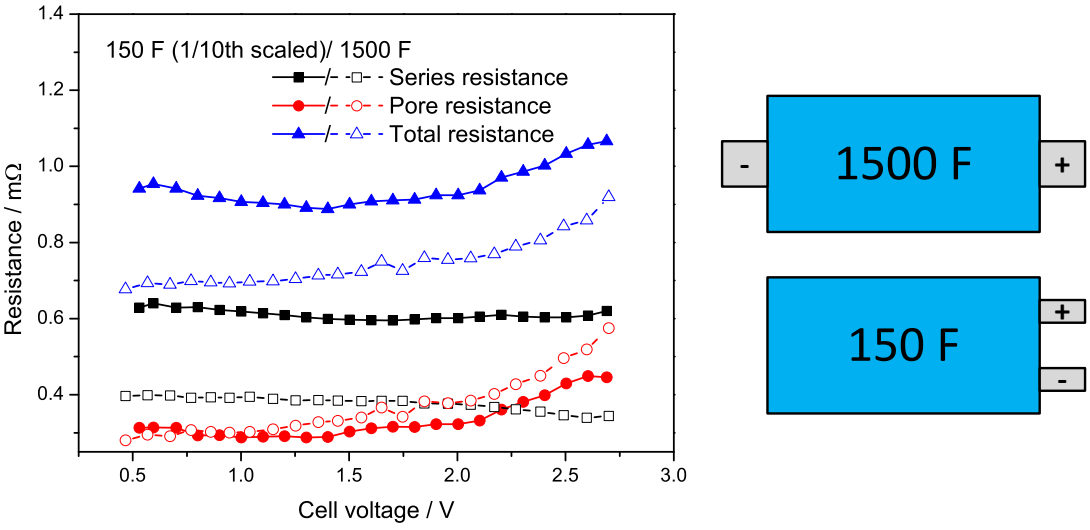


(a) (b)

Figure 5.9: (a) Normalised capacitance bode plot for a 150 F and 1500 F supercapacitor and (b) comparison of the knee frequencies

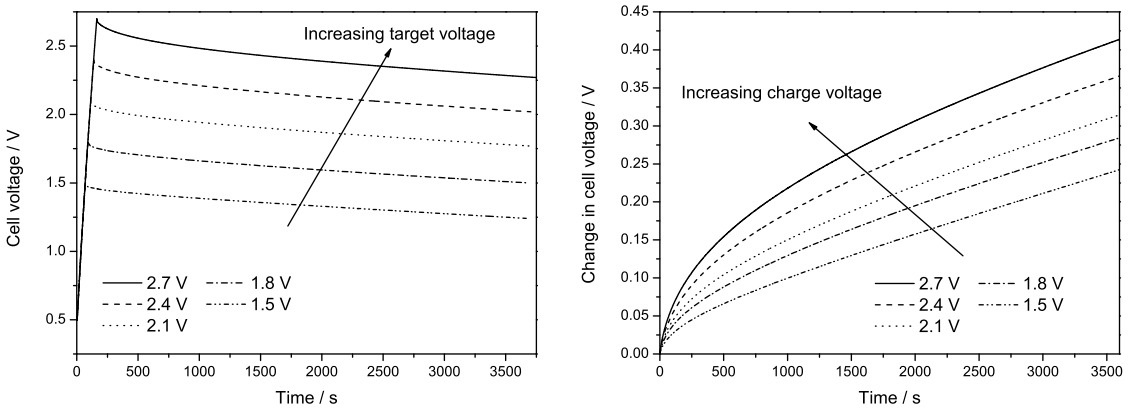
frequency than the smaller 150 F. One would assume that if the electrodes are the same, then they would have the same knee frequency characteristics.

Assuming that the 1500 F supercapacitors have a 10× greater area than the 150 F supercapacitor, and thus the 150 F supercapacitor electrode material if scaled up to 10× the surface area to reduce the resistance by the same factor it becomes apparent that the two devices do not scale linearly as shown in figure 5.10a. From the figure, if the impedance of the 150 F supercapacitor is scaled by a factor of 10, it can be seen that the pore resistance trend of both devices are in good agreement over the range of operation suggesting that the same electrode material is used. However, the relative series resistance of the 150 F supercapacitor is larger than that of the 1500 F one resulting in an overall greater total relative polarisation resistance. This would therefore be the reason for the lower knee frequency experienced by the 150 F supercapacitor. If the normalised resistance is higher then it would make sense that the high frequency drop off in capacitance would occur at a lower frequency.



(a) (b)

Figure 5.10: (a) Comparison between the impedance at different operating voltages for a 1500 F and 1/10th scale 150 F Maxwell supercapacitor and (b) cell tab configurations



(a) (b)

Figure 5.11: Charge redistribution effect seen in a 150 F Maxwell supercapacitor under a 2 A charge current at different target voltages (a) and change in voltage from target voltage (b)

This difference in the series resistance could possibly be attributed to the contact resistance since the 150 F and 1500 F supercapacitors have different cell tab configurations. The 150 F having both terminals on the same side and the 1500 F supercapacitors with cell terminals on opposite sides as shown in figure 5.10b. Thus, for high frequency applications the 1500 F, due to the lower normalised resistance seems more suited as the knee frequency is higher.

5.3.5 Constant current tests

One of the major areas of interest for the model to accurately replicate was the charge redistribution effect which has a time constant on the order to minutes to hours. To probe this, constant current tests were performed.

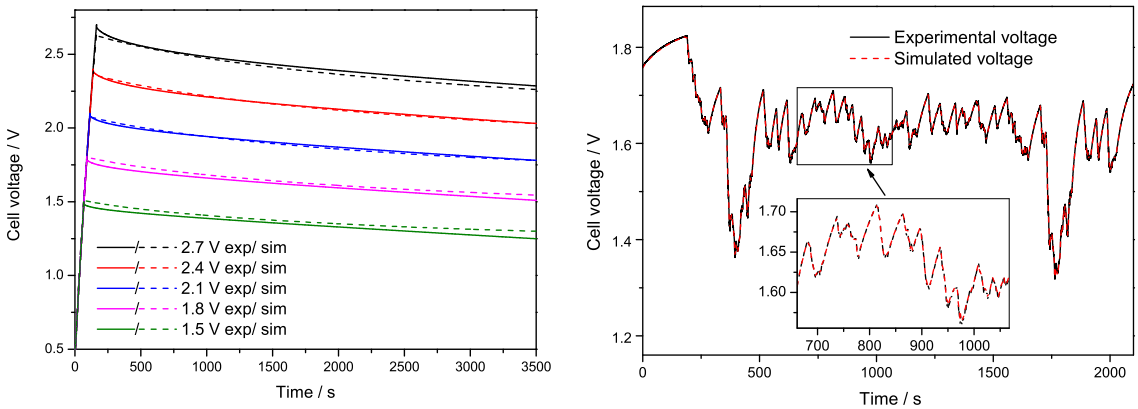
Figure 5.11 shows the voltage after a 2 A charge of a 150 F Maxwell supercapacitor, when charged to different target voltages. Once the cell reaches the target voltage the load is removed and the OCV is measured to monitor the charge redistribution effect. It can be seen that under constant current charging to different target voltages the highest target voltage exhibits the largest voltage relaxation. This is attributed to a longer charge period rather resulting in larger concentration gradients of the charge carrying species in the porous electrodes.

5.4 Model parameterisation

Using the data from the EIS measurements combined with constant current tests and the model parameterisation toolbox in Simulink, the model for the supercapacitor was parameterised by iteratively minimising the residuals of the error between the model and experimental results.

Using different data sets it was possible to parameterise different parts of the model with different time constants in order to get a better overall fit. Figure 5.12a shows the fit of the model to charge redistribution data which allows for more accurate parameterisation of the slower diffusion processes of ions in the mesopores of the electrode structure.

The fitting algorithm simultaneously evaluated the 5 sets of test data to minimise the overall residuals. Hence, the fit for the 2.1 V data set appears to be the best, whilst the 2.7 V simulated data overestimates the charge redistribution effect. Similarly, the 1.5 V data simulated data set underestimates the charge redistribution. This can be attributed to having a constant pore resistance over the whole range of operation. From



(a) (b)

Figure 5.12: (a) Comparison between experimental and simulated charging and then relaxation for a 150 F Maxwell supercapacitor after a 2A charge to different target voltages and (b) comparison between experimental and simulated voltages for a 150 F Maxwell supercapacitor during rapid power cycling

the EIS measurements it could be seen that at higher cell potentials the pore resistance was higher. Thus at 2.7 V the actual resistance is higher than the fitted value resulting in a faster ionic diffusion and vice versa for the lower operating potentials.

Fitting of the parameters which defines the shorter time constant behaviour was done with dynamic data typical of load cycling in HEV applications. This is shown in figure 5.12b. Results show that a good fit can be achieved with the transmission line model to both long term charge redistribution data and shorter term dynamic load variations.

By fixing the slower time constant parameters which were determined by the fitting of the model by the relaxation data, a better overall fit is achieved.

5.5 Conclusion

The work presented in this chapter covers the development, experimental validation and performance investigation of supercapacitors with the aim of developing a model that will be used in later chapters for whole system level analysis of powertrain efficiencies. The below thus summarises the key points of this chapter:

- A transmission line model that accounts for the charge redistribution effects in the porous electrodes has been created with tests performed on 150F and 1500F Maxwell supercapacitors to acquire data for parameterisation and experimental validation
- Investigation of performance metrics over the range of operation has shown that capacitance is both a function of the operating potential and frequency with the drop off in capacitance denoted by the knee frequency
- Further investigation of the knee frequency found that this was also frequency dependent with lower frequencies found at higher cell potentials. When comparing supercapacitors of different scales it was found that larger cells had a higher knee frequency than smaller ones. Analysis of the impedance response showed that the relative pore resistance of the two different sizes of supercapacitors was the same but the relative series resistance for the smaller supercapacitor was larger resulting in the smaller knee frequency
- Through analysis of the complex capacitance it was found that the simple approximation

of capacitance as a function of frequency typically overestimated the transition frequency between full performance and reduced high frequency performance. Both techniques however resulted in the same low-frequency capacitance

- Application of the complex components of capacitance then allowed for the development of a novel Nyquist capacitance plot, which if fitted to an equivalent circuit, allowed for the estimation of the low-frequency capacitance

Chapter 6

Powertrain comparison

6.1 Introduction

The powertrain comparison chapter aims to combine the works presented in the previous three chapters on the modelling and experimental validation of lithium-ion batteries, PEMFCs and supercapacitors with the aim of answering the original research question on how feasible a FCHEV powertrain is, relative to other EV powertrains. Analysis will only focus on FC based powertrain analysis and pure battery electric vehicles in order to restrict the scope of investigation. The contents of this chapter are thus listed below:

- **Development of a vehicle model**
  - This section presents the mathematical framework on the vehicle and motor model used to establish vehicle power requirements
- **Drive cycle analysis**
  - This section presents the work on analysing different vehicle drive cycles typical of automotive applications and provides a quantitative analysis to a normally qualitative metric. It also presents a novel method of dimensionless characterisation of drive cycles through a Reynolds-decomposition style analysis
- **Development of a scaled down hybrid vehicle test rig**
  - This section presents the development of a scaled down hybrid vehicle test rig constructed in order to validate the developed hybrid models
- **Comparison of different electric vehicle powertrain configurations**
  - This section presents the analysis of different vehicle powertrain configurations using the previously developed models and draws conclusions to answers the original research question of the thesis. The analysis of the following systems were performed:
    - Pure battery electric vehicles
    - Pure fuel cell vehicles
    - Fuel cell-battery active hybrids
    - Fuel cell-supercapacitor active hybrids
    - Fuel cell-supercapacitor passive hybrids
- **Development of a large scale 9.5 kW PEMFC-supercapacitor passive hybrid system**
  - This section presents the development work on a 9.5 kWe PEMFC-supercapacitor passive hybrid system used to validate models for larger systems and to act as a proof-of-concept of the feasibly of this configuration

The analysis of different hybrid vehicle configurations will not consider active hybrids with different power regulation strategies due to the shear scale of the different numbers of possible control algorithms which would affect the overall result. Rather, this section is

used to demonstrate the application of the developed tools and methodology in analysing different FC-hybrid vehicle configurations.

6.2 Vehicle modelling

Development of a vehicle and motor model is critical in determining the power and energy requirements of different vehicle drive cycles. When optimising the system in later sections it will be important to consider the variable mass of the devices which will have an impact on the overall energy consumption.

When considering vehicle modelling, there are two main types of modelling: forward and backwards facing. Backwards facing models start with a vehicle drive cycle which consists of a time-velocity trace. This then goes into a vehicle/motor model where the power requirements are calculated and then this power requirement is then imposed onto the powertrain devices of interest. Backwards facing models are typically faster than forward facing models which is why some authors implement this method however a forward facing model is much more indicative of real world conditions. In forward facing models a driver model determines the power requested from the device based on the current speed of the vehicle and the target speed. This power request then goes into the powertrain devices which provide the electrical power and then into a motor and vehicle model. This then determines the speed of the vehicle which is then fed back into the driver model. Figure 6.1 depicts the two types.

The work presented here after will use a backwards facing model due to the faster computational speed and numerical stability.

6.2.1 Equations of motion for the vehicle

The vehicle model is needed to calculate the speed of the vehicle for a given force input and assumes that the vehicle can be taken as a lumped mass. Figure 6.2a shows a free body diagram of a vehicle with the various motive and resistive forces annotated.

The vehicle model, which is based on the equations presented by Ehsani *et al.* [67], includes considerations of the the vehicles inertia, resistance causes by air resistance, mechanical resistance of the components, resistance caused by motion up an incline and the rolling resistance of the vehicle. Rolling resistance losses are caused by the viscous hysteresis of the tyre material and air resistance is caused by pressure differentials generated between the front and rear regions of a vehicle as it moves [67]. This is shown in equation 6.1. Where dV/dT is the vehicle acceleration (m.s^{-2}), m is the vehicle mass (kg), g is the acceleration due to gravity (m.s^{-2}), μ is the coefficient of friction, C_D is the coefficient of drag, A is the vehicle area (m^2), V is the vehicle velocity (m.s^{-1}), V_w is the wind velocity (m.s^{-1}), θ is the angle of incline for the vehicle(°), $\dot{\theta}$ is the angular

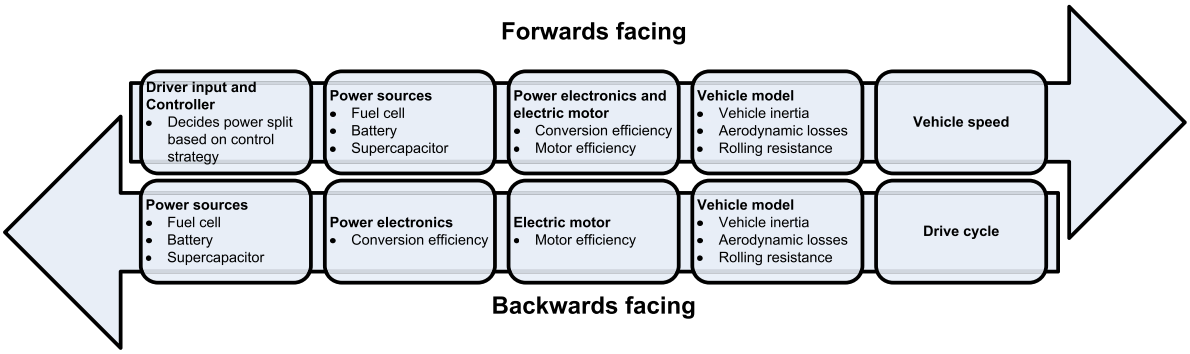
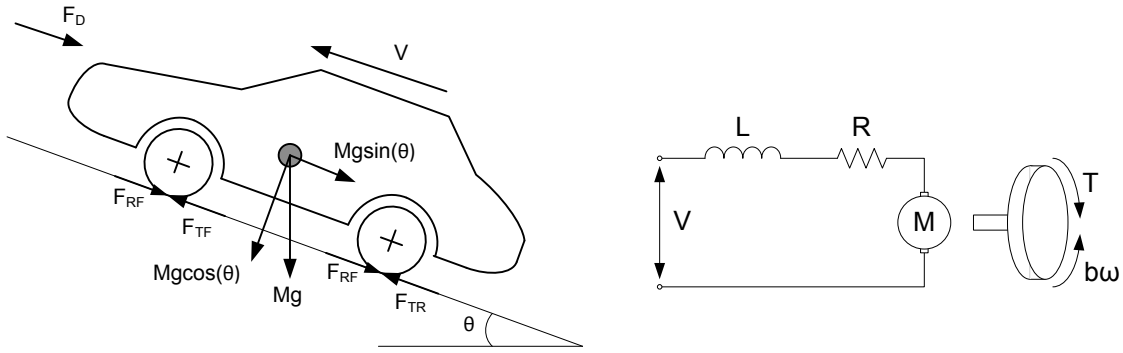


Figure 6.1: Illustration of how forward and backwards facing vehicle models work



(a) (b)

Figure 6.2: (a) Free body diagram of a car and (b) electrical and mechanical schematic of electric motor model

speed of a the vehicle shaft (rads^{-1}) and b is the damping coefficient which accounts for frictional losses.

$$m\frac{dV}{dt} = F - mg\mu - \frac{1}{2}C_D A(V - V_w)^2 - mg\sin(\theta) - b\dot{\theta} \tag{6.1}$$

Normally the coefficient of friction has a baseline value but it is also a function of velocity. This is because at higher velocities there are more viscous tyre losses. Values for coefficient of friction can vary depending on the road surface between 0.006 for a truck tire on concrete to 0.35 if driving on a field [67]. In performance calculations it is often sufficient to assuming the coefficient of friction as a linear function of speed. The most common approximation for passenger vehicle on a concrete road is shown in equation 6.2 [67].

$$\mu = 0.01\,(1 + 0.0017V) \tag{6.2}$$

6.3 Electric motors

The electric motor model used is based on a DC motor model to capture the dynamics of its operations and transient power consumption. This considers the mechanical characteristics of the system including inertia and frictional losses as well as electrical losses from ohmic resistances, inductance and back ElectroMotive Force (EMF). A schematic of the model is shown in figure 6.2b. The electrical equation for the DC motor is shown in equation 6.3.

$$\frac{di_{motor}}{dt} = \frac{1}{L}\left(V - Ri_{motor} - k_e\frac{d\theta}{dt}\right) \tag{6.3}$$

Where i_{motor} is the current drawn from the motor, L is the inductance, V is the motor voltage, θ is the angular position and k_e is the motor constant. Assuming that the generated torque is directly proportional to the current, the mechanical equations which govern the motor behaviour is shown in equation 6.4. Where J is the angular inertia of the motor, K_T is the armature constant and b is the damping coefficient, which is representative of frictional losses.

$$\frac{d^2\theta}{dt^2} = \frac{1}{J}\left(K_T i - b\frac{d\theta}{dt}\right) \tag{6.4}$$

The resulting rate of angular rotation is then directly coupled via a fixed gear ratio to the vehicle model. The radius of the wheel of the vehicle, allows for the translation of angular velocity of the motor to linear velocity of the vehicle.

Motor efficiency

As good as electric motors are there are still inefficiencies associated with their operation. In electric motors the main sources of losses are copper losses from the windings, eddy current losses, hysteresis losses, windage losses and mechanical losses from the bearings. Under equilibrium conditions the electrical torque (T_e) generated is related to the load torque (T_l) and frictional losses (T_f) as shown in equation 6.5.

$$T_e = T_l + T_f \tag{6.5}$$

The amount of electrical input energy to a motor can also be derived by using a $d-q$ frame model as shown by Shukla [188]. This is shown in equation 6.6.

$$P_{in} = \frac{3}{2}(v_q i_q + v_d i_d) = \frac{3}{2} i_q^2 R + T_e \omega_r \tag{6.6}$$

Assuming that the i_d current is 0 and electrical torque can be derived using equations 6.7 then the power in can be written in the form of equation 6.8.

$$T_e = \frac{3}{2} P \lambda_f i_q \tag{6.7}$$

$$P_{in} = \frac{3}{2} \left(\frac{2T_e}{3\lambda_f p} \right)^2 R + T_e \omega_r \tag{6.8}$$

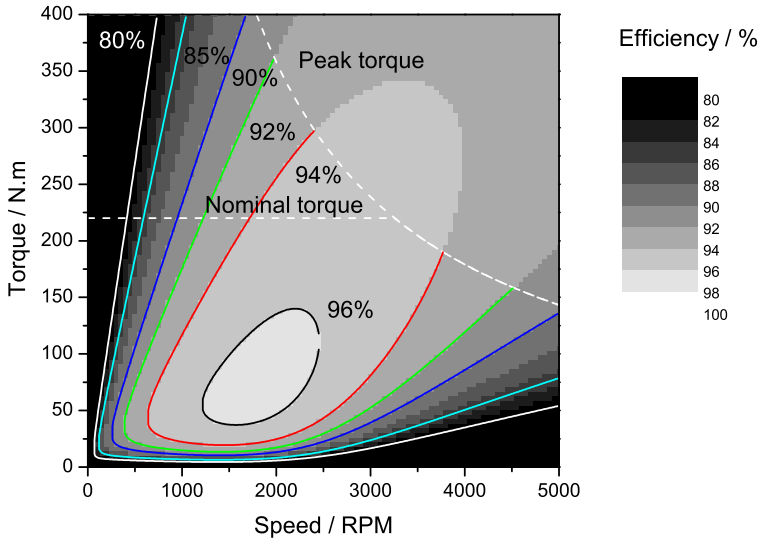


Figure 6.3: Generated efficiency map of a AFM-140 EVO Electric Axial Flux Machine Motor based on fitting to manufacturers data sheet [73] and coefficients from Shukla [188]

The power out (P_{out}) and efficiency (η) can then be defined as shown in equations 6.9 and 6.10.

$$P_{out} = T_l \omega_r \tag{6.9}$$

$$\eta = \frac{P_{out}}{P_{in}} \tag{6.10}$$

Combining all equations and rearranging the form into a quadratic then gives equation 6.11.

$$\frac{2R}{3\lambda_f^2 p^2} T_l^2 + \left(\frac{4RT_f}{3\lambda_f^2 p^2} + \omega_r - \frac{\omega_r}{\eta} \right) T_l + \frac{2RT_l^2}{3\lambda_f^2 p^2} + \omega_r T_f = 0 \tag{6.11}$$

This equation is quadratic with respect to T_l and can be rewritten as shown in equation 6.12. T_l for a certain efficiency can then be found by solving the quadratic equation.

$$aT_l^2 + bT_l + b = 0 \tag{6.12}$$

The efficiency of an electric motor is typically very high, often in excess of 90%; however, this is very dependent on the operating point. The efficiency of the machine is not constant over the whole operating range of the machine and the efficiency depends on the applied torque load and the rotational speed. Efficiency of the electrical machine is also typically not symmetrical, i.e. the performance is not the same in motor mode as it is in generator mode. Figure 6.3 shows the efficiency map of a 75 kW (167.5 kW peak) EVO Electric AFM-140 Axial Flux Machine Motor.

6.4 Drive cycle analysis

One of the main problems with designing systems suitable for mainstream automotive applications is the wide range of use. Some consumers will use their vehicle very economically whilst others will use them more aggressively. For a vehicle designer, this makes the task quite difficult as the operating envelope has to be considerably large to account for every eventuality without compromising on performance. The previously presented literature review showed that the majority of the works in the academic literature looking at system level analysis of vehicle powertrains used a single arbitrary load cycle. Specific drive cycle analysis works showed that depending on which load cycle is used, the requirements can vary significantly. Thus there is a motivation of developing a quantitative distinction of the different load cycles.

Typically, the variations in usage modes are interpreted by different vehicle drive cycles (i.e. a time-velocity trace). Figure 6.4 shows four different drive cycles which represent different modes of use. Figure 6.4a shows the NYCC cycle which is generally acknowledged as being a cycle which represents city driving. Here the average speed is low with many start-stop events but acceleration/deceleration events are frequent. Figure 6.4b shows the JC08 cycle which is typically used in Japan as the new standard cycle to represent urban/ extra urban driving. Here the average speed is slightly higher, than the NYCC, with fewer start-stop events. Figure 6.4c shows the HWFETDS which represents highway driving. Here the average velocity is high with almost no stop-start events. Velocity is generally quite constant. Figure 6.4d is the US06 cycle which represents the most aggressive cycle. Here average speed is high with large accelerations/ deceleration events.

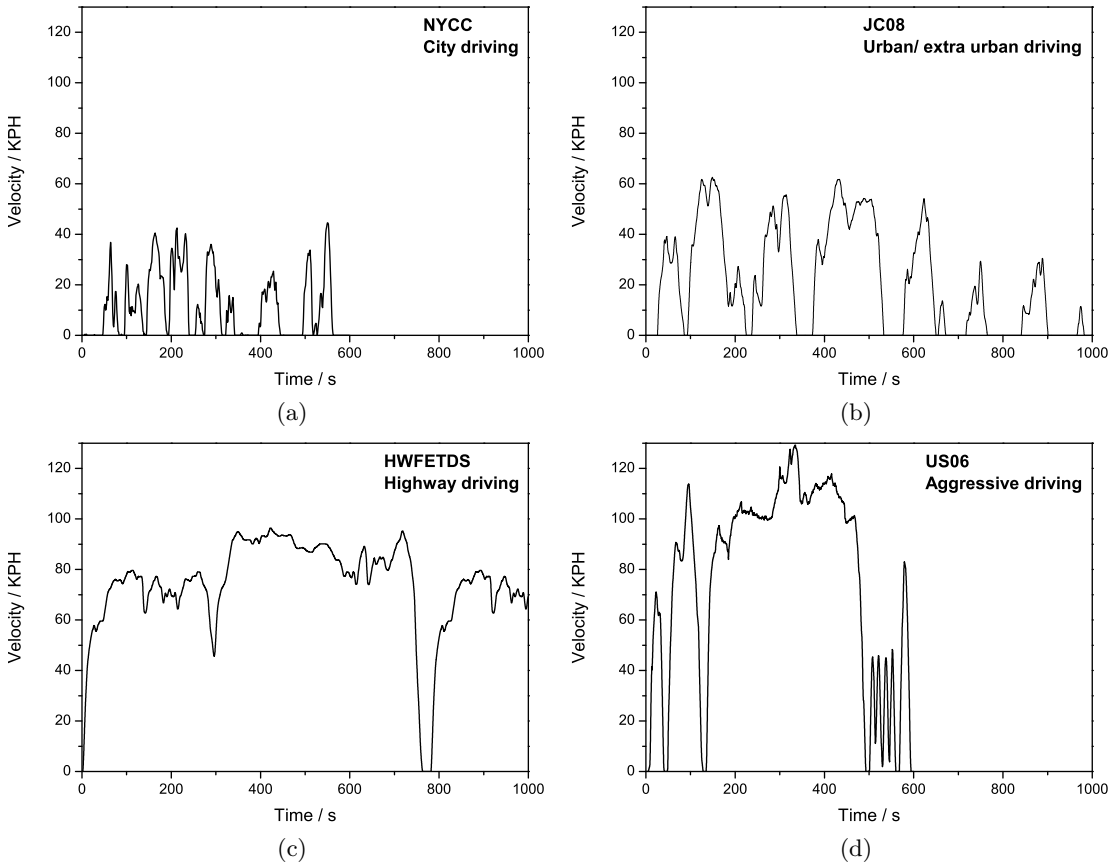
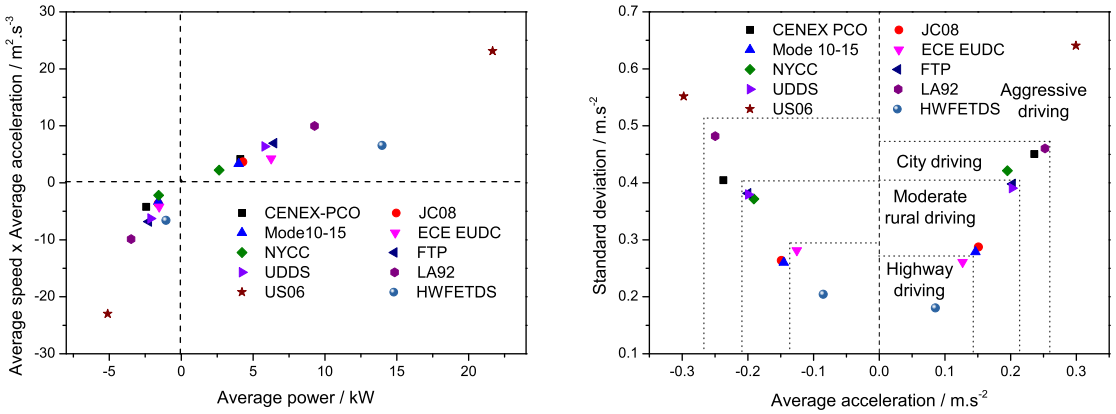


Figure 6.4: Time-velocity profiles for (a) NYCC (b) JC08, (c) HWFETDS and (d) US06 drive cycles

It becomes apparent from the drive cycles that different modes of use vary considerably and depending on which cycle is used may well favour one technology over another. Thus understanding the different power and energy requirements of the various load cycles becomes an important prerequisite for analysing the suitability of one vehicle powertrain over another. From the previously presented vehicle model, it can be seen that inertia losses and aerodynamic drag effects are the significant losses that have to be overcome by the vehicle powertrain. If the product of the average velocity and average acceleration is taken and plotted against the power requirement for the vehicle (without considering motor losses) it can be seen there is a correlation as shown in figure 6.5a. This would suggest that speed and acceleration are key metrics to consider and use as distinguishing features. Figure 6.5b then shows the average acceleration of the different drive cycles against the standard deviation of those cycles and again shows a correlation. This suggests that in more gentle cycles i.e. ones where the average acceleration is lower, there is very little variation whilst the more aggressive cycles have a larger variation. Thus, this suggests that there are limiting processes whereby the acceleration changes cannot instantaneously go from one level to another. This is thus the limitations imposed by the inertia of the vehicle. This also shows that general drive cycles categories can be divided up based on their average acceleration.

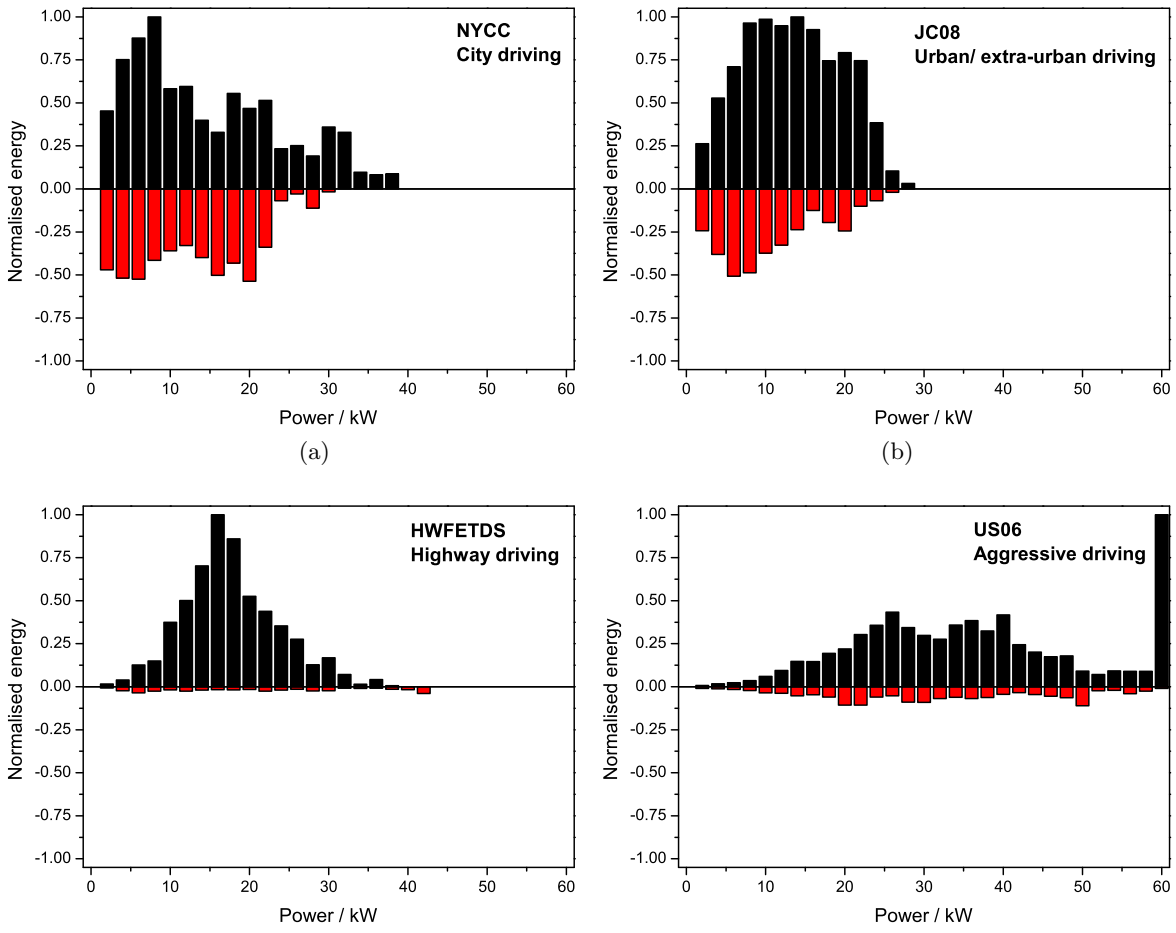
Further decomposition of the drive cycles and the information they contain can be extracted when combined with the vehicle model to extract the energy/ power requirements. Figure 6.6 shows the normalised energy against the power in histogram form for different drive cycles. This weights the power frequency histogram with the power value to give an indication of the absolute energy drawn at each power. The rational for this is that low power discharges are more frequent than high power ones; however, high power ones high more of an impact and thus should be weighted accordingly.



(a) (b)

Figure 6.5: (a) Average power of vehicle drive cycle assuming a vehicle with a mass of 1500 kg against the average speed × average acceleration of the respective drive cycle and (b) average acceleration against standard deviation of various standard vehicle drive cycles

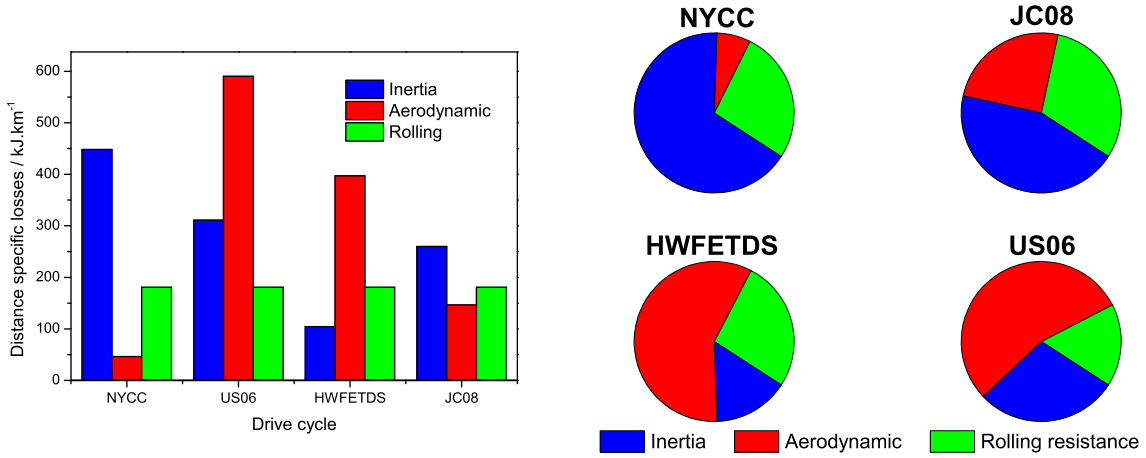
Figure 6.6 thus gives additional insight into the power and energy requirements of each drive cycle. In the NYCC cycle much of the energy requirements are low power bursts which was suggested by the low speed and frequent acceleration from the time-velocity



(a) (b)

(c) (d)

Figure 6.6: Energy distribution as a function of power for the (a) NYCC, (b) JC08, (c) HWFETDS and (d) US06 drive cycles



(a) (b)

Figure 6.7: (a) Distance specific losses associated with different drive cycles and (b) pie chart showing relative vehicle losses

plots. It can also be seen that in the NYCC cycle, a significant amount of regenerative energy can be recovered. In the JC08 cycle the energy requirements are higher due to more energy at higher powers. This is mainly due to the higher average speed operation. The fraction of regeneration energy is still significant but smaller than that of the NYCC cycle due to more energy lost via aerodynamic drag effects. In the HWFETDS cycle the average power is again higher but the standard deviation of the energy distribution is smaller as suggested by the lower average acceleration. Here there is very little regenerative breaking energy available due to the high aerodynamic losses and high velocity operation. In the US06 cycle, the average power requirement is still higher with a broad spread of energy, as suggested by the high velocity, high acceleration drive cycle. Here, more energy can be recovered but much of this is at higher powers.

Consideration of these plots is useful in considering which powertrain configuration would be best suited to each drive cycle. In city driving, the average power is relatively low with few excursions to higher powers. This cycle has a relatively large fraction of regenerative energy available and thus would suggest a supercapacitor hybrid powertrain would be suitable. In the JC08 cycle there are more high power excersions with still a reasonable amount of regeneration energy available but at lower powers. This may suggest a battery hybrid is more suitable in order to meet the higher energy requirements at higher powers. Fewer high power recharges from regeneration would also be advantageous for the battery to avoid premature failure. Highway driving has a higher average power but with few excursions to high powers. This may suggest a supercapacitor hybrid may be suitable. The US06 cycle has both high power and a large distribution and powers. This could suggest a triple hybrid using FC, battery and supercapacitor to be the best solution.

In reality a typical consumer vehicle will be expected to operate over all types of load cycles and thus consideration of the powertrain performance over this whole range of operation should be considered and not just restricted to a given load cycle.

6.4.1 Drive cycle decomposition

Typically, drive cycles are categorised in a very qualitative manner; however, with closer inspection of the nature of the drive cycles it is possible to divide these cycles in a more quantitative manner providing a more structured foundation for analysis of different load cycles. Ultimately, it is desirable to have vehicle independent metrics to compare one drive cycle against another.

The first stage in this process is to analyse the parameters of interest. From an automotive point of view, a typical starting point is the time-velocity trace. Depending on the design of the vehicle, this then cascades down to the individual powertrain components as a power requirement to achieve the desired performance. Equation 6.13 shows the main contributions of vehicle drag forces that the powertrain must overcome.

$$F_{Tractive} = \underbrace{M\frac{dV}{dt}}_{\text{Inertia}} + \underbrace{\frac{1}{2}C_D A V^2}_{\text{Aerodynamic}} + \underbrace{Mg\mu}_{\text{Rolling resistance}} + \underbrace{Mgsin\theta}_{\text{Incline}} - \underbrace{b\omega}_{\text{Friction}} \tag{6.13}$$

The retrospective torque that this applies on the drivetrain is then this force multiplied by the wheel radius. This is shown in equation 6.14 where it has been assumed that the rolling resistance, incline resistance and the frictional losses are negligible.

$$T_{Tractive} = F_{Tractive} r = Mr\frac{dV}{dt} + \frac{1}{2}C_D A r V^2 + \cancelto{0}{Mgr\mu} + \cancelto{0}{Mgrsin\theta} - \cancelto{0}{br\omega} \tag{6.14}$$

The power required of the powertrain is then the product of the torque and the angular speed of rotation as shown in equation 6.15.

$$P_{Tractive} = T_{Tractive}\omega = T_{Tractive}\frac{V}{r} = MV\frac{dV}{dt} + \frac{1}{2}C_D A V^3 \tag{6.15}$$

It then becomes apparent that two vehicle independent variables relating to the power required of the powertrain arises from this as shown in equations 6.16 and 6.17.

$$\frac{P_{Inertia}}{M} = V\frac{dV}{dt} \tag{6.16}$$

$$\frac{P_{Aerodynamic}}{\frac{1}{2}C_D A} = V^3 \tag{6.17}$$

In many cases, the power required to overcome the inertia of the vehicle, is the dominant source term. Since this is the product of two varying terms, a Reynolds Decomposition approach can be taken to separate the steady state and the fluctuation inertia contributions [79]. This is shown in equation 6.18.

$$\frac{P_{Inertia}}{M} = V\frac{dV}{dt} = \left(\bar{V} + V'\right)\left(\frac{d\bar{V}}{dt} + \frac{dV'}{dt}\right) \tag{6.18}$$

If this is then multiplied out and the average taken then this results in equation 6.19.

$$\frac{\overline{P}}{M} = \overline{\bar{V}\frac{d\bar{V}}{dt}} + \cancelto{0}{\overline{V'\frac{d\bar{V}}{dt}}} + \cancelto{0}{\overline{\bar{V}\frac{dV'}{dt}}} + \overline{V'\frac{dV'}{dt}} \tag{6.19}$$

It becomes apparent that two of the terms can drop out of the decomposition as $\overline{\frac{dV'}{dt}} = 0$ and $\overline{V'} = 0$ as the average of these variables over the positive power discharging portions of the drive cycle should be zero. As the vehicle is always moving forward it becomes apparent that $\overline{\frac{dV}{dt}} \neq 0$ as we are only looking at either the acceleration parts or deceleration parts of the cycle separately. In the case of the product of the two fluctuating terms, the average of the product cannot be assumed to be zero and therefore has to be considered as $\overline{V'\frac{dV'}{dt}} \neq 0$. This is normally termed the stress component which arises on

top of the steady state component when you have an oscillating component. Similarly, the mean of a mean is the original mean thus allowing the further simplification of equation 6.19 to equation 6.20.

$$\frac{\overline{P}}{M} = \underbrace{\overline{V\frac{dV}{dt}}}_{\text{Steady state component}} + \underbrace{\overline{V'\frac{dV'}{dt}}}_{\text{Fluctuating component}} \tag{6.20}$$

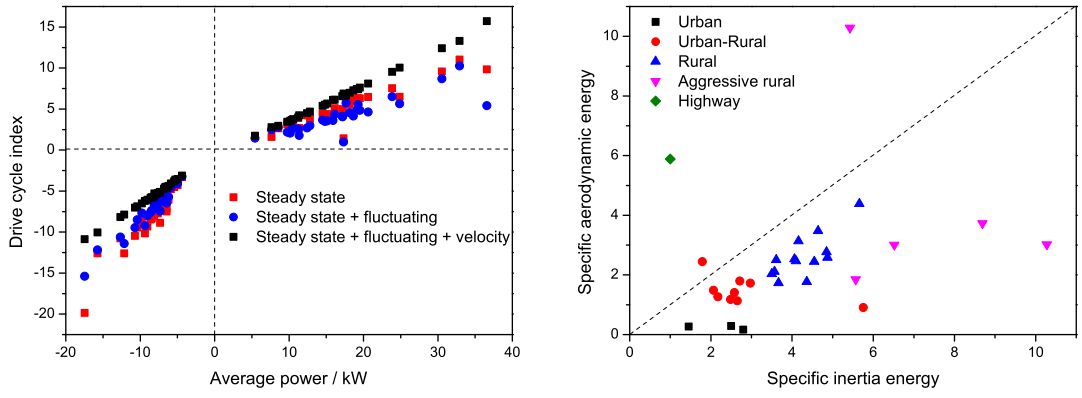
Figure 6.8a compares the simulated average power of different vehicle drive cycles assuming a 2000 kg vehicle mass with different aggregate components of the drive cycle.

In the case where only the average speed and the average acceleration of the cycle is considered, thus giving the steady state component of the specific inertia energy it can be seen that the correlation is roughly apt however there is a degree of deviation. At lower powers the correlation is better however at higher power this starts to deviate more suggesting an increased contribution from the aerodynamic component. When the fluctuating component is then also considered, the same trend is observed. When the specific energy from the aerodynamic drag losses are then considered with the steady state and fluctuating terms the correlation becomes nearly perfect.

This suggests that in low velocity drive cycles the steady state inertia term dominates the vehicle power requirement. The fluctuating component does not affect the correlation significantly. At higher velocities where the average power is greater this deviation increases when only considering the inertial energies. After the aerodynamic losses are considered the correlation between this index and the average power is nearly perfect.

Taking the specific aerodynamic and combined inertia forces then allows for comparison between these variables and drive cycle styles. Figure 6.8b shows how different drive cycle styles compare when plotted against each other for these two variables.

It can be seen that purely urban driving which is categorised as being low speed, high stop-start city driving has a low specific aerodynamical energy contribution and low end inertia energy. Drive cycles categorised as urban-rural has elements of city driving with more high velocity driving akin to rural driving have increasing aerodynamic energy



(a) (b)

Figure 6.8: (a) Comparison between average simulated drive cycle power assuming a 2000 kg vehicle and only the steady state component, steady state plus fluctuating components and steady state, fluctuating and velocity components and (b) Comparison between the specific aerodynamic and inertia forces for different vehicle drive cycles. The dotted line represents a 1:1 ratio of specific aerodynamic to inertia energy

contributions with similar inertia contributions to city driving. Purely rural driving has larger aerodynamic and inertia energy, whilst aggressive rural driving has similar aerodynamic energies but significantly larger inertia energies. Highway driving has a low inertia energy but high aerodynamic energy.

The dotted line on the figure represents the 1:1 ratio of the average power requirement of the driving cycle coming from the inertia losses and aerodynamic losses. Points which are below the line represent inertia dominates cycles whilst points above the line represent aerodynamic dominated cycles. Two extreme cases are city driving and highway driving. City driving shows the most inertia dominated characteristics owing to its low average velocity whilst highway driving is the converse with highly aerodynamically dominated losses due to its steadier high velocity operation.

6.5 Development of a scaled down powertrain simulator

In order to simulate and test various hybrid configurations a scale model of a FC hybrid powertrain simulator was constructed. The main component architecture of the rig is shown in figure 6.9. Here a host computer running NI LabVIEW handles the data logging and supervisory control. A custom made user interface allows for visualisation of relevant information. LabVIEW written drivers allow for the control for external devices such as power supplies and load banks. LabVIEW also communicates with a NI cRIO with RT and FPGA modules that allow for input and outputs required for data logging and control. C-series modules then interface with the FPGA chassis and extract the useful information from the device in question. The NI equipment and main powertrain components used in the construction of this rig is shown in table 6.1.

In order to simulate the drive cycle load and regenerative breaking power the system is connected to a separate load and power supply which was connected in parallel. The DC power supply was a Kikusui PLZ1004W which is rated at 1000 W over an operating range of 1.5-150 V and 0-200 A. The electronic load used was a Kikusui PWR1600L which is rated at 1600 W over an operating range of 0-80 V and 0-100 A. Whilst the devices output their terminal voltage this does not give an accurate measure of the

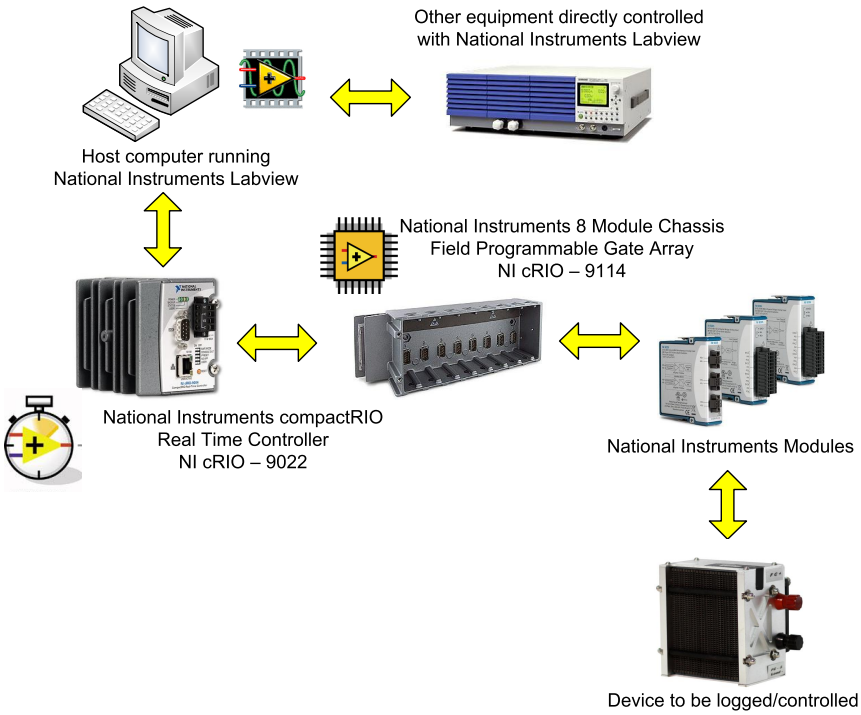
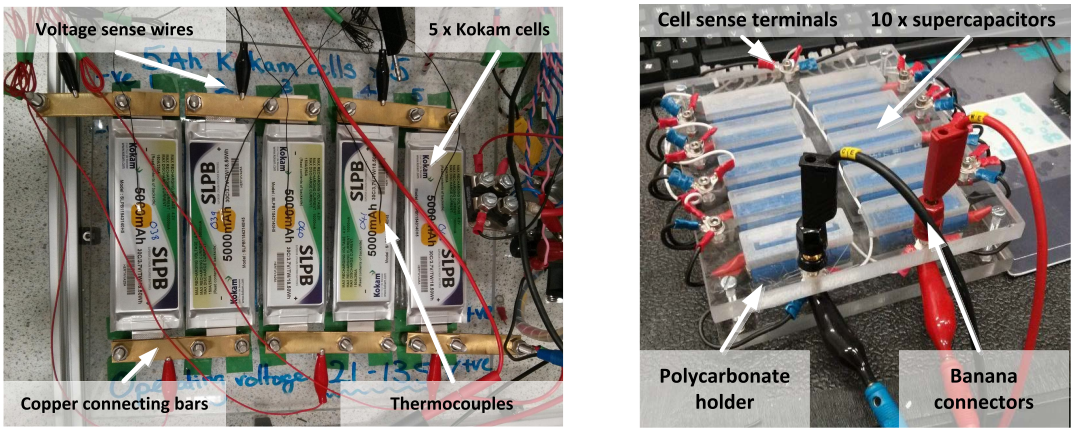


Figure 6.9: Diagram of the data logging and control architecture for the hybrid vehicle power train test rig



(a) (b)

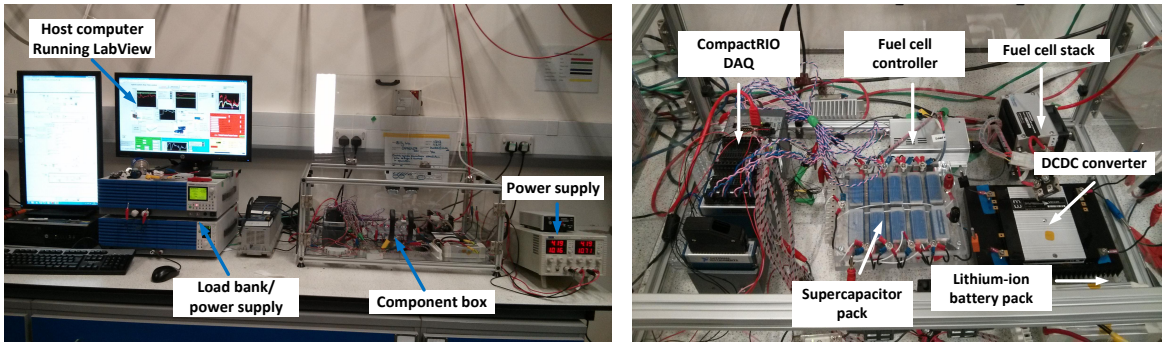
Figure 6.10: Picture of (a) 5 cell battery pack and (b) 10 cell supercapacitor pack

actual operating potential of the system due to the relatively large potential drops of the connectors. Thus, external potential measurements using the cRIO were used. Shunt resisters were deemed to have the best resolution for current measurements in this rig and the relative low currents allowed for their introduction to have minimal impact on the overall performance.

A 100 W self-humidifying Horizon PEMFC was used as the FC which has its own controller. An external power supply provided the 12 V low voltage BUS for the controller and a regulated hydrogen supply was set to 1.5 bar absolute. The lithium-ion battery pack was created in house with 6 Kokam 4.8 Ah lithium-polymer cells. These individual cells were connected in series via copper interconnects. No BMS was created but the cells were balanced before each test. A 10 × 150 F Maxwell supercapacitor pack was created in-house. A CNC-milled housing was created to hold the supercapacitors in place with soldered cell tab collectors providing electrical connections and two banana connectors providing safe and low resistance pack connection points. All components were connected together via banana clips which allowed for ease of inter-changeability, safety and low resistance. Pictures of the battery and supercapacitor pack are shown in figure 6.10. Pictures of the rig are shown in figure 6.11.

Table 6.1: National Instruments equipment and other components used in scaled down hybrid vehicle powertrain simulator rig

Component		Channels/Range	Use
Real Time controller	cRIO-9022		Real time data processor
FPGA chassis	cRIO-9114	8-slot	FPGA processor
Analog Output module	NI 9263	4-channel / ±10 V	Control DCDC converter
Thermocouple module	NI 9213	16-channel	Measure temperatures
Analog Input module	NI 9205	32-channel / ± 10 V	Measure low voltages
Universal Analog Input module	NI 9219	4-channel / ± 60 V	Measure high voltages
Digital Output module	NI 9472	8-channel / 24 V	Controls contactors
Component	Manufacturer	Description	
Fuel cell	Horizon fuel cell	100 W Self-humidifying PEMFC (10-18V)	
Battery pack	Dow Kokam	4.8 Ah × 6 in-house made pack	
Supercapacitor pack	Maxwell	150 F ×10 in-house made pacl	
DCDC converter	Vicor Power	Megamod chassis-mount (VI-200 series) step-up converter with 10-20V regulated output. Maximum output power of 100W	



(a) (b)

Figure 6.11: Picture of (a) the complete hybrid system rig and (b) the component box

6.6 Total Cost of Ownership

As previously mentioned, the TCO is the total cost of acquisition of a vehicle combined with the running costs over the lifetime of the vehicle. Cost is an important consideration for the selection of a powertrain and thus needs to be accounted for. The TCO presented here is based on the electricity and hydrogen costs presented in Offer *et al.* [148] which is shown in table 6.2.

Table 6.2: Predictions of fuel costs [149]

Fuel	Optimistic / $\$.GJ^{-1}$	Average / $\$.GJ^{-1}$	Pessimistic / $\$.GJ^{-1}$
Electricity	26.9	35.8	44.7
Hydrogen	14	35	55.9

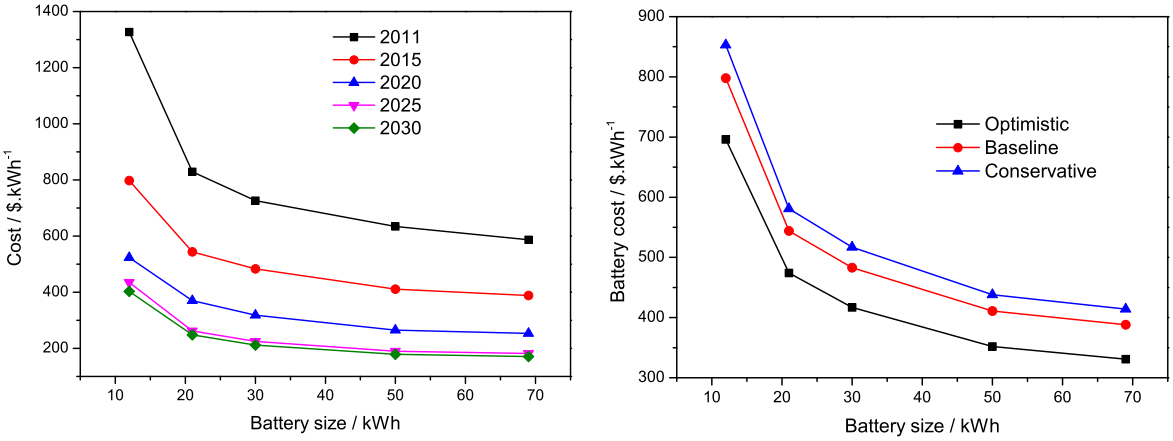
The TCO of the vehicle is calculated based on the base vehicle cost, capital cost of equipments and the cost of fuel based on the predicted 2015 values and the fuel efficiency calculated using the models.

Whilst cost numbers have been used in this analysis it should be mentioned that there is a high level of variation in these numbers based on many factors and no absolute conclusions should be drawn on the result. Rather, the introduction of a cost analysis should be used as a relative comparison.

6.6.1 Battery costs

The costs of lithium-ion batteries varies significantly in the academic and commercial literature due to factors such as cell chemistry, scale of production and other economic influences. Even with the same chemistry the cost of the cell can very depending on the internal cell construction, with earlier analysis showing that from a materials point of view high power cells are more expensive than high energy dense cells. The cost of an entire battery pack is also different to the predicted cost per kWh due to the need for pack assembly and other ancillary components required for the construction of a working pack. Figure 6.12a shows the predicted cost of a whole battery pack for different pack sizes installed in a vehicle and also the time. It is predicted that improvements in the manufacturing techniques and scale of production in the future will lower the unit cost of these devices. Figure 6.12b shows for the predicted 2015 battery cost the limits of this prediction under different scenarios.

It can be seen that the cost per kWh of smaller battery packs is higher than that of larger ones due to the fundamental baseline cost of component such as the packaging, wiring and management systems. For later analysis the trend for the 2015 battery cost per kWh was taken.



(a) (b)

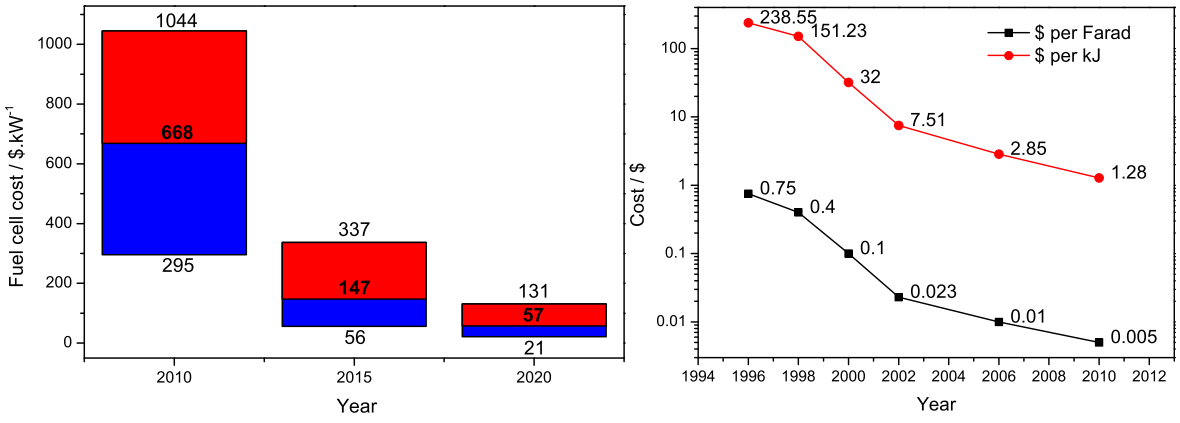
Figure 6.12: (a) Predicted cost of a battery pack as a function of the battery pack size and time [71] and (b) predicted cost of the battery under different scenarios for 2015

6.6.2 Fuel cell costs

The current cost of the FC systems is high but it has been predicted by many that this cost will decrease with a scale up of production. Figure 6.13a shows the predicted cost assumptions made in this analysis assuming values for a 2015 rollout of FCs.

6.6.3 Supercapacitor costs

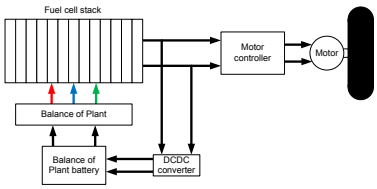
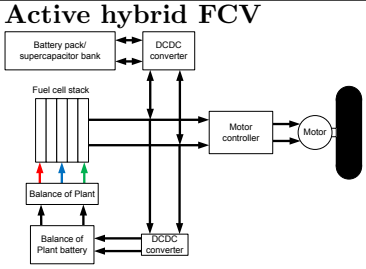
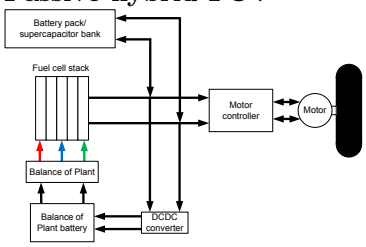
The cost of supercapacitors also needs to be considered when analysing their feasibility in hybrid vehicle applications. Figure 6.13b shows the historical cost of supercapacitors over time and it can be seen that there is a gradual decline, however this decrease is slowing down as indicated by the log-scale for cost. The analysis for the following sections will therefore assume a cost of 0.005 $\$/F$.



(a) (b)

Figure 6.13: (a) Predicted cost of a fuel cell stack in 2010, 2015 and 2020 with scenarios of optimistic, pessimistic and baseline costs [135] and (b) historical cost of supercapacitors [100]

Table 6.3: Comparison of different FC powertrains

Powertrain configuration	Advantages	Disadvantages
Pure FCV 	• Simple design	• Large FC • No regenerative braking • Large transient loads • Periodic no load operation • Relatively high cost
Active hybrid FCV 	• Smaller FC • Can capture regenerative braking • Load smoothing on FC • Can reduce time at OCV	• Requires additional DCDC converter
Passive hybrid FCV 	• Smaller FC • Can capture regenerative braking • Load smoothing on FC • Can reduce time at OCV • No additional DCDC converter	• Loss of active power control

6.7 Powertrain comparison

This section will look at comparing different electric vehicle powertrains with a focus on FC and FC-hybrid powertrains. ICE powertrains will not be covered nor FC-hybrid systems with complex active power control due to the shear number of possible permutations.

The pure FCV where the FC is the only motive power source has the advantage of simplicity of implementation; however, the FC has to be large in order to meet the entire range of expected operation. In addition the FC experiences all of the transient loads. In the active hybrid system the FC can be much smaller and has the capability to recover regenerative energy. The introduction of a second energy storage device allows for storage of regenerative energy and also load regulation of the FC. The disadvantage is that an additional DCDC converter is required. The passive system allows for the same benefits as the active hybrid system but does not require an additional DCDC converter saving of cost and the losses associated with an extra level of power conversion. The drawback of this is that the user loses active power regulation between the devices. This is summarised in table 6.3.

Quantifying the exact benefit gains from each of these powertrains will be the subject of the following sections.

The parameters used for the vehicle simulations is shown in table 6.4.

Table 6.4: Parameters used in simulations

Parameter	Value		Parameter	Value	
Mass	1200	kg	Frontal area	2.78	m^2
Hotel load	200	kg	Drag coefficient	0.46	

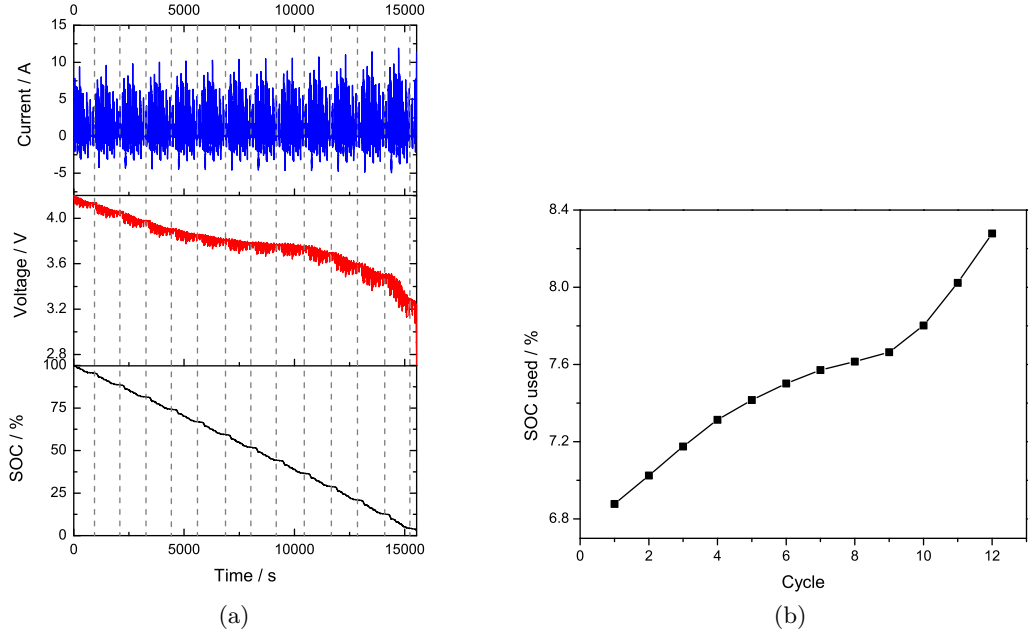
6.7.1 Pure battery electric vehicle

A pure BEV relies only on the energy stored in the vehicles' battery pack for motive power. Sizing of the battery pack for automotive applications requires consideration of design requirements such as range, drive cycle, vehicle mass, cost, durability and many other factors which are determined by the designer.

In theory, the average energy required for a vehicle to meet a certain drive cycle and the energy of the installed battery pack will define the range of a EV. In practice, the theoretical amount of energy stored in the battery is not often extracted under typical automotive load cycles due to the relatively high C-rate discharge leading to surface depletion of lithium in the electrodes meaning that the cell cut-off potentials are reached whilst bulk charge remains. The rate of solid phase lithium diffusion in the electrodes is therefore, often the limiting factor. Diffusion limitations combined with other electrochemical losses lead to inefficiencies which reduce the available energy.

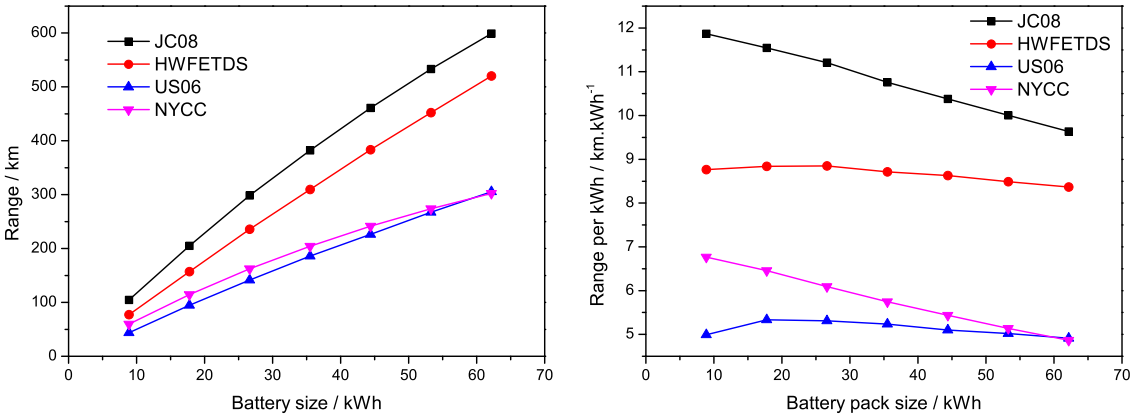
Increasing the capacity of the battery pack increases the range of the vehicle; however, this increase is not linear due to the increased mass of the resulting vehicle. An increase in the size of the pack also results in higher efficiency due to lower losses due to operation at lower reaction current densities. The main penalty paid for increasing the size of the battery pack is the resulting increase in cost and the additional energy requirement for the motive power of the additional mass.

The weight of the battery is a function of the number of batteries used and is based on a unit weight of 115 g for the parameterised Kokam 4.8 Ah cells used. Scaling of the battery pack is based on increasing the number of this base unit. It has been assumed that ancillary component and packaging for the battery pack accounts for an additional 10% of the mass of the cells. One of the metrics that will be compared is the range of the vehicles which is defined as the distance traveled from starting at 100% SOC until the 2.7 V cut-off is achieved. As the cell voltage of the battery decreases with decreasing SOC an increased current draw is required for the same power in later cycles as can be seen in figure 6.14a. As such, the SOC difference for the later cycles is also higher due to both higher resistances at lower SOCs and the lower potential, as seen in figure 6.14b.



(a) (b)

Figure 6.14: (a) Example JC08 load cycle on single cell with an 8.88 kWh battery pack (grey lines represent a single drive cycle) and (b) change in SOC for each cycle

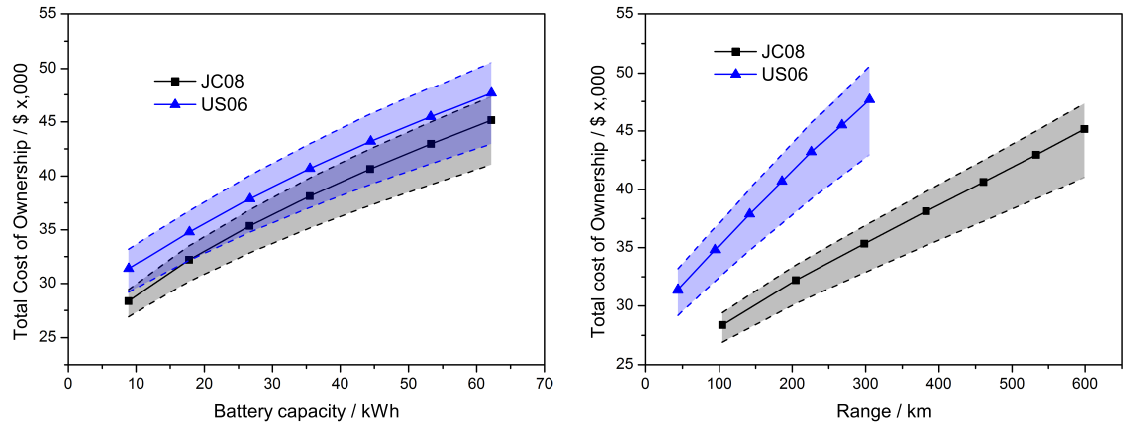


(a) (b)

Figure 6.15: (a) Simulated BEV range and (b) range per kWh for different battery sizes

The non-linear decrease in SOC thus means that to estimate the range of the vehicle, the entire load cycle should be run and not extrapolated from a single load cycle.

Previous analysis of typical vehicle load cycles indicate four distinct load cycles: city, urban/rural, highway and aggressive driving. These can be represented by the NYCC, JC08, HWFETDS and US06 drive cycles, and the following analysis will use these four load cycles. Figure 6.15a shows the simulated range of pure BEVs with different battery sizes under the different drive cycles with regenerative braking taken into account. It can be seen that, within the simulated range, in all cases the range increases with the battery capacity with the JC08 cycle showing the best range and the US06 the worst. Figure 6.15b then shows the range per kWh of battery capacity for different pack sizes and load cycles. It becomes more evident in this plot that there is a law of diminishing returns, whereby an increase in battery capacity results in a smaller gain in range. This is due to the increased mass of batteries and the resulting increase energy requirements to drive the vehicle. In the case of the HWFETDS and US06 cycles there is an optimum point around a battery capacity of 20-25 kWh due to the increase in efficiency gains of lower currents outweighing the decrease in efficiency due to the additional mass. The load cycle which exhibit the worst range is the US06 drive cycle. This is mainly due to the the high proportion of the energy requirements being made up of inertial losses and aerodynamic drag effects relative to the motive power.



(a) (b)

Figure 6.16: 10 year TCO of a BEV under the JC08 and US06 cycles in 2015 under optimistic, baseline and pessimistic scenarios showing (a) capacity and (b) range

With the simulation results the TCO of the vehicle under the different load cycles and battery sizes can be considered. Figure 6.16a shows the 10 year TCO varies under the two extremes of load cycles (JC08 and US06) in 2015 under optimistic, baseline and pessimistic scenarios assuming an annual usage of 20,000 km. It can be seen that the US06 consistently costs more due to the lower range per kWh of the load cycle resulting in higher running costs however due to the relatively low cost of electricity and high efficiency of batteries the difference in the TCO between the two extremes of load cycles is only 5.7% for the baseline case relative to the JC08 TCO. Figure 6.16b then shows the 10 year TCO against the range of the vehicles, which highlights the range sensitivity of BEVs.

From the analysis of pure BEVs the following can be concluded:

- BEVs exhibit a high sensitivity to the selected load cycle with respect the to range
- The load cycles which represent the extremes of operation for a BEV are the JC08 and the US06 which represent the most conservative and aggressive in terms of range
- There is a law of diminishing returns for increasing battery capacity due to the dominating effect of battery mass, although in higher power cycles (HWFETDS and US06) there is an optimum battery size between 20-25 kWh due to operation at a more efficient point
- Due to the high efficiency of batteries and low relative cost of electricity there is little variation in the 10 year TCO of equivalent vehicles under different load cycles

6.7.2 Pure fuel cell vehicle

Pure FCVs have a relatively large FC system that provides all of the motive power for the motors. The advantage of FCVs are that their gravitmetric energy density is higher than that of BEVs, resulting in a far superior range; however, their power density is lower, meaning that the FC has to be sized to the peak power requirement of the load cycle. Combined with the fact that their refueling times are comparable to that of an ICE vehicle means many automotive OEMs have invested heavily in their development as a low-carbon technology.

The disadvantage of pure FCVs is that highly transient performance impacts both the efficiency and the durability of the FC system. Large current ramp rates are often not allowed with a certain current slew rate limit imposed to prevent localised fuel starvation in the FC stack.

In this analysis the coolant pump is run at a constant fixed flow rate with a PID controlled fan that has a target temperature of 65°C, whilst the blower is operated with a PID based controller that maintains the air stoichiometry at target value of 2. This therefore allows for the model to capture the effects of cold start-up which is often neglected and can lead to discrepancies in the efficiency. The power drawn from the FCV will be both the motive power required from the vehicle to follow the time-velocity trace and also the BOP power required to maintain its operation. The blower is limited by a minimum flow rate as air should alway be flowing through the stack even during idle operation to prevent damage. A hydrogen storage capacity of 5.6 kg has been assumed with the assumption that the range can be estimated from the hydrogen consumption of a single cycle.

Figure 6.17 shows the efficiency and range for a pure FCV with different stack sizes and load cycles. It can be seen that in certain cases, increasing the stack size also increases the efficiency of the FC and thus the range, but in other cases the trend is opposite indicating a high sensitivity to the load conditions. In the cases where the efficiency

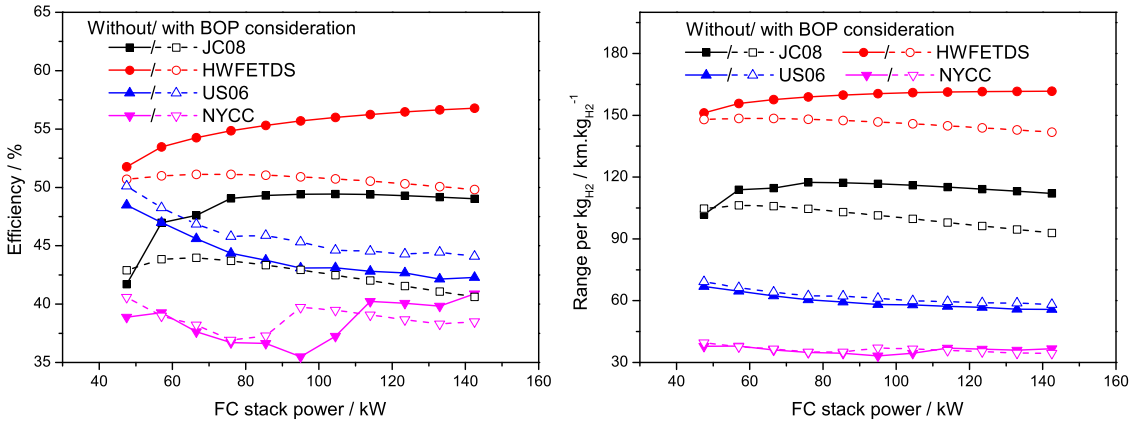


Figure 6.17: (a) Efficiency and (b) range of a pure FCV for different stack sizes and drive cycles with and without BOP power consumption consideration

decreases these are load cycles with heavy acceleration component. In these load cycles, increases in mass result in significantly larger power consumptions due to inertial losses. This increase in power requirement offsets any potential gain from having a larger FC to reduce current density and thus losses. In the case of the highway driving, this is less sensitive to mass increases from a larger FC in terms of power requirements. Thus the increase in FC efficiency comes from operation at lower current densities.

The city drive cycles also suffer from higher losses due to high rates of transient load changes. In addition, the city drive cycle suffers from lower range and efficiency due to the larger proportion of stop periods. During stop periods the blower must still be active and thus power must be generated to do this during periods whilst the vehicle do not require motive power. The constant flowing of air through the FC when no considerable power is being drawn lowers the stack temperature and humidity leading to further inefficiencies. It can also be seen that if the BOP energy was not considered then the range estimations for the FCVs would in general be overestimated.

The variation of the fuel efficiency of a FC is shown in figure 6.18a for a static case. In the case of the less dynamic highway driving the increase in range and efficiency is due to the fact that the increase in stack size allows for operation at lower current densities which results in higher efficiencies. This gain in FC efficiency is greater than the additional losses incurred from the additional mass. In the case of the city driving, increasing the stack size increases the baseline power requirement which initially isn't offset by the increases in efficiency during operation until a certain size after which overall efficiency increases again. In the aggressive driving the additional energy of the mass has a dominant effect such that efficiency is always decreasing.

In this case the HWFETDS and NYCC represents the best and worst case load cycle for a FCV. If the TCO of the for the FCVs are then calculated clear differences in the cost after 10 years becomes apparent from the different load cycles. This is shown in figure 6.18b. From this analysis it becomes apparent that the efficiency gains from having a larger FC do not offset the higher capital costs in all drive cycles. The most favorable driving style for the FCV powertrain appears to be the highway driving due to low transient losses. The most unfavourable appears to be city driving. Here the highly transient load and frequent stop events results in considerable losses due to mass transport and idling losses from the BOP.

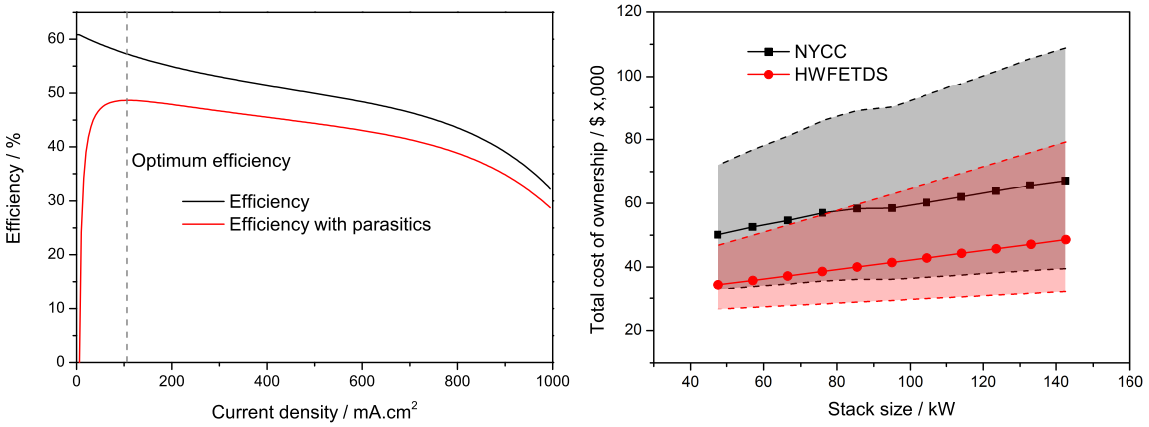


Figure 6.18: (a) Fuel efficiency of FC with and without consideration of parasitic power consumption. Here assuming a base value plus 10% of power and (b) 10 year total cost of ownership for the simulated FCVs under different drive cycles assuming a 20,000 km annual usage showing baseline, optimistic and pessimistic scenarios (shaded regions)

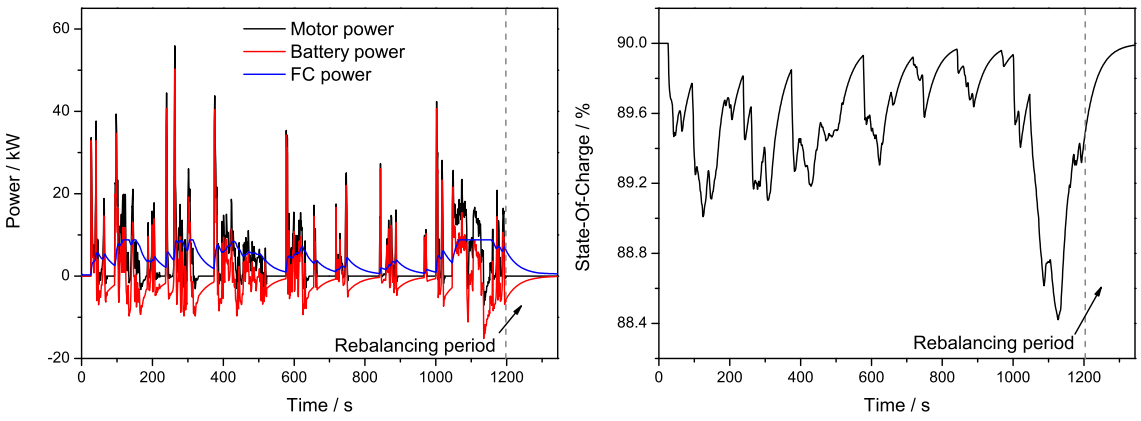
From the analysis of pure FCVs the following can be concluded.

- Pure FCVs are not ideal for city driving due to the relatively large idle power losses and associated lower temperature operation leading to inefficiencies
- Pure FCVs favour highway driving due to the low transient variation of the loads
- Increases in the stack power typically result in higher efficiency due to operation at lower current densities up to a certain point depending on the load cycle. Increases beyond that result in lower efficiencies due to the increase in vehicle mass power requirements and also the colder operation resulting in slower chemical kinetics
- The impact of the BOP power consumption is important and changes the trends in efficiency and range

6.7.3 Fuel cell-battery active hybrid

FC-battery active hybrid systems have been investigated as a means of aggressively downsizing the FC. In this configuration a relatively small FC is combined with a small battery pack (relative to a pure BEV) to meet to vehicle load requirements. A DCDC converter is used to regulate power between the FC, battery and motors allowing for significant reductions in the load dynamics of the FC and allowing for operation at a more optimal efficiency point. This therefore allows the vehicle designer to decouple the power and energy requirements of a vehicle. This has the advantage of potentially lowering the cost of the overall system as well as improving durability of the FC by operating it in more preferable conditions, i.e. away from high potentials and rapid load cycling.

In the FC-battery hybrid configuration, the FC provides a more steady load and the battery handles the majority of the rapid power fluctuations. In this analysis a charge sustaining strategy for controlling the FC was used. The power requirement of the FC is controlled by a PID controller which tries to regulate the SOC of the battery around the same steady state value. After each load cycle, the simulation is allowed to continue until the FC has recharged the battery to the initial SOC. This allows for a fairer comparison of the results. If this was not done then the different battery SOCs would vary the results, potentially overestimating the range of the vehicle due to high utilisation of the battery SOC from the beginning to end of the load cycle. This is shown in figure 6.19

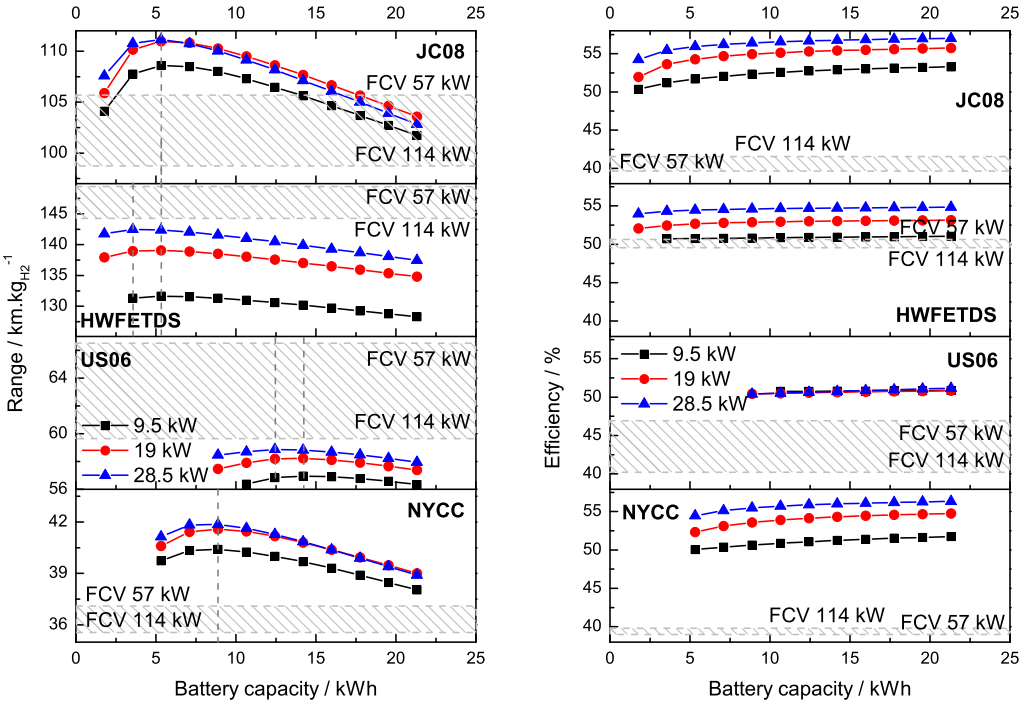


(a) (b)

Figure 6.19: (a) Simulated power for a FC-battery hybrid powertrain with a 9.5 kW FC and 8.88 kWh battery pack under the JC08 cycle and (b) variation in SOC

which shows the power split between the devices and the variation of SOC. Decreasing the battery size will allow for a greater range of the battery SOC to be used up to a certain limit as the overpotentials associated with higher current operation results in reaching the cut-off potentials earlier. In this study a non-valid solution is assumed if the battery potential goes outside of the 4.2-2.7 V single cell range.

The simulations run were based on three FC sizes: 9.5, 19 and 28.5 kW where the BOP power was scaled appropriately. In each case the battery size was allowed to vary. Figure 6.20 shows the results of the simulations under the four exemplar load cycles. In figure 6.20a it can be seen in all load cycle cases there is an optimum battery



(a) (b)

Figure 6.20: Simulated range (a) and FC efficiency (b) of a FC-battery active hybrid system with charge sustaining operating mode with different battery and FC sizes. Shaded regions represent the equivalent FCV performance

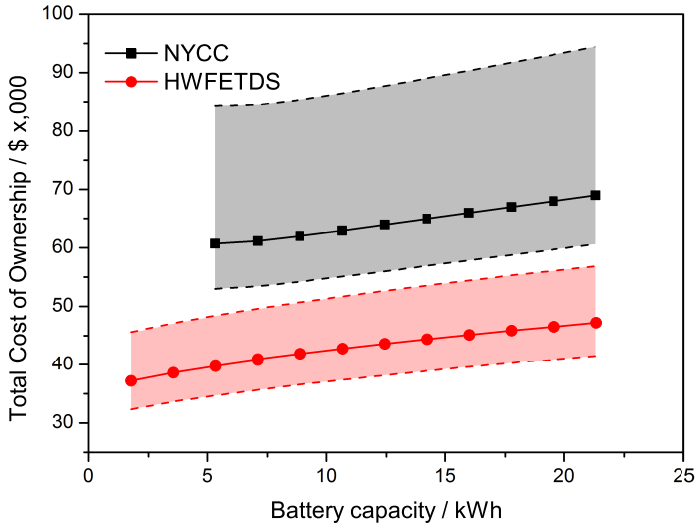


Figure 6.21: 10 year total cost of ownership for a 19 kW FC-battery hybrid under the NYCC and HWFETDS cycles with baseline, optimistic and pessimistic cost assumptions (shaded regions)

size to maximise the range of the vehicle. In hybrid systems with small battery packs the load experienced by the battery is more aggressive leading to more significant losses. Increasing the battery size for a fixed FC size allows for lower currents and more efficient operation; however, after a certain point the mass required for the additional batteries increases the energy requirements of the vehicle more than the amount of energy saved through the efficiency gains. In all cases a battery size smaller than 15 kWh allows for maximum benefit in terms of range. This is in agreement with literature values quoting an optimum of approximately 5-15 kWh [149].

The plots also show a comparison against the pure FCV mode. In the case of the NYCC cycle the range per unit mass of fuel increased by between 5.9-12.7% when comparing between worst and best case for a 28.5 kW FC in the battery hybrid configuration. This gain comes about due to the lower idling losses in the FC-battery hybrid configuration, whereby the FC recharges the battery during periods of idling, whereas in the pure FCV there is a net negative energy from the FC due to the power requirements of the BOP. In the case of the HWFETDS the FC-battery hybrid typically performs worse with respect to range due to the batteries being largely unused whilst their weight adds an additional power requirement. The operation point of the FC is also in a more efficient region due to lower current density operation in pure FCV mode. Here fuel efficiency is upto 7.4% worse in the FC-battery hybrid configuration.

When increasing the FC size it can be seen in general a larger FC results in a greater range due to operation at lower current densities in the FC and thus more efficient operation as seen in figure 6.20b. However, in the lower speed cycles with more aggressive acceleration/ deceleration, increases in the FC size results in lower ranges due to the relatively large inertial losses relative to the speed. When considering all 4 load cycles it would appear that the optimum FC stack size is around 19 kW.

When comparing the efficiency of the FC in hybrid mode to pure FC mode it can be seen that the efficiency is consistently above that of pure FC mode. This is due to the fact that in hybrid mode the FC is operated under near constant conditions, reducing losses associated with manifolding and compressor inertia effects. In addition, there are considerably fewer idling events where zero net power is produced but power is wasted on maintaining a baseline BOP power. Also, under constant power operation the FC stack can achieve a higher temperature operation, whereby the pure FC mode the temperature varies more considerably due to the more frequent idling events where the need for a continuous air flow results in excessive cooling.

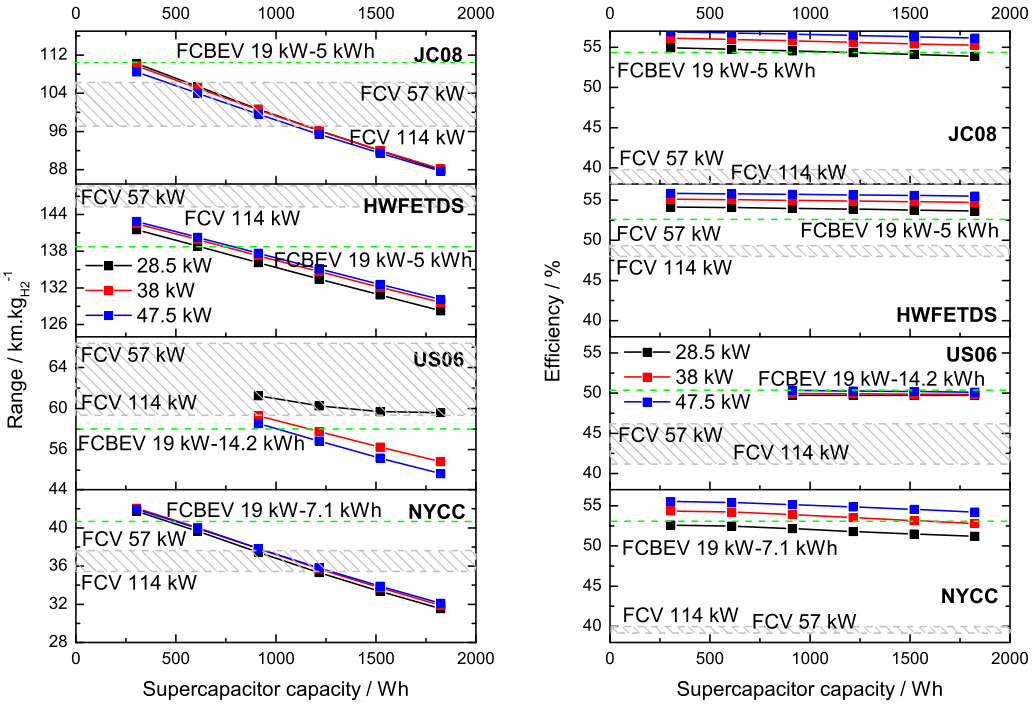
Figure 6.21 shows the TCO for a 19 kW FC under baseline, pessimistic and optimistic cost scenario with a varying battery size. Here it can be seen that the NYCC cycle performs worse than the HWFETDS. In this case the running costs are lower but the capital costs are higher

From the analysis of FC-battery active hybrids the following can be concluded.

- Maximum benefit in range is achieved with battery sizes in the range of 5-15 kWh and a FC stack size of 19 kW for most drive cycles. Smaller packs result in excessive electrochemical losses
- FC efficiency in battery hybrid mode is higher than in pure FC mode due to slower load transients
- The FC-battery shows fuel efficiency benefits of between 5.9-12.7% under the NYCC cycle, compared to th due to fewer idling losses but shows a reduced fuel efficiency for the HWFETDS of upto 7.4% due to the operation at higher current densities in the hybrid configuration and the relative inactivity of the battery pack

6.7.4 Fuel cell-supercapacitor active hybrid

The previous section investigated the performance and TCO of a FC-battery active hybrid system using a charge sustaining operational strategy for a relative small FC. An alternative to the FC-battery hybrid system is the FC-supercapacitor system. Due to the absence of a charge transfer process in supercapacitors, their internal impedance is much lower than batteries and thus offers a more efficient means of energy storage than lithium-ion batteries; however, their limitations lie in their reduced energy density. The following thus analyses the performance metrics of a FC-supercapacitor active hybrid system using the same parameters as the FC-battery system allowing for direct comparison.



(a) (b)

Figure 6.22: Simulated (a) range and (b) FC efficiency of a FC-supercapacitor hybrid system

In the previously analysis with the FC-battery active hybrid simulations, a stack sizes of 9.5, 19 and 28.5 kW was simulated. In the FC-SC active hybrid system not all of the load cycles completed with these stack sizes due to the supercapacitor voltage falling too low. Therefore, in the FC-supercapacitor simulations, sizes of 28.5, 38 and 47.5 kW were simulated as these were able to complete the load cycles. This highlights one of the drawbacks of the FC-supercapacitor system in that, due to the lower density density of the supercapacitors, a larger FC is typically required and prolonged pulses of high power requirements drive the system to low operating potentials. Figure 6.22a shows for the four example load cycles the range per kg unit mass of fuel.

By varying the number of supercapacitors to increase the capacity, it can be seen that in general a decrease in range is experienced when increasing the number of supercapacitors. This can be attributed to the fact that in the FC-supercapacitor system the supercapacitor losses are not significant due to the inherently low impedance. As such, an increase in capacity and thus a decrease in the average operating current density results in a negligible improvement in the efficiency. The increase in the mass of the vehicle that comes with the increase in the capacity is the dominating factor here. Increasing the size of the FC stack also has a negligible impact on the overall range. Comparison between the FC-battery and FC-supercapacitor hybrid systems shows the most significant improvements in range being achieved in aggressive driving.

Figure 6.22b then shows the FC efficiency under the different load cycles. Again, an increase in supercapacitor capacity reduces FC efficiency due to the dominating effect of mass on increasing in energy requirement of the vehicle and shifting the average operating current density of the FC to higher values and thus increases the losses. Increasing the FC stack size in this case increases the FC efficiency due to a shift of the current density to lower values, however the increase in efficency of the FC is again not enough to compensate for the increase in energy requirements for the load cycle due to the extra mass of the FC and the supercapacitors.

Figure 6.23 shows the 10 year TCO for the FC-supercapacitor hybrid system under conservative, baseline and pessimistic conditions for the NYCC and HWFETDS load cycles which represent the extremes of operation. Again the NYCC is consistently higher in cost due to the higher running costs. Increasing the supercapacitor has a negative impact on the TCO. Direct comparison with the FC-battery TCO shows that in both

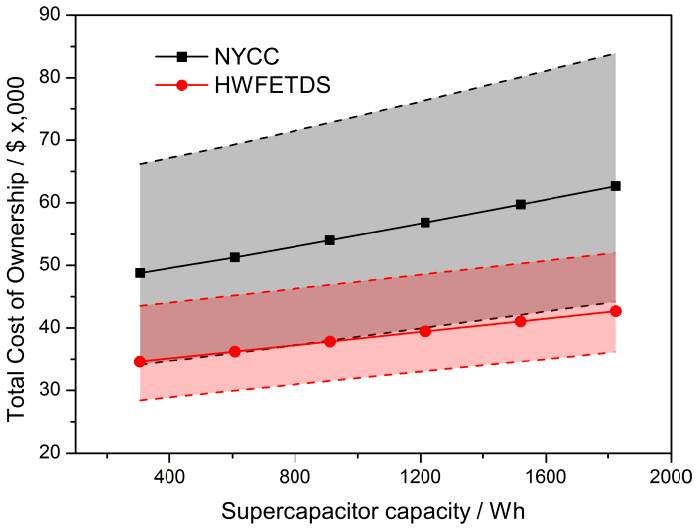


Figure 6.23: 10 year total cost of ownership for a 38 kW FC-supercapacitor hybrid under the NYCC and HWFETDS cycles with baseline, optimistic and pessimistic cost assumptions (shaded regions)

cases the FC-supercapacitor hybrid is lower.

From the analysis of the FC-supercapacitor active hybrid the following can be concluded

- Relative to the FC-battery hybrid system, the FC-supercapacitor system requires a large FC in order to complete the 4 example load cycles due to the lower energy density of supercapacitors
- An increase in supercapacitor capacity results in an overall reduction in the vehicle range due to the dominant effect of mass
- Most benefit in terms of range is achieved with aggressive driving
- The TCO for both the NYCC and HWFETDS cycles are lower for the FC-supercapacitor hybrid than compared to the FC-battery hybrid

6.7.5 Passive hybrid system

The previous analysis on FC-battery and FC-supercapacitor hybrid systems have shown that hybridisation offers possible reduction in the FC size as well as range improvements under certain load cycles. During the initial stage of commercialisation the FC cost is still anticipated to be high. The cost of any EV thus need to be further reduced. The concept of the passive hybrid system is to eliminate the need for costly DCDC converters that usually regulate power between different devices in a hybrid vehicle as well as their associated electrical losses. The passive system achieves this by the direct coupling of these such that their operating voltages must match. Power split between the devices is achieved by the difference in either the thermodynamic potential of the device or a difference in impedance. This means that the DCDC converter is not needed and the associated losses are not encountered. The drawback of this system is that the user loses active control of the power flow between devices. Therefore, in passive hybrid applications the sizing of components becomes a critical metric to consider.

The basic principle of a passive hybrid system can be schematically represented in figure 6.24 which illustrates a FC-supercapacitor passive hybrid system. The division of power is a inherent feature of the system when the impedance of the coupling devices is different and also the rate of change of thermodynamic potential. Under steady no load conditions, the thermodynamic OCV of both the FC and the supercapacitors are equal and the two devices have the same potential. Upon application of a load, the

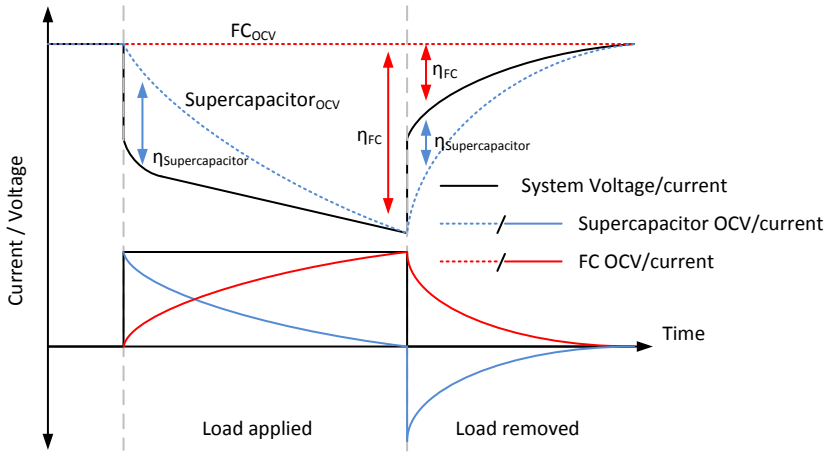


Figure 6.24: Figurative representation of voltage, current and overpotentials during dynamic operation for a FC-supercapacitor passive hybrid system

system potential drops. Initially the overpotential of both devices is the same and due to the supercapacitors lower impedance it gives a larger proportion of the current. As the OCV of the supercapacitors fall due to decreasing SOC, the supercapacitor overpotential gradually decreases until the system working potential is the same as the supercapacitor OCV potential at which point all of the current is handled by the FC since the OCV is relatively constant and not a function of current throughput. Upon load removal the difference between the OCV of the FC and supercapacitor results in the FC charging the supercapacitors until the potentials are equal again.

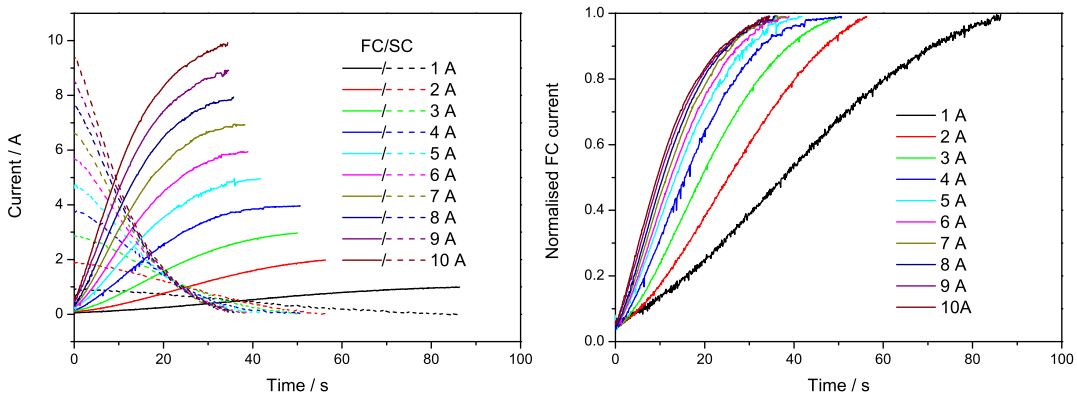
The principle operating mechanism is the same for FC-battery passive hybrids and FC-battery-supercapacitor triple hybrids but the analysis will focus on the dynamic behaviour of the FC-supercapacitor passive hybrid hereafter due to the gap in the literature in the area previously identified in section 2.5.6.

6.7.6 Fuel cell-supercapacitor passive hybrid

It has been shown in the academic literature that excessive cycling of batteries at high C-rates can lead to accelerated degradation due to the onset of mechanical failure of the electrode materials. Supercapacitors on the other hand have exceptional cycle lives due to the absence of Faradaic processes in addition to their low impedances. Previous analysis has also shown the potential benefits of FC-supercapacitor active hybrids and this section will focus on the performance of FC-supercapacitor passive hybrid systems.

As mentioned previously, due to the difference in impedances of the devices (supercapacitors having a much lower impedance than FCs), a passive FC-supercapacitor hybrid system will result in the supercapacitor initially providing the peak power requirements. Figures 6.25a and 6.25b shows the response of a FC-supercapacitor passive hybrid system to step loads of varying current. Here a 100 W Horizon FC was coupled to a 10×150F Maxwell supercapacitor pack. Upon application of the load to the system the supercapacitors initially handle the majority of the load. As their SOC drops the FC gradually ramps up. It can be seen that as the load current increases the time taken for the FC to take the full proportion of the load decreases in a logarithmic fashion.

When varying the load, it can be seen from the normalised plot of the current load on the FC that transient buffering effects are less effective at higher currents, however, this converges to a uniform normalised profile. This can be attributed to the decrease in the polarisation resistance of the FC when under load as suggested by the Butler-Volmer



(a) (b)

Figure 6.25: (a) Currents for a FC-SC passive hybrid system under varying step loads and (b) normalised FC currents in the same FC-SC passive hybrid system

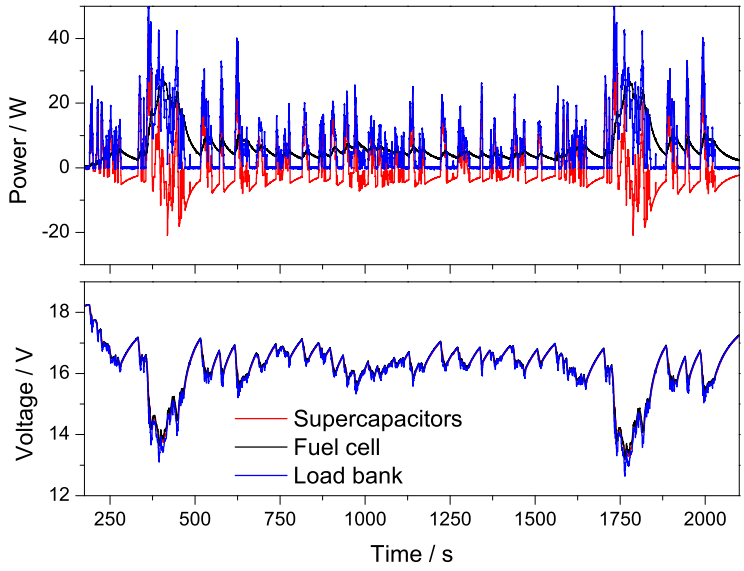


Figure 6.26: Power split between a 100 W PEMFC and 10 x 150 F supercapacitor pack under a scaled down FTP load cycle with a 50 W peak load

equation. At lower step loads, the charge transfer resistance is higher and thus the ratio of supercapacitor to FC resistance is very small, resulting in slower load dyanmics for the FC.

Figure 6.26 then shows the response of the system to a FTP vehicle load cycle for the scaled down 100 W PEMFC directly coupled to a 10 x 150 F supercapacitor pack to highlight the dynamic performance characteristics of the system. Here the voltages of the load bank, FC and SC pack are all the same due to the passive coupling. There are slight variations due to contact resistances between the devices. As the impedance of the SC pack is smaller than that of the FC, the SC pack provides the peak power requirements of the load cycle. This enables the FC load to meet the average of the load cycle rather than the peak allowing for the possibility of FC downsizing and further cost savings. The fact that the majority of the transients are handled by the SC pack means that the FC load is much smoother. This means the FC is allowed to operate much more efficiently as mass transport losses aren't as much of an issue.

During the FTP cycle however it could be seen that there were long periods of high power consumption whereby the supercapacitors became increasingly depleted resulting in the FC power having to ramp up. This therefore highlights one of the limitations of the FC-supercapacitor hybrid system in that the limited energy density of the supercapacitors may restrict downsizing of the FC depending on the load cycle.

To highlight this further figure 6.27 shows the response of the system to a HWFETDS drive cycles. Here it can be seen that the FC constantly operates at a higher power with periods where it handles all of the power requirements of the load cycle. The HWFETDS which is characteristic of highway driving, by nature, has fewer stop-start events, which in the FTP load cycle allowed for the FC to recharge to supercapacitors such that the subsequent load events did not require the FC power to be as high. Figure 6.28 then shows the current histograms for the FC-SC passive hybrid system under both the FTP and HWFETDS cycles.

It can be seen that in both cases the peak FC load and the peak in its average operating point is shifted to a lower current however the peak shaving benefits are more apparent on the FTP load cycle. The distribution of the current loading in the case of the supercapacitor however exhibits a Gaussian distribution around a mean load of zero thus

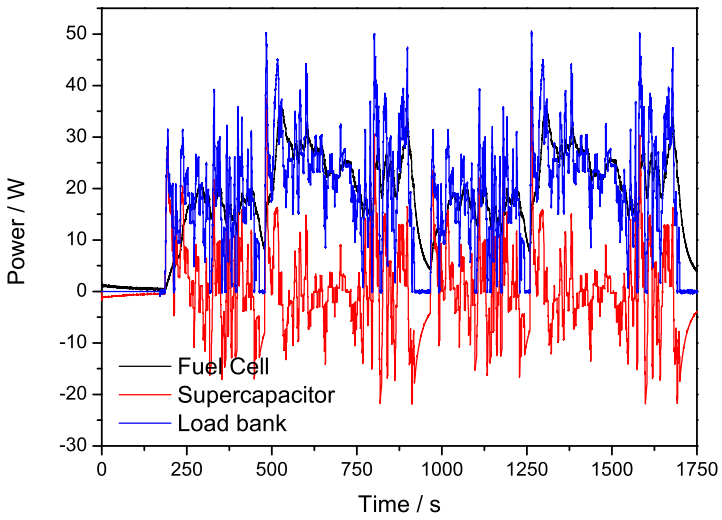
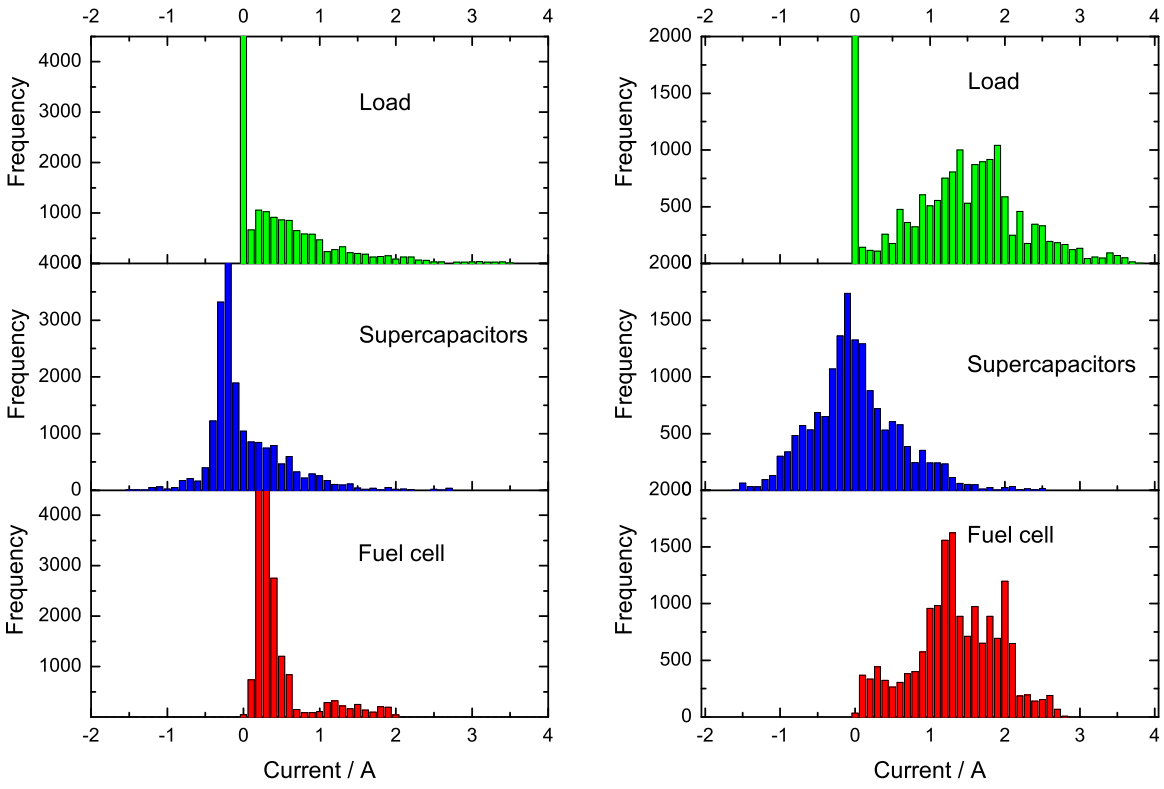


Figure 6.27: Power split between a 100 W PEMFC and 10 x 150 F supercapacitor pack under a scaled down HWFETDS load cycle with a 50 W peak load

showing that the supercapacitor acts as a load buffer and thus provides an approximately zero net current contribution. In the case of the FTP drive cycle where there is a large amount of idling which would normally leave the FC at elevated potentials and thus accelerating carbon corrosion it can be seen that there is very little no load idling due to the constant charging of the supercapacitors.



(a) (b)

Figure 6.28: Current histograms for the (a) FTP and (b) HWFETDS

From this experimentally based study of the FC-supercapacitor passive hybrid system the following can be concluded:

- FC-supercapacitor hybrids vastly reduce the transient loading on FCs, with the benefits most evident at lower step currents due to the higher resistance of the FC
- Some downsizing of the FC is possible however this depends on the load cycle, whereby a frequent stop-start cycle achieves the greatest benefit relative to a near constant highway driving cycle
- In most load cycles the FC-supercapacitor passive hybrid allows for a vast reduction in time spend at OCV inferring a reduction in the degradation of the carbon supported catalyst and various components within a FC MEA

From the scaled down system analysis of the FC-supercapacitor system it has been shown that there is potential benefit to be gained from this system and the previous literature review has indicated that this is an area which is currently lacking. Thus, the subsequent section will focus on the development and analysis of a larger scale system which is more representative of a system which would be in a vehicle. The scaled down experimental rig uses a open cathode PEMFC with a prescribed controller which operates at extremely high stoichiometries. These open cathode systems are often limited to lower powers (< 5 kW) due to thermal management issues. Closed cathode systems with active liquid cooling are the more likely candidate for automotive FC systems and highlights the need to consider scaling effects.

6.7.7 Large scale fuel cell-supercapacitor passive hybrid system

As systems are scaled up, inhomogenities in the performance of the system become increasingly evident. If these effects are not considered then errors in the system performance may result. Therefore, to validate the advantages of the FC-supercapacitor passive hybrid system a large scale 9.5 kWe PEMFC was hybridised with a 33×1500 F supercapacitor pack. The rig was constructed with the intension of validating the established models as well as acting as a portable power generate at music festivals and thus was named, "Project Rock Band".

The FC system architecture used in this rig was the same as described as in section 4.4.

Electrical system architecture

Figure 6.29 shows the wiring diagram for the powertrain system. For the purposes of testing, a 12 kW resistive load bank was used. In the full system a 5 kW DCAC inverter was used.

Mechanical contactors between the FC, supercapacitor and load provided controllable electrical isolation for each component. A 310 A fuse in-line with the FC and supercapacitors provides additional passive protection in the case of large in-rush currents. A diode was placed in front of the FC to prevent possible charging of the FC stack from the supercapacitors in case the thermodynamic OCP of the stack drops below that of the supercapacitors.

All BOP components were powered by a 24VDC supply via a low voltage bus. During start-up/shut-down events, the BOP was powered by two 12 V lead acid batteries connected in series. During normal operation, two parallel DCDC converters parallel delivered power to the low voltage bus. A contactor allowed for the switching in and out of the lead acid battery. During operation this was charged by either the inverter or an external power supply via a manufacturers recommended charger. The lead acid battery was not charged by the low voltage DCDC converters due to the fact that the charge

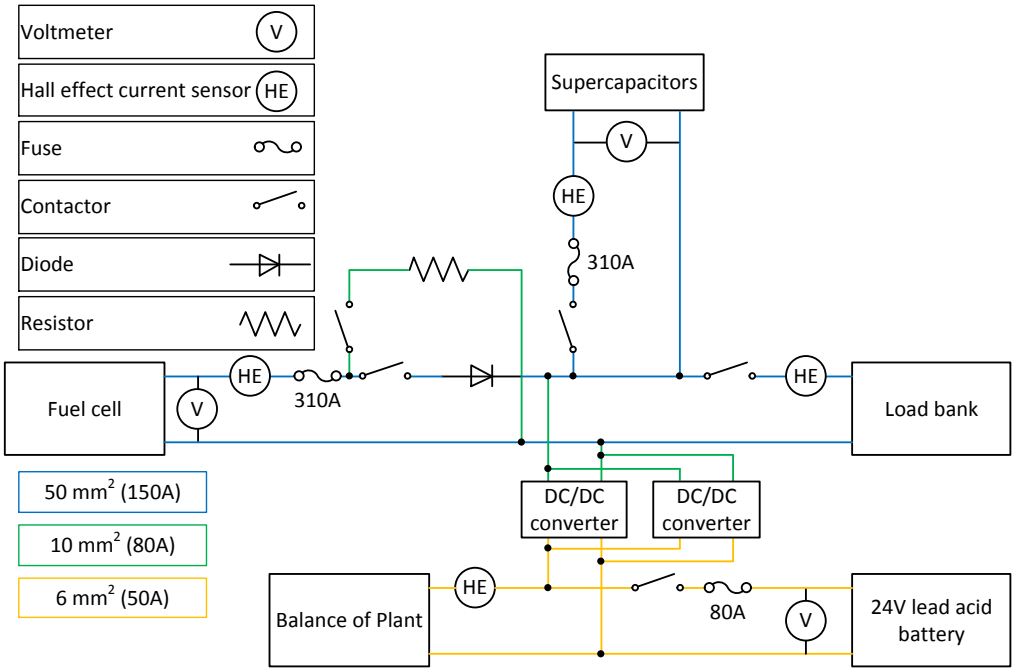


Figure 6.29: Wiring diagram for powertrain components in 9.5 kWe PEMFC-supercapacitor passive hybrid system. Adapted from Wu *et al.* [225]

impedance of the battery is relatively high and thus a significant overpotential is required for rapid charging which is not possible via the DCDC converters which maintained a constant potential of 24 V.

Prior to connecting the FC and supercapacitors to the main power bus, the supercapacitors were pre-charged to just below the FC OCP via an external charging circuit to prevent large inrush current from the FC to the supercapacitors when the two devices are initially connected. This is required after long periods of inactivity due to the relatively fast self-discharge rate of the supercapacitors.

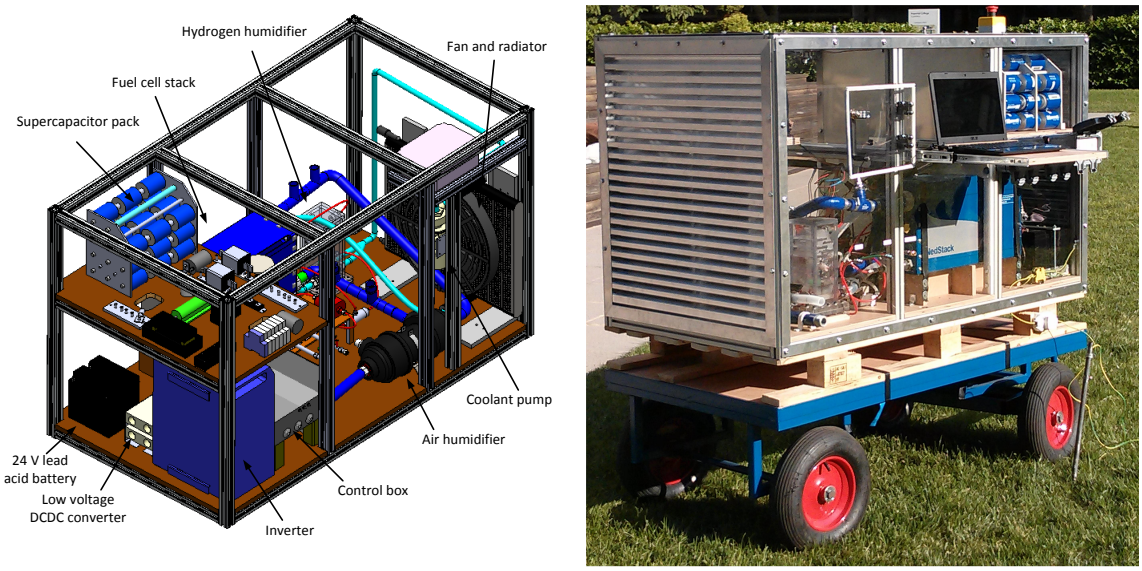
A resistor was wired in parallel to the FC and connected through a contactor. This resistor was used during the shut-down procedure under autonomous operation. Upon shut-down, the hydrogen supply was closed, however residual amounts of reactants in the gas diffusion electrodes and flow channels gave rise to an elevated OCP until the reagents were consumed. As elevated potentials are detrimental for carbon corrosion, the resistor was used to apply a load to the FC to facilitate the consumption of residual hydrogen.

A Computer Aided Design (CAD) model and picture of the FC-supercapacitor system is shown in figure 6.30.

Control system

The control system is based on the work described in section 4.4.1 with additional features included. Control was achieved through the use of a NI cRIO with RT and FPGA capabilities which was controlled by a host computer running NI LabVIEW with a custom made control program. Table 6.5 lists the cRIO component used and their application.

The cRIO was also connected to the 24V low voltage BUS and shared the common ground. The Hall effect sensors used to measuring current required a 5 V power supply which was provided via a 24 V-5 V linear regulator. All other transducers worked from the 24 V BUS.



(a) (b)

Figure 6.30: (a) CAD model of the fuel cell-supercapacitor passive hybrid system and (b) picture of actual system [225]

During operation, the air system could be operated with either a feed forward controller based on the current drawn for the blower to maintain a certain stoichiometry with a baseline value or in manual model. Similarly the cooling system could be operated either in manual control mode or through a PID controller for the fan with a fixed coolant flow rate which was found to the be most efficient means of heat dissipation with these two degrees of freedom.

Table 6.5: National Instruments equipment for the 9.5 kW FC-supercapacitor passive hybrid system

Component		Channels/Range	Use
Real Time controller	cRIO-9022		Real time data processor
FPGA chassis	cRIO-9114	8-slot	FPGA processor
Analog Output module	NI 9263	4-channel / ±10 V	Controls coolant pump, fan and recirculation pump
Thermocouple module	NI 9213	16-channel	Measure temperatures
Analog Input module	NI 9205	32-channel / ± 10 V	Measure output signals from pressure transducers and hydrogen flow meter
Universal Analog Input module	NI 9219	4-channel / ± 60 V	Measure FC, supercapacitor and lead acid battery voltages
Digital Output module	NI 9472	8-channel / 24 V	Provides PWM signal for blower control
Solid State Relay module	NI 9485	8-channel	Controls contactors and gas solenoids
CAN BUS module	NI 9853	2-port High speed	Reads in CAN BUS data from FC cell voltage monitoring system

6.7.8 FC-supercapacitor passive system test

The concept of the FC-supercapacitor passive hybrid system is that the supercapacitors will act as a low-pass filter to high frequency oscillating loads which are detrimental to FC efficiency and durability. EIS measurements as presented in section 5.3.2 indicated that the total polarisation resistance of the 33 cell supercapacitor pack would be 22.4-30.4 mΩ. Current interrupt measurements showed total polarisation resistances for the FC ranged from 500-225 mΩ. Since the supercapacitor resistance is an order of magnitude smaller than the FC, it will initially handle the majority of the load until the thermodynamic potential of the supercapacitors drops to the operating potential as suggested in figure 6.24.

Understanding the dynamic response of the system is the first stage of characterising the system benefits. Figure 6.31 shows the response of the FC-supercapacitor passive hybrid system to a 100 A step load. It can be seen that the supercapacitors provide the peak load due to their lower impedance, however as their cell potential drops under discharge the FC current ramps up as the deviation from the OCV increases. This continues until the FC handles 100% of the load current. Upon removal of the load, the FC recharges the supercapacitors.

The immediate advantage of this passive coupling is that under step load conditions the FC, and associated BOP, have sufficient time to ramp up. The more gradual increase in load means that the additional losses from initial mass transport and also from the additional power required from the BOP to increase blower speed is not experienced. The peak power of the system under step loads is also increased as the voltage is higher for the same, pure FC, load. In terms of system durability, the supercapacitors act as a low pass filter to the FC. This increases system efficiency due to lower transient mass transport losses and improves system durability from the point of view of reduced power cycling and thus reduce platinum dissolution and also decreased time at elevated potentials thereby reducing the rate of catalyst carbon support corrosion.

Figure 6.32 then shows the dynamic response of the system to step loads of varying amplitudes. Prior to application of the step load, current between the FC and supercapacitor was allowed to equilibrate until the system voltage was 69 V, indicating a charge current of < 1 A. Choosing a voltage datum is preferable to current due to the measurement resolution of the hall effect current transducers which were $\pm$ 3 A.

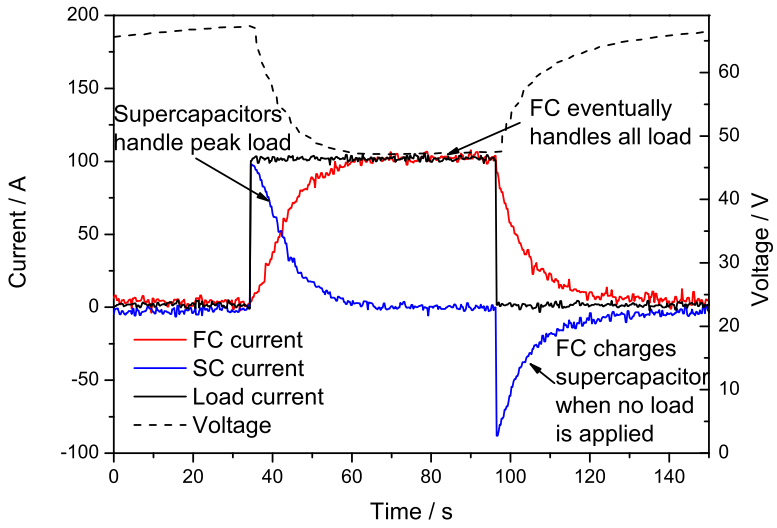


Figure 6.31: Dynamic response of a P9.5-75 Nedstack PEMFC and 33×1500 F supercapacitor pack under a 100 A load [225]

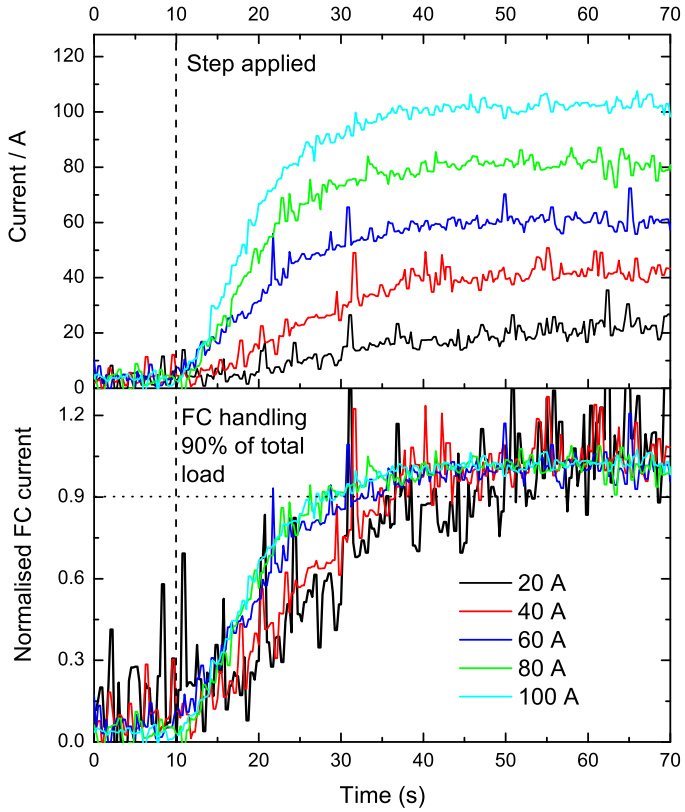
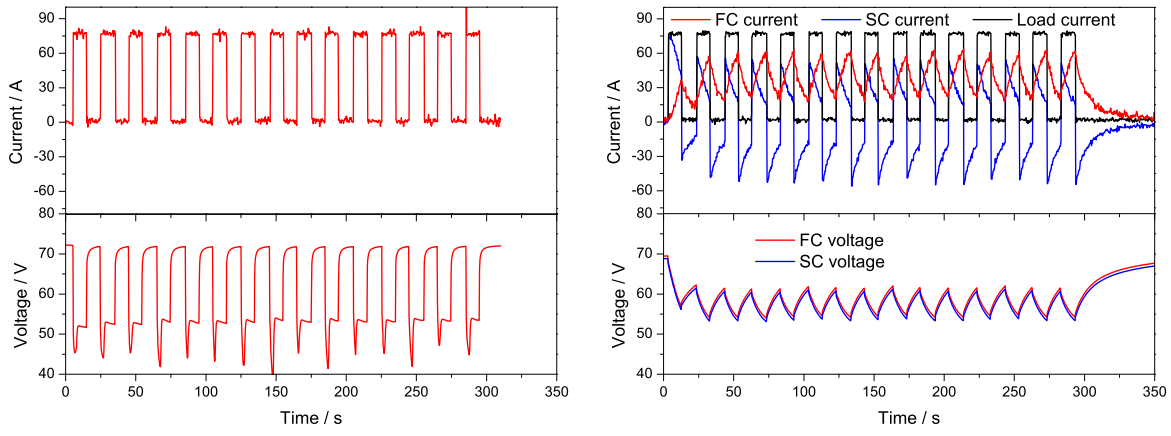


Figure 6.32: Comparison of dynamic fuel cell response to step load in FC-supercapacitor passive hybrid mode [225]

It can be seen that upon application of the step load, the supercapacitors give the FC approximately 20 s time to ramp to 90% of the applied load. This is true for all loads as they converge to a normalise current profile. Lower step loads experience a system response due to operation in the non-linear activation region of the FC polarisation curve. Above a step load of 40 A the normalised FC response time converges to the same profile due to less time operated in the activation region and a proportionally longer time in the linear ohmic region as the system ramps up.

The air subsystem uses a low pressure blower that works at an operating stoichiometry of 2. A feed forward controller controls the power to the blower however upon application of a step load in current, the blower has a finite transient time to ramp up and also gas



(a) (b)

Figure 6.33: Comparison between pure FC (a) and FC-supercapacitor passive hybrid under 75 A step loads (b) with a frequency of 0.2 Hz [225]

manifolding effects result in the observed voltage sag. Once the blower overcomes the impeller inertia and the reactant is delivered to the stack the voltage recovers. These voltage sags under step loads therefore lead to additional inefficiencies as observed in figure 6.33a when a 75A step load is applied with a 0.2 Hz frequency. In Figure 6.33b, the same load profile is applied but this time the supercapacitor pack is coupled passively. The result is the supercapacitors handle the peak load initially and subsequentially, after reaching a dynamic equilibrium operates around an average load of zero as it removes the peaks from the load cycle. The FC therefore meets the average load with sufficient time for the air blower to meet the transient loads. The result is therefore a removal of the voltage sag due to additional mass transport losses due to blower inertia and gas manifolding.

Figure 6.34 shows the efficiency comparison between the pure FC and FC-SC passive hybrid system under the 0.2 Hz pulse load with varying amplitude. It can be seen that in both cases the efficiency of the FC decreases with increasing pulse load amplitudes due to the increased losses associated with higher current densities. Comparison between the pure FC and FC-SC passive hybrid system shows that a 5% efficiency gain is achieved. This is mainly due to fewer ohmic losses due to operation at a lower current density despite the increased polarisation resistance and also the system being able to handle the transients much better resulting is fewer mass transport related under voltage sags. Here the efficiency of the FC is defined as shown in equation 6.21. Where $-\Delta\bar{h}_f$ is the enthalpy of formation assuming the Higher Heating Value (HHV) for a PEMFC reaction which is -285.84 kJ.mol^{-1}.

$$\eta_{FC} = \frac{\text{Energy per mol of hydrogen}}{-\Delta\bar{h}_f} \tag{6.21}$$

Of course an idealised step load is not very indicative of real world load conditions. As such the system was run under a 1/10th scale Highway Fuel Economy Test (HWFET) drive cycle which is representative of highway driving. A power profile assuming a 1500 kg massed vehicle accounting for inertia, aerodynamic and rolling resistance losses was generated. A constant motor efficiency of 95% was assumed. Figure 6.35 shows the dynamic response of the system under a 1/10th scale HWFET drive cycle. Just

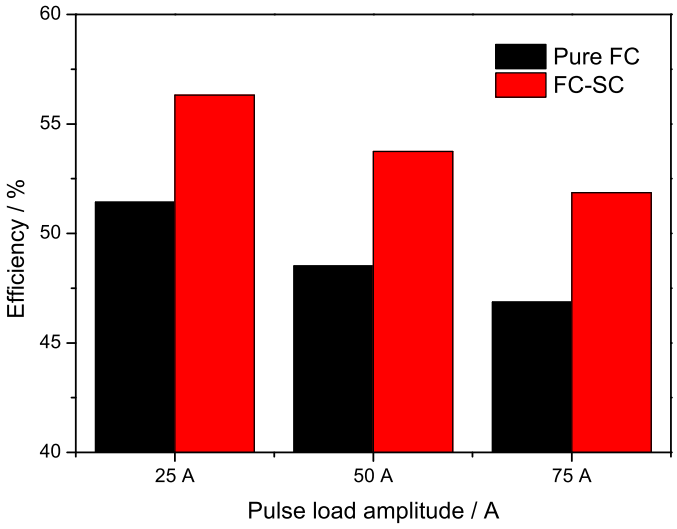


Figure 6.34: Comparison of fuel cell efficiency between pure FC and FC-SC passive hybrid system with the fuel cell operating with an air stoichiometry of 2 [225]

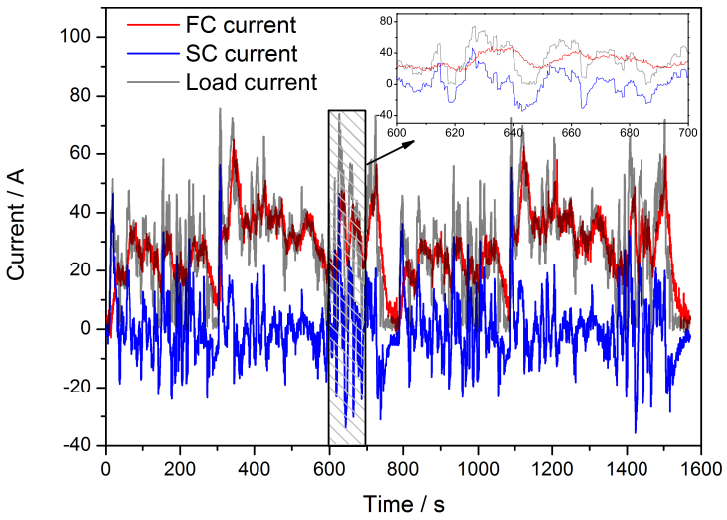


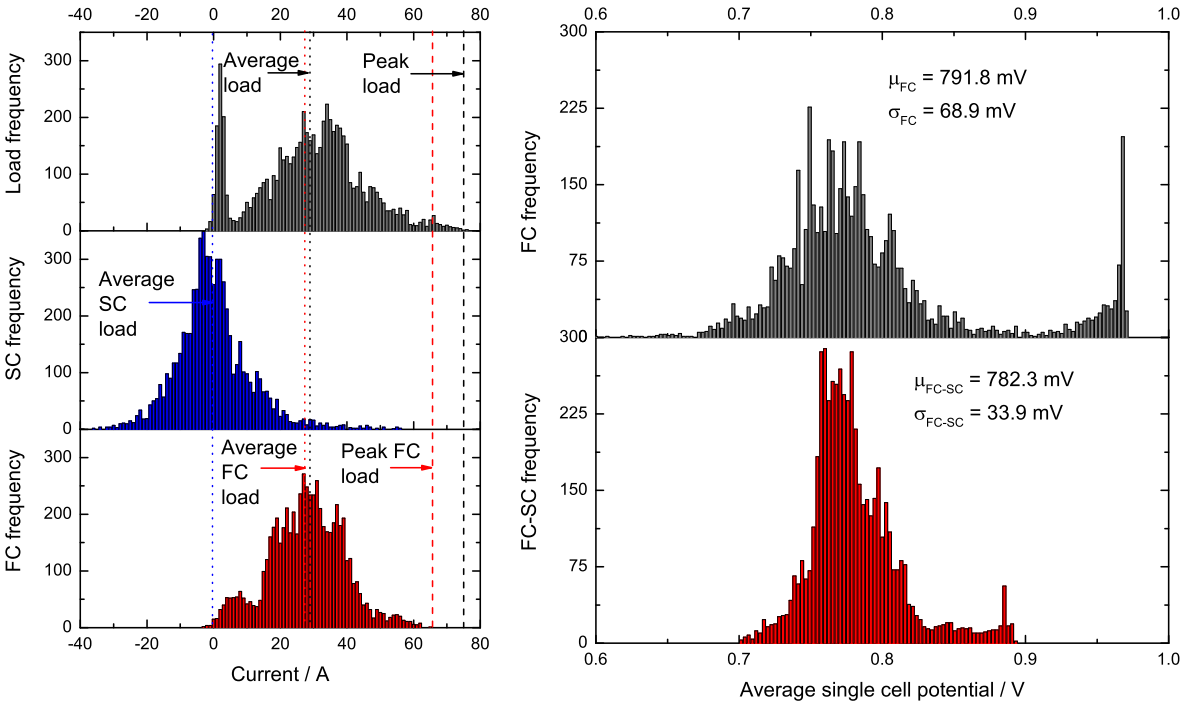
Figure 6.35: Dynamic response for the 9.5 kW FC-SC passive hybrid system under a 1/10th scale HWFET drive cycle [225]

like in the scaled down system the supercapacitors meets the high frequency transient loads, smoothing the FC load. It can be seen that the FC follows the load profile however doesn't see the majority of the higher frequency loads which are buffered out by the supercapacitors. When no load is applied to the system the FC recharges the supercapacitors due to the higher OCV. The apparent advantages therefore of this system are they this addresses two of the main automotive PEMFC degradation modes: rapid power cycling leading to catalyst dissolution and no load idling leading to accelerated rate of carbon support corrosion. From an efficiency point of view this reduces the voltage sag issue in pure FC mode experienced when large step loads are applied. This reduces the inertial losses of the blower reducing BOP losses of which the air subsystem is a substantial contributor.

The decoupling of the load cycle power to FC power becomes more apparent when considering figure 6.36a which shows a histogram of the load currents during the HWFETDS cycle. It can be seen that in the FC-supercapacitor hybrid configuration the supercapacitors peak shave the load from 76 A to 62 A for the FC resulting in an 18.4% decrease in peak load. There is also a decrease in the average load current of the FC from 28.5 A for the applied load to 27.9 A but this 2% decrease is not significant. The supercapacitors operate at an average load of 0 A but show a Gaussian distribution with standard deviation of 11.2 A.

Further to this the FC potential operating window is also changed. Figure 6.36b shows the average cell potential of the FC stack during operation in pure FC mode and FC-supercapacitor mode under the HWFETDS. Due to the hybridisation the FC can be operated away from higher potentials which will result in greater durability. The benefits of this shift in potential are known to be nonlinear as shown by Mathias *et al.* [134] who empirically showed that corrosion currents of conventional carbon supported MEA followed the empirical relationship in equation 6.22 for 100% relative humidity, where i_{CO_2} is the carbon corrosion current (A), E is the potential (V), TS is the gradient of the Tafel Slope (mV/decade), R is the universal gas constant, T is temperature (K), E_a is the activation energy (J.mol^{-1}), t is the time (s) and m is is a power law exponent.

$$i_{CO_2} \propto 10^{E/TS} \exp^{-E_a/RT} t^{-m} \tag{6.22}$$



(a) (b)

Figure 6.36: (a) Current histogram for the FC-SC passive hybrid system under a HWFETDS and (b) voltage histogram for the FC-SC passive hybrid system under a HWFETDS in pure FC mode and FC-SC mode [225]

6.7.9 Estimating buffering effect of the supercapacitors

Quantifying the buffering effect, seen by the FC, to a first order approximation can be achieved by considering the standard equation for a capacitor as shown in equation 6.23, where I_{SC}, V_{SC} and C represents the supercapacitor current, voltage and capacitance respectively.

$$I_{SC} = C\frac{dV_{SC}}{dt} \tag{6.23}$$

In a passive system, neglecting interconnection losses, the voltage of the supercapacitor pack and that of the FC stack (V_{FC}) are approximately equal ($V_{SC} = V_{FC}$). Applying Kirchoffs current law, then allows us to express the supercapacitor current in terms of the FC (I_{FC}) and load (I_{Load}) currents ($I_{SC} = I_{Load} - I_{FC}$) as shown in equation 6.24.

$$I_{Load} - I_{FC} = C\frac{dV_{FC}}{dt} \tag{6.24}$$

Assuming that the FC is operated in a region where its resistance is largely unchanged, it can be assumed that the FC voltage can be related to the FC current by its resistance ($V_{FC} = V_{OCP} - I_{FC}R_{FC} - IR_{FCCT}$). Here V_{OCP} represents FC OCP, R_{FC} represents the ohmic resistance of the FC and R_{FCCT} represents the charge transfer resistance. Assuming the OCP of the FC is time invariant and the current is sufficiently large such the charge transfer polarisation losses are sufficiently small relative to the ohmic

resistance and that ohmic resistance is time invariant results in equation 6.25.

$$I_{Load} - I_{FC} = CR_{FC}\frac{dI_{FC}}{dt} \tag{6.25}$$

When compared to experimental data this simple approximation shows good agreement as shown in figure 6.37. The first pulse and settling period exhibit the highest deviation from simulated data due to the large contribution of resistance from the polarisation resistance due to operation at low current densities.

It is therefore possible to compare the impact of the passive load filtering offered for different numbers of supercapacitors as shown in figure 6.38a. Here, the rate of change of the FC is plotted against the applied system load from no load conditions. A lower rate of change is preferable to reduce the level of dynamic loading on the FC. It can be seen that at relatively low currents, the FC-supercapacitor hybrid offers a good level of load filtering to the FC and this is independent of the number of supercapacitors. However, with increasing load it becomes apparent that having a larger pack is actually detrimental to the load filtering characteristics.

The reason for this is evident by considering equation 6.26 and 6.27. Neglecting losses, the FC voltage and supercapacitor voltage are approximately equal. The rate of change of supercapacitor voltage is therefore the same as the rate of change of the FC voltage. The resulting change in FC voltage would therefore result in a proportional change in the rate of change of FC current.

$$V_{SC} = V_{FC} \tag{6.26}$$

$$\frac{dV_{SC}}{dt} = \frac{dV_{FC}}{dt} \propto \frac{dI_{SC}}{dt} \tag{6.27}$$

By considering figure 6.38b, it can be seen that given the same current flow through the supercapacitors, increasing the number of supercapacitors in series will increase the rate of change of voltage seen by the entire pack. This translates to an increased rate

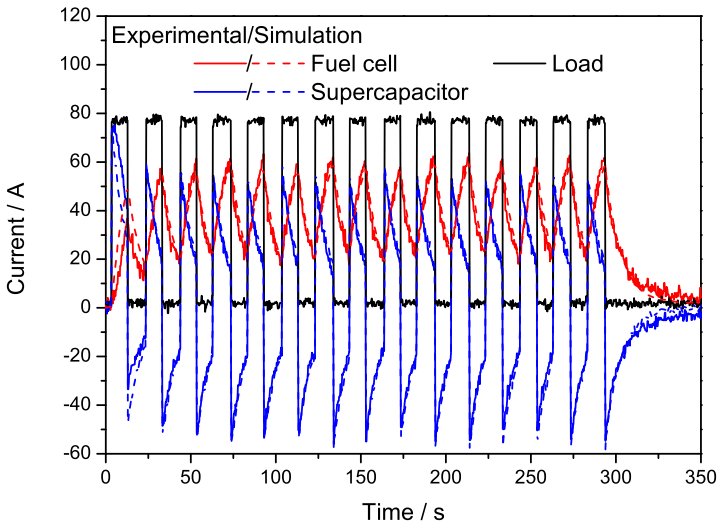
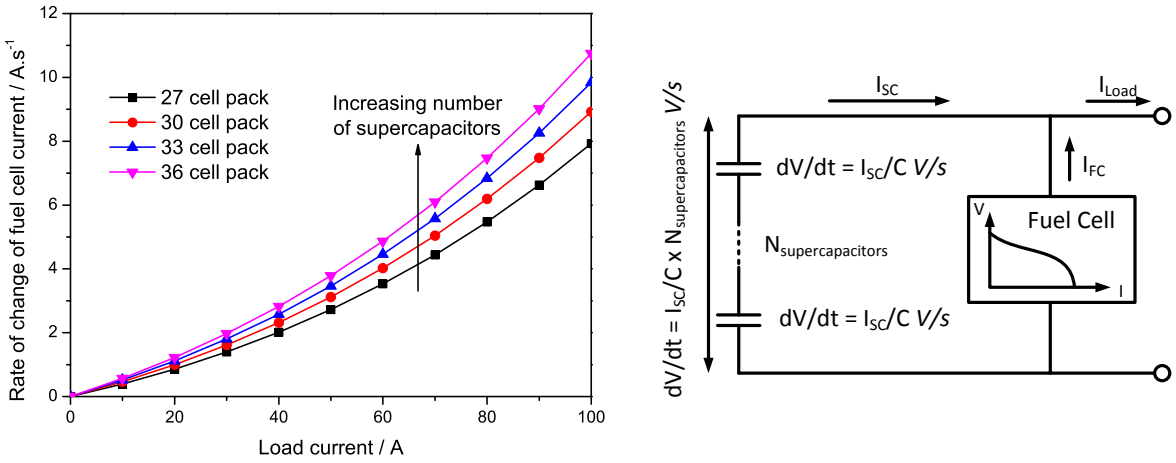


Figure 6.37: Comparison between experimental and simulated data for the FC-supercapacitor passive hybrid system under a 75A 0.2 Hz step load [225]



(a) (b)

Figure 6.38: (a) Comparison of different step loads and supercapacitor pack size with the response time of the FC current assuming the same 1500 F supercapacitors used in this study and (b) Figure showing how increasing the number of supercapacitors in series for the same capacitance increases the pack rate of change of voltage for the same current. The faster the rate of change of voltage for the supercapacitor pack results in faster rate of change of load experienced by the FC [225]

of change of FC voltage and therefore FC current. It therefore becomes apparent that the maximum benefit of the FC-supercapacitor system is achieved when the number of supercapacitors in series is sized such that it matches the maximum OCP of the FC stack to both reduce the rate of change of voltage of the supercapacitor pack for a given current and also increase the average operating voltage of a single supercapacitor, thereby increasing the working capacitance.

This analysis, however, is only applicable within certain operating conditions. It was shown previously that the capacitance of a supercapacitor is a function of the operating frequency due to the porous nature of the supercapacitors with high frequency operation resulting in a drop in capacitance beyond the knee frequency. In the FC-supercapacitor passive hybrid system therefore, the knee frequency represents the frequency limit that the load cycle should have for the FC-supercapacitor system to be useful. If a load cycle has considerable frequency components above the knee frequency then the benefit of the system is vastly reduced.

From the analysis work on passive FC-supercapacitor hybrid systems the following can be concluded:

- FC-supercapacitor passive hybrid systems allow for load smoothing of the FC during automotive load cycles due to its lower impedance
- Whilst some downsizing of the FC is possible this is highly dependent on the load cycle
- Efficiency gains from the reduced transient loads and shifting of the operational point have been shown with values of up to 5% during step loads
- FC-battery passive hybrids potentially offer further reductions in the FC dynamics but is highly sensitive to component sizing for the voltage windows
- The knee frequency also suggests that load cycles with significant frequency components above this will be be favorable for the FC-supercapacitor system

6.7.10 Direct comparison of fuel cell hybrid powertrains

The previous sections have largely looked at the performance metrics of the individual subdivisions of FCVs, FCHEVs and the BEV. This section aims to bring it all together and compare the technologies against each other. It should be explicitly mentioned at this stage that the results here are presented as a case study for demonstrating the tools and techniques developed. The high variability of many of the factors such as cost, mileage and vehicle weight will change the result on a case by base basis and thus the results presented are only applicable to the numbers used. As previously shown, the NYCC and HWFETDS cycles represent two extremes of operation for the FCV, i.e. city and highway driving. The analysis hereafter will thus focus on the performance and cost metrics of these two cycles.

Figure 6.39 shows the TCO of different simulated vehicle powertrains under the NYCC and HWFETDS load cycles. From this analysis it becomes apparent that under city load cycles the hydrogen costs result in a higher 10 year TCO than the BEV option. This is due to the highly transient nature of the load cycles. However, in the highway drive cycles, the FC based powertrains offer significant advantages over the BEV due to operation at higher efficiencies resulting in a significantly lower running cost. Highway driving favours the pure FCV the most, which has the lowest running costs. The FC-supercapacitor hybrid has slightly higher running costs due to the additional mass of the supercapacitors whilst the FC-battery hybrid has the highest running costs due to the further additional mass of the batteries which under constant high speed cruising do not add any benefit to the vehicle.

Of course TCO is not the only metric the powertrain which needs to be considered. The range, and its interplay with the TCO, is also a critical metric to consider. Figure 6.40 shows for the different powertrains explored what this relationship is. Here is can be seen that due to the relative inefficiency and higher cost of hydrogen, that if only city driving was considered then the BEV should always be the powertrain of choice due

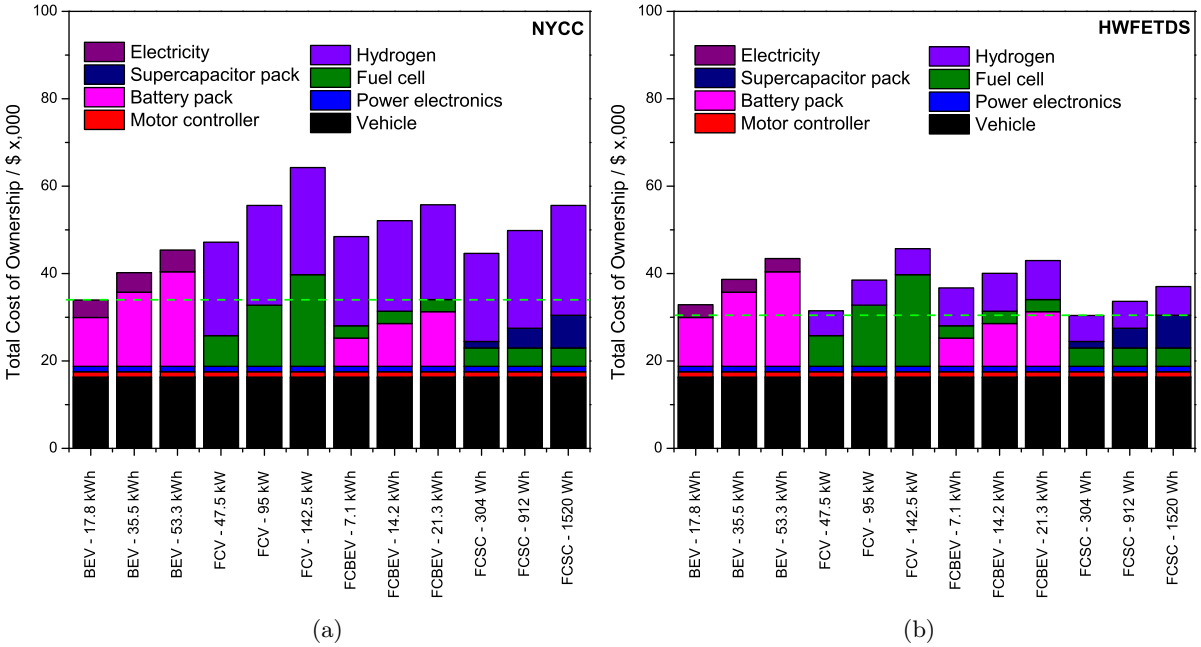


Figure 6.39: 10 year total cost of ownership for different vehicle configurations for (a) the NYCC and (b) HWFETDS cycles. FC size for the FCBEV and FCSC vehicles were 19 and 38 kW respectively for 2015 baseline values

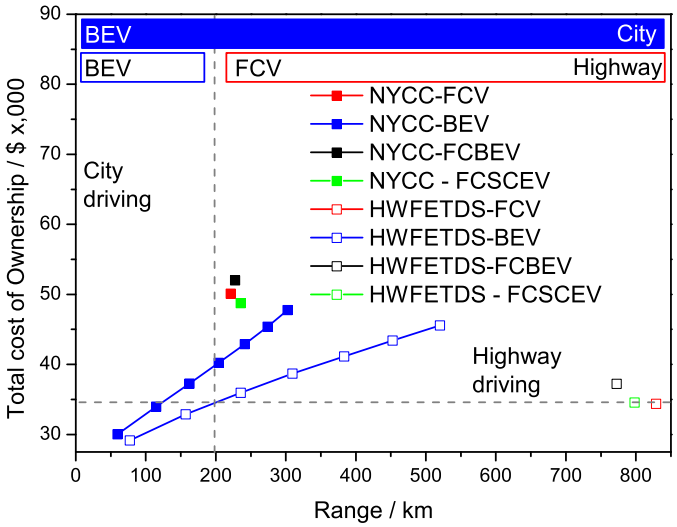


Figure 6.40: 10 year total cost of ownership of different vehicle types against range for two extreme drive cycles: city and highway

to the greater range for equivalent TCO. Of the FC powertrains the FC-supercapacitor hybrid system offers the best range/TCO for city driving. BEV is also the preferred powertrain when considering highway driving upto a range of 200 km. Beyond that there is a large transition where it becomes favourable for the FCV powertrain due to the greater gravitmetric energy density and increased efficiency.

Between the three different FC based powertrains there is little difference between the lowest cost options. Assuming that a typical vehicle should experience both types of load cycles with a range comparable to that of an ICE powered vehicle then an FC based powertrain becomes a cost effective option relative to the BEV with the FC-supercapacitor powertrain offering most benefit in city driving in terms of cost reduction.

From the analysis of all of the simulated vehicle powertrains the following can be concluded:

- For pure city driving a BEV powertrain consistently offers greater TCO and range
- For highway driving there is a transitions between BEV and a FC based powertrain being preferred with the transition ranging being approximately 200 km

6.8 Conclusion

This chapter was aimed at combining the developed models of lithium-ion batteries, supercapacitors and fuel cells in order to evaluate different EV and HEV configurations as a demonstration of the developed tools described in previous chapters. The below is therefore a summary of the key point of this chapter:

6.8.1 Drive cycle analysis

Analysis of different drive cycles that are used as standardised load cycles vary considerably and highlights the need for consideration of the load cycle when performing any analysis of a vehicle system. Simple analysis of the acceleration profiles of the cycles, which is vehicle independent shows 4 main categories of load cycle exist: highway, rural/urban, city and aggressive. Development of a novel means of categorising these load cycles in a quantitative manner based on a Reynold's decomposition style analysis was presented and showed good agreement with simulated power requirements of the load cycles.

6.8.2 Powertrain comparison

A vehicle model was developed and combined with models of the FC, battery and supercapacitor (as presented in previous chapters) in different configurations. A scaled-down powertrain simulator was also created and used to acquire experimental data. Based on this the following conclusions were made about the different vehicle configurations analysed.

- **Battery Electric Vehicles**
  - Pure BEVs exhibit a low electricity cost sensitivity to varying the battery size over the lifetime of use due to the relatively high efficiency of batteries at the scale required for pure BEVs
  - An optiminal battery size in terms of efficiency was predicted to be between 20-25 kWh
- **Fuel Cell Vehicles**
  - Pure FCVs are not ideal for city driving with many stop periods due to the relatively large idling losses and higher transient losses thus impacting efficiency and lifetime
  - Pure FCVs exhibit the best performance under highway driving
- **Fuel Cell-Battery hybrid**
  - Under a charge sustaining operation mode, an optimal battery size between 5-15 kWh was found with a 19kW FC stack for most drive cycles
  - Most benefits are gained, relative to the pure FCV, under the city drive cycles where the frequent idling losses are replaced by charging of the battery
- **Fuel Cell-Supercapacitor hybrid**
  - The FC-supercapacitor hybrid system requires a larger FC than in the FC-battery hybrid due to lower energy density
  - Most benefit in terms of range, relative to the FC-battery and FCV, are achieved under aggressive driving due to the lower impedance of the supercapacitor
- **Fuel Cell-Supercapacitor passive hybrid system**
  - A small scale FC-supercapacitor passive hybrid system was created and it was shown that passive coupling of the FC with the supercapacitor reduced FC dynamics
  - Downsizing of the FC is possible however this depends on the load cycle, with more benefits exhibited in cycles with more stop-start events
  - A 9.5 kWe-33×1500F FC-supercpacitor passive hybrid system was created in order to expand the idea further. Experimental results showed that fuel efficiency gains of approximately 5% were achieved under step loads in the passive system compared to the pure FC mode due to the reduction in transient losses
  - Maximum load buffering was found to be achieved with fewer supercapacitors and a physical limitation of the knee frequency was identified as being the limit at which the FC-supercapacitor system begins to lose most of its benefits
  - Passive coupling was also shown to reduce the residence time at elevated potentials, inferring a reduction in the carbon corrosion degradation mode

Chapter 7

Conclusions

The aim of this work was to develop the tools, methodology and techniques required to investigate the performance metrics of different FC vehicle powertrain configurations to a level that captures the relevant physical processes of interest to find the optimum configuration. In doing this several vehicle configurations have been investigated as case studies of the capabilities of the developed tools, however it should be highlighted that this is not a complete analysis due to the sheer number of different possible configurations. In order to answer this question robust models for the three main electrochemical devices of interest needed to be developed, with these being: the lithium-ion battery, PEMFC and supercapacitor. In the course of developing these models to answer the overarching research question a number of novel contributions have been made.

Within the work on lithium-ion batteries the following has been presented in this thesis:

- **Lithium-ion batteries**
  - Analysis of the existing academic literature has shown that physics based models provide the most insight into the fundamental processes occurring within a battery allowing for a deeper understanding of the rate limiting processes occurring in their application to electric vehicles. Whilst, extensive works have been published on their characterisation under well controlled lab conditions, in-situ diagnosis tools were limited to simple techniques. In addition, scale up effects from the developed single cell models to multi-cell systems suitable for electric vehicles was mostly absent. This thus provided the motivation for the presented works
  - A physics based pseudo 2D thermally coupled electrochemical model of a lithium-ion battery was created and experimentally validated using a genetic algorithm based parameterisation technique. The usefulness of this model was demonstrated through worked examples of model lead design of the battery which compared changing the internal structure of the battery to tailor the ideal power to energy density of the cell
  - Many different battery degradation mechanisms were identified as occurring in lithium-ion batteries, with these being agitated by different operating modes and conditions. It has generally been acknowledged that the formation and growth of the SEI layer is the most critical degradation mode to consider and as such an SEI based degradation model was integrated into the developed electrochemical model
  - Using the model, novel techniques around monitoring the stoichiometric drift of lithium-ion batteries were presented by simulating the SRCV. Further to this a DTV technique which monitored surface temperature and related this to the SRCV results was also presented as a novel technique of in-situ monitoring. Results suggest that over the lifetime of operation the operational potential window should be shifted based on the loss of active material to avoid damage to the electrode
  - Scale up of the single cell model to pack level modelling showed that pack architecture and the magnitude of the interconnect resistances can have a significant impact on the performance of different cells in a highly parallel pack

Within the work on PEMFCs the following has been presented in this thesis:

- **Proton Exchange Membrane Fuel Cells**
  - A literature review looking at PEMFCs for automotive applications showed that models of FCs varied considerably in the literature with many large systems works neglecting to account for effects such a water management, thermal effects and BOP power consumption. The three main modes of automotive FC degradation were identified as being start-up/shut down, no load idling and rapid power cycling. Whilst detailed models accounting for these degradation modes do not exist at the levels of computation required for system analysis their consideration was accounted for in a qualitative manner. Development of models and experimental work thus focused on the areas identified as being critical
  - A model of a PEMFC stack which considers electrochemical, thermal and membrane hydration effects has been presented. This was combined with models of the BOP components and thus represents a full system
  - A 9.5 kWe 75-cell stack with in-house developed BOP systems was developed in order to validate the developed model and showed a good level of agreement
  - Experimentally lead investigation of pin-hole formation in large PEMFC, caused by flooding, was also presented. Results showed that U-shaped stack configurations operating with low pressure cathode systems suffer from significant risk of failure. Pin-hole formation caused by the flooding lead to a cascading potential decay originating from the failed cell to neighboring cells due to the mixing of anode gases in the cathode until the stack potential is zero at no load conditions. The bipolar nature of the FC stack gave rise to performance fluctuations being observed in cells next to poor performing cells

Within the work on supercapacitors the following has been presented in this thesis:

- **Supercapacitors**
  - Review of the academic literature showed that the majority of models of supercapacitors were based on equivalent circuit models of varying degrees of fidelity. The electrochemical nature of their performance resulted in voltage and frequency dependent performance which many authors fail to capture. Relative to batteries and FCs, their temperature dependency and degradation rates are not as significant. Thus the subsequent modelling and experimental work focused on these findings
  - A transmission line based model which accounts for the charge redistribution effect which occurs in supercapacitors was presented and validated against experimental data for a 150F and 1500 F supercapacitor
  - Analysis of the limitations on performance of supercapacitors was performed with detailed analysis of the rate limiting frequency known as the knee frequency
  - A novel method of extracting the low-frequency capacitance using a Capacitance Nyquist plot was presented for the first time and results showed good agreement with capacitance measurements using different techniques

Combination of all the individual models allowed for analysis of the whole vehicle powertrain with different configurations. The following were presented in this thesis regarding powertrain comparison.

- **Powertrain comparison**
  - Review of the literature on the high level system analysis showed that the selection of a suitable load cycle needs to be considered and that much of the techno-economic work considering EVs used oversimplified models. Passive hybridisation was identified as one means of cost reduction through through the removal of a DCDC converter with FC-battery and FC-battery-supercapacitor configurations already explored. FC-supercapacitor passive hybrids were however not found in the literature. This therefore motivated the subsequent work
  - A vehicle and motor model was developed and presented that allowed for generation of power profiles for base vehicles
  - A drive cycle analysis was performed and a novel dimensionless analysis of different vehicle drive cycles was presented using a Reynold decomposition style analysis. Four main modes of driving were identified as being city, urban, highway and aggressive with city and highway representing the two extremes of operation
  - Assuming an annual mileage of 20,000 km, BEVs offer the best TCO of all electric vehicle powertrains if only considering city driving, however if considering only highway driving for vehicles with ranges over 200 km the FCV powertrain offers the lowest TCO. It is important to consider that conclusions drawn based on the cost and usage assumptions are only valid within the prescribed limits. The results may change based on the boundaries set and the case studies presented are purely as a demonstrator of the tools developed
  - FCVs exhibit a lower range when only considering city driving due to the frequent idling events leading to significant losses. Hybridisation was shown to improve this. The FC-battery hybrid was shown to allow for more aggressive downsizing of the FC relative to the FC-supercapacitor hybrid however the FC-supercapacitor hybrid exhibited a lower TCO especially under aggressive drive cycles
  - Using a developed scaled down powertrain test rig, it was shown that a FC-supercapacitor passive hybrid system could significantly reduce load dynamics seen on the FC. Downsizing of the FC is possible however highly depends on the load cycle, with most benefits being achieved in load cycles with frequent stop-start events to allow for recharging of the supercapacitors. Further experimental validation of the system was achieved with the development of a 9.5 kW-33×1500F supercapacitor passive hybrid system. Fuel efficiency gains of up to 5% were achieved under step loads and it was shown that the most significant buffering gains were achieved through a lower number of supercapacitors in series

The contents of the thesis therefore presents current state-of-the-art models relevant to system level modelling of electric vehicles which captures of the relevant physical effects occurring in these devices. The aim of this thesis was to develop the tools and techniques to explore different FC powertrain configurations. Whilst the author acknowledges the near exhaustive different number of possible configurations and control strategies, a number of different case studies were investigated as a demonstration of the tools as well as a more extensive study of FC-supercapacitor passive hybrid systems which were identified as being a gap in the literature.

7.1 Future Work

Within the time constraints of the 3 year funded PhD period, the author feels that a significant amount of progress has been made but acknowledges many areas of the modelling and experimental work could have benefited from more work given more time. The suggested future works are listed below:

- **Lithium-ion batteries**
  - Whilst the developed model does work the method of reducing residual errors could be improved upon to decrease computational time. In addition to this the model developed is done with a static spatial and temporal mesh. Many commercial CFD and FEA softwares offer dynamic time steps and spatial meshing to decrease computational time further
  - The degradation model presented based on the growth of the SEI layer on the anode has not been experimentally validated and values taken were from literature. The degradation model by all means is not complete and does not claim to be. Many other mechanisms relating to degradation of lithium-ion batteries exist which have not been captured. Thus further improvement and validation of the battery model is required
- **Proton Exchange Membrane Fuel Cells**
  - The developed stack level model, whilst suitable for this application, could be improved by discretising the lumped MEA model into a 1D model
  - Development of a degradation model for the FC
- **Supercapacitors**
  - The developed equivalent circuit model currently does not take into consideration heat generation and the impact on performance. Further improvements in the model in this respect could be made as well as the development of a physics based model
  - Integration of thermal and degradation effects
- **Powertrain comparison**
  - More accurate power profile generation through the integration of a incline profile
  - No comparison between the examined powertrains and an ICE vehicle was made due to the lack of an ICE model. A comparison between these technologies would be useful
  - Further market segmentation of drive cycles to take into account the different usage of different load cycles, i.e. different annual mileages
  - More accurate models of power electronics and motors with validation
  - Comparison of different control strategies for the various powertrain configurations

References

[1] T. Akita, A. Taniguchi, J. Maekawa, Z. Siroma, K. Tanaka, M. Kohyama, and K. Yasuda. Analytical TEM study of Pt particle deposition in the proton-exchange membrane of a membrane-electrode-assembly. *Journal of Power Sources*, 159(1):461–467, September 2006.

[2] M. A. R. S. Al-Baghdadi. Modelling of proton exchange membrane fuel cell performance based on semi-empirical equations. *Renewable Energy*, 30(10):1587–1599, August 2005.

[3] M. Al Sakka, H. Gualous, J. Van Mierlo, and H. Culcu. Thermal modeling and heat management of supercapacitor modules for vehicle applications. *Journal of Power Sources*, 194(2):581–587, December 2009.

[4] J. C. Amphlett, R. M. Baumert, R. F. Mann, B. A. Peppley, P. R. Roberge, and T. J. Harris. Performance Modeling of the Ballard Mark IV Solid Polymer Electrolyte Fuel Cell. I. Mechanistic model development. *Journal of The Electrochemical Society*, 142(1), 1995.

[5] L. Andaloro, G. Napoli, F. Sergi, G. Dispenza, and V. Antonucci. Design of a hybrid electric fuel cell power train for an urban bus. *International Journal of Hydrogen Energy*, 38(18):7725–7732, June 2013.

[6] M. André and M. Rapone. Analysis and modelling of the pollutant emissions from European cars regarding the driving characteristics and test cycles. *Atmospheric Environment*, 43(5):986–995, February 2009.

[7] M. André, R. Joumard, R. Vidon, P. Tassel, and P. Perret. Real-world European driving cycles, for measuring pollutant emissions from high- and low-powered cars. *Atmospheric Environment*, 40(31):5944–5953, October 2006.

[8] M. André. The ARTEMIS European driving cycles for measuring car pollutant emissions. *The Science of the total environment*, 334-335:73–84, December 2004.

[9] G. Appetecchi, G. Kim, M. Montanino, F. Alessandrini, and S. Passerini. Room temperature lithium polymer batteries based on ionic liquids. *Journal of Power Sources*, 196(16):6703–6709, August 2011.

[10] P. Arora, R. E. White, and M. Doyle. Capacity Fade Mechanisms and Side Reactions in Lithium-Ion Batteries. *Journal of The Electrochemical Society*, 145(10):3647, 1998.

[11] P. Arora, M. Doyle, A. S. Gozdz, R. E. White, and J. Newman. Comparison between computer simulations and experimental data for high-rate discharges of plastic lithium-ion batteries. *Journal of Power Sources*, 88(2):219–231, June 2000.

[12] D. Aurbach. Review of selected electrodesolution interactions which determine the performance of Li and Li ion batteries. *Journal of Power Sources*, 89(2):206–218, August 2000.

[13] B. Avasarala, R. Moore, and P. Haldar. Surface oxidation of carbon supports due to potential cycling under PEM fuel cell conditions. *Electrochimica Acta*, 55(16):4765–4771, June 2010.

[14] T. Banjac, F. Trenc, and T. Katrašnik. Energy conversion efficiency of hybrid electric heavy-duty vehicles operating according to diverse drive cycles. *Energy Conversion and Management*, 50(12):2865–2878, December 2009.

[15] P. Baptista, J. a. Ribau, J. a. Bravo, C. Silva, P. Adcock, and A. Kells. Fuel cell hybrid taxi life cycle analysis. *Energy Policy*, 39(9):4683–4691, September 2011.

[16] A. J. Bard and L. R. Faulkner. *Electrochemical methods - Fundamentals and applications*. 2000.

[17] E. Barsoukov and J. R. Macdonald. *Impedance Spectroscopy: Theory, Experiment, and Applications*. 2005.

[18] E. Beguin, Francois; Frackowiak. *Supercapacitors. Materials, systems and applications*. 2012.

[19] F. Belhachem, S. L. Ral, and B. Davat. A physical based model of power electric double-layer supercapacitors. *IEEE*, (Upresa 7037):3069–3076, 2000.

[20] J. Bernard, M. Hofer, U. Hannesen, A. Toth, A. Tsukada, F. N. Büchi, and P. Dietrich. Fuel cell/battery passive hybrid power source for electric powertrains. *Journal of Power Sources*, 196(14):5867–5872, July 2011.

[21] J. Black and H. A. Andreas. Effects of charge redistribution on self-discharge of electrochemical capacitors. *Electrochimica Acta*, 54(13):3568–3574, May 2009.

[22] J. Black and H. A. Andreas. Prediction of the self-discharge profile of an electrochemical capacitor electrode in the presence of both activation-controlled discharge and charge redistribution. *Journal of Power Sources*, 195(3):929–935, February 2010.

[23] O. Bohlen and J. Kowal. Ageing behaviour of electrochemical double layer capacitors. *Journal of Power Sources*, 173(1):626–632, November 2007.

[24] O. Bohlen, J. Kowal, and D. U. Sauer. Ageing behaviour of electrochemical double layer capacitors. *Journal of Power Sources*, 172(1):468–475, October 2007.

[25] C. Bonnet, S. Didierjean, N. Guillet, S. Besse, T. Colinart, and P. Carré. Design of an 80kWe PEM fuel cell system: Scale up effect investigation. *Journal of Power Sources*, 182(2):441–448, August 2008.

[26] R. L. Borup, J. R. Davey, F. H. Garzon, D. L. Wood, and M. A. Inbody. PEM fuel cell electrocatalyst durability measurements. *Journal of Power Sources*, 163(1):76–81, December 2006.

[27] G. G. Botte, V. R. Subramanian, and R. E. White. Mathematical modeling of secondary lithium batteries. *Electrochimica Acta*, 45(15-16):2595–2609, May 2000.

[28] O. Briat, J.-M. Vinassa, N. Bertrand, H. El Brouji, J.-Y. Delétage, and E. Woirgard. Contribution of calendar ageing modes in the performances degradation of supercapacitors during power cycling. *Microelectronics Reliability*, 50(9-11):1796–1803, September 2010.

[29] P. Bubna, D. Brunner, J. J. Gangloff, S. G. Advani, and A. K. Prasad. Analysis, operation and maintenance of a fuel cell/battery series-hybrid bus for urban transit applications. *Journal of Power Sources*, 195(12):3939–3949, June 2010.

[30] F. N. Büchi, A. B. Geiger, and R. P. Neto. Dependence of current distribution on water management in PEFC of technical size. *Journal of Power Sources*, 145(1):62–67, July 2005.

[31] F. N. Büchi, M. Inaba, and T. J. Schmidt. *Polymer Electrolyte Fuel Cell Durability*. Springer, 2009.

[32] K. Çaatay Bayindir, M. A. Gözüküçük, and A. Teke. A comprehensive overview of hybrid electric vehicle: Powertrain configurations, powertrain control techniques and electronic control units. *Energy Conversion and Management*, 52(2):1305–1313, February 2011.

[33] Q. Cai, D. Brett, D. Browning, and N. Brandon. A sizing-design methodology for hybrid fuel cell power systems and its application to an unmanned underwater vehicle. *Journal of Power Sources*, 195(19):6559–6569, October 2010.

[34] S. Campanari, G. Manzolini, and F. Garcia de la Iglesia. Energy analysis of electric vehicles using batteries or fuel cells through well-to-wheel driving cycle simulations. *Journal of Power Sources*, 186(2):464–477, January 2009.

[35] J.-L. Carpentier and J.-L. Dellis. Nelder and Mead algorithm in impedance spectra fitting. *Solid State Ionics*, 62:119–123, 1993.

[36] S. Caux, J. Lachaize, M. Fadel, P. Shott, and L. Nicod. Modelling and control of a Fuel Cell System and Storage Elements in transport applications. *Journal of Process Control*, 15(4):481–491, June 2005.

[37] M. Ceraolo, C. Miulli, and A. Pozio. Modelling static and dynamic behaviour of proton exchange membrane fuel cells on the basis of electro-chemical description. *Journal of Power Sources*, 113(1):131–144, January 2003.

[38] C. Chan. The state of the art of electric and hybrid vehicles. *Proceedings of the IEEE*, 90(2):247–275, 2002.

[39] Y.-J. Chang and C.-C. Wang. A generalized heat transfer correlation for louver fin geometry. *International Journal of Heat and Mass Transfer*, 40(3), 1997.

[40] N. Chaturvedi and R. Klein. Algorithms for advanced battery-management systems. *Control Systems, ...*, (June 2010):49–68, 2010.

[41] J. Chen and B. Zhou. Diagnosis of PEM fuel cell stack dynamic behaviors. *Journal of Power Sources*, 177(1):83–95, February 2008.

[42] M. Chen, S. Member, and G. A. Rinc. Accurate Electrical Battery Model Capable of Predicting Runtime and I V Performance. *IEEE Transactions on Energy Conversion*, 21(2):504–511, 2006.

[43] Y.-D. Cho, G. T.-K. Fey, and H.-M. Kao. Physical and electrochemical properties of La-doped LiFePO4/C composites as cathode materials for lithium-ion batteries. *Journal of Solid State Electrochemistry*, 12(7-8):815–823, March 2008.

[44] J. Christensen. Modeling Diffusion-Induced Stress in Li-Ion Cells with Porous Electrodes. *Journal of The Electrochemical Society*, 157(3):A366, 2010.

[45] J. Christensen. Modeling Diffusion-Induced Stress in Li-Ion Cells with Porous Electrodes. *Journal of The Electrochemical Society*, 157(3):A366, 2010.

[46] D. Chu and R. Jiang. Comparative studies of polymer electrolyte membrane fuel cell stack and single cell. *Journal of Power Sources*, 80(1-2):226–234, July 1999.

[47] A. M. Colclasure and R. J. Kee. Thermodynamically consistent modeling of elementary electrochemistry in lithium-ion batteries. *Electrochimica Acta*, 55(28):8960–8973, December 2010.

[48] P. Corbo, F. Migliardini, and O. Veneri. An experimental study of a PEM fuel cell power train for urban bus application. *Journal of Power Sources*, 181(2):363–370, July 2008.

[49] J. Crank. *The Mathematics of Diffusion*. 1956.

[50] Y. Dandeville, P. Guillemet, Y. Scudeller, O. Crosnier, L. Athouel, and T. Brousse. Measuring time-dependent heat profiles of aqueous electrochemical capacitors under cycling. *Thermochimica Acta*, 526(1-2):1–8, November 2011.

[51] S. Dargaville and T. Farrell. A comparison of mathematical models for phase-change in high-rate LiFePO4 cathodes. *Electrochimica Acta*, 111:474–490, November 2013.

[52] R. Darling and J. Newman. Modeling Side Reactions in Composite LiMn2O4 Electrodes. *Journal of The Electrochemical Society*, 145(3):990–998, 1998.

[53] R. De Levie. On porous electrodes in electrolyte solution - IV. *Electrochemica Acta*, 9(November 1963), 1964.

[54] D. W. Dees, V. S. Battaglia, and A. Bélanger. Electrochemical modeling of lithium polymer batteries. *Journal of Power Sources*, 110(2):310–320, August 2002.

[55] A. J. del Real, A. Arce, and C. Bordons. Development and experimental validation of a PEM fuel cell dynamic model. *Journal of Power Sources*, 173(1):310–324, November 2007.

[56] C. Delacourt and M. Safari. Life Simulation of a Graphite/LiFePO4 Cell under Cycling and Storage. *Journal of the Electrochemical Society*, 159(8):A1283–A1291, July 2012.

[57] A. D'Entremont and L. Pilon. First-principles thermal modeling of electric double layer capacitors under constant-current cycling. *Journal of Power Sources*, 246:887–898, January 2014.

[58] S. Dhanushkodi, M. Tam, S. Kundu, M. Fowler, and M. Pritzker. Carbon corrosion fingerprint development and de-convolution of performance loss according to degradation mechanism in PEM fuel cells. *Journal of Power Sources*, 240:114–121, October 2013.

[59] Y. Diab, P. Venet, H. Gualous, and G. Rojat. Self-Discharge Characterization and Modeling of Electrochemical Capacitor Used for Power Electronics Applications. *IEEE Transactions on Power Electronics*, 24(2):510–517, February 2009.

[60] Dow Kokam. Dow Kokam Material Safety Data Sheet. Technical report, 2009.

[61] M. Doyle and J. Newman. The use of mathematical modelling in the design of lithium/polymer battery systems. *Electrochemica Acta*, 40(13), 1995.

[62] M. Doyle and J. Newman. Comparison of Modeling Predictions with Experimental Data from Plastic Lithium Ion Cells. *Journal of The Electrochemical Society*, 143(6):1890, 1996.

[63] M. Doyle, T. F. Fuller, and J. Newman. Modeling of Galvanostatic Charge and Discharge of the Lithium / Polymer / Insertion Cell. *Journal of the Electrochemical Society*, 140(6):1526–1533, 1993.

[64] M. Doyle, J. P. Meyers, and J. Newman. Computer Simulations of the Impedance Response of Lithium Rechargeable Batteries. *Journal of The Electrochemical Society*, 147(1):99, 2000.

[65] M. Dubarry, N. Vuillaume, and B. Y. Liaw. From single cell model to battery pack simulation for Li-ion batteries. *Journal of Power Sources*, 186(2):500–507, January 2009.

[66] S. Dutta, S. Shimpalee, and J. Van Zee. Numerical prediction of mass-exchange between cathode and anode channels in a PEM fuel cell. *International Journal of Heat and Mass Transfer*, 44(11):2029–2042, June 2001.

[67] M. Ehsani, Y. Gao, and A. Emadi. *Modern electric, hybrid electric, and fuel cell vehicles: fundamentals, theory and design*. CRC Press, Boca Raton, 2010.

[68] H. El Brouji, O. Briat, J.-M. Vinassa, N. Bertrand, and E. Woirgard. Comparison between changes of ultracapacitors model parameters during calendar life and power cycling ageing tests. *Microelectronics Reliability*, 48(8-9):1473–1478, August 2008.

[69] H. El Brouji, O. Briat, J.-M. Vinassa, H. Henry, and E. Woirgard. Analysis of the dynamic behavior changes of supercapacitors during calendar life test under several voltages and temperatures conditions. *Microelectronics Reliability*, 49(9-11):1391–1397, September 2009.

[70] Electropedia. Lithium-ion battery failures, 2013.

[71] Element Energy. Cost and performance of EV batteries. Technical report, 2012.

[72] C. Erk, T. Brezesinski, H. Sommer, R. Schneider, and J. Janek. Toward silicon anodes for next-generation lithium ion batteries: a comparative performance study of various polymer binders and silicon nanopowders. *ACS applied materials & interfaces*, 5(15):7299–307, August 2013.

[73] EVO Electric. Axial Flux Electric Motor AF-240, 2013.

[74] R. Faranda. A new parameters identification procedure for simplified double layer capacitor two-branch model. *Electric Power Systems Research*, 80(4):363–371, April 2010.

[75] T. R. Ferguson and M. Z. Bazant. Nonequilibrium Thermodynamics of Porous Electrodes. *Journal of The Electrochemical Society*, pages 1–27, 2012.

[76] J. C. Forman, S. J. Moura, J. L. Stein, and H. K. Fathy. Genetic identification and fisher identifiability analysis of the DoyleFullerNewman model from experimental cycling of a LiFePO4 cell. *Journal of Power Sources*, 210:263–275, July 2012.

[77] N. Fouquet, C. Doulet, C. Nouillant, G. Dauphin-Tanguy, and B. Ould-Bouamama. Model based PEM fuel cell state-of-health monitoring via ac impedance measurements. *Journal of Power Sources*, 159(2):905–913, September 2006.

[78] M. W. Fowler, R. F. Mann, J. C. Amphlett, B. a. Peppley, and P. R. Roberge. Incorporation of voltage degradation into a generalised steady state electrochemical model for a PEM fuel cell. *Journal of Power Sources*, 106(1-2):274–283, April 2002.

[79] R. Fox, P. Pritchard, and A. McDonald. *Introduction to Fluid Mechanics*. Wiley, 2006.

[80] L. Franck-Lacaze, C. Bonnet, E. Choi, J. Moss, S. Pontvianne, H. Poirot, R. Datta, and F. Lapicque. Ageing of PEMFCs due to operation at low current density: Investigation of oxidative degradation. *International Journal of Hydrogen Energy*, 35(19):10472–10481, October 2010.

[81] T. F. Fuller and J. Newman. Water and Thermal Management in Solid-Polymer-Electrolyte Fuel Cells. *Journal of The Electrochemical Society*, pages 1218–1225, 1993.

[82] T. F. Fuller, M. Doyle, and J. Newman. Relaxation Phenomena in Lithium-Ion-Insertion Cells. *Journal of The Electrochemical Society*, 141(4):982–990, 1994.

[83] P. García, J. Torreglosa, L. Fernández, and F. Jurado. Viability study of a FC-battery-SC tramway controlled by equivalent consumption minimization strategy. *International Journal of Hydrogen Energy*, 37(11):9368–9382, June 2012.

[84] S. J. Gerssen-Gondelach and A. P. Faaij. Performance of batteries for electric vehicles on short and longer term. *Journal of Power Sources*, 212:111–129, August 2012.

[85] R. E. Gerver and J. P. Meyers. Three-Dimensional Modeling of Electrochemical Performance and Heat Generation of Lithium-Ion Batteries in Tabbed Planar Configurations. *Journal of The Electrochemical Society*, 158(7):A835, 2011.

[86] J. Gomez, R. Nelson, E. E. Kalu, M. H. Weatherspoon, and J. P. Zheng. Equivalent circuit model parameters of a high-power Li-ion battery: Thermal and state of charge effects. *Journal of Power Sources*, 196(10):4826–4831, May 2011.

[87] J. W. Graydon, M. Panjehshahi, and D. W. Kirk. Charge redistribution and ionic mobility in the micropores of supercapacitors. *Journal of Power Sources*, 245:822–829, January 2014.

[88] H. Gualous and R. Gallay. Supercapacitor Module Sizing and Heat Management under Electric, Thermal, and Aging Constraints. In *Supercapacitors*, pages 373–436. Wiley-VCH Verlag GmbH & Co. KGaA, 2013.

[89] H. Gualous, H. Louahlia-Gualous, R. Gallay, and A. Miraoui. Supercapacitor Thermal Modeling and Characterization in Transient State for Industrial Applications. *IEEE Transactions on Industry Applications*, 45(3):1035–1044, 2009.

[90] M. Guo and R. E. White. A distributed thermal model for a Li-ion electrode plate pair. *Journal of Power Sources*, 221:334–344, January 2013.

[91] M. Guo, G.-H. Kim, and R. E. White. A three-dimensional multi-physics model for a Li-ion battery. *Journal of Power Sources*, 240:80–94, October 2013.

[92] M. Hahn, O. Barbieri, F. Campana, R. Kötz, and R. Gallay. Carbon based double layer capacitors with aprotic electrolyte solutions: the possible role of intercalation/insertion processes. *Applied Physics A*, 82(4):633–638, November 2005.

[93] O. Haik, S. Ganin, G. Gershinsky, E. Zinigrad, B. Markovsky, D. Aurbach, and I. Halalay. On the Thermal Behavior of Lithium Intercalated Graphites. *Journal of The Electrochemical Society*, 158(8):A913, 2011.

[94] H. He, R. Xiong, H. Guo, and S. Li. Comparison study on the battery models used for the energy management of batteries in electric vehicles. *Energy Conversion and Management*, 64:113–121, December 2012.

[95] E. Hosseinzadeh, M. Rokni, A. Rabbani, and H. H. Mortensen. Thermal and water management of low temperature Proton Exchange Membrane Fuel Cell in fork-lift truck power system. *Applied Energy*, 104:434–444, April 2013.

[96] Y. Hou, M. Zhuang, and G. Wan. A transient semi-empirical voltage model of a fuel cell stack. *International Journal of Hydrogen Energy*, 32(7):857–862, May 2007.

[97] D. Howey, R. North, and R. Martinez-botas. Road transport technology and climate change mitigation. *Grantham Institute for Climate Change - Briefing paper*, (2), 2010.

[98] J. J. Hwang and W. R. Chang. Characteristic study on fuel cell/battery hybrid power system on a light electric vehicle. *Journal of Power Sources*, 207:111–119, June 2012.

[99] J. J. Hwang. Transient power characteristic measurement of a proton exchange membrane fuel cell generator. *International Journal of Hydrogen Energy*, 38(9):3727–3740, March 2013.

[100] Ioxus. Ultracapacitor sizing and packaging for cost effictive micro-hybrids. Technical report, 2013.

[101] K. Jiao, I. E. Alaefour, G. Karimi, and X. Li. Cold start characteristics of proton exchange membrane fuel cells. *International Journal of Hydrogen Energy*, 36(18):11832–11845, September 2011.

[102] M. Kaus, J. Kowal, and D. U. Sauer. Modelling the effects of charge redistribution during self-discharge of supercapacitors. *Electrochimica Acta*, 55(25):7516–7523, October 2010.

[103] T. Keränen, H. Karimäki, J. Viitakangas, J. Vallet, J. Ihonen, P. Hyötylä, H. Uusalo, and T. Tingelöf. Development of integrated fuel cell hybrid power source for electric forklift. *Journal of Power Sources*, 196(21):9058–9068, November 2011.

[104] B. Key, R. Bhattacharyya, M. Morcrette, V. Seznéc, J.-M. Tarascon, and C. P. Grey. Real-time NMR investigations of structural changes in silicon electrodes for lithium-ion batteries. *Journal of the American Chemical Society*, 131(26):9239–49, July 2009.

[105] M. Kilic, M. Bazant, and A. Ajdari. Steric effects in the dynamics of electrolytes at large applied voltages. II. Modified Poisson-Nernst-Planck equations. *Physical Review E*, 75(2):021503, February 2007.

[106] M.-J. Kim and H. Peng. Power management and design optimization of fuel cell/battery hybrid vehicles. *Journal of Power Sources*, 165(2):819–832, March 2007.

[107] G.-H. Kim, A. Pesaran, and R. Spotnitz. A three-dimensional thermal abuse model for lithium-ion cells. *Journal of Power Sources*, 170(2):476–489, July 2007.

[108] J. King. The King Review of low-carbon cars. Part I: The potential for CO2 reduction. Technical report. Technical report, 2007.

[109] J. Kowal, E. Avaroglu, F. Chamekh, A. Šenfelds, T. Thien, D. Wijaya, and D. U. Sauer. Detailed analysis of the self-discharge of supercapacitors. *Journal of Power Sources*, 196(1):573–579, January 2011.

[110] S. Kreitmeier, M. Michiardi, A. Wokaun, and F. N. Büchi. Factors determining the gas crossover through pinholes in polymer electrolyte fuel cell membranes. *Electrochimica Acta*, 80:240–247, October 2012.

[111] E. Kristina, G. Torbjörn, and T. Josh. *Lithium-Ion Batteries: Solid-Electrolyte Interphase. The cathode-electrolyte interface in a Li-ion battery.* 2004.

[112] A. Kucernak. Fuel Cells and Renewable Energy Systems. Technical report, Imperial College London, 2010.

[113] A. Kuperman, I. Aharon, A. Kara, and S. Malki. A frequency domain approach to analyzing passive batteryultracapacitor hybrids supplying periodic pulsed current loads. *Energy Conversion and Management*, 52(12):3433–3438, November 2011.

[114] W. Lajnef, J.-M. Vinassa, O. Briat, S. Azzopardi, and E. Woirgard. Characterization methods and modelling of ultracapacitors for use as peak power sources. *Journal of Power Sources*, 168(2):553–560, June 2007.

[115] J. Larminie and A. Dicks. *Fuel Cell Systems Explained*. Wiley, 2nd edition, 2009.

[116] A. Lasia. *Electrochemical Impedance Spectroscopy and its Applications*. Kluwer Academic/Plenum Publishers, New York, 1999.

[117] N. Legrand, B. Knosp, P. Desprez, F. Lapicque, and S. Raël. Physical characterization of the charging process of a Li-ion battery and prediction of Li plating by electrochemical modelling. *Journal of Power Sources*, 245:208–216, January 2014.

[118] R. D. Levie. On porous electrodes in electrolyte solutions. 1: Capacitance effects. *Electrocehmica Acta*, 8, 1963.

[119] J. Li and M. S. Mazzola. Accurate battery pack modeling for automotive applications. *Journal of Power Sources*, 237:215–228, September 2013.

[120] H. Li, Y. Tang, Z. Wang, Z. Shi, S. Wu, D. Song, J. Zhang, K. Fatih, J. Zhang, H. Wang, Z. Liu, R. Abouatallah, and A. Mazza. A review of water flooding issues in the proton exchange membrane fuel cell. *Journal of Power Sources*, 178(1):103–117, March 2008.

[121] X.-G. Li, L.-L. Cao, Z.-X. Liu, and C. Wang. Development of a fast empirical design model for PEM stacks. *International Journal of Hydrogen Energy*, 35(7):2698–2702, April 2010.

[122] D. Li, T. Zhang, X. Liu, P. He, R. Peng, M. Wang, M. Han, and H. Zhou. A hybrid phase-transition model of olivine LiFePO4 for the charge and discharge processes. *Journal of Power Sources*, 233:299–303, July 2013.

[123] D. Liang, Q. Shen, M. Hou, Z. Shao, and B. Yi. Study of the cell reversal process of large area proton exchange membrane fuel cells under fuel starvation. *Journal of Power Sources*, 194(2):847–853, December 2009.

[124] B. Y. Liaw and M. Dubarry. From driving cycle analysis to understanding battery performance in real-life electric hybrid vehicle operation. *Journal of Power Sources*, 174(1):76–88, November 2007.

[125] R. Lin, E. Gulzow, M. Schulze, and K. a. Friedrich. Investigation of Membrane Pinhole Effects in Polymer Electrolyte Fuel Cells by Locally Resolved Current Density. *Journal of The Electrochemical Society*, 158(1):B11, 2011.

[126] R. Lin, C. Cao, J. Ma, E. Gülzow, and K. Andreas Friedrich. Optimizing the relative humidity to improve the stability of a proton exchange membrane by segmented fuel cell technology. *International Journal of Hydrogen Energy*, 37(4):3373–3381, February 2012.

[127] X. Lin, J. Park, L. Liu, Y. Lee, a. M. Sastry, and W. Lu. A Comprehensive Capacity Fade Model and Analysis for Li-Ion Batteries. *Journal of the Electrochemical Society*, 160(10):A1701–A1710, August 2013.

[128] H. Liu and P. Li. Maintaining equal operating conditions for all cells in a fuel cell stack using an external flow distributor. *International Journal of Hydrogen Energy*, 38(9):3757–3766, March 2013.

[129] D. D. Macdonald. Reflections on the history of electrochemical impedance spectroscopy. *Electrochimica Acta*, 51(8-9):1376–1388, January 2006.

[130] T. Mahlia, S. Tohno, and T. Tezuka. A review on fuel economy test procedure for automobiles: Implementation possibilities in Malaysia and lessons for other countries. *Renewable and Sustainable Energy Reviews*, 16(6):4029–4046, August 2012.

[131] G. Maranzana, C. Moyne, J. Dillet, S. Didierjean, and O. Lottin. About internal currents during start-up in proton exchange membrane fuel cell. *Journal of Power Sources*, 195(18):5990–5995, September 2010.

[132] J. Marcinkoski, B. D. James, J. a. Kalinoski, W. Podolski, T. Benjamin, and J. Kopasz. Manufacturing process assumptions used in fuel cell system cost analyses. *Journal of Power Sources*, 196(12):5282–5292, June 2011.

[133] E. Martínez-Rosas, R. Vasquez-Medrano, and A. Flores-Tlacuahuac. Modeling and simulation of lithium-ion batteries. *Computers & Chemical Engineering*, 35(9):1937–1948, September 2011.

[134] M. F. Mathias, R. Makharia, H. A. Gasteiger, J. J. Conley, T. J. Fuller, C. J. Gittleman, S. S. Kocha, D. P. Miller, C. K. Mittelsteadt, T. Xie, S. G. Yan, P. T. Yu, U. S, and H. Hoover. Two Fuel Cell Cars In Every Garage. *The Electrochemical Society Interface*, 14(3):24–35, 2005.

[135] McKinsey & Company. A portfolio of power-trains for Europe: a fact-based analsis. Technical report, 2010.

[136] S. Mekhilef, R. Saidur, and A. Safari. Comparative study of different fuel cell technologies. *Renewable and Sustainable Energy Reviews*, 16(1):981–989, January 2012.

[137] M. Miansari, K. Sedighi, M. Amidpour, E. Alizadeh, and M. Miansari. Experimental and thermodynamic approach on proton exchange membrane fuel cell performance. *Journal of Power Sources*, 190(2):356–361, May 2009.

[138] M. Miller and A. Bazylak. A review of polymer electrolyte membrane fuel cell stack testing. *Journal of Power Sources*, 196(2):601–613, January 2011.

[139] J. R. Miller. Electrochemical capacitor thermal management issues at high-rate cycling. *Electrochimica Acta*, 52(4):1703–1708, December 2006.

[140] S. Miyatake, Y. Susuki, T. Hikihara, S. Itoh, and K. Tanaka. Discharge characteristics of multicell lithium-ion battery with nonuniform cells. *Journal of Power Sources*, 241:736–743, November 2013.

[141] P. Moraal and I. Kolmanovsky. Turbocharger modeling for automotive control applications. *SAE papers*, 01(0908), 1999.

[142] M. V. Moreira and G. E. da Silva. A practical model for evaluating the performance of proton exchange membrane fuel cells. *Renewable Energy*, 34(7):1734–1741, July 2009.

[143] F. Musio, F. Tacchi, L. Omati, P. Gallo Stampino, G. Dotelli, S. Limonta, D. Brivio, and P. Grassini. PEMFC system simulation in MATLAB-Simulink environment. *International Journal of Hydrogen Energy*, 36(13):8045–8052, July 2011.

[144] A. Nishizawa, J. Kallo, O. Garrot, and J. Weiss-Ungethüm. Fuel cell and Li-ion battery direct hybridization system for aircraft applications. *Journal of Power Sources*, 222:294–300, January 2013.

[145] J. Nolan and J. Kolodziej. Modeling of an automotive fuel cell thermal system. *Journal of Power Sources*, 195(15):4743–4752, August 2010.

[146] R. J. North, R. B. Noland, W. Y. Ochieng, and J. W. Polak. Modelling of particulate matter mass emissions from a light-duty diesel vehicle. *Transport Research: Part D*, 11:344–357, 2006.

[147] P. Novak, J. Panitz, F. Joho, M. Lanz, R. Imhof, and M. Coluccia. Advanced in situ methods for the characterization of practical electrodes in lithium-ion batteries. *Journal of Power Sources*, pages 52–58, 2000.

[148] G. Offer, D. Howey, M. Contestabile, R. Clague, and N. Brandon. Comparative analysis of battery electric, hydrogen fuel cell and hybrid vehicles in a future sustainable road transport system. *Energy Policy*, 38(1):24–29, January 2010.

[149] G. Offer, M. Contestabile, D. Howey, R. Clague, and N. Brandon. Techno-economic and behavioural analysis of battery electric, hydrogen fuel cell and hybrid vehicles in a future sustainable road transport system in the UK. *Energy Policy*, 39(4):1939–1950, April 2011.

[150] G. J. Offer, V. Yufit, D. A. Howey, B. Wu, and N. P. Brandon. Module design and fault diagnosis in electric vehicle batteries. *Journal of Power Sources*, 206:383–392, May 2012.

[151] I. J. Ong and J. Newman. Double-Layer Capacitance in a Dual Lithium Ion Insertion Cell. 146(12):4360–4365, 1999.

[152] M. Outeiro, R. Chibante, A. Carvalho, and A. de Almeida. A parameter optimized model of a Proton Exchange Membrane fuel cell including temperature effects. *Journal of Power Sources*, 185(2):952–960, December 2008.

[153] M. Özbek, S. Wang, M. Marx, and D. Söffker. Modeling and control of a PEM fuel cell system: A practical study based on experimental defined component behavior. *Journal of Process Control*, 23(3):282–293, March 2013.

[154] V. Paladini, T. Donateo, A. de Risi, and D. Laforgia. Super-capacitors fuel-cell hybrid electric vehicle optimization and control strategy development. *Energy Conversion and Management*, 48(11):3001–3008, November 2007.

[155] C. Panos, K. Kouramas, M. Georgiadis, and E. Pistikopoulos. Modelling and explicit model predictive control for PEM fuel cell systems. *Chemical Engineering Science*, 67(1):15–25, January 2012.

[156] P. Pathapati, X. Xue, and J. Tang. A new dynamic model for predicting transient phenomena in a PEM fuel cell system. *Renewable Energy*, 30(1):1–22, January 2005.

[157] E. Peled, D. Golodnitsky, and G. Ardel. Advanced Model for Solid Electrolyte Interphase Electrodes in Liquid and Polymer Electrolytes. 144(8):208–210, 1997.

[158] E. Peled. The Electrochemical Behavior of Alkali and Alkaline Earth Metals in Nonaqueous Battery Systems– The Solid Electrolyte Interphase Model. *Journal of the Electrochemical Society*, (1):2047–2051, 1979.

[159] W. Pell and B. Conway. Voltammetry at a de Levie brush electrode as a model for electrochemical supercapacitor behaviour. *Journal of Electroanalytical Chemistry*, 500(1-2):121–133, March 2001.

[160] M. B. Pinson and M. Z. Bazant. Theory of SEI Formation in Rechargeable Batteries: Capacity Fade, Accelerated Aging and Lifetime Prediction. *Journal of the Electrochemical Society*, 160(2):A243–A250, December 2012.

[161] B. G. Pollet, I. Staffell, and J. L. Shang. Current status of hybrid, battery and fuel cell electric vehicles: From electrochemistry to market prospects. *Electrochimica Acta*, 84:235–249, April 2012.

[162] R. Ponnappan and T. Ravigururajan. Contact thermal resistance of Li-ion cell electrode stack. *Journal of Power Sources*, 129(1):7–13, April 2004.

[163] J. T. Pukrushpan, A. G. Stefanopoulou, and H. Peng. *Control of Fuel Cell Power Systems: Principles, modeling, analysis and feedback analysis*. Springer, 2004.

[164] F. Rafik, H. Gualous, R. Gallay, A. Crausaz, and A. Berthon. Frequency, thermal and voltage supercapacitor characterization and modeling. *Journal of Power Sources*, 165(2):928–934, March 2007.

[165] P. Ramadass, B. Haran, P. M. Gomadam, R. White, and B. N. Popov. Development of First Principles Capacity Fade Model for Li-Ion Cells. *Journal of The Electrochemical Society*, 151(2):A196, 2004.

[166] P. Ramadass, B. Haran, P. M. Gomadam, R. White, and B. N. Popov. Development of First Principles Capacity Fade Model for Li-Ion Cells. *Journal of The Electrochemical Society*, 151(2):A196, 2004.

[167] A. Randall, R. D. Perkins, X. Zhang, and G. L. Plett. Controls oriented reduced order modeling of solid-electrolyte interphase layer growth. *Journal of Power Sources*, 209:282–288, July 2012.

[168] T. B. Reddy. *Linden's Handbook of Batteries*. 2010.

[169] C. a. Reiser, L. Bregoli, T. W. Patterson, J. S. Yi, J. D. Yang, M. L. Perry, and T. D. Jarvi. A Reverse-Current Decay Mechanism for Fuel Cells. *Electrochemical and Solid-State Letters*, 8(6):A273, 2005.

[170] S. Renganathan and R. E. White. Semianalytical method of solution for solid phase diffusion in lithium ion battery electrodes: Variable diffusion coefficient. *Journal of Power Sources*, 196(1):442–448, January 2011.

[171] Y. Reynier, R. Yazami, and B. Fultz. The entropy and enthalpy of lithium intercalation into graphite. *Journal of Power Sources*, 119-121:850–855, June 2003.

[172] P. Rodatz, F. Büchi, C. Onder, and L. Guzzella. Operational aspects of a large PEFC stack under practical conditions. *Journal of Power Sources*, 128(2):208–217, April 2004.

[173] P. Rodatz, G. Paganelli, A. Sciarretta, and L. Guzzella. Optimal power management of an experimental fuel cell/supercapacitor-powered hybrid vehicle. *Control Engineering Practice*, 13(1):41–53, January 2005.

[174] E. Roth, D. Doughty, and D. Pile. Effects of separator breakdown on abuse response of 18650 Li-ion cells. *Journal of Power Sources*, 174(2):579–583, December 2007.

[175] M. Safari and C. Delacourt. Aging of a Commercial Graphite/LiFePO4 Cell. *Journal of The Electrochemical Society*, 158(10):A1123, 2011.

[176] G. Salitra, A. Soffer, L. Eliad, Y. Cohen, and D. Aurbach. Carbon Electrodes for Double-Layer Capacitors I. Relations Between Ion and Pore Dimensions. *Journal of The Electrochemical Society*, 147(7):2486, 2000.

[177] D. G. Sanchez, A. Ortiz, and K. a. Friedrich. Oscillation of PEFC under Low Cathode Humidification: Effect of Gravitation and Bipolar Plate Design. *Journal of the Electrochemical Society*, 160(6):F636–F644, April 2013.

[178] S. Santhanagopalan and R. E. White. Online estimation of the state of charge of a lithium ion cell. *Journal of Power Sources*, 161(2):1346–1355, October 2006.

[179] M. Santis, S. A. Freunberger, M. Papra, A. Wokaun, and F. N. Büchi. Experimental investigation of coupling phenomena in polymer electrolyte fuel cell stacks. *Journal of Power Sources*, 161(2):1076–1083, October 2006.

[180] M. Saxe, A. Folkesson, and P. Alvfors. Energy system analysis of the fuel cell buses operated in the project: Clean Urban Transport for Europe. *Energy*, 33(5):689–711, May 2008.

[181] Ultracapacitors - www.ultracapacitors.org/img2/ultracapacitor-image.jpg.

[182] J. Schiffer, D. Linzen, and D. U. Sauer. Heat generation in double layer capacitors. *Journal of Power Sources*, 160(1):765–772, September 2006.

[183] W. Schmittinger and A. Vahidi. A review of the main parameters influencing long-term performance and durability of PEM fuel cells. *Journal of Power Sources*, 180(1):1–14, May 2008.

[184] B. Scrosati and J. Garche. Lithium batteries: Status, prospects and future. *Journal of Power Sources*, 195(9):2419–2430, May 2010.

[185] Y. Shao, J. Wang, R. Kou, M. Engelhard, J. Liu, Y. Wang, and Y. Lin. The corrosion of PEM fuel cell catalyst supports and its implications for developing durable catalysts. *Electrochimica Acta*, 54(11):3109–3114, April 2009.

[186] Y. Shao-Horn, P. Ferreira, G. J. lo O, D. Morgan, H. A. Gasteiger, and R. Makharia. Coarsening of Pt Nanoparticles in Proton Exchange Membrane Fuel Cells upon Potential Cycling. *ECS Transactions*, 1(8):185–195, 2006.

[187] R. Shimoi, T. Aoyama, and A. Iiyama. Development of fuel cell stack durability based on actual vehicle test data: current status and future work. *SAE International Journal ...*, 4970, 2009.

[188] A. Shukla. *Parametric modelling and simulation of hybrid electric vehicle*. PhD thesis, 2009.

[189] K. Smith and C.-Y. Wang. Power and thermal characterization of a lithium-ion battery pack for hybrid-electric vehicles. *Journal of Power Sources*, 160(1):662–673, September 2006.

[190] K. Smith and C.-Y. Wang. Solid-state diffusion limitations on pulse operation of a lithium ion cell for hybrid electric vehicles. *Journal of Power Sources*, 161(1):628–639, October 2006.

[191] K. Smith, C. Rahn, and C. Wang. Control oriented 1D electrochemical model of lithium ion battery. *Energy Conversion and Management*, 48(9):2565–2578, September 2007.

[192] H.-K. Song, H.-Y. Hwang, K.-H. Lee, and L. H. Dao. The effect of pore size distribution on the frequency dispersion of porous electrodes. *Electrochimica Acta*, 45(14):2241–2257, March 2000.

[193] R. Spotnitz and J. Franklin. Abuse behavior of high-power , lithium-ion cells. *Journal of Power Sources*, 113:81–100, 2003.

[194] T. E. Springer, T. A. Zawodzinski, and S. Gottesfeld. Polymer Electrolyte Fuel Cell Model. *Journal of The Electrochemical Society*, 138(8):2334–2342, 1993.

[195] P.-L. Taberna and P. Simon. Electrochemical Techniques. In *Supercapacitors*, pages 111–130. Wiley-VCH Verlag GmbH & Co. KGaA, 2013.

[196] W. Tang, Y. Zhu, Y. Hou, L. Liu, Y. Wu, K. P. Loh, H. Zhang, and K. Zhu. Aqueous rechargeable lithium batteries as an energy storage system of superfast charging. *Energy & Environmental Science*, 6(7):2093, 2013.

[197] A. Taniguchi, T. Akita, K. Yasuda, and Y. Miyazaki. Analysis of electrocatalyst degradation in PEMFC caused by cell reversal during fuel starvation. *Journal of Power Sources*, 130(1-2):42–49, May 2004.

[198] C. Thomas. Fuel cell and battery electric vehicles compared. *International Journal of Hydrogen Energy*, 34(15):6005–6020, August 2009.

[199] P. Thounthong, S. Raël, and B. Davat. Control strategy of fuel cell/supercapacitors hybrid power sources for electric vehicle. *Journal of Power Sources*, 158(1):806–814, July 2006.

[200] P. Thounthong, S. Raël, and B. Davat. Energy management of fuel cell/battery/supercapacitor hybrid power source for vehicle applications. *Journal of Power Sources*, 193(1):376–385, August 2009.

[201] U. Troltzsch, O. Kanoun, and H. Trankler. Characterizing aging effects of lithium ion batteries by impedance spectroscopy. *Electrochimica Acta*, 51(8-9):1664–1672, January 2006.

[202] Y. Troxler, B. Wu, M. Marinescu, V. Yufit, Y. Patel, A. J. Marquis, N. P. Brandon, and G. J. Offer. The effect of thermal gradients on the performance of lithium-ion batteries. *Journal of Power Sources*, pages 1–8, June 2013.

[203] O. van Vliet, A. S. Brouwer, T. Kuramochi, M. van den Broek, and A. Faaij. Energy use, cost and CO2 emissions of electric cars. *Journal of Power Sources*, 196(4):2298–2310, February 2011.

[204] M. W. Verbrugge and P. Liu. Microstructural Analysis and Mathematical Modeling of Electric Double-Layer Supercapacitors. *Journal of The Electrochemical Society*, 152(5):D79, 2005.

[205] P. Verma, P. Maire, and P. Novák. A review of the features and analyses of the solid electrolyte interphase in Li-ion batteries. *Electrochimica Acta*, 55(22):6332–6341, 2010.

[206] J. Vetter, P. Novák, M. Wagner, C. Veit, K.-C. Möller, J. Besenhard, M. Winter, M. Wohlfahrt-Mehrens, C. Vogler, and A. Hammouche. Ageing mechanisms in lithium-ion batteries. *Journal of Power Sources*, 147(1-2):269–281, September 2005.

[207] J. Vetter, P. Novák, M. Wagner, C. Veit, K.-C. Möller, J. Besenhard, M. Winter, M. Wohlfahrt-Mehrens, C. Vogler, and A. Hammouche. Ageing mechanisms in lithium-ion batteries. *Journal of Power Sources*, 147(1-2):269–281, September 2005.

[208] C. A. Vincent and B. Scrosati. *Modern Batteries 2nd edition*. 2003.

[209] H. Wang and L. Pilon. Intrinsic limitations of impedance measurements in determining electric double layer capacitances. *Electrochimica Acta*, 63:55–63, February 2012.

[210] H. Wang and L. Pilon. Mesoscale modeling of electric double layer capacitors with three-dimensional ordered structures. *Journal of Power Sources*, 221:252–260, January 2013.

[211] C. Wang and V. Srinivasan. Computational battery dynamics (CBD)electrochemical/thermal coupled modeling and multi-scale modeling. *Journal of Power Sources*, 110(2):364–376, August 2002.

[212] Y. Wang and C.-Y. Wang. Ultra large-scale simulation of polymer electrolyte fuel cells. *Journal of Power Sources*, 153(1):130–135, January 2006.

[213] Y. Wang, S. Basu, and C.-Y. Wang. Modeling two-phase flow in PEM fuel cell channels. *Journal of Power Sources*, 179(2):603–617, May 2008.

[214] Y. Wang, K. S. Chen, J. Mishler, S. C. Cho, and X. C. Adroher. A review of polymer electrolyte membrane fuel cells: Technology, applications, and needs on fundamental research. *Applied Energy*, 88(4):981–1007, April 2011.

[215] Y. Wang, J. Yi, and Y. Xia. Recent Progress in Aqueous Lithium-Ion Batteries. *Advanced Energy Materials*, 2(7):830–840, July 2012.

[216] M. Watanabe. Activity and Stability of Ordered and Disordered Co-Pt Alloys for Phosphoric Acid Fuel Cells. *Journal of The Electrochemical Society*, 141(10):2659, October 1994.

[217] A. Z. Weber and J. Newman. Effects of Microporous Layers in Polymer Electrolyte Fuel Cells. *Journal of The Electrochemical Society*, 152(4):A677, 2005.

[218] J. Wilson, D. Schwartz, and S. Adler. Nonlinear electrochemical impedance spectroscopy for solid oxide fuel cell cathode materials. *Electrochimica Acta*, 51(8-9):1389–1402, January 2006.

[219] P. Wingelaar, J. Duarte, and M. Hendrix. PEM fuel cell model representing steady-state, small-signal and large-signal characteristics. *Journal of Power Sources*, 171(2):754–762, September 2007.

[220] J. Wishart, Z. Dong, and M. Secanell. Optimization of a PEM fuel cell system based on empirical data and a generalized electrochemical semi-empirical model. *Journal of Power Sources*, 161(2):1041–1055, October 2006.

[221] J. Wu, X. Z. Yuan, J. J. Martin, H. Wang, J. Zhang, J. Shen, S. Wu, and W. Merida. A review of PEM fuel cell durability: Degradation mechanisms and mitigation strategies. *Journal of Power Sources*, 184(1):104–119, September 2008.

[222] B. Wu, M. Matian, and G. J. Offer. Hydrogen PEMFC system for automotive applications. *International Journal of Low-Carbon Technologies*, 7(1):28–37, January 2012.

[223] C. Wu, Y. Hung, and C. Hong. On-line supercapacitor dynamic models for energy conversion and management. *Energy Conversion and Management*, 53(1):337–345, January 2012.

[224] B. Wu, V. Yufit, M. Marinescu, G. J. Offer, R. F. Martinez-Botas, and N. P. Brandon. Coupled thermal-electrochemical modelling of uneven heat generation in lithium-ion battery packs. *Journal of Power Sources*, 243:544–554, June 2013.

[225] B. Wu, G. Offer, R. Martinez-Botas, and N. Brandon. Investigation of optimal fuel cell, battery and capacitor powertrain set-up for automotive applications. Technical report, 2014.

[226] H. Yang and Y. Zhang. Self-discharge analysis and characterization of supercapacitors for environmentally powered wireless sensor network applications. *Journal of Power Sources*, 196(20):8866–8873, October 2011.

[227] M. Yaniv and A. Soffer. The Transient Behavior of an Ideally Polarized Porous Carbon Electrode at Constant Charging Current. *Journal of The Electrochemical Society*, 123:506–511, 1972.

[228] Y. Ye, Y. Shi, and A. a.O. Tay. Electro-thermal cycle life model for lithium iron phosphate battery. *Journal of Power Sources*, 217:509–518, November 2012.

[229] Y. Ye, Y. Shi, N. Cai, J. Lee, and X. He. Electro-thermal modeling and experimental validation for lithium ion battery. *Journal of Power Sources*, 199:227–238, February 2012.

[230] X. Yu, B. Zhou, and A. Sobiesiak. Water and thermal management for Ballard PEM fuel cell stack. *Journal of Power Sources*, 147(1-2):184–195, September 2005.

[231] V. Yufit and N. Brandon. Development and application of an actively controlled hybrid proton exchange membrane fuel cellLithium-ion battery laboratory test-bed based on off-the-shelf components. *Journal of Power Sources*, 196(2):801–807, January 2011.

[232] V. Yufit, P. Shearing, R. Hamilton, P. Lee, M. Wu, and N. Brandon. Investigation of lithium-ion polymer battery cell failure using X-ray computed tomography. *Electrochemistry Communications*, 13(6):608–610, June 2011.

[233] Y. Zhai, H. Zhang, D. Xing, and Z.-G. Shao. The stability of Pt/C catalyst in H3PO4/PBI PEMFC during high temperature life test. *Journal of Power Sources*, 164(1):126–133, January 2007.

[234] Q. Zhang and R. E. White. Calendar life study of Li-ion pouch cells. *Journal of Power Sources*, 179(2):785–792, May 2008.

[235] Y. Zhang and H. Yang. Modeling and characterization of supercapacitors for wireless sensor network applications. *Journal of Power Sources*, 196(8):4128–4135, April 2011.

[236] Q. Zhang, Q. Guo, and R. E. White. Semi-empirical modeling of charge and discharge profiles for a LiCoO2 electrode. *Journal of Power Sources*, 165(1):427–435, February 2007.

[237] S. Zhang, X.-Z. Yuan, J. N. C. Hin, H. Wang, K. A. Friedrich, and M. Schulze. A review of platinum-based catalyst layer degradation in proton exchange membrane fuel cells. *Journal of Power Sources*, 194(2):588–600, December 2009.

[238] G. Zhang. Simulating the Electrical Double Layer Capacitance. In *COMSOL Conference Boston*, 2010.

[239] Y. Zheng, X. Han, L. Lu, J. Li, and M. Ouyang. Lithium ion battery pack power fade fault identification based on Shannon entropy in electric vehicles. *Journal of Power Sources*, 223:136–146, February 2013.

[240] M. Zhu, C. Weber, Y. Yang, M. Konuma, U. Starke, K. Kern, and A. Bittner. Chemical and electrochemical ageing of carbon materials used in supercapacitor electrodes. *Carbon*, 46(14):1829–1840, November 2008.

[241] C. Ziogou, S. Voutetakis, S. Papadopoulou, and M. C. Georgiadis. Modeling, simulation and experimental validation of a PEM fuel cell system. *Computers & Chemical Engineering*, 35(9):1886–1900, September 2011.

[242] Y. Zong, B. Zhou, and A. Sobiesiak. Water and thermal management in a single PEM fuel cell with non-uniform stack temperature. *Journal of Power Sources*, 161(1):143–159, October 2006.